SAPIENZA
UNIVERSITÀ DI ROMA

Numerical modeling of subduction zones and implications for mantle convection

Dottorato di Ricerca in Scienze della Terra – XXXI ciclo
Settore Scientifico Disciplinare GEO/03

Candidata
Eleonora Ficini

Coordinatore	Tutor	Co-tutor
Prof. Giovanni B. Andreozzi	Prof. Carlo Doglioni	Dott. Marco Cuffaro

2019

Nothing in life is to be feared,
it is only to be understood.
Now is the time to understand more,
so that we may fear less.
Marie Curie

One, remember to look up at the stars
and not down at your feet.
Two, never give up work.
Work gives you meaning and purpose
and life is empty without it.
Three, if you are lucky enough to find love,
remember it is there and don't throw it away.
Stephen Hawking

Contents

RIASSUNTO

Le interazioni tra la tettonica delle placche e la convezione del mantello sono continuamente oggetto di investigazione nel campo della geodinamica e tettonica delle placche. Questa tesi di dottorato contribuisce ad ampliare le conoscenze su queste interazioni, integrando la modellazione numerica effettuata in differenti geometrie con dati geofisici e cinematici. Questi dati suggeriscono un forte carattere asimmetrico della tettonica delle placche, sia lungo i margini convergenti che estensionali. Un moto globale verso "ovest" della litosfera potrebbe esserne il principale responsabile, causando interazioni asimmetriche tra la litosfera ed il mantello sottostante. A partire da modelli numerici in geometria piana, è stata simulata l'interazione tra una placca oceanica in subduzione e un flusso orizzontale del mantello. I risultati hanno mostrato come la dinamica di subduzione sia fortemente influenzata da questo flusso orizzontale, riproducendo alcune delle principali caratteristiche di subduzioni attuali, come ad esempio la pendenza dello slab, lo stato di stress della placca a tetto ed il movimento della cerniera della subduzione. La litosfera che rientra nel mantello attraverso la subduzione è uno degli aspetti principali quando si analizzano le interazioni tra la tettonica delle placche ed i movimenti del mantello ed è strettamente legato al tipo di movimento della cerniera dello slab in subduzione. In un sistema di riferimento in cui la placca a tetto è fissa, una cerniera che si muove verso di essa contribuisce a diminuire il tasso di subduzione e viceversa. È stata effettuata quindi una analisi cinematica globale, calcolando i tassi di subduzione ed il volume di litosfera attualmente in subduzione per ogni subduzione. I risultati hanno mostrato tassi di subduzione e volumi di litosfera subdotti maggiori in corrispondenza della maggior parte delle subduzioni con polarità geografica dello slab verso "ovest" rispetto alle subduzioni con polarità opposta. Il tasso di subduzione è un parametro-chiave per la caratterizzazione della dinamica delle subduzioni poiché racchiude la velocità di convergenza della placca in subduzione ed il comportamento della cerniera. Perciò i modelli numerici sono stati migliorati per includere questa velocità come condizione al contorno, usando i tassi di subduzione ottenuti tramite l'analisi cinematica. L'asimmetria delle subduzioni è stata riprodotta dai modelli numerici, supportando l'analisi cinematica. Per verificare infine la dinamica di subduzione in geometria sferica, il moto delle placche è stato simulato in sistemi di riferimento assoluti e relativi: 1) hotspot profondi, 2) hotspot superficiali, 3) placca a tetto fissa. I risultati forniscono materiale di riferimento per futuri lavori di ricerca.

ABSTRACT

Relationships between plate tectonics and mantle convection are under relentless investigation in the field of geodynamics and plate tectonics. This dissertation contributes to the understanding of this interplay, integrating numerical models in different geometries with both geophysical and kinematic data. These data would suggest an asymmetric character of plate tectonics, along both extensional and convergent margins. A global "westward" displacement of the lithosphere with respect to the underlying mantle could be responsible for that, causing asymmetries in lithosphere-mantle interactions. Starting from numerical models in a rectangular box, interactions between subducting oceanic plates and a horizontal mantle flow have been simulated. Results showed that subduction dynamics is strongly affected by the horizontal flow, reproducing some of the main features of present-day subduction zones such as slab dip, state of stress within the upper plate and motion of the subduction hinge. Lithosphere re-entering into the mantle through subduction is one of the main aspects when analyzing the interplay between mantle motion and plate tectonics and it is highly affected by the displacement of the subduction hinge. In the fixed upper plate framework, the hinge moving towards the upper plate contributes to decrease the subduction rate and vice-versa. Thus, a worldwide kinematic analysis was performed, eventually calculating the subduction rate and volumes of subducted lithosphere for each subduction zone. Results showed both faster subduction rates and higher volumes of subducted lithosphere along most of the "westward"-directed subduction zones with respect to the opposite ones. The subduction rate could be considered as a key-parameter for subduction zones dynamics, enclosing both the plate convergence velocity and the motion of the subduction hinge. Therefore, the numerical simulations have been improved to include this velocity as boundary condition, using subduction rate estimations obtained from the kinematic analysis. The numerical models reproduced subduction zones asymmetries, supporting the kinematic analysis. Finally plate reconstructions have been computed to verify subduction dynamics in a spherical domain using both mantle- and relative-reference frameworks, e.g., 1) deep hotspots; 2) shallow hotspots; 3) upper plate fixed. Results provide reference material for future research works.

PREFACE

This thesis explores the range of interactions between plate tectonics processes (particularly subduction and its features), the "westward" rotation of the lithosphere and mantle convection. Thus, the main aim of this dissertation is the development of 2d (in plane and spherical geometry) and 3d (in spherical geometry) numerical models which simulate subduction zones dynamics and their relations with mantle circulation. This dissertation is organized in four chapters and two appendices in which frameworks, methods, results and their implications are shown step by step. Chapter 1 is a brief introduction on the Earth's interior, plate tectonics and kinematics. In Chapter 2 are described numerical models that test the asymmetric interaction between a horizontal mantle flow and subduction zones, in a fixed upper plate reference frame. This asymmetric behaviour was then tested without the imposition of the horizontal mantle flow in Chapter 3. Here, in a fixed upper plate reference frame, a kinematic analysis of the subduction hinge motion and of volumes of lithosphere currently subducting worldwide was made to this scope. Chapter 4 represents a numerical analysis that aimed to investigate subduction dynamics in absolute reference frames (considering both deep and shallow hotspots source). Using the ASPECT code for mantle convection allowed to communicate with its broad and active community. During the tests, I identified a bug which have been then fixed by the ASPECT's developers. Finally, Appendix A and Appendix B show further results of Chapter 2 and Chapter 4, respectively.

Some of these chapters were used to produce related papers, for instance, Chapter 2 (Ficini et al., 2017) and Chapter 3 (Ficini et al., submitted). The external reviews of these works were extremely useful to improve the validity of the results. In Ficini et al. (2017) I elaborated the modeling strategy, performed and analyzed the numerical experiments, discussed the results, commented and contributed to write the paper. In Ficini et al. (submitted) I elaborated the modeling strategy and designed the model setup, performed the kinematic analysis and numerical experiments, discussed the results, contributed to write and commented on the paper.

Chapter 1

Introduction

Before going into details with subduction zones and mantle convection dynamics it is useful to provide the reader with background informations about the Earth's interior and plate tectonics, in order to make the reading of the next chapters as smooth as possible.

1.1 Interior of the Earth

Although the Earth's interior is one of the most explored topic in geosciences and geodynamics, there still are several outstanding issues and questions with no univocal answers.

The interior of the Earth could be partitioned in layers on a compositional basis or on its mechanical behaviour (i.e., rheology). Following the conventional compositional criterion, three layers can be identified: the crust, the mantle and the core (Figure 1.1). This assumes a chemical stratification bound to density of minerals for which lighter elements (e.g., Si, Al, Mg) rise toward the surface whereas heavier ones (e.g., Fe, Ni) sink at depth. We can also identify a useful rheological (i.e., based on its mechanical behaviour) layering of the Earth's interior (Figure 1.1). With this criterion, we can detect the lithosphere, the asthenosphere, the mesosphere, the outer and the inner core.

The crust is the outermost and thinnest (0-10 to 20-50 km) layer and can be either oceanic and continental. Its average density is within the range of 2600-2800 kg/m^3, reaching thicknesses up to ~70 km below high mountain ranges (e.g., the Himalayas or the Andes). The oceanic crust is younger (0-180 Myr; Artemieva, 2011) with respect to the continental one (up to ~4 Gyr; Artemieva, 2011) pointing to its higher mobility. Mohorovičić discontinuity (at ~30 km depth, on average) splits the crust and the mantle below. Here an abrupt increase of the seismic velocities occurs (e.g., P-waves velocity varies from ~6.50–7.00 to ~8.00 km/s, whereas S-waves goes from ~3.90 to ~4.50 km/s), due to the higher rigidity of the rocks of the mantle below the crust.

The mantle is mainly peridotitic and can be divided in an upper (between ~30 km and ~670 km) and a lower (between ~670 km and ~2891 km) part, with some important discontinuities in it, as for example the 410 km discontinuity. This discontinuity marks the olivine-spinel phase change with an increase in the seismic velocities, i.e., P-waves from ~8.90 to ~9.13 km/s and S-waves from ~4.76 to ~4.93 km/s. At 670 km, the boundary between the upper and lower mantle is emphasized by a rise in

the seismic velocities, i.e., P-waves from ~10.26 to ~10.75 km/s and S-waves from ~5.57 to ~5.94 km/s, due to the phase change from spinel to perovskite and magnesiowüstite, higher in density and viscosity. At the base of the mantle (i.e., ~2891 km depth) the Gutenberg discontinuity marks the boundary between the mantle and the core. At this depth, the pressure is of ~140 GPa.

The Earth's core is made of Fe and Ni alloys and is twice as dense as the mantle (10000-13000 kg/m^3). It spans from ~2891 km depth to the center of the Earth, having a radius of ~3500 km.

The lithosphere has variable thicknesses depending on the geological setting, i.e., thinner the oceanic (~20-100 km) and thicker (~50-250 km) the continental one, but on average could be considered as 100 km thick. It is the combination between the crust plus the lithospheric mantle (LID). This is the shallower part of the mantle above the 1300°C isotherm that can be, thus, considered as the bottom of the lithosphere. At this depth P- and S-waves velocities are ~8.07 and ~4.46 km/s.

The asthenosphere goes from ~100 km to ~410 km. At its top (~100-200 km), right under the lithosphere (Doglioni et al., 2011; Gutenberg, 1959; Lambert & Wyllie, 1970; Thybo, 2006;), a layer can be detected in which a small amount, i.e., probably the 0.2-2% (Chantel et al., 2016; Doglioni et al., 2005; Green & Falloon, 1998; Green & Liebermann, 1976), of melt allows a drop in seismic velocities, that reach ~7.98 and ~4.41 km/s for P- and S-waves, respectively. For this reason, this layer is called Low Velocity Zone (LVZ) but it could be known also as Low Velocity Layer or asthenospheric mantle and it can reach the lowest viscosity values (~10^{15}-10^{19} Pa s; Asimow & Langmuir, 2003; Chantel et al., 2016; Grove et al., 2006; Hu et al., 2016; Jin et al., 1994; Karato et al., 2008; Korenaga & Karato, 2008; Pollitz et al., 1998) among the Earth's layers depending on its water content. It is one of the most important layer for the Earth's dynamic since it allows the relative movements between the lithosphere and the mantle below. At ~410 km depth an increase in seismic velocities can be observed. They go from ~8.90 to ~9.13 km/s for P-waves and from ~4.76 to ~4.93 km/s for S-waves: this is commonly addressed to the exothermic transition of olivine to its denser spinel-like phase.

The mesosphere is the last layer belonging to the upper mantle. It extends from ~410 km to the 670 km depth discontinuity. The bottom of the mesosphere is considered as the maximum depth at which subduction zones earthquakes occur. However, the 670 km discontinuity depth could be variable, e.g., Izu Bonin subduction zone at which the bottom of the mesosphere seems to reach ~690 km depth (Obayashi et al., 2017; Porrit & Yoshioka, 2016). At this depth P-waves velocity increases from ~10.26 to ~10.99 km/s, whereas S-waves go from ~5.57 to ~5.94 km/s.

Below the mesosphere, the lower mantle extends down to a depth of ~2891 km, where the core-mantle boundary (CMB) is located.

The core could be divided in an outer (liquid) and an inner (solid) part. In its outer part, the S-waves

disappear together with an abrupt drop of the P-waves velocity (that decrease to 8.06 km/s) and the temperature should be in the range of 4000-5000°C. The Lehmann discontinuity, at about 5100 km depth, marks the boundary between the outer and the inner core. Here the mantle physical state changes from liquid to solid and the pressure is ~330 GPa for a temperature that spans in the range of 5000-6500°C. The inner core has a radius of 1221 km and its solid state can be detected thanks to an abrupt increase of the seismic P-waves and S-waves velocity, that go from ~10.35 to ~11.02 km/s and from 0 to 3.50 km/s, respectively. This solid inner part of the core is thought to exist since 1.5 Gyr and it is currently expanding because of the outer core secular cooling from the bottom. Moreover, the inner core has P-waves higher in velocity in a N-S direction, aligned to the Earth's rotation axis (Godwin et al., 2018 and references therein). The inner core appears to rotate eastward ~3° yr^{-1} faster with respect to the mantle and with the anisotropy axis tilted by ~10° with respect to the Earth's rotation axis (Su et al., 1996). The inner core anisotropy is due to the alignment and orientation of the Fe crystals along the Earth's rotation axis suggesting a rotational control on it.

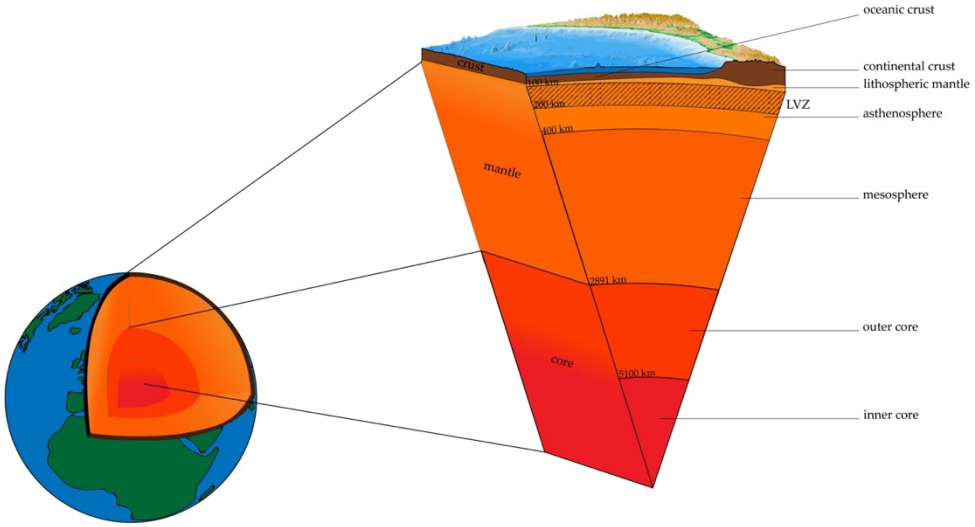

Figure 1.1 – The interior of the Earth. Cartoon sketch (not in scale) of the Earth's interior that sums up both compositional and mechanical partitions.

One of the most important work of the last 40 years is the Dziewonski and Anderson's (1981) PREM (Preliminary Reference Earth Model), a one-dimensional model of the Earth's interior (Figure 1.2) that still represents the reference model for several Earth's parameters with depth (i.e., density, seismic waves velocities, etc.) and from which seismic velocities in this Chapter 1 have been taken.

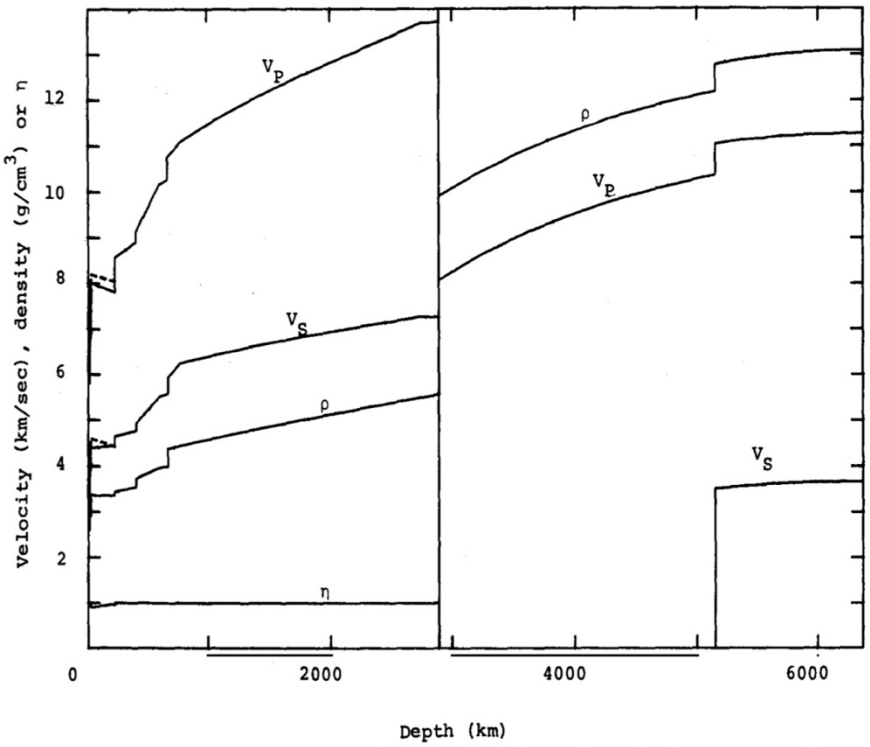

Figure 1.2 – The PREM model. Dashed lines are the horizontal components of velocity. η is a non-dimensional parameter, ρ is the density, V_P is the P-waves velocity and V_S is the S-waves velocity. Where η is 1 the model is isotropic (from Dziewonski and Andersons, 1981).

1.2 Basic concepts of plate tectonics

Plate tectonics has certainly been the main revolutionary theory for Earth sciences since it was first set out, in the first decades of the 1900s, and validated, in the late 1950s-early 1960s. It concerns and explains the evolution of the Earth's outer shell, i.e., the lithosphere, which is broken in plates that are in relative motion with respect to the mantle and with respect to each other. The foundation of the more recent theories about plate tectonics has been laid by Alfred Wegener, with his "continental drift" concept. His conclusions were presented for the first time to the German Geological Society in Frankfurt, on the 6th of January 1912, and published in 1915 with the paper "The origin of continents and oceans" (Wegener, 1915; 1924). Behind Wegener's theory there was a superocean, that he called Panthalassa (from the ancient Greek *pan*, all, and *thàlassa*, sea), which surrounded a supercontinent named Pangaea (from the ancient Greek *pan*, all, and *gaia*, Earth), which broke up in several portions each referred to as "continent" (Figure 1.3). Wegener intuition was confirmed through the observation of African and South American plate margins: in fact, if connected, these boundaries fit almost perfectly. Furthermore, analysis on their rocks and fossils were found to be in strong agreement.

Despite evidence in its support, the continental drift theory was not accepted for many years, in fact, its complete acceptance occurred around 1967. During these years, geophysicists Morgan, McKenzie and Parker set out revised versions of plate tectonics theory, integrating John Tuzo Wilson discoveries about hotspots (Wilson, 1963) and transform faults (Wilson, 1965). His findings, plus Vine and Matthews (1963) paleomagnetic studies, contributed to the universal acceptance of Hess's (1962) model on seafloor spreading.

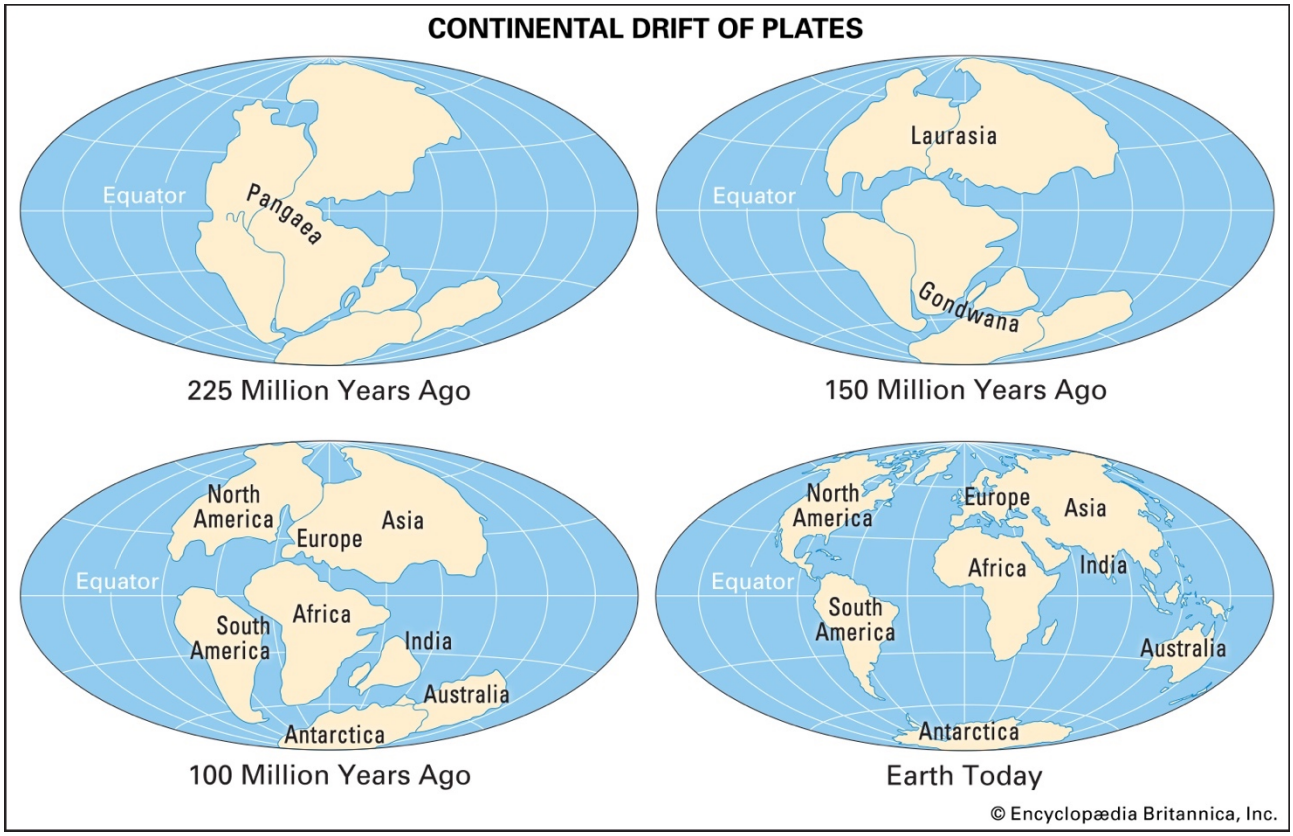

Figure 1.3 – Continental drift of plates. Evolution of the location of Earth's continents at various times between 225 Myr and Present time (by courtesy of Encyclopaedia Britannica, Inc., copyright 2017; used with permission).

There are eight major plates, such as Pacific (PA), North America (NA), Eurasia (EU), Africa (AF), Antarctica (AN), Australia (AU), India (IN), South America (SA), as well as some minor plates, i.e., Nazca, Philippines Sea, Caribbean, Cocos, Scotia, Juan de Fuca etc., and a constantly evolving number of microplates, i.e., Kermadec, Tonga, Okinawa, Aegean Sea, Banda Sea etc. (Figure 1.4). Most of the geological features, such as earthquakes, orogens and oceanic trenches formation, active volcanoes and mid-ocean ridges occur along plate boundaries. Movements of plate relative to each other can be of three types, leading to three different plate margins (Figure 1.4): i) convergent margins (destructive), at which plates move towards each other with one plate eventually subducting below the other; ii) divergent margins (constructive), at which plates move apart from each other, eventually

leading to seafloor spreading (ridge axis); iii) transform margins (conservative), at which plates slide with respect to each other. Although plates are made by both oceanic and continental material, usually only the oceanic part of any plate is continuously recycled, as it is subducted at ocean trenches and accreted at ocean ridges.

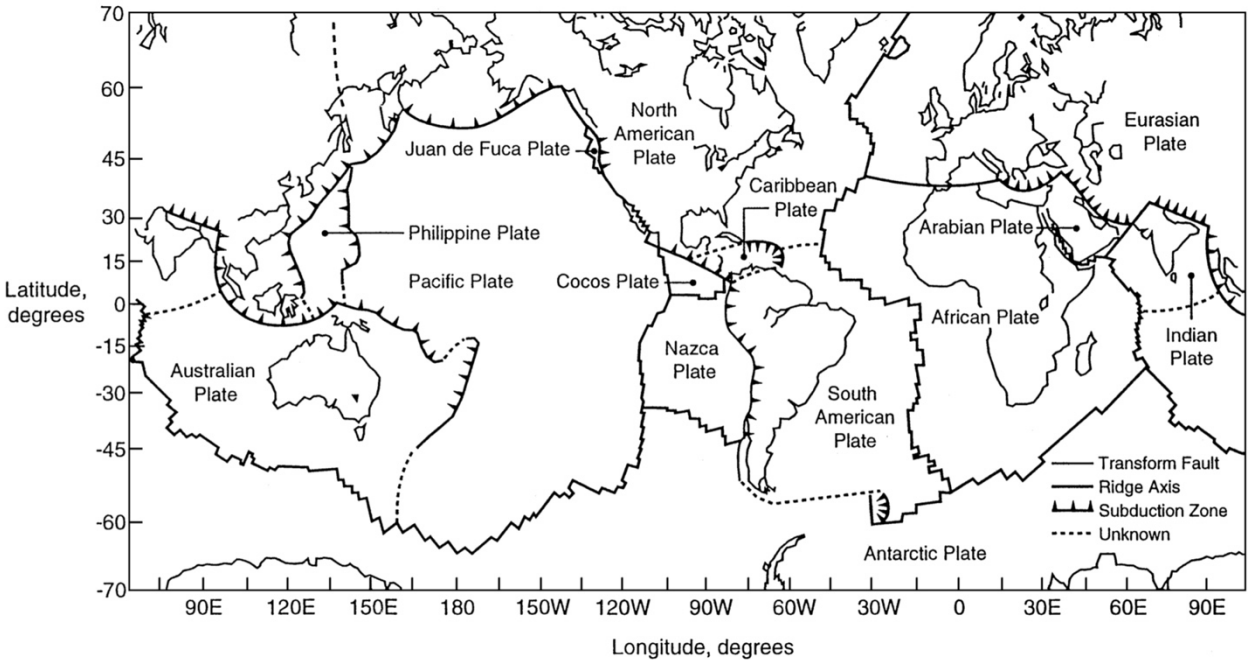

Figure 1.4 - Distribution of the major and minor plates. The ocean ridge axis (divergent plate margins), subduction zones (convergent plate margins) and transform faults that make up the plate boundaries are shown (from Turcotte and Schubert, 1982).

1.2.1 Plate kinematics

The décollement plane is the most important element for plate tectonics as we know it. It is the rheologically weak sub-lithospheric layer which allows the relative motion between the lithosphere and the mantle below. For the Earth, this layer corresponds to the LVZ, at the top of the asthenosphere (Figure 1.1). Plates movements are in the order of a few tens of millimeters per year and observable plate velocities are related to lateral heterogeneities in viscosity within the LVZ, leading to different decoupling extent. Connecting vectors of extensional and compressional stresses within lithospheric plates it can be seen a main direction in their motion, in an absolute reference frame (Figure 1.5). This preferential flow of plates is faster along the tectonic equator (Figure 1.5) and has a mainly E-W direction, being ondulated in a NE-SW direction between western Pacific Ocean and eastern Africa. It seems to persist at least over the last 100 Myr (Doglioni & Panza, 2015).

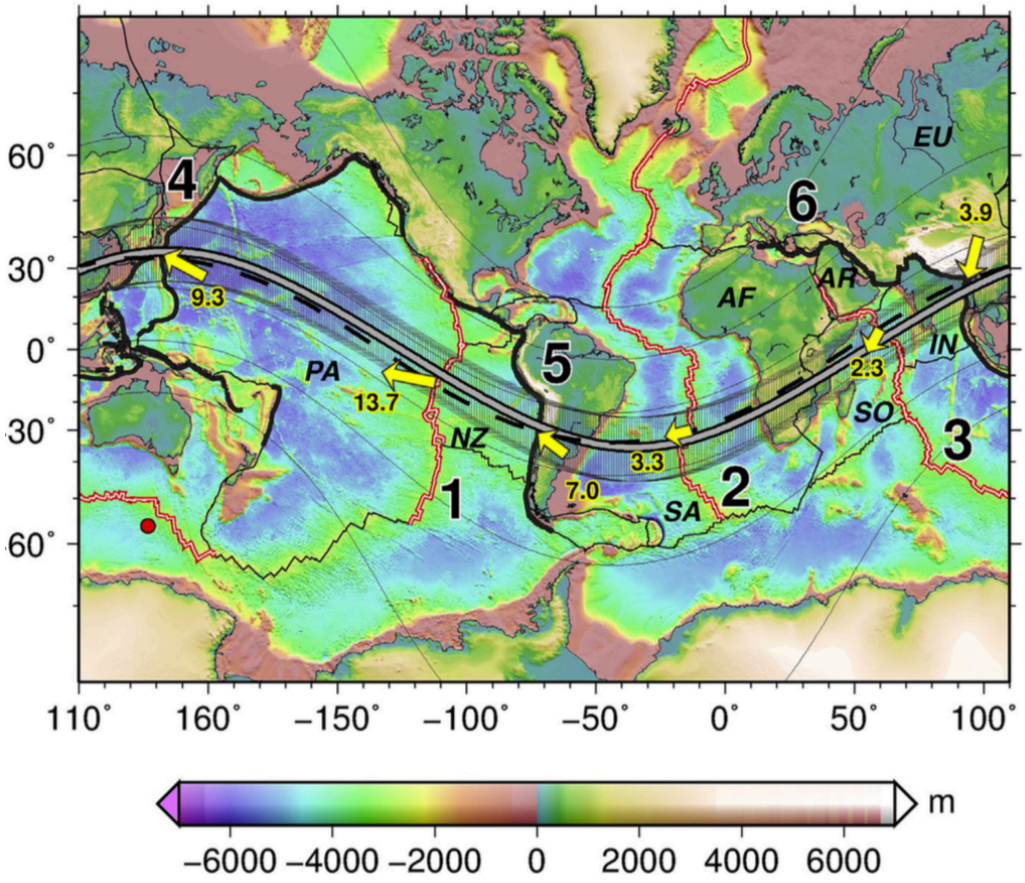

Figure 1.5 - Present-day plate motions. Different shapes of the tectonic equator, starting from the Pacific motion direction and linking all the other relative motions in a global circuit using first order tectonic features such as the East Pacific Rise (1), the Atlantic rift (2), the Red Sea, the Indian Ocean rift (3) for the rift zones, and the west Pacific subduction (4), the Andean subduction (5), and the Zagros-Himalayas subduction (6) for convergent margins. The grey curve is the tectonic equator provided by Crespi et al. (2007), with latitude error band containing the net-rotation equator for shallow hotspot reference frame (dashed black curve) with a pole located at −56.4 °N 136.7 °E (red circle). Yellow arrows are the relative plate velocities along the tectonic equator with units of cm/yr from DeMets et al. (2010). Every deviation of velocity direction with respect to the main azimuth of tectonic equator can be attributed to oblique components of relative plate motions, generating transtension and transpression at rift and subduction zones respectively. Thin lines are the small circles of the Euler pole. PA-Pacific, NZ - Nazca, SA - South America, AF - Africa, SO - Somalia, AR - Arabia, IN - India, EU - Eurasia.

From Figure 1.5 a global "westward" drift of plates would be supported, although they move with different velocities with respect to each other (Figure 1.6). This geodynamic model of plates motion can suggest constraints for a global model of mantle circulation (Doglioni & Anderson, 2015; Doglioni & Panza, 2015): at a global scale the mantle would be flowing "eastward" relative to the lithosphere, generating a first order flow. Subductions and rift zones provide then a second order turbulence disturbing the main "eastward" relative mantle flow (Doglioni et al., 2015). In fact, there are subduction zones and orogens that do not follow the "westward" lithospheric flow, e.g., the Pyrenees, resulting from these second order subrotations of plates (Cuffaro et al., 2008). Mantle anisotropies provide evidence for the existence of this mantle flow, e.g., below the Nazca plate (Russo & Silver, 1994), below the Tyrrhenian backarc basin (Margheriti et al., 1996), below north-western America (Silver & Holt, 2002) and below southern Pacific ridges (Wolfe & Solomon, 1998). Kennedy et al. (2002) demonstrated how some mantle xenoliths recorded evidence for a shear stress

within the lithosphere-asthenosphere interface. These informations would support the existence of an upper mantle flow and a décollement layer at the bottom of the lithosphere (Russo & Silver, 1996; Doglioni et al., 1999; Bokelmann & Silver, 2000).

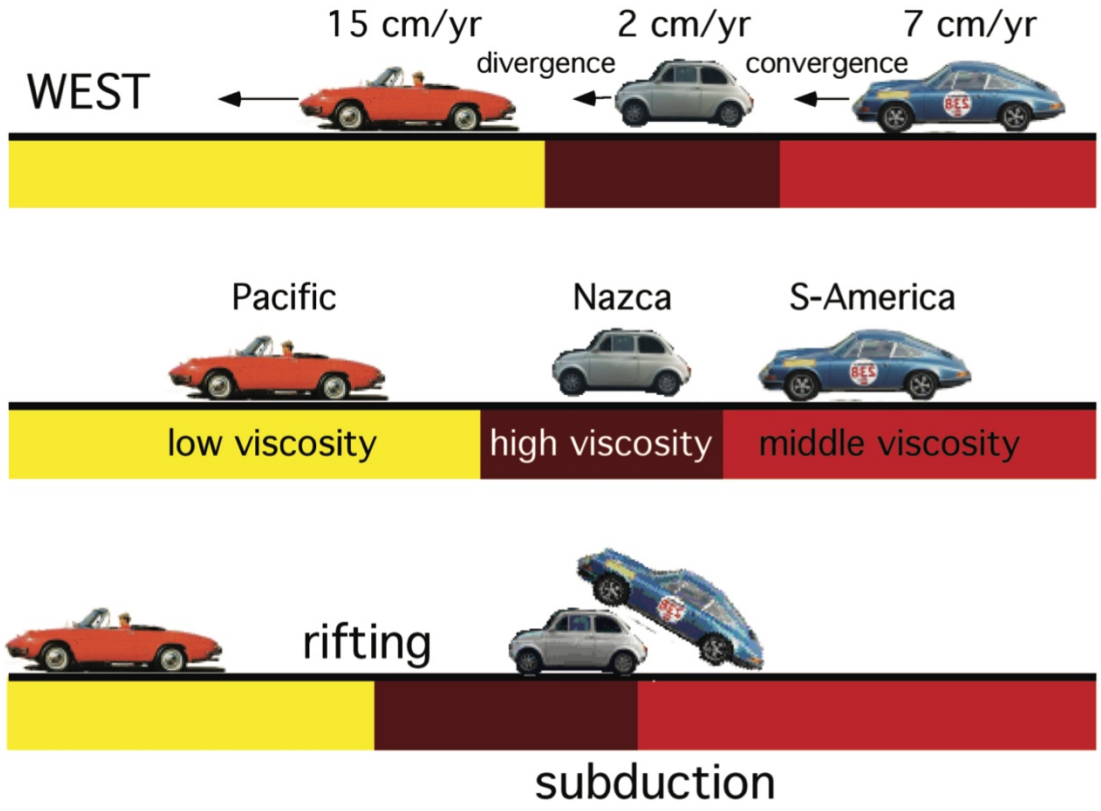

Figure 1.6 - Cartoon illustrating the plates (cars) moving westward along their preferential direction, but having different velocities. The differential velocities control the tectonic environment and result from different viscosities of the asthenosphere. There is extension when the western plate moves westward faster with respect to the plate to the east, whereas convergence occurs when the plate to the east moves westward faster with respect to the plate to the west. When the plate in the middle is subducted, the tectonic regime switches to extension, because the car to the west moves faster, e.g., the Basin and Range (from Cuffaro & Doglioni, 2007).

However, since the "westward" drift has been described (Wegener, 1915; 1924), a conspicuous number of scientists (Bostrom, 1971; Conrad & Behn, 2010; Cuffaro & Doglioni, 2007; Cuffaro & Jurdy, 2006; Gordon, 1995; Gripp & Gordon, 2002; Knopoff & Leeds, 1972; Le Pichon, 1968; O'Connel et al., 1991; Ricard et al., 1991; Rittman, 1942; Torsvik et al., 2010) suggested and analyzed some net or global measurements of it and there are also several hypotheses on its origin, such as the lithosphere density and viscosity, lateral LVZ heterogeneities, etc. (Riguzzi et al., 2010; Stegman et al., 2010; Steinberger, 2000; Scoppola et al., 2006), and driving mechanisms for it (Bostrom, 1971; Carcaterra & Doglioni, 2018; Jeffreys, 1975; Jordan, 1974; Knopoff & Leads, 1972; Moore, 1973; Ranalli, 2000; Riguzzi et al., 2010; Scoppola et al., 2006; Solomon et al., 1975; Torsvik et al., 2010). Furthermore, geological and geophysical evidence would suggest an astronomical polarization of plate tectonics, e.g., plate velocities and seismic distribution which tend to decrease towards

geographic poles (De Mets et al., 1990; Engdahl & Villasenor, 2002; Riguzzi et al., 2010; Solomon et al., 1975; Sun, 1992; Varga et al., 2012), the fact that transform faults are longer in equatorial areas and thermal minimum within the mantle are clustered at equatorial latitudes, suggesting a migration of cold and heavy materials towards lower latitudes being this related to the redistribution of masses due to the centrifugal force effect (Doglioni & Panza, 2015).

1.2.2 Reference frames

Describing plate kinematics, the reference frame choice is essential. Plates motion can be described both in relative or absolute reference frames. Relative plate motions are useful to describe how plates sharing a boundary move along the boundary itself. Absolute reference frames are useful to analyze movements of the entire lithosphere with respect to the mesosphere. One of the most convenient absolute reference frame to study plate kinematics and dynamics is the hotspot reference frame. This is based on the assumption that hotspots are fixed with respect to the mesosphere and relative to each other (Morgan, 1971; Wilson, 1973). There are several issues related to the hotspot reference frame that needs to be addressed every time it is used to compute plates motion relative to the mantle, such as whether hotspots are fixed relative to the mantle, fixed relative to each other and their feeding depth (Cuffaro & Doglioni, 2007). Since plate boundaries move relative to one another and relative to the underlying mantle, any hotspot located on a plate boundary cannot be used for a fixed-hotspot reference frame and relevant ones are those located within plates. For example, in an analysis by Norton (2000) the only hotspots resulted reasonably well fixed relative to one another during the last 80 Myr are Pacific hotspots (O'Neill et al., 2005; Steinberger & Torsvik, 2008).

The lithosphere shows a net "westward" rotation (Bostrom, 1971; Crespi et al., 2006; Gripp & Gordon, 2002; O'Connell et al., 1991; Ricard et al., 1991; Torsvik et al., 2010). Geophysical data and geological observations of subductions and rift zones, independently, show a global polarity of current plate motions, suggesting a "westward" displacement of the whole lithosphere relative to the underlying mantle (Doglioni et al., 1999; 2003; Cuffaro & Doglioni, 2007). This drift is not an average feature due to the larger weight of the Pacific plate in the global plate motions computation, but indeed computed plate motions with respect to a shallow hotspot reference frame (Cuffaro & Doglioni, 2007), show a westward displacement of the entire lithosphere and produce faster plate motions with respect to the mesosphere. To have an idea, a net rotation of the lithosphere of about 49 mm/yr (0.44 ± 0.11°/Myr about a pole of 70°E, 56°S) was computed by Gripp and Gordon (2002), that would increase to 1.49°/Myr (i.e., about 90 mm/yr, with a pole of rotation located in the southeast Indian ocean at about 56°S 136°E) in a shallow-fed hotspots reference frame (Cuffaro & Doglioni,

2007). Thus, hotspots can be interpreted as having a deep or a shallow source, which inevitably leads to two distinct reference frames: i) a deep hotspot reference frame, in which plates move westward but there still are few plates, i.e., Nazca, Cocos and Juan de Fuca, moving eastward with respect to the mantle and in which rotation poles al largely scattered (Figure 1.7); ii) a shallow hotspot reference frame in which all plates move towards the west, albeit having different velocities, and in which rotation poles are mostly located in a narrow area at a mean latitude of 58°S (Figures 1.5 and 1.8c). This shallow hotspot reference frame fits better the geological and geophysical asymmetries observed worldwide at ridges and subduction zones (which will be addressed in the next sections). This would indicate a global tuning (i.e., a complete "westward" rotation of the lithosphere relative to the mantle) rather than a simple average of plate motions (i.e., considering the westward drift only a residual motion of plates that move both westward and eastward relative to the mantle).

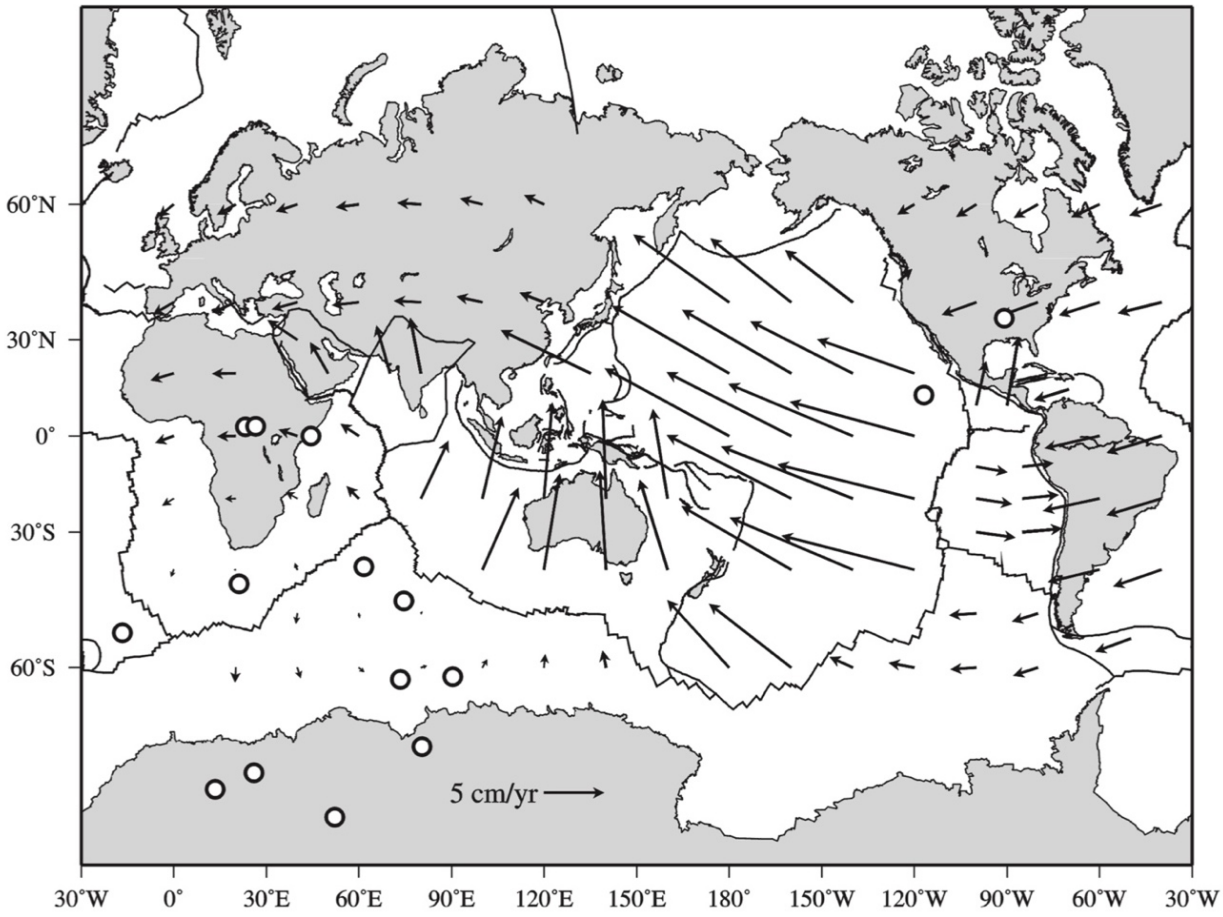

Figure 1.7 - Current velocities with respect to the deep hotspot reference frame. Open circles are the rotation poles. Data from HS3-NUVEL1A (Gripp & Gordon, 2002). In this reference frame plates move westward but there still are few plates, i.e., Nazca, Cocos and Juan de Fuca, moving eastward with respect to the mantle and in which rotation poles al largely scattered (from Cuffaro & Doglioni, 2007).

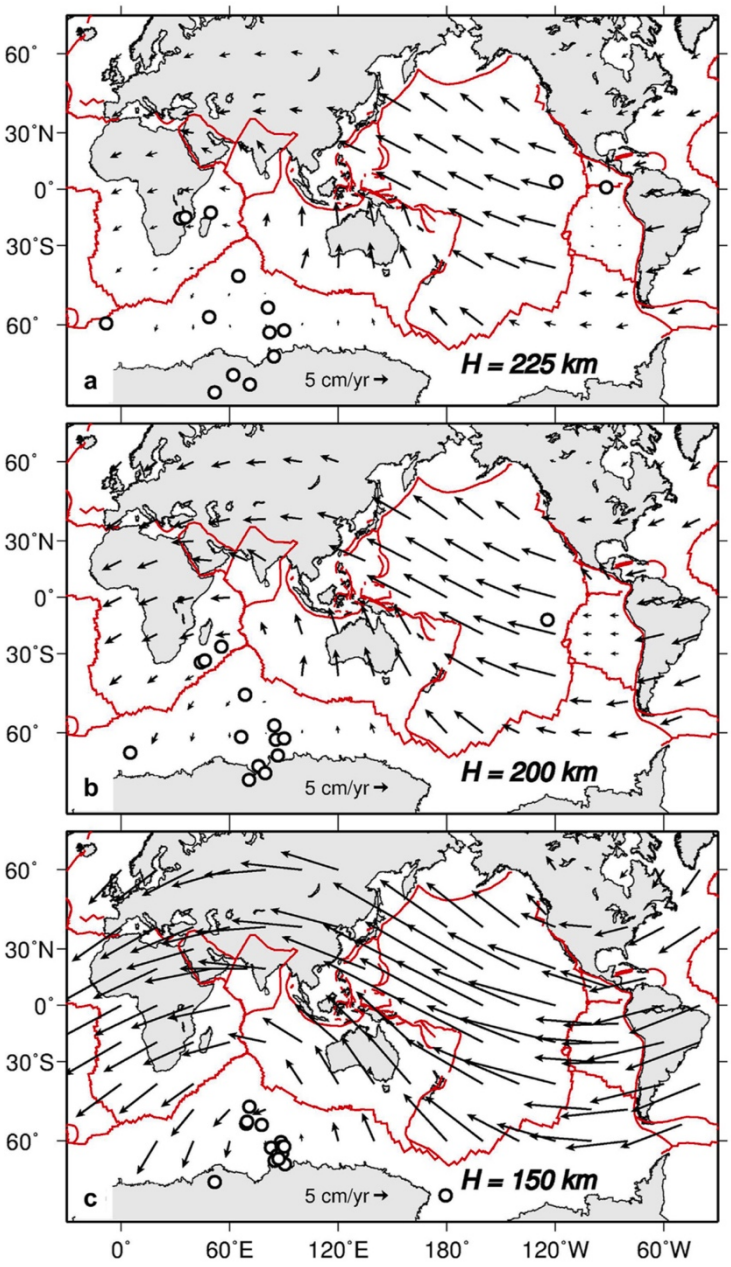

Figure 1.8 - Present-day plate motions with respect to the Pacific shallow hotspot reference frame. This was computed incorporating the NUVEL1A current plate motion model (DeMets et al., 1994) and assuming hotspots source (H) at different depths, shallower going from (a) to (b). Note that in (a) plates move generally toward the west except for the Nazca plate that moves slowly toward the East. In (b) and (c) plates move with faster velocities and they are strongly W-directed. Open circles are the Euler poles for plates that in (c) are located close to the net rotation pole, suggesting a global and polarized westward drift of the lithosphere. In red are tectonic plate boundaries. From Doglioni et al., 2015).

1.3 Subduction zones

As discussed in the previous section, the possibility of a net rotation of the lithosphere relative to the mantle is generally neglected since it depends on the adopted reference system. However, there is relevant evidence that terrestrial plate tectonics has a strongly asymmetric character along both extensional (Cuffaro & Miglio, 2012) and convergent plate boundaries (Doglioni et al., 2006), which could be related to a global asymmetry of the lithosphere-mantle interactions moving along the undulated mainstream of plates motion, i.e., the tectonic equator, in Figure 1.5 (Cuffaro & Miglio, 2012; Doglioni et al., 2006; Doglioni & Panza, 2015 and references therein).

Subduction, at convergent margins, is a geological process with a key-role in plate tectonics. It is considered by some as its main driving mechanism ("slab pull" and "trench suction" models; Conrad & Lithgow-Bertelloni, 2002 and references therein). Besides, this process significantly changes the mantle thermal and chemical structure and is responsible for most of the seismic energy release on Earth (Lallemand & Funiciello, 2009). Subduction zones are the places on Earth where the lithosphere (always oceanic, except for collision zones) enters the mantle along ~70-75000 km worldwide. Several outstanding issues concerning subduction dynamics currently remain unaddressed (Bellahsen et al., 2005; Boutelier & Cruden, 2008; Capitanio et al., 2007; Doglioni, 2008; Doglioni et al., 2006; Hager & O'Connell, 1978; Petricca & Carminati, 2016; Rodríguez-González et al., 2014; Schellart, 2007; Tao & O'Connell, 1992). For instance, it is not understood why most of today's subducting plates interact differently with the mantle, which inevitably results in significant variations in slab morphology and dynamics worldwide (Doglioni et al., 2007; Riguzzi et al., 2010). When comparing "westward" versus "eastward" (or "northeastward") directed subduction zones, there are systematic differences in their morphology, kinematics of the subduction hinge, gravity anomalies, heat flow, subsidence and uplift rates, etc. (Artemieva et al., 2016; Doglioni et al., 2006; Doglioni et al., 2007; Doglioni et al., 1999; Harabaglia & Doglioni, 1998). The most remarkable feature that can be inferred from geophysical signatures is that W-directed slabs (Figure 1.9) are generally very steep and deep, they have a cogenetic backarc basin, low-topography single-verging accretionary prism associated with them and a very deep, fast subsiding (>1 mm/yr) foredeep basin or trench, e.g., Marianas (Doglioni et al., 1999; Lenci and Doglioni, 2007; Uyeda and Kanamori, 1979). Furthermore, this kind of prisms involve young and shallow rocks coming from superficial offscraping of the plates involved in the subduction process. In this case the basal décollement of the subducting plate is never connected to the surface but is rather folded and swallowed down inside the subduction zone (e.g., Tonga-Kermadec and Barbados), being thus unable to feed the accretionary prism with rocks coming from higher depths. On the other hand, E- or NE-directed slabs (Figure 1.9) are shallower, seismicity

generally ends at about 300 km, apart from some deeper clusters close to the upper-lower mantle transition (Artemieva et al., 2016; Omori et al., 2004) and are less steep; furthermore, there is no typical backarc basin opening but instead they build high-topography double-verging orogens with associated two shallower, slow subsiding (<0.1-0.3 mm/yr) trench or foreland basins (Doglioni & Panza, 2015).

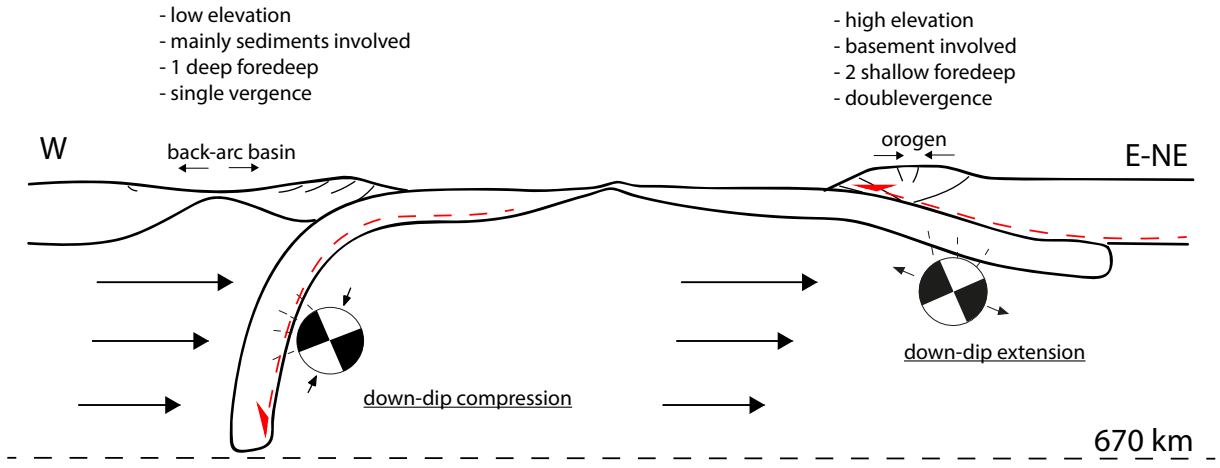

Figure 1.9 – Subduction zones asymmetries. W-directed subduction zones are steeper and deeper with respect to E-to-NE directed ones. The décollement layer (dashed red line) is deformed and subducted for W-directed subductions, whereas is shallower for E-to-NE-directed ones, allowing the involvement of rocks coming from higher depths in the orogen building. Focal mechanisms are representative of the state of stress within the subducting slabs. Arrows point to the mantle flow direction. Modified after Doglioni et al., 1999.

These orogens involve older and deeper rocks because of the deeper décollement planes (e.g., American cordilleras, Alps, Zagros, Himalayas), being thus able to involve the basement of the subducted plate during the collisional stage (Carminati & Doglioni 2012; Doglioni et al., 1999; Uyeda, 1981; Uyeda & Kanamori, 1979). These asymmetries are striking when comparing the western Pacific slabs and orogens (low topography and backarc spreading in the upper plate) and the eastern Pacific subduction zones (high topography and deep rocks involved in the upper plate), which cannot be explained solely by variations in the age-dependent negative buoyancy of the subducting lithosphere (Riguzzi et al., 2010; Doglioni & Panza, 2015; Cruciani et al., 2005; Conrad & Lithgow-Bertelloni, 2002). The same asymmetric features can be recognized worldwide, for instance, comparing the W-directed Atlantic subduction zones and the NE-directed Dinarides-Zagros-Himalayas-Indonesia subduction zones, and it seems rather to be related to the geographic polarity of subduction. Moreover, the asymmetry between the two subduction end-members is supported by (observable and modeled) different/opposite state of stress within the subducting slabs (Figure 1.9): down-dip compression for mostly of the W-directed slabs and down-dip extension for mostly of the E- to NE-directed slabs (Bailey et al., 2012; Carminati & Petricca, 2010; Doglioni et al., 2007;

Petricca & Carminati, 2016). Moreover, there is a seismic gap occurring at depth in the range of about 300-550 km only for the E- to NE-directed slabs (Artemieva et al., 2016; Riguzzi et al., 2010).
In support of this hypothesis, thus, the geometrical asymmetries and geophysical constraints along subduction zones would point to the already mentioned "westerly" polarized drift of plates (Cuffaro & Doglioni, 2007), which implies a relative opposed flow of the underlying Earth's mantle (that is, easterly-directed "mantle wind"). This relative motion is presumably allowed by the presence of a rheologically weak sub-lithospheric low seismic velocity zone (LVZ) located at about 100-200 km depth, where low-degree (~1-2%) melting causes an abrupt drop in the velocity of seismic waves and a low viscosity of the asthenosphere ($\sim 10^{17}$–10^{19} Pa s) (Jin et al., 1994; Stevenson, 1994; Pollitz et al., 1998). The above-mentioned asymmetries (Figure 1.9) have been related by some (Spence et al., 1987) to the age of the subducting lithosphere. Nonetheless, it has been noticed how the negative buoyancy of the slab (if any) alone cannot thoroughly explain all subduction zones feature (Artemieva et al., 2016; Brandmayr et al., 2011; Carminati & Petricca, 2010; Cruciani et al., 2005; Doglioni et al., 2007; Petricca & Carminati, 2016). Furthermore, there are plates, such as Africa or Eurasia, that move without slabs attached in their direction of motions, thus, in these cases both the "slab-pull" and "trench suction" models would not be applicable (Doglioni et al., 2015; Doglioni et al., 2007).

1.3.1 The importance of the subduction hinge

Measurable parameters for evaluating subduction zones dynamics are: uplift rate of the fold-and-thrust belt (or accretionary prism) and depth of the décollement surface at its base (Dahlstrom, 1969; 1970), structural and morphologic elevation of thrust belts, dip of the foreland regional monocline (Lenci & Doglioni, 2007), foredeep subsidence rates, erosion rates, metamorphic evolution, type of magmatism. Some other important parameters are age, thickness and composition of the upper and lower plates, together with their thermal state and observed gravity and magnetic anomalies, involved plates convergence rates, subduction rates (i.e., the velocity with which the subducting lithosphere enters the mantle), stress within the upper plate (i.e., the opening or not of a backarc basin), seismicity and slab dip (Heuret & Lallemand; 2005; Lallemand et al., 2005; Malinverno, 2012; Malinverno & Ryan, 1986; Schellart, 2007; Schellart & Lister, 2004). These features have to be taken into account when analyzing subduction zones dynamics since they directly affect its geometry and evolution. However, there is still one important element that needs to be considered in subduction zones analysis that will have a key-role in the next chapters of this dissertation: the behaviour of the subduction hinge. The subduction hinge is the maximum curvature point within the subducting slab and its behaviour represents a diagnostic feature for subduction zones that can be distinguished indeed on it

basis. For a subduction zone, reference frames with three points should be considered: U attached to the upper plate, L attached to the lower plate and H on the transient subduction hinge (Doglioni et al., 2006). Considering a reference frame in which L and H move with respect to a fixed U, subduction zones with W-directed slab have generally H moving away from U, whereas subduction zones with opposite directed slab have H moving towards U. V_S corresponds to the subduction rate. This velocity is defined as the rate at which the subducting lithosphere enters the subduction zone and can be calculated with the formula:

$$V_S = V_H - V_L, \tag{1.1}$$

where V_L is the velocity of the lower plate and V_H is the velocity of the hinge. In that relation, V_H and V_L are considered positive and negative when the hinge and the lower plate are diverging and converging relative to the upper plate respectively. Thus, the subduction hinge can either diverge from the upper plate or approach it (e.g., Doglioni et al., 2006; Figure 1.10).

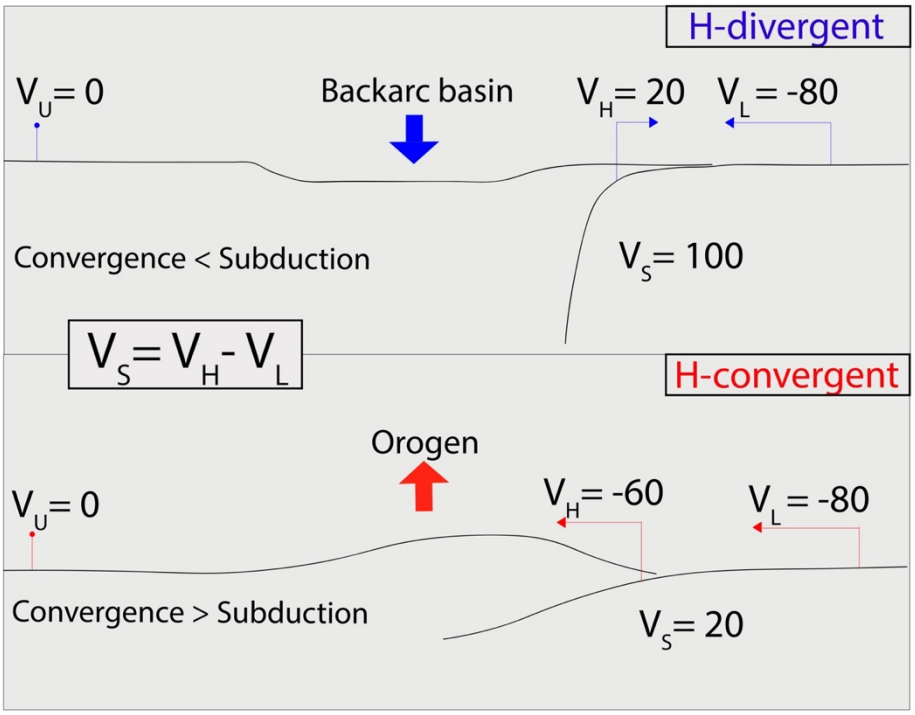

Figure 1.10 - Kinematic model. The kinematics of H-divergent and H-convergent subduction zones is shown. In a reference frame where the upper plate U is taken as fixed, the hinge H can either move towards or away with respect to U. This kinematics occurs for each subduction zone and is essential for the computation of V_S using the formula $V_S = V_H - V_L$. The kinematics of H-divergent (blue) and H-convergent (red) subduction zones is shown. In the first case (upper panel) the subduction rate is increased by the positive motion of the subduction hinge towards the lower plate. In the second case (lower panel), the subduction rate is lowered by the negative motion of the subduction hinge that moves towards the upper plate. V_H is the subduction hinge velocity, V_L is the lower plate velocity, V_U is the upper plate velocity, V_S is the subduction rate.

Regardless of the reference frame, the subduction hinge behaviour has a determining role in increasing or decreasing the subduction rate V_S (see the next chapters for a detailed analysis) that wouldn't have, thus, the same meaning and values of the convergence rate. In fact, for W-directed subduction zones there is generally extensional stress within the upper plate and the subduction rate corresponds to the sum of the convergence rate with the opening rate of the backarc basin (that can be approximated as the motion of the subduction hinge), whereas for E- to NE-directed subduction zones there is high compressional stress within the upper plate, leading to mountain building, and the subduction rate is lowered by the amount of the upper plate shortening, being the subduction hinge motion towards the upper plate. The shortening, in turn, depends on the upper plate viscosity: the higher the viscosity, the lower the shortening within the orogen, conversely, the lower the viscosity of the upper plate, the higher the orogen shortening.

1.4 Mantle Convection

The occurrence of mantle convection is evident either from plate boundary kinematics and numerical modeling. It is obvious that subduction zones are part of the mantle convection, regardless of the slab penetration into the lower mantle. In fact, subduction zones and oceanic ridges yet effectively contribute to upper mantle circulation.

The Earth could be considered as an isolated system that is cooling by conduction through the top. It is characterized by narrow active downwellings, i.e., subducting slabs, and broad upwellings regions, characterized by extension and low wave speed, i.e., ridges (Doglioni & Anderson, 2015). Internal heating slows down the reduction in temperature. However, mantle convection dynamics is still under debate. Three classical models for mantle convection have been proposed (Turcotte & Schubert, 1982): i) whole mantle convection, in which the mantle acts as a whole convection system (the subducted lithosphere enters the 670 km discontinuity with a complementary mantle upwelling); ii) layered mantle convection, in which two separated convective systems operates in the upper and lower mantle (the 670 km discontinuity acts as a barrier between the upper and lower mantle, although there are evidence of slabs penetrating it); iii) hybrid models, in which the 670 km discontinuity acts as a partial barrier, inducing a time-dependence in mantle convection.

A major challenge has been to evaluate and reconcile the range of observations and constraints provided by different scientific disciplines (e.g., chemical geodynamics studies, geophysical observations, plate boundaries asymmetries and kinematics, etc.). Earth's heat budget (the balance between heat production and heat loss) and geochemical analyses of ocean floor basalts suggest that distinct mantle reservoirs have retained their identity for 2 billion years or more (Condie, 2016;

Korenaga, 2008; Turcotte & Schubert, 1982). One reservoir boundary is typically placed at 670 km depth, i.e., between the upper and lower mantle. Seismic imaging and computational geodynamics indicate, however, that this interface is not an effective barrier to mantle flow and suggest that convective circulation occurs at a larger scale (Kárason & van der Hilst, 2000). Although many models have been proposed so far, mantle kinematics and its internal dynamics are far to be fully understood. Thus, some of the still prominent questions are: in how many layers of the Earth mantle convection actively occur? What are the paths of mantle particles? It can be considered as chaotic or polarized? And lastly, the most important to this dissertation purposes is: what is its relationship with plate motions and subduction zones?

Mantle convection does not need a decoupling at the lithosphere base. Depending on the assumption behind its mechanisms (such as mantle drag), it is rather more effective if the lithosphere is fully coupled to the mantle. However, from the Pacific hot-spots we have kinematic evidence that the lithosphere is decoupled relative to the mantle in the LVZ. From these considerations, mantle convection appears driven from the top rather than from the deep mantle (e.g., mantle plume model by Wilson, 1963). This means that plate motions, in a way, is responsible for driving mantle convection (e.g., Anderson, 2001). Therefore, the shearing of the lithosphere and its penetration into the mantle should trigger internal motion. Thus, the question is: what is determining the shearing? The usual answer is the negative buoyancy of slabs, which are pulling plates, i.e., the slab pull (e.g., Royden, 1993), but we have already mentioned how evidence casts doubt on this feature as the "one and only" guiding mechanism for geodynamic processes.

1.5 State of the art of modeling approaches, geophysical data and geodynamic model

During the past decades, several authors (e.g., Tackley et al., 1993; Tackley, 2000; Gerya et al., 2008; Steinberger et al., 2012; Becker, 2017; Colli et al., 2018, etc.) examined the interplay between plate tectonics and mantle convection using 2d and 3d numerical models in spherical or rectangular geometries. Efforts were made in the understanding of mantle i) temperature distribution, e.g., Bunge et al. (2001) in which, assuming the mantle as compressible and heated purely from within, isoviscous reference calculations were obtained (Figure 1.11). When dealing with mantle convection it is important to introduce the concepts of adiabaticity, superadiabaticity and subadiabaticity. The first one points to processes that occur without any heat gain or loss; the second one is a condition which imply a tendency to rise of the hotter material, which is likely less dense; the third one is the tendency

to sink of the hotter and denser material within the mantle. In literature superadiabaticity is concentrated into narrow thermal boundary layers, whereas the geotherm is subadiabatic for the intervening region; ii) phase transitions representative of internally heated whole-mantle models (Figure 1.12), e.g., Tackley et al. (1993), Honda et al. (1993) and references therein, in which the influence of the main discontinuities (~410 km and ~670 km) within the interior of the Earth were tested; iii) composition and rheology, e.g., Barry et al. (2017) or Rolf et al. (2017), in which the authors investigated rheological controls on evolution of surface tectonics, mantle structure and dynamics using the tectonic patterns to infer the Earth's mantle viscosity structure (Figure 1.13); iv) dynamics and mixing properties, e.g., Coltice and Schmalzl (2006), van Keken and Zhong (1999), or Ballmer et al. (2017), in which the authors systematically vary density and viscosity, pointing that the difference in mantle-mixing efficiency between observed regimes highlights the role of compositional rheology (Figure 1.14).

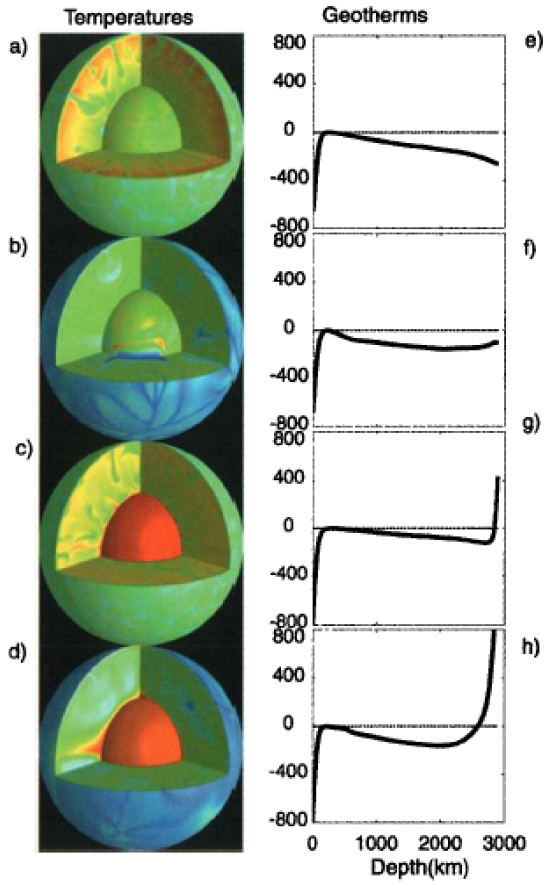

Figure 1.11 – Temperature distribution within the mantle. a) internally heated reference case, with non-adiabatic temperatures and isoviscous. Blue is cold and red is hot. The authors removed the top 100 km of the mantle. b) Same as (a) with increased lower mantle viscosity. c/d) same as (a/b) with the addition of 50% core heating. (e)-(h) Corresponding non-adiabatic geotherms (from Bunge et al., 2001).

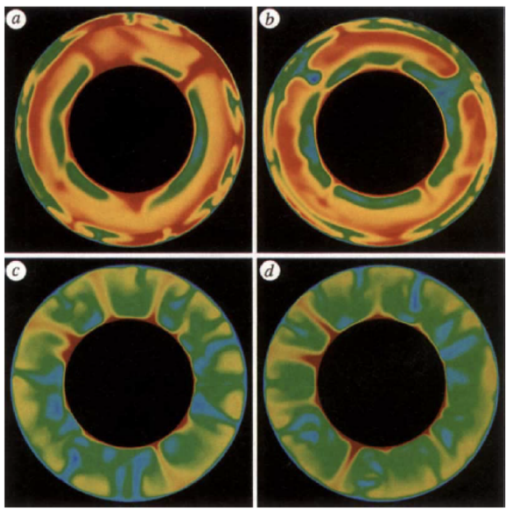

Figure 1.12 – Studies on phase transitions. In (Tackley, 1993) a and b are the final frame of the simulation including phase change, whereas models in c and d are case with no phase change (from Tackley et al., 1993).

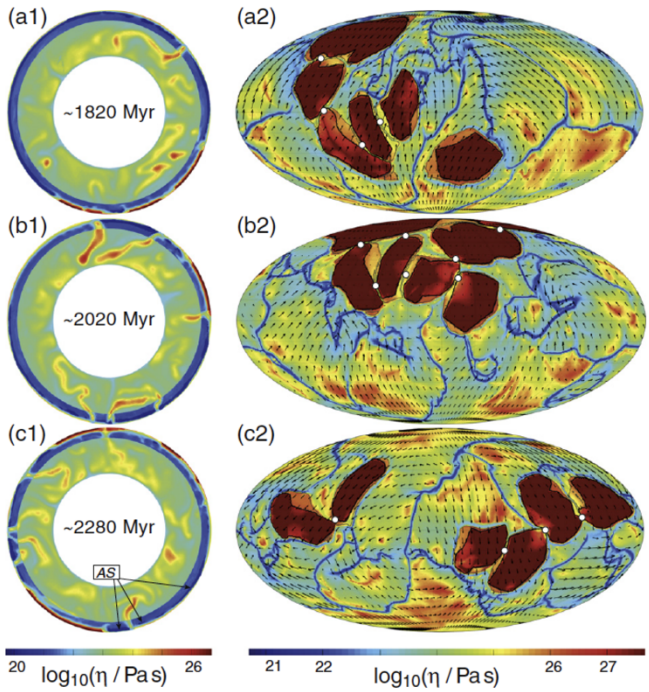

Figure 1.13 – Models about mantle composition. In this figure equatorial cross-sections and Mollweide projections at different time are shown. In cross-sections, the low viscosity asthenosphere is in dark-blue patches. In the Mollweide projections, black arrows denote surface velocities. Cratons are contoured by black lines (from Rolf et al., 2017).

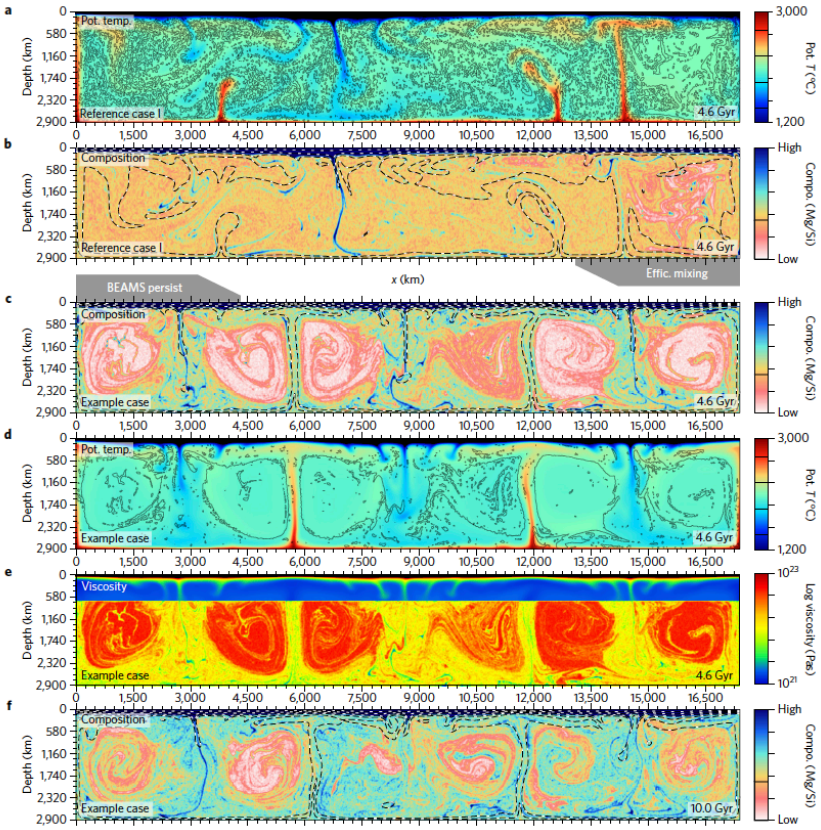

Figure 1.14 - Predicted evolution of the mantle for two regimes of mixing. Models a–f show efficient mixing and persistence of large-scale heterogeneity, respectively (model time as annotated). b, c, f are snapshots of composition with isotherms. The authors observed two regimes in their numerical experiments: 1) in which materials are readily mixed and the mantle becomes largely homogenized over timescales shorter than the age of the Earth; 2) in which intrinsically strong SiO2-enriched material can avoid significant entrainment and mixing for model times greater than the age of the Earth (from Ballmer et al., 2017)

Several mantle convection models are computed considering the mantle as a homogeneous medium (i.e., having the same composition throughout the entire model), whereas mantle convection is often guided by thermal, i.e., density, (Capitanio et al., 2010; Crameri et al., 2012; Stegman et al., 2010) differences (Figure 1.15). However, the mantle presents in nature lateral heterogeneities and vertical chemical stratifications (e.g., Anderson, 2006; Doglioni & Anderson, 2015; Frost et al., 2018; Lebedev & van der Hilst, 2008; Ritsema, 2005) shown by tomographic models, that should be, thus, representative also for chemical heterogeneities and not just for cold and hot volumes of mantle material (Anderson, 2006; Foulger et al.,2013; Tackley, 2000; Thybo, 2006; Trampert et al., 2004; Figures 1.16-1.17).

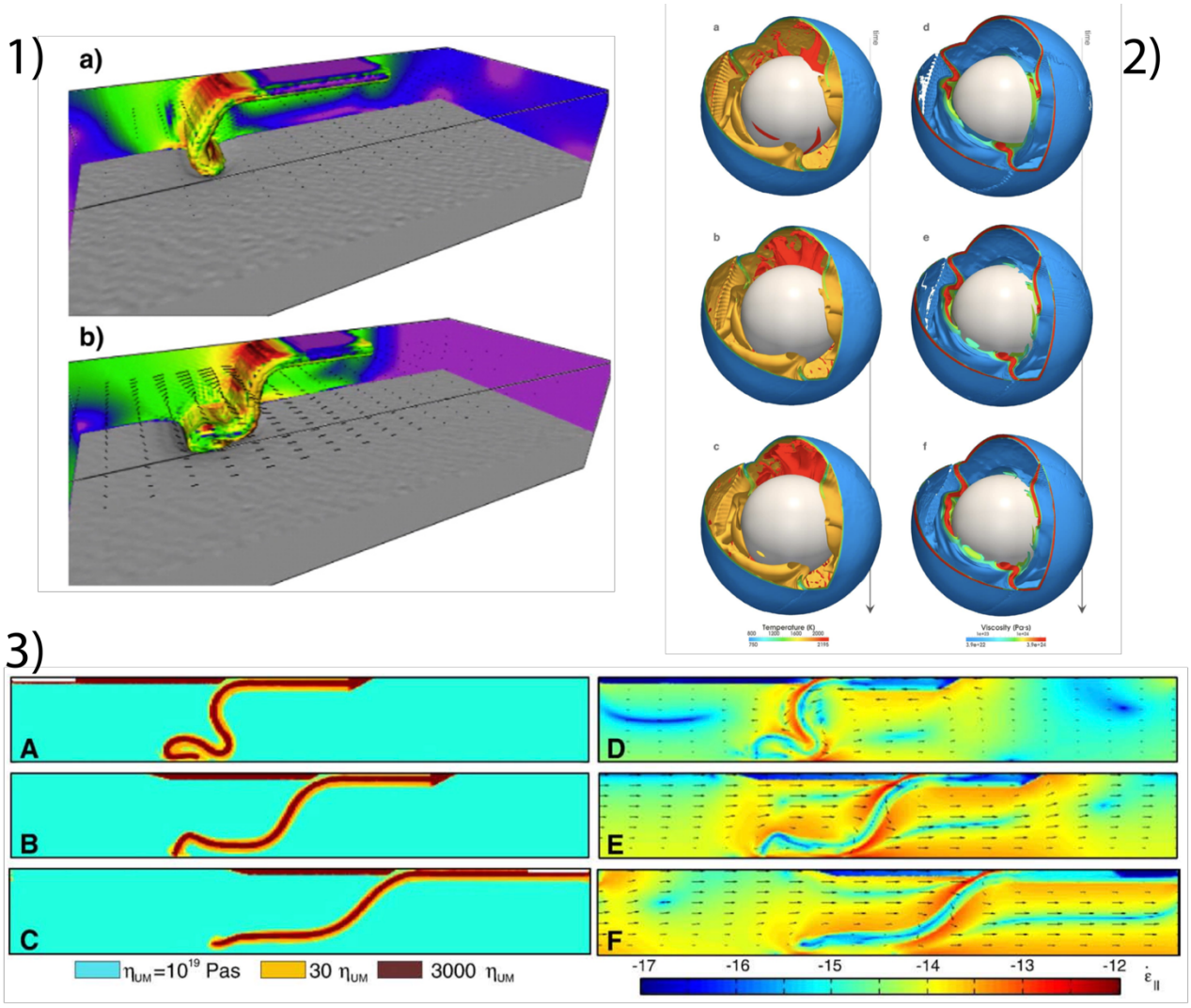

Figure 1.15 – Subduction zones in numerical models. Panel 1: Evolution of subduction subducting slab showing second invariant of the strain rate during (a) slab–tip interaction with the lower mantle, (b) recumbent fold slab geometry denoting the switch from advancing to retreating trench motion with backwards-draping slab (modified after Stegman et al., 2010). Panel 2: Three-dimensional single-sided subduction in a spherical geometry in 3-D spherical mantle convection. Temperature (a-c) and viscosity isosurfaces (d-f) are plotted (modified after Crameri et al., 2012). Panel 3: Viscosity, strain rates and velocity distribution subduction zones having fixed upper plate (A, D), free upper plate (B,E) and fixed subducting plate (C, F). The white area in A and C is where the imposed velocity is zero (modified after Capitanio et al., 2010).

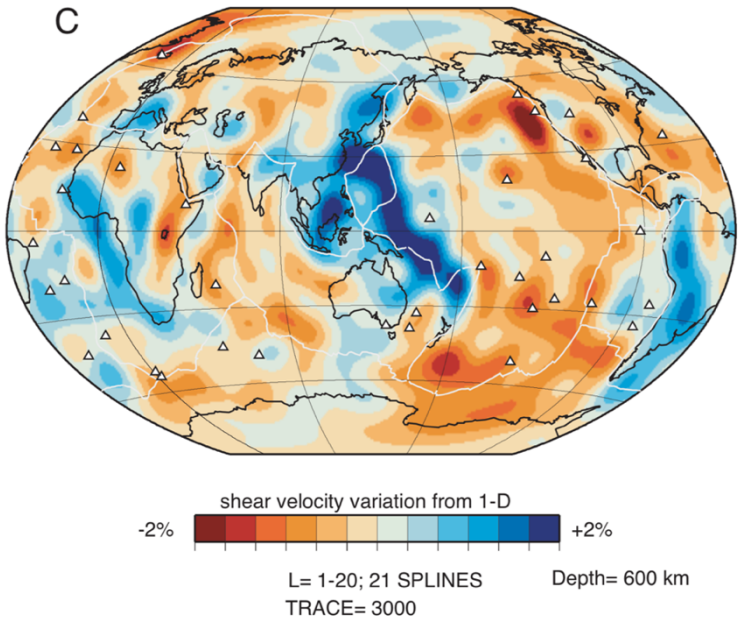

Figure 1.16 – Tomography of the bottom of the upper mantle. Maps of shear velocity heterogeneity according to model S20RTS at 600 km depth. In regions colored red (blue) the shear velocity is lower (higher) than the average shear velocity at that depth. Triangles represents hotspots location catalogue by Sleep (1990). Approximate positions of plate boundaries are shown with white lines (modified after Ritsema, 2005).

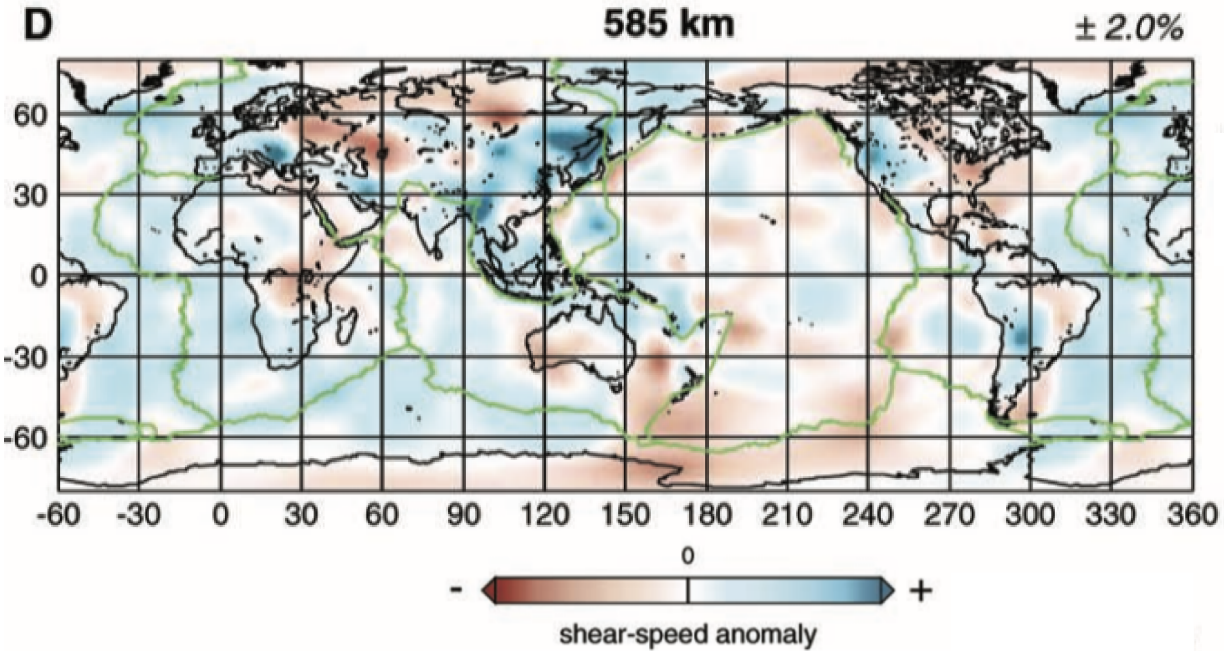

Figure 1.17 – Tomography of the bottom of the upper mantle. Cross-sections through the tomographic model at 585 km depth. Approximate plate boundaries are the green lines. The reference shear-wave velocity value is 5.34 km/s (modified after Lebedev & van der Hilst, 2008).

Moreover, processes which represents the interplay between plate tectonics (i.e., subduction zones) and mantle convection were thoroughly analyzed by a great number of authors, which didn't include any mantle polarization but reflects the classic mantle convection models described above. For instance some plate tectonics features and origin hypotheses were explored by Gerya et al. (2015) and Gerya et al. (2008), in which the authors investigated about the cause of one-sided subduction demonstrating that they require a weak hydrated slab interface and high slab strength (Figure 1.18), whereas plate tectonic-mantle interactions were largely modeled by a number of authors, e.g., Conrad & Behn (2010), Gurnis (1988), Bonnardot et al. (2008), Crameri et al. (2012), Rolf et al. (2012), Yoshida & Santosh (2014), Yoshida (2013), Phillips and Bunge (2005), in which the authors explored continental motions in 3d spherical convection models, focusing on the influence of continent size, mantle heating mode and an increase in lower mantle viscosity (Figure 1.19).

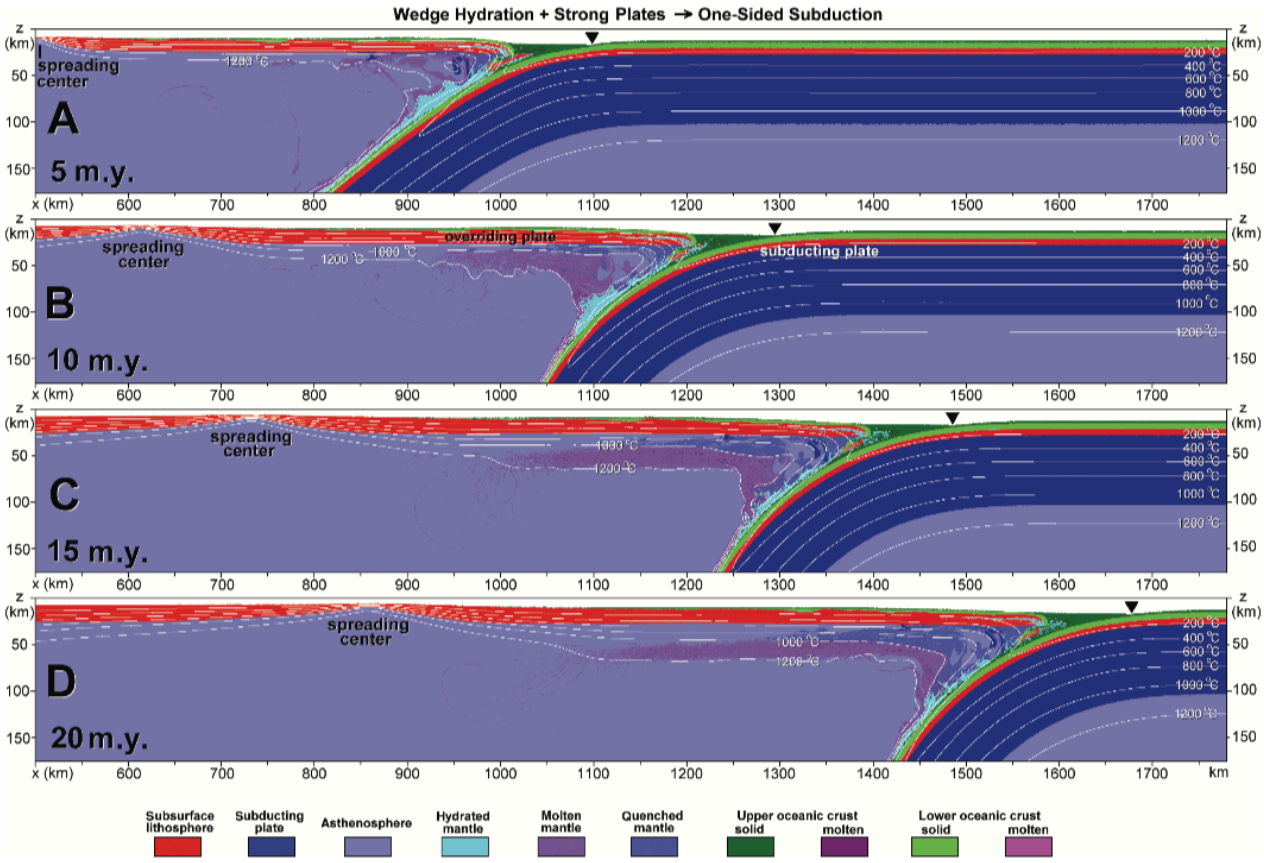

Figure 1.18 – Models investigating some subduction typical features. Results of numerical experiments showing typical dynamics of self-sustaining one-sided subduction development. Solid triangle shows trench position (from Gerya et al., 2008).

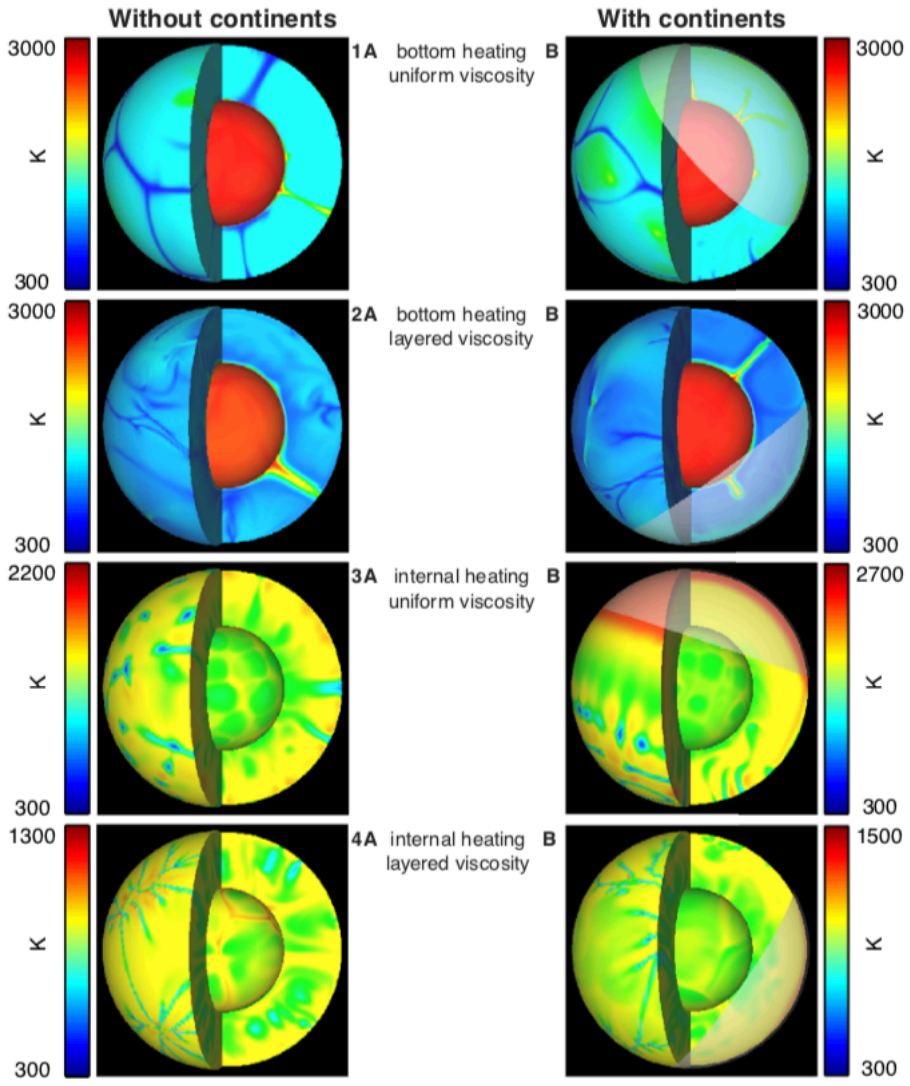

Figure 1.19 – Plate tectonics-mantle interactions. Temperature field snapshots for cases with bottom or internal heating and uniform or layered viscosity. Temperatures run from hot (red) to cold (blue) expressed in Kelvin. The inner and outer spherical boundaries correspond to the core–mantle boundary (CMB) and 90 km depth, respectively. Cases lA–4A correspond to convection calculations without continents. Models lB–4B show cases with a supercontinent covering 30% of the surface (gray cap) (from Phillips & Bunge, 2005).

Anderson (2001) proposed a top-driven plate tectonic model, in which the Earth's internal heat allows convection within the mantle. At the base of this model, integrated by Doglioni & Anderson (2015), are the following seminal concepts, some of which have been already mentioned in the sections above: i) the low viscosity of the LVZ decoupling layer, at the lithosphere base; ii) the superadiabaticity of the LVZ (Anderson, 2013), in which the potential temperature (T_P) is higher and local fluids and melts occur (Crépisson et al., 2014; Green et al., 2010; Naif et al., 2013; Panza, 1980); iii) the subadiabaticity of parts of the mantle below the LVZ down to the CMB (e.g., Anderson, 2013; Moore, 2008); iv) geophysical and geological asymmetries at worldwide plate margins; v) a volcanic source within the shallow mantle (i.e., within the LVZ) for volcanic chains, instead of a source within the deeper mantle (e.g., Anderson, 2011; Presnall & Gudfinnsson, 2011); vi) intraplate basalts comes

from the LVZ upper part and MORB from the transition zone (Anderson & Sammis, 1970; Ligi et al., 2005); vii) the shallow hotspot reference frame which supports a faster and globally "westward" directed motion of the lithosphere with respect to the mantle (Crespi et al., 2007; Cuffaro & Doglioni, 2007).

In this system, secular cooling, lateral temperature gradients and the motion of the LID can be driving features for mantle convection, in which narrow active downwellings (i.e., slabs) have to be compensated by broad passive upwelling (i.e., subadiabatic upper mantle material). Being the negative buoyancy of slabs alone (Anderson, 2001) or the influence of the Earth's rotation and its lag due to tidal friction and thermal cooling (Carcaterra & Doglioni, 2018; Riguzzi et al., 2010; Varga et al., 2012) the main driving force for plate motions, the "westward" drift of plates may regulate convection and its polarization leading to a shearing from the top (Figure 1.20).

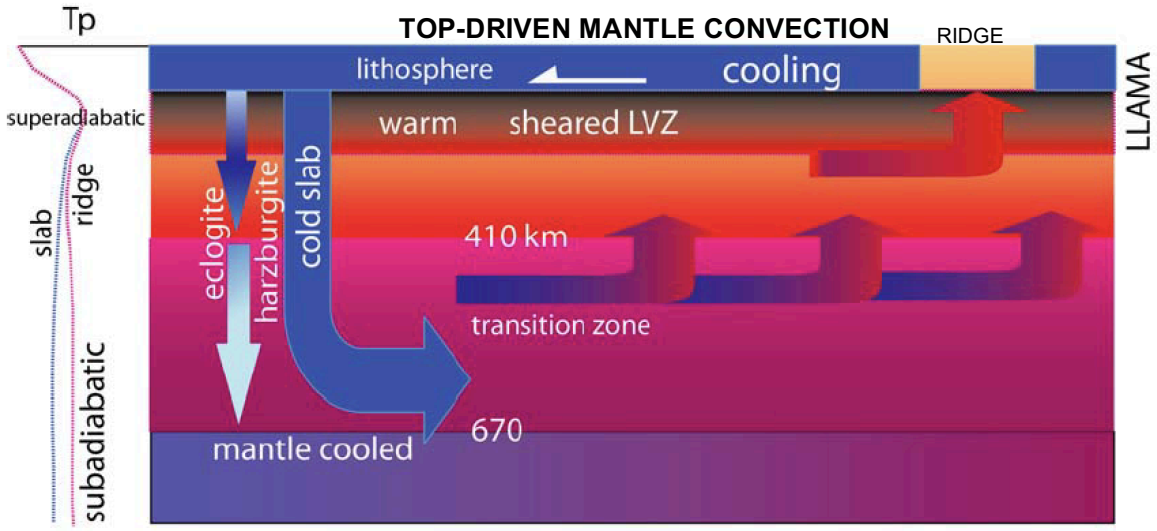

Figure 1.20 – Mantle convection driven from the top (after Doglioni & Anderson, 2015). Counterclockwise convection (red and blue arrows) leads to lateral variations in the mantle potential temperature. The host mantle along subduction zones is cooler than elsewhere. The thermal buffer exerted by the cold lithosphere, the radiogenic decay and the shear heating in the LVZ point to a superadiabatic upper asthenosphere and a subadiabatic lower upper mantle. In this model, mantle convection is polarized by the "westward" drift of the lithosphere (white arrow into the lithosphere) and the relative "easterly" directed compensating mantle (red and blue arrows), balancing slab loss along W-directed subduction zones. The intrinsically buoyant harzburgite component of slabs contributes to the upward return flow. westward drift of the lithosphere. Subduction of the cold slab with its components (eclogite and harzburgite) are the blue and white arrows.

There are, however, a number of authors who explored the interaction between the polarized mantle described in this system and the subducting lithosphere with simplified approaches, e.g., analytical methods (Hager & O'Connell, 1978), mechanical-physical methods (Boutelier & Cruden, 2008), mechanical (Petricca & Carminati, 2016) and thermomechanical models by Rodríguez-González et al. (2014), in which the authors investigate the influence of a mantle flow relative to the lithosphere on subduction dynamics testing different mantle flow velocities, as well as different directions of

flow, either sustaining or opposing slab dip, evaluating the effects of different inflow/outflow velocity profiles, slab strengths and upper–lower mantle viscosity contrasts (Figure 1.21).

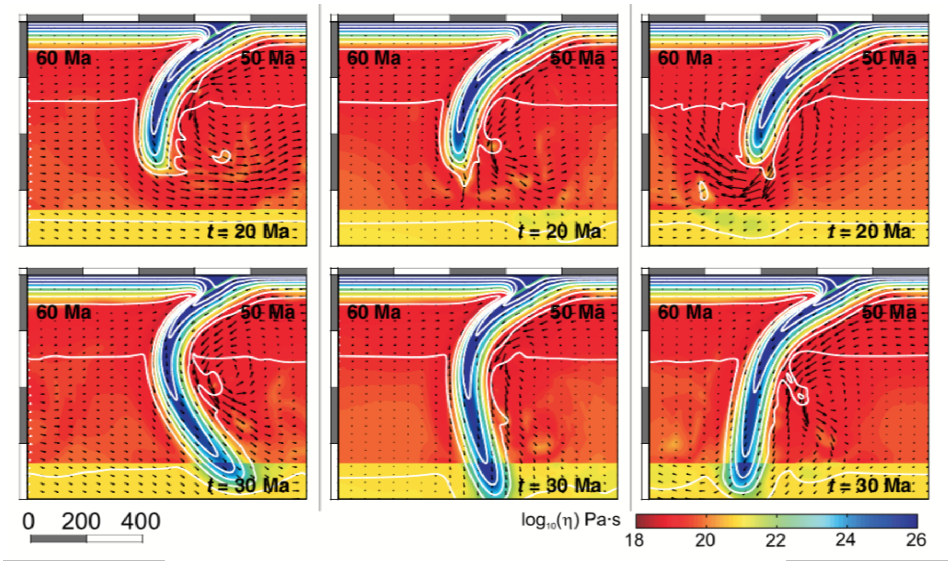

Figure 1.21 - Models testing the influence of a horizontal mantle flow. In these models the overriding plate is 60 Ma and the subducting plate is 50 Ma. Here different mantle flow velocities were tested: (a) imposed horizontal upper mantle flow (IHMF) opposite to subduction direction, (b) without IHMF; (c) IHMF in the same direction as subduction (modified after Rodríguez-González et al., 2014)

Nevertheless, in literature there is a lack of numerical models including togheter three of the main important geodynamical and geophysical constraints: i) the horizontal mantle flow which interacts with tectonic plates; ii) the subduction hinge motion, that allows the correct estimation of the effective velocity with which subducting plates enter the mantle; iii) the LVZ decoupling layer between the lithosphere and the mantle, which allows their relative motion; iv) the global "westward" drift of the lithosphere as a constrain for global subduction dynamics.

The starting point for this research work was, thus, the system described by Doglioni and Anderson (2015) with particular interest in including its kinematics, geophysical and geodynamical constraints in numerical models.

Chapter 2

Horizontal mantle flow controls subduction dynamics

As already mentioned in Chapter 1, it is generally accepted that subduction is driven by downgoing-plate negative buoyancy. Yet plate age –the main control on buoyancy– exhibits little correlation with most of the present-day subduction velocities and slab dips (Cruciani et al., 2005; Doglioni, 2007). W-directed subduction zones are on average steeper (~65°) than E-directed (~27°) (Doglioni et al., 2015; Riguzzi et al., 2010). Also, a "W"-directed net rotation of the lithosphere relative to the mantle has been detected in the hotspot reference frame. Thus, the existence of an "E"-directed horizontal mantle wind could explain this subduction asymmetry, favouring steepening or lifting of slab dip angles. In this Chapter, we test this hypothesis using high-resolution two-dimensional numerical thermomechanical models of a subducting oceanic plate interacting with a mantle flow. Results show that when subduction polarity is opposite to that of the mantle flow, the descending slab dips subvertically and the hinge retreats, thus leading to the development of a backarc basin. In contrast, concordance between mantle flow and subduction polarity results in shallow dipping subduction, hinge advance and pronounced topography of the overriding plate, regardless of their age-dependent negative buoyancy. These results are consistent with seismicity data and tomographic images of subduction zones. Thus, these models may explain why subduction asymmetry is a common feature of convergent margins on Earth.

2.1 Introduction

The potential influence of westward lithospheric drift (or relative eastward mantle wind) on the subduction zones asymmetry (Figure 2.1) has been already explored in the past decades on the basis of simplified approaches. For instance, an analytical model (Hager & O'Connell, 1978) has been proposed to stress the importance of a background mantle flow in influencing slabs geometry.

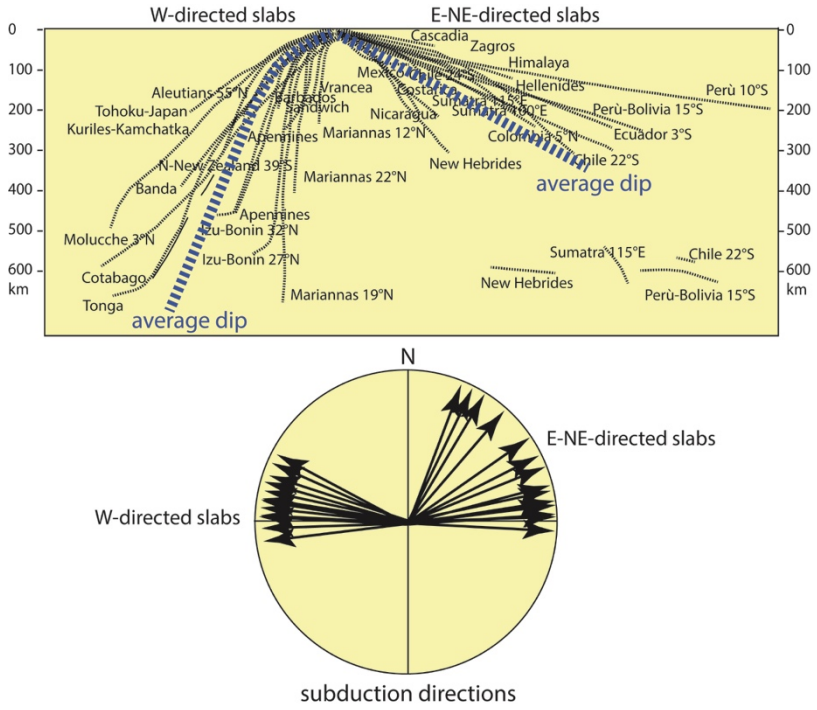

Figure 2.1 - Slab dip of the main subduction zones of the world measured parallel to the convergence direction among upper and lower plates. Subduction directions appear concentrated into two main trends, i.e., W-ward and E-ward or N-NE-ward. W-directed subduction zones are steeper than E- or NE-ward directed subduction zones. Modified after Riguzzi et al., (2010) and Sottili et al. (2015).

This model suggests that the dip angle of subducted slabs are strongly controlled by a large-scale flow imposed within the mantle by tectonic plates moving in their observed geometry and, more importantly, the slabs are orientated as if they were responding passively to the flow driven by the surface motion of the plates. Moreover, this model shows how important the decoupling role of a Low Viscosity Layer (LVZ) between lithosphere and mantle would be. In fact, the match between the direction of mantle flow and the direction of the subducted slab, given by the trend in earthquakes hypocentres, is good for most of the subduction zones and is usually improved by the inclusion of this decoupling level (Hager & O'Connell, 1978). More recently, a purely mechanical physical model (Boutelier & Cruden, 2008) has been used to investigate the influence of a regional convective (i.e., combined horizontal and vertical) mantle flow on the geometry of subducted slabs and the deformation regime of the overriding plates. It has been demonstrated that an imposed circulation of a simplified Newtonian asthenospheric mantle with rates of 1–10 cm/yr in the direction of subduction can cause the flattening of slab angles from vertical to ~60^{o}. These modeling results have been applied to explain geophysical observations in some regional subduction settings (NE-Japan, Central America). Further numerical thermomechanical models (Rodriguez-Gonzalez et al., 2014) have been used to understand how much of the slab-dip variability found in nature can be attributed to the interaction between the slab and a background mantle flow. The number of salient features of mantle-

lithosphere interaction that these models do succeed in reproducing provides useful insights. However, these thermomechanical numerical models did not employ realistic free upper surface condition, which is crucial for subduction zones asymmetry (Crameri et al., 2012), and used highly simplified rheology of the mantle that is in conflict with available geochemical, experimental and theoretical data (Ranalli, 1995; Afonso et al., 2007; van Keken et al., 2011). Hence, the validation of the mantle wind hypothesis, through a realistic state of the art numerical thermomechanical model, stands as a challenge that motivated the work done in this Chapter.

Here, we explore and integrate the effects of a priori defined mantle flow on the subduction zone morphology and slab dynamics, improving the modeling by means of self-consistent two-dimensional rheologically realistic thermomechanical numerical experiments with a free surface. In these experiments an oceanic plate sinks beneath a continental plate under the control of non-Newtonian temperature-, pressure- and strain rate-dependent viscous-plastic rheologies (with viscosity magnitude ranging from 10^{18} and 10^{25} – Table 2.1) in a fully thermodynamically coupled model accounting for mineralogical phase changes (Gerya & Yuen, 2003). A troughgoing (Rodríguez-González et al., 2014) purely horizontal (0-3 cm/yr) asthenospheric mantle flow (i.e., not related to any regional mantle circulation (Boutelier & Cruden, 2008) is imposed at both lateral boundaries in the same or opposite direction with respect to pre-defined rightward subduction polarity. We also tested the potential influence of the LVZ decoupling level (with a constant viscosity value of 10^{18} Pa s) on mantle-lithosphere interactions.

2.2 Numerical Modeling

The numerical experiments were carried out with the code I2VIS (Gerya & Yuen, 2003). This code is based on a combination of the finite-difference method with a marker-in-cell technique. In the I2VIS code, the conservative finite-difference schemes are designed over a non-uniformly spaced fully staggered Eulerian grid. The initial set-up is shown in Figures 2.2 and 2.3. The momentum, continuity and energy equations are solved in the Eulerian frame and physical properties are advected by Lagrangian markers according to a computed velocity field using a fourth-order in space, first order in time explicit Runge-Kutta scheme. The material properties are interpolated from the markers to the grid by using a distance-dependent averaging. Full details on this method, allowing for its reproduction, are provided elsewhere (Gerya & Yuen, 2003; Gerya, 2010). We use non-Newtonian viscous-plastic rheologies (Table 2.1) in a model that is fully thermodynamically coupled and accounts for mineralogical phase changes (Faccenda & Dal Zilio, 2017), as well as for adiabatic, radiogenic and frictional internal heating sources. The viscous-ductile rheological term accounts for

power-law and diffusion creep as well as for Peierls creep at depth. The free surface upper boundary is simulated using the "sticky air" technique (Gerya & Yuen, 2007), enhanced by the high-density marker distribution in the near-surface. For all models presented in this Chapter, periodic boundary conditions have been implemented on the left and right boundaries following the same approach as in previous numerical experiments (Dal Zilio et al., 2017), and free slip condition is applied at the top and the bottom of the computational domain. A low viscosity zone between a 100 and 200 km depth and an imposed throughgoing asthenospheric mantle flow of -3 to +3 cm/yr are implemented in the models. The occurrence of any vertical component of the mantle flow has been neglected due to the assumption of a prevalent horizontal component related to the "eastward" mantle flow. The viscosity of this weak layer and the mantle flow velocities applied are listed in Tables 2.1, 2.2 and A.1. Full details on the method, allowing its reproduction, are provided below and in Gerya and Yuen (2003). This algorithm has been thoroughly tested in two dimensions and used for lithospheric deformation experiments in a number of previous studies. All data used in this Chapter can be accessed from the sources provided in the reference list, below and in Appendix A.

2.2.1 Governing equations

The I2VIS code solves for the conservation of mass, momentum and energy. Conservation of mass is approximated by the incompressible continuity equation:

$$\frac{\partial v_x}{\partial x} + \frac{\partial v_y}{\partial y} = 0; \tag{2.1}$$

where x and y denote horizontal and vertical Cartesian coordinates. The momentum equations are presented in the form of the Stokes flow approximation:

$$\frac{\partial \sigma'_{ij}}{\partial x_j} - \frac{\partial P}{\partial x_i} + \rho g_i = 0 \tag{2.2}$$

which in 2D reads:

$$\frac{\partial \sigma'_{xx}}{\partial x} + \frac{\partial \sigma'_{xy}}{\partial y} - \frac{\partial P}{\partial x} = 0 \tag{2.3.1}$$

$$\frac{\partial \sigma'_{yy}}{\partial y} + \frac{\partial \sigma'_{yx}}{\partial x} - \frac{\partial P}{\partial y} = -\rho g_y \tag{2.3.2}$$

where σ'_{ij} are the components of the viscous deviatoric stress tensor, ρ is the density dependent on rock composition, temperature and pressure, and g_y is the acceleration due to gravity. The components of the deviatoric stress tensor (σ'_{ij}) are calculated using the incompressible viscous constitutive relationship between stress and strain rate ($\dot{\varepsilon}$), as follows:

$$\sigma'_{ij} = 2\eta \dot{\varepsilon}_{ij} \; ; \tag{2.4}$$

$$\dot{\varepsilon}_{ij} = \frac{1}{2}\left(\frac{dv_i}{dx_j} + \frac{dv_j}{dx_i}\right). \tag{2.5}$$

The conservation of energy equation describes the temperature changes in a continuum due to internal heat generation/consumption and advective/conductive heat transport:

$$\rho c_{P\_eff}\left(\frac{\partial T}{\partial t} + v\ grad(T)\right) = -\frac{\partial q_x}{\partial x} - \frac{\partial q_y}{\partial y} + H_r + H_a + H_s, \tag{2.6}$$

where q_x and q_y are heat flux components; $k = f(P, T, C)$ is the thermal conductivity which depends on the pressure-temperature conditions and composition. H_r, H_a and H_s are, respectively, radioactive, adiabatic and shear heat production. Radioactive heat production depends on the rock type and it is assumed to be constant through time. The adiabatic heat production/consumption is related to pressure changes (compression-decompression):

$$H_a = T\alpha_{eff}\left(v_x \frac{\partial P}{\partial x} + v_y \frac{\partial P}{\partial y}\right). \tag{2.7}$$

The shear heat production is given by the dissipation of mechanical energy during viscous deformation and depends on the deviatoric stress and deviatoric strain rate:

$$H_s = \sigma'_{xx}\dot{\varepsilon}'_{xx} + \sigma'_{yy}\dot{\varepsilon}'_{yy} + 2\sigma'_{xy}\dot{\varepsilon}'_{xy}\,. \tag{2.8}$$

The effect of latent heating related to the phase transformations of the rocks is included implicitly by calculating the effective heat capacity (c_{P_eff}) and the effective thermal expansion (α_{eff}) through

thermodynamic relations (Gerya, 2010). Phase transitions are parameterized as a function of thermodynamic state variables (*P*, *T*, *V*) and composition by using polynomials to interpolate the reaction boundary (Faccenda & Dal Zilio, 2017). For instance, the olivine polymorphic transformations and the post-spinel reaction are parameterized with the linear *P–T* relationship:

$$P = P_0 \frac{\partial P}{\partial T} \Delta T = P_0 + \gamma \Delta T \; ; \tag{2.9}$$

where γ is the Clapeyron slope of the reaction, P_0 is the pressure at reference temperature (T_0) and $\Delta T = T - T_0$.

The visco-plastic behaviour is implemented via evaluation of the effective viscosity of the material. The viscous properties are computed by taking into account the contribution of different creep mechanisms such as diffusion, dislocation and Peierls creep, as:

$$\frac{1}{\eta_{eff}} = \frac{1}{\eta_{diff}} + \frac{1}{\eta_{disl}} + \frac{1}{\eta_{peierls}} , \tag{2.10}$$

where η_{diff}, η_{disl} and $\eta_{peierls}$ are calculated from flow laws (Ranalli, 1995). The strength of the material is limited by:

$$\eta_{eff} = \frac{\sigma_{yield}}{2\dot{\varepsilon}_{II}} , \tag{2.11}$$

where the yield stress is described at shallow depths by the Drucker-Prager yield criterion:

$$\sigma_{yield} = cos\phi C + \; sin\phi \; P\left(1 - \lambda_{fluid}\right) . \tag{2.12}$$

Here, ϕ is the internal friction angle, C is the cohesion, and λ_{fluid} is the assumed pore fluid pressure factor.

2.2.2 Model setup

The initial setup for our models is shown in Figures 2.2-2.3, while the rheological (Ranalli, 1995) and thermal (Clauser & Huenges, 1995) parameters used in the numerical experiments are shown in Table 2.1. The computational domain size is 4000 x 1400 km and is discretized with 1361 x 351 Eulerian

nodes, with more than 12 million randomly distributed Lagrangian particles. This allowed a minimum grid resolution of 1 km in the area subject to largest deformation. Elsewhere, the resolution increases gradually from 1 km up to 5 km. Vertical resolution is 1 km for the first 100 km and then increases with depth to a maximum of 5 km. Two 1700-km-long continental plates were separated by a 700-km-long oceanic plate. Both continental plates and an oceanic are composed of an upper crust, lower crust and lithospheric mantle. The initial continental geotherm was set using values of 0 °C (273 K) at the top and 1344 °C (1617 K) at the bottom of the lithosphere (100-km-thick). The thermal structure of the initial plate set-up is computed according to the half-space cooling model (Turcotte & Schubert, 2014) for a given age between 20 and 150 Ma. The thermal gradient used within the mantle was quasi-adiabatic (0.5 K/km). To ensure an efficient heat transfer from the surface of the crust, the temperature of the "sticky air" is kept constant at 0 °C. Gravitational acceleration of g_y = 9.81 m/s was used in the model. Subduction starts as the result of the imposed rightward convergence rate of 5 cm/yr imposed for the first 6 Ma on the left plate. The subduction is localised along a prescribed inclined rheologically weak (hydrated) intra-plate zone characterized by low plastic strength of 1 MPa (Faccenda & Dal Zilio, 2017) (Figure 2.2). The subducting plate is also decoupled from the left model boundary by a low viscosity zone. We also impose low plastic strength for the fluid-saturated subducting basaltic crust (see Table 2.1) acting as a lubricating layer (Faccenda et al., 2009; Gerya et al., 2008). This ensures that the induced one-sided subduction can continue spontaneously after 6 Myr period of initial plate convergence. A low viscosity layer (10^{18} Pa s) between 100-200 km depth has been included in some numerical experiments (see Table 2.1) in order to test the role of a weak and partially melted asthenosphere, as suggested in Doglioni et al. (2011). Finally, as the main additional ingredient of our models, we impose a throughgoing horizontal asthenospheric mantle flow (see Boundary conditions section).

During numerical experiments, a suite of parameters have been tested to investigate how they affect the dynamic of the model itself. In particular, we considered the activation volume, the coefficient of thermal expansion, the age of the subducting lithosphere, the direction and velocity of the horizontal mantle flow (Tables 2.1, 2.2 and A.1). We chose to observe the behaviour of the models changing these parameters to see how variations in effective viscosity and in density, with temperature and depth, influence subduction dynamics (Tables 2.2 and A.1), in the set of conditions of a mantle flow acting as a push or as a sustain for a subducting slab, including the effect of a décollement level. Furthermore, also the age of the subducting oceanic plate was taken into account: in fact, we wanted to numerically and physically demonstrate that the horizontal mantle flow has a sufficient strength to generate a steep dip angle also in slabs that are made of young (and therefore hot) oceanic lithosphere. This latter represents a further evidence that the dynamics of a subducting slab and, more generally,

of plate tectonics is far from being completely known, not being the slab pull force (if any) alone a full explanation for these mechanisms.

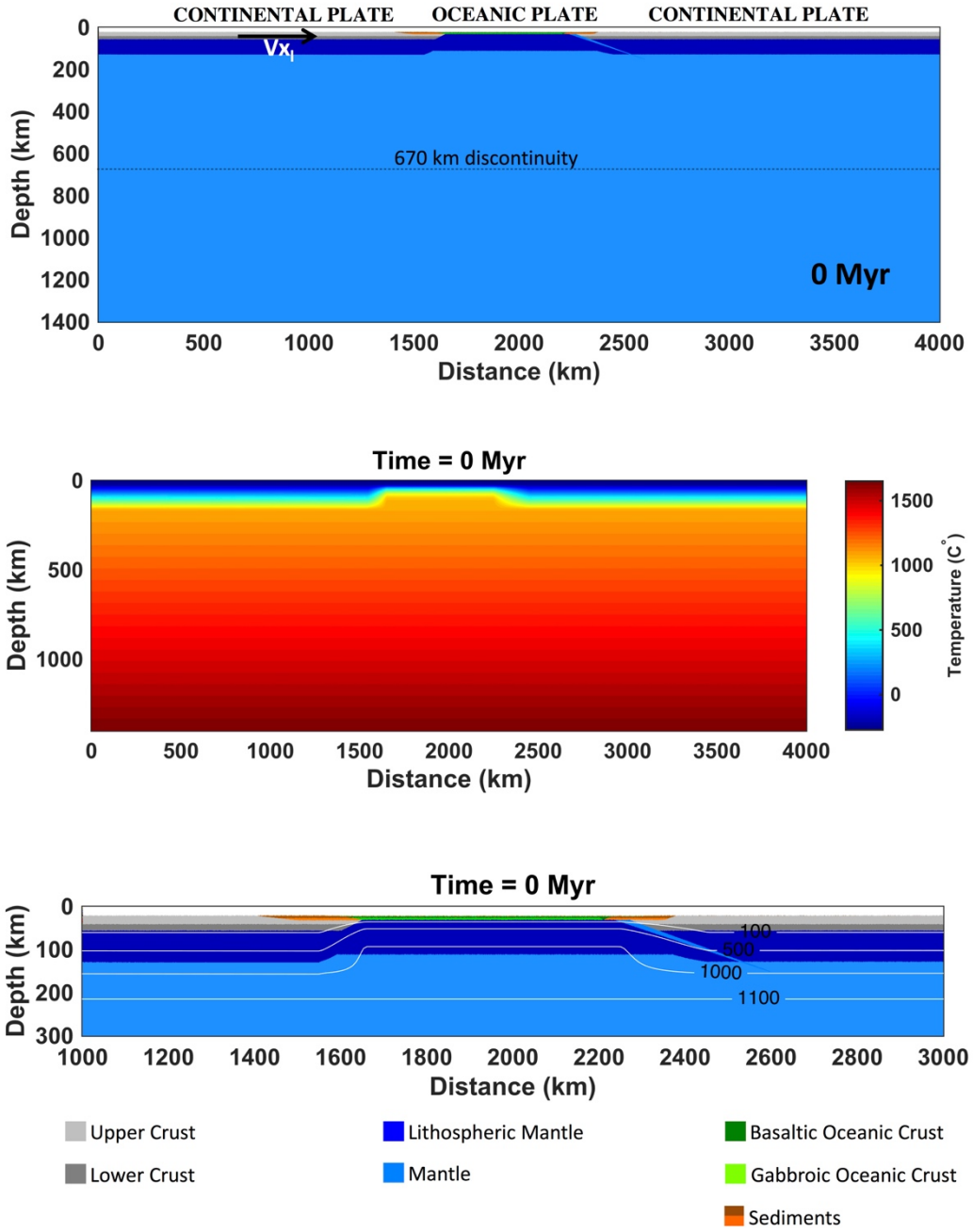

Figure 2.2 - Model setup. The top panel shows the initial composition of the entire domain (see the bottom panel for correspondence with materials). The black arrow within the lithosphere shows the convergence direction of the lower subducting plate. Plate convergence rate of 5 cm yr-1 is applied at 1000 km for 6 Myr to initialize the subduction process. The dashed line points to the 670 km discontinuity. The middle panel shows the initial temperature of the domain. In the bottom panel isotherms are the white lines. The light blue line in the lower panel (between the oceanic, lower plate and the upper continental right plate) is the weak zone. Color code for different materials is shown at the bottom of the figure.

Material	k (W/m/K)	H_r (W/m^3)	Cp (J/kg)	sin(ϕ)	C (MPa)	Flow Law	η_0 (Pa^n s)	n	λ
Sediments	$0.64+\frac{807}{T+77}$	1.5×10^{-6}	1000	0.150	1	Wet Qz.	1.97×10^{17}	2.3	1.00
Upper cont. crust	$0.64+\frac{807}{T+77}$	1.00×10^{-6}	1000	0.150	1	Wet Qz.	1.97×10^{17}	2.3	1.00
Lower cont. crust	$1.18+\frac{474}{T+77}$	0.25×10^{-6}	1000	0.150	1	Pl. (An75)	4.80×10^{22}	3.2	1.00
Upper oceanic crust	$0.64+\frac{807}{T+77}$	0.25×10^{-6}	1000	0.000	1	Wet Qz.	1.97×10^{17}	2.3	1.00
Lower oceanic crust	$1.18+\frac{474}{T+77}$	0.25×10^{-6}	1000	0.600	1	Pl. (An75)	4.80×10^{22}	3.2	1.00
Low Velocity Zone	$0.73+\frac{1293}{T+77}$	2.20×10^{-8}	1000	0.600	1	Dry Ol.	3.98×10^{18}*	3.5	1.00
Mantle	$0.73+\frac{1293}{T+77}$	2.20×10^{-8}	1000	0.600	1	Dry Ol.	3.98×10^{16}	3.5	1.00
Weak Zone	$0.73+\frac{1293}{T+77}$	2.20×10^{-8}	1000	0.000	1	Wet Ol.	5.01×10^{20}	4.0	1.00

Table 2.1 – Rheological (Ranalli, 1995) and thermal (Clauser & Huenges, 1995) parameters of materials used for the experiments. * $\eta_0 = \eta_{eff}$

2.2.3 Boundary conditions

For all models presented in this Chapter, the boundary conditions are set to be periodic on the left and right boundaries, while a free slip condition is applied at the top and the bottom of the computational domain. A free slip condition requires that the normal velocity component on the boundary is set to zero whereas the tangential component do not change across the boundary. This condition also implies zero shear strain rates and stresses along the boundary. The free slip condition at the top and bottom boundaries is then defined as follows:

$$v_y = 0; \tag{2.13}$$

$$\frac{\partial vx}{dy} = 0\ . \tag{2.14}$$

Additionally, a 10–km–thick layer of "sticky air" (ρ_{air} = 1 kg/m^3, η_{air} = 10^{18} Pa s) was employed to mimic the effect of a free surface and the development of topography (Crameri et al., 2012). To simulate a polarized troughgoing asthenospheric mantle flow, periodic boundary conditions are set on the left and right boundaries by discretizing the fundamental equations across the boundaries and by prescribing the horizontal velocity (v_x) and the temperature (T) unknowns on both sides of each boundary as identical. From a physical point of view, this implies that these two boundaries are open and that flow leaving the model through one boundary immediately re-enters through the opposite side. This condition is often used in mantle convection modeling to simulate part of a cylindrical shell domain, or mimic it, in Cartesian coordinates (Dal Zilio et al., 2017), and is formulated as follows:

$$v_{x_{(N-1)}} = v_{x_{(1)}}\ ; \tag{2.15}$$

$$T_{(N-1)} = T_{(1)} \,, \tag{2.16}$$

where N is the number of nodes. Periodic boundary conditions at the right boundary was combined with prescribed horizontal velocity at the left boundary: zero horizontal velocity was prescribed for the lithosphere, whereas constant inflow/outflow horizontal velocity condition was applied for the entire asthenosphere (Figure 2.3). To evaluate the role of mantle flow velocity we conducted numerical experiments with mantle wind rates covering the full spectrum from -3 to +3 cm/yr (Table 2.2).

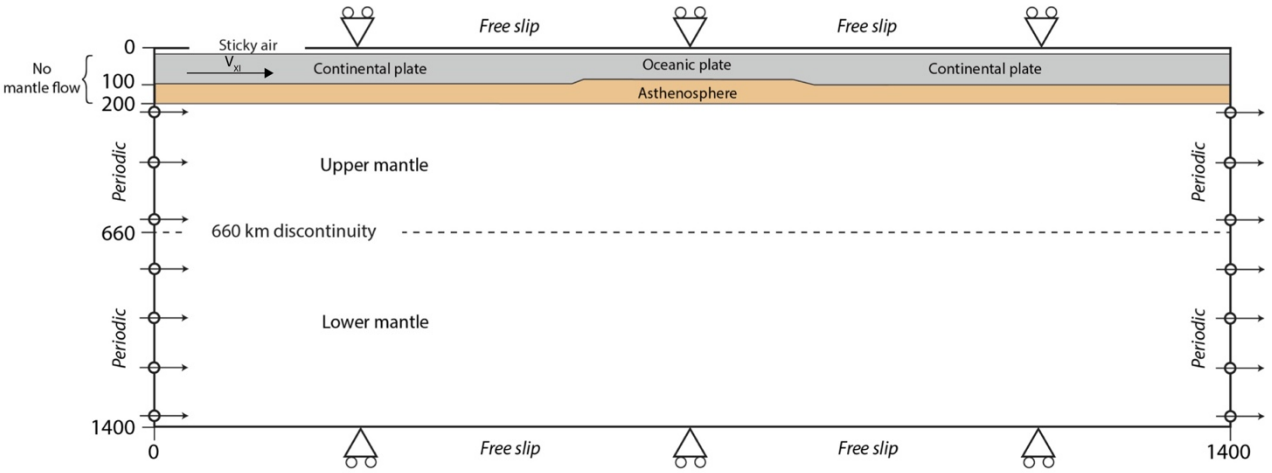

Figure 2.3 - Schematic model setup used for standard 2D experiments in Cartesian geometry and mechanical boundary conditions. The black arrow within the lithosphere shows the convergence direction of the lower subducting plate. Plate convergence rate of 5 cm yr-1 is applied at 1000 km for 6 Myr to initialize the subduction process. In grey the lithosphere, in orange the LVZ, the dashed line is the 670 km discontinuity. Free slip boundary conditions are applied to the top and bottom of the numerical domain, whereas periodic boundary conditions are applied to the right and left side of it.

2.3 Results

The use of mantle wind, in conjunction with a weak asthenospheric layer, produce sustained asymmetric subduction for most of models run in this study (see also Appendix A Figures A.1–A.6 and Appendix A Table A.1). The temporal evolution of two end-member models, one with discordant mantle flow and one with concordant mantle flow with respect to the subduction polarity, validate the defining features of the evolution of all models. In the following sections we describe our end-member models, divided by direction of the mantle flow with respect to the subduction polarity (Figure 2.4).

2.3.1 Models with discordant mantle flow and subduction polarity

Results from a model simulating an "eastward" mantle flow imposed against a "westward" directed subduction (Figure 2.4a) show a sub-vertical slab. Subduction initiates via slip along the interplate weak zone (see Figures 2.2 and 2.3 for further details on the model setup). As some of the initial plate boundary interface material gets subducted, it is replenished by material from the upper layer of the subducting plate, and the hinge begins to retreat. Before the slab tip flattens in the transition zone, the slab is pushed backwards and downwards by the flow. The hinge continues to retreat, allowing the spontaneous formation of backarc extension at a distinct location with respect to the trench, and causing an uplift of the asthenospheric mantle. The subduction hinge moves away from the upper plate and subduction rates are faster than the convergence rates (Doglioni et al., 2007), leading to a faster recycling of the lithosphere into the mantle (Doglioni & Anderson, 2015). Hinge retreat correlates with the intensity of the mantle wind, regardless of subducting plate strength or age-dependent density. Age variations of the subducting oceanic plate have indeed negligible effects on subduction dynamics (Appendix A Table A.1), thus suggesting that mantle wind intensity is a more critical subduction parameter compared to the slab age.

During incipient collision, a large volume of weak crustal material is interposed between the plates. The negative pressure gradient caused by mantle flow and dense retreating slab favor sucking of the mantle into the accretionary prism. As collision proceeds, the rheologically weak part of the crust is scraped off from the retreating lithosphere by the mantle wedge above the subducting slab that acts as a backstop moving in the opposite direction to convergence.

2.3.2 Models with concordant mantle flow and subduction polarity

Numerical results from the model simulating an "eastward" mantle flow interacting with an "eastward" directed subduction are strikingly different (Figure 2.4b); the "eastward" mantle flow holds the subducting slab up, thus resulting in a less steep dip angle and a shallower depth of the slab itself. In this case the subduction hinge is moving toward the upper plate, which is set under compression, and the subduction rates are slower than the convergence rates (Doglioni et al., 2007). The strong correlation between topography and slab dip angle with corresponding variations in mantle flow direction suggests a strong relationship with the underlying subduction dynamics. This should be the reason why this kind of subductions is correlated with the highest mountain ranges (i.e., the Andes, the Cascade Range, the Alps etc.). It is worth noting that the shallow subduction also

produces slower recycling of the oceanic lithosphere into the mantle (Doglioni & Anderson, 2015). As in the previous model, the age of the subducting plate has subordinate effects on subduction dynamics: low dip angle can be reached either by younger and older oceanic plates, despite having different values of activation volume and isobaric thermal expansion (Table 2.2). The persistence of a mantle flow is therefore crucial to determine the dip angle of the slab and the state of stress within the upper plate. At the onset of collision, the buoyancy of the continental crust slows down the convergence rate. As collision continues, crustal material is accreted at the margin, raising the topography and thus building up the compressional stresses within the upper plate. The final structure is that of a narrow and thick collisional zone delimitated by a shallow-dipping slab and characterized by diffuse deformation.

These results thus suggest that when these heterogeneities (that are, concordant mantle wind and a weak asthenospheric layer) are combined in a single model, the dynamics of the subducting plate and the topography evolution of the overriding plate can all be reconciled.

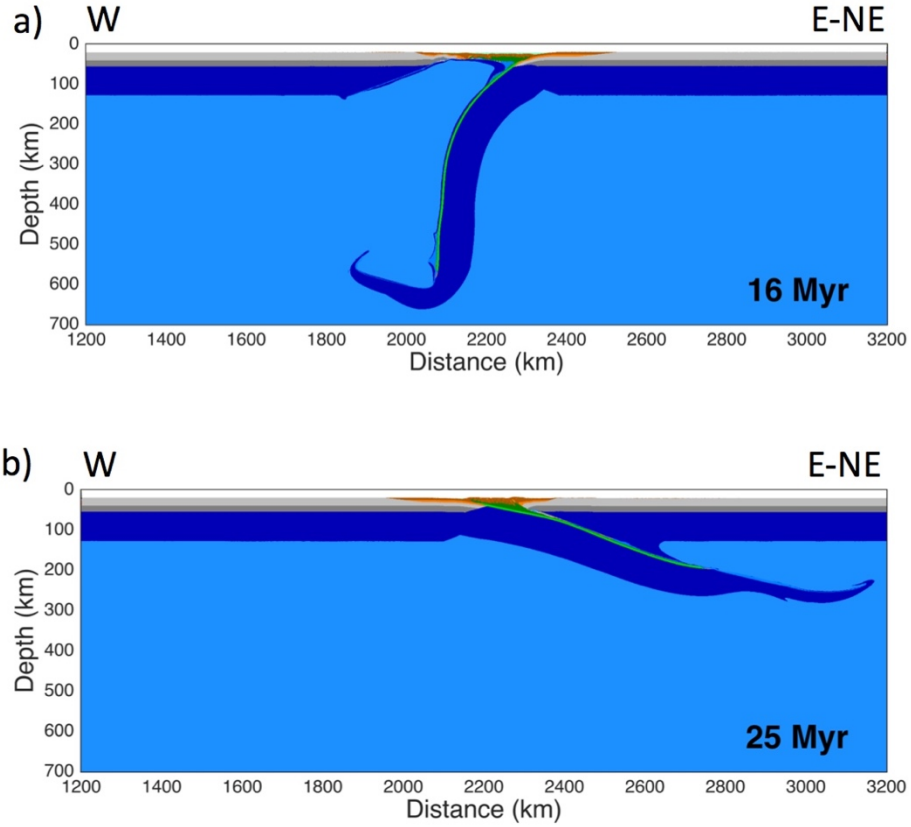

Figure 2.4 – Results. Panel (**a**) shows a W-directed slab. All numerical models present pre-defined rightward subduction polarity; therefore this model was mirrored for better comparison with nature. In panel (**b**) a slab along E or NE-subduction zone is designed. In each model a horizontal mantle flow is imposed, having concordant or opposite direction with respect to the subduction polarity. The difference in dip of the slab is striking: the "westerly" dipping slab is steeper and deeper, whereas "easterly or northeasterly" dipping slab is shallower and less steep. The difference is also remarkable comparing backarc spreading or not: in fact this latter only occurs in "westwardly" directed slab model (**a**). See Figure 2.2 for the color legend

Results demonstrate that symmetric changes in the mantle wind direction have an impact on the total force propagated to the upper plate and influences the plate motions, dips and vertical stresses, reflected as a topographic high in the overriding plate.

Model	V_a (J/bar)	α (1/K)	Low Velocity Zone	Mantle Flow Direction	Mantle Flow Velocity (cm/yr)	Slab Dip Angle (°)	Back-arc spreading	Oceanic plate age (Myr)
a	1.20	2.00×10^{-5}	Yes	Negative	3.00	74	Yes	20
b	1.20	2.00×10^{-5}	Yes	Positive	3.00	17.5	No	40

Table 2.2 - Conditions and results of 2D numerical models. Slabs dip of 74° was found for the W-directed slab, while the dip found for the E-directed slab was 17.5°, for models in Fig. 2.4

2.4 Discussion

Our numerical models suggest that the dip of the slab consistently changes as a function of intensity of the mantle wind, whereas the presence or absence of the LVZ plays only a collateral role (Appendix A Figures A.3-A.4). This is confirmed by the fact that in our models, negative buoyancy does not influence the slab dip angle and the density contrast between the lithosphere and the hosting mantle is about 35-40 kg/m^3 on average (for example, in Figure 2.4a) (Afonso et al., 2007; van Keken et al., 2011). The resulting dip angle associated to a horizontal mantle flow mimics the natural data, providing a different clue to explain the global asymmetry of slab dip. Comparing our numerical experiments with a global compilation of slab dips (Figure 2.5) measured along cross-sections perpendicular to respective trenches (Riguzzi et al., 2010), a good fit can be obtained, assuming a mantle flow intensity of 3 cm/yr. Dip angle of our "westward" directed slab lies indeed within the average of the W-directed subduction zones worldwide (being ~73.7° the average dip angle for our "westward" directed slab, Figure 2.5). Following the same line of reasoning, our "eastward" directed slab (being its dip angle ~17.5°, Figure 2.5) correlates remarkably with the average dip of slabs along E to NE-subduction zones. The catalogue in Figure 2.5 includes several sections for western and eastern sides of the Pacific Ocean, ranging from 55N to 40S latitude degrees and from 50N to 22S latitude degrees, respectively. These can be used as representative for W- and E- to NE-directed subduction zones spread out in opposite Pacific Ocean sides. Also, looking at tomography (Fukao & Obayashi, 2014; Zhao et al., 2017) (considering the segment of the slab on which seismicity is plotted) and other seismicity data (Cahill & Isacks, 1992; Fischer et al., 1991; McCrory et al., 2012), a quite good correlation between slab dip and subduction polarity can be observed. Exceptions are for northern-Japan, the Aegean Sea, Java and central America, these latter two being more likely related to the obliquity of the slab direction with respect to the main convergence direction. The northern-

Japan setting is peculiar because the subduction hinge is now converging relative to the upper Eurasian plate, hence inverting the previous slab retreat relative to the upper plate and the contemporaneous opening of the Japan Sea (Doglioni et al., 2007).

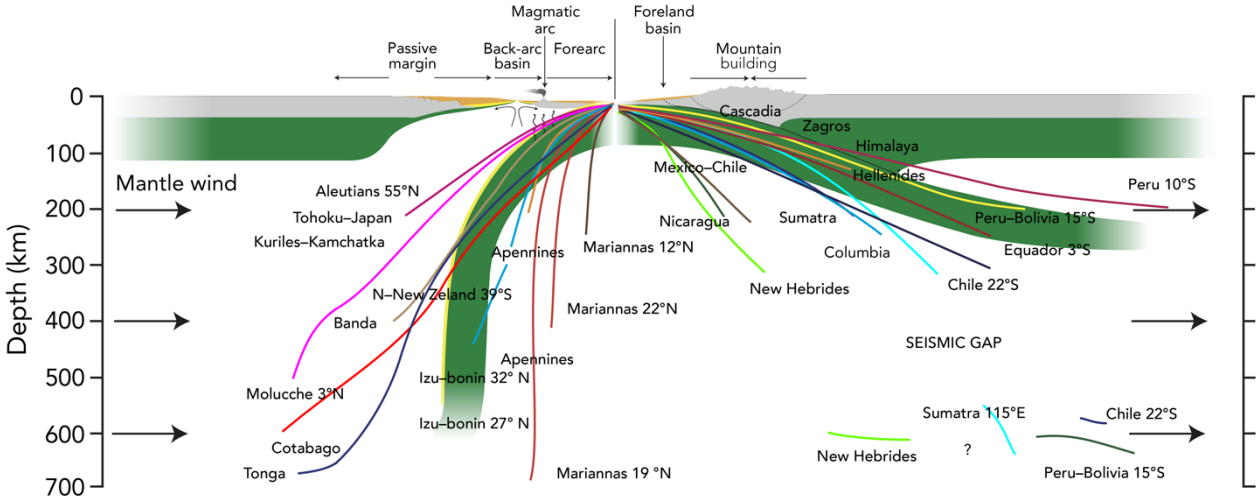

Figure 2.5 - This picture shows our two models (in green), compared with a compilation of the slab dip measured along cross-sections perpendicular to the trench of most subduction zones. Each line represents the mean trace of the seismicity along every subduction. Some E- or NE-subduction zones present a deeper scattered cluster of hypocentres between 550–670 km. Dominant down-dip compression occurs in the W-directed intraslab seismicity, whereas down-dip extension prevails along the opposed E- or NE-directed slabs. The W-directed slabs are, on average, dipping 65.6°, whereas the average dip of the E- or NE-directed slabs, to the right, is 27.1° (modified after Riguzzi et al., 2010). In our models the dip of the slab fits within this average by assuming intensity of the horizontal mantle flow of 3 cm/yr. In this figure the differences in topography and state of stress between the upper plates of both models can be seen.

Although a possible link between slab dip, deformation of the overriding plate and trench motion has been already proposed (Schellart, 2007; Tao & O'Connell, 1992), our results could be useful to explain some of the different features between Andean- and Mariana-type subductions in a different way. In the past (Tao & O'Connell, 1992), differences between these two subduction types were explained by ablation extent during subduction process. In our conceptual and numerical models, the absence of crustal shortening in Mariana-type subductions should be due to the backarc basin opening, as a consequence of the slab rollback associated to the retreat of the subduction hinge relative to the upper plate, and shallow décollement levels determine mostly thin skinned tectonics. In such settings most of the crust and the lithospheric mantle are completely subducted instead of being involved in the accretionary prism building. In the opposite subduction setting, the slab hinge converges relative to the upper plate and the deep décollement levels allow involvement of rocks coming from a higher depth in orogens building. Some authors (Lallemand et al., 2005; Schellart, 2007), then, used seismicity data coming from deeper and shallower parts of the slab, separately, to study relations between slab dip and subduction direction. However, it is important to notice that splitting a slab in a shallow and a deep part of it could be misleading: 1) in subduction zones where there is a continental upper crust (approximately all E- to NE-directed), the behaviour of the first 125

km is mostly influenced by the thickness of the lithosphere and by the slab angle with respect to convergence direction. Slab dip might not even show such a different dip in its shallow part because of the presence of the décollement level (LVZ, considered in our numerical models), located between a 100 and 200 km depth. However, regional monocline dip reveals the same asymmetry between W-directed an E- to NE-directed subduction zones (Doglioni et al., 1999). 2) Seismicity below W-directed and E- to NE-directed subduction zones is quite different: E- to NE-directed subduction zones have a seismic gap between 250-300 km and a 500 km depth, and seismic isolated events at deeper depth origin are still unclear (Doglioni, 2008).

Another issue that should be considered when evaluating relationship between subduction zones direction and slab dip, is that most of subductions worldwide show an arcuate geometry (Doglioni, 2008; Schellart et al., 2011); therefore slabs could form different angles with subduction direction and, consequently, they have different dip angles according to their obliquity with respect to the main convergence direction. 3D modeling may be necessary to properly model these arcuate subduction zones. Furthermore, some works (Schellart, 2007) consider trench-perpendicular migration velocities but, doing this, an assumption is made: in fact, when having an oblique trench with respect to subduction direction the hinge moves obliquely too, due to stress deviation from the convergence direction and strain partitioning. Moreover, hinge velocity cannot be measured in a precise way, especially when calculated with respect to the mantle (Doglioni, 2008).

However, here we analyse the possibility that a global feature –such as the mantle wind– could be the first-order controlling parameter of slab dip and stress regime within the upper plate (Doglioni, 2008). Our results show a backarc basin opening only in models with "westward" directed slabs, as it can be seen along W-directed subduction zones worldwide (i.e., Appenines, Marianas, Tonga-Kermadec, Sandwich etc.). This opening could thus be critically related to the slab rollback, due to the push exerted from the "eastward" mantle flow on a "westward" directed subducting slab. In fact, it has to be considered that extension within the overriding plate, in the two subduction end-members, has different geologic origins: along W-directed subduction zones, backarc spreading occurs as a consequence of slab rollback and of the asthenospheric replacement for the retreated lithosphere (as it can be seen also from our W-directed subduction model), whereas for E-NE-directed subductions backarc basins open in few places where the upper plate lithosphere is split into two sub-plates that have different velocity with respect to the same lower plate (Doglioni et al., 2007). Moreover, the first one are characterized by fast backarc opening, widely distributed throughout the upper plate and eventually arriving to oceanization (e.g., the Western Mediterranean) whereas, in the second one, extension within the upper plate is confined in areas close to the transfer zones (e.g., the Aegean Sea) and rarely reaching the oceanization stage (e.g., the Andaman Sea).

2.5 Conclusions

Our experiments suggest, thus, that the existence of a predominantly “eastward” horizontal mantle flow (along the so-called, undulated, tectonic equator) may explain several contrasting characteristics of subduction zones worldwide. The subduction of the Nazca plate beneath the Andes provides a key test for this analysis. In fact, in the kinematic model of a slow net rotation of the lithosphere driven only by the slab negative buoyancy, beneath the Nazca plate and the slab of the south America cordillera, the mantle flow should be westerly directed, providing a steep slab. However, as shown in the numerical modeling presented here, the shallow dip of the Andean slab is consistent with an eastward mantle flow even beneath the Nazca plate as evident by shear wave splitting results (Russo & Silver, 1994) and providing indirect support for the fast lithospheric rotation rates relative to the mantle (Crespi et al., 2007).

While geophysical constraints support the hypothesis of an E-directed mantle flow over at least the last 100 Myr (Doglioni & Panza, 2015), how mantle structure and kinematics may have behaved in the geological past is still unclear. One possible explanation is that the lithosphere is sheared “westward” relative to the asthenospheric mantle, along the mainstream of plate motions in which W-directed subduction zones contribute to a three times larger fraction of global lithospheric recycling, compared to E- and NE-directed subduction zones (Doglioni & Anderson, 2015). As a result, a larger fraction of the asthenospheric mantle material has to move to the east, thus creating a global mantle wind. However, understanding of physical origin and distribution of the horizontal mantle flow requires self-consistent global mantle convection and plate tectonics modeling (Crameri et al., 2012) and remains as a challenge for future research.

Chapter 3

Asymmetric dynamics at subduction zones derived from plate kinematic constraints

Computing the volume of lithosphere recycled within the mantle by subducting slabs quantifies the equivalent amount of mantle that should be displaced, for the mass conservation criterion. The rate of subduction is constrained by the convergence rate between upper and lower plates and the motion of the subduction hinge H that may either converge or diverge relative to the upper plate. See Section 1.3.1 for an extensive discussion about the importance of the subduction hinge. Here, starting from the analysis of the slab hinge kinematics, we evaluate the subduction rate at subduction zones worldwide, useful to compute volumes of sinking lithosphere into the mantle. Our results show that ~190 km^3/yr and ~91 km^3/yr of lithospheric slabs are currently subducting below H-divergent and H-convergent subduction zones, respectively. We also propose supporting numerical models providing asymmetric volumes of subducted lithosphere, using the subduction rate instead of plate convergence, as boundary condition. Furthermore, H-divergent subduction zones appears to be coincident with subductions having "westward"-directed slabs, whereas H-convergent are compatible with those that have "eastward-to-northeastward"-directed slabs. On the basis of this geographical polarity, our lithospheric volume estimation gives ~214 km^3/yr and ~91 km^3/yr of subducting lithosphere, respectively. This entails that W-directed subduction zones contribute more than twice in lithospheric sinking into the mantle with respect to E-to-NE-directed ones. In accordance with the conservation of mass principle, this volumetric asymmetry in the mantle suggests a displacement of ~120 km^3/yr of mantle material from west to east, which is a first order component that we expect in global mantle convection, providing a constraint for a global asymmetric mantle convection.

3.1 Introduction

Subduction zones dynamics and the evolution of the lithosphere-mantle system at convergent margins have been thoroughly investigated in the last decades by the scientific community (Capitanio et al., 2010; Coltice et al., 2017; Conrad & Hager, 1999; Jarrard, 1986). Several parameters seem to influence subduction zones behaviour and different models have been invoked to explain the initiation of the slab sinking, as well as the driving forces of plate tectonics and related mantle convection (Carcaterra & Doglioni, 2018; Faccenna et al., 2001; Forsyth & Uyeda, 1975; Garfunkel et al., 1986). However, regardless the origins and driving mechanisms for plate tectonics, it is generally accepted that subduction zones dynamics is strongly affected by the motion of the trench (Doglioni et al., 2007; Heuret & Lallemand, 2005; Schellart & Rawlinson, 2013).

In this Chapter, we compute the volumes of subducting lithosphere at subduction zones worldwide (Figure 3.1), taking into account the different subduction hinge kinematics, also improving the study of Doglioni and Anderson (2015). Indeed, relative to the fixed upper plate, the slab hinge can move either towards the lower plate (e.g., Marianas, Tonga-Kermadec or Sandwich subduction zones, etc.) or towards the upper plate (e.g., South America, Cascadia or Burma-Sumatra subduction zones, etc.) (Figure 1.10).

For every subduction zones, we collected a data set including the velocities of the lower plate and the subduction hinge, from which we derived the subduction rate; also, we computed the length of each subduction trench (Figures 3.3-3.5 and Tables 3.1-3.7). Finally, to support our analysis, we included these results in numerical models of subducting lithosphere, for both the end-member cases, using the subduction rate instead of plate convergence, as boundary condition, and considering or not the influence of the Low Velocity Zone (LVZ).

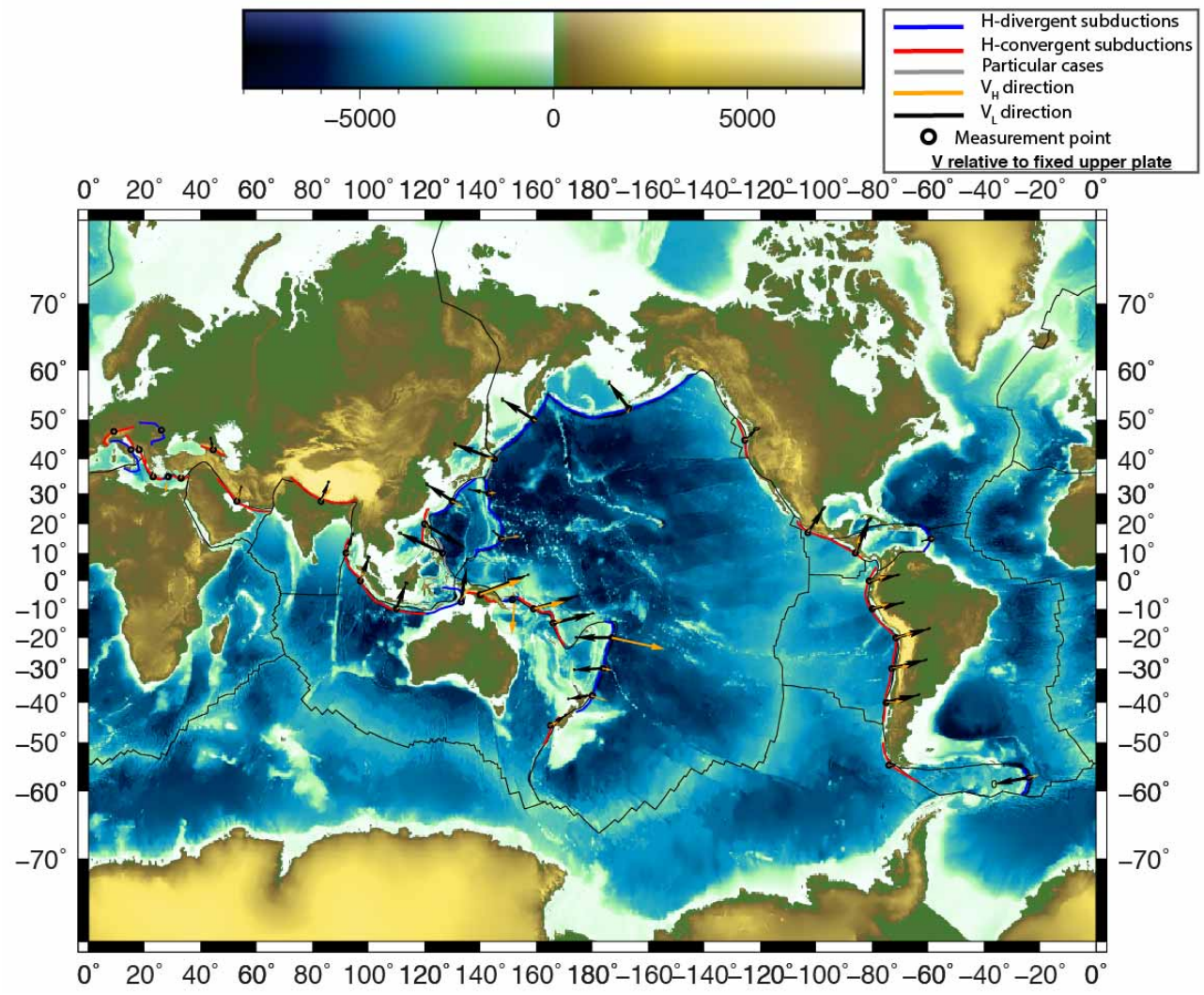

Figure 3.1 - Analyzed subduction zones. In red are H-convergent subduction zones, whereas in blue are H-divergent ones. Subductions marked by gray lines are the two outliers of our dataset such as the Philippines and Northern-Japan subduction zones. Empty circles are the point where plate velocities were computed at each subduction zone. Black arrows show the average direction of the lower plates. Orange arrows show the direction of the subduction hinge. Velocities are computed relative to the upper plate, taken as fixed.

3.2 Geodynamic model

To compute volumes of lithosphere currently subducting below the principal subduction zones, we considered their kinematics in a reference frame with three points, one attached to the upper plate U, a second attached to the lower plate L, and the third on the subduction hinge H. The point U located on the upper plate is taken as fixed, i.e., its velocity $V_U = 0$. The motion of the two remaining points is thus considered relative to the fixed upper plate, so that V_L is the velocity of the lower plate and V_H is the velocity of the hinge (Figure 1.10).

We calculated the lithospheric volume LV using the relation:

$$LV = l\ V_S\ d, \tag{3.1}$$

where l is the length of the trench, d is the thickness of the slab, which is assumed to be 100 km for each subduction zone, whereas V_S corresponds to the subduction rate. This velocity is defined as the rate at which the subducting lithosphere enters the subduction zone and can be calculated with the formula (1.1), already mentioned in Chapter 1 (Doglioni et al., 2007). When using the equation (1.1), observations of V_H present many uncertainties principally related to the exact location of the subduction hinge. This is due to the wide area in which the hinge could be located from the horizontal lower plate to the inclined downgoing slab. Thus, V_H values at subduction zones were investigated using GPS data, previously published in literature. In very few cases, the motion of the hinge zone was inferred from the state of stress within the upper plate (Lallemand et al., 2005; Parson & Wright, 1996). However, for an extensive discussion about the subduction hinge the reader is referred to Section 1.3.1 of this dissertation. Conversely, V_L was derived from current plate motions models (DeMets et al., 2010) and, in some cases, from GPS data (Devoti et al., 2008; Doglioni et al., 2007; Mason et al., 1998). A detailed description of measured and computed kinematic parameters is given below and in Tables 3.1-3.7.

3.3 Geodynamic and kinematic analysis

3.3.1 Rationale

The following section includes description of data, used parameters and references taken into account for our computations. For an amount of 31 analyzed subduction zones (Tables 3.1-3.7), V_L was estimated from plate kinematic models (DeMets et al., 2010) in the 90% of the cases, whereas we had to refer to literature (Devoti et al., 2008; Doglioni et al, 2007; Mason, 1998) for the 10% of the subduction zones. The 95% of the hinge data were estimated on the basis of GPS data taken from literature, whereas only 5% were taken in other forms (i.e., state of stress of the upper plate, from Lallemand et al., 2005; Parson & Wright, 1996). In the next section, we show in detail our analysis, starting from H-convergent subduction zones, moving on to H-divergent subduction zones, and concluding with outliers, representing the 52%, 42%, and 6%, of the analyzed database.

However, a detailed recap of all the following data is available in Tables 3.1-3.7. All data are computed in correspondence, or close, to points illustrated in Figure 3.1 and in Table 3.7, collected every 10° of latitude. For longer subduction zones (i.e., South America, Indonesia, Central America, Tonga-Kermadec and Izu Bonin-Marianas), averaged parameters are considered, as they were

calculated at several reference points (Figure 3.1 and Table 3.7).

Measurement Points		
Subduction	Latitude Degrees	Longitude Degrees
S-America	0.00	– 81.00
	– 10.00	– 80.50
	– 20.00	– 71.50
	– 30.00	– 73.00
	– 40.00	– 75.50
	– 55.00	– 73.50
Indonesia	10.00	92.00
	0.00	97.00
	– 10.00	108.00
Central America	10.00	– 86.00
	17.00	– 103.00
Taiwan	20.00	120.00
New Hebrides-Vanuatu Islands	– 15.00	166.00
Cascadia	45.00	– 125.50
S-New Zealand	– 46.00	165.00
Himalaya	27.50	83.00
Zagros	27.50	53.00
Solomon Islands	– 10.00	159.00
Papua-New Guinea	– 2.50	144.00
Caucasus	42.50	44.50
Dinarides	42.50	18.00
Hellenides	35.00	23.00
Cyprus	35.00	33.00
Alps	47.20	9.00
Tonga-Kermadec	– 20.00	– 173.00
	– 30.00	– 176.00
Banda Arc	– 5.00	133.50
Aleutians	52.50	– 167.00
Izu-Bonin-Marianas	15.00	147.50
	30.00	143.50
Ryukyu-Japan	27.50	130.00
Kuril-Kamchatka	50.00	159.00
New Britain	– 6.50	151.50
New Scotia-Sandwich	– 57.50	– 24.00
N-New Zealand	– 38.00	179.00
Caribbean	15.00	– 59.00
Crete	35.00	28.00
Apennines	42.50	15.00
Carpathians	47.50	26.00
N-Japan	40.00	145.00
Philippines	10.00	126.50

Table 3.1 - Measurement points. All kinematics data were collected and/or calculated on or close to these points for each subduction zone.

3.3.2 Geological and kinematic data

The following correspond the H-convergent subduction zones ordered for decreasing computed volumes (summary in Tables 3.2-3.3).

South America, is one of the most extensive subduction zone in the world, when considering the range of latitude. It goes from 5°N to about 60°S, for a total length of about 7060 km. Plate kinematics related to this subduction zone involve Nazca moving and South America fixed (from 4°S to 45°S) and Antarctica moving and Scotia fixed (from 52°S to 58°S) (DeMets et al., 2010; Hayes et al., 2012). The average V_L is of about 59.5 mm/yr (DeMets et al., 2010) and it is differently distributed along the entire subduction length. Indeed, velocity decreases toward the south (e.g., Liu et al., 2000; Doglioni et al., 2007; Mora-Paez et al., 2018; Smalley et al., 2007). Data from Liu et al., (2000) was used for points corresponding to the latitude interval ranging from 10°S to 40°S whereas, for the Equator point at latitude 0° and the 55° latitude point, GPS data provided by Mora-Páez et al. (2018) and Smalley et al. (2007) respectively were used. V_H for this subduction zone has an average value of -31.6 mm/yr. Average V_S value is about 27.9 mm/yr, computed with equation (3.2), whereas LV, obtained with equation (3.1) is about 18.9 km^3/yr.

The Indonesian subduction zone is the second for extension worldwide. In fact, it has a length of about 4811 km, from 15°N to about 10°S and could be divided in three major segments (i.e., Andaman, Sumatra and Java). Plates involved in the different segments are India moving and Sunda fixed (from 15°N to 2°N); Capricorn moving and Sunda fixed (from 2°N to 12°S) (DeMets et al., 2010; Hayes et al., 2012). For this subduction zone, average V_L is about 40.1 mm/yr (DeMets et al., 2010). V_H (on average -19.1 mm/yr) values were considered from literature as GPS data (Koulali et al., 2017; Michel et al., 2001; Yong et al., 2017). Average V_S and total LV, obtained using equation (3.2) and (3.1), respectively, are about 34.4 mm/yr and 17.1 km^3/yr.

Central America subduction zone extends from about latitude 10°N to about 20°N, for a total length of 2986 km. Tectonic plates involved in this subduction zone are Cocos moving and Caribbean fixed (from 8°N to 15°N); Cocos moving and North America fixed (from 15°N to 21°N) (DeMets et al., 2010; Hayes et al., 2012). Average V_L has a value of about 69.2 mm/yr (DeMets et al., 2010), whereas average V_H, in this area, should be of about -18.5 mm/yr, obtained using GPS data (Márquez-Azúa & DeMets, 2003; Outerbridge et al., 2010). Having these values, an average V_S of 50.7 mm/yr and a total LV of 15 km^3/yr are easily derived from equations (3.2) and (3.1).

The Taiwan subduction zone is located northward with respect to Philippines Islands, between 25°N and 15°N, for a total length of about 1476 km. Plates that take part to the subduction process here are Sunda moving and Philippine Sea fixed (DeMets et al., 2010). V_L used for our calculation here is 93.9

mm/yr (DeMets et al., 2010). V_H of -2.70 mm/yr was taken from GPS data (Hsu et al., 2012), V_S, obtained using equations (3.2), is of 91.2 mm/yr whereas LV, from equation (3.1) is 13.5 km^3/yr.

New Hebrides-Vanuatu Islands are part of a 1951 km long subduction zone that falls in a range of latitude that goes from about 20°S to about 10°S. Plates involved in this subduction are Australia moving and Pacific fixed (DeMets et al., 2010; Hayes et al., 2012). V_L in this zone is 88.4 mm/yr (DeMets et al., 2010) and, together with a V_H of -32.7 mm/yr (GPS data from Calmant et al., 2003), were used to calculate V_S value with equation (3.2), that results being of 55.7 mm/yr. The resulting LV, from equation (3.1), is of 10.9 km^3/yr.

Cascadia subduction zone extends for about 1083 km, covering a range of latitude that goes from 40°N to 50°N. Plates involved in subduction process are Juan de Fuca moving and North America fixed (DeMets et al., 2010; Hayes et al., 2012). V_L from plates velocity calculator (DeMets et al., 2010) has a value of 35 mm/yr. V_H is -6.7 mm/yr at the trench and it decreases to zero toward the inner upper plate, taken as fixed (Krogstad et al., 2016). With these two parameters, then, we could estimate V_S, with equation (3.2), that has a value of 28.2 mm/yr. LV, then, calculated with equation (3.1), is 3.1 km^3/yr.

Southern New Zealand subduction zone extends within a latitude range of about 40°S-50°S, for a total length of about 1243 km. Plates involved in this subduction zone are Australia moving and Pacific fixed (DeMets et al., 2010). V_L measured (DeMets et al., 2010) is 38.8 mm/yr and was used, together with a V_H of -15 mm/yr (GPS data from Beavan et al., 2016), to calculate V_S with equation (3.2), that results having a value of 23.8 mm/yr. LV, obtained here from equation (3.1), is 3 km^3/yr.

Himalaya subduction zone (now collision zone) is about 2596 km long and it extends from a latitude of 25°N to a latitude of 35°N. Plates playing a role in this tectonic area are India moving and Eurasia fixed (DeMets et al., 2010). V_L is 44.2 mm/yr (DeMets et al., 2010), whereas V_H, estimated from GPS data (Jade et al., 2017) is -34.4 mm/yr. V_S has a calculated value of 9.8 mm/yr, from equation (3.2), whereas LV has a value of 2.5 km^3/yr, calculated from equation (3.1).

Zagros subduction zone extends from a latitude of about 25°N to 35°N for a total length of about 2516 km. Plates involved in this zone are Arabia moving and Eurasia fixed (DeMets et al., 2010). V_L is 31.5 mm/yr (DeMets et al., 2010) and V_H is -22.5, taken from GPS data (Walters et al., 2017). With all these numbers, we obtained a V_S value of 9 mm/yr, with equation (3.2), and LV found using equation (3.1) is 2.3 km^3/yr.

Solomon Islands subduction zone length reaches a value of about 1161 km, extending from 10°S to 5°S. Plates involved in the subduction process are the Australia moving and the Pacific fixed (DeMets et al., 2010; Hayes et al., 2012). Measured V_L is 97.1 mm/yr (DeMets et al., 2010) and V_H has a value

of -84 mm/yr (GPS data from Kuo et al., 2016). V_S, obtained from equation (3.2), is 12.7 mm/yr, whereas LV, calculated with equation (3.1) is 1.5 km^3/yr.

Papua-New Guinea subduction zone length is of approximately 1293 km, extending from a latitude of about 7°S to 5°N. Plates playing a role in this subduction zone are Australia moving and Pacific fixed (DeMets et al., 2010). Plate motions calculator (DeMets et al., 2010) shows a V_L velocity in this area of 108.7 mm/yr. V_H in this area, from GPS data (Koulali et al., 2015), is found to be -100.1 mm/yr. V_S, obtained using equation (3.2), is 8.6 mm/yr, whereas, with equation (3.1), LV was found to have a value of 1.1 km^3/yr.

Caucasus is a complex subduction zone that is placed within a latitude of 40°N and 45°N and it extends for a total length of 763 km. It is located within a zone of wide continental collision, between the still converging Arabian plate moving and Eurasian fixed. V_L here is 25.3 mm/yr (DeMets et al., 2010). V_H (GPS data from Ahadov and Jin, 2017) is -11.4 mm/yr. V_S obtained from equation (3.2) is 13.9 mm/yr whereas LV, from equation (3.1), is 1.1 km^3/yr.

Dinarides subduction zone extends for 10° of latitude, between 40°N and 45°N, for a total length of about 1086 km. Plates involved in this tectonic area are Adriatic moving and Eurasia fixed (Bennet et al., 2008; Serpelloni et al., 2016). DeMets et al., 2010 suggest a value of 9 mm/yr for V_L in this area, whereas a V_H of -2.7 mm/yr is obtained from GPS data (Métois et al., 2015). Calculated V_S, with equation (3.2), is 6.3 mm/yr whereas LV, from equation (3.1), is 0.7 km^3/yr.

Hellenides subduction zone is located between 35°N and 40°N approximately and it extends for about 620 km. Plates involved in subduction process are Africa moving and Eurasia fixed (DeMets et al., 2010). Measured V_L is 9.4 mm/yr (DeMets et al., 2010), whereas we used a V_H value of -2.8 mm/yr (England et al., 2016). With equation (3.2) we found a V_S value of 6.6 mm/yr and, with equation (3.1), a LV of 0.4 km^3/yr.

Cyprus subduction zone extends along the 35th latitude degree, for a length of about 581 km. Plates taking part to subduction here are Africa moving and Eurasia fixed (DeMets et al., 2010). V_L here was estimated as 10.8 mm/yr (DeMets et al., 2010), whereas V_H, taken from GPS data (Devoti et al., 2017), is -6.7 mm/yr. We obtained a V_S value of 4.1 mm/yr, with equation (3.2), and LV found using equation (3.1) is 0.2 km^3/yr.

Alps subduction zone (now collision zone) covers a latitude that goes from about 45°N to about 50°N, reaching a total length of approximately 1218 km. Plates converging in this tectonic area are Eurasia moving and Adriatic plate fixed (Carminati and Doglioni, 2012; Serpelloni et al., 2016). V_L for this

subduction is 1 mm/yr (Doglioni et al., 2007) and V_H is.4 mm/yr (GPS data from Serpelloni et al., 2016). V_S, calculated with equation (3.2) is found to be 0.6 mm/yr, and, using equation (3.1), calculated LV is 0.1 km^3/yr.

H-convergent Subduction Zones			
Subduction	**Moving Plate**	**Fixed Plate**	**Reference for hinge motion**
S-America	Nazca	S-America	*Doglioni et al.*, 2007; *Liu et al.*, 2000; *Mora-Paez et al.*, 2018
	Antarctica	Scotia	*Smalley et al.*, 2007
Indonesia	India	Sunda	*Michel et al.*, 2001
	Capricorn	Sunda	*Koulali et al.*, 2017; *Yong et al.*, 2017
Central America	Cocos	Caribbean	*Outerbridge et al.*, 2010
	Cocos	N-America	*Marquez-Azua and DeMets*, 2003
Taiwan	Sunda	Philippines Sea	*Hsu et al.*, 2012
New Hebrides-Vanuatu Islands	Australia	Pacific	*Calmant et al.*, 2003
Cascadia	Juan de Fuca	N-America	*Krogstad et al.*, 2016
S-New Zealand	Australia	Pacific	*Beavan et al.*, 2003
Himalaya	India	Eurasia	*Jade et al.*, 2017
Zagros	Arabia	Eurasia	*Walters et al.*, 2017
Solomon Islands	Australia	Pacific	*Kuo et al., 2016*
Papua-New Guinea	Australia	Pacific	*Koulali et al.*, 2015
Caucasus	Arabia	Eurasia	*Ahadov and Jin*, 2017
Dinarides	Eurasia	Adriatic	*Metois et al.*, 2015
Hellenides	Africa	Eurasia	*England et al.*, 2015
Cyprus	Africa	Eurasia	*Devoti et al.*, 2017
Alps	Eurasia	Adriatic	*Serpelloni et al.*, 2016

Table 3.2 - Useful information for the H-convergent subduction zones. The star symbol points to cases in which V_H was inferred from the state of stress of the upper plate (contraction, neutral or extension).

H-convergent Subduction Zones					
Subduction	**Length** (km)	V_L (mm/yr)	V_H (mm/yr)	V_S (mm/yr)	**Volumes** (km^3/yr)
S-America**	7060.0	59.5	−31.6	27.9	18.9
Indonesia**	4810.8	40.1	−19.1	34.4	17.1
Central America**	2985.6	69.2	−18.5	50.7	15.1
Taiwan	1475.9	93.9	−2.7	91.2	13.5
New Hebrides-Vanuatu Islands	1951.0	88.4	−32.7	55.7	10.9
Cascadia	1082.6	34.9	−6.7	28.2	3.1
S-New Zealand	1242.7	38.8	−15.0	23.8	3.0
Himalaya	2596.2	44.2	−34.4	9.8	2.5
Zagros	2515.8	31.5	−22.5	9.0	2.3
Solomon Islands	1160.9	97.1	−84.4	12.7	1.5
Papua-New Guinea	1293.2	108.7	−100.1	8.6	1.1
Caucasus	763.0	25.3	−11.4	13.9	1.1
Dinarides	1086.1	9.0	−2.7	6.3	0.7
Hellenides	619.6	9.4	−2.8	6.6	0.4
Cyprus	581.2	10.8	−6.7	4.1	0.2
Alps	1218.4	1.0	−0.4	0.6	0.1

Table 3.3 - Parameters used and calculated for the H-convergent subduction zones. The double stars point to long subduction zones for which average values for V_L, V_H and V_S are shown.

The following are the H-divergent subduction zones ordered for decreasing computed volumes (summary in Tables 3.4 and 3.5).

Tonga-Kermadec subduction zone has a length of about 2896 km, included between about 15°S and 35°S of latitude. Plates that play a role in this area are Pacific moving and Australia fixed (DeMets et al., 2010; Hayes et al., 2012). V_L estimated with plate motions calculator (DeMets et al., 2010), is 68.7 mm/yr, on average; V_H in this case is 76.1 mm/yr (Parson and Wright, 1996; Ribeiro et al., 2017), on average, whereas averaged V_S, obtained from equation (3.2), and LV, from equation (3.1), are 144.8 mm/yr and 40.1 km^3/yr, respectively.

Banda subduction zone includes the Northern, Central and Southern segment of the Banda Arc and it is 2407 km long. It extends mostly from a latitude of 0°S to 10°S. Plates that take part in this subduction zones are Australia moving and Sunda fixed (DeMets et al., 2010). V_L, measured with plate motions models (DeMets et al., 2010), in this area reaches a value of 76.9 mm/yr, whereas V_H, obtained from Koulali et al. (2016), is of 60 mm/yr. V_S, from equation (3.2), turned out to be 136.9 mm/yr and LV, from equation (3.1), 33 km^3/yr.

Aleutians subduction zone length is about 3935 km, extending from a latitude of 50°N to about 60°N. Plates involved in the subduction process are Pacific moving and North America fixed (DeMets et al., 2010; Hayes et al., 2012). V_L value is around 69 mm/yr (DeMets et al., 2010), whereas we used a 5.0 mm/yr value for V_H (Kogan et al., 2017). With equation (3.2) we obtained a V_S of about 74.1 mm/yr and, using equation (3.1), we had a LV of approximately 29.2 km^3/yr.

Izu-Bonin-Marianas subduction zone has a length of 3591 km, and an extension in latitude of about 25°, from around 10°N to 35°N. Plates involved in this tectonic area are Pacific moving and Philippine Sea fixed (DeMets et al., 2010; Hayes et al., 2012). V_L is estimated to have a value of 33.4 mm/yr on average, whereas V_H has a value of about 25.0 mm/yr (Arisa & Heki, 2016; Kato et al., 2003). V_S, obtained from equation (3.2) and LV, from equation (3.1), are 58.3 mm/yr and 21.2 km^3/yr on average, respectively.

The Japan-Ryukyu subduction zone has a total length of about 2180 km, covering a latitude range that goes from about 35°N to 25°N. Plates converging in this area are Philippine Sea moving and Eurasia fixed (DeMets et al., 2010; Hayes et al., 2012). Computed V_L is 65.4 mm/yr (DeMets et al., 2010) and V_H is 25.0 mm/yr (GPS data from Sagiya et al., 2004). V_S, from equation (3.2), and LV, from equation (3.1), are estimated to be 90.4 mm/yr and 19.7 km^3/yr, respectively.

The Kuril-Kamchatka subduction zone extends from a latitude of about 35°N and 55°N, along 1929 km. Plates involved are Pacific moving and North America fixed (DeMets et al., 2010; Hayes et al., 2012). V_L estimated from plate motions calculator (DeMets et al., 2010) is 79.3 mm/yr, and V_H is 5.0

mm/yr (GPS data from Apel et al., 2006). With equations (3.2) and (3.1) we calculated a V_S and a LV of 84.3 mm/yr and 16.3 km^3/yr, respectively.

New Britain subduction zone ranges from a latitude of 5°S to 10°S, for an overall length of about 611 km. Plates involved in this area are Australia moving and Pacific fixed (DeMets et al., 2010; Hayes et al., 2012). Calculated V_L for this subduction zone is 103.5 mm/yr (DeMets et al., 2010), whereas V_H has a value of 110.0 mm/yr (Wallace et al., 2004). V_S and LV, calculated with equation (3.2) and (3.1), are 213.5 mm/yr and 13.0 km^3/yr, respectively.

New Scotia-Sandwich Arc has a length of 754 km, for a latitude extension that goes from 55°S to 60°S. Plates playing a role in this tectonic area are South America moving and Sandwich fixed (DeMets et al., 2010; Hayes et al., 2012). V_L calculated for Sandwich plate is 71.3 mm/yr (DeMets et al., 2010) and V_H was found to be 10.0 mm/yr (Smalley et al., 2007). Equation (3.2) was used to calculate a V_S value of 81.3 mm/yr whereas a LV of 6.1 km^3/yr was estimated starting from equation (3.1).

Northern New Zealand subduction zone has a length of barely 785 km and it extends in the range of 45°S to 35°N latitude. Plates converging in this area are Pacific moving and Australia fixed (DeMets et al., 2010). V_L obtained from plate motions calculator (DeMets et al., 2010) is 46.0 mm/yr and V_H is 30.0 mm/yr (GPS data from Beavan et al., 2016). V_S, calculated with equation (3.2), is 76.0 mm/yr whereas, from equation (3.1), we obtained a LV of 6.0 km^3/yr.

Caribbean subduction has a total length of 1063 km, for a latitude extension of about 10°, from 10°N to 20°N. Plates converging are South America moving and Caribbean fixed (DeMets et al., 2010). V_L in this area is 19.1 mm/yr (DeMets et al., 2010), whereas V_H is 1.6 mm/yr (Weber et al., 2001). V_S, from equation (3.2), is 20.7 mm/yr, whereas LV, calculated with equation (3.1), is 2.2 km^3/yr.

Crete subduction is a short segment of the Hellenides subduction zone that has subduction hinge moving away from the upper plate. It has a length of 323 km, at a latitude of about 35°N. In this area converging plates are Africa moving and Eurasia fixed (DeMets et al., 2010). V_L reaches the value of 10.1 mm/yr (DeMets et al., 2010), and a V_H of 33.3 mm/yr (GPS data from Devoti et al., 2017). V_S has a value of 43.4 mm/yr and LV of 1.4 km^3/yr, obtained using equations (3.2) and (3.1), respectively.

Apennines subduction zone length reaches about 2067 km and its latitude extension goes from 35°N to 45°N. Plates involved in the subduction process are Adriatic moving and Eurasian fixed (Carminati and Doglioni, 2012; Devoti et al., 2008; Di Bucci and Mazzoli, 2002; Métois et al., 2015). V_L in this area reaches 2.0 mm/yr (Devoti et al., 2008) and V_H is thought to be 4.5 mm/yr (Métois et al., 2015). V_S, calculated with equation (3.2), in this area has a value of 6.5 mm/yr, whereas LV, obtained from equation (3.1), is 1.3 km^3/yr.

Carpathians subduction zone is about 1227 km long, for a latitude extension that goes from almost 40°N to 50°N. Plates involved in this area are a subplate, the intra-Carpathian basin system, moving and the European plate fixed (Fan et al., 1998; Linzer, 1996; Mason et al., 1998), moving. V_L in this area is less than 0.2 mm/yr (Mason et al., 1998) and V_H, obtained from GPS data (Serpelloni et al., 2016), is 0.2 mm/yr. V_S in this area is estimated to be 0.4 mm/yr, using equation (3.2), and LV is 0.1 km^3/yr, calculated starting from equation (3.1).

H-divergent Subduction Zones			
Subduction	**Moving Plate**	**Fixed Plate**	**Reference for hinge motion**
Tonga-Kermadec	Pacific	Australia	*Ribeiro et al.*, 2017; *Parson and Wright*, 1996*
Banda Arc	Australia	Sunda	*Koulali et al.*, 2016
Aleutians	Pacific	N-America	*Kogan et al.*, 2017
Izu-Bonin-Marianas	Pacific	Philippine Sea	*Arisa and Heki*, 2016; *Kato et al.*, 2003
Japan-Ryukyu	Philippine Sea	Eurasia	*Sagiya*, 2004
Kuril-Kamtchatka	Pacific	N-America	*Apel et al.*, 2006
New Britain	Australia	Pacific	*Wallace et al.*, 2004
New Scotia-Sandwich Arc	S-America	Sandwich	*Smalley et al.*, 2007
N-New Zealand	Pacific	Australia	*Beavan et al.*, 2003
Caribbean	S-America	Caribbean	*Weber et al.*, 2001
Crete	Africa	Eurasia	*Devoti et al.*, 2017
Apennines	Adriatica	Eurasia	*Metois et al.*, 2015
Carpathians	Intra-Carpathian Basin	Eurasia	*Serpelloni et al.*, 2016

Table 3.4 - Useful information for H-divergent subduction zones. The star symbol points to cases in which V_H was inferred from the state of stress of the upper plate (contraction, neutral or extension).

H-divergent Subduction Zones					
Subduction	**Length** (km)	V_L (mm/yr)	V_H (mm/yr)	V_S (mm/yr)	**Volumes** (km^3/yr)
Tonga-Kermadec**	2895.5	68.7	76.1	144.8	40.1
Banda Arc	2406.7	76.9	60.0	136.9	33.0
Aleutians	3935.0	69.1	5.0	74.1	29.2
Izu-Bonin-Marianas**	3591.3	33.4	25.0	58.3	21.2
Ryukyu-Japan	2180.0	65.4	25.0	90.4	19.7
Kuril-Kamchatka	1929.2	79.3	5.0	84.3	16.3
New Britain	611.0	103.5	110.0	213.5	13.0
New Scotia-Sandwich	753.5	71.3	10.0	81.3	6.1
N-New Zealand	785.1	46.0	30.0	76.0	6.0
Caribbean	1063.4	19.1	1.6	20.7	2.2
Crete	323.1	10.1	33.3	43.4	1.4
Apennines	2067.2	2.0	4.5	6.5	1.3
Carpathians	1227.1	0.2	0.2	0.4	0.1

Table 3.5 - Parameters used and calculated for the H-divergent subduction zones. The double stars point to long subduction zones for which average values for V_L, V_H and V_S are shown.

Exceptions in our dataset are (summary in Tables 3.6 and 3.7):

i) Northern Japan subduction zone, that extends from a latitude of about 35°N and 45°N, along 1067 km. Plates involved are North America fixed and Pacific Ocean moving (from 42° to 40°); Eurasia fixed and Pacific Ocean moving (from 40° to 35°) (DeMets et al., 2010; Hayes et al., 2012). V_L estimated from plate motions calculator (DeMets et al., 2010) is 90.8 mm/yr, and V_H from GPS data (Sagiya, 2004) is -12.5 mm/yr. With equations (3.2) and (3.1) we calculated a V_S and a LV of 78.3 mm/yr and 8.4 km^3/yr, respectively.

ii) Philippines subduction zone reaches a length of about 1565 km, for a latitude extension that goes from 15°N to 0°N. Plates that are involved in this area are Sunda fixed and Philippines Sea moving (DeMets et al., 2010; Hayes et al., 2012). V_L calculated for this subduction is about 101.1 mm/yr (DeMets et al., 2010). V_H of this subduction zone is taken from information about the state of stress of the upper plate in this area. In Lallemand et al. (2005) the Sunda upper plate is considered in a neutral state (neither in extension nor in compression). For this reason, we considered a stable subduction hinge for this subduction zone (i.e., $V_H = 0$). V_S obtained with equation (3.2) is 101.1 mm/yr, whereas LV, from equation (3.1), turned out to be 15.8 km^3/yr.

Particular cases			
Subduction	**Moving Plate**	**Fixed Plate**	**Reference for hinge motion**
Philippine	Philippine Sea	Sunda	*Lallemand et al.*, 2005*
N-Japan	Pacific	Eurasia	*Sagiya*, 2004

Table 3.6 - Useful information for the outliers of our dataset (Philippines and N-Japan subduction zones). The star symbol points to cases in which V_H was inferred from the state of stress of the upper plate (contraction, neutral or extension).

Particular cases					
Subduction	**Length** (km)	V_L (mm/yr)	V_H (mm/yr)	V_S (mm/yr)	**Volumes** (km^3/yr)
N-Japan	1066.7	90.8	-12.5	78.3	8.4
Philippines	1564.8	101.1	0.0	101.1	15.8

Table 3.7 - Parameters used and calculated for the outliers of our dataset (Philippines and N-Japan subduction zones.

3.4 Results

Our kinematic analysis result in that, usually, the hinge kinematics is constant along the length trench at each subduction zone, showing convergent and divergent displacement of the subduction hinge H. Two exceptions occur along northern Japan and Philippine subductions. For the first zone, in the southern region the hinge moves toward the lower plate, i.e., the Philippine Sea, whereas in the northern area the subduction hinge is rather converging relative to the upper plate, i.e., the Eurasia. For the second zone, instead, the extension within the upper plate is no longer active (Lallemand et al., 2005).

When computing volumes of sinking slabs into the mantle with the equations (3.1), we obtain that there are currently about 190 km^3/yr of lithosphere subducting below H-divergent subduction zones, whereas about 91 km^3/yr of lithosphere are subducting below H-convergent subduction zones. In this computation, northern Japan and Philippines subduction zones were not taken into account, representing outliers for our database.

While the total length of H-convergent subduction zones is ~32443 km and present differences with respect to the length of H-divergent subduction zones, i.e., ~23768 km (Figure 3.2), on the contrast, the average V_L shows no significant variation between the two end-members, being 52.0 mm/yr for H-convergent and 49.8 mm/yr for H-divergent (Figure 3.3). Conversely, a considerable difference can be observed in the average computed V_S, obtained for the two subduction settings, e.g., approximately 82 mm/yr for H-divergent subduction zones and about 27 mm/yr for H-convergent ones (Figure 3.4).

Uncertainties of computed volumes reach a maximum value confined under the 15% by using the error propagation function. This value was firstly obtained by (i) considering a null uncertainty associated with the thickness of the lithosphere *d*, taken constant – 100 km – in our calculation, (ii) an error equal to the 10% of the average trench length l for each subduction zone, corresponding to 200 km for H-divergent and H-convergent slabs and (iii) alternatively imposing errors equal to 10 mm/yr, 50 mm/yr and 100 mm/yr on the subduction hinge velocity V_H. Then, we computed a propagated V_L mean error of 1.2 mm/yr for H-divergent and 0.9 mm/yr for H-convergent subduction zones, integrating velocity uncertainties provided by DeMets et al. (2010) and a propagated uncertainty on V_S, resulted very similar to the error assigned to V_H. Errors obtained for lithospheric volumes are 1, 4 and 8% and 2, 7 and 15% for H-divergent and H-convergent subduction zones, respectively, using uncertainties of 10, 50 and 100 mm/yr on V_H.

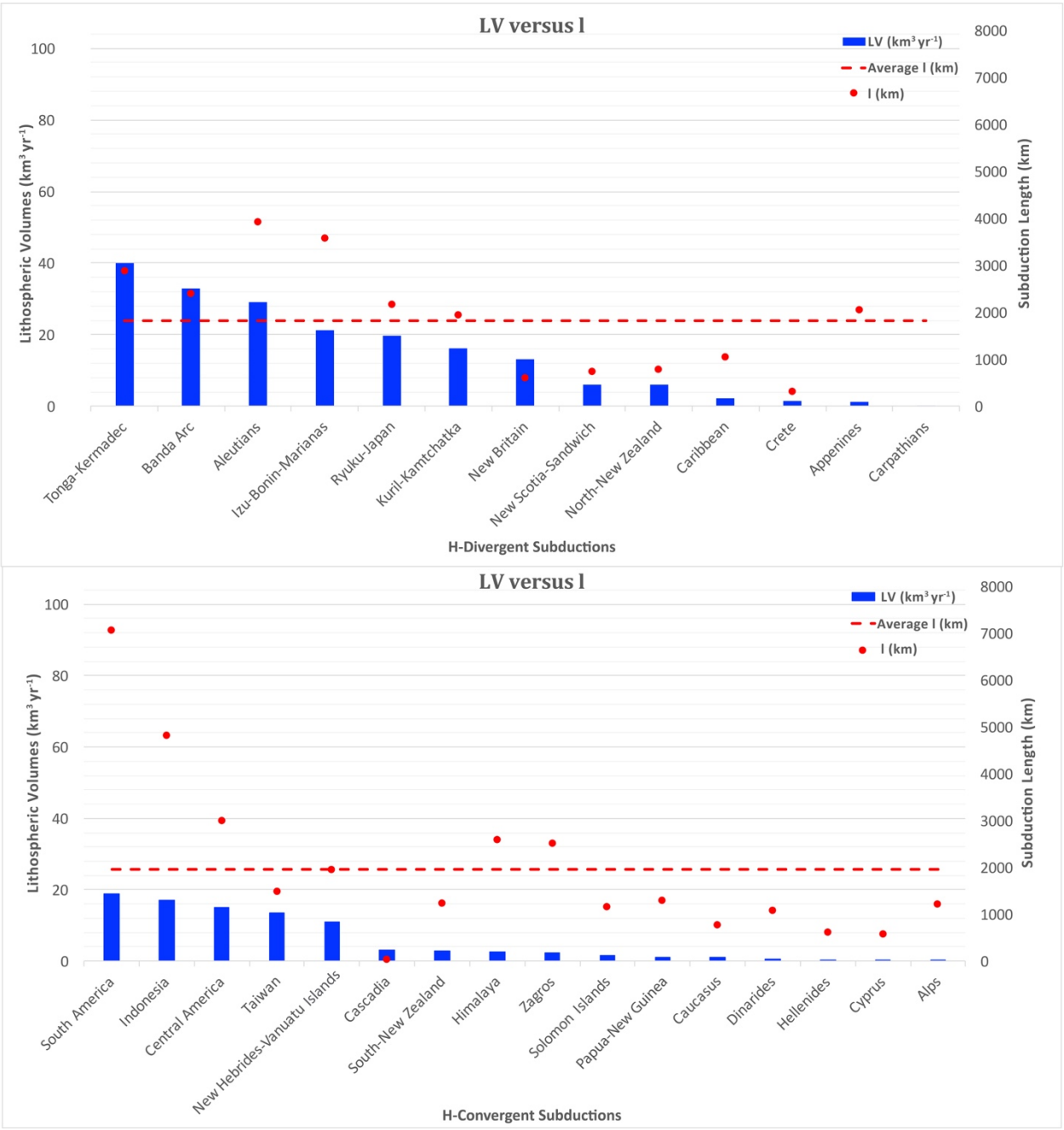

Figure 3.2- Lithospheric volumes (LV, blue histogram) vs. Subduction length (l, red dots). Total length for H-convergent ~32443 km – Total length for H-divergent subductions ~23768 km. Average *l* in dashed line is ~2000 km for H-convergent and 1800 for H-divergent subduction zones. A clear relation between role of length l and differences of worldwide subducted lithosphere volumes cannot be detected

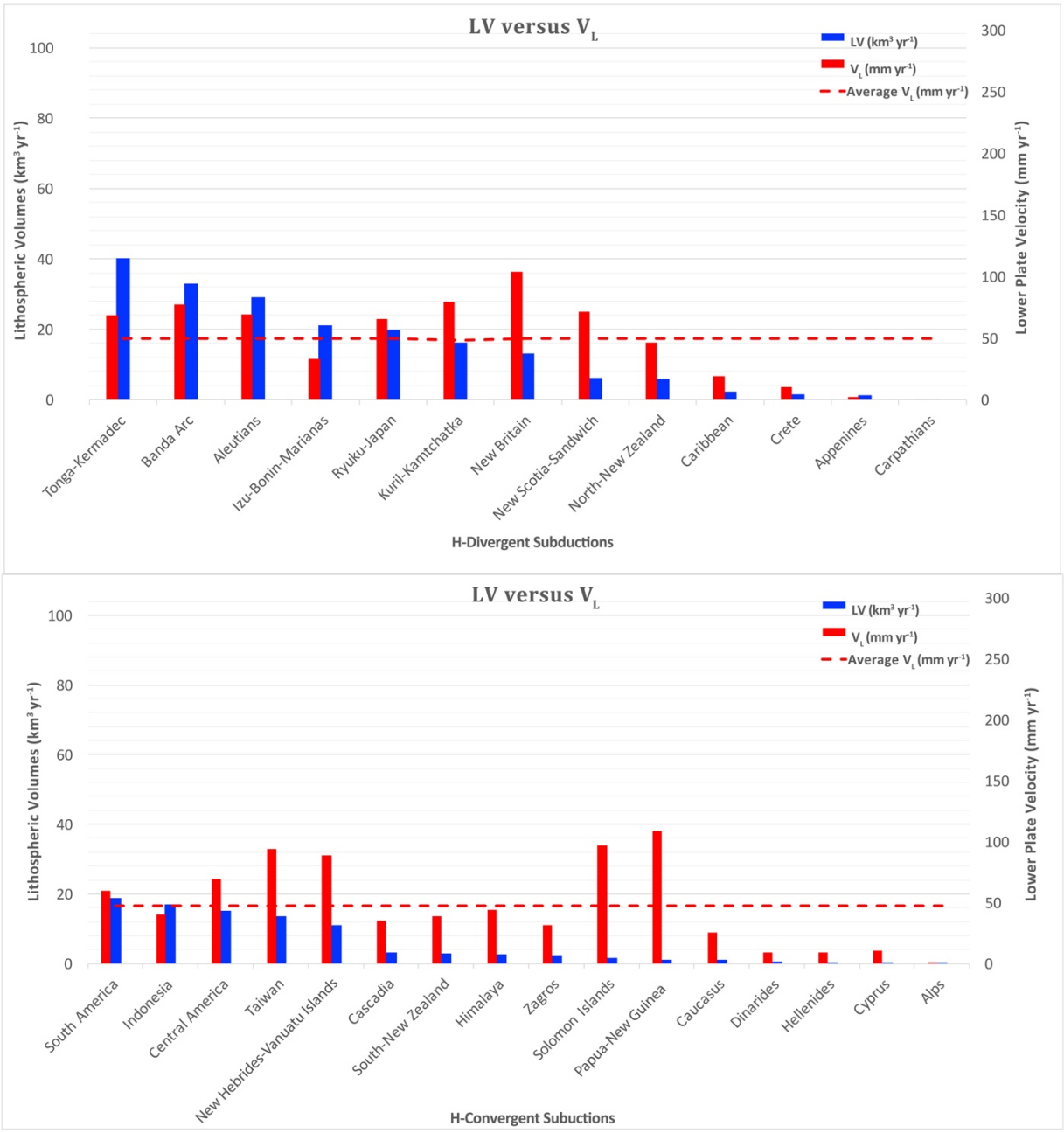

Figure 3.3 - Lithospheric volumes (LV, blue histogram) vs. Lower plate velocity (V_L, red histogram). Average V_L in dashed line is 50 mm/yr for H-divergent and 52 mm/yr for H-convergent subduction zones. An evident correlation between the velocity V_L and differences of worldwide subducted lithosphere volumes cannot be noticed.

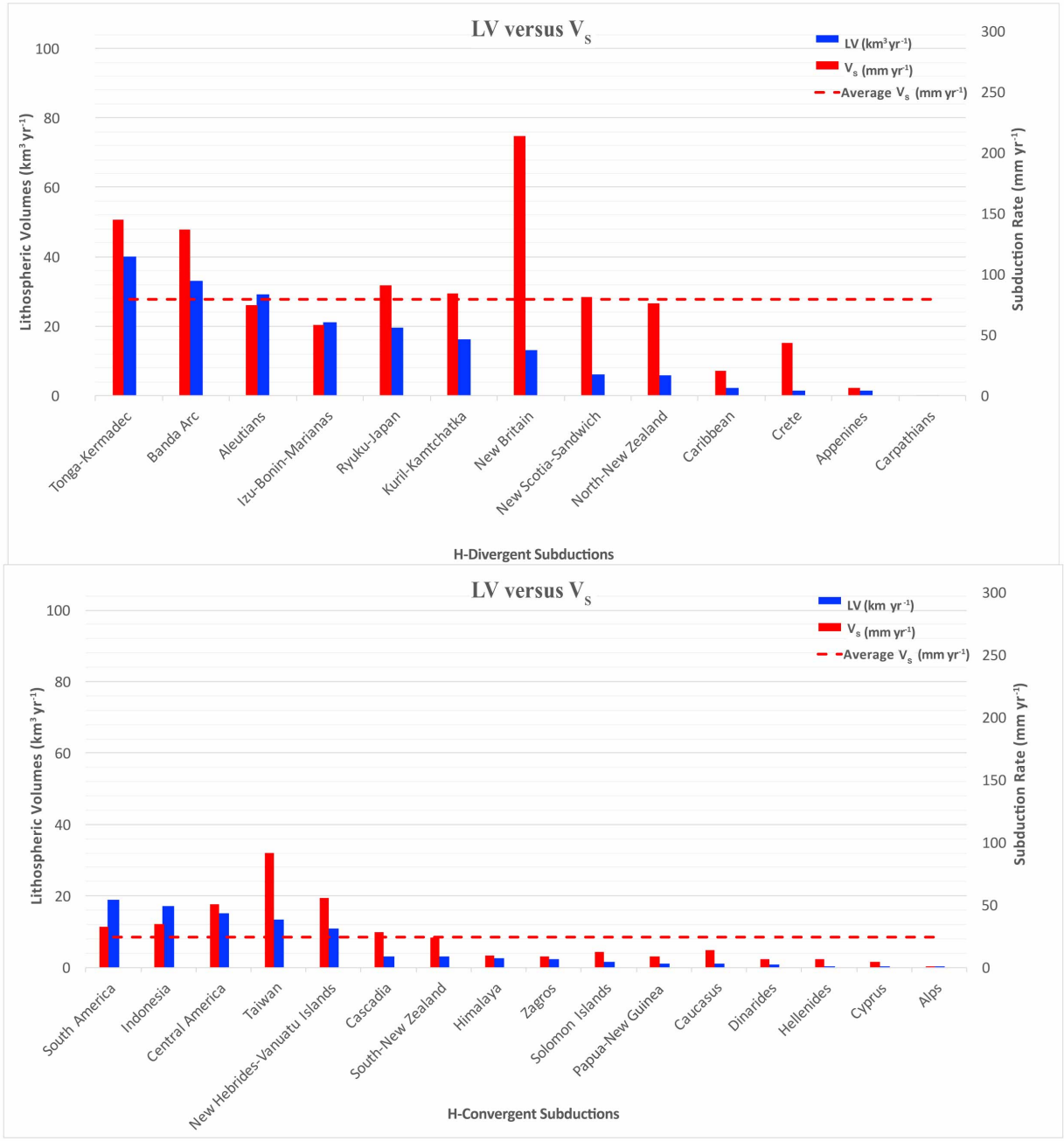

Figure 3.4 - Lithospheric volumes (LV, blue histogram) vs. Subduction rate (V_S, red histogram). Average V_S in dashed line is 82 mm/yr for H-divergent and 27 mm/yr for H-convergent subduction zones. Being the first value almost four times higher than the second, this could affect difference in volumes of subducted lithosphere for H-divergent and H-convergent subduction zones.

3.5 Supporting numerical modeling

The previously presented results show a difference of lithospheric slab volumes currently subducting below H-divergent and H-convergent subduction zones. This volume discrepancy is principally due to the difference in the two-end-member subduction rate V_S, that takes into account the hinge kinematics. To support our kinematic results, here, we carried out numerical experiments using the subduction rate V_S instead of plate convergence V_L, as boundary condition, to verify whether subduction rate affects slab dynamics at subduction zones.

We used a visco-elasto-plastic thermomechanical code proposed by Gerya (2010) and Gerya and Yuen (2007). This code is based on a combination of the finite difference method applied on a staggered Eulerian grid with a marker-in-cell technique. The momentum, continuity and energy equations are solved in the Eulerian frame, and physical properties are transported by Lagrangian markers that move according to the velocity field interpolated from the fixed grid. We use non-Newtonian realistic pressure-, temperature- and stress-dependent visco-elasto-plastic rheology in a model that is fully thermally and thermodynamically coupled and accounts for adiabatic, radiogenic and frictional internal heating sources. The viscous-ductile rheological term accounts for power-law and diffusion creep.

Conservation of mass is approximated by a compressible time-dependent 2D continuity equation:

$$\frac{\mathrm{D}\ln\rho}{\mathrm{Dt}} + \frac{\partial \mathrm{v_x}}{\partial \mathrm{x}} + \frac{\partial \mathrm{v_y}}{\partial \mathrm{y}} = 0, \tag{3.4}$$

where $\frac{\mathrm{D}}{\mathrm{Dt}}$ is the Lagrangian time derivative (for a moving point of reference) x and y denote horizontal and vertical Cartesian coordinates, whereas ρ (kg/m^3) is the local density, which characterizes the amount of mass per unit volume, and v (m/s) is the local velocity.

The momentum equations are presented in the form of the Stokes flow approximation:

$$\frac{\partial \sigma'_{\mathrm{ij}}}{\partial \mathrm{x_j}} - \frac{\partial \mathrm{P}}{\partial \mathrm{x_i}} + \rho \mathrm{g_i} = 0 \tag{3.5}$$

which in 2D reads:

$$\frac{\partial \sigma'_{\mathrm{xx}}}{\partial \mathrm{x}} + \frac{\partial \sigma'_{\mathrm{xy}}}{\partial \mathrm{y}} - \frac{\partial \mathrm{P}}{\partial \mathrm{x}} = 0 \tag{3.5.1}$$

$$\frac{\partial \sigma'_{\mathrm{yy}}}{\partial \mathrm{y}} + \frac{\partial \sigma'_{\mathrm{yx}}}{\partial \mathrm{x}} - \frac{\partial \mathrm{P}}{\partial \mathrm{y}} = -\rho \mathrm{g_y} \tag{3.5.2}$$

where σ'_{ij} are the components of the deviatoric stress tensor, ρ is the density dependent on rock composition, temperature and pressure, and g_y is the acceleration due to gravity.
The conservation of energy equation describes the temperature changes in a continuum due to internal heat generation/consumption and advective/conductive heat transport:

$$\rho c_{P\_eff}\left(\frac{\partial T}{\partial t} + v\,\nabla(T)\right) = -\frac{\partial q_x}{\partial x} - \frac{\partial q_y}{\partial y} + H_r + H_a + H_s, \tag{3.6}$$

where q_x and q_y are heat flux component (where $q_i = -k\frac{\partial T}{\partial x_i}$ and $k = f(P, T, C)$ is thermal conductivity which depends on the pressure-temperature conditions and composition). H_r, H_a and H_s are, respectively, radioactive, adiabatic and shear heat production. Radioactive heat production depends on the rock type and it is assumed to be constant through time. The adiabatic heat production/consumption is related to pressure changes (compression-decompression):

$$H_a = T\alpha\frac{DP}{Dt} = T\alpha\left(v_x\frac{\partial P}{\partial x} + v_y\frac{\partial P}{\partial y}\right), \tag{3.7}$$

where α is the thermal expansion and P is the pressure.
Since elastic deformation is reversible and does not contribute to mechanical energy dissipation, this deformation has to be excluded from shear heating calculation and therefore:

$$H_s = 2\sigma'_{xx}(\dot{\varepsilon}'_{xx} - \dot{\varepsilon}'_{xx(elastic)}) + 2\sigma_{xy}(\dot{\varepsilon}_{xy} - \dot{\varepsilon}_{xy(elastic)}). \tag{3.8}$$

The effect of latent heating related to the phase transformations of the rocks is included implicitly by calculating the effective heat capacity and the effective thermal expansion through thermodynamic relations (Gerya, 2010, pp.128).
With the previously described methods, we carried out four synthetic experiments where the first two models were made with an oceanic lower plate subducting beneath to a continental upper plate stated fixed (Figures 3.5, 3.6a, 3.6b). The other two experiments were performed with an oceanic subducting lower plate relative to another fixed oceanic upper plate (Figures 3.5, 3.6c, 3.6d). Every lithospheric plate subducting into the asthenospheric mantle is designed with an upper crust, a lower crust and a lithospheric mantle, considering the age of the subducting plate equal to 30 Myr and a time evolution of 7 Myr in all the numerical simulations. Furthermore, we divided the four experiments in models M1 and M2. In the M1 models (Figure 3.6a, 3.6c) no low velocity zone (LVZ) decoupling layer has

been integrated and the initial velocity conditions V_S has been applied along the entire lateral boundary of the domain, as proposed by Gerya (2010), when simulating the subducting lower plate motion. In models M2 (Figures 3.6b, 3.6d), V_S has been applied only on subducting lower plate and we added a LVZ layer of 100 km, with a constant viscosity value of 10^{18} Pa s. Synthetic velocity $V_S = 3$ cm/yr is assigned as boundary condition to the H-convergent subduction zones, whereas a synthetic $V_S = 8$ cm/yr for the H-divergent ones is used (Figure 3.6, a, b, and c, d panels, respectively). Model setup is shown in Figure 3.5.

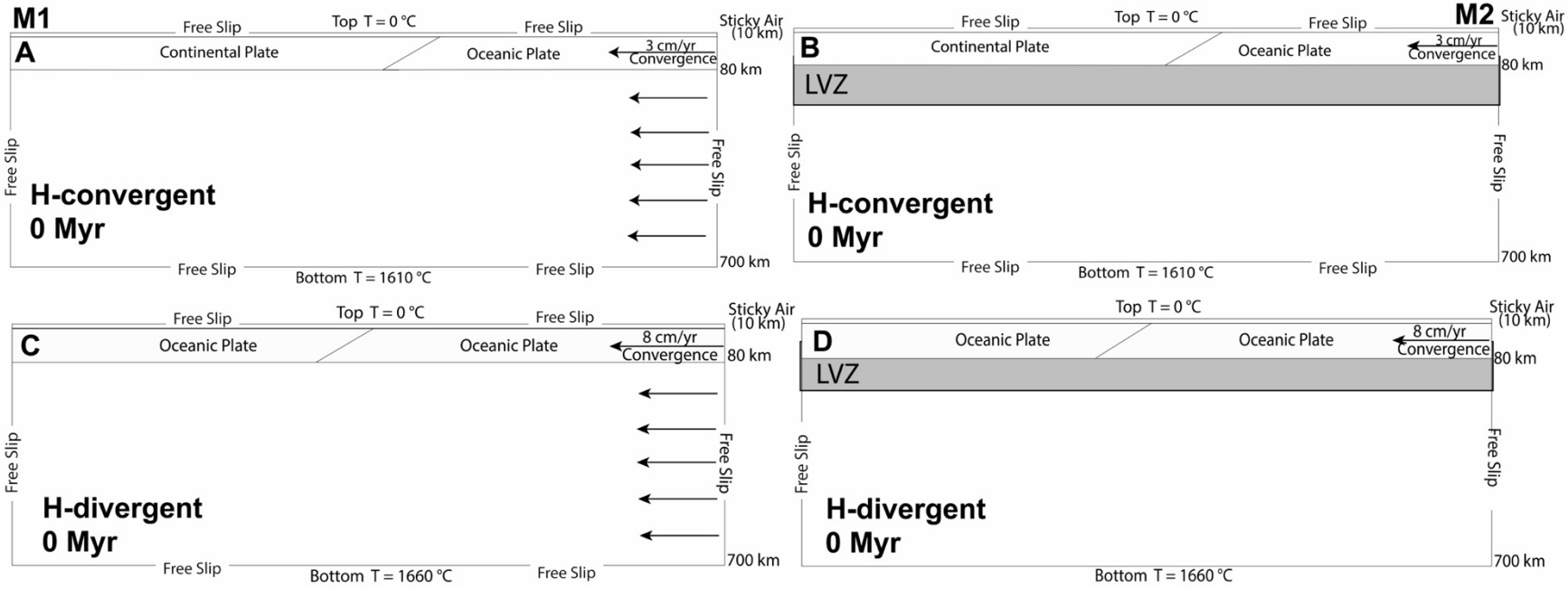

Figure 3.5 - Model setup. The experiments are performed in a 2000 x 700 km computational domain and they begin with two plates juxtaposed along a fault with a weak zone between upper and lower plates, having a 30° dip angle. Properties of the weak zone and all the quantities are reported in Tab. S8. Synthetic velocity $V_S =$ 3 cm/yr is assigned as boundary condition to the H-convergent subduction zones, whereas a synthetic $V_S = 8$ cm/yr for the H-divergent ones is used. In grey the LVZ décollement layer.

The experiments were performed in a 2000 x 700 km computational domain (Figure 3.5). The grid has a resolution of 201 x 61 nodes with variable grid spacing. This allowed a minimum grid resolution of 2 x 2 km in the area affected by the largest deformation. Around 1400000 randomly distributed Lagrangian markers carrying material properties were used in each experiment. A free surface upper boundary is simulated using the "sticky air" technique (Gerya & Yuen, 2007), for the first 10 km of all models, enhanced by the high-density marker distribution in the near-surface. To investigate slab subduction, we used an initial setup for subduction initiation across a pre-existing fault (Hall et al., 2003). The experiments begin with two plates juxtaposed along a fault with a weak zone between upper and lower plates, having a 30° dip angle (Figure 3.5), with no plastic strength (sin (φ) = 0), which creates favourable conditions for subduction to initiate (Gerya, 2010, pp. 274-275). Free slip boundary conditions were used on all boundaries and for all tests (Figure 3.5). Full details on the method are provided in Gerya (2010) and Gerya and Yuen (2007). Values of the used quantities are reported in Table 3.8 (Ranalli, 1995; Clauser & Huenges, 1995) .

Material	ρ (kg/m^3)	k (W/m/K)	H_r (W/m^3)	Cp (J/kg)	sin(φ)	α (1/K)	Flow Law	η_0 (Pa^n s)	n	Thickness (km)
Sediments	2700	$0.64+\frac{807}{T+77}$	1.00×10^{-6}	1000	0.030	3×10^{-5}	Wet Qz.	1.97×10^{17}	2.3	1
Upper cont. crust	2800	$0.64+\frac{807}{T+77}$	1.00×10^{-6}	1000	0.200	3×10^{-5}	Wet Qz.	1.97×10^{17}	2.3	20
Lower cont. crust	2900	$1.18+\frac{474}{T+77}$	5.00×10^{-7}	1000	0.200	3×10^{-5}	Pl. (An75)	4.80×10^{22}	3.2	15
Upper oceanic crust	3200	$1.18+\frac{474}{T+77}$	2.50×10^{-7}	1000	0.030	3×10^{-5}	Wet Qz.	1.97×10^{17}	2.3	2
Lower oceanic crust	3200	$1.18+\frac{474}{T+77}$	2.50×10^{-7}	1000	0.200	3×10^{-5}	Pl. (An75)	4.80×10^{22}	3.2	5
Low Velocity Zone	3300	$0.73+\frac{1293}{T+77}$	2.20×10^{-8}	1000	0.600	3×10^{-5}	Dry Ol.	$3.00\times10^{18*}$	3.5	120
Mantle	3300	$0.73+\frac{1293}{T+77}$	2.20×10^{-8}	1000	0.600	3×10^{-5}	Dry Ol.	3.98×10^{16}	3.5	664-692
Weak Zone	3300	$0.73+\frac{1293}{T+77}$	2.20×10^{-8}	1000	0.030	3×10^{-5}	Wet Ol.	5.01×10^{20}	4.0	-

Table 3.8 - Reference rheological (Ranalli, 1995) and thermal (Clauser & Huenges, 1995) parameters of materials used for the experiments. In this table $\boldsymbol{\rho}$ corresponds to the density, k to the thermal conductivity, H_r to the radiogenic heat production, Cp to the heat capacity, sin(ϕ) to the friction, α to the thermal expansion, η_0 to the initial viscosity, n to the stress exponent.

* $\boldsymbol{\eta}0 = \boldsymbol{\eta}\ eff$

Results of our numerical analysis show that in H-divergent models (Figures 3.6c and 3.6d) the slab reach a higher depth and has a steep angle, whereas in H-convergent ones is standing close to shallow depths and is less steep. In fact, in Figure 3.6c, the slab has a dip angle that goes from about 30° (at a depth of 150 km) to about 60° at the tip (~550 km), whereas model in Figure 3.6d maintains a slab dip of about 50° from the point at which the slab enters the mantle to its tip (at a depth of ~350 km).

Slab dip angles for H-convergent models (Figures 3.6a and 3.6b) are about 20° on average, with no significant changes of inclination.

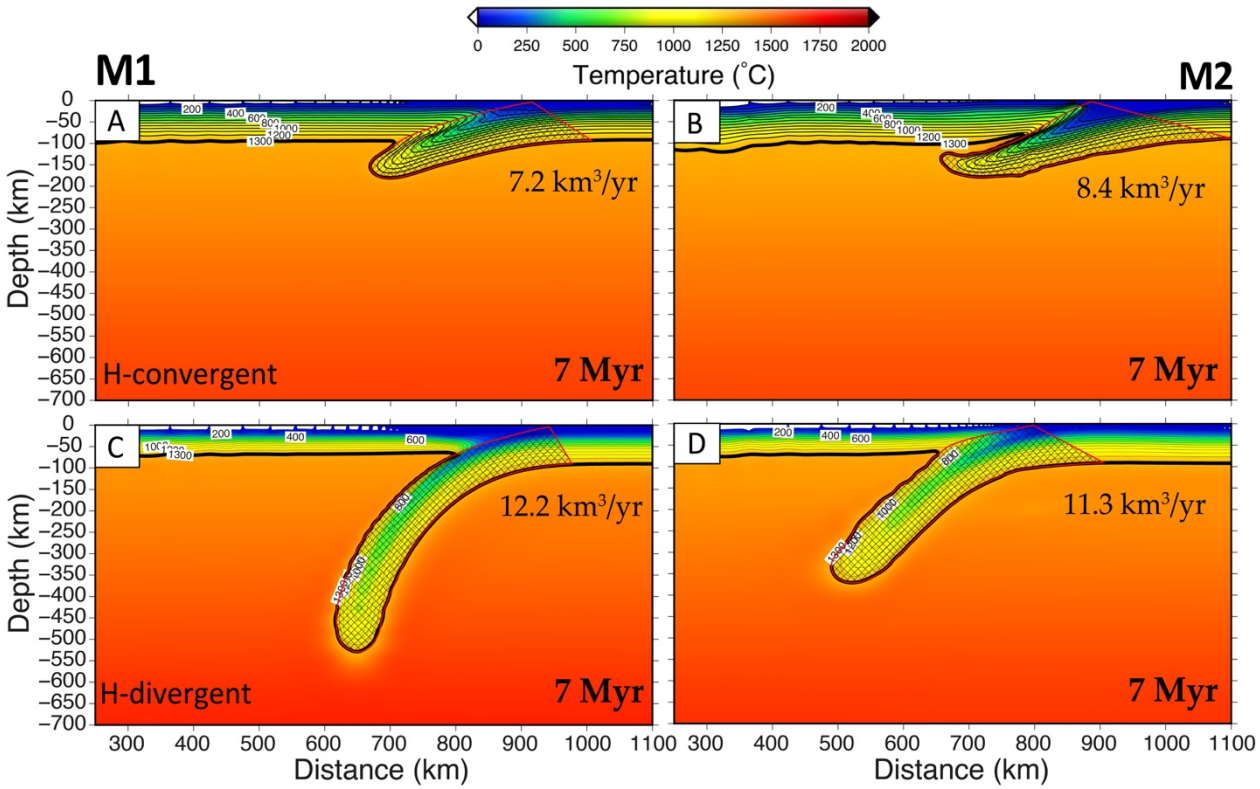

Figure 3.6 - Supporting numerical model results. This figure follows the same order of the Figure 3.5, where model setup is shown. Evolution of subducting plate is shown at 7 Myr. Models M1 (a, c) are models without LVZ and with subduction rate V_S applied all along the lateral boundary of the domain. Models M2 (b, d) are models in which LVZ is integrated and the subduction rate V_S is applied only to the lithosphere. Numbers are volumes LV, obtained by the product of the subducted area - the crossed lines - by length of 1800 km for H-divergent and of 2000 km for H-convergent subductions. Results are about 7.8 km^3/yr for H-convergent models and about 11.8 km^3/yr for H-divergent ones, supporting our kinematics analysis.

Finally, we evaluate the area of each subducted slab and together with an average trench length of 1800 km for H-divergent and of 2000 km for H-convergent subduction zones we compute the resulting volume of the lithosphere subducted per year (Figure 3.6). To compute the area of the subducted slabs obtained from our numerical analysis, we digitalized the data starting from the point of incipient curvature, considering the lithosphere above the 1300°C isotherm (i.e., the bottom of the lithosphere). The selected slab points were then used to compute the slab area with the method of coordinates (i.e., Gauss's area formula). During the selected time interval of 7 Myr, the slab in Figure 3.6c is approximately 200 km deeper than the one in Figure 3.6d, and volumes of subducting lithosphere are about 11.8 km^3/yr for H-divergent (Figures 3.6c and 3.6d) and about 7.8 km^3/yr for H-convergent models (Figures 3.6a and 3.6b).

3.6 Discussion

The kinematic analysis proposed in this Chapter provides an asymmetric slab dynamics at subduction zones. Many asymmetries in geological and geophysical observations can be detected at subduction zones in their slab dip, kinematics of the subduction hinge, morphology, structural elevation, gravity anomalies, heat flow, metamorphic evolution, subsidence and uplift rates, depth of the décollement planes, mantle wedge thickness, magmatism, backarc development or not (e.g., Cuffaro and Doglioni, 2018; Doglioni et al., 2009; Harabaglia & Doglioni, 1998; Marotta & Mongelli, 1998; Nelson & Temple, 1972; Stevenson & Turner, 1977; Tovish et al., 1979). Results reported in Figures 3.2-3.4 and 3.6 shows that subduction zones with opposite motion of the subduction hinge, i.e., convergent or divergent with respect to the fixed upper plate, provide differences in the velocity of the subduction process and, consequently, distinct amounts of lithosphere volume recycled within the mantle can be computed, e.g., about 190 km^3/yr and 91 km^3/yr for H-divergent and H-convergent slabs respectively. This occurs even though (i) the H-convergent slabs have a greater total length with respect to the H-divergent ones (about 32443 km and 23768 km, respectively, Figure 3.2), and (ii) the average V_L in the H-divergent subduction zones appears to be comparable to the average $V_L$of the H-convergent ones (49.8 mm/yr and 52.0 on average, respectively, Figure 3.3). Comparisons among the obtained data (Figures 3.2-3.4) show that, with respect to the quantities V_L and l, there is no relation between the discrepancy of the computed volumes LV at subduction zones with H-divergent and H-convergent hinge. On the contrary, the variation of the velocity V_S (Figure 3.4) contributes to the volume LV changes, pointing out the importance of the role of subduction rate in subduction zones dynamics.

Numerical experiments where V_S is used as boundary condition, i.e., the subducting slab velocity, enforce this crucial role. In our models, regardless the used setup, slabs characterized by a V_S that takes into account the divergent motion of the subduction hinge are steeper and deeper, allowing a deeper recycling within the mantle. On the contrary, slabs with a V_S that accounts for a convergent motion of the subduction hinge are shallower and less steep. This implies that, on the same time interval equal to 7 Myr, different volumes of lithosphere sink into the mantle being 11.8 km^3/yr and 7.8 km^3/yr for H-divergent and H-convergent hinge (Figure 3.6).

The integration of a LVZ decoupling layer in the models and the use of velocity V_S as boundary condition applied to the lithosphere only, instead of the lateral boundary (Gerya, 2010), provide new insights on the dynamics of the sinking slabs at subduction zones. This condition produces different coupling/decoupling, and related dragging effects, between the lithosphere and the mantle. In fact, a higher depth of the slab in Figure 3.6c, can be addressed to the absence of the LVZ that, because of a higher coupling between the lithosphere and the mantle, provides a strong dragging effect of the

slab at higher depths. This is also enhanced by V_S applied to the entire boundary of the model and results in a higher depth of the subducting slab of about 200 km with respect to the one in Figure 3.6d. This latter seems not to be affected by these constraints, being V_S applied to the lithosphere only, and also for the presence of the LVZ, that acts as a decoupling layer.

The work done in this Chapter suggests that plate kinematic constraints contribute on the knowledge of subduction zone dynamics. Only if considering the V_S subduction rate as the main kinematic initial and boundary condition, numerical modeling provides results comparable with the asymmetries observed by geological and geophysical data at subduction zone worldwide. This parameter V_S, in fact, is the only one including variation carried by the transient motion of the subduction hinge. When analyzing subduction zones kinematics and dynamics, thus, convergence rate should be substituted with subduction rate to avoid any underestimation or overestimations in both numerical and kinematic analysis.

Furthermore, H-divergent subduction zones appears to be coincident with subduction zones having "westward"-directed slabs, whereas H-convergent are compatible with those that have "eastward-to-northeastward"-directed slabs (Doglioni & Panza, 2015). The exceptions to this geographic polarity are due to the Philippines and northern Japan subduction zones. Especially for the northern Japan, this subduction zone could be considered as transitional, i.e., an intermediate case of subduction where the Neogene W-directed subduction system is presently starting to flip, having the backarc basin started to shrink (Doglioni et al., 2007; Doglioni et al., 2006; Mazzotti et al., 2001). However, on the basis of this geographical polarity of subducting slabs, the computed volumes given by Japan and Philippine slabs can contribute on the lithosphere sinking at the W-directed subduction zones.

Under this assumption, the obtained lithospheric volume estimation gives ~214 km^3/yr and ~91 km^3/yr of subducting lithosphere at subduction zones with W-directed and E-to-NE-directed slabs, respectively. This enforces the contribution in lithosphere recycling of the W-directed subduction zones and entails that W-directed slabs produce more than twice the lithospheric sinking into the mantle with respect to E-to-NE-directed ones. In accordance with the conservation of mass principle, this volumetric asymmetry in the mantle suggests a displacement of ~120 km^3/yr of mantle material from the west to the east, providing a constraint for a global asymmetric mantle convection (Figure 3.7). Here we consider the larger fraction of the displacement occurring in a mainly horizontal direction, neglecting the other components.

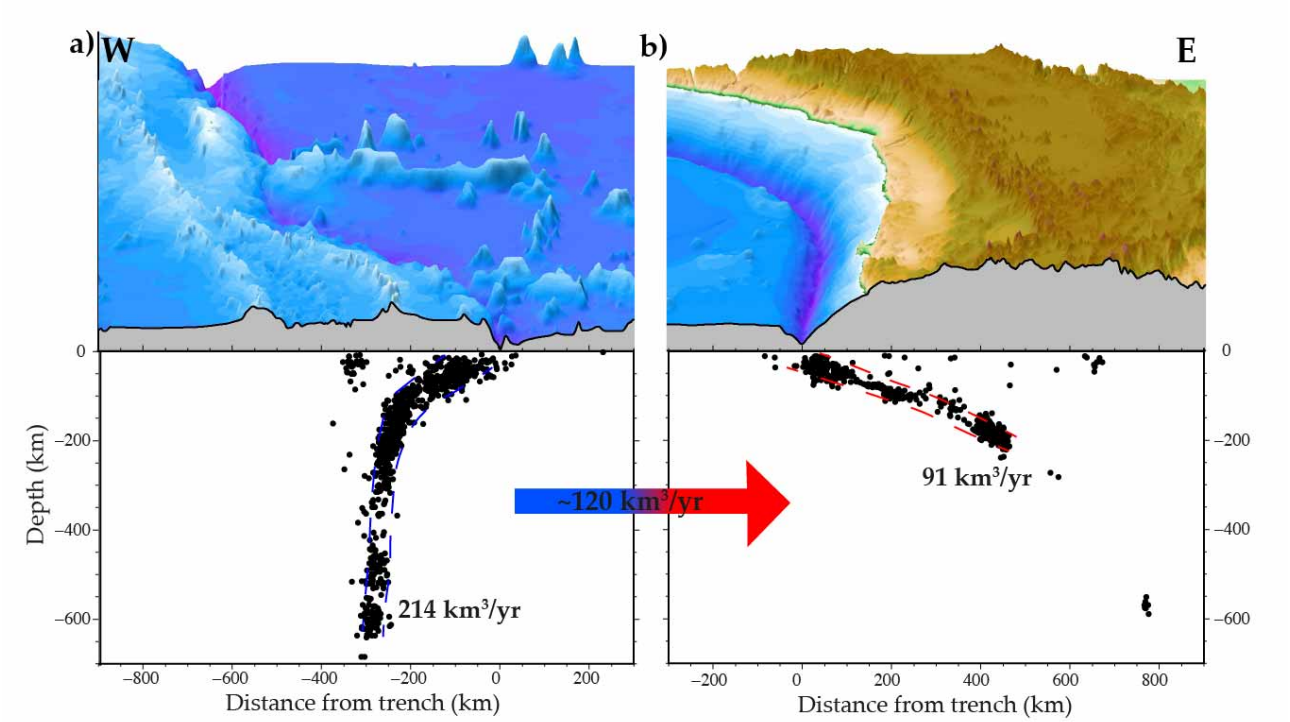

Figure 3.7 - Subduction asymmetries and related global mantle flow. Topography and earthquakes hypocenters (Heuret & Lallemand, 2005) at subduction zones that point to their asymmetries, due to the kinematics of the subduction hinge and the geographical polarity. Here the asymmetry in volumes of subducted lithosphere is striking. Since ~214 km^3/yr of lithosphere are currently subducting below subduction zones with mainly W-directed slabs (in blue) whereas only ~91 km^3/yr are subducting below subduction zones with mainly E to NE-directed slabs (in red), we would expect that about 120 km^3/yr of material moves from W to E within the mantle, consequently leading to a global "eastward" mantle flow.

3.7 Conclusions

In this Chapter, we analyzed subduction zones on the basis of the different kinematics of their subduction hinge with respect to the fixed upper plate. It produces a discrepancy in volumes of subducted lithosphere, e.g., ~190 km^3/yr vs ~91 km^3/yr and suggests asymmetric dynamics at subduction zones. This difference in subducted lithospheric volumes is related to the almost four times higher V_S of the H-divergent subductions with respect to the H-convergent subduction zones. It is important to note that this analysis is entirely independent from any mantle reference frame and holds regardless any dynamic model of subduction driving mechanism. Numerical modeling of subducting lithosphere into the mantle with the use of subduction rate V_S instead of the convergence rate V_L enforces the obtained asymmetries.

Lastly, it is worth noting that most of the subduction zones in which the hinge is moving away from the upper plate is characterized by a mainly W-directed slab and extensional stresses within the upper plate, that consequently leads to the opening of a backarc basin. In the most of the W-directed subduction zones, e.g., along the western side of the Pacific Ocean, there is the absence of high orogens. Conversely, subduction zones with a hinge moving towards the upper plate are mostly

characterized by a mainly E-to-NE-directed slab, e.g., along the eastern side of the Pacific Ocean, and a strong compressional stress within the upper plate can be observed, leading to the building of the highest mountain belts in the world.

Chapter 4

Plate tectonics and mantle convection: a numerical study

4.1 Introduction

The analysis about different kind of interactions between plate tectonics and mantle convection at convergent plate boundaries tackled in this dissertation has been realized, up to now, using 2d numerical models in rectangular boxes numerical domain.

In this section, 2d and 3d numerical models in a spherical domain will be shown. The aim of this analysis was to test the interplay between subduction dynamics and mantle convection in absolute and relative reference frames on a spherical geometry. To do this, we used the Advanced Solver for Problems in Earth's ConvecTion (ASPECT, Bangerth et al., 2018; Kronbichler et al., 2012) finite element parallel code, with the purpose of testing the asymmetries of subduction zones related to the "westward" drift of the lithosphere. This preferential motion of plates along the tectonic equator was simulated integrating plate motions in a shallow hotspot reference frame (Cuffaro & Doglioni, 2007) within the code. However, this reference frame was compared with angular vectors provided by Seton et al. (2012), in a conventional deep hotspot reference frame.

Nevertheless, being this the very first analysis of the interaction between global plate motions and mantle convection (particularly referring to the use of a shallow hotspot reference frame) using the ASPECT code, here strengths and weaknesses of this method were evaluated, in view of a possible future research.

The use of a spherical shell domain for these numerical models was important to avoid side boundary effects due to the rectangular box geometry domain and, furthermore, to consider the Earth's sphericity. Previously the flux was allowed to enter and flow out with periodic boundary conditions (Chapter 2) or was not allowed to flow in or out the computational domain (Chapter 3).

Two absolute plate motions reconstructions (data provided by Seton et al., 2012 and data in Table 4.1) have been used to constrain plate kinematics as boundary conditions in almost all the models that were realized. Exception are two numerical models in which relative reference systems were used, i.e., with respect to South America and Marianas plate fixed. Relative reference frames were taken

with respect to these two subduction zones because they clearly represent the two end-members of subduction zones described in this dissertation. Furthermore, the faster Pacific plate subducting below the Marianas plate leads to a clearer subducting slab with respect to the slower Philippine Sea plate.
Starting from our computational framework, moving on to the choice of the method used and its description, a characterization of both kinematic and rheological applied boundary conditions will be made for each model. Then, the results will be shown. In the last part of this section, discussion and critical issues will be addressed, togheter with future possibilities of improvement for the obtained results.

4.2 Numerical modeling

Numerical modeling tool used for the realization of this section was the ASPECT 2.0.0 code (Bangerth et al., 2018; Kronbichler et al., 2012), published under the GPL2 license. ASPECT is an advanced code based on the Finite Element Method (FEM) and it was mainly developed to solve convection problems in the Earth's mantle.
The cornerstones on which ASPECT is built (Bangerth et al., 2018) are also the principal reasons why it has been chosen to realize numerical model of this thesis last Chapter. In fact, among others, i) it is extendible by other users, whom constantly can contribute to determine which are the essential feature in the Earth's convection that needs to be included or improved; ii) it efficiently solves complex algorithms (such as, adaptive mesh refinement, linear and nonlinear solvers, etc.); iii) it involves the entire community of ASPECT users, that are welcomed to give their contribution and actively develop the code.
Thus, since it is a continuously evolving code, subsequent versions may differ from the one used to realize this dissertation numerical models. A short summary of the governing equations solved by ASPECT, as well as method used for their solution and the time discretization is given in Section 4.2.2. For more information, the reader is referred to Kronbichler et al. (2012) and Bangerth et al. (2018).
For this dissertation ~160 models were realized. Nonetheless, 16 models will be shown that were the most representative of the carried analysis and are, for instance, 14 in 2d and two in 3d. 14 are in absolute reference frames (seven in a deep hotspot reference frame and seven in a shallow hotspot reference frame), whereas two in relative reference frames (in a South American reference frame and in Marianas plate reference frame). Basically, it is again important to mention that each model realized in an absolute reference frame has been tested both in a deep and in a shallow hotspot reference frame.

4.2.1 Computational Framework

The available computational framework during the realization of these numerical models was composed of one MacBook Pro with a 2.6 GHz Intel Core i5 processor, one iMac with a 4GHz Intel Core i7 processor, two DELL workstations both with a native Ubuntu 16.04 LTS OS and a 3.60GHz × 8 Intel Core i7-7700 CPU processor. On the first two machines an Ubuntu operative system was mount using the Oracle VirtualBox virtual machine (Version 5.1.26 r117224 (Qt5.6.2)) on a macOS 10.13.6 version.

Although ASPECT is designed to support hundreds or thousands of processors working together (Bangerth et al., 2018), we used at maximum 6 processors working together. This allowed a total computational time spent of about 36 weeks, of which just 6 were used for the computation of one 3d model.

4.2.2 ASPECT

Like numerical codes previously presented in this dissertation solving the Stokes equation, ASPECT assumes a highly viscous fluid-like behaviour of the Earth solid part. Thus, its continuum mechanics mathematic formulations include the solution of the governing conservation of momentum (4.1), mass (4.2) and energy (4.3) equations (Schubert et al., 2001). ASPECT solves this system in a 2- or 3-dimensional domain Ω and can solve it for both compressible and incompressible flow using the Boussinesq approximation and omitting the inertial term (i.e., using an infinite Prandtl number). The governing equations are:

$$-\nabla \cdot \left[2\eta\left(\varepsilon(\mathbf{u}) - \tfrac{1}{3}(\nabla\cdot\mathbf{u})\mathbf{1}\right)\right] + \nabla p = \rho\mathbf{g} \quad \text{in } \Omega, \tag{4.1}$$

$$\nabla\cdot(\rho\mathbf{u}) = 0 \quad \text{in } \Omega, \tag{4.2}$$

$$\begin{aligned}\rho C_p\left(\frac{\partial T}{\partial t} + \mathbf{u}\cdot\nabla T\right) - \nabla\cdot k\nabla T = \rho H \\ +2\eta\left(\varepsilon(\mathbf{u}) - \tfrac{1}{3}(\nabla\cdot\mathbf{u})\mathbf{1}\right) : \left(\varepsilon(\mathbf{u}) - \tfrac{1}{3}(\nabla\cdot\mathbf{u})\mathbf{1}\right) \\ +\alpha T(\mathbf{u}\cdot\nabla p) \\ +\rho T\Delta S\left(\frac{\partial X}{\partial t} + \mathbf{u}\cdot\nabla X\right) \quad \text{in } \Omega,\end{aligned} \tag{4.3}$$

$$\frac{\partial c_i}{\partial t} + u\cdot\nabla c_i = 0 \quad \text{in } \Omega, i = 1\ldots C \tag{4.4}$$

where, η is the viscosity, $\varepsilon(\mathbf{u}) = \frac{1}{2}(\nabla\mathbf{u} + \nabla\mathbf{u}^T)$ is the symmetric gradient of velocity, i.e., the strain rate, $\mathbf{u}$ is the velocity vector, assuming a linear dependence of density $\rho = \rho_0\big(1 - \alpha(T - T_0)\big)$, being ρ_0 and T_0 the reference density, α the linear thermal expansion coefficient, temperature, respectively, T is the temperature, $\mathbf{g}$ is the gravity vector, C_p is the specific heat capacity, t is time, k is the thermal conductivity, H is the intrinsic specific heat production, p is the pressure, ΔS is the change in entropy at a phase transition, together with the derivatives of the phase function X = X(p, T, **c**, **x**), where **c** is the compositional field and **x** the spatial variable, with respect to temperature and pressure, thus c_i is a set of advected quantities, called compositional fields by the authors (Bangerth et al., 2018). Equation (4.1) and (4.2) togheter are the compressible Stokes equation. Equation (4.3) is the temperature equation, coupled to the Stokes system, that has the heat conduction terms and the advection with the flow velocity **u**. The right-hand side terms of this equation are the i) internal heat production, e.g., radioactive decay, ii) frictional heating, iii) adiabatic compression of material and iv) phase change. The last term of the temperature equation represents the latent heat generated or consumed in when phase change of material occurs. Furthermore, for each compositional field c_i, this formulation introduces an additional advection equation (4.4) to the system of described equations (4.1)-(4.3). All models in this Chapter use the Anelastic Liquid Approximation (ALA) variation for equations (4.1)-(4.3). This approximation considers the perturbation p' and T' much smaller than reference quantities values $\bar{p}$ and $\bar{T}$. This influences terms in the continuity equation, i.e., $\nabla \cdot (\rho u) = 0$, and in the temperature equation, i.e., $\rho(p, T)$. Thus, here the density variations $\rho(p, T) - \bar{\rho}$ can be described by its Taylor expansion:

$$\rho(p, T) \approx \bar{\rho} + \frac{\partial \rho(\bar{p}, \bar{T})}{\partial p} p' + \frac{\partial \rho(\bar{p}, \bar{T})}{\partial T} T' \tag{4.5}$$

where, second term is related to the compressibility k and the third to the thermal expansion coefficient α. Moreover, the ALA approximation assumes that density variations with respect to the reference value can be neglected in mass conservation and temperature equations (see Bangerth et al., 2012 and King et al., 2010). To solve the system of equations presented above, ASPECT uses the FEM (Finite Element Method). With this method, the domain is discretized into smaller quadrilateral/hexahedral finite elements and the solution, i.e., velocity, pressure, temperature and compositional fields, is then assembled into the larger system of equations using Lagrange polynomials as interpolating basis functions. The model geometry is a spherical shell going from the surface to the CMB, mostly taking into account fase transitions, such as the lithosphere thickness, i.e., 100 km, the 410 km discontinuity and 670 km discontinuity. The model is initially defined on a

regular grid, i.e., cells having the same height, width and depth, i.e., in 3d domains (Figure 4.1). In all the 2d models the coarsest mesh was refined five times globally, i.e., every cell was refined into four children five times. In 3d models the coarsest mesh was refined three times globally, i.e., every cell was refined into four children three times, globally. This was principally made to shorten the computational time. In its calculations, ASPECT uses the Adaptive Mesh Refinement (AMR) method, which allows the local refinement and coarsening of the grid during the simulation, being hundred and thousand times faster (in 2d and 3d, respectively) than using a regular grid keeping the same high resolution (Bangerth et al., 2018; Kronbichler et al., 2012). For the evolution through time of numerical simulations, the Courant-Friedrich-Lewy (CFL) condition (Anderson, 1995) is used in ASPECT and must be satisfied for every cell K in the domain (4.6).

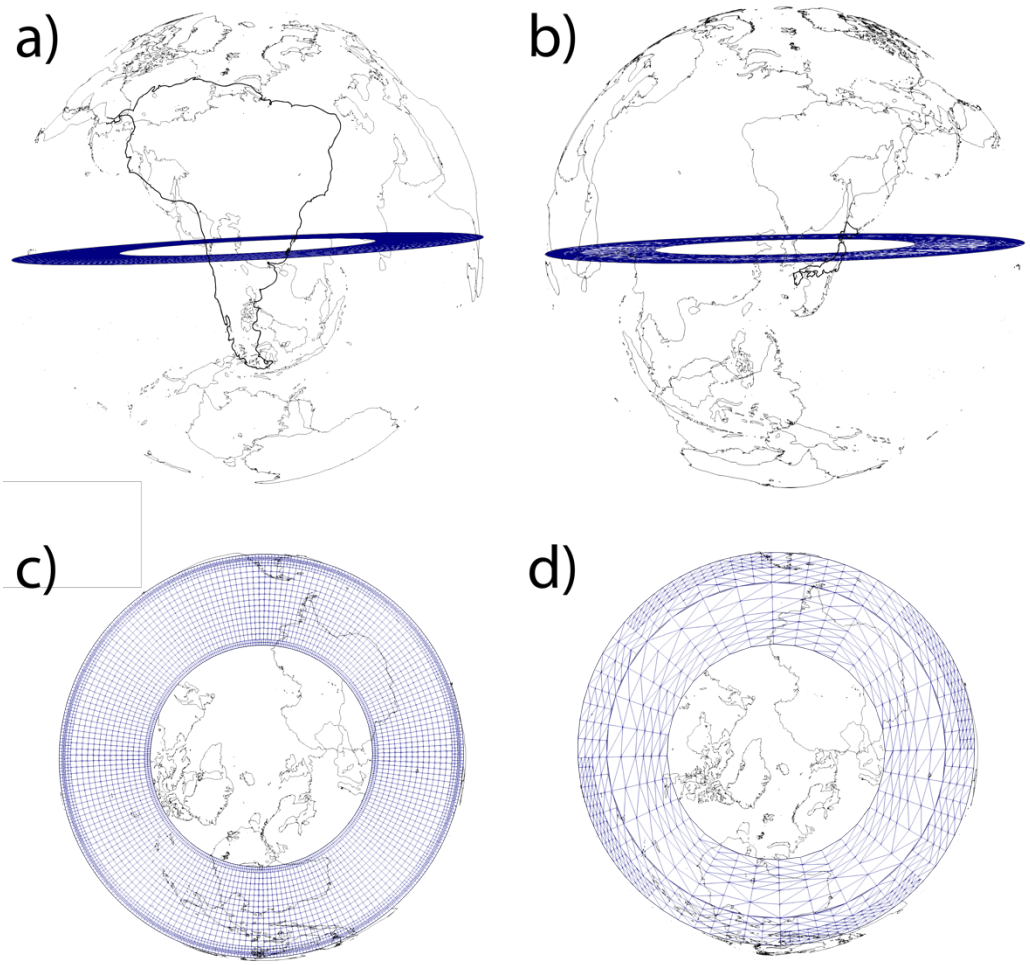

Figure 4.1 – Example of the 2d (panel c) and 3d (panel d) mesh grid at the initial stage. The view is from the South Pole in panels c) and d). Panel (a) shows a view on the model slice from South America (in bold), whereas panel (b) shows the model slice from a Pacific point of view (Japan in bold). The models are initially defined on a regular grid, i.e. cells having the same height, width and depth (in 3d). In its calculations, ASPECT uses the Adaptive Mesh Refinement (AMR) method, which allows the local refinement and coarsening of the grid during the simulation.

$$\frac{\delta t \|\mathbf{u}\|_{\infty,K}}{h_K} \leq C. \qquad (4.6)$$

This means that for each model the timestep is chosen so that a point in an advected cell does not move further than C times its diameter. This value is usually stable between zero and one, although values higher than one are stable as well in ASPECT (Kronbichler et al., 2012). In this dissertation models C is always set to 1.0. The CFL method is an efficient solution to the important problem of choosing the timestep size in numerical models. In fact, for too large or too small timesteps, the solver may not be able to find a good solution, wasting a lot of computational time. ASPECT is a modular code. The core code which solves basic equations communicates with attached plugins (i.e., small codes covering a single function, that can be easily attached and detached from ASPECT core, e.g., the plugin which calculates the model initial temperature field) and libraries on which ASPECT is built that are: i) p4est (Burstedde et al., 2011), that contains code to build adaptive meshes; ii) deal.II (Bangerth et al., 2007), a finite element library that implements the use of meshes built by p4est and discretization; TRILINOS (Heroux et al., 2005), that contains solvers to perform linear algebra calculations. Moreover, to prevent the users from recompiling ASPECT at each model run, an external input file (example in Figure 4.2), including runtime parameters defined and changed by the user, is read by ASPECT every time a model starts to run. In this file, parameters are divided in subsections, whereas global parameters are outside the subsection.

```
set Dimension                              = 2
set Use years in output instead of seconds = true
set End time                               = 14e7
set Output directory                       = output
set Adiabatic surface temperature          = 1600


subsection Material model
  set Model name = simple

  subsection Simple model
    set Viscosity                   = 1e21
    set Thermal viscosity exponent  = 5.0
    set Reference temperature       = 1600
  end
end


subsection Geometry model
  set Model name = spherical shell

  subsection Spherical shell
    set Inner radius  = 3481000
    set Outer radius  = 6336000
  end
end


subsection Model settings
  set Prescribed velocity boundary indicators = outer:gplates
  set Tangential velocity boundary indicators =

  set Fixed temperature boundary indicators   = inner, outer
```

Figure 4.2 – External input file. This is an example of external input file in which global parameters are the first five rows, outside of the subsections.

4.3 Plate motions boundary conditions

To achieve plate motions simulation on numerical models in a spherical shell domain, the ASPECT code efficiently interfaces to the widely used plate reconstruction software GPlates. This allowed to include plate surface velocities as boundary condition for the outer shell of the model domain, to prescribe its velocity according to a specific plate motions reconstruction. As already mentioned, the purpose was to test a proposed geological model and investigate lithosphere-mantle interactions.

4.3.1 GPlates

GPlates (Boyden et al., 2011) is an open-source software for plate tectonics interactive visualization developed by the EarthByte Project (School of Geosciences – University of Sydney, Division of Geological and Planetary Sciences – CalTech, Center for Geodynamics – Norwegian Geological Survey). For extensive documentation, the reader is referred to the GPlates website (http://www.gplates.org). To effectively take plate reconstruction models from GPlates and include it into ASPECT, several steps were followed, starting from the acquisition of closed dynamic polygons proposed by Seton et al. (2012) and rotation files covering the entire model domain corresponding to the plate reconstruction model. GPlates software, in fact, considers plates as polygons, which rotate around a pole with a specific assigned velocity. For this Chapter, we used Pacific angular vectors by Wessel and Kroenke (2008) including relative plate and microplates motions provided by Seton et al. (2012) for the deep hotspot reference frame hypothesis. Concerning the shallow hotspot reference frame, Pacific angular vectors proposed by Wessel and Kroenke (2008) were used, which we have first integrated into the Pacific shallow hotspots, following the methods proposed by Doglioni et al. (2005), Cuffaro and Doglioni (2007), Doglioni et al. (2015) and Cuffaro and Doglioni (2018), so that we obtained results reported in Table 4.1. Considering that ASPECT needs velocity vectors defined at individual surface points, the second step is to generate the "velocity domain points", i.e., discrete points at which velocity information are evaluated by GPlates. The output of this operation is a general Latitude/Longitude grid, which has nodes on all crossing points, so that it is easy for ASPECT to interpolate it to the nodes position during the model run. This is due to the adaptive mesh refinement used by ASPECT that does not make possible for GPlates to import velocities for a specific surface node position. Furthermore, since the GPlates velocity output is always 3d, its ASPECT plugin allows for both 2d and 3d numerical calculations. ASPECT's 2d simulations projects plate velocities into the model plane, that is rotated according to an orientation

specified by the user. This is done prescribing two points that define the plane, considering that in the used ASPECT's version only great-circle slices are allowed. Coordinates for these two points need to be expressed in radians and in spherical coordinates θ (i.e., the colatitude, with its 0 corresponding to the north pole) and φ (i.e., having its 0 at the Greenwich meridian, with positive eastwards). Through this approach, computations are performed on 2d slices chosen with arbitrary Earth's coordinates, using realistic plate motions velocities as surface boundary conditions. 2d numerical models presented in this dissertation has been carried out on 2d slices corresponding to the tectonic equator (as described in Section 1.2.1). On this equator, lithospheric plates show a mean faster motion and, besides, it perpendicularly crosses two of the most important and different subduction zones in the world, i.e., Japan and South America, that can be, thus, taken as reference for comparison on subduction dynamics. Furthermore, here numerical models are carried out in both absolute and relative reference frames. For instance, 14 models are described in absolute reference frames (seven in a deep hotspot reference frame and seven in a shallow hotspot reference frame), whereas two in relative reference frames (i.e., in a South America and Marianas plates fixed reference frame). 3d numerical models were carried out in absolute reference frames (one in a deep hotspot and one in a shallow hotspot reference frame). However, surface plate kinematics included in this thesis models is shown in Figures 4.3-4.7, so that an overall vision of what is happening on the surface of each model computed is always available for the reader. A picture of the surface kinematics corresponding to the specific model step will be also shown as a small feature in figures of each result that will be presented in the results section.

Pacific ID	Time (Ma)	Latitude (°N)	Longitude (°E)	Angle (°)	Fixed Plate ID
901	0.78	49.30	-49.5	2.04	002b
901	2.58	53.72	-56.88	5.32	002b
901	5.89	59.65	-66.05	10.78	002b
901	8.86	62.87	-70.87	16.46	002b
901	12.29	65.37	-68.68	20.60	002b
901	17.47	68.25	-61.53	31.00	002b
901	24.06	68.78	-69.83	40.80	002b
901	28.28	67.72	-70.80	47.20	002b
901	33.54	66.57	-68.73	55.40	002b
901	40.10	65.43	-64.25	63.20	002b
901	47.91	63.02	-66.68	69.20	002b
901	53.35	60.60	-69.67	72.20	002b
901	61.10	56.93	-72.93	76.80	002b
901	74.50	50.03	-78.35	88.00	002b
901	83.50	47.30	-82.10	97.60	002b
901	95.00	46.90	-82.68	108.20	002b
901	106.20	51.32	-85.12	120.20	002b
901	112.30	52.17	-85.80	124.80	002b
901	118.40	52.53	-80.33	133.00	002b
901	125.00	54.13	-88.18	139.20	002b
901	131.90	56.22	-112.25	157.20	002b

Table 4.1 – Shallow hotspot reference frame rotations. Pacific Plate (ID: 901) finite rotations with respect to the shallow hotspot reference frame (ID: 002b) in the time interval 140–0 Ma. Modified after Wessel and Kroenke (2008) and reported as Seton et al. (2012).

4.3.2 Surface boundary conditions

Numerical models carried out in absolute reference frames were realized using both a deep hotspot reference frame (angular vectors provided by Seton et al., 2012) and a shallow hotspot reference frame (Table 4.1). Two among the 14 models in absolute reference frames were realized using the current day plate motions velocities applied continuously for 140 Myr, whereas for the others the plate motions evolution (i.e., from 140 Myr to 0 Myr) were implemented (Table 4.2).

Plate kinematics evolution through the last 140 Myr, corresponding to the two reference frames, are shown in Figures 4.3, 4.4 and Figures 4.5, 4.6, respectively. In these figures the tectonic equator corresponds to the black solid line and points to the plane on which the models lie.

However, the following Table 4.2 describes the models surface boundary conditions.

MODEL NAME	EQUATOR	PLATE MOTIONS VELOCITY	REFERENCE FRAME
basic1	tectonic	current day	deep hotspot
basic2	tectonic	current day	shallow hotspot
basic3	tectonic	evolution	deep hotspot
basic4	tectonic	evolution	shallow hotspot
vp1	tectonic	evolution	deep hotspot
vp2	tectonic	evolution	shallow hotspot
isehar1	tectonic	evolution	deep hotspot
isehar2	tectonic	evolution	shallow hotspot
majol1	tectonic	evolution	deep hotspot
majol2	tectonic	evolution	shallow hotspot
majfo89_1	tectonic	evolution	deep hotspot
majfo89_2	tectonic	evolution	shallow hotspot
majol_sa	modified tectonic	current day	relative to South America
majol_ma	modified tectonic	current day	relative to Marianas
majol3d_1	tectonic	evolution	deep hotspot
majol3d_2	tectonic	evolution	shallow hotspot

Table 4.2 - Surface boundary conditions for all described models. Seven main models, each done in both deep and shallow hotspot reference frames, give 14 models in absolute reference frames plus two in relative reference frame (wrt South America and Marianas fixed plates). In this table are the model name, the equator on which the model lie and the implemented plate kinematics, both in terms of evolution of plate motions or not and corresponding reference frame. Rotation pole coordinates for the modified tectonic equator are longitude 100°E and latitude 65°S.

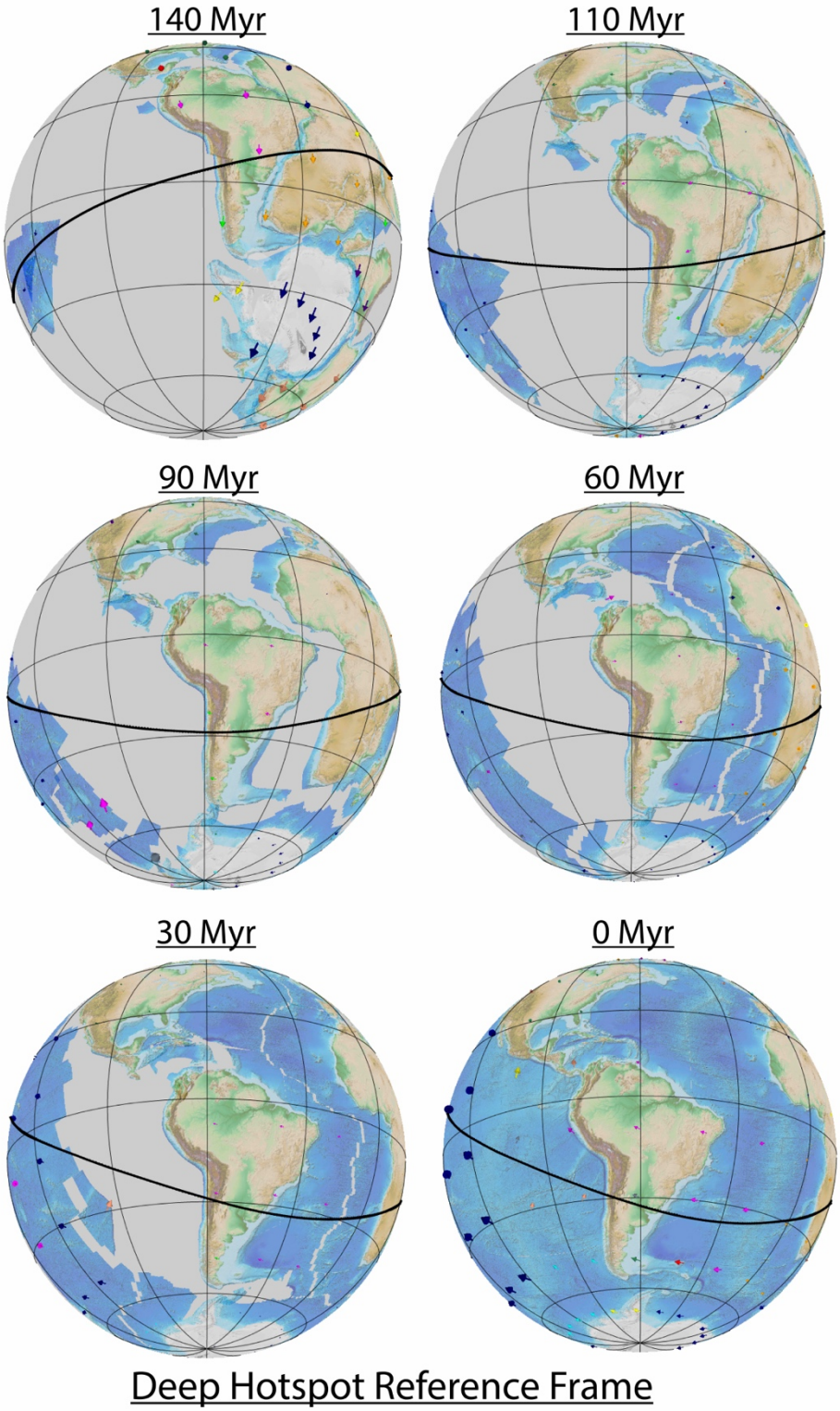

Figure 4.3 - Plate kinematics in the deep hotspot reference frame. These pictures are plate motion evolution through the last 140 Myr from a South America point of view. Rotations collected by Seton et al. (2012). In black the numerical models plane, i.e., the tectonic equator.

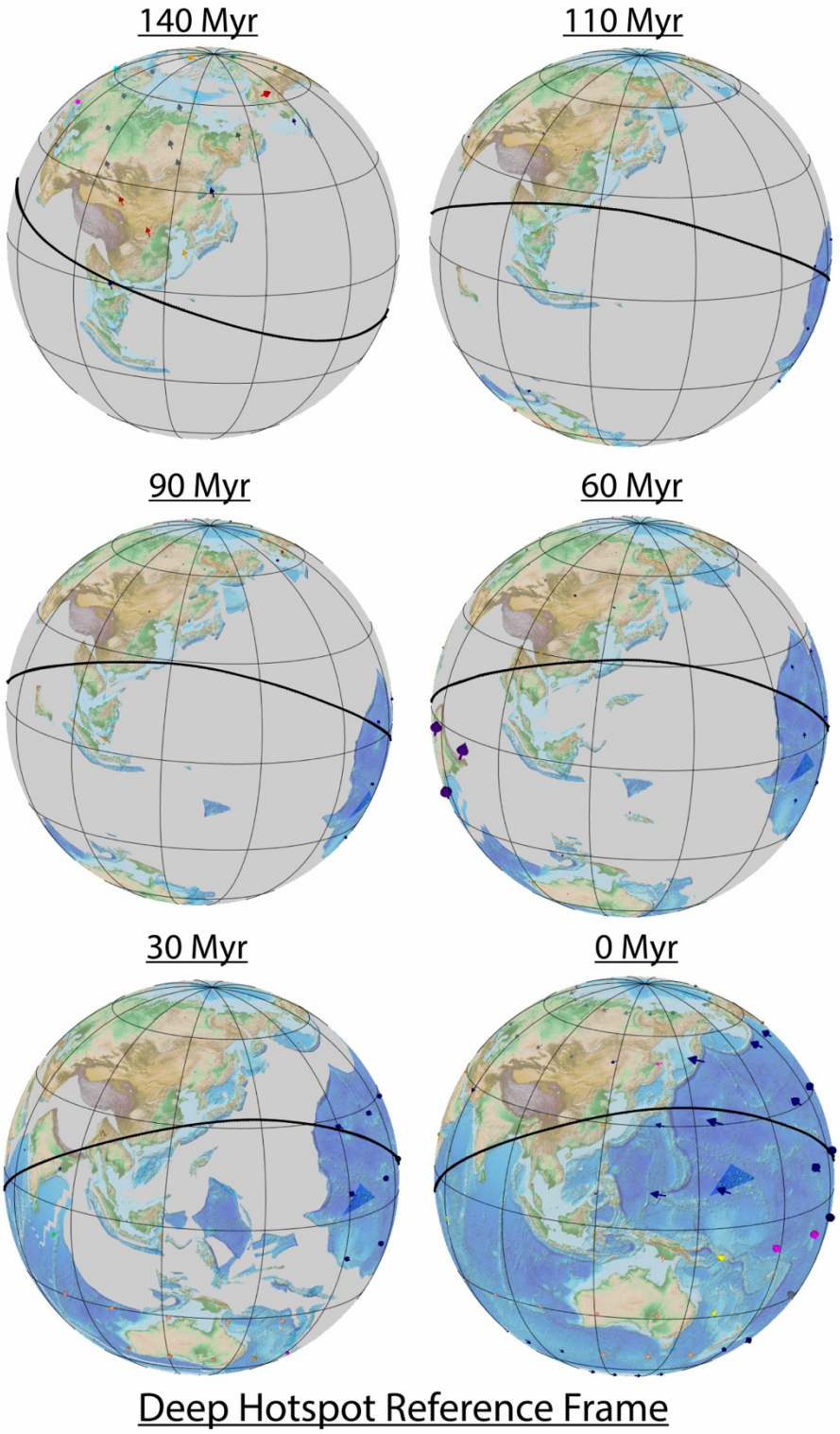

Figure 4.4 - Plate kinematics in the deep hotspot reference frame. These pictures are plate motion evolution through the last 140 Myr from a Pacific point of view. Data about angular vectors provided by Seton et al. (2012). In black the numerical models plane, i.e., the tectonic equator.

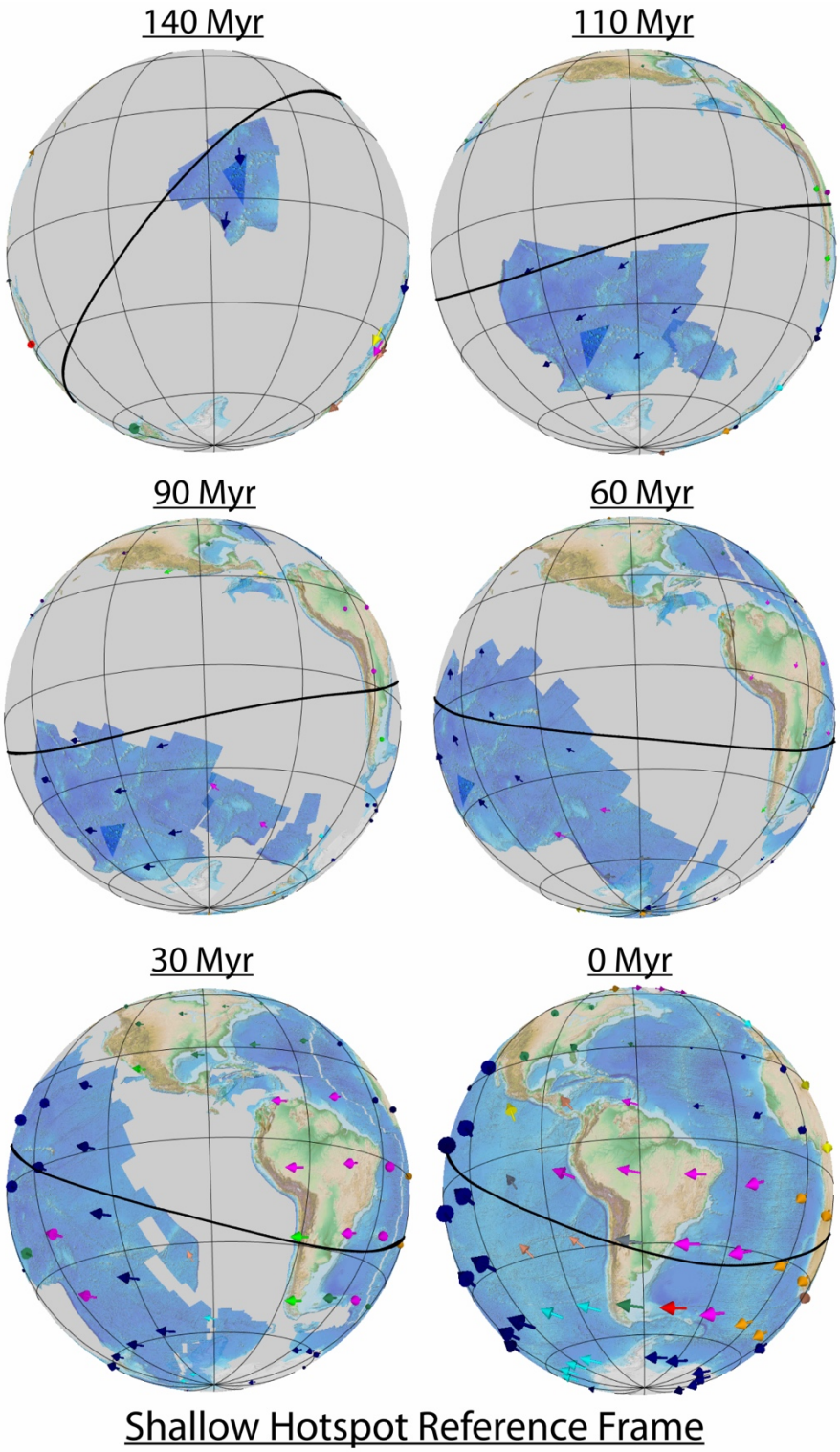

Figure 4.5 - Plate kinematics in a the shallow hotspot reference frame. These pictures are plate motion evolution through the last 140 Myr from a South America point of view in a shallow hotspot reference frame (Table 4.1). In black the numerical models plane, i.e., the tectonic equator.

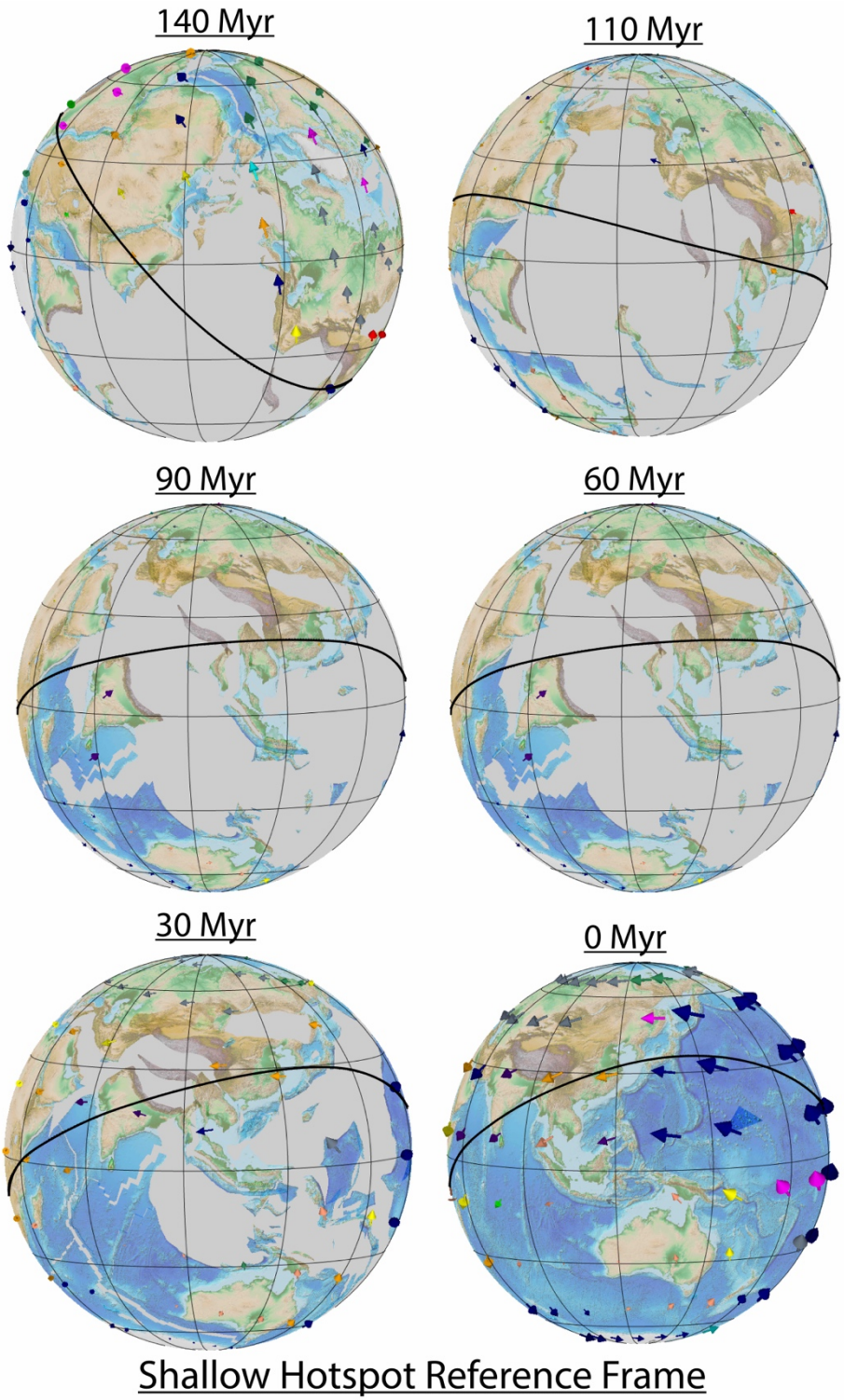

Figure 4.6 - Plate kinematics in a shallow hotspot reference frame. These pictures are plate motion evolution through the last 140 Myr from a Pacific point of view, in a shallow hotspot reference frame (Table 4.1). In black the numerical models plane, i.e., the tectonic equator.

To allow a comparison with models shown in the previous Chapter of this thesis two models in a relative reference frame were realized. Plate kinematics for the reference frame relative to fixed South America and Marianas plates are in Figure 4.7. Constant current plate velocities with respect to South America and Marianas plate were used cutting the numerical model slices on a tectonic equator slightly modified to be orthogonal to both these subduction zones (Figures 4.7a and 4.7b, solid black line). This modified version of the tectonic equator has rotation pole coordinates of longitude 100°E and latitude 65°S.

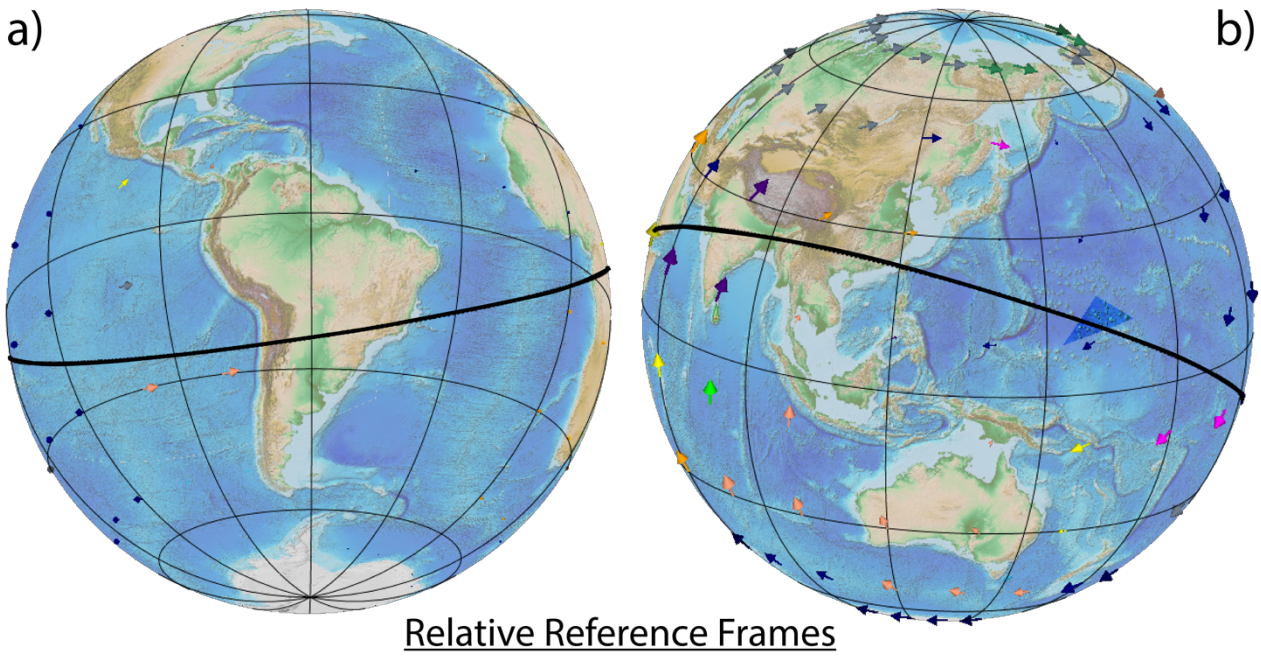

Figure 4.7 - Plate kinematics in a relative reference frame. This picture represents plate motions in both South America and Pacific point of view, in a relative reference frame. Panel a represents velocities for plates in a South America reference frame, whereas panel b shows velocities in a Marianas reference frame. In black the numerical models plane, i.e. the tectonic equator, slightly modified to be orthogonal to both reference plates. The modified version of the tectonic equator has rotation pole coordinates of longitude 100°E and latitude 65°S.

4.4 Rheology

Numerical models of this numerical analysis were realized also testing rheologies, starting from a simple one to a more complicated one. As mentioned before, the ASPECT code is a modular code, i.e., it is composed from a number of modules (e.g., for mesh refinement, boundary conditions, initial condition etc.). One of them is the Material model module, within which rheologies are implemented. In this way, ASPECT allows for the usage of several rheologies through the computation of functions for the principal rheological parameters, e.g., density, viscosity, specific heat, thermal expansion, conductivity and diffusivity.

In the next sections, rheologies used for numerical models showed in this Chapter will be described starting from the simple to the complex one. For instance, in this order, four models were realized using the Simple Material model, two with the Visco Plastic Material model and 10 using reference profiles read from ASCII data files specified by the user. These ASCII data files were generated using the BurnMan (Cottaar et al., 2014; Cottaar et al., 2017) open source software, a thermodynamic and geophysics toolkit for the Earth and planetary sciences (http://www.burnman.org), that will be quickly introduced in the following sections.

4.4.1 Simple Material model

This Material model is one of the simplest that the ASPECT code can offer. In this model density and viscosity have thermic and compositional dependencies, whereas the other coefficients are kept constant. For viscosity and density this material model uses the following set of equations:

$$\eta(p,T,\mathbf{c}) = \tau(T)\zeta(\mathbf{c})\eta_0, \tag{4.7}$$

$$\rho(p,T,\mathbf{c}) = \big(1-\alpha(\mathrm{T}-T_0)\big)\rho_0 + \Delta\rho\, c_0 \tag{4.8}$$

In these equations, if compositional fields are used, c_0 represents the first component of the compositional vector **c**. If compositional fields are not used, like in this thesis models, then its value is zero. $\tau(T)$ is the viscosity temperature pre-factor and it is defined as follows:

$$\tau(T) = H\left(e^{-\frac{\beta(T-T_0)}{T_0}}\right), \qquad H(x) = \begin{cases} \tau_{min} & \text{if } x < \tau_{min}, \\ x & \text{if } 10^{-2} \le x \le 10^{2}, \\ \tau_{max} & \text{if } x > \tau_{max}, \end{cases} \tag{4.9}$$

where T and H are again the temperature and intrinsic heat capacity respectively, whereas β is the thermal viscosity exponent and T_0 is the reference temperature and can be both set by the user in the input parameter file. τ_{max} and τ_{min} are the maximum and minimum temperature pre-factors values. If compositional fields are used, $\zeta(\mathbf{c})$ corresponds to the viscosity compositional pre-factor, whereas α and $\Delta\rho$ are, respectively, the thermal expansion coefficient and the density differential for compositional fields. This model uses an incompressible medium and pressure and temperature are computed in adiabatic conditions. Its adiabatic domain temperature is always chosen significantly higher (~1330 °C or 1600 K) with respect to the actual surface temperature (~0°C or ~273 K). The bulk mantle, in fact, is in thermal equilibrium with a temperature that is ~1600 K, thus for temperature and pressure to be good starting points for nonlinear solvers, this is a reasonable adiabatic surface temperature to have a well-mixed temperature within the entire domain (Bangerth et al., 2018). Otherwise, the very low actual Earth's surface temperature and the very high one at the core-mantle boundary, would simply induce characteristic thermal boundary layers (at 0 km and 2900 km, i.e., the top and bottom of the domain) from which plumes rise and sink (Bangerth et al., 2018). In numerical models of this section a fixed temperature is prescribed at the top and bottom of the domain, so that there is heat flux throughout these two boundaries. Models that were carried out with this Simple Material model are four, i.e., *basic1*, *basic2*, *basic3* and *basic4* and their main parameters are in Table 4.3. These models differ for their surface velocities boundary conditions: i) models *basic1* and *basic2* use the current day plate motions velocity all along the entire model run (140 Myr), whereas models *basic3* and *basic4* implement plate motions evolution for the last 140 Myr (Table 4.2); ii) models *basic1* and *basic3* are in a deep hotspot reference frame, whereas models *basic2* and *basic4* are in a shallow hotspot reference frame (Table 4.2)

GLOBAL PARAMETERS	
MODEL NAME	basic1, basic2, basic3, basic4
DIMENSION	2
END TIME	140 Myr
ADIABATIC SURFACE TEMPERATURE	1600 K
MATERIAL MODEL	
MODEL NAME	Simple
REFERENCE VISCOSITY	1.00E+22
THERMAL VISCOSITY EXPONENT	5.00
GEOMETRY MODEL	
MODEL NAME	Spherical Shell
INNER RADIUS	3481000 m
OUTER RADIUS	6336000 m
MODEL SETTINGS	
FIXED TEMPERATURE BOUNDARY INDICATORS	inner, outer
BOUNDARY TEMPERATURE MODEL	
MODEL NAME	Spherical Constant
OUTER TEMPERATURE	273 K
INNER TEMPERATURE	2600 K
INITIAL TEMPERATURE MODEL	Adiabatic
GRAVITY MODEL	
MODEL NAME	Radial Constant
MAGNITUDE	10
MESH REFINEMENT	
INITIAL GLOBAL	5
INITIAL ADAPTIVE	1
TIME STEPS BETWEEN MESH REFINEMENT	2

Table 4.3 – Main input parameters of the *basic1-4* models. Models *basic1* and *basic2* use the current day plate motions velocity all along the entire model run (140 Myr), whereas models *basic3* and *basic4* implement plate motions evolution for the last 140 Myr (Table 4.2); ii) models *basic1* and *basic3* are in a deep hotspot reference frame, whereas models *basic2* and *basic3* are in a shallow hotspot reference frame (Table 4.2).

4.4.2 Visco Plastic Material model

This Material model takes into account both plastic and non-linear viscous deformation. It allows the usage of different flow laws, such as dislocation creep, diffusion creep or combinations of them. Viscous stresses are bounded from the Drucker-Prager yield criterion and, for dislocation and diffusion creep, the viscosity, in ASPECT, is characterized as follows (Billen & Hirth, 2007):

$$v = 0.5\, A^{-\frac{1}{n}}\, d^{\frac{m}{n}}\, \dot{\varepsilon}_{ii}^{\frac{1-n}{n}}\, exp\left(\frac{E+PV}{nRT}\right). \qquad (4.10)$$

In the formula above, A is the pre-factor, n is the stress exponent, d is the grain size, m is the grain

size exponent, $\dot{\varepsilon}_{ii}$ is the square root of the second invariant of the deviatoric strain rate tensor, E is the activation energy, P is the pressure, V is the activation volume, R is the gas exponent and T is the temperature. Here A is determined by Viscosity. The viscosity change depends on a list of Viscosity pre-factors and of depths at which each pre-factor should be applied. In these models, viscosity jumps are set at 150, 410 and 660 km depth. The equation above assumes different forms depending on the chosen flow law. The diffusion form v_{diff} has $n = 1$ and $m! = 0$, whereas the dislocation form v_{disl} assumes values of $n > 1$ and $m = 0$. A form in which both the previous ones are combined is also possible, in this case the equation becomes $\frac{v_{diff} \times v_{disl}}{v_{diff} + v_{disl}}$.

Since models that uses such visco-plastic rheology in this thesis are in 2d, the corresponding form for the yield stress is:

$$\sigma_y = C\cos(\phi) + P\sin(\phi), \tag{4.11}$$

where C is the cohesion and ϕ is the angle of internal friction. The above form corresponds to the Mohr-Coulomb yield surface whereas, if $\phi = 0$ then σ_y is constant and equal to C (i.e., Von Mises yield criterion).

In numerical models of this section the fixed temperature is prescribed at the top of the domain, so that there is heat flux throughout this boundary.

Models that were carried out with this Visco Plastic Material model are two, i.e., *vp1* and *vp2*, and their main parameters are in Table 4.4. These models differ only for their surface velocities boundary conditions. In fact, model *vp1* is in a deep hotspot reference frame, whereas model *vp2* is in a shallow hotspot reference frame (Table 4.2).

GLOBAL PARAMETERS	
MODEL NAME	vp1, vp2
DIMENSION	2
END TIME	140 Myr
ADIABATIC SURFACE TEMPERATURE	1600 K
MATERIAL MODEL	
MODEL NAME	Visco Plastic
REFERENCE VISCOSITY	1.00E+21
THERMAL VISCOSITY EXPONENT	0.00
VISCOSITY PRE-FACTORS	10.0, 0.1, 1.0, 10.0
GEOMETRY MODEL	
MODEL NAME	Spherical Shell
INNER RADIUS	3481000 m
OUTER RADIUS	6336000 m
MODEL SETTINGS	
FIXED TEMPERATURE BOUNDARY INDICATORS	outer
BOUNDARY TEMPERATURE MODEL	
MODEL NAME	Spherical Constant
OUTER TEMPERATURE	273 K
INNER TEMPERATURE	2600 K
INITIAL TEMPERATURE MODEL	Adiabatic
GRAVITY MODEL	
MODEL NAME	Radial Constant
MAGNITUDE	10
MESH REFINEMENT	
INITIAL GLOBAL	5
INITIAL ADAPTIVE	1
TIME STEPS BETWEEN MESH REFINEMENT	2

Table 4.4 – Main input parameters of the *vp1* and *vp2* models. These models differ only for surface velocities boundary conditions. In fact, model *vp1* is in a deep hotspot reference frame (see Table 4.2) and model *vp2* is in a shallow hotspot reference frame (see Table 4.2).

4.4.3 ASCII Reference Profile Material model

The ASCII classes, in ASPECT, allow ASCII data files to be read by plugins (i.e., boundary and initial conditions, material models, etc.). This ASCII data file has to contain information about depth, pressure, temperature, density, gravity, thermal expansion, specific heat and compressibility for each point of the numerical domain.

These data were generated using the BurnMan thermodynamic toolkit (Cottaar et al., 2014; Cottaar et al., 2017) and used in models providing a constraint for material model, adiabatic conditions and gravity model. In this model, the viscosity is computed as a function of the depth direction z of the model geometry and on its dependence on temperature T, as follows:

$$\eta(z,T) = \eta_r(z)\eta_0 exp\left(-A\frac{T-T_{adiab}}{T_{adiab}}\right). \quad (4.12)$$

In this expression, the constants A and η_0 are set by Viscosity and Thermal viscosity exponent parameters. $\eta_r(z)$ is the viscosity profile function, with which the viscosity changes depending on a list of Viscosity pre-factors and of depths at which each pre-factor should be applied. In these models, viscosity jumps are set at 150, 410 and 660 km depth and pre-factors determine an asthenosphere with a low viscosity and a lower mantle with high viscosities. Harmonic averaging of material properties is implemented to avoid numerical problems due to viscosity jumps, so that accurate solutions and acceptable computational time are preserved. Basically, an evaluation on each computed quantity (i.e., viscosity, density, compressibility etc.) is made at every quadrature point, replacing the values with their harmonic average:

$$\bar{x} = \left(\frac{1}{N}\sum_{i=1}^{N}\frac{1}{x_i}\right)^{-1} \quad (4.13)$$

In numerical models of this section the fixed temperature is prescribed at the top of the domain, so that there is heat flux throughout this boundary.

Models that were carried out with this Material model are 10, i.e., *isehar1*, *isehar2*, *majol1*, *majol2*, *majfo89_1*, *majfo89_2*, *majol_sa*, *majol_ma*, *majol3d_1* and *majol3d_2* and their main parameters are in Tables 4.4-4.7. These models differ i) for their surface velocities boundary conditions, in fact, model *isehar1*, *majol1*, *majfo89_1* and *majol3d_1* are in a deep hotspot reference frame; models *isehar2*, *majol2*, *majfo89_2* and *majol3d_2* are in a shallow hotspot reference frame, whereas *majol_sa*, and *majol_ma* are in reference frames relative to South America and Marianas plate (Table 4.2); their rheologic profiles were generated using the BurnMan Thermodynamic Toolkit (Cottaar et al., 2014; Cottaar et al., 2017), that will be briefly introduced in the next section.

4.4.3.1 The BurnMan Thermodynamic Toolkit and the initial compositions

This software allows the calculus of the Earth's and other planets physical properties (e.g., isotropic thermoelastic moduli). It solves the equations-of-state (EoS) for a mixture of minerals given by the user, that can either select them from the available extensive mineral database (Holland & Powell, 2011; Stixrude & Lithgow-Bertelloni, 2005) or easily create them. For the models of this thesis, first the isentropic harzburgitic mantle composition (models *isehar1* and *isehar2*) given in the ASPECT cookbook was used from 0 km to 2900 km (Bangerth et al., 2018). Then, a majoritic composition was

used down to 100 km (Griffin et al., 2009), i.e., characterizing the lithosphere, whereas two olivinic composition were used as simple starting mantle composition: i) Fo50, i.e., models *majol1*, *majol2*, *majol_sa*, *majol_ma*, *majol3d*_1 and *majol3d_2* (Boneh et al., 2017; Nekvasil et al., 2004) and then ii) Fo89, i.e., models *majfo89_1* and *majfo89_2* (Bina, 1998; Mitra, 2004; Raye et al., 2011). Furthermore, to obtain the thermodynamic properties of both given lithospheric and mantle compositions, temperature and pressure were calculated starting from the PREM model (Dziewonsky & Anderson, 1981) and then given to the BurnMan software as an additional constraint. The physical properties, i.e., density, thermal expansivity, specific heat and compressibility were calculated by BurnMan using the Birch-Murnaghan (Birch, 1947; Murnaghan, 1944) with thermal correction EoS (Mie-Grüneisen-Debye; Stixrude & Lithgow-Bertelloni, 2005).

The Birch-Murnaghan isothermal equation relates volume and pressure and is defined as follows:

$$f = \frac{1}{2}\left[\left(\frac{V}{V_0}\right)^{-2/3} - 1\right], \tag{4.14}$$

where V_0 is the volume at a reference pressure and V is the volume at a given pressure. For an isotropic material, pressure P , isothermal bulk modulus K_T and shear modulus G are obtained, respectively, using:

$$P = 3K_0 f(1+2f)^{5/2}\left[1 + \frac{3}{2}(K_0' - 4)f\right], \tag{4.15}$$

$$K_T = (1+2f)^{5/2}\left[K_0 + (3K_0K_0' - 5K_0)f + \frac{27}{2}(K_0K_0' - 4K_0)f^2\right], \tag{4.16}$$

$$G = (1+2F)^{5/2}\left[G_0 + (3K_0G_0' - 5G_0)f + (6K_0G_0' - 24K_0 - 14G_0 + \frac{9}{2}K_0K_0')f^2\right], \tag{4.17}$$

in which K_0 and G_0 correspond to reference bulk and shear modulus, whereas K_0' and G_0' are derivative of the same moduli with respect to pressure. Correction from Stixrude and Lithgow-Bertelloni (2005) were applied to equation (4.15-4.17), giving:

$$P_{th}(V,T) = \frac{\gamma \Delta U}{V}, \tag{4.18}$$

$$K_{th}(V,T) = (\gamma + 1 - q)\frac{\gamma \Delta U}{V} - \gamma^2 \frac{\Delta(C_V T)}{V}, \tag{4.19}$$

$$G_{th}(V,T) = -\frac{\eta_S \Delta U}{V}. \tag{4.20}$$

In these set of equations, γ is the Grüneisen parameter (which describes the effect that change on temperature has on size and dynamics of a crystal; Grüneisen, 1912), q represents its logarithmic

volume derivative, η_S its shear strain derivative, each Δ refers to the difference from the reference temperature, C_V is the heat capacity at a constant volume and U the internal energy for temperature T. For a detailed description, the reader is referred to Stixrude and Lithgow-Bertelloni (2005), Cottaar et al. (2014) and Cottaar et al. (2017).

Numerical models realized using these Material model constraints are: i) *isehar1*, *isehar2* which have the same rheologic profile (isentropic harzburgitic mantle; Bangerth et al., 2018) and deep and shallow hotspot reference frames respectively (Table 4.2); ii) *majol1*, *majol2* with the majoritic lithosphere and the Fo50 mantle (Boneh et al., 2017; Griffin et al., 2009; Nekvasil et al., 2004), and, respectively, deep and shallow hotspot reference frames (Table 4.2); iii) *majfo89_1* and *majfo89_2*, with a majoritic lithosphere and the Fo89 mantle (Bina, 1998; Mitra, 2004; Raye et al., 2011), and deep and shallow hotspot reference frames as surface velocities boundary conditions (Table 4.2); iv) models *majol_sa*, *majol_ma*, in reference frames relative to South America and Marianas, respectively (Table 4.2), using the majorite-Fo50 rheology and, lastly, v) models *majol3d_1*, *majol3d_2*, carried out using this same rheology, but in 3d and using absolute reference frames and, in particular, deep hotspot and shallow hotspot reference frame, respectively (Table 4.2). However, in Tables 4.5-4.8 a summary of the principal input used to perform these numerical models are shown.

GLOBAL PARAMETERS	
MODEL NAME	isehar1, isehar2
DIMENSION	2
END TIME	140 Myr
MATERIAL MODEL	
MODEL NAME	ASCII Reference Profile: isentrope harzburgitic
REFERENCE VISCOSITY	1.00E+21
THERMAL VISCOSITY EXPONENT	10.00
VISCOSITY PRE-FACTORS	1.0, 0.1, 1.0, 10.0
GEOMETRY MODEL	
MODEL NAME	Spherical Shell
INNER RADIUS	3481000 m
OUTER RADIUS	6336000 m
MODEL SETTINGS	
FIXED TEMPERATURE BOUNDARY INDICATORS	outer
BOUNDARY TEMPERATURE MODEL	
MODEL NAME	ASCII Reference Profile: isentrope harzburgitic
OUTER TEMPERATURE	273 K
INNER TEMPERATURE	3500 K
INITIAL TEMPERATURE MODEL	Adiabatic
GRAVITY MODEL	
MODEL NAME	ASCII Reference Profile: isentrope harzburgitic
MESH REFINEMENT	
INITIAL GLOBAL	5
INITIAL ADAPTIVE	1
TIME STEPS BETWEEN MESH REFINEMENT	5

Table 4.5 – Main input parameters of the *isehar1* and *isehar2* models. These models differ only for surface velocities boundary conditions. In fact, model *isehar1* is in a deep hotspot reference frame (see Table 4.2) and model *isehar2* is in a shallow hotspot reference frame (see Table 4.2).

GLOBAL PARAMETERS	
MODEL NAME	majol1, majol2, majol_sa, majol_ma
DIMENSION	2
END TIME	140 Myr
MATERIAL MODEL	
MODEL NAME	ASCII Reference Profile: majorite-Fo50
REFERENCE VISCOSITY	1.00E+21
THERMAL VISCOSITY EXPONENT	10.00
VISCOSITY PRE-FACTORS	1.0, 0.1, 1.0, 10.0
GEOMETRY MODEL	
MODEL NAME	Spherical Shell
INNER RADIUS	3481000 m
OUTER RADIUS	6336000 m
MODEL SETTINGS	
FIXED TEMPERATURE BOUNDARY INDICATORS	outer
BOUNDARY TEMPERATURE MODEL	
MODEL NAME	ASCII Reference Profile: majorite-Fo50
OUTER TEMPERATURE	273 K
INNER TEMPERATURE	3500 K
INITIAL TEMPERATURE MODEL	Adiabatic
GRAVITY MODEL	
MODEL NAME	ASCII Reference Profile: majorite-Fo50
MESH REFINEMENT	
INITIAL GLOBAL	5
INITIAL ADAPTIVE	1
TIME STEPS BETWEEN MESH REFINEMENT	5

Table 4.6 – Main input parameters of the *majol1*, *majol2* and *majol_sa*, *majol_ma* models. These models differ only for surface velocities boundary conditions. In fact, model *majol1* is in a deep hotspot reference frame (see Table 4.2) and model *majo2* is in a shallow hotspot reference frame (see Table 4.2), whereas models *majol_sa* and *majol_ma* are in reference frames relative to South America and Marianas plate fixed, respectively (Table 4.2).

GLOBAL PARAMETERS	
MODEL NAME	majfo89_1, majfo89_2
DIMENSION	2
END TIME	140 Myr
MATERIAL MODEL	
MODEL NAME	ASCII Reference Profile: majorite-Fo89
REFERENCE VISCOSITY	1.00E+21
THERMAL VISCOSITY EXPONENT	10.00
VISCOSITY PRE-FACTORS	1.0, 0.1, 1.0, 10.0
GEOMETRY MODEL	
MODEL NAME	Spherical Shell
INNER RADIUS	3481000 m
OUTER RADIUS	6336000 m
MODEL SETTINGS	
FIXED TEMPERATURE BOUNDARY INDICATORS	outer
BOUNDARY TEMPERATURE MODEL	
MODEL NAME	ASCII Reference Profile: majorite-Fo89
OUTER TEMPERATURE	273 K
INNER TEMPERATURE	3500 K
INITIAL TEMPERATURE MODEL	Adiabatic
GRAVITY MODEL	
MODEL NAME	ASCII Reference Profile: majorite-Fo89
MESH REFINEMENT	
INITIAL GLOBAL	5
INITIAL ADAPTIVE	1
TIME STEPS BETWEEN MESH REFINEMENT	5

Table 4.7 – Some of the main input parameters of the *majfo89_1* and *majfo89_2* models. These models differ only for surface velocities boundary conditions. In fact, model *majfo89_1* is in a deep hotspot reference frame (see Table 4.2) and model *majfo89_2* is in a shallow hotspot reference frame (see Table 4.2).

GLOBAL PARAMETERS	
MODEL NAME	majol3d_1, majol3d_2
DIMENSION	3
END TIME	140 Myr
MATERIAL MODEL	
MODEL NAME	ASCII Reference Profile: majorite-Fo50
REFERENCE VISCOSITY	1.00E+21
THERMAL VISCOSITY EXPONENT	10.00
VISCOSITY PRE-FACTORS	1.0, 0.1, 1.0, 10.0
GEOMETRY MODEL	
MODEL NAME	Spherical Shell
INNER RADIUS	3481000 m
OUTER RADIUS	6336000 m
MODEL SETTINGS	
FIXED TEMPERATURE BOUNDARY INDICATORS	outer
BOUNDARY TEMPERATURE MODEL	
MODEL NAME	ASCII Reference Profile: majorite-Fo50
OUTER TEMPERATURE	273 K
INNER TEMPERATURE	3500 K
INITIAL TEMPERATURE MODEL	Adiabatic
GRAVITY MODEL	
MODEL NAME	ASCII Reference Profile: majorite-Fo50
MESH REFINEMENT	
INITIAL GLOBAL	3
INITIAL ADAPTIVE	0
TIME STEPS BETWEEN MESH REFINEMENT	10

Table 4.8 – Main input parameters of the *majol3d_1* and *majol3d_2* models. These models are in 3-dimensions and differ only for surface velocities boundary conditions. In fact, model *majol3d_1* is in a deep hotspot reference frame (see Table 4.2) and model *majol3d_2* is in a shallow hotspot reference frame (see Table 4.2).

4.5 2d results in absolute reference frames

In the following subsections, results of this numerical study will be described. They will be divided first for the reference frame, the geometry used and then, when needed, for their rheologic profile. We referred the reader to the previous recap Tables 4.2-4.8 for quantities used in these numerical models. For each model, figures with the initial thermal stage for the entire spherical domain will be shown at the beginning of each subsection, whereas the last step, i.e., 0 Myr - current day stage, of each model will be described in a quarter annulus which is ~8000 km wide. However, figures showing steps corresponding to 110, 90, 60 and 30 Myr of each model can be found in the Appendix B (Figures B.1-B.60). Moreover, the spherical shell of each model will be shown first from a South America point of view, then from a Pacific point of view. At the end of each description, the data analysis will be shown, with information about both depth and velocity evolution of the lithosphere deepest point (picked following a line of reasoning like in Figure 4.8) using timesteps evolution: each timestep corresponds to 10 Myr (e.g., timestep 14 = 140 Myr, timestep 7 = 70 Myr, etc., to timestep 0 = 0 Myr, i.e., current day).

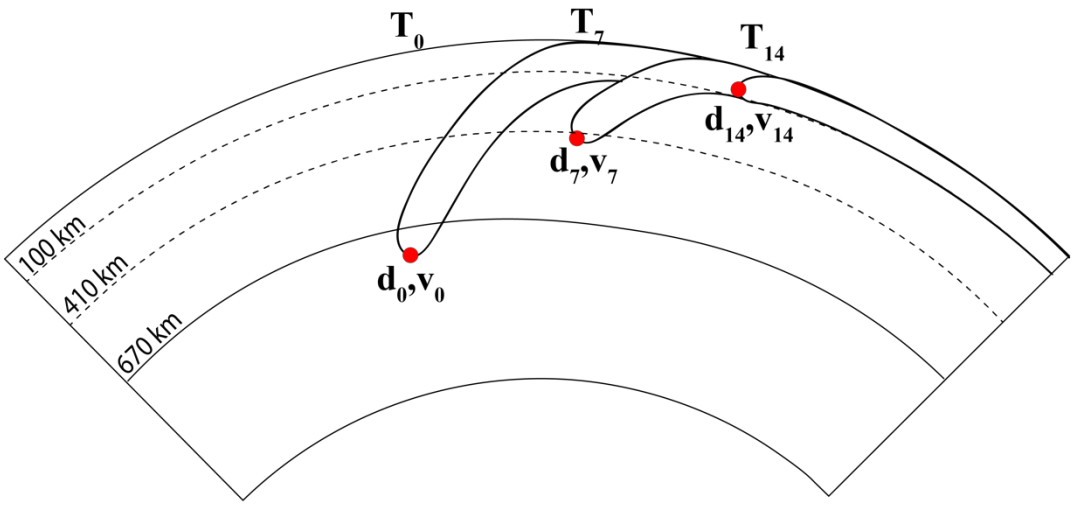

Figure 4.8 – Determination of the chosen deepest lithosphere point for the depth and velocity data analysis. At each timestep, depth (d_n) and velocity (v_n) data were evaluated for the deepest point within the lithospheric slabs, pointed from red circles. In this picture Tn corresponds to the timesteps, dashed and plain lines represents 100 km, 410 and 670 km depths. Figure not in scale. n=14,…,0

These data are the result of a long-term evolution of plate motions that obviously leads to a sequence of subducting slabs and/or thickening lithosphere through time (as shown in Figure 4.9 and in Appendix B Figures B.1-B.60). However, to characterize the current subduction dynamics, only the depth and velocity evolution of the tectonic setting described at step 0, i.e., 0 Myr, is shown (e.g., Figure 4.9). Moreover, to allow a better comparison between the two end-members subduction zones,

on the basis of their geographical polarity useful to test the westward drift of the lithosphere along the tectonic equator, data will be shown only for points in correspondence of South America (E-to-NE-directed and H-convergent subduction zone) and Japan-Marianas subduction zones (W-directed, H-divergent subduction zones); e.g., in Figure 4.9, different slabs, in black, are spread all around the Indo-Pacific area , but only the red-squared data, that corresponds to the Japanese slab, will be shown for Figure 4.20).

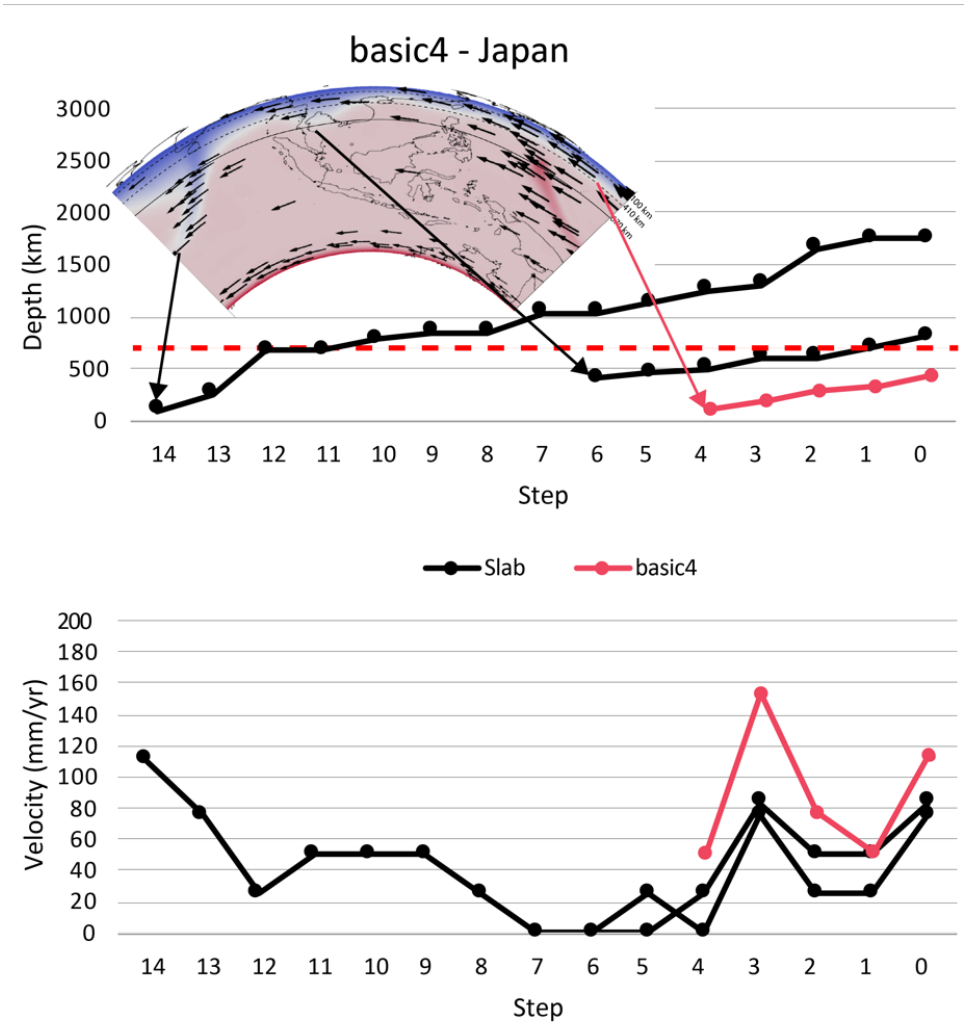

Figure 4.9 - Data description example. To characterize the current subduction dynamics, in this results section, only the depth and velocity evolution of the tectonic setting described at step 0, i.e. 0 Myr, is shown. Moreover, to allow a better comparison between the two end-members subduction zones, on the basis of their geographic polarity useful to test the westward drift of the lithosphere along the tectonic equator, data will be shown only for points in correspondence of South America and Japan-Marianas subduction zones. E.g., different slabs, in black, are spread all around the Indo-Pacific area , but only the magenta-colored data, that corresponds to the current Japanese lithosphere, will be shown for Figure 4.20. As can be seen from its miniature in the upper left part of the Figure, older shifted slabs correspond to older shown data.

Here numerical results in absolute reference frames will be shown. For instance, 2d models realized with a Simple Material model, i.e., *basic1*, *basic2*, *basic3*, *basic4*, with a Visco Plastic Material model, i.e., *vp1*, *vp2*, and with an ASCII Material model, i.e. *isehar1*, *isehar2* isentrope harzburgitic

models; *majol1*, *majol2* majorite-Fo50 models; *majfo89_1*, *majfo89_2* majorite-Fo89 models. It is important to remember that models with plate motions evolution as surface boundary conditions start with velocities corresponding to 140 Myr and end with current plate motions velocities (i.e., 0 Myr).

4.5.1 Model *basic1*

In Figure 4.10 the thermal initial stage of the entire spherical domain is shown. This initial stage is the same for all models presented in this subsection, i.e., models *basic1*, *basic2*, *basic3* and *basic4*, since they were carried out using the same Simple Material model.

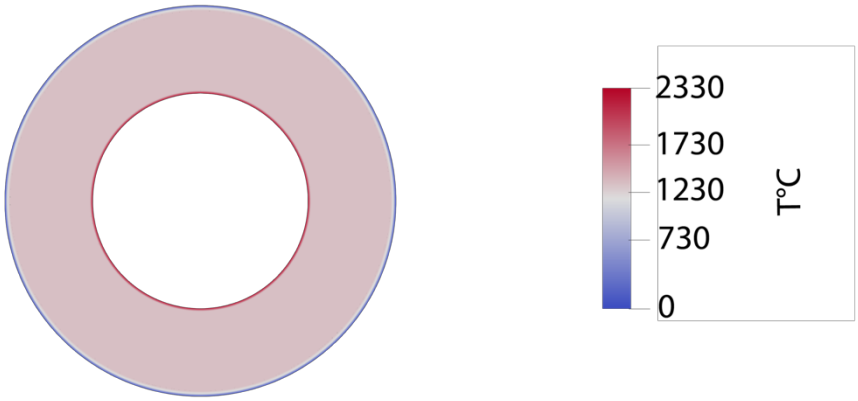

Figure 4.10 – Initial thermal stage for models basic1, basic2, basic3, basic4. This is the thermal state at the initial stage. Two thermal boundary layers can be seen at the top and the bottom of the domain, corresponding to the minimum (i.e., the lithosphere) and the maximum (i.e., the core-mantle boundary) temperature. The temperature is expressed in C°.

In this Figure 4.10, the lithosphere (in blue) is 100 km thick along the entire spherical shell and two thermal boundary layers can be seen at the top and the bottom of the domain, corresponding to the minimum, i.e., the surface at 0°C, and the maximum, i.e., the core-mantle boundary at 2330°C, temperature.

The last step of *basic1* model is shown in Figure 4.11. This model is made applying constant current plate motions velocity (i.e., at 0 Myr) in a deep hotspot reference frame (data about angular vectors provided by Seton et al., 2012) as boundary conditions for the entire model run, i.e., 140 Myr that were arbitrary divided for sake of simplicity in 14 Steps of 10 Myr each. **South America (Figure 4.11, upper panel):** starting from the western part of the model, the lithosphere, in blue, is thinner with respect to the initial stage, at which its thickness is 100 km. The lithospheric thickness increase towards the South American continent, going eastward, reaching its maximum close to the slab, with a wedge that has a thickness of about 400 km. The slab reaches the depth of 1300 km. Velocity vectors show a subduction direction that goes from E to W. Note that in this model there is an unexpected

slab direction. Velocities on the surface are higher towards the W for the Pacific plate, whereas are lower towards the E on the surface of the Nazca plate. Velocity vectors increase again on the South American plate surface, in the easternmost part of the quarter annulus.

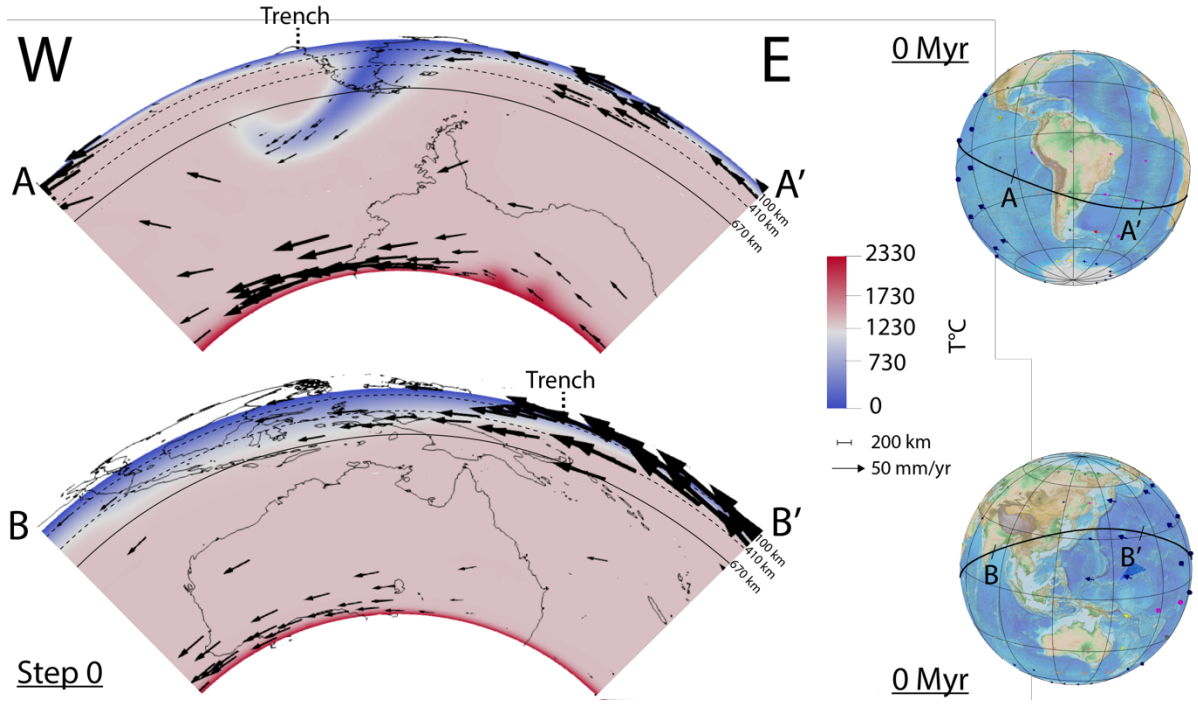

Figure 4.11 - Step 0 relative to the model *basic1*. A view on South America in the upper panel, shows that the slab reaches the depth of 1300 km, whereas velocity vectors show a subduction direction that goes from E to W. The lower panel shows the Pacific side of the quarter annulus. Here an almost homogeneously ~600 km thick lithosphere is shown. Velocity vectors are noticeably high under the Pacific plate, pointing to an E-W direction of the subduction direction. Globes in the right part of this figure show surface plate kinematics at this stage in a deep hotspot reference frame, with the black line suggesting the position of the tectonic equator, along which the 2d slice of this model is cut. Profiles A-A' and B-B' show the lateral extension of the quarter annulus, whereas the dashed Trench line points to the location where the trench should approximately be.

Velocity vectors at the bottom of the domain follow the CMB thermal boundary layer, and are smaller in the westernmost part of the model domain, increase in its central part, decreasing again in its easternmost part of the annulus. The temperature at the bottom of the lithosphere is of ~1230°C, whereas at the CMB is constant at about 2330°C. In the central part of the domain the temperature is homogeneous, having a value of ~1330°C. However, this layer is ~160 km thick, and shows incipient plumes rising in its easternmost part. **Pacific (Figure 4.11, lower panel):** starting from the W, the lithosphere is about 410 km thick. Then it thickens extending from Indonesia to Japan, being ~600 km depth in its deepest part, below the Sunda plate. Then the lithosphere thickness decrease towards the E, reaching a depth of ~150 km on the easternmost part of the spherical domain. Velocity vectors are short under the Indo-Australian and Eurasia plates, whereas they noticeably increase under the Pacific plate. In fact, the increasing thickness of the lithosphere follows an E-W direction. At the CMB, the maximum thermal boundary layer has a constant thickness of ~100 km. Here, the velocity

vectors are higher in the western part of the quarter annulus and decrease towards the E. The temperature at the bottom of the lithosphere is of ~1230°C, whereas at the CMB is constant at about 2330°C. In the central part of the domain the temperature is homogeneous, having a value of ~1330°C.

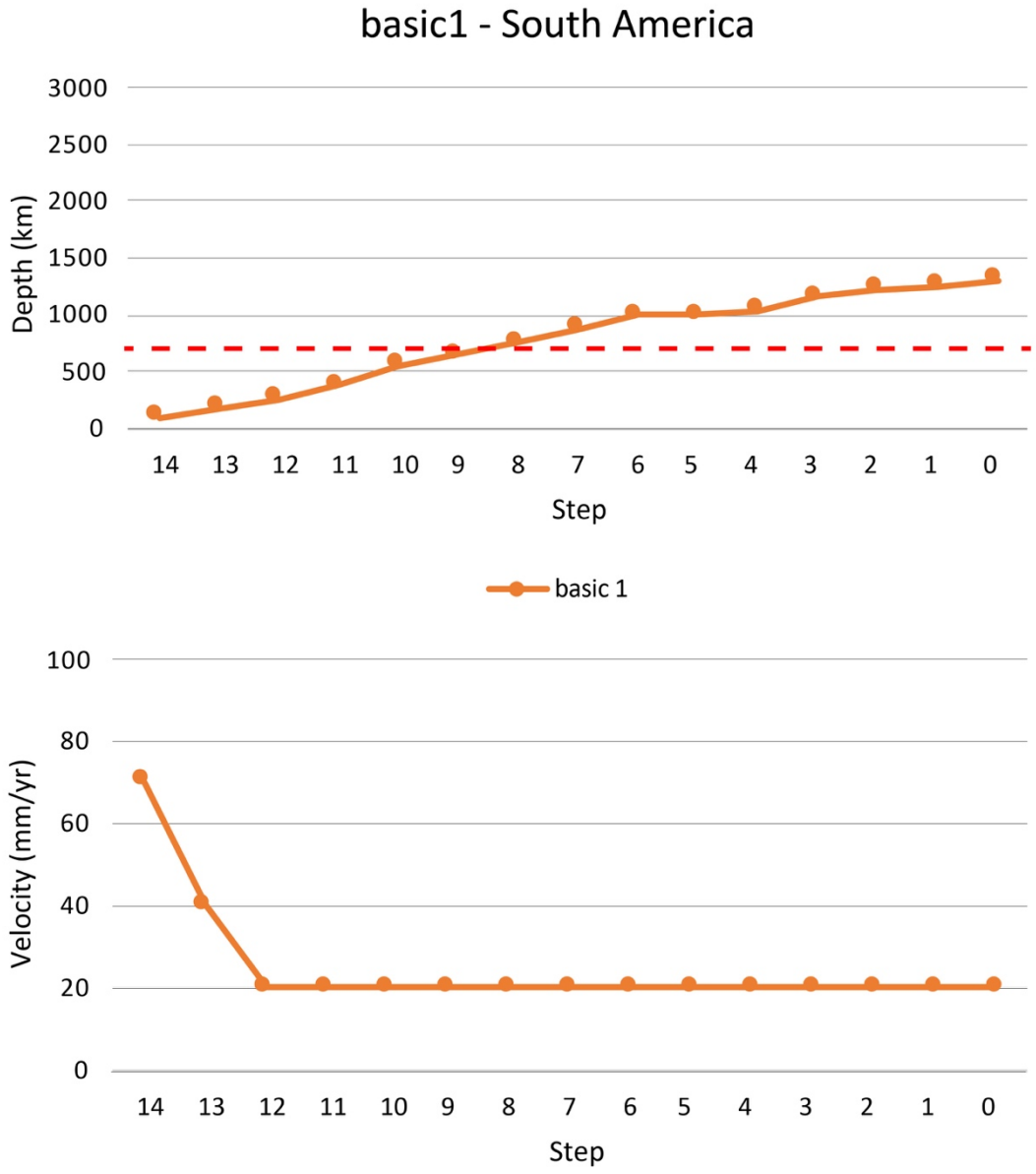

Figure 4.12 – Depth (upper panel) and velocity (lower panel) data for the South American area of model basic1. The slab depth (upper panel) increases with time, passing over the 670 discontinuity (red dashed line) at about 80 Myr. Velocities (lower panel) abruptly decrease from about 75 mm/yr to 20 mm/yr, value that is kept constant until the end of the model run.

In Figures 4.12 and 4.13 depth and velocity data are shown for this model, at each 10 Myr step.

For South America (Figure 4.12, upper panel), the increase in depth is more or less constant at 500 km depth each 40 Myr for the first 80 Myr of the model run, passing over the 670 km discontinuity (red dashed line) at about 80 Myr. The slab depth is almost constant at 1000 km between 60 and 40

Myr and it increase again of 500 km in the last 40 Myr of the model run. The slab tip velocity (Figure 4.12, lower panel) is on average very fast at the beginning (~80 mm/yr) but it decreases during the first 30 Myr of the model run, being constant at 20 mm/yr for the remaining time.

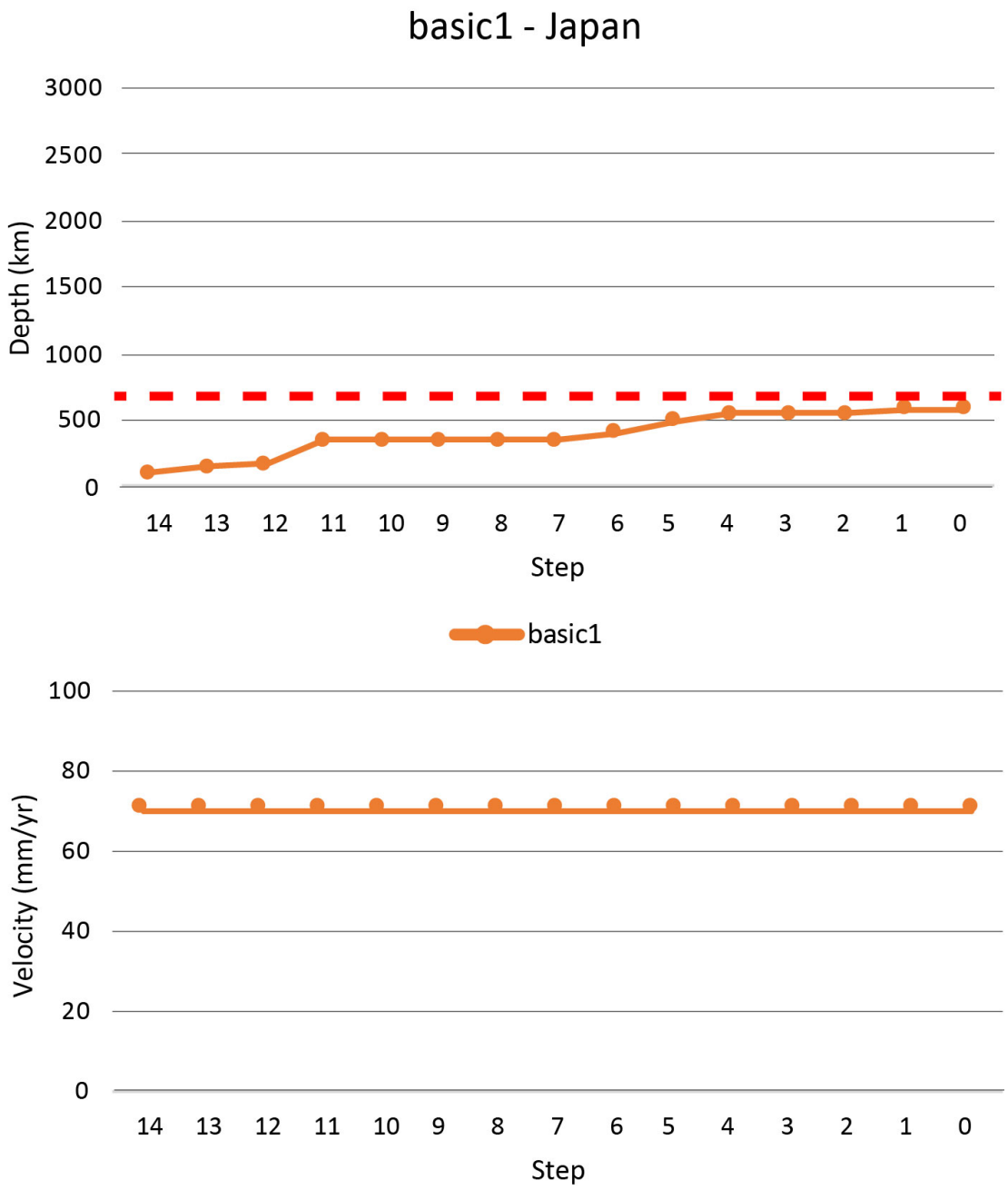

Figure 4.13 – Depth and velocity data for Japanese area in model *basic1*. The slab depth (upper panel) slowly increases with time, doesn't passing over the 670 discontinuity (red dashed line). Velocity (lower panel) for the thickened lithosphere segment in the Japanese area is constant for the entire model run at about 75 mm/yr.

Below the Japanese area (Figure 4.13, upper panel), the lithosphere thickens almost homogeneously slowly during the entire model run, increasing consistently its depth for the first 30 Myr of the model run. Between 110 and 70 Myr its thickness is constant, whereas it starts to slowly increase again

between 60 and 40 Myr. It is constant for the last steps of the model run. The velocity (Figure 4.13, lower panel) of the thickened lithosphere portion is high (~75 mm/yr).

4.5.2 Model *basic2*

In Figure 4.14, the last step of the *basic2* model is shown. This model is made applying constant current plate motions velocity (i.e., at 0 Myr) in a shallow hotspot reference frame (Table 4.1) as boundary conditions for the entire model run, i.e., 140 Myr arbitrary divided into 14 Steps of 10 Myr each. **South America (Figure 4.14, upper panel):** the lithosphere is ~100 km thick at the westernmost boundary of the quarter annulus, increasing its depth going towards the E, reaching the maximum depth of approximately 400 km below the South American continent and decreasing at the easternmost boundary of the annulus to ~300 km depth. Velocity vectors have a westward direction along the entire quarter annulus surface, but are slightly faster in the eastern part, for the South American plate with respect to the westernmost Nazca and Pacific. Furthermore, the Pacific plate is faster with respect to the Nazca plate, having both the same westward direction. Note that in this model there is an unexpected slab direction. Velocity vectors at the CMB layer have the same velocity, and seem to have a vigorous motion. Velocity vectors within the mantle, however, show a shorter length with respect to the superficial vectors. Temperature at the top of the model domain is 0°C and its of ~1230°C at the bottom of the lithosphere. The bottom thermal boundary layer, at the CMB is homogeneously ~200 km thick, whereas in the middle of the model domain the temperature is constant at ~1330°C. **Pacific (Figure 4.14, lower panel):** looking at this side of the spherical shell domain, the lithosphere is homogeneously thick ~400 km almost along the entire annulus. Velocity vectors are westward directed but are shorter in the westernmost part of the domain, in correspondence of the Indo-Australian and Eurasia plates, whereas are noticeably longer for the Pacific plate that shows, thus, the higher velocities.

Velocities decrease within the mantle, reaching the CMB thermal boundary layer that however shows a vigorous westward rotation, although at a slower velocity with respect to the surface. In Figure 4.14, the temperature at the top boundary layer is 0°C and its of ~1230°C all along the entire model lithosphere bottom. The CMB, at ~2900 km depth, is ~170 km thick, whereas at the W and E boundaries of the model domain incipient plumes starts to rise. In the middle of the model domain the temperature is constant at ~1330°C.

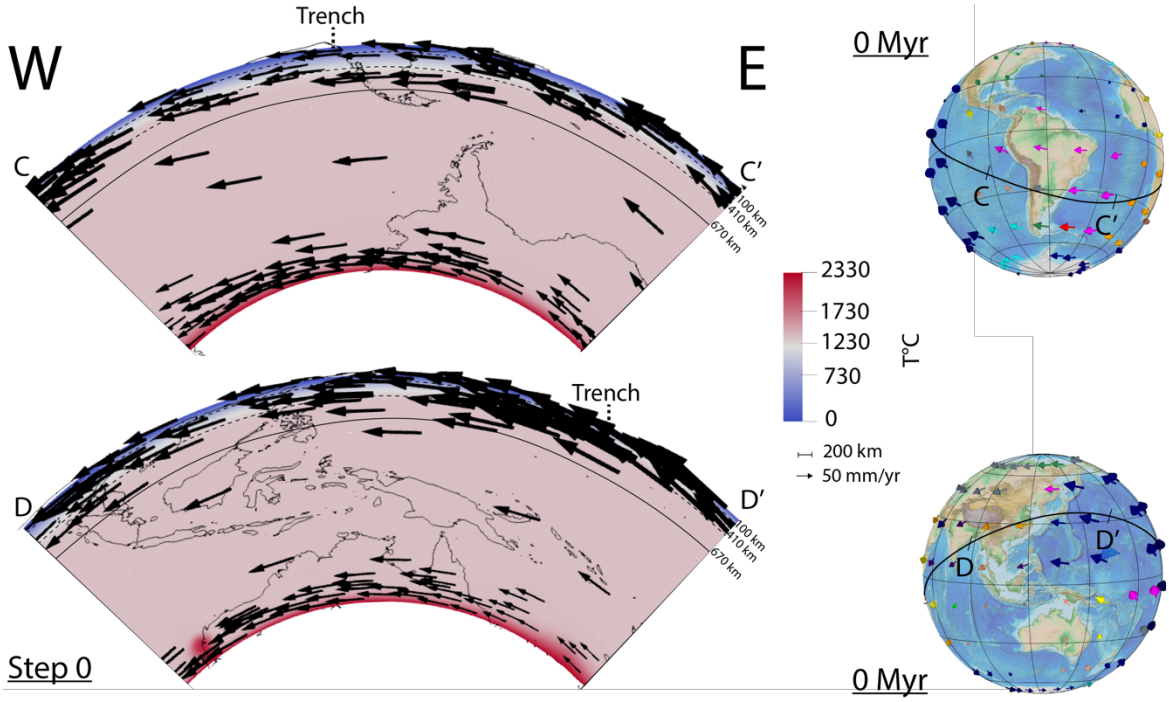

Figure 4.14 - Step 0 relative to the model *basic2*. A view on South America in the upper panel shows that the lithosphere reaches the depth of ~400 km with an almost homogeneous thickness, whereas velocity vectors show an overall westward direction of the plate motion, although at different velocities. The lower panel shows the Pacific side of the annulus. Here an almost homogeneously ~400 km thick lithosphere is shown. Velocity vectors are noticeably high under the Pacific plate, pointing to an E-W direction of plate motion. Globes in the right part of this figure show surface plate kinematics in a shallow hotspot reference frame at this stage, with the black line suggesting the position of the tectonic equator, along which the 2d slice of this model is cut. Profiles C-C' and D-D' show the lateral extension of the quarter annulus. The dashed Trench line points to the approximate position of where the subduction trench should be.

The following Figures 4.15 and 4.16 show depth and velocity data for model *basic2*, respectively for the South American and Indo-Pacific area, every 10 Myr step. In Figure 4.15 (upper panel), for the first 30 Myr of the model run the lithospheric thickness below the South American plate is constant at the initial condition of 100 km. The lithosphere thickness then increases homogeneously throughout the entire model domain, slowly reaching ~400 km depth at the last step. The velocity (Figure 4.15, lower panel) along the lithosphere bottom is constant throughout the entire model run at about 83 mm/yr.

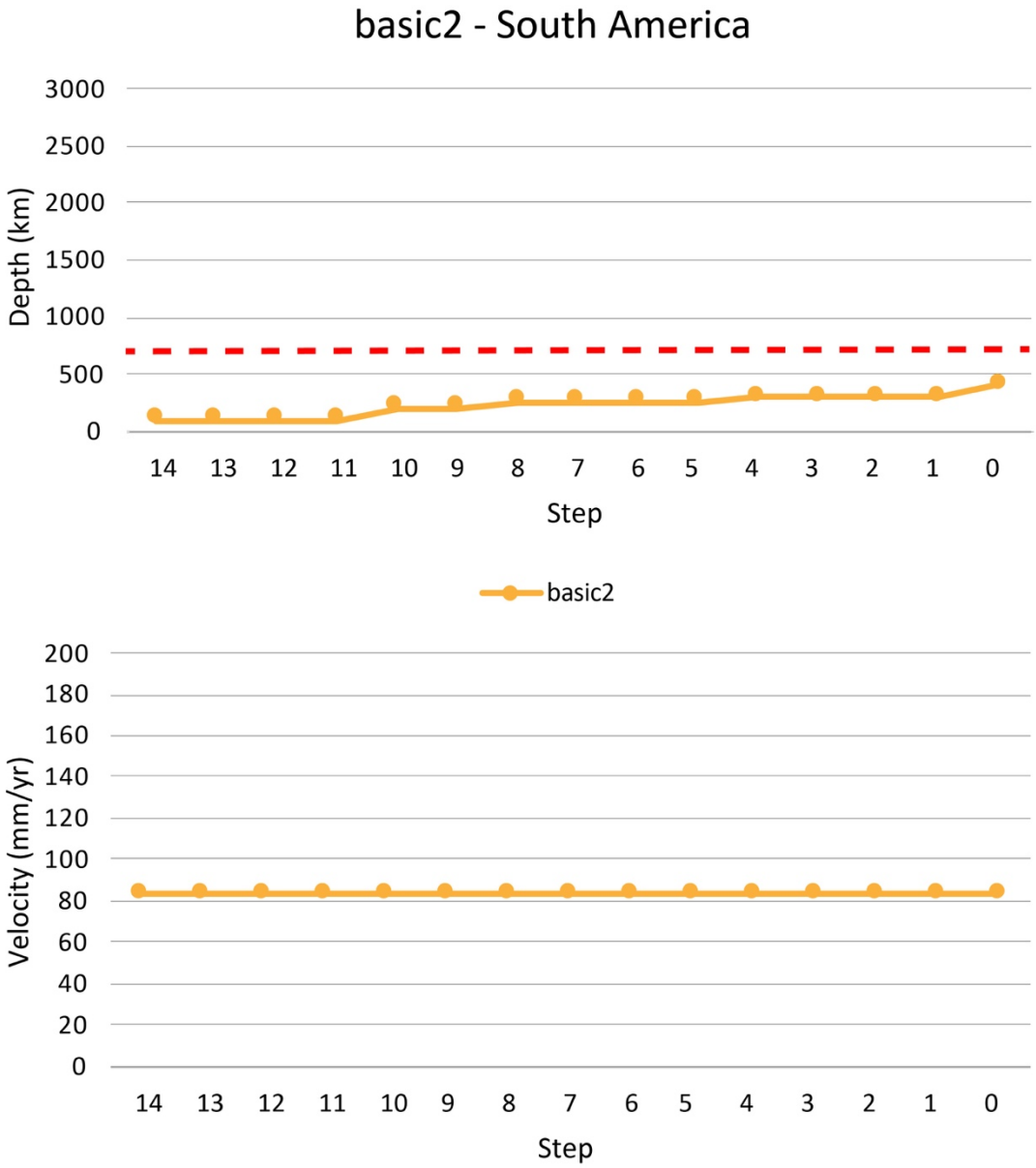

Figure 4.15 – Depth (upper panel) and velocity (lower panel) data for the South American area of model *basic2*. After an initial stagnant phase, the slab depth (upper panel) slowly increases with time, reaching about 400 km depth, being far from the 670 km discontinuity (red dashed line). Velocities (lower panel) are constant from the start to the end of the model run at about 83 mm/yr.

In the Japanese area (Figure 4.16, upper panel), until 110 Myr, the thickness of the lithosphere is constant at the initial condition of 100 km. Its thickness increases homogeneously throughout the entire model surface, slowly reaching ~400 km depth at the last step. The velocity (Figure 4.16, lower panel) at the lithosphere bottom is constant throughout the entire model run at about 180 mm/yr.

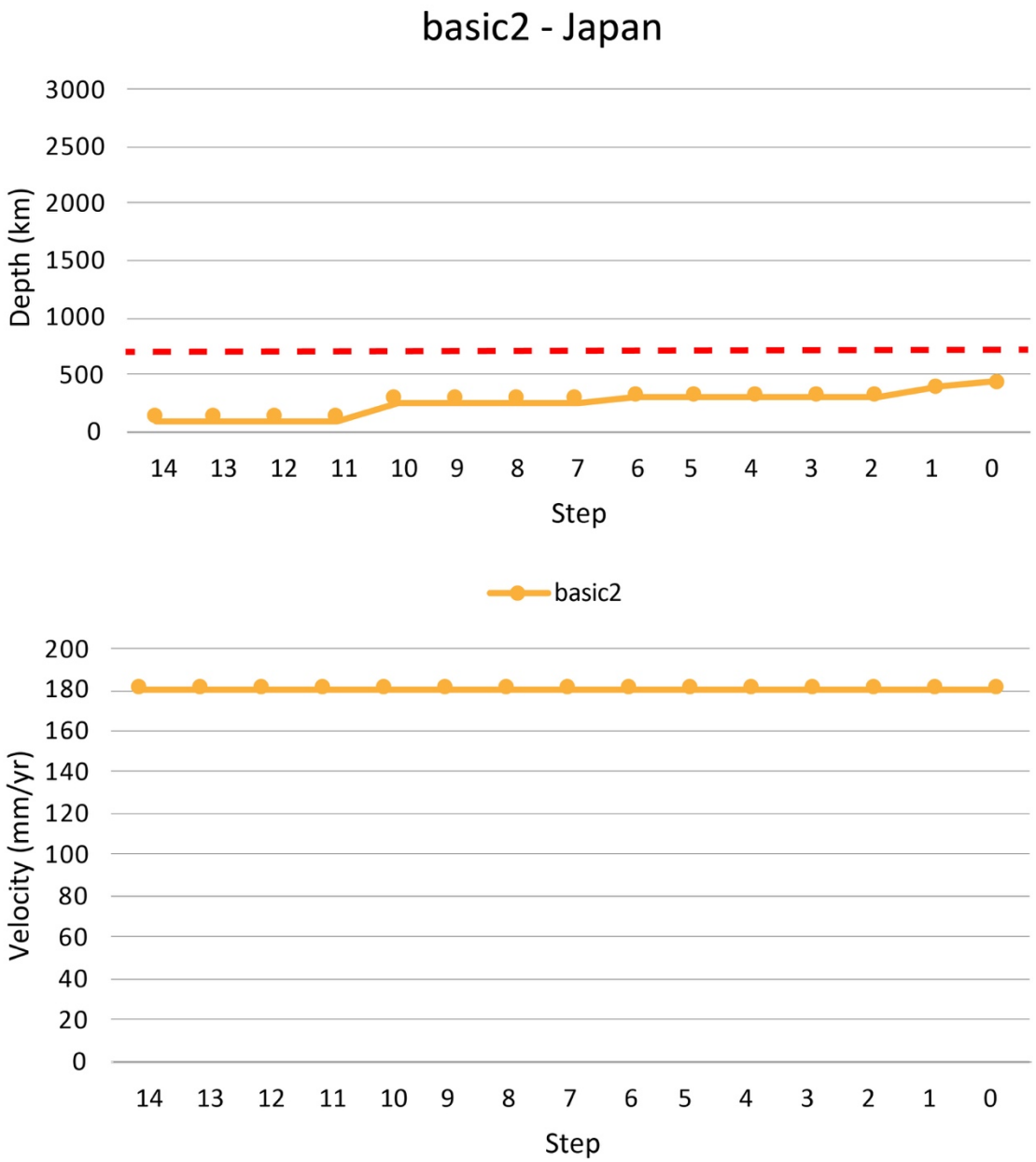

Figure 4.16 – Depth (upper panel) and velocity (lower panel) data for Japanese area in model *basic2*. The slab depth (upper panel) slowly increases with time does not crossing over the 670 km discontinuity (red dashed line). Velocity (lower panel) for the thickened lithosphere segment in the Japanese area is constant for the entire model run at about 180 mm/yr.

4.5.3 Model *basic3*

Figure 4.17 shows the step 0 of the model *basic3*. In this model the evolution of plate motions velocity, i.e., from 140 to 0 Myr, in a deep hotspot reference frame (rotation data provided by Seton et al., 2012) is applied as surface boundary conditions, for a total runtime of 140 Myr corresponding to arbitrary defined 14 Steps of 10 Myr each.

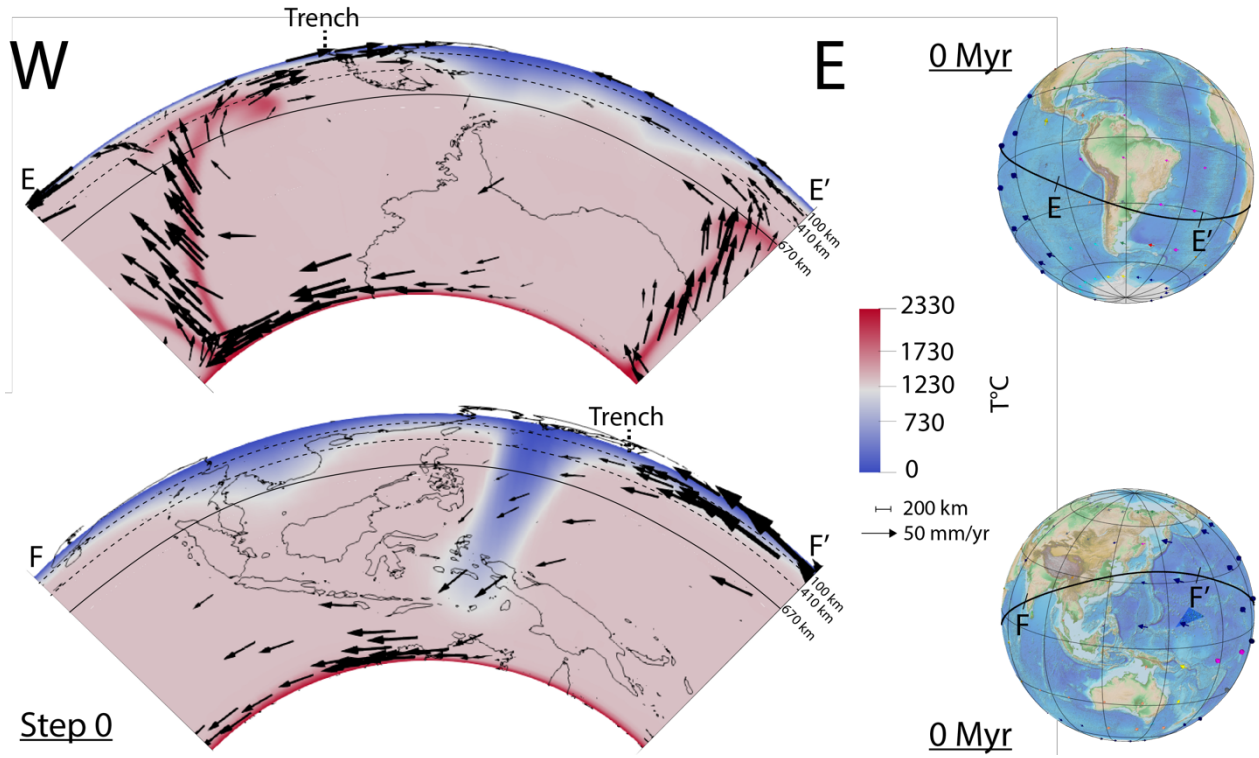

Figure 4.17 - Step 0 relative to the model *basic3*. A view on South America in the upper panel, shows that the lithosphere reaches the depth of ~700 km on the westernmost side of the Atlantic Ocean, almost below the eastern side of the South American continent, whereas below central Atlantic Ocean it reaches ~580 km depth. Velocity vectors show an eastward direction of the plate motion for the Nazca plate, so that the western thickened area direction of accumulation seems to be from W to E. The easternmost boundary of the South American plate is going westward at this stage. In the lower panel the Pacific side of the annulus is shown. At this stage two slabs can be seen, a shallower one below Indonesia (~810 km) and a deeper one below Japan (~2400 km). Velocity vectors are very high under the Pacific plate, pointing to an E-W direction of plate motion. Globes in the right part of this figure show surface plate kinematics in a deep hotspot reference frame at this stage, with the black line suggesting the position of the tectonic equator, along which the 2d slice of this model is cut. In profiles E-E' and F-F' the lateral extension of the described annulus can be seen whereas the dashed Trench line indicates where the subduction trench should be.

South America (Figure 4.17, upper panel): at current plate motions, after 140 Myr of plate surface velocity evolution, starting from the westernmost boundary of the domain, a very thin lithosphere can be observed. Going eastward along the model domain, the lithosphere reaches the depth of ~700 km on the westernmost side of the Atlantic Ocean, almost below the eastern side of the South American continent, whereas below central Atlantic Ocean it reaches ~580 km depth. The lithosphere becomes again thinner at the easternmost boundary of the domain.

In the westernmost boundary of the model domain, velocity vectors show a spreading ridge between the Pacific and the Nazca plates. Furthermore, a plume coming from the CMB arises in the middle of the ridge, curving slightly towards the E and reaching a superficial depth of about 350-400 km. Another plume arises from the CMB at the easternmost side of the domain, as shown by both temperature field and velocity vectors, touching the depth of the 670 km discontinuity. Furthermore, velocity vectors show an eastward direction of motion for the Nazca plate, so that the thickened area almost below the South American coastline seems to have a direction of accumulation that goes from

W to E. The easternmost boundary of the South American plate is going westward at this stage, suggesting an E-W direction of accumulation for the thickened area that is located almost below the mid-Atlantic Ocean. Velocities decrease from the surface to the bottom of the domain, but they are higher close to the CMB and in the plume zones. In fact, velocity vectors along the bottom thermal boundary layers point to a vigorous motion of the bottom part of the domain, being higher in correspondence of the two arisen plumes, towards the surface. Temperature at the bottom of the lithosphere is of about 1230°C, whereas it is about 0°C at its top. At the CMB the temperature is of about 2330°C and the thickness of this layer is very thin, except for the two areas where plumes arisen towards the surface of the model domain, maintaining a temperature of ~2330°C. in the middle of the domain, the temperature is constant at about 1330°C. **Pacific (Figure 4.17, lower panel):** the Pacific side of the annulus shows a 100 km thick lithosphere at its westernmost boundary, that thickens towards the east reaching a depth of ~810 km below Indonesia. Below the Eurasian plate, between Indonesia and Japan, an almost homogeneous zone of 350 km thickness can be observed. This zone ends in correspondence of Japan, where a very wide and ~2400 km deep slab can be seen. The lithosphere then becomes thinner again, reaching the initial condition of ~100 km at the easternmost side of the domain, below the Pacific Ocean. Velocity vectors are very high under the Pacific plate, pointing to an E-W direction of plate motions and, thus, of the subducting lithosphere. Velocity vectors are very small within the mantle, but they increase from the slab tip to the CMB, towards the W. Temperature at the lithosphere bottom is of about 1230°C along the entire model domain, whereas it is about 0°C at its top. At the CMB the temperature is of about 2330°C and the thickness of this layer is about 100 km, that increases to ~170 towards the W, together with corresponding velocity vectors along this same surface. Its temperature is of about 2330°C and in the middle of the domain, the temperature is constant at about 1330°C.

In Figures 4.18 and 4.19 data about depth and velocities for each arbitrary defined step of 10 Myr of the model run are shown.

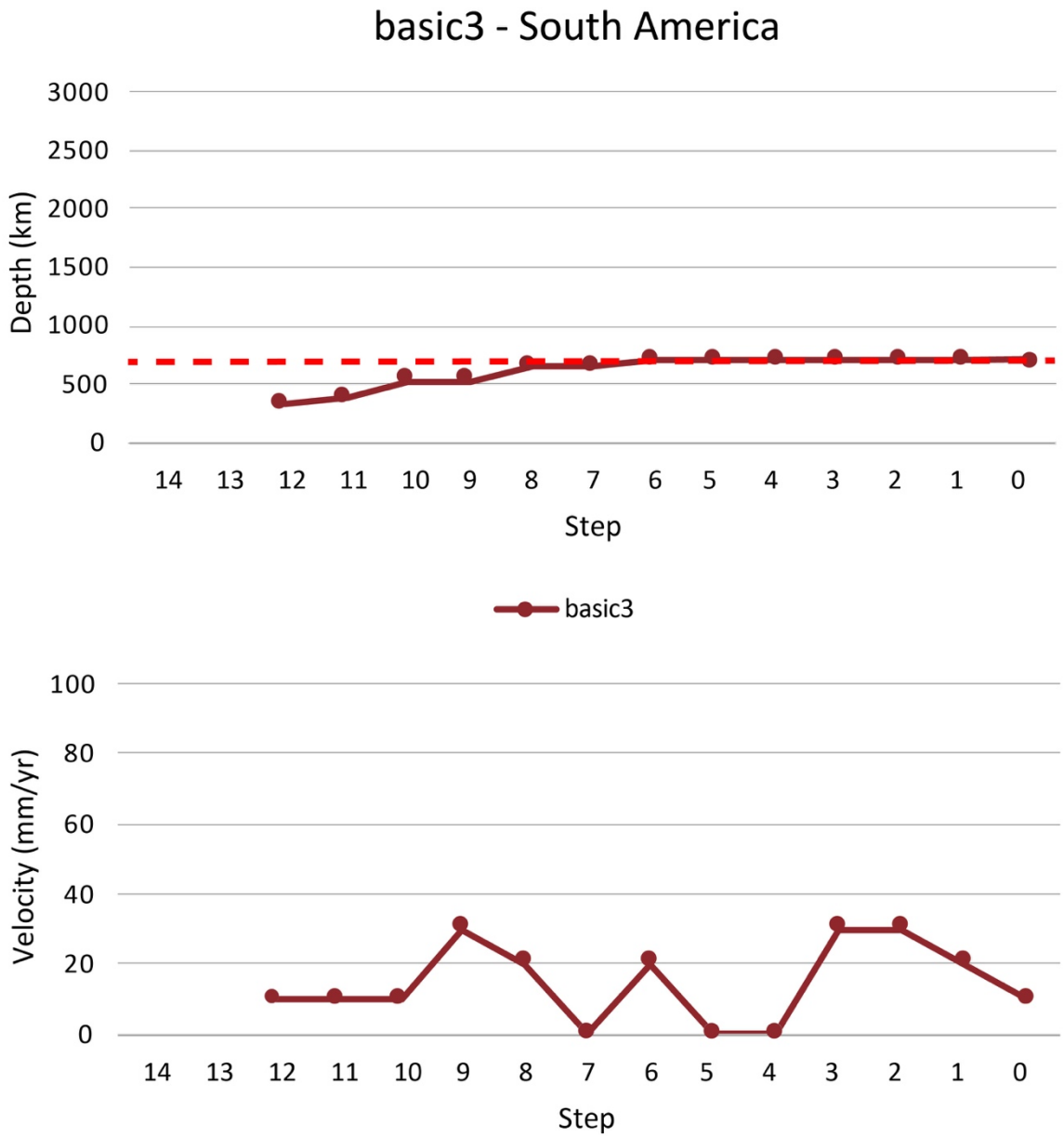

Figure 4.18 – Depth (upper panel) and velocity (lower panel) data for the South American area of model *basic3*. The thickened zone increases its depth with time (upper panel) and, when reaching the 670 km discontinuity at about 80 Myr, it stagnates at this depth until the end of the model run. For what regards the velocity data (lower panel), the lithosphere velocities reach their maximum value of 10 mm/yr at 90 Myr and 30-20 Myr, whereas its minimum value of 0 mm/yr is reached at step 7, 5 and 4.

Figure 4.18 shows the evolution of depth and velocities of the two lithospheric thickened zones for South America. The thickened zone increases its depth (Figure 4.18, upper panel) with time and, when reaching the 670 km discontinuity at about 80 Myr, it stagnates at this depth until the end of the model run. For what regards the velocity data (Figure 4.18, lower panel), the lithosphere velocity evolution starts from about 10 mm/yr at 120 Myr. It is constant until 100 Myr, increasing up to 30 mm/yr at 90 Myr. Velocity then has a value 0 mm/yr from 70 to 40 Myr, with a peak to 20 mm/yr at 60 Myr. At 30 Myr it reaches 30 mm/yr, decreasing down to 10 mm/yr at 0 Myr.

For the Japanese area, depth and velocity data are shown by Figure 4.19. The slab depth (Figure 4.19,

upper panel) starts to constantly increase with time until about 100 Myr, time at which it reaches the 670 discontinuity (red dashed line) and stagnate on it for about 20 Myr. After that, the slab depth increases again, stagnating for about 10 Myr at 1500 km depth. It starts then to deepen again, reaching 2400 km depth at 0 Myr. Velocity evolution (Figure 4.19, lower panel) of this slab is high at the beginning (~60 mm/yr) and abruptly decreases to 10 mm/yr at 130 Myr.

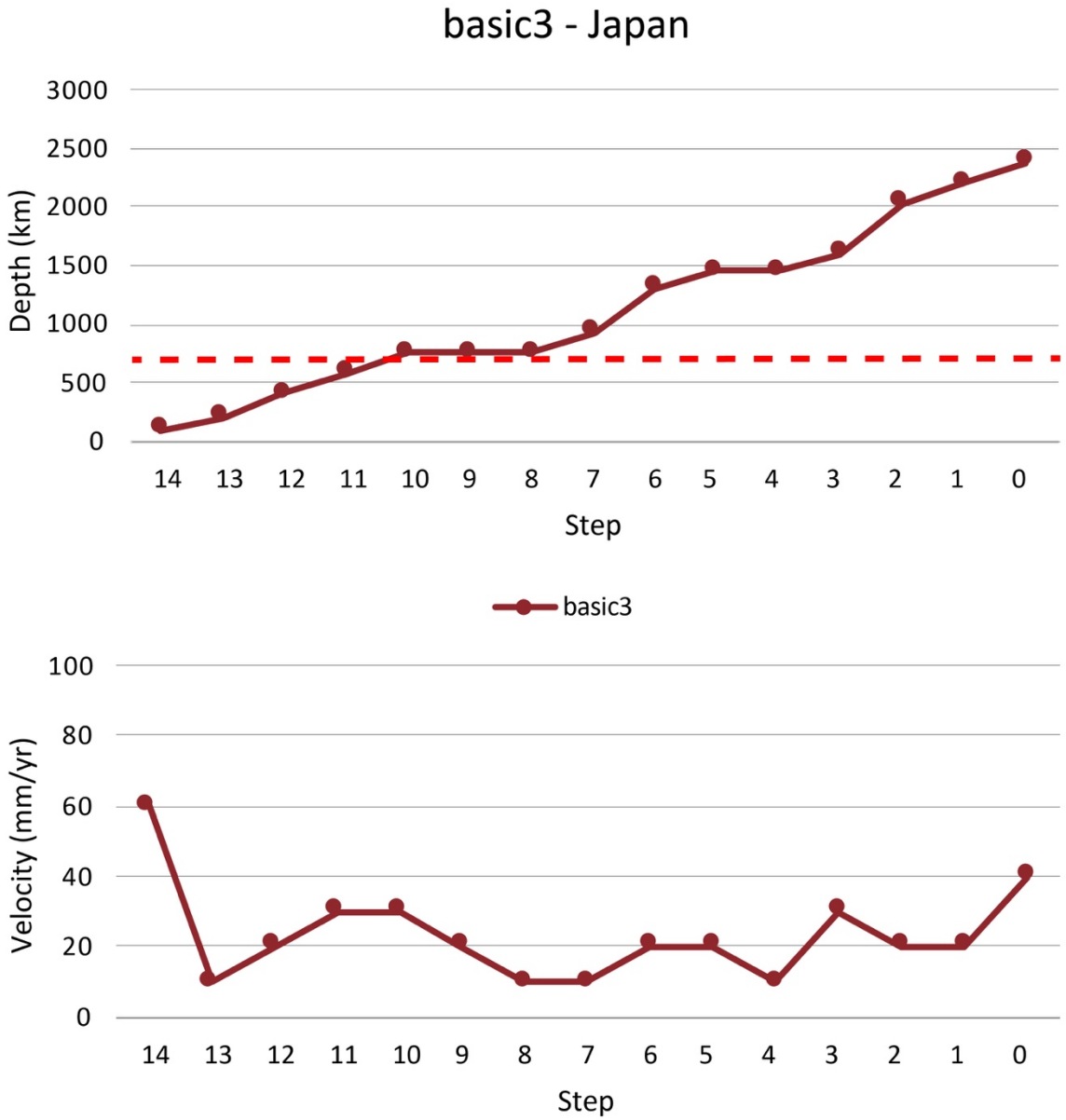

Figure 4.19 – Depth (upper panel) and velocity (lower panel) data for Japanese area in model *basic3*. For the Japanese area, the slab depth (upper panel) starts to constantly increase with time until about 100 Myr, time at which it reaches the 670 discontinuity (red dashed line) and stagnate on it for about 20 Myr. After that, the slab depth increases again, stagnating for about 10 Myr at 1500 km depth. It starts then to deepen again, reaching 2400 km depth at 0 Myr. Velocity values (lower panel) have their maximum at step 14, with a value of 60 mm/yr, reaching a minimum of 10 mm/yr at steps 13, 8-7 and 4.

It increases and then it is stable at 30 mm/yr during 110 and 100 Myr, whereas it decreases down to 10 mm/yr, being stable to this velocity during 10 Myr between 80 and 70 Myr. Between 60 and 50 Myr the velocity is stable at 20 Myr, whereas it decreases at 10 mm/yr at 40 Myr. At 30 Myr the velocity has a value of 30 mm/yr that decreases at 20 mm/yr during the 10 Myr between 20 and 10 Myr. At the current day stage, i.e., 0 Myr, the slab tip velocity is 40 mm/yr.

4.5.4 Model *basic4*

The step 0 of the model *basic4* is shown in Figure 4.20. In this model the evolution of plate motions velocity (from 140 to 0 Myr) in a shallow hotspot reference frame (Table 4.1) is applied as boundary condition, for a total runtime of 140 Myr corresponding to the arbitrary defined 14 steps of 10 Myr each. **South America (Figure 4.20, upper panel):** in model *basic4*, at 0 Myr stage of the plate motions evolution (current plate motions velocity) the lithosphere is thin at the western boundary of the numerical domain. Going towards the east, under the South American continent, below the current position of the South American trench, a slab that reaches 1650 km depth can be observed. From its wedge, the slab is almost wide as the South American continent. The lithosphere then, right eastward of the South American coastlines becomes thin again, reaching its undeformed initial condition of 100 km thickness until the end of the model domain, to the E.

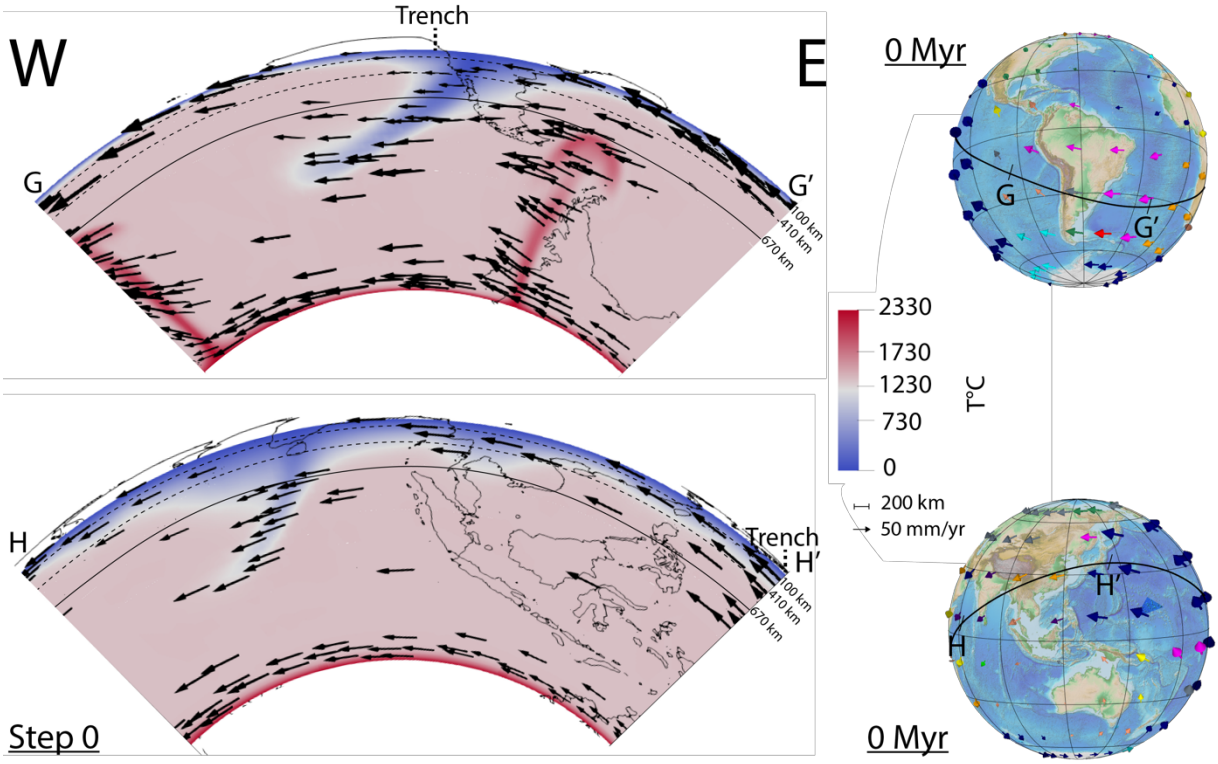

Figure 4.20 - Step 0 relative to model *basic4*. Looking at South America (upper panel) the lithosphere is thin at the western boundary of the numerical domain. Going towards the east, under the South American continent, below the current position of the South

American trench, a slab that reaches 1650 km depth can be observed. From its wedge, the slab is almost wide as the South American continent. The lithosphere then, right eastward of the South American coastlines becomes thin again, reaching its undeformed initial condition of 100 km thickness until the end of the model domain, to the E. Velocity vectors are slightly shorter within the mantle, but are higher in correspondence of two rising plume, one at the westernmost boundary of the numerical domain, reaching 670 km depth, and one (reaching 670 km depth) below the western side of the Atlantic ocean. In the Pacific side (lower panel) the slab below India, has a depth of ~1740 km and it is very thin if compared to its wedge thickness. Towards the E, a slab that has a ~700 km depth can be seen below Indonesia. Velocity of the lithosphere surface is high in correspondence of the Pacific plate, whereas it is slightly slower for the Indo-Australia plate. Globes in the right part of this figure show surface plate kinematics in a shallow hotspot reference frame at this stage, with the black line suggesting the position of the tectonic equator, along which the 2d slice of this model is cut. Profiles G-G' and H-H' show the lateral extension and geographical location of the quarter annulus. The dashed Trench line points to the possible location of where the subduction trench should be.

Velocity vectors are almost of the same length for Pacific and South American plates, at the westernmost and easternmost sides of the domain, whereas they are shorter for the Nazca plate in the middle. Although maintaining different velocities, plates direction is globally towards the W. Again, note the unexpected direction of the subducting slab. Velocity vectors are slightly shorter within the mantle, but are higher in correspondence of two rising plume, one at the westernmost boundary of the numerical domain, reaching 670 km depth, and one below the western side of the Atlantic Ocean. This plume reaches the depth of 670 km. The temperature is about 1220° at the bottom of the lithosphere and 0°C at the top of the model domain. At the CMB the temperature is of about 2330°C and the thickness of this layer is about 100 km. Temperature of about 2330°C is constant for both the plumes and in the middle of the domain the temperature is constant and homogeneous at about 1330°C. **Pacific (Figure 4.20, lower panel):** the Pacific area from the westernmost side of the numerical domain, shows a rapidly increasing depth of the lithosphere. In fact, a subducting slab is observable below India, preceded by a wide wedge zone, that has a maximum thickness of about 750 km. The slab below India has a depth of ~1740 km and it is very thin if compared to its wedge thickness. Towards the E, a slab that has a ~700 km depth can be seen below Indonesia. The lithosphere between the Indian and the Indonesian slab is about 400 km deep. This is the depth of the lithosphere also going from the Indonesian slab towards Japan. Below Japan the lithosphere deepens to about 410 km, pointing to an incipient slab. A rising plume coming from the eastern boundary of the quarter annulus can be observed right below the Pacific plate. Velocity of the lithosphere surface is high in correspondence of the Pacific plate, whereas it is slightly slower for the Indo-Australian and Eurasian plates. This points to a subduction direction that goes from E to W. Velocity vectors slightly decrease towards the bottom of the model domain but pointing to a vigorous motion of the entire mantle that is following the lithosphere motion, even though at a slightly lower velocity. Temperature of the lithosphere is 0°C at its top and reaches 1230°C at its bottom. The CMB layer is thin, at a constant temperature of about 2330°C. Within the mantle, the temperature is constant at about 1330°C except for the rising plume, which has a temperature of about 2330°C.

In the following Figures 4.21 and 4.22 depth and velocity data relative to this same model *basic4* are shown. In Figure 4.21, data for the South American side are represented. The slab rapidly increases

its depth (Figure 4.21, upper panel) for the first 50 Myr of the model run. Its depth become 1130 km at 90 Myr. The depth of the slab is constant until ~60 Myr.

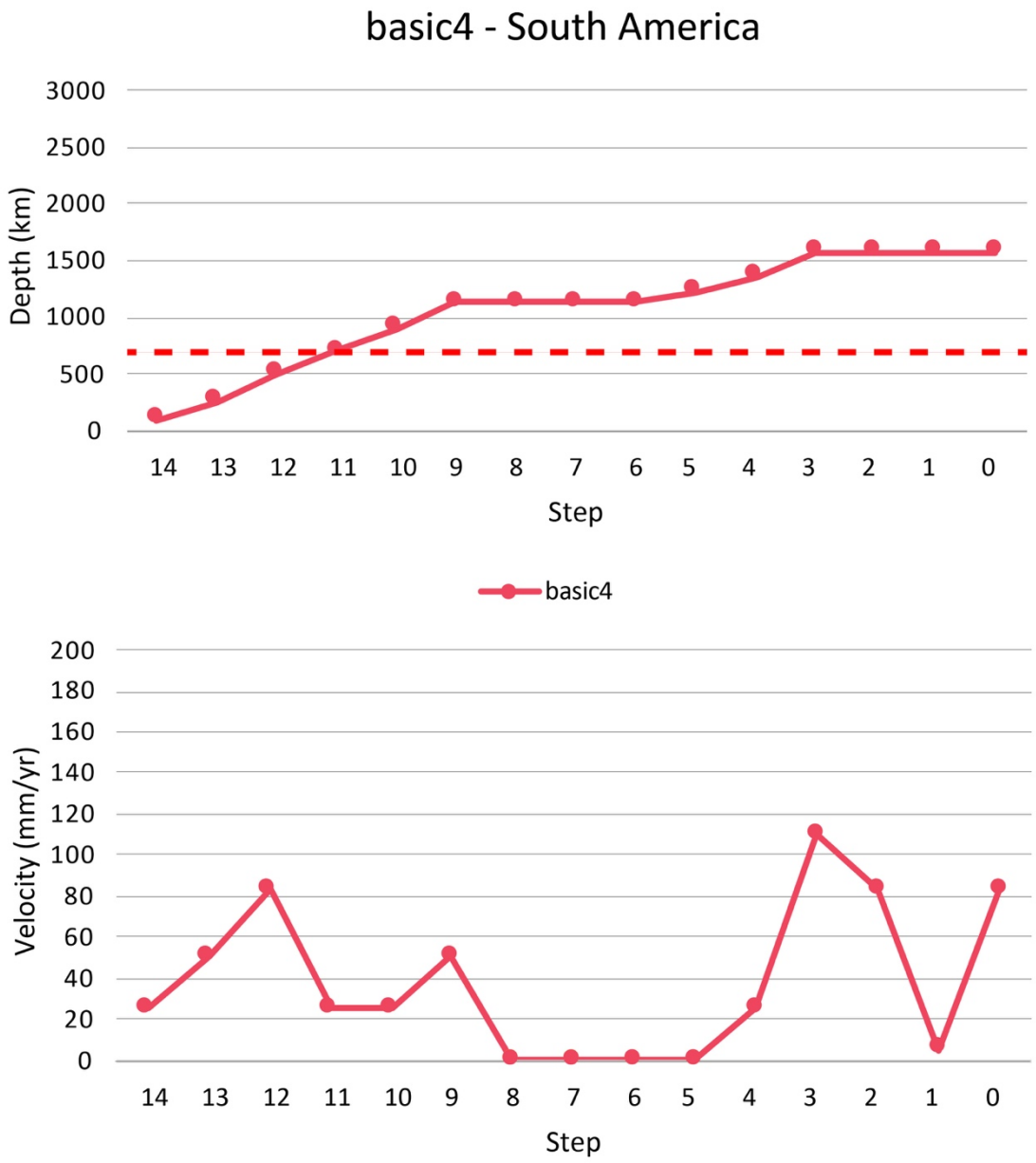

Figure 4.21 – Depth (upper panel) and velocity (lower panel) data for model *basic4.* The slab rapidly increases its depth (upper panel) for the first 50 Myr of the model run. Its deep become 1130 km at 90 Myr. The depth of the slab is constant until ~60 Myr. The slab at 50 Myr starts to increase its depth again, reaching 1220 km depth. At 30 Myr, the slab reaches a depth of about 1600 km that is kept constant until the current day plate motions setting (0 Myr). Velocities (lower panel) are discontinuous, increasing and decreasing with time. They reach a minimum value of 0 mm/yr during steps 8-5, whereas its maximum peak is at step 3, with a value of 110 mm/yr.

The slab at 50 Myr starts to increase its depth again, reaching 1220 km depth. At 30 Myr, the slab reaches a depth of about 1600 km that is kept constant until the current day plate motions setting (0 Myr). Velocities (Figure 4.21, lower panel) are discontinuous in time. They start from ~25 mm/yr at 140 Myr and reach ~83 mm/yr at 120 Myr. At 110 and 100 Myr their value is ~25 mm/yr, whereas they increase up to about 50 mm/yr to decrease abruptly to 0 at 80 Myr. This velocity is constant until

50 Myr, increasing up to ~110 mm/yr at 30 Myr and decreasing again to 10 mm/yr at 10 Myr. The last 10 Myr of the model run are characterized by an increase of the slab tip velocity up to ~83 mm/yr. In the Japanese area (Figure 4.22, upper panel), the lithosphere depth evolution starts at 40 Myr, at which it has a depth of about 100 km. It constantly deepens reaching about 410 km depth at step 0. Velocities for the deepest points of the lithosphere in the Japanese area, in Figure 4.22 (lower panel) starts at 40 Myr, with a velocity of about 50 mm/yr. Velocity increase to 150 mm/yr at 30 Myr, decreasing to 50 mm/yr at 10 Myr, whereas at 0 Myr it has a value of 110 mm/yr.

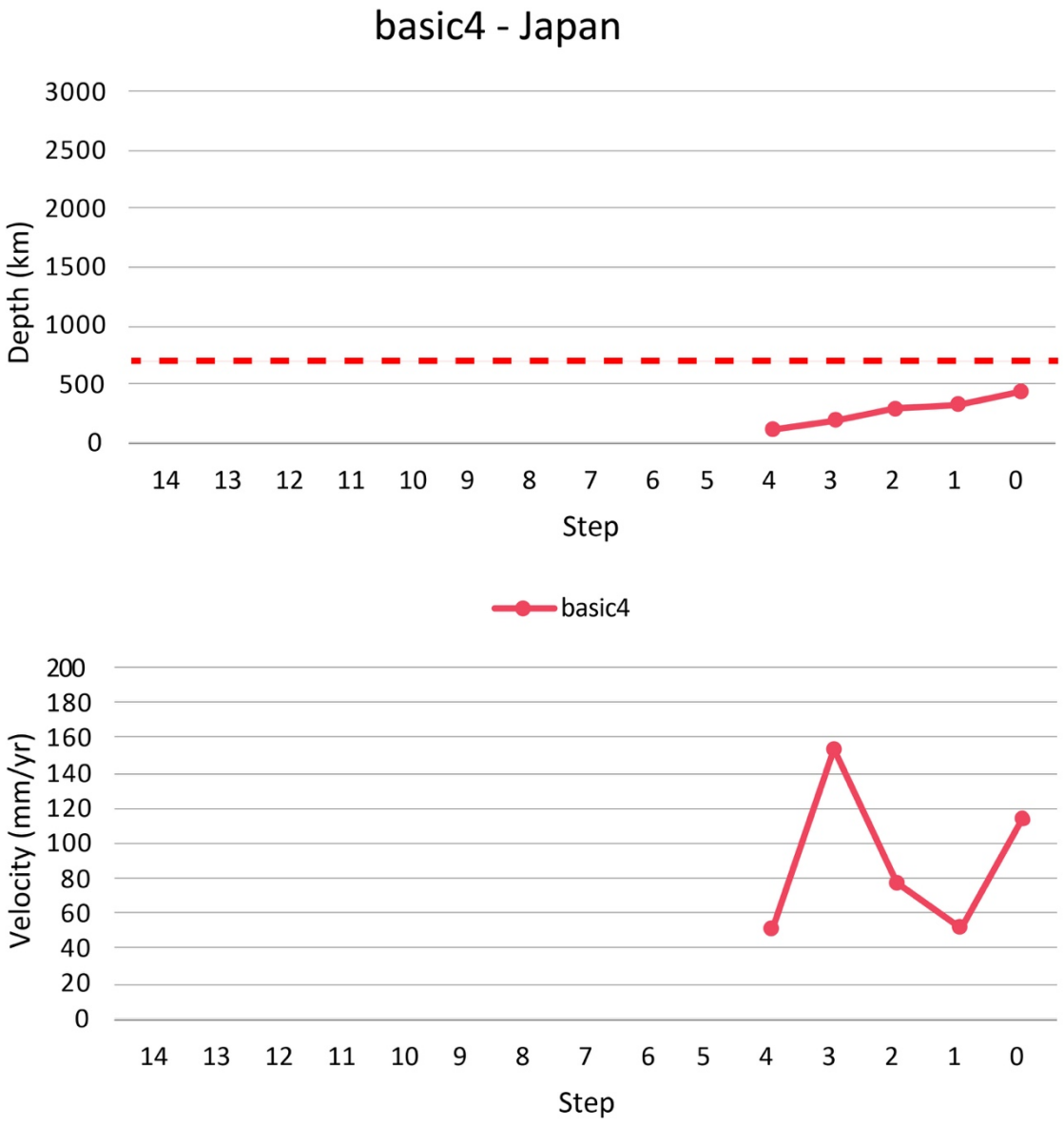

Figure 4.22 – Depth (upper panel) and velocity (lower panel) data for Pacific area in model *basic4*. Initially (upper panel) an almost defined slab tip reaches 670 km depth, stagnating here for about 10 Myr. At 100 Myr, the slab starts to slowly but continuously deepen again, reaching throughout the whole model running time 1740 km depth at 0 Myr. Velocities (lower panel) are discontinuous with some phases at which they are kept constant. Their maximum value is of about 150 mm/yr, reached at 30 Myr, whereas their minimum value is 50 mm/yr, reached at 40 and 10 Myr.

4.5.5 Model *vp1*

In Figure 4.23 the thermal initial stage of the entire spherical domain for Visco Plastic models is shown. This initial stage is the same for all models presented in this subsection, i.e., models *vp1* and *vp2*, since they were carried out using the same Visco Plastic Material model.

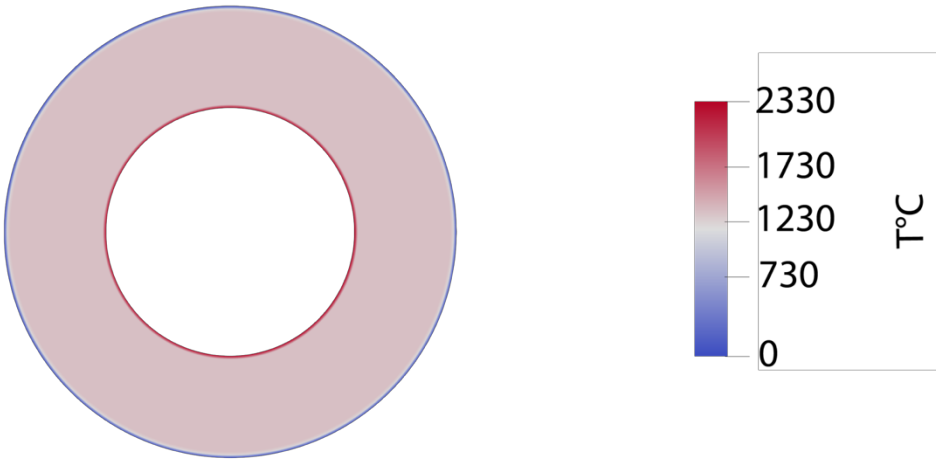

Figure 4.23 – Initial thermal stage for models *vp1* and *vp2*. This is the thermal state at the initial stage. Two thermal boundary layers can be seen at the top and the bottom of the domain, corresponding to the minimum (i.e., the lithosphere) and the maximum (i.e., the core-mantle boundary) temperature. The temperature is expressed in C°.

For this Material model the lithosphere (in blue) is 100 km thick along the entire spherical shell and two thermal boundary layers can be seen at the top and the bottom of the domain, corresponding to the minimum, i.e., the surface, at 0°C, and the maximum, i.e., the core-mantle boundary, at 2330°C, temperature.

Figure 4.24 shows the step 0 of the model *vp1*. In this model the evolution of plate motion velocities (from 140 to 0 Myr) in a deep hotspot reference frame (angular vectors collected by Seton et al., 2012) is applied as boundary conditions, for a total runtime of 140 Myr corresponding to arbitrary defined 14 Steps of 10 Myr each.

South America (Figure 4.24, upper panel): in model *vp1*, at current plate motion stage (0 Myr) the lithosphere is thin at the western boundary of the numerical domain and thickens going towards the east, exceeding the 410 km discontinuities of few km, starting from the mid-South American continent.

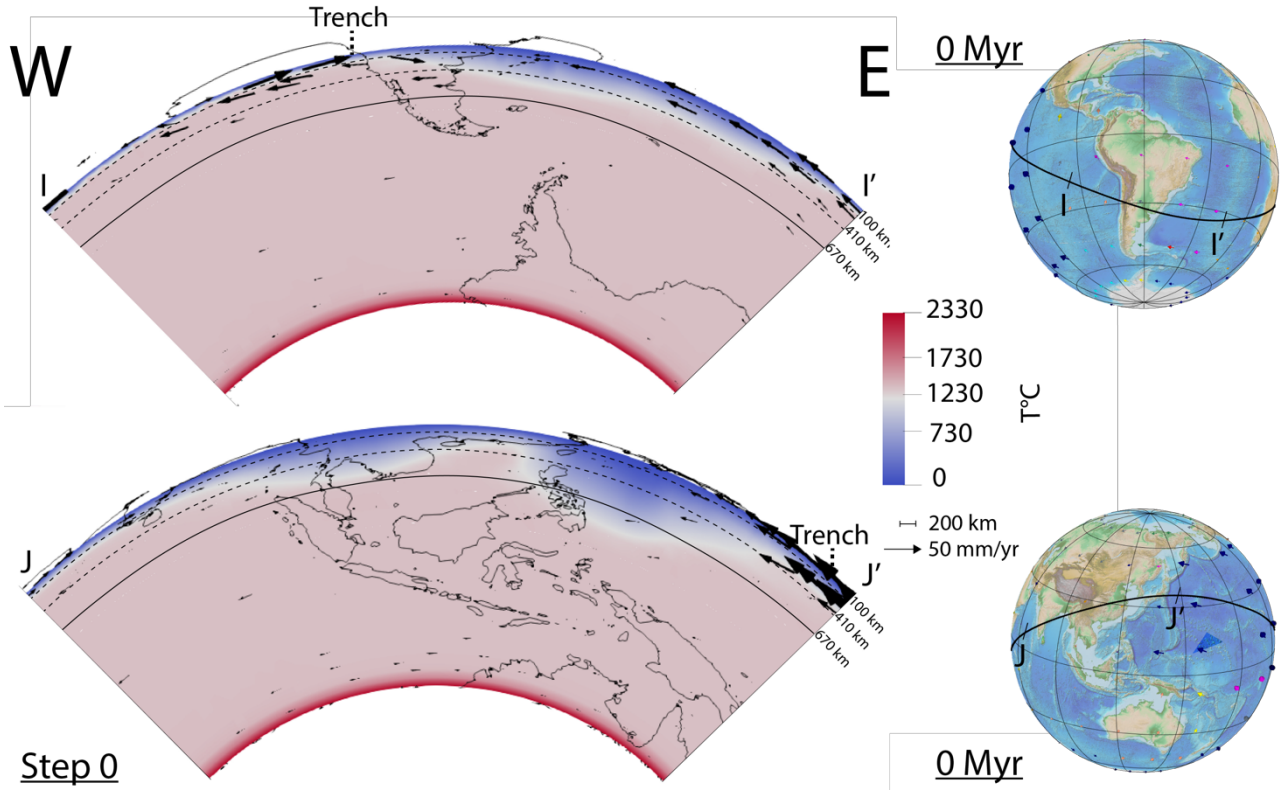

Figure 4.24 - Step 0 relative to model *vp1*. Looking at South America (upper panel) the lithosphere is thin at the western boundary of the numerical domain and thickens going towards the east, exceeding the 410 km discontinuity of few km under the South American continent whereas it remains uniformly thick eastward, below the Atlantic Ocean, reaching its undeformed initial condition of 100 km thickness right at the end of the model domain. Velocity vectors are almost of the same length for Pacific and South American plates, at the westernmost and easternmost sides of the domain, keeping also the same westward direction, whereas they are longer for the Nazca plate, in the middle, that moves towards the east. The Pacific area (lower panel) from the westernmost side of the numerical domain, shows a depth of the lithosphere of ~100 km. Below Indonesia a wide thick zone can be seen reaching a depth of about 600 km. This zones almost continuously connects with the deformed thickened zone below the Philippines Sea and Japan, that is 1000 km depth. Globes in the right part of this figure show surface plate kinematics in a shallow hotspot reference frame at this stage, with the black line suggesting the position of the tectonic equator, along which the 2d slice of this model is cut. In the profiles I-I' and J-J' are shown the lateral extension and geographical position of the quarter annulus, whereas the dashed Trench line points to the geographical position of where the subduction trench should be.

The lithosphere is almost uniformly thick eastward, below the Atlantic Ocean, reaching its undeformed initial condition of 100 km thickness right at the end of the model domain, to the E. Velocity vectors are almost of the same length for Pacific and South American plates, at the westernmost and easternmost sides of the domain, keeping also the same westward direction, whereas they are longer for the Nazca plate, in the middle, that moves towards the east. This points to a W to E direction of the lithospheric accumulation. Velocity vectors are shorter, almost close to be 0, within the mantle and at the bottom boundary layer. The temperature is about 1220°C at the bottom of the lithosphere and 0°C at the top of the model domain. At the CMB the temperature is of about 2330°C and the thickness of this layer is about 175 km. Temperature in the middle of the domain is constant at about 1330°C. **Pacific (Figure 4.24, lower panel):** the Pacific area from the westernmost side of the numerical domain shows a depth of the lithosphere of ~100 km. Below Indonesia a wide thick

zone can be seen reaching a depth of about 600 km. This zones almost continuously connects with the deformed thickened zone below the Pacific plate and Japan, towards the E. This zone below Japan has a depth of ~1000 km. The lithosphere rapidly decreases its thickness, going back to the initial condition of 100 km thickness at easternmost boundary of the model domain. Velocity of the lithosphere surface is high in correspondence of the Pacific plate, whereas it is noticeably slower for the Eurasian and the Indo-Australian plates. This points to a subduction direction that goes from E to W. Velocity vectors further decrease towards the bottom of the model domain. Temperature of the lithosphere is 0°C at its top and reaches 1230°C at its bottom. The CMB layer is ~175 km thick, at a constant temperature of about 2330°C. Within the mantle the temperature is constant at about 1330°C. In Figures 4.25 and 4.26 data relative to the depth and velocities of the South American and Japanese thickened zones for *vp1* model are respectively shown. In Figure 4.25 (upper panel) the thickened area slowly increases its thickness from 100 km at 140 Myr to 400 km at 40 Myr, remaining stable at this depth until the end of the model run. Velocity (Figure 4.25, lower panel) for the South American thickened zone, starting from ~50 mm/yr, decreases to about 20 mm/yr at 100 Myr. Then, it is constant until 70 Myr, time at which it increases abruptly to about 30 mm/yr to then decrease again to 0 mm/yr at 50 and 40 Myr. From 30 to 0 Myr the velocity is constant at 20 mm/yr. In Figure 4.26, Japanese slab data can be seen. From the start of the model run (140 Myr) to its end (0 Myr) the slab depth (Figure 4.26, upper panel) slowly and continuously increase, reaching 1000 km depth at 10 Myr, depth that is constant also at 0 Myr. Velocities (Figure 4.26, lower panel) for this slab increase from about 10 mm/yr to almost 40 mm/yr during the first 30 Myr of the model run. Then they decrease to 20 mm/yr at 80 Myr, remaining constant at this value until 60 Myr. After a discontinuous phase at which the velocity jumps from 40 mm/yr to 0 mm/yr then again to 30 mm/yr and 10 mm/yr, at the end of the model run (10-0 Myr), the velocity of the bottom of the thickened lithosphere is constant at 20 mm/yr.

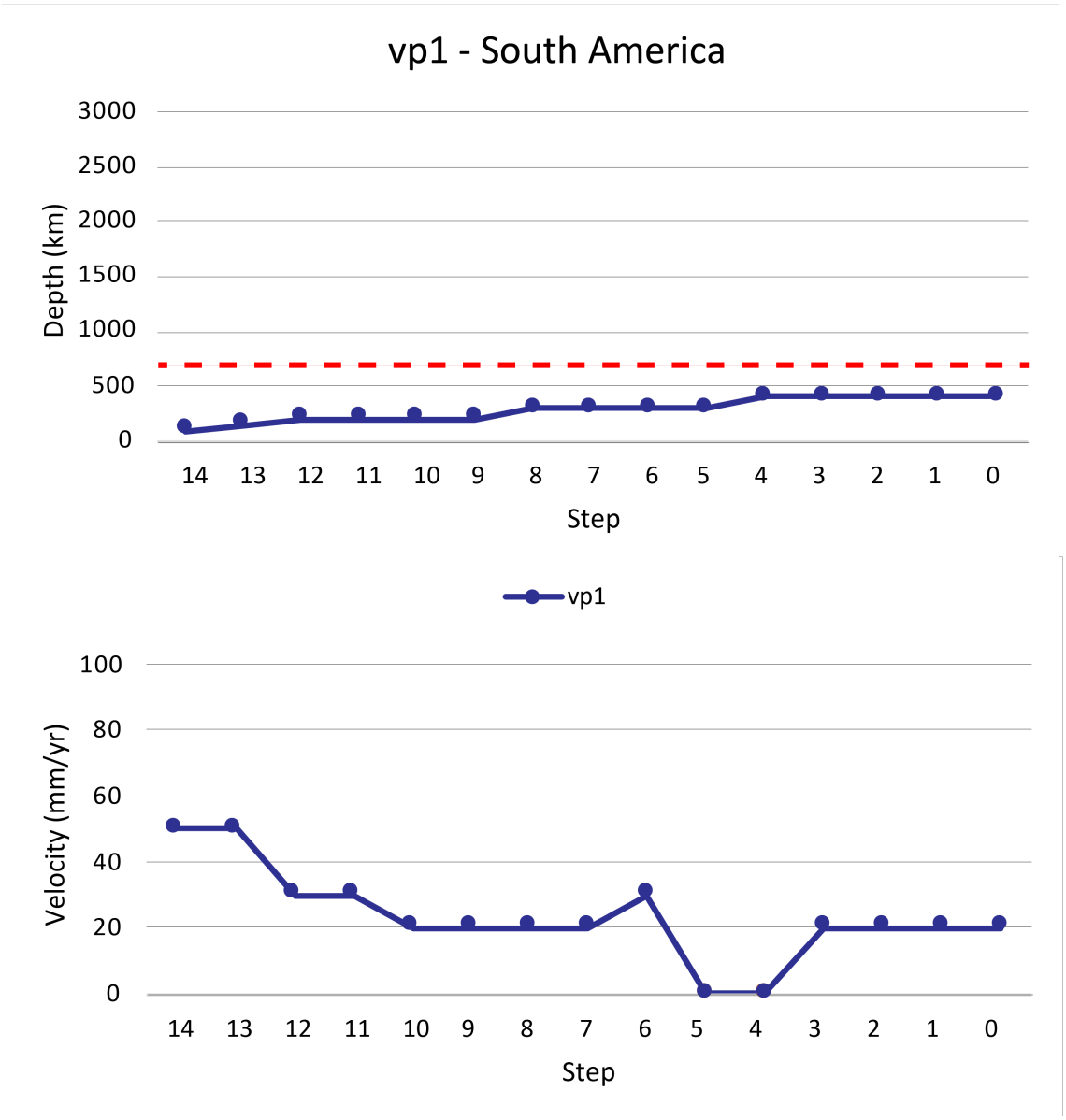

Figure 4.25 – Depth (upper panel) and velocity (lower panel) data for the South American lithosphere. In the upper panel the thickened area slowly increases its thickness from 100 km at 140 Myr to 400 km at 40 Myr, remaining stable at this depth until the end of the model run. Velocity (lower panel) for the South American thickened zone reaches a maximum of 50 mm/yr between 140 and 130 Myr and a minimum of 0 mm/yr between 50 and 40 Myr.

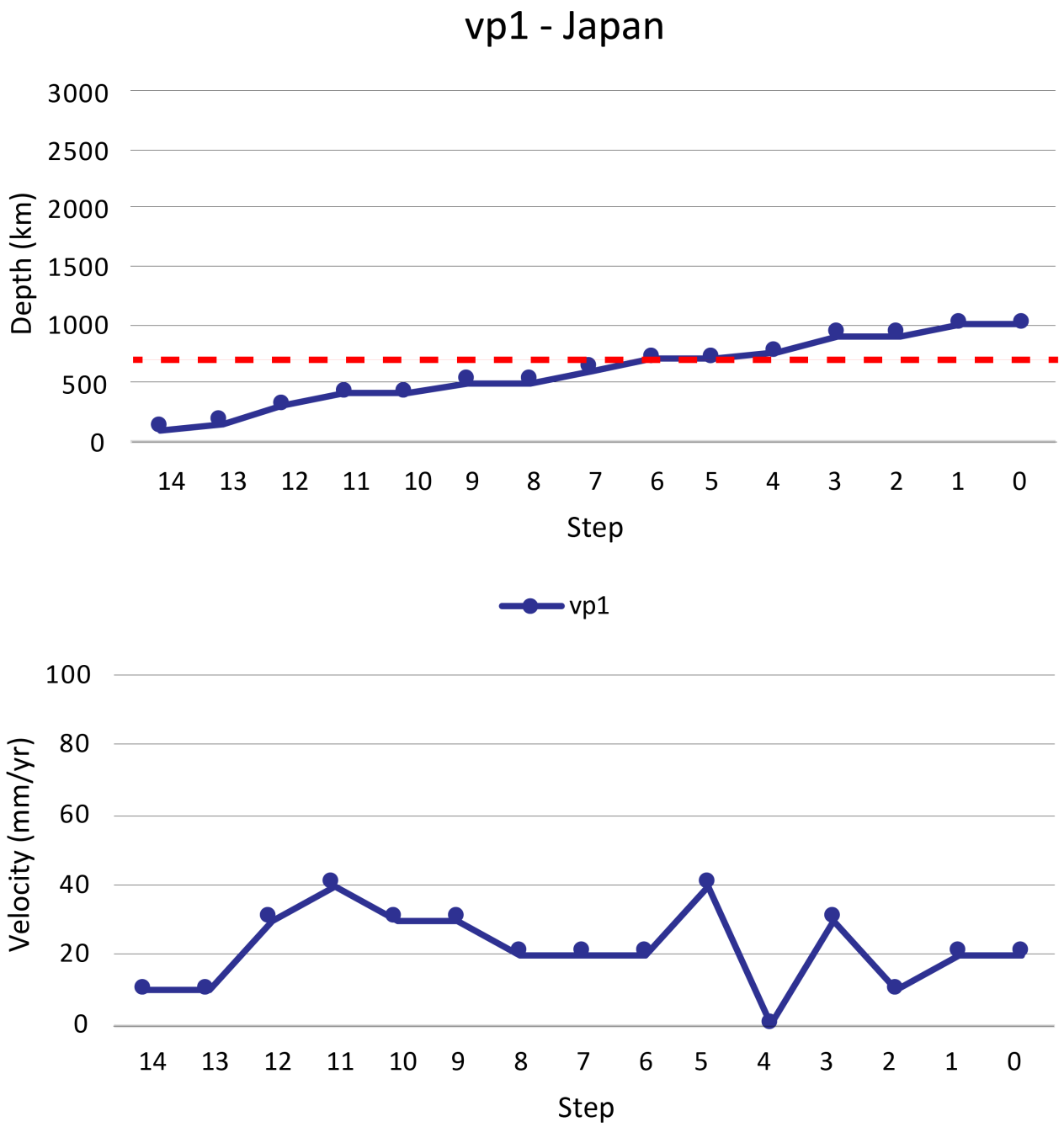

Figure 4.26 – Depth (upper panel) and velocity (lower panel) data for the Japanese slab. From the start of the model run (140 Myr) to its end (0 Myr) the slab depth (upper panel) slowly and continuously increase, reaching 1000 km depth at 10 Myr, constant also at 0 Myr. Velocities (lower panel) for this slab increase from about 10 mm/yr to almost 40 mm/y during the first 30 Myr of the model run. Then they decrease to 20 mm/yr at 80 Myr, remaining constant at this value until 60 Myr. After a discontinuous phase at which the velocity jumps from 40 mm/yr to 0 mm/yr and then again to 30 mm/yr and 10 mm/yr. At the end of the model run (10-0 Myr) the velocity of the bottom of the thickened lithosphere is constant at 20 mm/yr.

4.5.6 Model *vp2*

Figure 4.27 shows the step 0 of the model *vp2*. In this model the evolution of plate motion velocity (from 140 to 0 Myr) in a shallow hotspot reference frame (Table 4.1) is applied as boundary condition, for a total runtime of 140 Myr arbitrary divided into 14 Steps of 10 Myr each.

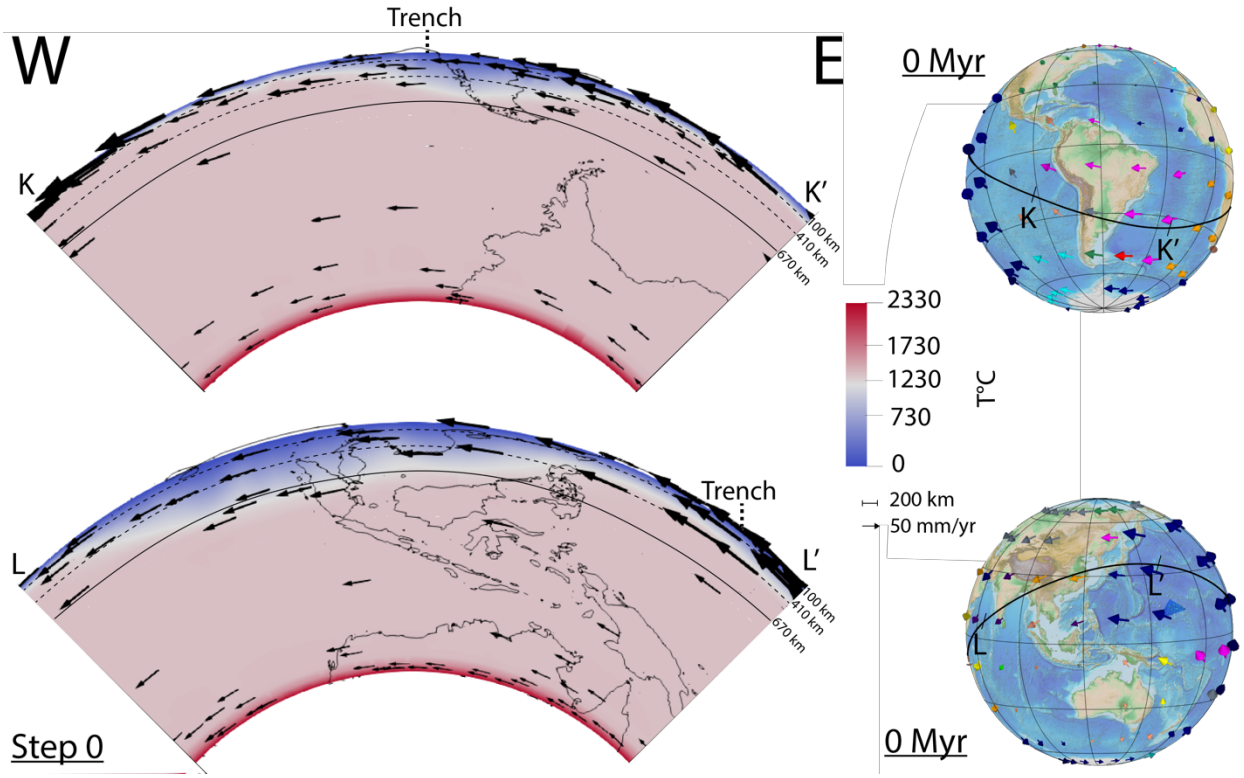

Figure 4.27 - Step 0 relative to model *vp2*. Looking at South America (upper panel) the lithosphere is thin at the western boundary of the numerical domain and thickens going towards the east, reaching the maximum depth of about 550 km under the South American continent. Towards the East, below the Atlantic ocean, its thickens goes back to the initial condition, reaching again 100 km depth. Velocity vectors points to a westward direction of the lithospheric accumulation under the South American continent. The Pacific area (lower panel) from the westernmost side of the numerical domain, shows a depth of the lithosphere of ~100 km. Then, from about India to the Sunda and Eurasian plates a wide thick zone that reaches a depth of about 700 km can be observed. Velocities at the surface, as well as at the bottom of the model domain, point to an E-W direction of the lithospheric accumulation. Globes in the right part of this figure show surface plate kinematics in a shallow hotspot reference frame at this stage, with the black line suggesting the position of the tectonic equator, along which the 2d slice of this model is cut. In the profiles K-K' and L-L' are shown the lateral extension and geographical position of the quarter annulus. The dashed Trench line represents where the subduction trench should be geographically located.

South America (Figure 4.27, upper panel): in model *vp2*, at current plate motion stage (0 Myr) the lithosphere is thin at the western boundary of the numerical domain and thickens going towards the east, reaching the maximum depth of about 550 km under the South American continent. Further eastward, below the Atlantic Ocean, its thickness goes back to the initial conditions, reaching again 100 km depth. Velocity vectors are almost of the same length for Pacific and South American plates, at the westernmost and easternmost sides of the domain, keeping also the same westward direction whereas they are shorter for the Nazca plate, in the middle, that is moving towards the west. This points to a W to E direction of the lithospheric accumulation. Velocity vectors are shorter within the mantle and at the bottom boundary layer. The temperature is of about 1220°C at the bottom of the lithosphere, along the entire spherical annulus, and 0°C at its top. At the CMB the temperature is of about 2330°C and its thickness is of about 175 km. Temperature in the middle of the domain is homogeneously at ~1330°C. **Pacific (Figure 4.27, lower panel):** the Pacific area from the

westernmost side of the numerical domain, shows a depth of the lithosphere of ~100 km. Then, from about India to the Eurasian plate a wide thick zone that reaches a depth of about 700 km can be observed. The lithosphere then slowly decreases its thickness, reaching the depth of about 400 km at easternmost boundary of the model domain. Velocity of the lithosphere surface is high in correspondence of the Pacific plate, whereas it decreases towards the Eurasia and Indo-Australia plates, at W. This points to a subduction direction that goes from E to W. Velocity vectors decrease towards the bottom of the model domain where the CMB layer is 175 km thick. Temperature of the lithosphere is 0°C at its top and reaches 1230°C at its bottom. The CMB layer has a constant temperature of about 2330°C. Within the mantle, the temperature is constant at about 1330°C.

In Figures 4.28 and 4.29 data relative to the depth and velocities respectively of the South American and Japanese thickened zones for *vp2* model can be seen. In Figure 4.28 (upper panel) the depth evolution data through time relative to the South American thickened zone are shown. In this area the thickness of the lithosphere reaches ~350 km at 80 Myr. This situation is stable until 40 Myr. Here the lithosphere starts to increase its thickness, reaching 400 km depth at 30 Myr. At 10 Myr, the slab depth is ~500 km reaching ~550 km at 0 Myr. Figure 4.28 (lower panel) shows the velocity evolution of the South American deepest lithosphere point. Starting from a null velocity (i.e., 0 mm/yr), the velocity of its tip starts to increase, up to a peak of ~80 mm/yr at 30 Myr. After that, the velocity decreases again to 0 mm/yr at 10 Myr and increases up to 80 mm/yr at 0 Myr.

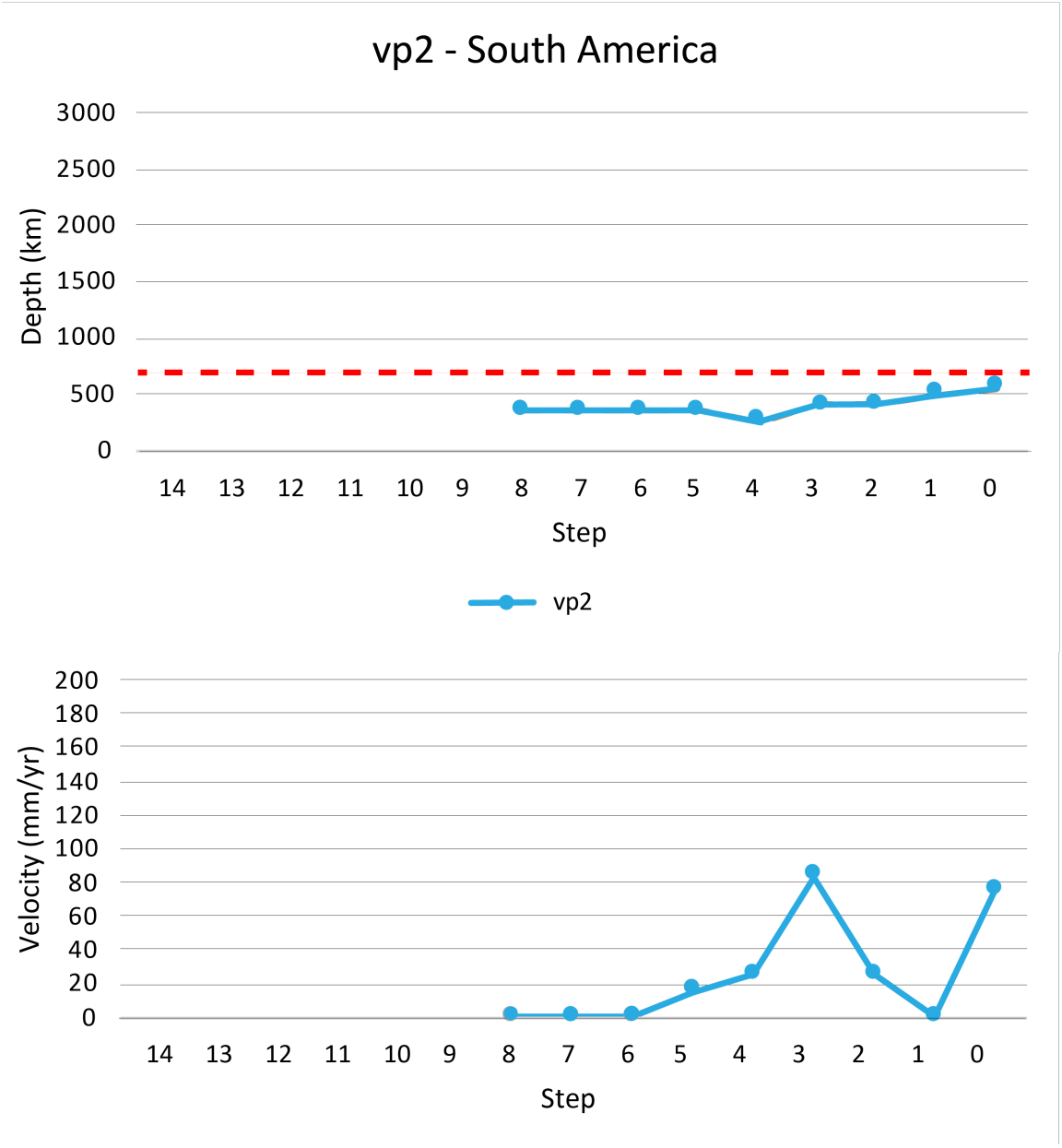

Figure 4.28 – Depth (upper panel) and velocity (lower panel) data for the South American lithosphere. In the upper panel, the depth evolution data through time relative to the South American thickened zone are shown. In this area, the thickness of the lithosphere reaches ~350 km at 80 Myr. This situation is stable until 40 Myr. Here the lithosphere starts to increase its thickness, reaching 400 km depth at 30 Myr. At 10 Myr, the slab depth is ~500 km reaching ~550 km at 0 Myr. The lower panel shows the velocity evolution of the South American slab. Maximum velocity value is about 83 mm/yr reached at 30 Myr, whereas the minimum value is 0 mm/yr, that is reached by the lithosphere between 80 and 60 Myr and at 10 Myr.

Figure 4.29 shows depth and velocities evolution for the lithosphere on the Pacific side of the spherical shell. After an increasing phase of the lithospheric depth (Figure 4.29, upper panel) up to about 500 km, this thickness is stable until 20 Myr. After that the lithosphere depth reaches 700 km, being stable during the last 10 Myr of the model run.

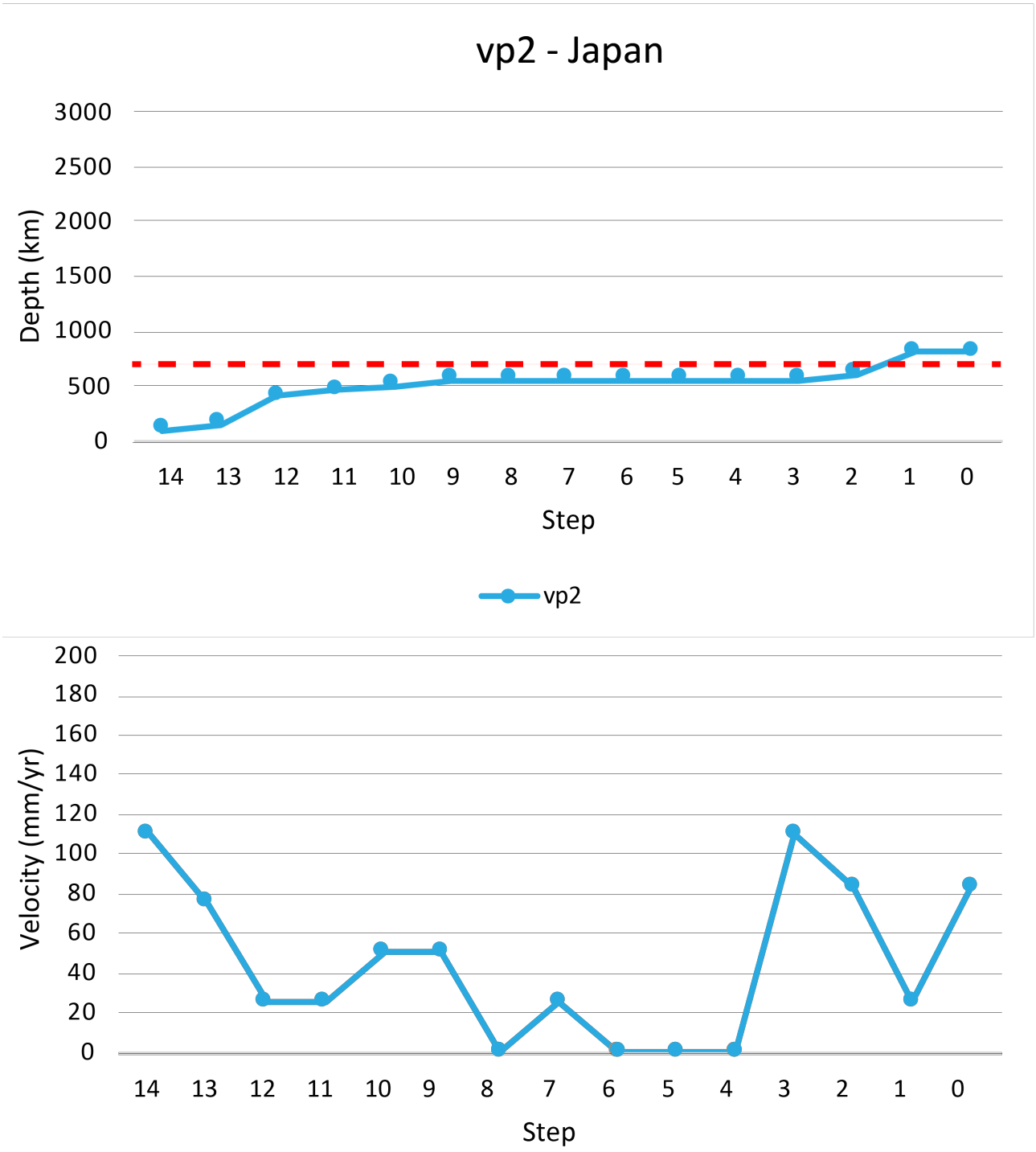

Figure 4.29 – Depth (upper panel) and velocity (lower panel) data for the Japanese lithosphere. In the upper panel, after an increasing phase of the lithospheric depth up to about 500 km, this thickness is stable until 20 Myr. After that the lithosphere depth reaches 700 km, being stable during the last 10 Myr of the model run. In the lower panel, velocities of the lithosphere reach their maximum value of 110 mm/yr at 140 and 30 Myr, whereas their minimum value is 0 mm/yr, reached at 80 Myr and kept between 60 and 40 Myr.

Initial velocity (Figure 4.29, lower panel) for the Pacific lithosphere is high, reaching ~110 mm/yr. After this initial stage, it starts to decrease, reaching about 20 mm/yr at 120 Myr. At 100 Myr the velocity is around 50 mm/yr, stable also at 90 Myr. At 80 Myr an abrupt decrease occurs, reaching 0 mm/yr. The velocity then has an increasing phase at 70 Myr to decrease again at 0 mm/yr, velocity

kept during 60-40 Myr. Between 40 and 30 Myr, the velocity reaches again about 110 mm/yr, but then decreases again to 20 mm/yr, at 10 Myr. The stage of 0 Myr is characterized by an increase in the velocity of the thickened lithosphere that reaches about 80 mm/yr.

4.5.7 Model *isehar1*

In Figure 4.30 the thermal initial stage of the entire spherical domain for models using the isentrope harzburgic (Bangerth et al., 2018) mantle rheological profile is shown. This initial stage is valid for models presented in this subsection, i.e. models *isehar1* and *isehar2*, since they were carried out using the same ASCII Reference Profile model.

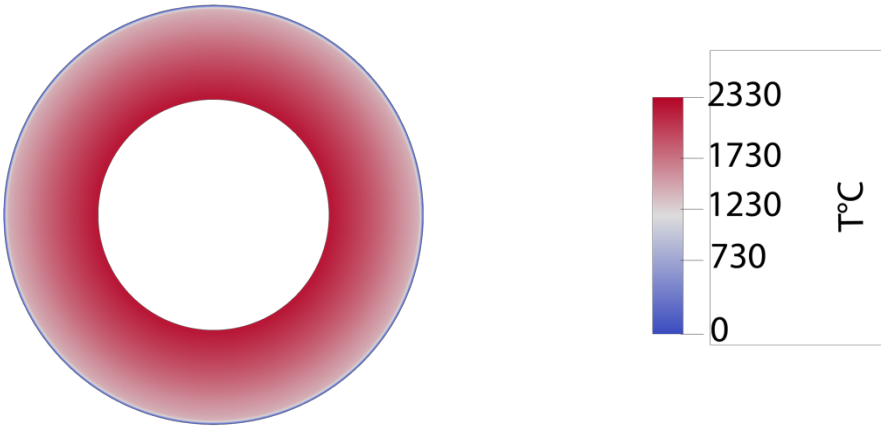

Figure 4.30 – Initial thermal stage for models *isehar1* and *isehar2*. This is the thermal state at the initial stage. One thermal boundary layer can be seen at the top of the domain, corresponding to the minimum (i.e., the lithosphere) temperature. The temperature is expressed in C°.

For this rheological profile, the lithosphere (in blue) is 100 km thick along the entire spherical shell and a single thermal boundary layer can be seen at the top of the spherical domain, corresponding to the minimum, i.e., the surface at 0°C, temperature.

Figure 4.31 shows the step 0 of the model *isehar1*. In this model the evolution of plate motion velocity (from 140 to 0 Myr) in a deep hotspot reference frame (rotation provided by Seton et al., 2012) is applied as boundary conditions, for a total runtime of 140 Myr corresponding to 14 arbitrary defined Steps of 10 Myr each.

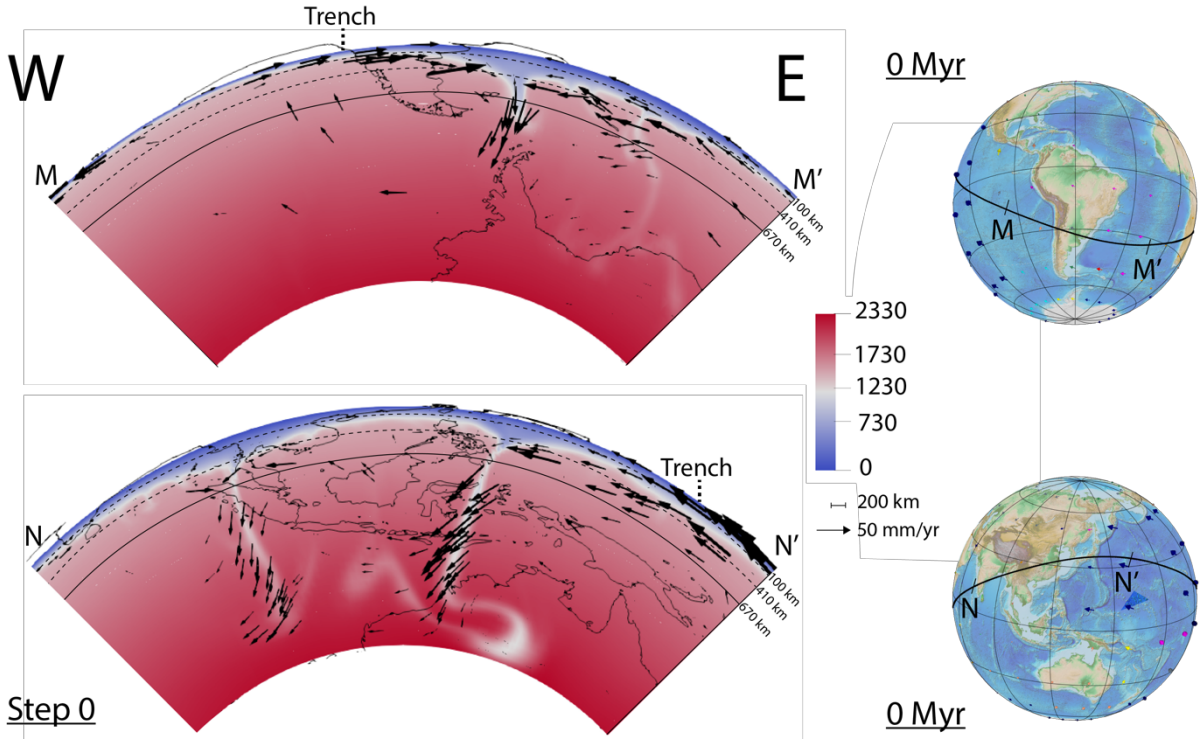

Figure 4.31 - Step 0 relative to model *isehar1*. Looking at South America (upper panel) the lithosphere is less than 100 km thick at the western boundary of the numerical domain. It thickens towards the east, reaching a depth of 960 km in correspondence of the subducting slab, right eastward of the South American continent and on the western side of the Atlantic Ocean. Going eastward, in the middle of the Atlantic ocean a very thin and deformed slab can be seen. It reaches a depth of about 2400 km. Velocity vectors are shorter within the mantle and point to a counterflow behind the subducting slab, with the upwelling in correspondence of the East Pacific Rise. Velocities are almost null at the CMB layer. A wide delamination zone can be observed from about India to Indonesia (Pacific area, lower panel). Then, almost below the Eurasian plate a thin and localized subducting slab reaches the depth of ~2500 km. This slab is surrounded by a zone of thickened lithosphere that reaches the depth of about 410 km both westward and eastward of the slab. Velocity vectors decrease towards the bottom of the model domain, but they are of the same intensity of the surface along the subducting slabs, this seems to enhance a weak circulation into the mantle, towards the W. Globes in the right part of this figure show surface plate kinematics in a deep hotspot reference frame at this stage, with the black line suggesting the position of the tectonic equator, along which the 2d slice of this model is cut. Profiles M-M' and N-N' show the lateral extension and geographical location of the quarter annulus surface. The location where the subduction trench should be is pointed by the dashed Trench line.

South America (Figure 4.31, upper panel): in model *isehar1*, a very thin lithosphere can be seen at the western boundary of the numerical domain. It thickens towards the east, reaching a depth of 960 km in correspondence of the subducting slab, right eastward of the South American continent and on the western side of the Atlantic ocean. Going eastward, in the middle of the Atlantic ocean, a very thin and deformed slab can be seen. It has a depth of about 2400 km. From 670 km the temperature of the slab becomes higher throughout its boundaries; at about 1000 km the slab almost faded away into the mantle. On the eastern boundary of the numerical domain the lithosphere thickness goes back to the initial condition, reaching again 100 km depth. Velocity vectors are longer and have a westward direction on the Pacific plate surface at the westernmost side of the annulus quarter, whereas they are shorter for the Nazca plate, right eastward, that has an eastward motion direction. Vectors within the subducting slab are slightly shorter with respect to vectors of the Nazca plate, however they point to an eastward direction of motion for the subducting slab. Velocities are slower on the surface of the

South American plate, that has a E-W direction of motion. Velocity vectors are shorter within the mantle and point to a counterflow behind the subducting slab, with the upwelling in correspondence of the East Pacific Rise. Velocities are almost null at the CMB layer. The temperature is of about 1330°C at the bottom of the lithosphere, along the entire spherical annulus, and 0°C at its top. At the CMB the temperature is of about 2330°C. Temperature gradually increases within the mantle. **Pacific (Figure 4.31, lower panel):** the Pacific area from the westernmost side of the numerical domain shows a depth of the lithosphere of ~100 km. Moving eastward a wide delamination zone can be observed from about India to Indonesia. Then, almost below the Eurasian plate a thin and localized subducting slab reaches the depth of ~2500 km. This slab is surrounded by a zone of thickened lithosphere that reaches the depth of about 410 km right westward and eastward of the slab. Towards the east, below the Eurasian plate, the lithosphere goes back to a thickness of about 100 km and it thickens again to about 400 km in correspondence of the subducting slab localized under Japan. Here the slab reaches a depth of 2430 km. After this depth, it starts to bend assuming an S shape and accumulates at the bottom of the numerical domain, i.e., at 2900 km. The last part of the slab, starting from ~2400 km, is hotter and the slab is increasingly thinner. Velocity vectors on the lithosphere surface are small for the Indo-Australian and Eurasian plates, whereas it is high in correspondence of the Pacific plate. This points to a subduction direction that goes from E to W for both the observable slabs in Figure 4.31 (lower panel). Velocity vectors decrease towards the bottom of the model domain but they are of the same intensity of the surface along the subducting slabs, this seems to enhance a weak circulation into the mantle, towards the W, that shows a lower intensity with respect to the surface. Temperature of the lithosphere is 0°C at its top and reaches ~1330°C at its bottom. The bottom of the domain has a temperature of about 2330°C. Within the mantle, the temperature increases from the top to the bottom.

In Figures 4.32 and 4.33 data on the depth and velocity evolution through time for model *isehar1* are shown. In Figure 4.32 (upper panel), the depth evolution of the young South American slab can be observed. It starts to subduct at about 10 Myr, reaching rapidly the depth of about 600 km. At 0 Myr, it reaches ~1000 km depth. Velocity (Figure 4.32, lower panel) is very high for the tip of this slab. It starts with a velocity of 40 mm/yr to end at 0 Myr with a velocity of ~50 mm/yr.

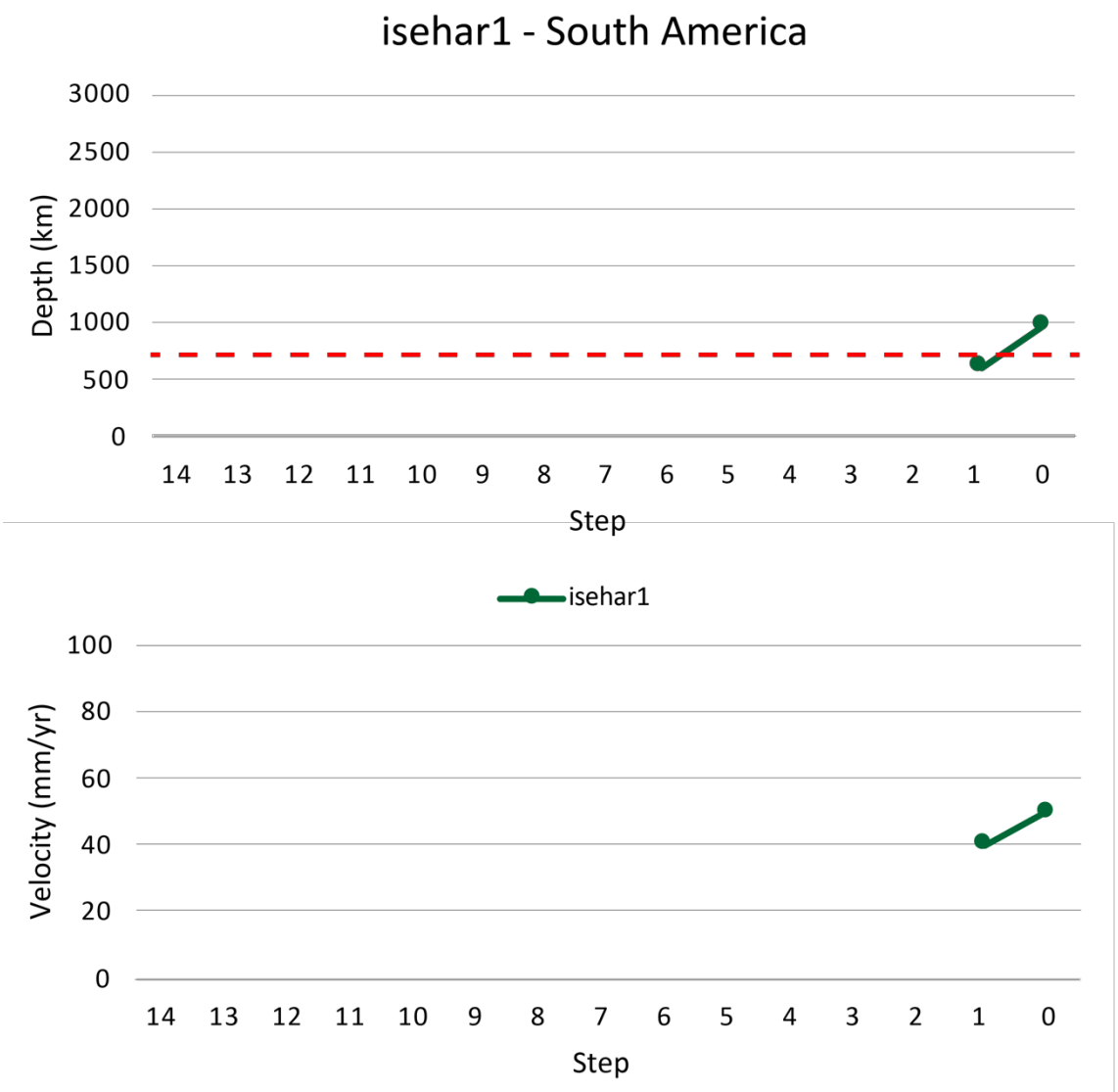

Figure 4.32 – Depth (upper panel) and velocity (lower panel) data for the South American slab. The depth (upper panel) evolution of the young South American slab starts at about 10 Myr, reaching rapidly the depth of about 600 km. At 0 Myr, it reaches ~1000 km depth. Velocity (lower panel), in fact, is very high for the tip of this slab. It starts with a velocity of 40 mm/yr (its minimum value), to end at 0 Myr with a velocity of ~50 mm/yr (its maximum value).

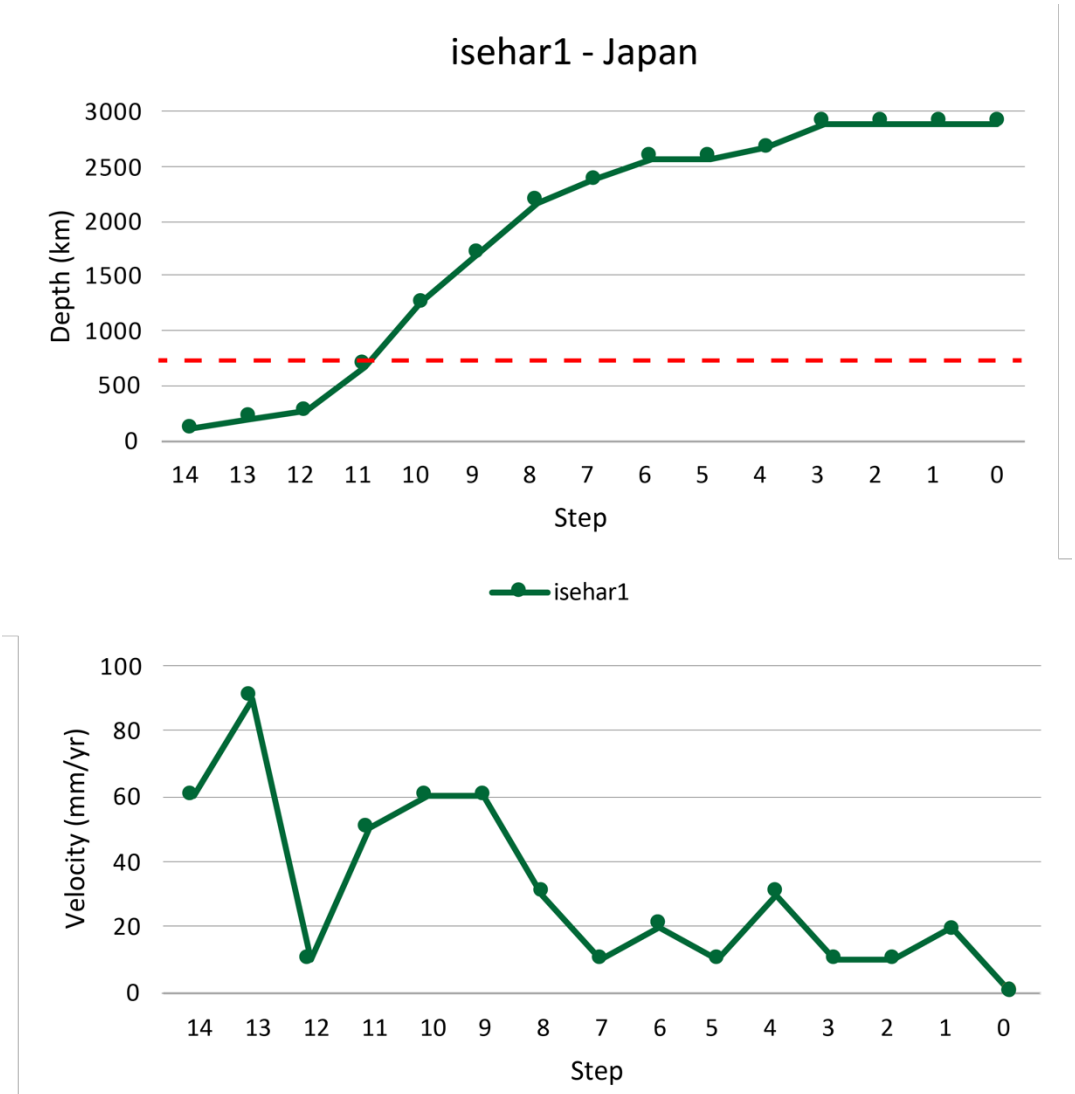

Figure 4.33 – Depth (upper panel) and velocity (lower panel) data for the Japanese slab. Depth (upper panel) evolution started at 140 Myr, time at which the lithosphere is homogeneously thick (100 km). At 130 Myr the lithosphere starts to thickens below Japan, reaching 260 km depth at 120 Myr. At 110 Myr the slab starts to increase more rapidly its depth, reaching 2580 km depth at 60 Myr. Its depth is constant until about 40 Myr, time at which its depth start to increase again. At 40 Myr, the deepest part of the Japanese slab is at 2670 km, reaching the bottom of the model domain at 30 Myr. Velocity (lower panel) evolution for the Japanese slab is discontinuous and variable. Among a number of up and downs, the maximum velocity value reached at 130 Myr is about 90 mm/yr whereas the minimum is 0 at the current stage (0 Myr).

In Figure 4.33 (upper panel), the depth evolution of the Pacific area shows a long-lived Japanese slab. Its evolution started at 140 Myr, time at which the lithosphere is homogeneously thick (100 km). At 130 Myr, the lithosphere starts to thickens below Japan, reaching 260 km depth at 120 Myr. At 110 Myr the slab starts to increase more rapidly its depth, reaching ~2580 km depth at 60 Myr. Its depth is constant until about 40 Myr, time at which its depth start to increase again. At 40 Myr the deepest part of the Japanese slab is at 2670 km, reaching the bottom of the model domain, i.e., 2900 km, at 30 Myr. Velocity evolution for the Japanese slab (Figure 4.33, lower panel) is discontinuous and variable. Maximum velocity value reached at 130 Myr is about 90 mm/yr but then suddenly decreases

to about 10 mm/yr at 110 Myr. Its value increases again, being constant at 60 mm/yr between 100 and 90 mm/yr. At 70 Myr, the velocity decreases again at 10 mm/yr, increasing to 30 mm/yr at 40 Myr, reaching its minimum value of 0 mm/yr at the current stage (0 Myr).

4.5.8 Model *isehar2*

Figure 4.34 shows the step 0 of the model *isehar2*. In this model the evolution of plate motion velocity (from 140 to 0 Myr) in a shallow hotspot reference frame (Table 4.1) is applied as boundary conditions, for a total runtime of 140 Myr corresponding to 14 Steps arbitrary divided in 10 Myr each. **South America (Figure 4.34, upper panel):** in model *isehar2*, the lithosphere at the western boundary of the numerical domain is about 100 km thick. It thickens towards the east, right under the South American trench, forming a mantle wedge that is about 410 km thick. Here the South American slab can be observed. It has a total depth of ~2900 km depth. The slab almost preserve its initial temperature and thickness until about 1400 km depth. From this depth, at which the slab is not subject to deformation, the deformed part of the slab starts, reaching 2900 km depth. This slab segment is way hotter than the one above 1400 km depth, starting to mix with the hosting mantle. It is important to notice that, although very warped in this last segment, the slab is always in connection with all its part. Towards the East, on the eastern boundary of the numerical domain, the lithosphere thickness goes back to the initial condition, reaching again 100 km depth. Velocity vectors are longer and have a westward direction on the Pacific and South American plate surfaces, at the westernmost and easternmost side of the annulus, whereas they are shorter for the Nazca plate, in the middle, that maintain a westward motion direction. Vectors within the subducting slab are of the same length if compared with vectors of the South American plate, pointing to a westward subduction direction. Velocity vectors are shorter within the mantle rising towards the East Pacific Rise and the Pacific plate. Velocities are almost null at the CMB layer, except for vectors within the slab segment lying above the CMB. The temperature is of about 1330°C at the bottom of the lithosphere, along the entire spherical annulus, and 0°C at its top. At the CMB the temperature is of about 2330°C. Temperature gradually increases within the mantle

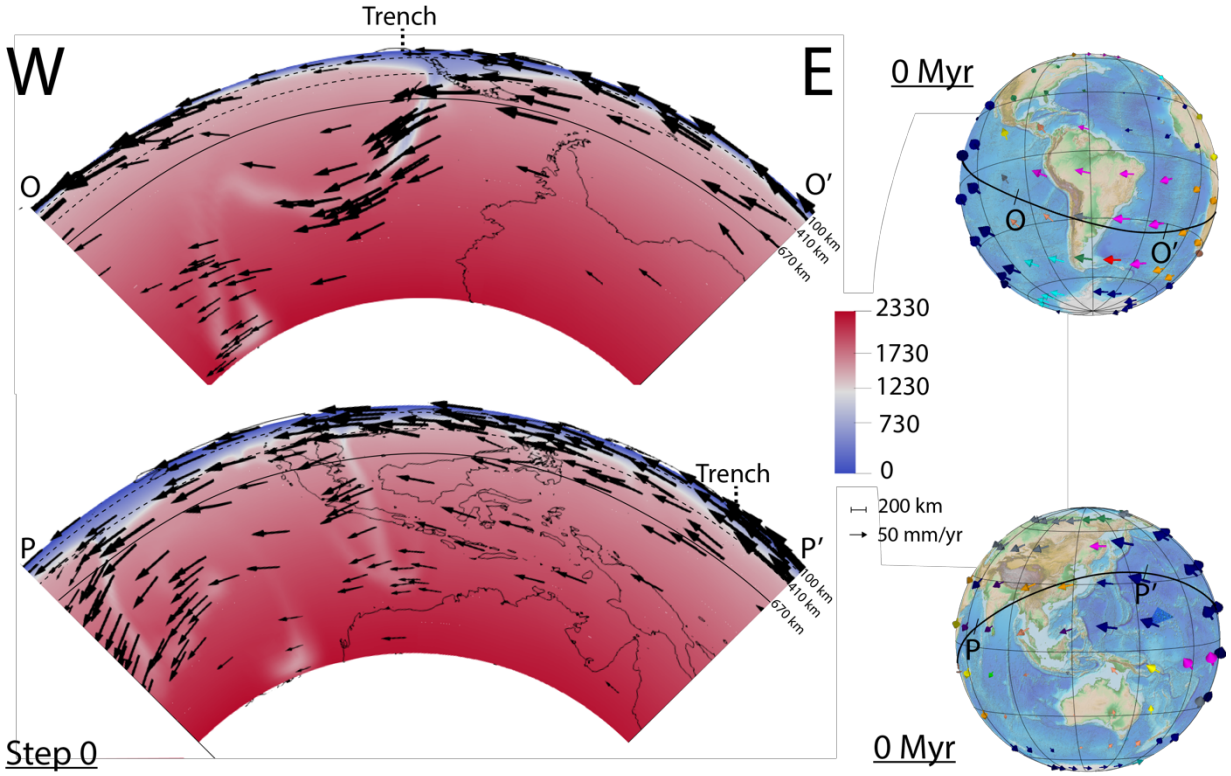

Figure 4.34 - Step 0 relative to model *isehar2*. In the upper panel (South America) the lithosphere at the western boundary of the numerical domain is about 100 km thick. It thickens towards the east, right under the South American trench, forming a mantle wedge that is about 410 km thick. Here the South American slab can be observed. It has a total depth of ~2900 km depth. The slab preserve almost its initial temperature and thickness until about 1400 km depth. From this depth, at which the slab is not subject to deformation, the deformed part of the slab starts reaching 2900 km depth. All plates show a westward direction, although keeping different velocities. The Pacific area (lower panel) from the westernmost side of the numerical domain shows a depth of the lithosphere of ~100 km. Its depth rapidly increases eastward, where a wedge (410 km thick) and a slab that reaches 2200 km depth below the Indian Ocean can be seen. The bottom of this subducting slab is at ~410 km, but the lithosphere thickness decreases up to about 350 km towards the east. Below Indonesia another slab can be seen. It reaches a depth of ~2200 km. Velocity vectors have a westward direction, showing different velocities. Globes in the right part of this figure show surface plate kinematics in a shallow hotspot reference frame at this stage, with the black line suggesting the position of the tectonic equator, along which the 2d slice of this model is cut. In profiles O-O' and P-P' the lateral extension and geographical position of the quarter annulus surface are shown. The position where the subduction trench should be is represented by the dashed trench line.

Pacific (Figure 4.34, lower panel): the Pacific area from the westernmost side of the numerical domain shows a depth of the lithosphere of ~100 km. Its depth rapidly increases eastward, where a wedge (410 km thick) and a slab that reaches 2200 km depth can be seen below the Indian Ocean. The bottom of this subducting slab is at ~410 km but the lithosphere thickness decreases up to about 350 km towards the east. Below Indonesia a slab can be seen. It reaches a depth of ~2200 km. Below Japan a delaminated lithosphere zone reaches 380 km depth. Velocity vectors on the lithosphere surface are small for the Indo-Australian plate but increase eastward for the lithosphere of the Eurasian plate whereas it slightly decrease for Pacific plate. All plates show a westward direction, although keeping different velocities. Subduction direction for both slabs goes from E to W. Velocity vectors slightly decrease towards the bottom of the model domain but they are of the same intensity of the surface along the subducting slab, especially for the one below the Indian plate. This produce

a circulation into the mantle that has the same direction of the lithosphere, but with a minor intensity with respect to it. Temperature of the lithosphere is 0°C at its top and reaches ~1330°C at its bottom. The bottom of the domain has a temperature of about 2330°C. Within the mantle, the temperature increases from the top to the bottom.

In Figures 4.35 and 4.36 depth (upper panel) and velocity (lower panel) evolution for South American and Japanese slabs, respectively, are shown. In Figure 4.35 (upper panel) the lithosphere at the initial stage of 140 Myr is 100 km thick for all the spherical shell, then it starts to slowly but constantly increase its thickness up to 500 km at 110 Myr. The lithosphere thickness deepens in a faster way until 70 Myr, time at which it reaches 2500 km depth. After this time, the slab tip decreases its velocity, reaching 2900 km depth at 30 Myr and keeping it constant until the end of the model run. Velocity evolution (Figure 4.35, lower panel) starts from ~50 mm/yr at 140 Myr. Velocity increases up to almost 80 mm/yr, then decreases again to almost 50 mm/yr, at 110 Myr. After this time, velocity has a high peak around 100 mm/yr at 90 Myr, but then decreases again reaching almost 20 mm/yr at 60 Myr and keeping it constant until 40 Myr. This velocity is kept constant for the last 20 Myr of the model evolution except for a peak at 100 mm/yr, in correspondence of 30 Myr.

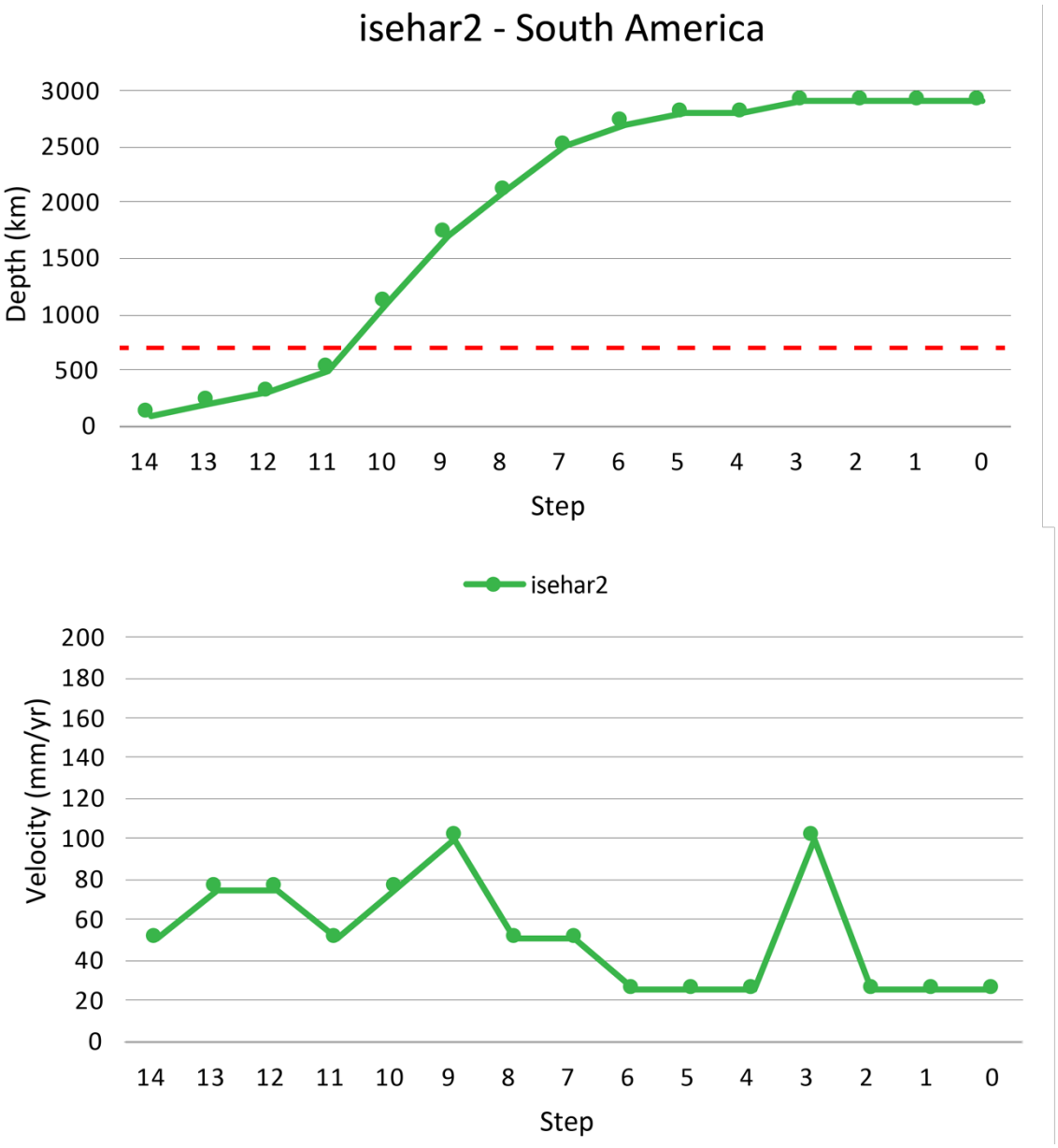

Figure 4.35 – Depth (upper panel) and velocity (lower panel) data for the South American side of model *isehar2*. In the upper panel the lithosphere at the initial stage of 140 Myr is 100 km thick for all the spherical shell, then it starts to slowly but constantly increase its thickness up to 500 km, at 110 Myr. The lithosphere thickness deepens in a faster way until 70 Myr, time at which it reaches 2500 km depth. After this time, the slab dip decreases its velocity, reaching 2900 km depth at 30 Myr and keeping it constant until the end of the model run. Velocities for this model follow a discontinuous evolution. Maximum peaks are two in correspondence of 90 and 30 Myr, whereas minimum velocity is about 20 mm/yr, kept constant between 60 and 40 Myr and from 20 to 0 Myr.

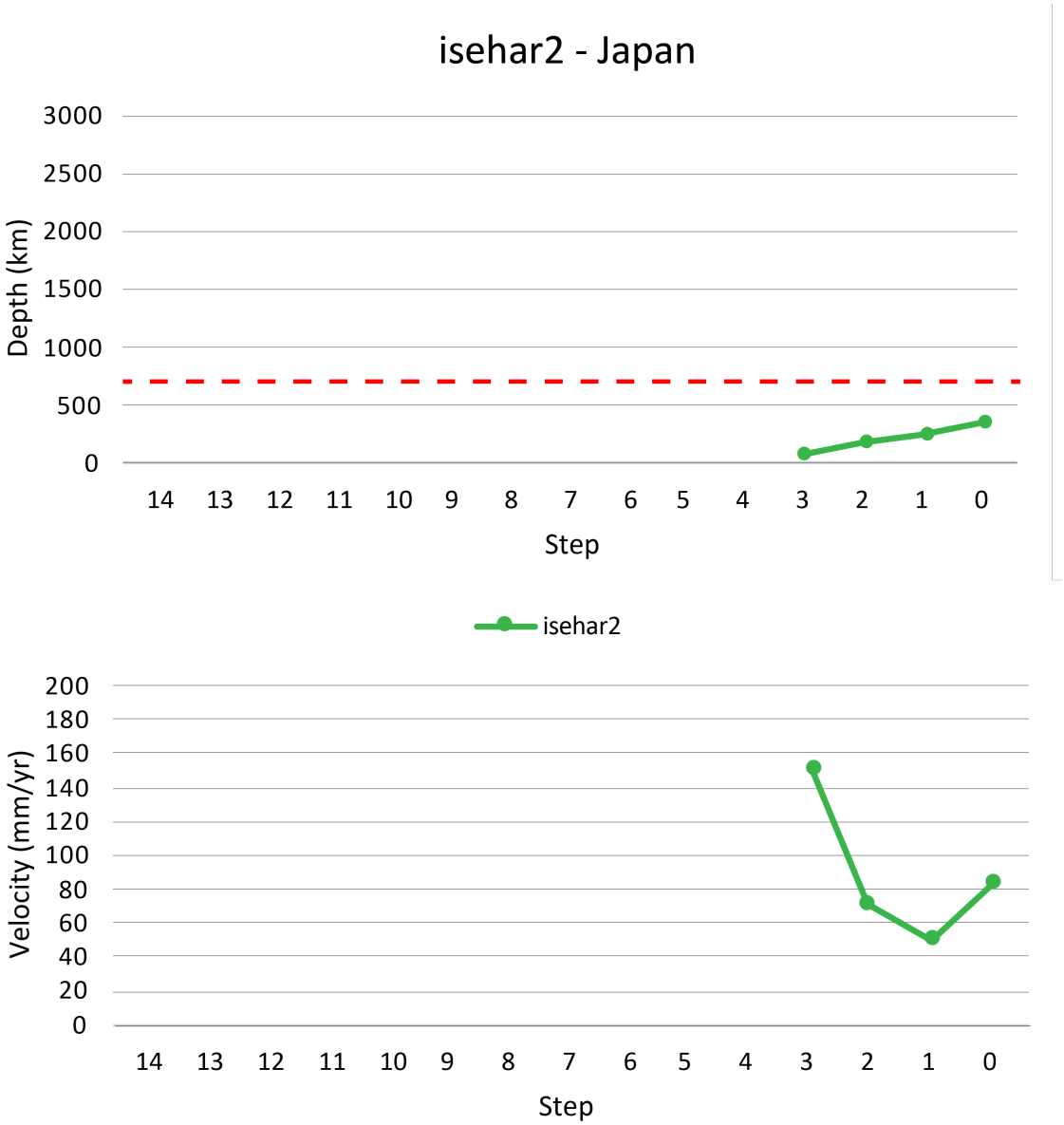

Figure 4.36 – Depth (upper panel) and velocity (lower panel) data for the Japanese slab. The depth evolution of the Japanese slab (upper panel) starts at about 30 Myr with a depth of about 100 km. The depth of the slab tip increases almost continuously, following the same trend, up to almost 380 km depth at 0 Myr. During velocity evolution at the slab tip the maximum velocity reached is about 150 mm/yr whereas the minimum is 50 at and 10 Myr.

In Figure 4.36 (upper panel) the depth evolution of the Japanese slab starts at about 30 Myr, with a depth of about 100 km. The depth of the slab tip increases almost continuously, following the same trend, up to almost 380 km depth at 0 Myr. Velocity of the slab tip (Figure 4.36, lower panel) at 30 Myr is about 150 mm/yr. It abruptly decreases to 50 mm/yr at 10 Myr, whereas it starts increasing again reaching 85 mm/yr at 0 Myr.

4.5.9 Model *majol1*

In Figure 4.37 the thermal initial stage of the entire spherical domain for models using the majorite-Fo50 (Boneh et al., 2017; Griffin et al., 2009; Nekvasil et al., 2004) rheological profile is shown. This initial stage is valid for models presented in this subsection, i.e., models *majol1* and *majol2*, since they were carried out using the same ASCII Reference Profile model.

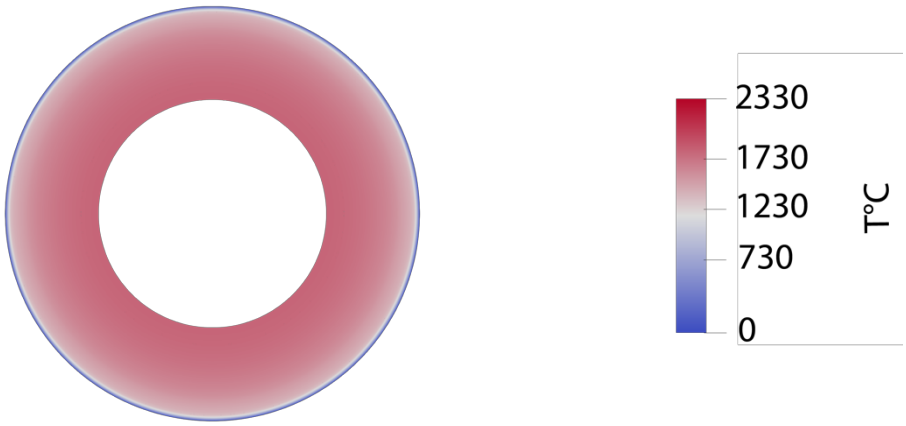

Figure 4.37 – Initial thermal stage for models *majol1* and *majol2*. This is the thermal state at the initial stage. One thermal boundary layer can be seen at the top of the domain, corresponding to the minimum (i.e., the lithosphere) temperature. The temperature is expressed in C°.

For this rheological profile the lithosphere (in blue) is 100 km thick along the entire spherical shell and a single thermal boundary layer can be seen at the top of the spherical domain, corresponding to the minimum (i.e., the surface at 0°C) temperature.

Figure 4.38 shows the step 0 of the model *majol1*. In this model the evolution of plate motion velocity (from 140 to 0 Myr) in a deep hotspot reference frame (rotation data collected by Seton et al., 2012) is applied as boundary conditions, for a total runtime of 140 Myr corresponding to 14 Steps of 10 Myr each, arbitrarily defined. **South America (Figure 4.38, upper panel):** in model *majol1* the lithosphere at the western boundary of the numerical domain is about 100 km thick. It thickens towards the east, eastward with respect to the South American coastlines, reaching a depth of ~780 km. Right eastward, a thick zone of delaminated lithosphere is observable. Its thickness is of about 410 km, with delaminated lithospheric nails reaching about 670 km depth. However, the lithosphere is homogeneously 410 km thick until the central Atlantic Ocean. After that, at the easternmost boundary of the model domain, the lithosphere is 100 km thick.

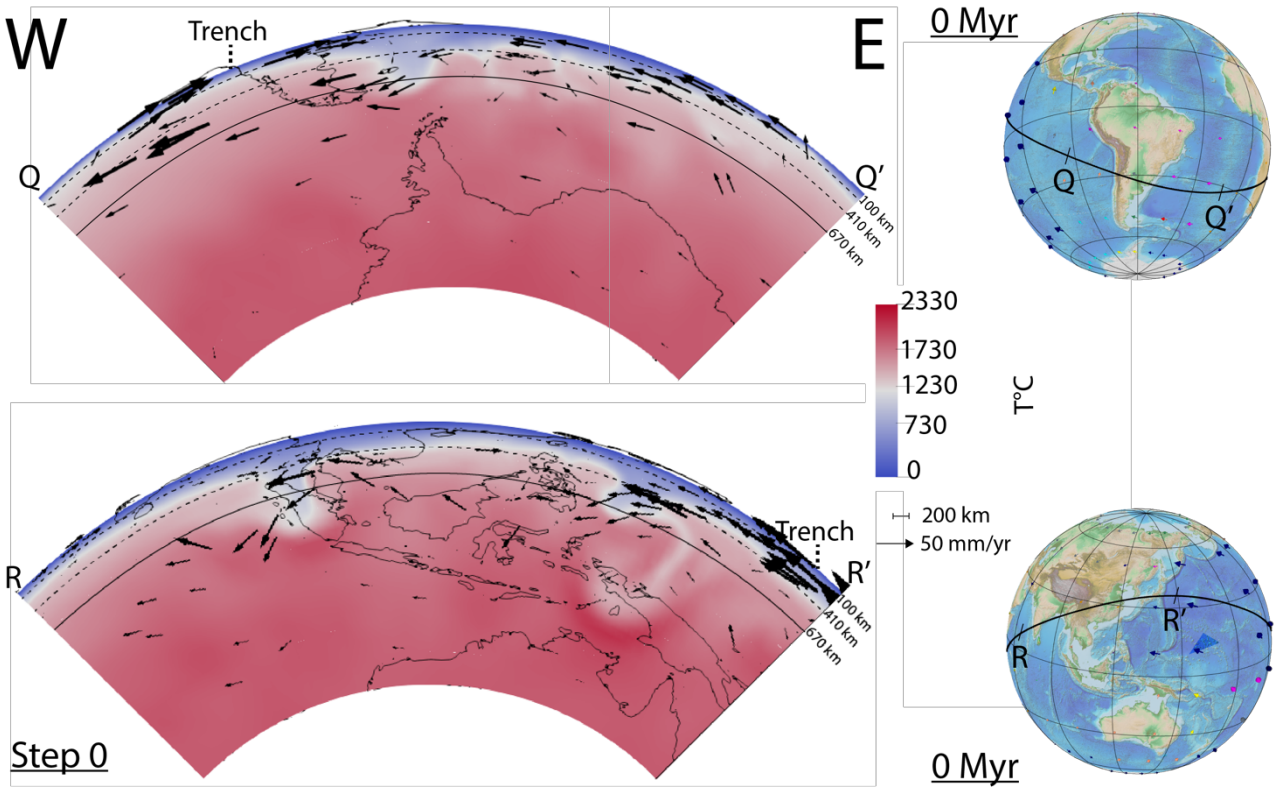

Figure 4.38 - Step 0 relative to model *majol1*. Looking at South America (upper panel) the lithosphere at the western boundary of the numerical domain is about 100 km thick. It thickens towards the east, right eastward with respect to the South American coastlines, reaching a depth of ~780 km. Velocity vectors show an eastward direction for the Nazca plate, with a higher velocity with respect to the South American plate, which has a westward motion of its surface. In the Pacific area (lower panel), the lithosphere at the westward boundary of the annulus has a depth of about 175 km. It increases going eastward and below Indonesia a mantle wedge in front of the slab can be seen, with a depth of about 410 km. The slab here reaches a depth of 1100 km. Under Japan, the slab reaches a depth of 700 km. Velocity vectors on the lithosphere surface are very small for the Indo-Australian and Eurasian plates, whereas they are higher towards the Pacific plate. Globes in the right part of this figure show surface plate kinematics in a deep hotspot reference frame at this stage, with the black line suggesting the position of the tectonic equator, along which the 2d slice of this model is cut. In profiles Q-Q' and R-R' the lateral extension and geographical position of the quarter annulus surface are shown. The dashed vertical Trench line points to the location where the subduction trench should be.

Velocity vectors show an eastward direction for the Nazca plate with a higher velocity with respect to the South American plate, which has a westward motion of its surface. This points to an eastward direction of the subducting lithosphere. Furthermore, velocity vectors behind the slab show a counterflow with an upwelling of mantle material towards the East Pacific Rise. Within the mantle, at depth, velocity vectors become shorter, pointing to a more vigorous circulation within the upper mantle, with respect to the lower mantle. Temperature of the lithosphere is 0°C at its top and reaches ~1300°C at its bottom. The bottom of the domain has a temperature of about 2300°C. Within the mantle, the temperature increases from the top to the bottom. **Pacific (Figure 4.38, lower panel):** the lithosphere at the westward boundary of the annulus has a depth of about 175 km. It increases going eastward and a mantle wedge with a depth of about 410 km in front of the slab can be seen below Indonesia. The slab here reaches a depth of 1100 km. Under Japan the slab reaches a depth of 700 km. Starting from the tip of the Japanese slab an old faded slab segment can be observed. It first rises at about 500 km, eastward of the current active slab, then it deepens again fading within the

surrounding mantle reaching a depth of 1800 km. Velocity vectors on the lithosphere surface are very small for the Indo-Australian and Eurasian plates, whereas they are higher in correspondence of the Pacific plate. This points to a subduction direction that goes from E to W for both the observable slabs in Figure 4.38 (lower panel). Velocity vectors decrease towards the bottom of the model domain but they are high as the vectors of the Pacific plate along both the subducting slabs, this seems to enhance a weak circulation into the mantle towards the W. A counterflow is visible right in front of the Indonesian slab rising up towards the Indian continent, whereas a westward motion of the mantle towards the shallow portion of the Indonesian slab arise from the Japanese slab.

In Figures 4.39 and 4.40 depth and velocity evolution of the slabs in Figure 4.38 is shown. In the upper panel of Figure 4.39, depth evolution of the South American slab can be observed. At 20 Myr the slab has a depth of 440 km. At 10 Myr, the active slab reaches 700 km depth, merely exceeding the 670 discontinuity. At this depth its deepening process is slowered down. At the last stage (0 Myr) the slab reaches a depth of 780 km. In Figure 4.39 (lower panel), velocity of the tip of the slab is 30 mm/yr at 20 Myr, slows down to 10 mm/yr at 10 Myr and increase again to 30 mm/yr at the last evolution stage. In Figure 4.40 (upper panel), the young Japanese slab at 40 Myr has a depth of about 550 km, whereas its depth is constant around the 670 km discontinuity between 30 and 10 Myr, reaching 730 km depth at 0 Myr. Velocities for this slab (Figure 4.40, lower panel) are constant at 10 mm/yr from 40 to 10 Myr and increase at 0 Myr, reaching 20 mm/yr.

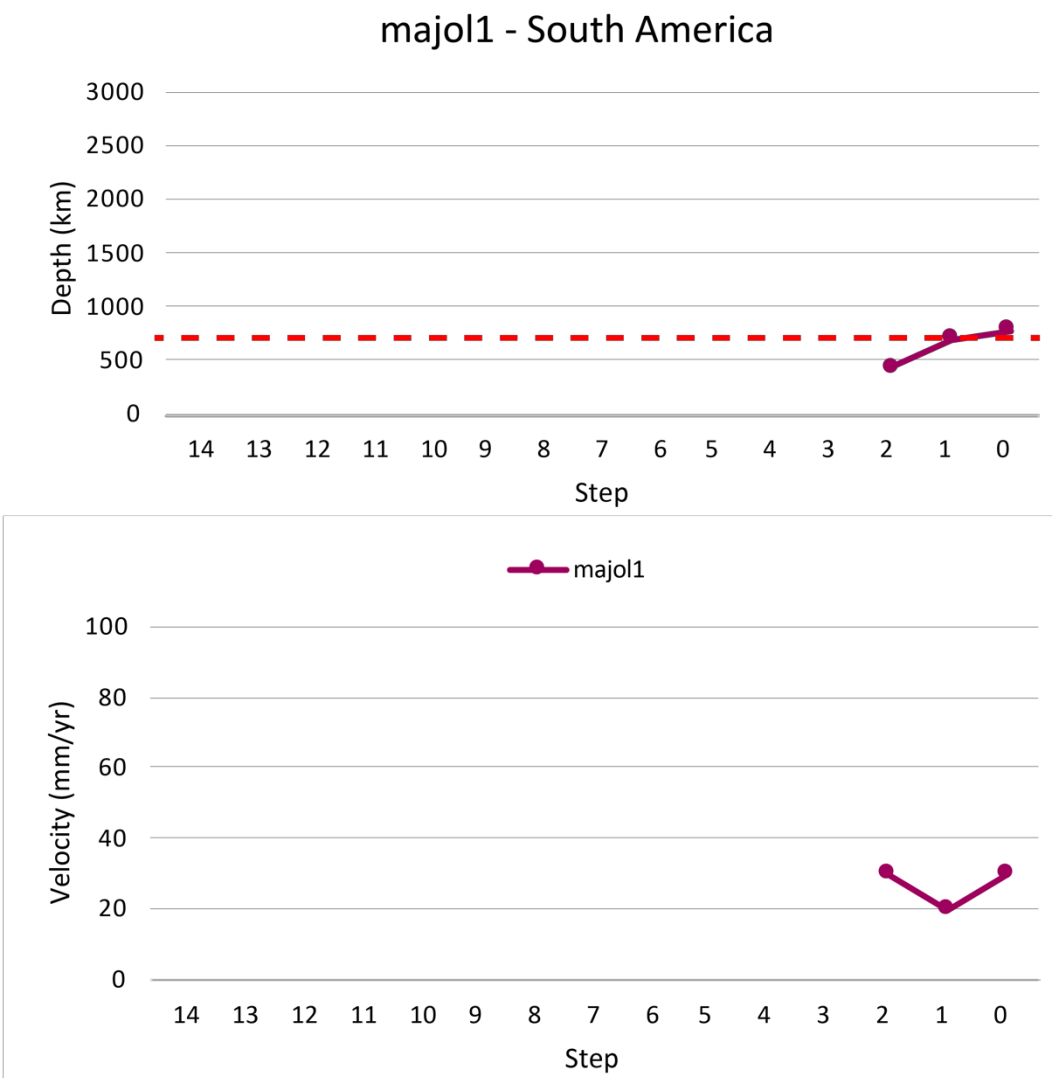

Figure 4.39 – Depth (upper panel) and velocity (lower panel) data for the South American slab of model *majo1*. In the upper panel depth evolution of the South American slab can be observed. At 20 Myr the slab has a depth of 440 km. At 10 Myr the active slab reaches 700 km depth, merely exceeding the 670 discontinuity. At this depth its deepening process is slowered down. At the last stage (0 Myr) the slab reaches a depth of 780 km. Maximum velocity (lower panel) for this slab is ~30 mm/yr at 20 and 0 Myr, whereas minimum velocity is 20 mm/yr at 10 Myr.

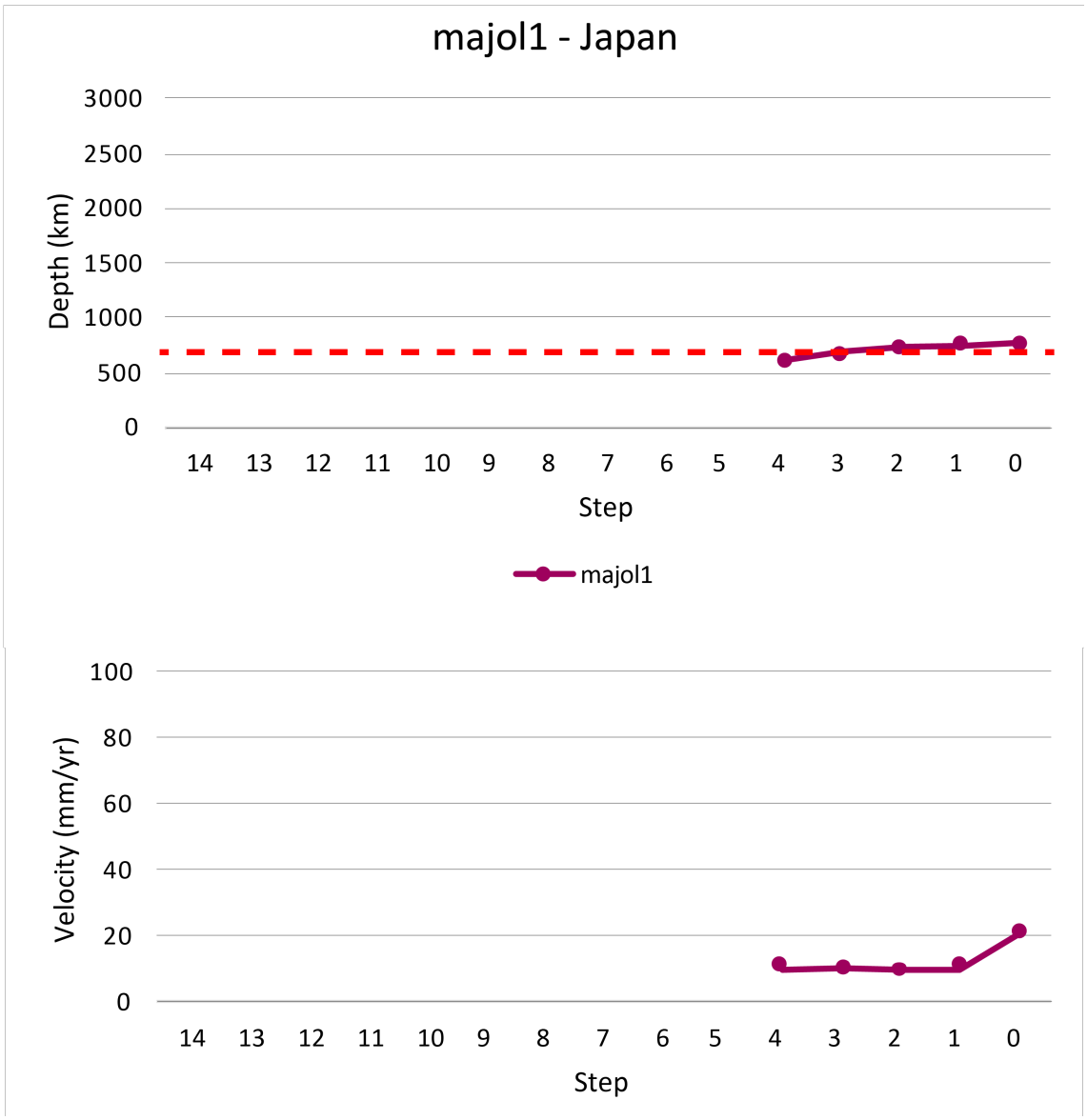

Figure 4.40 – Depth (upper panel) and velocity (lower panel) data for the Japanese slab of model *majol1*. Looking at the depth evolution of the young Japanese slab (upper panel), at 40 Myr it has a depth of about 550 km, whereas it is constant around the 670 discontinuity between 30 and 10 Myr, reaching 730 km depth at 0 Myr. The minimum velocity for this slab (lower panel) is 10 mm/yr, constant 40 to 10 Myr and its maximum is 20 mm/yr at 0 Myr.

4.5.10 Model *majol2*

Figure 4.41 shows the step 0 of the model *majol2*. In this model the evolution of plate motion velocity (from 140 to 0 Myr) in a shallow hotspot reference frame (Table 4.1) is applied as boundary conditions, for a total runtime of 140 Myr arbitrarily divided into 14 Steps of 10 Myr each. **South America (Figure 4.41, upper panel):** model *majol2* shows a lithosphere that is about 100 km thick at the western boundary of the quarter annulus. It thickens towards the east, right westward of the South American coastlines where the wedge in front of the South American slab reaches a depth of ~410 km.

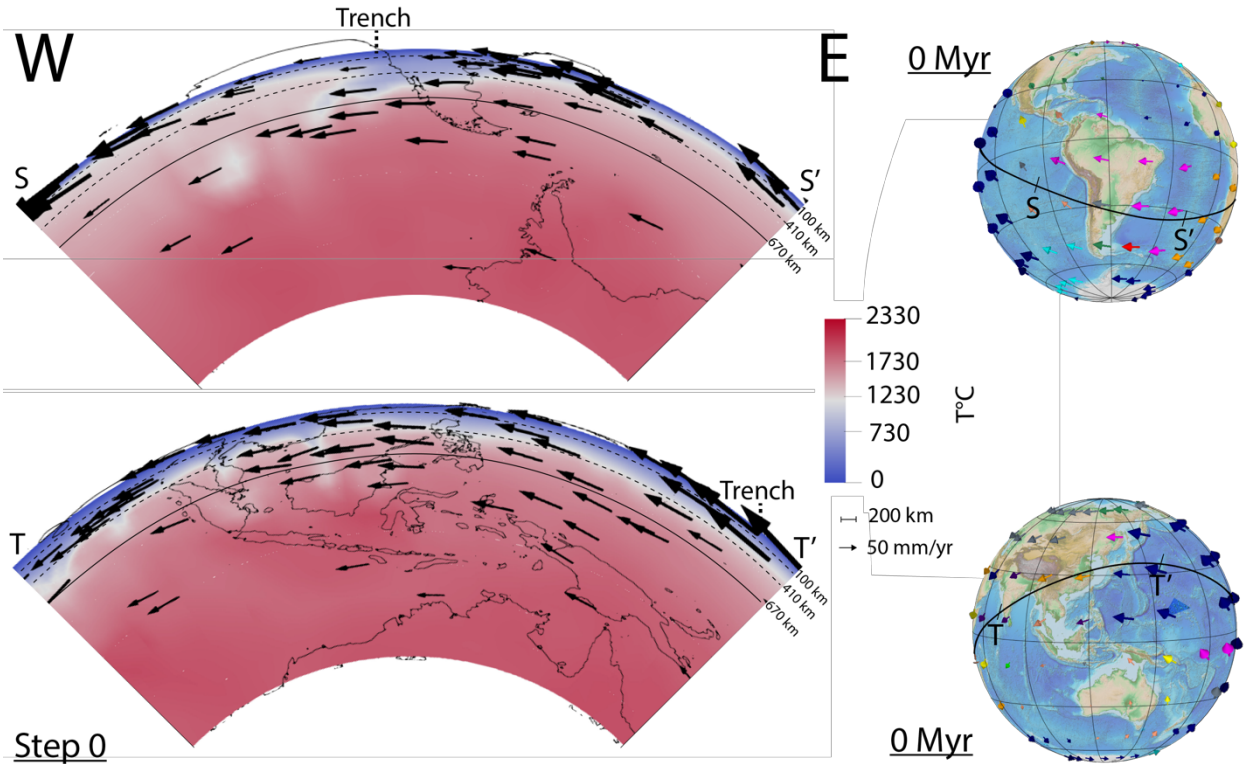

Figure 4.41 - Step 14 relative to model *majol2*. In the upper panel (South America) the model shows a lithosphere that is about 100 km thick at the western boundary of the quarter annulus. It thickens towards the east, right westward of the South American coastlines, where the wedge in front of the South American slab reaches a depth of ~410 km. Right eastward, the slab is about 700 km depth, whereas a segment of it, detached and localized slightly westward, reaches 900 km depth. Velocity vectors have a westward direction for all the plate surfaces. Pacific and South America plates show comparable velocities, higher with respect to the Nazca plate that has shorter velocity vectors. The lower panel shows the Pacific area where, from the westernmost side of the numerical domain, the lithosphere has a uniform depth of ~400 km. This side of the quarter annulus shows a delaminated lithosphere. More nails of lithosphere enters the mantle form the Indian ocean to the Eurasian plate. They start all from about the 410 km discontinuity and they stop at the 670 km discontinuity, except for a slab below the Eurasian plate, which penetrate the 670 km discontinuity, reaching almost 900 km depth. Under Japan the lithosphere is about 410 km thick but no slabs are observable. Velocity vectors on the lithosphere surface follow a global westward direction. Vectors of the Indo-Australian plate lithosphere are shorter if compared to Eurasian vectors, whereas they further increase in length for Pacific plates. Globes in the right part of this figure show surface plate kinematics in a shallow hotspot reference frame at this stage, with the black line suggesting the position of the tectonic equator, along which the 2d slice of this model is cut. Profiles S-S' and T-T' show the lateral extension and geographical location of the quarter annulus surface. The dashed Trench line points to where the subduction trench should be.

Towards the east the slab is about 750 km depth, whereas a segment of an old slab is located slightly westward, reaching 900 km depth. In correspondence of the eastern boundary of the numerical domain the lithosphere has a thickness of ~150 km. Velocity vectors have a westward direction for all the plate surfaces. Pacific and South America plates show comparable velocities, higher with respect to the Nazca plate that has shorter velocity vectors. Vectors within the subducting slab are of the same length if compared with vectors of the South American plate, pointing to a westward subduction direction. Velocity vectors are shorter within the mantle and rise towards the East Pacific Rise and the Pacific plate, showing a vigorous circulation within the upper mantle. Velocities decrease further at depth, however the circulation seem to be consistent also for the lower mantle. The temperature is of about 1300°C at the bottom of the lithosphere along the entire spherical annulus and 0°C at its top. At the CMB the temperature is of about 2300°C. The temperature gradually

increases within the mantle. **Pacific (Figure 4.41, lower panel):** from the westernmost side of the numerical domain, shows a uniform depth of the lithosphere of ~400 km. This side of the quarter annulus shows a delaminated lithosphere. More nails of lithosphere enters the mantle from the Indian ocean to the Eurasian plate. They start all from about the 410 km discontinuity and stop at the 670 km discontinuity, except for a slab below the Eurasian plate which penetrates the 670 km discontinuity, reaching almost 900 km depth. However they all contribute to cool down the upper mantle temperature in this region. Under Japan, in correspondence of the Pacific plate, the lithosphere is about 410 km thick but no slabs are observable. Velocity vectors on the lithosphere surface here follow a global westward direction. Vectors of the Indo-Australian plate lithosphere are shorter if compared to Eurasian vectors, whereas vectors further increase in length for the Pacific plate. They slightly decrease at depth within the mantle, maintaining, however, a consistent value. This produces a circulation into the mantle, with the same direction of the lithosphere but with a minor intensity with respect to it. However velocities within the mantle are slower below the Indo-Australian plates and higher below the Pacific plate. Temperature of the lithosphere is 0°C at its top and reaches ~1300°C at its bottom. The bottom of the domain has a temperature of about 2300°C. Within the mantle the temperature increases from the top to the bottom.

In Figures 4.42 and 4.43, depth (upper panel) and velocity (lower panel) evolution for the South American and Japanese slabs are respectively shown. The South American slab evolution (Figure 4.42, upper panel) starts at a depth of about 500 km at 50 Myr from the end of the model run. This slab slowly deepens through the last steps of the model run, reaching about 750 km depth, kept constant for the last 10 Myr of the model evolution.

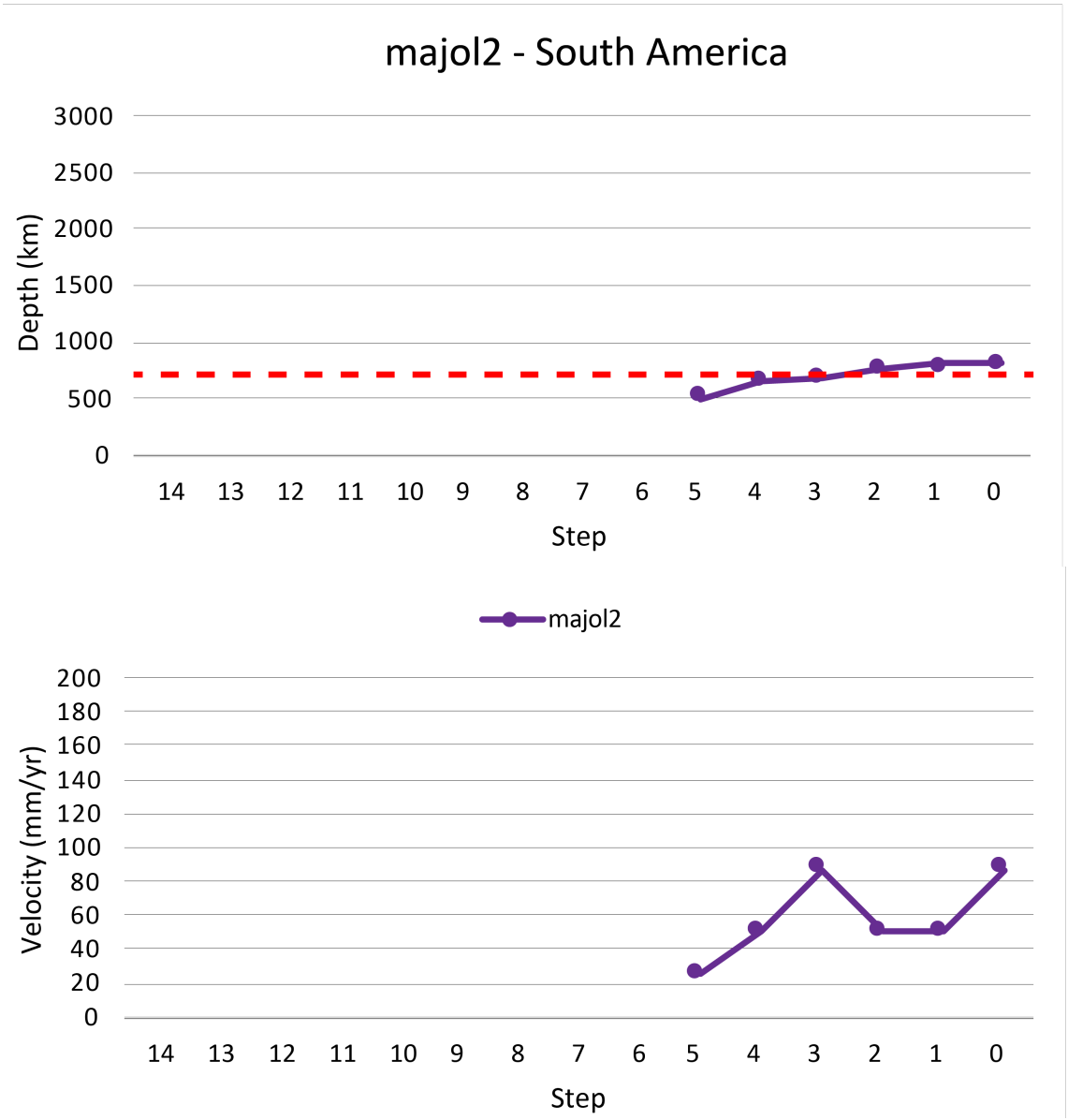

Figure 4.42 – Depth (upper panel) and velocity (lower panel) data for the South American slab of model *majol2*. In the upper panel the South American slab evolution starts at a depth of about 500 km at 50 Myr from the end of the model run. This slab slowly deepen through the last steps of the model run, reaching about 750 km depth, kept constant for the last 10 Myr of the model evolution. Velocities for the South American slab (lower panel) show a maximum value of about 90 mm/yr at 30 and 0 Myr, whereas they show the minimum value of about 25 mm/yr at 50 Myr.

The South American slab tip (Figure 4.42, lower panel) shows an initial velocity of about 25 mm/yr at 50 Myr. This velocity increases up to ~85 mm/yr at 30 Myr. Then it is stable at 30 mm/yr between 20 and 10 Myr, increasing again at ~85 mm/yr at the last stage, i.e., 0 Myr. The evolution of the lithosphere thickening below Japan (Figure 4.43, upper panel) is younger and starts at about 10 Myr and at a depth of ~200 km. The thickness of the lithosphere increases up to ~410 km at the current plate motion stage (0 Myr). The lithosphere velocity evolution (Figure 4.43, lower panel) starts at the same 10 Myr time, with a velocity of ~50 mm/yr and ends with a velocity of ~110 mm/yr.

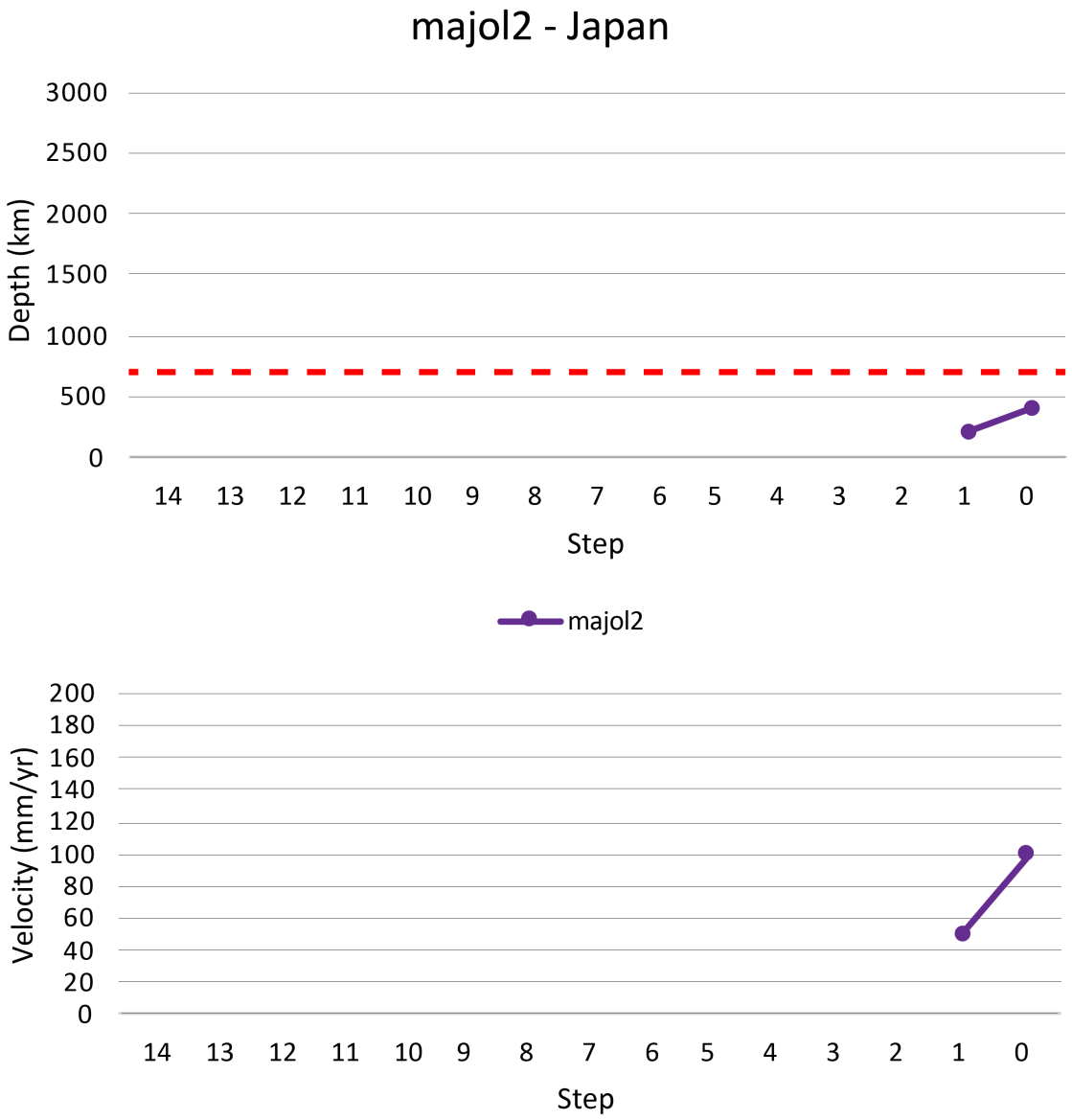

Figure 4.43 – Depth (upper panel) and velocity (lower panel) data for the Japanese lithosphere of model *majol2*. The evolution of the lithosphere thickening below Japan (upper panel) is younger and starts at about 10 Myr and at a depth of ~200 km. The thickness of the lithosphere increases up to ~410 km at the current plate motion stage (0 Myr). The lithosphere velocity evolution (lower panel) starts at the same 10 Myr time, with a velocity of ~50 mm/yr and ends with a velocity of ~110 mm/yr, which correspond thus to maximum and minimum values.

4.5.11 Model *majfo89_1*

In Figure 4.44 the thermal initial stage of the entire spherical domain for models using the majorite-Fo89 (Bina, 1998; Mitra, 2004; Raye et al., 2011), the last rheological profile, is shown. This initial stage is valid for models presented in this subsection, i.e., models *majfo89_1* and *majfo89_2*, since they were carried out using the same ASCII Reference Profile model.

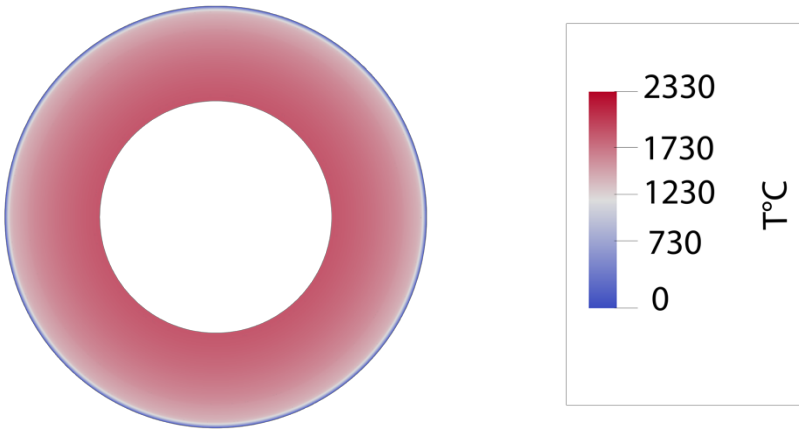

Figure 4.44 – Initial thermal stage for models *majfo89_1* and *majfo89_2*. This is the thermal state at the initial stage. One thermal boundary layer can be seen at the top of the domain, corresponding to the minimum (i.e., the lithosphere) temperature. The temperature is expressed in C°.

For this rheological profile the lithosphere (in blue) is 100 km thick along the entire spherical shell and a single thermal boundary layer can be seen at the top of the spherical domain, corresponding to the minimum (i.e., the surface at 0°C) temperature.

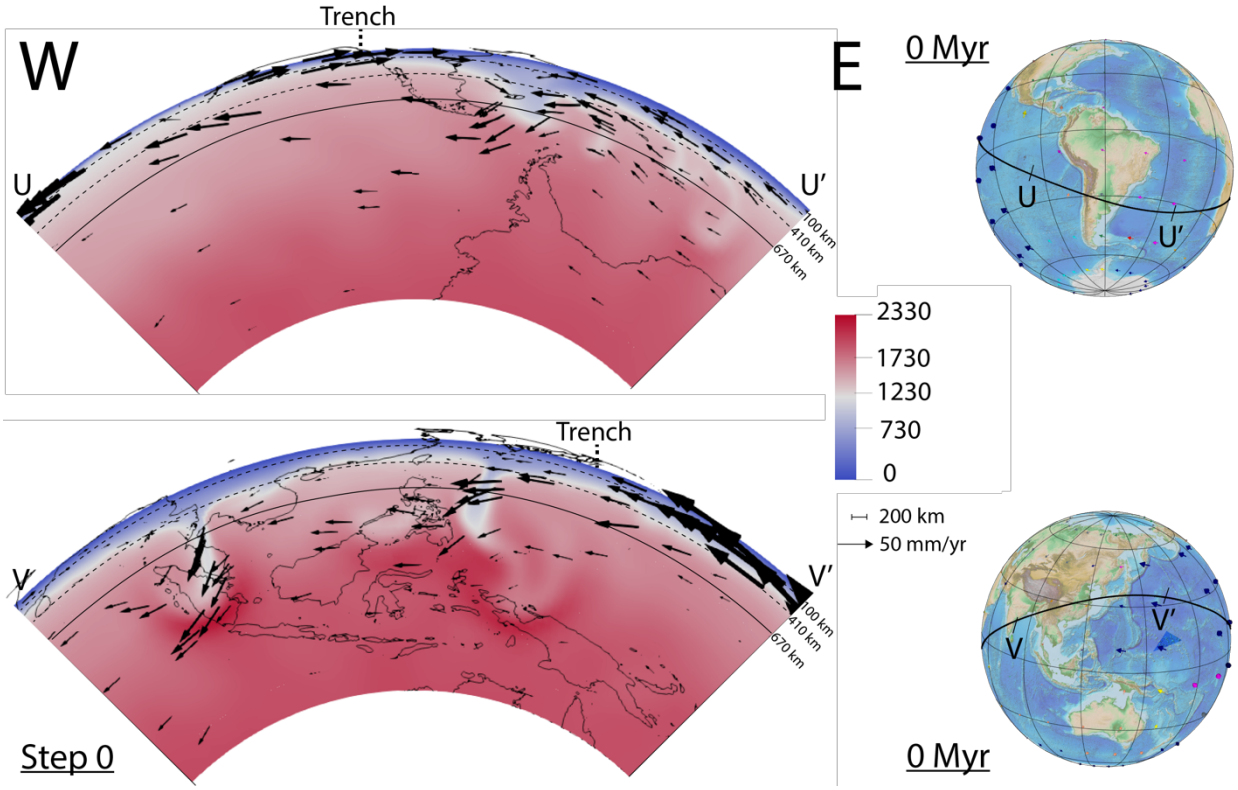

Figure 4.45 - Step 0 relative to model *majfo89_1.* In the upper panel, the Pacific lithosphere at the western boundary of the numerical domain is about 100 km thick. It thickens towards the east. Eastward of the South American coastlines a slab that is about 750 km depth can be observed. It is rather wide and, right eastward, a thick wedge zone reaching a depth of about 410 km can be seen. Towards the East the lithosphere is homogeneously ~400 km thick until almost the end of the spherical annulus. At this point it becomes thinner, reaching the undeformed initial condition of 100 km of thickness. Velocity vectors show a westward direction of the Pacific plate, at the westward boundary of the domain, whereas the Nazca plate has an eastward direction of motion, with a higher velocity with respect to the South American plate, which has a westward slower motion of its surface. The lithosphere in the Pacific area (lower panel) is 100 km thick at the beginning of the spherical annulus, then suddenly starts to increase in thickness, reaching ~410 km right westward

of the slab subducting below the Indonesian subduction zone. Here the slab reaches about 1450 km depth, whereas the lithosphere has a thickness of ~410 km towards the east, reaching the Japanese area and the Japanese slab. This slab reaches below Japan ~1220 km depth, but a hotter and almost faded segment can be seen prosecuting after its end. Eastward with respect to the slab the lithosphere maintain a thickness of about 410 km until the end of the spherical annulus. Velocity vectors on the lithosphere surface are very small for the Indo-Australian and Eurasian plates, whereas they are slightly higher in correspondence of the the Pacific plate. Globes in the right part of this figure show surface plate kinematics in a deep hotspot reference frame at this stage, with the black line suggesting the position of the tectonic equator, along which the 2d slice of this model is cut. Profiles U-U' and V-V' show the lateral extension and geographical position of the correspondent quarter annulus surface. The location of where the subduction trench should be is pointed by the dashed Trench line.

Figure 4.45 shows the step 0 of the model *majfo89_1*. In this model the evolution of plate motion velocity (from 140 to 0 Myr) in a deep hotspot reference frame (data about angular vectors collected by Seton et al., 2012) is applied as boundary conditions, for a total runtime of 140 Myr corresponding to 14 Steps of 10 Myr each, defined arbitrarily. **South America (Figure 4.45, upper panel):** in model *majfo89_1* the lithosphere at the western boundary of the numerical domain is about 100 km thick. It thickens towards the east. Eastward of the South American coastlines, a slab that is about 800 km depth can be observed. It is rather wide and, right eastward, a thick wedge zone reaching a depth of about 410 km can be seen. Towards the East the lithosphere is homogeneously ~400 km thick until almost the end of the spherical annulus, point at which it becomes thinner reaching the undeformed initial condition of 100 km of thickness. Velocity vectors show a westward direction of the Pacific plate, at the westward boundary of the domain, whereas the Nazca plate has an eastward direction of motion with a higher velocity with respect to the South American plate, which has a westward slower motion of its surface. This points to an eastward direction of the subducting lithosphere. Furthermore, velocity vectors behind the slab show a counterflow with an upwelling of mantle material towards the Pacific plate and the East Pacific Rise. The circulation is rather active in the upper mantle, with velocity vectors almost comparable with the surface vectors, especially along the subducting slab and towards the upwelling location. However, within the lower mantle, at depth, velocity vectors become shorter. Temperature of the lithosphere is 0°C at its top and reaches ~1300°C at its bottom. The bottom of the domain has a temperature of about 2300°C and the temperature increases from the top to the CMB. **Pacific (Figure 4.45, lower panel):** the lithosphere in this model is 100 km thick at the beginning of the spherical annulus, then suddenly starts to increase in thickness, reaching ~410 km right westward of the slab subducting below the Indonesian subduction zone. Here the slab reaches about 1450 km depth, whereas the lithosphere has a thickness of ~410 km towards the east, reaching the Japanese area and the Japanese slab. This slab reaches below Japan ~1220 km depth but a hotter and almost faded segment can be seen prosecuting after its end. Eastward with respect to the slab the lithosphere maintain a thickness of about 410 km until the end of the spherical annulus. Velocity vectors on the lithosphere surface are very small for the Indo-Australian and Eurasian plates whereas they are slightly higher in correspondence of the Pacific plate. This points to a subduction direction

that goes from E to W for both the observable slabs in Figure 4.45 (lower panel). Velocity vectors decrease towards the bottom of the model domain, but they are higher along both the subducting slabs: this seems to enhance a weak westward circulation into the lower mantle.

Figures 4.46 and 4.47 show depth (upper panel) and velocity (lower panel) evolution for the South American and Japanese slab in Figure 4.45. The depth evolution (Figure 4.46, upper panel) for the South American slab starts at about 30 Myr, at a depth of about 450 km. Its depth slowly increases up to the 670 km discontinuity at 10 Myr, then it deepens abruptly at 0 Myr, reaching ~800 km depth. Velocity evolution (Figure 4.46, lower panel) for this slab starts at 30 Myr with a velocity of 10 mm/yr. Between 20 and 10 Myr the slab tip velocity is constant at 20 mm/yr, increasing to 30 mm/yr at 0 Myr. For the Japanese slab the depth evolution (Figure 4.47, upper panel) starts at 60 Myr and at a depth of ~800 km. Its depth increases constantly up to about 1800 km, depth that is kept constant for 20 and 10 Myr. At 0 Myr its depth is instead shallower, reaching 2200 km. Velocity evolution (Figure 4.47, lower panel) for this slab starts at 60 Myr with a velocity of about 30 mm/yr that increases up to 50 mm/yr at 50 Myr. The velocity of the slab tip then decreases down to 0 mm/yr at 10 Myr. At 0 Myr it has a value of 30 mm/yr.

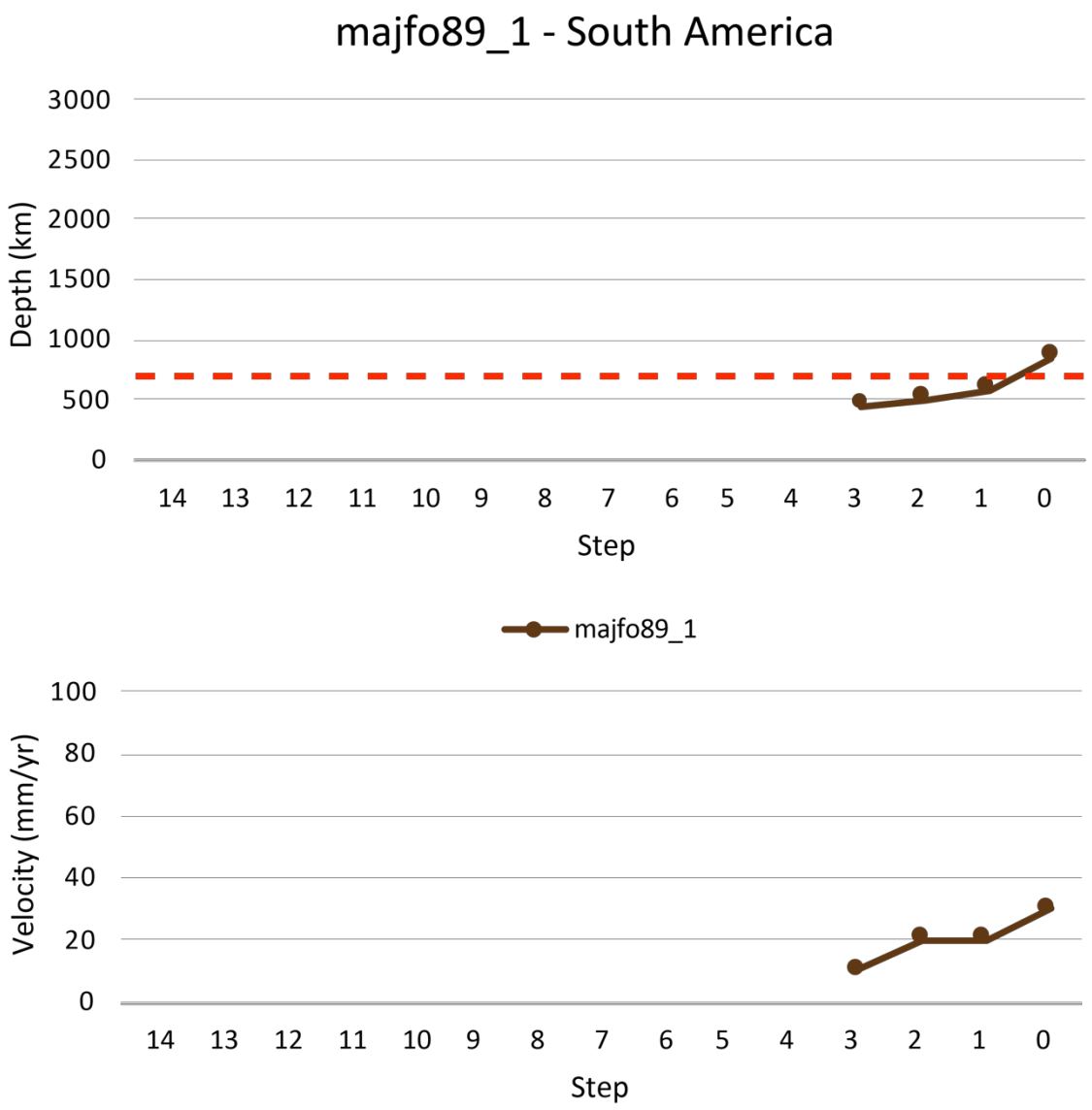

Figure 4.46 – Depth (upper panel) and velocity (lower panel) data for the South American slab of model *majfo89_1*. The depth evolution (upper panel) for the South American slab starts at about 30 Myr, at a depth of about 450 km. Its depth slowly increases up to the 670 km discontinuity, at 10 Myr, the it deepens abruptly at 0 Myr, reaching ~800 km depth. Velocity evolution (lower panel) for this slab starts at 30 Myr, with a velocity of 10 mm/yr. Between 20 and 10 Myr the slab tip velocity is constant at 20 mm/yr, increasing to 30 mm/yr at 0 Myr.

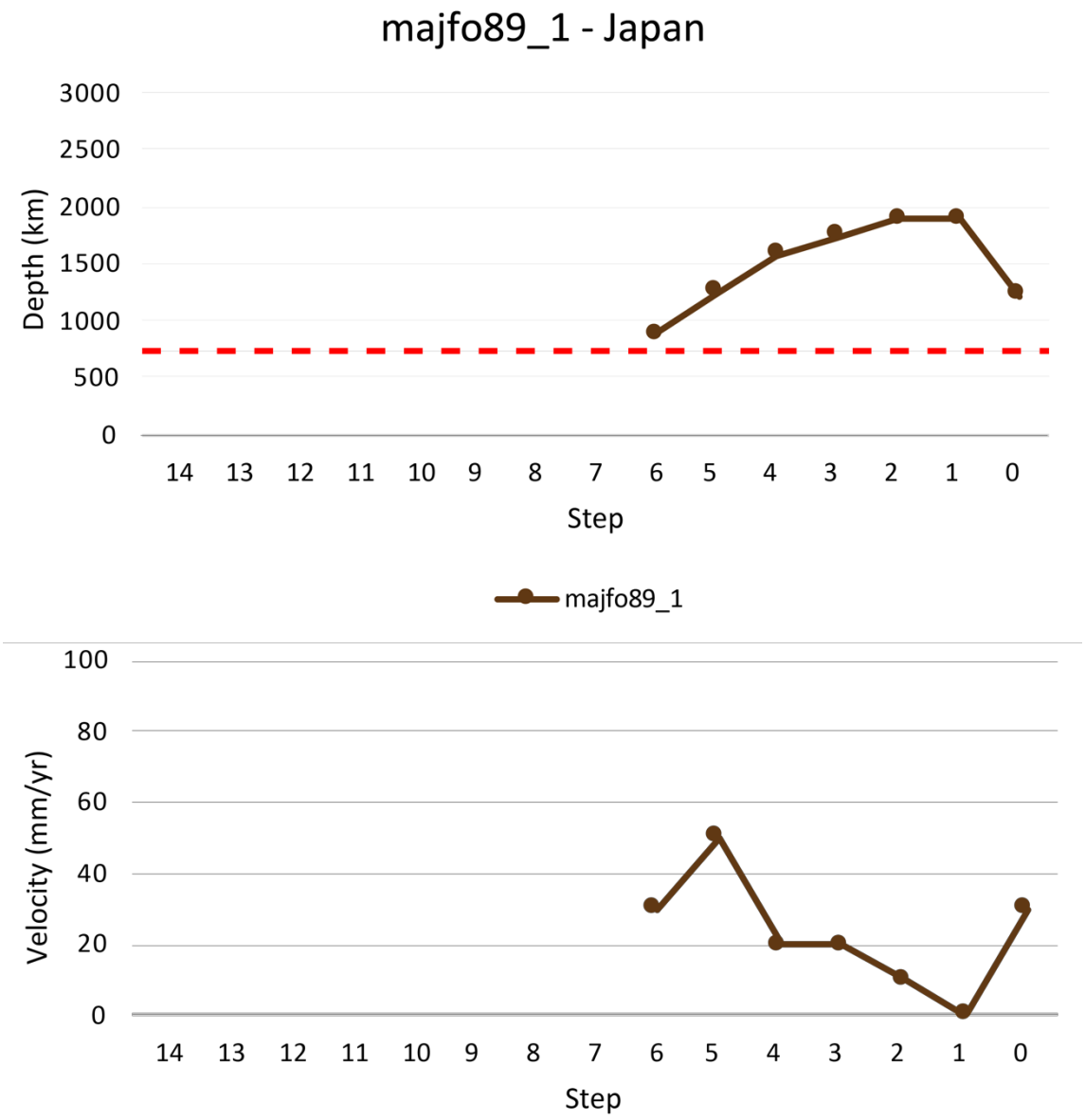

Figure 4.47 – Depth (upper panel) and velocity (lower panel) data for the Japanese slab of model *majfo89_1*. For the Japanese slab, the depth evolution (upper panel) starts at 60 Myr and at a depth of ~800 km. Its depth increases constantly up to about 1800 km, depth that is kept for 20 and 10 Myr. At 0 Myr, its depth is instead shallower, reaching 2200 km. Velocity evolution for this slab has a maximum peak of the velocity value of 50 mm/yr at 50 Myr, whereas it has a minimum peak of 0 mm/yr at 10 Myr.

4.5.12 Model *majfo89_2*

Figure 4.48 shows the step 0 of the model *majfo89_2*. In this model the evolution of plate motion velocity (from 140 to 0 Myr) in a shallow hotspot reference frame (Table 4.1) is applied as boundary conditions, for a total runtime of 140 Myr corresponding to 14 arbitrary defined Steps of 10 Myr each.

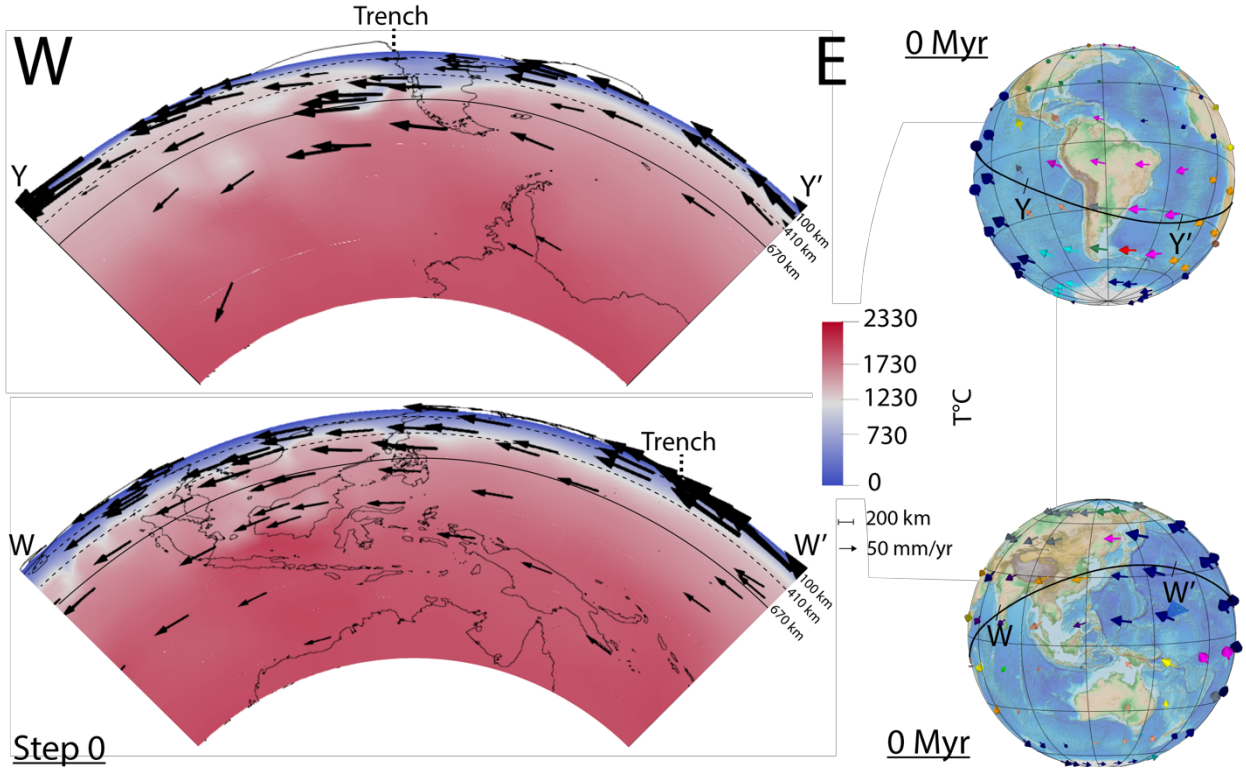

Figure 4.48 - Step 0 relative to model *majfo89_2*. In the upper panel model majfo89_2 shows a lithosphere that is about 100 km thick at the western boundary of the quarter annulus. It thickens towards the east, right westward of the South American coastlines, where the wedge in front of the South American slab reaches a depth of ~410 km. Here, the slab is about 730 km depth. In correspondence of the eastern boundary of the numerical domain the lithosphere has a thickness of ~150 km. Velocity vectors have a westward direction for all the plate surfaces. Pacific and South America plates show comparable velocities, higher with respect to the Nazca plate that has shorter velocity vectors. The Pacific area (lower panel) from the westernmost side of the numerical domain shows a uniform depth of the lithosphere of ~410 km. This side of the quarter annulus shows more nails of lithosphere that enters the mantle below the Indo-Australian and Eurasian plates. They start all from about the 410 km discontinuity and stop at about 500 km depth, exceeding the 670 km discontinuity only in correspondence of an old faded slab below Eurasia, which penetrate the 670 km discontinuity, reaching almost 1160 km depth. However, they all contribute to cool down the upper mantle temperature in this region. Under Japan the lithosphere is about 410 km thick, but no slabs are observable. Velocity vectors on the lithosphere surface follow a global westward direction. Velocities of the Indo-Australian plate lithosphere are high and velocity vectors are of the same length with respect to the Eurasia and they increase in length within the Pacific plates. Globes in the right part of this figure show surface plate kinematics in a shallow hotspot reference frame at this stage, with the black line suggesting the position of the tectonic equator, along which the 2d slice of this model is cut. In profiles Y-Y' and W-W' the lateral extension and geographical location of the correspondent quarter annulus surface are shown. The dashed Trench line represents where the subduction trench should be.

South America (Figure 4.48, upper panel): here the lithosphere is about 100 km thick at the western boundary of the quarter annulus. It thickens towards the east, right westward of the South American coastlines, where the wedge in front of the South American slab reaches a depth of ~410 km. Here the slab is about 730 km depth. In correspondence of the eastern boundary of the numerical domain the lithosphere has a thickness of ~150 km. Velocity vectors have a westward direction for all the plate surfaces. Pacific and South America plates show comparable velocities, higher with respect to the Nazca plate that has shorter velocity vectors. Vectors within the subducting slab are of the same length if compared with vectors of the South American plate, pointing to a westward subduction direction. Velocity vectors are shorter within the mantle and rise towards the East Pacific Rise and the Pacific plate, showing a consistent circulation within the upper mantle. Velocities decrease further at depth, however the circulation seem to be consistent in the upper part of the lower mantle. The

temperature is of about 1300°C at the bottom of the lithosphere, along the entire spherical annulus, and 0°C at its top. At the CMB the temperature is of about 2300°C. Temperature gradually increases within the mantle. **Pacific (Figure 4.48, lower panel):** the Pacific area from the westernmost side of the numerical domain, shows a uniform depth of the lithosphere of ~410 km. This side of the quarter annulus shows more nails of lithosphere that enters the mantle below the Indo-Australian and Eurasian plates. They start all from about the 410 km discontinuity and stop at about 500 km depth, exceeding the 670 km discontinuity only in correspondence of an old faded slab below the Eurasian plate, which penetrate the 670 km discontinuity reaching almost 1160 km depth. However, they all contribute to cool down the upper mantle temperature in this region. Under Japan the lithosphere is about 410 km thick, but no slabs are observable.

Velocity vectors on the lithosphere surface follow a global westward direction. Velocities of the Indo-Australian plate lithosphere are high and velocity vectors are of the same length with respect to Eurasia, whereas they further increase in length within the Pacific plates. Velocity vectors slightly decrease at depth, within the mantle, maintaining a consistent value. This produces a circulation into the mantle which has the same direction of the lithosphere but with a minor intensity with respect to it. Temperature of the lithosphere is 0°C at its top and reaches ~1300°C at its bottom. The bottom of the domain has a temperature of about 2300°C. Within the mantle, the temperature increases from the top to the bottom.

In Figures 4.49 and 4.50, depth (upper panel) and velocity (lower panel) evolution for the South American and Japanese slabs, respectively, are shown. The South American slab depth evolution (Figure 4.49, upper panel) starts at a depth of about 200 km. Its depth increases up to ~1390 km at 60 Myr. After this timestep, the active tip of the subducting slab becomes shallower reaching a depth of about 520 km.

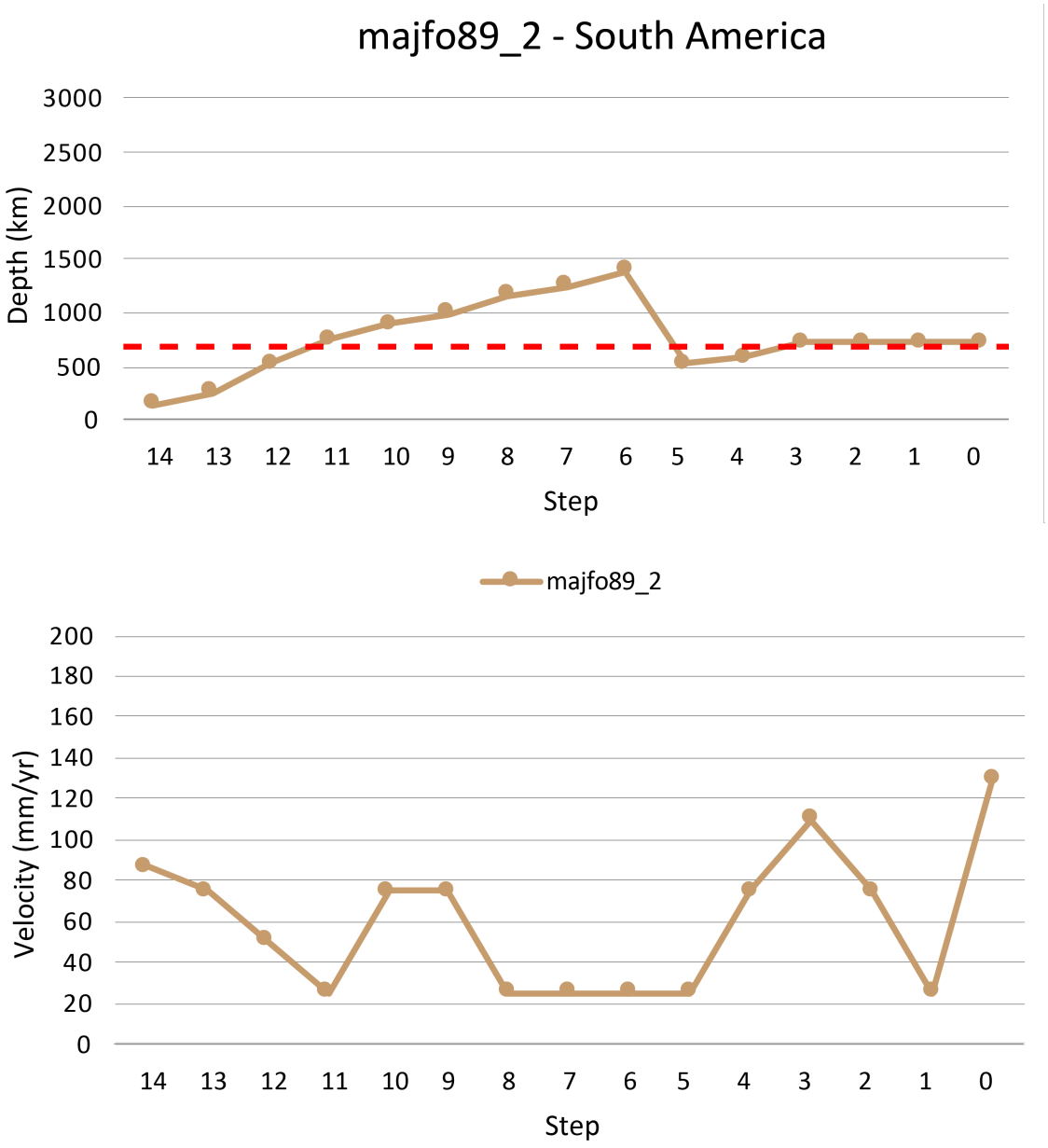

Figure 4.49 – Depth (upper panel) and velocity (lower panel) data for the South American slab of model *majfo89_2.* The South American (upper panel) slab depth evolution starts at a depth of about 200 km. Its depth increases up to ~1390 km at 60 Myr. After this timestep, the active tip of the subducting slab becomes shallower, at a depth of about 520 km. At 40 Myr, the slab reaches 580 km depth, whereas it is 730 km depth during the last 30 Myr of the model run, between 30 and 0 Myr. Velocity evolution of this slab (lower panel) has its minimum value at about 25 mm/yr, reached at 110, 80-50 and 10 Myr, whereas its maximum peak is at 0 Myr, where the slab tip reaches a velocity of about 130 mm/yr.

At 40 Myr the slab reaches 580 km depth, whereas it is 730 km depth during the last 30 Myr of the model run, between 30 and 0 Myr. Velocity evolution of this slab (Figure 4.49, lower panel) starts at about 90 mm/yr at 140 Myr. This value decreases down to 25 mm/yr at 110 Myr and increases again up to 75 mm/yr during the 10 Myr between 100 and 90 Myr. Then the velocity of the slab tip goes back to ~25 mm/yr and this value is kept constant during the 30 Myr between 80 and 50 Myr. Then it rises up to 110 mm/yr at 30 Myr, decreasing again to 25 mm/yr, at 10 Myr. The last 10 Myr of the model run are characterized by an increasing velocity, reaching a value of about 130 mm/yr at 0 Myr.

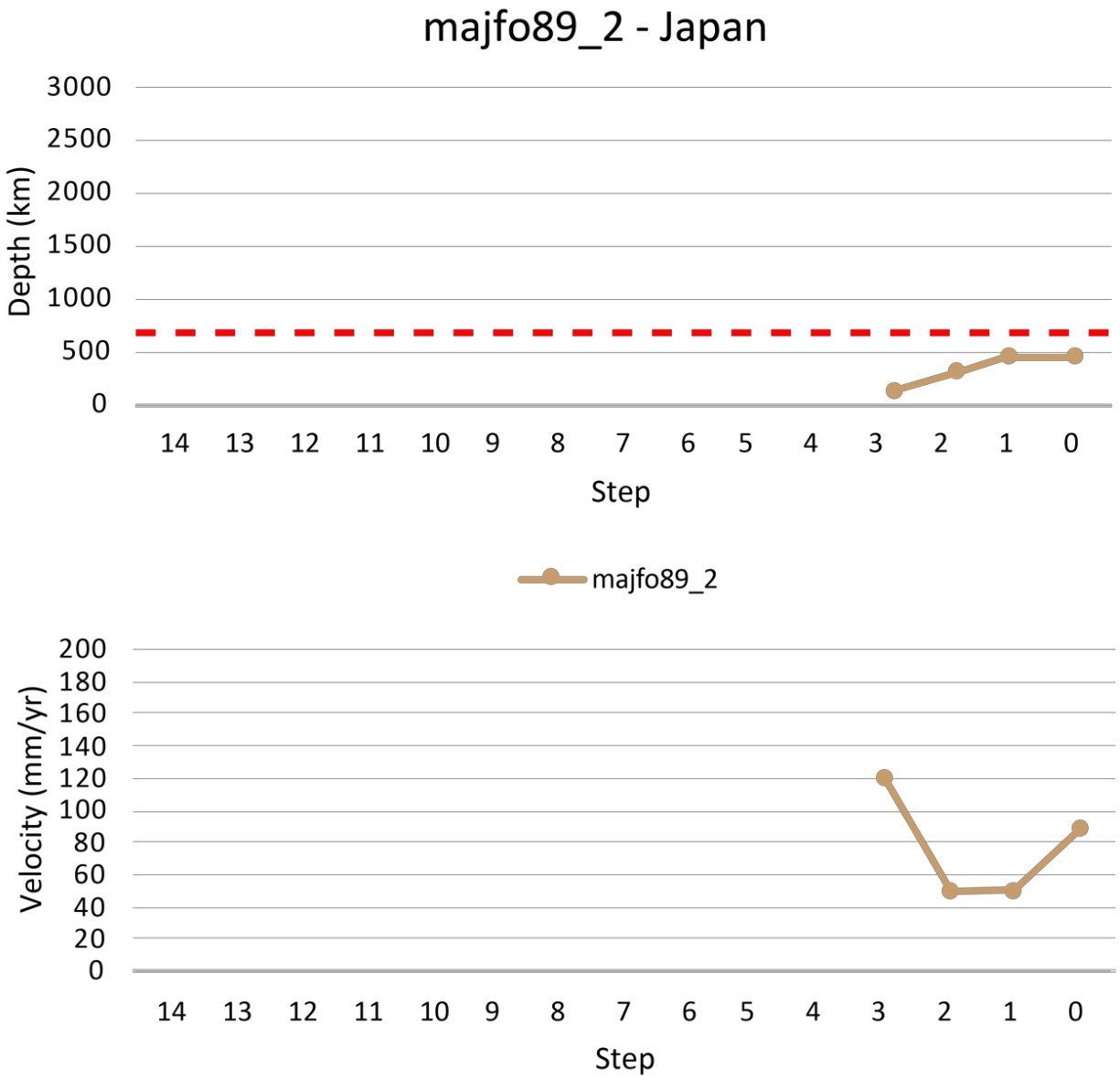

Figure 4.50 – Depth (upper panel) and velocity (lower panel) data for the Japanese lithosphere of model *majfo89_2*. The depth evolution (upper panel) for this part of lithosphere starts at 30 Myr, with a thickness of about 200 km. It reaches the maximum depth of ~490 km, that is maintained at 0 Myr. Evolution for velocities of the lithosphere (lower panel) in this area has its maximum value at 30 Myr, when it reaches ~120 mm/yr, whereas its minimum peak is reached between 20 and 10 Myr, at about 50 mm/yr.

In Figure 4.50 the depth (upper panel) and velocity (lower panel) evolution through time for the Japanese lithosphere in Figure 4.48 is shown. The depth evolution (Figure 4.50, upper panel) for this part of lithosphere starts at 30 Myr, with a thickness of about 200 km. It reaches the maximum depth of ~490 km, that is maintained at 0 Myr. Evolution for velocities (Figure 4.50, lower panel) of the lithosphere in this area starts at 30 Myr, at a value of about 120 mm/yr. It then decreases at 50 mm/yr, between 20 and 10 mm/yr, increasing again at 0 Myr, having a value of about 90 mm/yr.

4.6 2d results in relative reference frames

In this section two models in relative reference frames will be shown. In particular, model *majol_sa* and *majol_ma* (Figure 4.51) were realized using the majorite-Fo50 rheological profile (Boneh et al., 2017; Griffin et al., 2009; Nekvasil et al., 2004; see Figure 4.37 for the initial thermal setup). These models were carried out applying the current plate motion velocities for 140 Myr. However, since these boundary conditions are rather constrained and to allow a better comparison with numerical models previously showed in this thesis which are realized using an upper fixed plate reference frame, these models will be shown at a timestep of 70 Myr. This was the most reasonable compromise between subduction zones dynamics in the ASPECT's models, due to the rheological profile, and duration of the model run. These models has been carried out on 2d slices corresponding to a slightly modified tectonic equator which has its rotation pole coordinates at longitude 100°E and latitude 65°S. Its coordinates were slightly modified to cross the two subduction zones whose upper plate was taken as reference frame.

Furthermore, although a model using the majorite-Fo89 rheological profile (Bina, 1998; Mitra, 2004; Raye et al., 2011) was realized, it will not be shown in this section. It presents localization problems of the subducting slab due to the combination between the long-term applied velocity to the lower plate and the low resistance of the upper plate. However, it will be shown in the Appendix B (Appendix B, Figure B.61).

Figure 4.51 (upper panel) shows the step 7 of the model *majol_sa*. In this model the current plate motion velocities with respect to fixed South America were applied as boundary conditions, for a total runtime of 70 Myr corresponding to 7 steps of 10 Myr each that were arbitrarily defined.

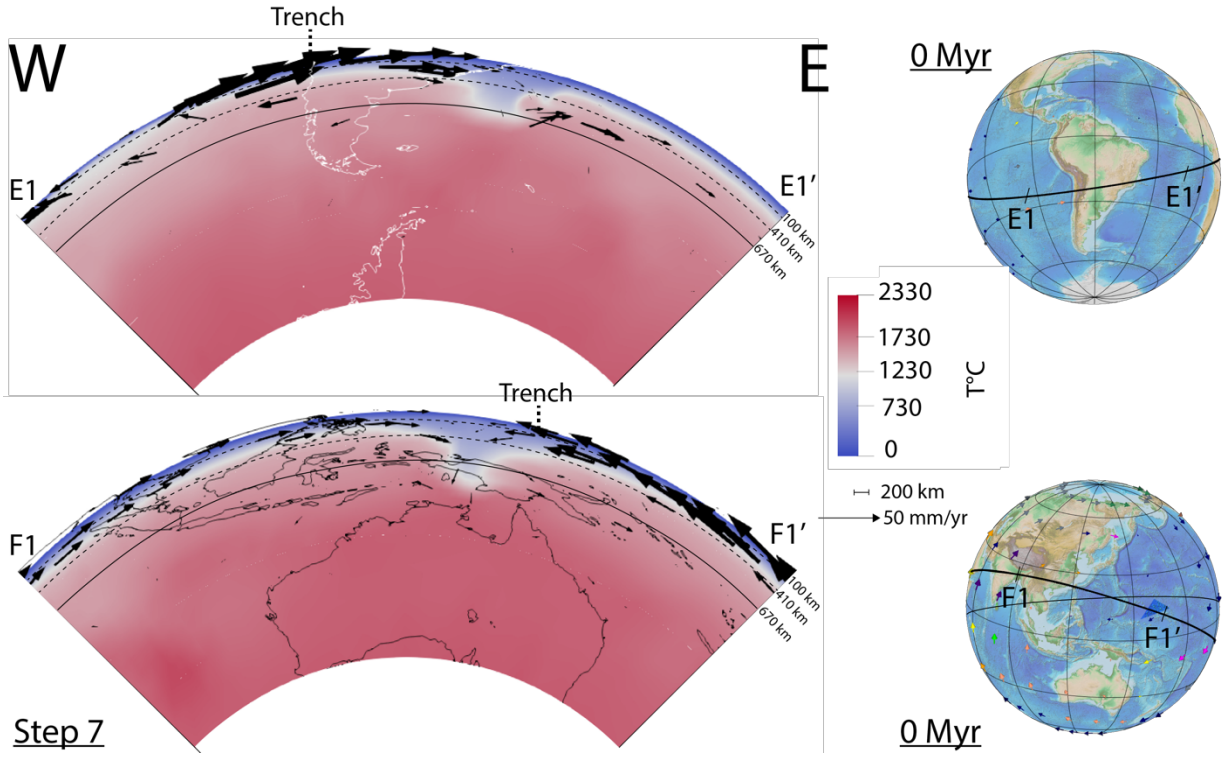

Figure 4.51 - Step 7 relative to model *majol_sa* (upper panel) and model *majol_ja* (lower panel). In model *majol_sa* (upper panel), the lithosphere at the western boundary of the numerical domain is about 100 km thick. Right eastward with respect to the South American coastlines a lithospheric slab can be observed with a maximum depth of about 750 km. Velocity vectors show a westward direction of the Pacific plate, at the western boundary of the domain, whereas they become consistently faster and with an eastward direction of motion in correspondence of the Nazca plate. The South American plate is fixed. In model *majol_ma* (lower panel), the lithosphere at the western boundary of the numerical domain is about 300 km thick. This depth is constant until the Marianas region, towards the east, where a lithospheric slab can be observed with a maximum depth of about 1020 km. It has a regular shape within the mantle. From the Marianas slab the lithosphere thickness goes back to ~350 km depth. Velocity vectors show an eastward direction of the Indo-Australian plate, as well as the Eurasian plate. Between this latter and the Pacific plate the fixed Marianas plate can be seen. Globes in the right part of this figure show surface plate kinematics in a South American fixed reference frame (upper panel) and in a Marianas plate fixed reference frame (lower panel) at this stage, with the black line suggesting the position of the modified tectonic equator (which has the rotation pole at coordinates of longitude 100°E and latitude 65°S), along which the 2d slices of the models are cut. Profiles E1-E1' and F1-F1' show the geographical position and the lateral extension of the quarter annulus represented in this figure. The dashed Trench line represents where the subduction trench should be located.

In this model (Figure 4.51, upper panel) the lithosphere at the western boundary of the numerical domain is about 100 km thick. Right eastward with respect to the South American coastlines a lithospheric slab can be observed with a maximum depth of about 750 km. It has a wedge shape, with an irregular top boundary. It ends just on the western boundary of the Atlantic ocean, whereas eastward the lithosphere is ~200 km thick, reaching the easternmost boundary of the quarter annulus. Velocity vectors show a westward direction of the Pacific plate at the westward boundary of the domain, whereas they become consistently faster and with an eastward direction in correspondence of the Nazca plate. The South American plate is fixed. Thus, subduction direction in this case occurs from W to E. Moreover, velocity vectors show an active circulation within the upper mantle having a westward direction, i.e., towards the East Pacific Rise, below the Nazca plate and an eastward direction in front of the subducting slab. No circulation appears to occur within the lower mantle. Temperature of the lithosphere is 0°C at its top and reaches ~1300°C at its bottom. The bottom of the

domain has a temperature of about 2000°C as well as almost all the lower mantle.

Figure 4.51 (lower panel) shows the step 7 of the model *majol_ma*. In this model the current plate motion velocities with respect to fixed Marianas plate were applied as boundary conditions, for a total runtime of 70 Myr corresponding to 7 arbitrarily defined steps of 10 Myr each. Here the lithosphere at the western boundary of the numerical domain is about 300 km thick. This depth is constant until the Marianas region, towards the east, where a lithospheric slab can be observed with a maximum depth of about 1020 km. It has a regular shape within the mantle. From the Marianas slab the lithosphere thickness goes back to ~350 km depth. Velocity vectors show an eastward direction of the Indo-Australian plates, as well as the Eurasian plate. Between this latter and the Pacific plate the fixed Marianas plate can be seen. The Pacific plate has the fastest motion towards the west among all the above described plates. Thus, subduction direction in this case occurs mainly from E to W. No circulation appears to occur within both the upper and lower mantle. Temperature of the lithosphere is 0°C at its top and reaches ~1300°C at its bottom. The bottom of the domain has a temperature of about 2000°C as well as almost all the lower mantle.

In Figures 4.52 and 4.53 depth and velocity evolution for model *majol_sa* and model *majol_ma*, respectively, are shown. Depth evolution for model *majol_sa* (Figure 4.52, upper panel) starts from 70 Myr at a depth of about 100 km. Since the starting runtime for this model the slab depth increases constantly up to 750 km at 0 Myr. Velocity evolution (Figure 4.52, lower panel) starts at a value of 20 mm/yr at 70 Myr, this value decreases down to 10 mm/yr and it is constant between 50 and 10 Myr.

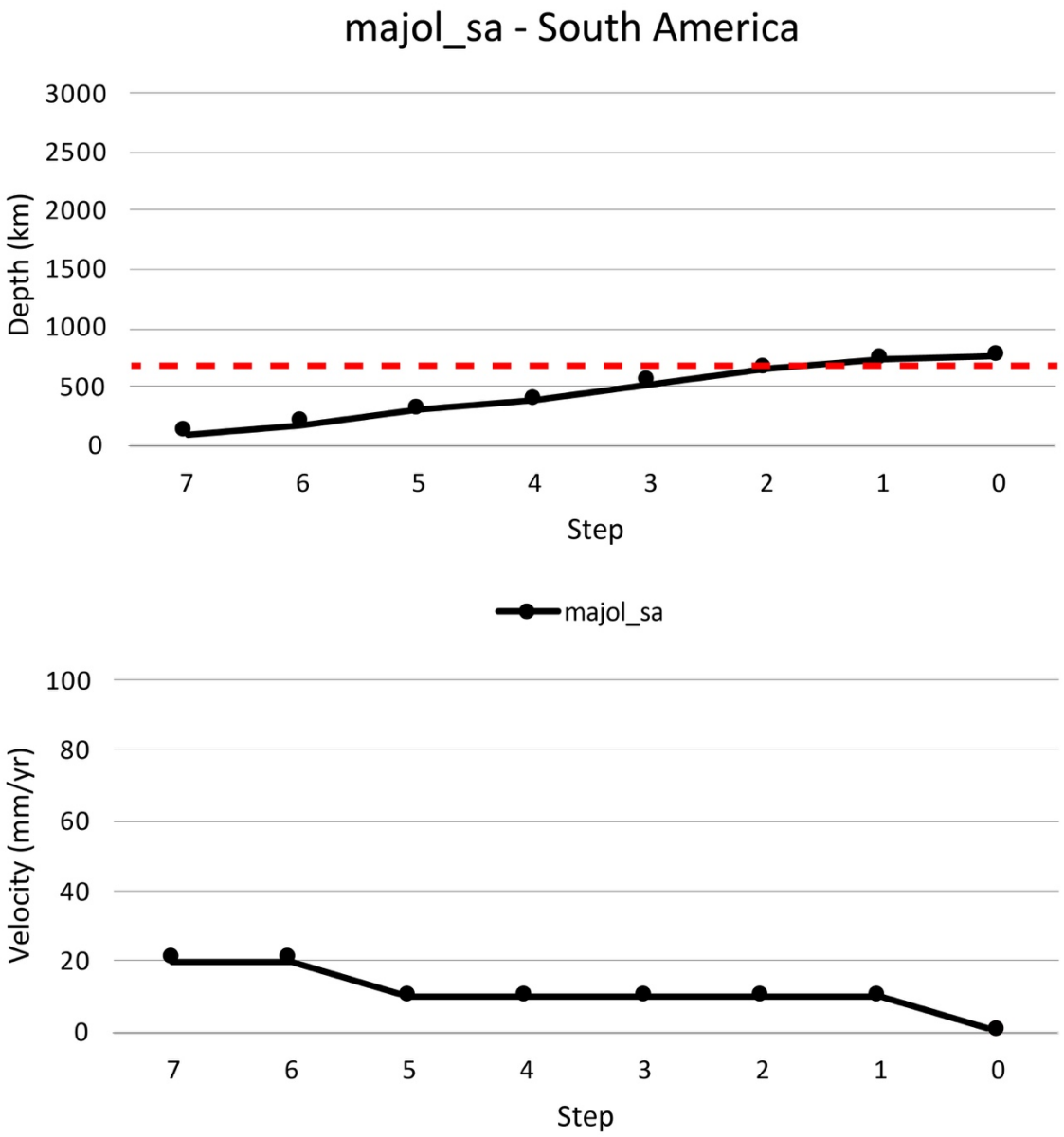

Figure 4.52 – Depth (upper panel) and velocity (lower panel) data for the South American side of model *majol_sa.* The South American slab depth evolution (upper panel) for model *majol_sa* starts from 70 Myr, at a depth of about 100 km. Since the starting runtime for this model the slab depth increases constantly up to 750 km at 0 Myr. Velocity evolution (lower panel) starts at 70 Myr. For this evolution the slab tip has a maximum velocity of about 20 mm/yr at 70 and 60 Myr, whereas its minimum peak is 0 mm/yr at 0 Myr.

At 0 Myr, velocity of the subducting slab is 0 mm/yr. Depth evolution (Figure 4.53, upper panel) for model *majol_ma* starts from 70 Myr at a depth of about 100 km. Since the starts of this model run the slab depth constantly rises up until 1020 km depth at 0 Myr. Velocity evolution (Figure 4.53, lower panel) starts at a value of 20 mm/yr during 70 and 60 Myr, this value decreases down to 10 mm/yr and it is constant between 50 and 10 Myr.

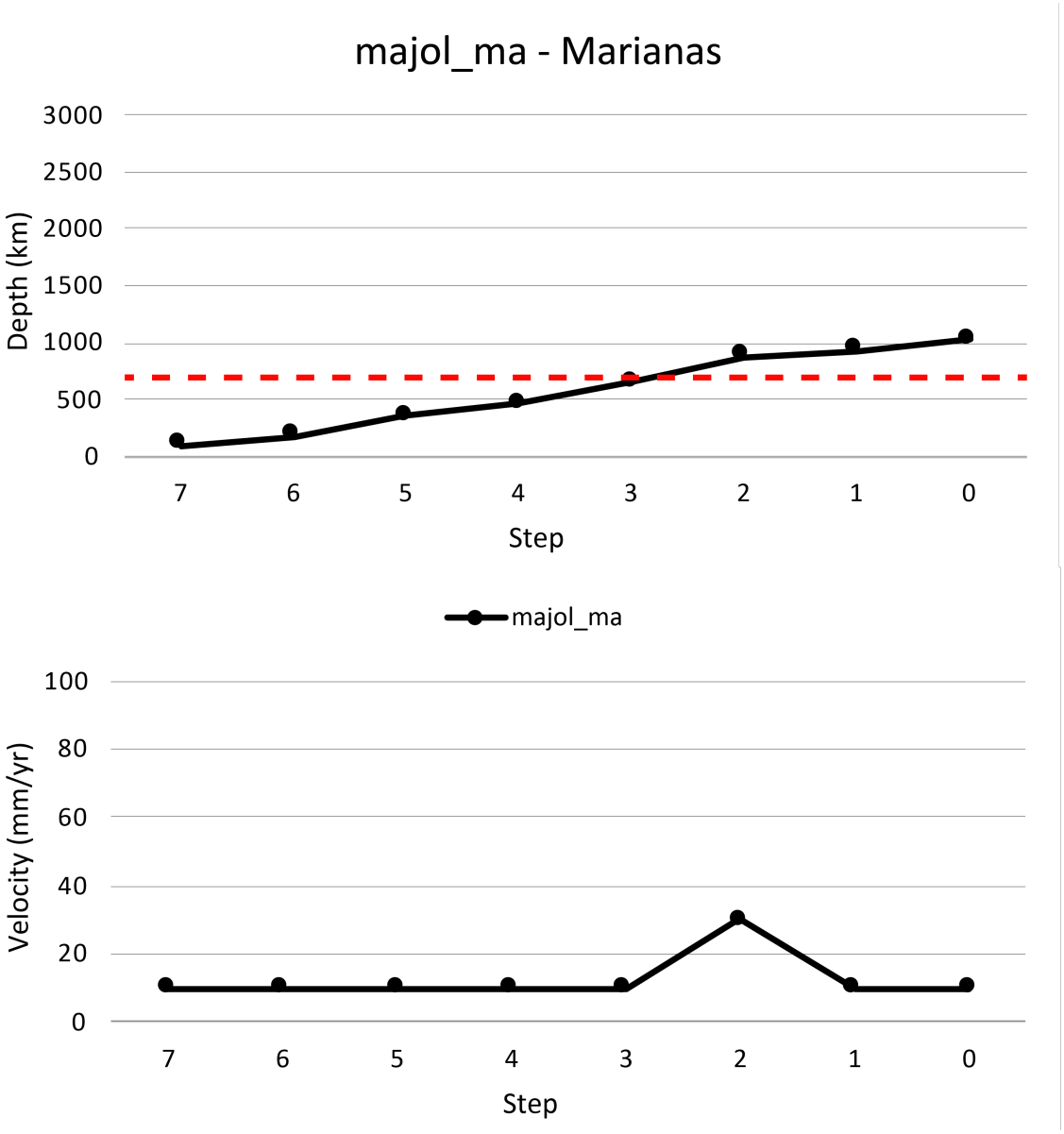

Figure 4.53 – Depth (upper panel) and velocity (lower panel) data for the Marianas lithosphere of model *majol_ma*. Depth evolution for the Marianas slab (upper panel) starts from 70 Myr, at a depth of about 100 km. Since the starts of this model run the slab depth constantly rises up until 1020 km depth, at 0 Myr. Velocity evolution (lower panel) starts at a value of 20 mm/yr during 70 and 60 Myr, this value decreases down to 10 mm/yr and it is constant between 50 and 10 Myr.Velocity evolution (lower panel) shows its maximum peak at 20 mm/yr, whereas the minimum peaks are reaches 50 mm/yr for the remaining timesteps of the model.

4.7 3d results in absolute reference frames

Using the ASCII Reference Profile Material model two 3-dimensional experiments were made. In these models the majorite-Fo50 rheological profile (Boneh et al., 2017; Griffin et al., 2009; Nekvasil et al., 2004) was used, whose thermal initial stage for the entire spherical domain was shown in Figure 4.37. Thus, that initial stage is valid for both models presented in this subsection, i.e., models *majol3d_1* (Figures 4.54 and 4.56) and *majol3d_2* (Figures 4.57 and 4.59) since they were carried out using the same ASCII Reference Profile model, in a deep hotspot reference frame (angular velocity provided by Seton et al., 2012) and a shallow hotspot reference frame (Table 4.1) respectively.

4.7.1 Model *majol3d_1*

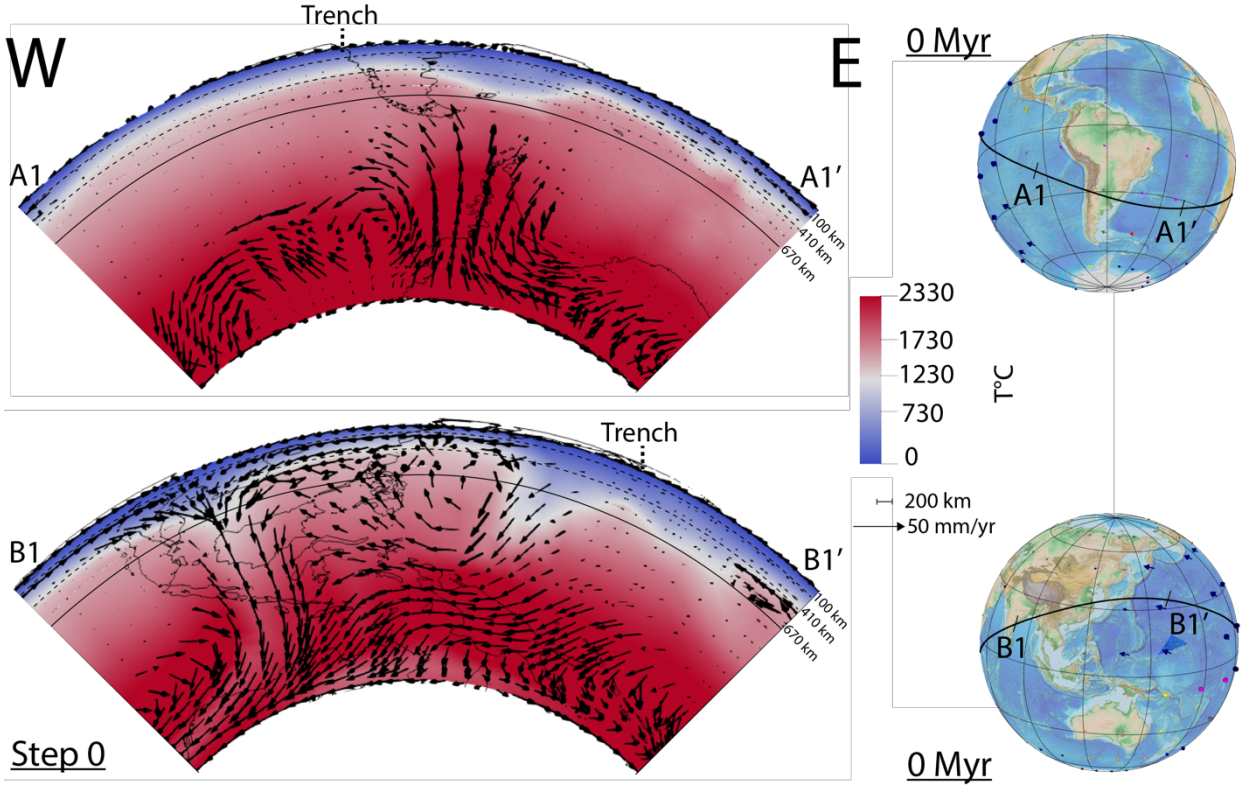

Figure 4.54 - Step 0 relative to model *majol3d_1.* In the upper panel, model majol3d_1 shows a lithosphere, at the western boundary of the numerical domain, that is about 410 km thick. Right eastward with respect to the South American coastlines a lithospheric thickening can be observed, with a maximum depth of about 640 km. Going towards the east, the lithosphere thickness becomes ~410 km depth again until the easternmost boundary of the annulus. Velocity vectors show a westward direction of the Pacific plate, at the western boundary of the domain, a N-S direction for the East Pacific Rise, where velocity vectors reverse their motion direction in correspondence of the Nazca plate, that has an eastward direction of motion. The South American plate has a westward-directed lithospheric motion and its direction inversion occurs below the eastern boundary of the South American coastline. The lithosphere is ~410 km thick at the western boundary of the spherical annulus in the Pacific area (lower panel). Under Indonesia a segment of descending lithosphere into the mantle can be seen, reaching a depth of about 1280 km. However, an older and hotter prosecution of it at depth can be seen, being almost mixed with the surrounding mantle, reaching the bottom of the model domain. Eastward, the lithosphere has a thickness of ~410 km, reaching the Japanese area and the Japanese slab. This slab reaches here ~1620 km depth.

Velocity vectors on the lithosphere surface are eastward-directed for the Indo-Australian plate, whereas they invert their motion direction in correspondence of the Eurasian plate, becoming strictly westward-directed on the Pacific plates surface. Globes in the right part of this figure show surface plate kinematics in a deep hotspot reference frame at this stage, with the black line suggesting the position of the tectonic equator, along which the 2d slice within the 3d model is cut. Profiles A1-A1' and B1-B1' are shown to point out to the surface of the correspondent quarter annulus geographical location and lateral extension. The dashed Trench line points to where the subduction trench should be.

Figure 4.54 shows the step 0 of the model *majol3d_1*. In this model the evolution of plate motion velocity (from 140 to 0 Myr) in a deep hotspot reference frame (rotation data collected by Seton et al., 2012) is applied as boundary conditions, for a total runtime of 140 Myr arbitrarily divided into 14 Steps of 10 Myr each. **South America (Figure 4.54, upper panel):** in model *majol3d_1*, the lithosphere at the western boundary of the numerical domain is about 410 km thick. Right eastward with respect to the South American coastlines a lithospheric thickening can be observed, with a maximum depth of about 640 km. Going towards the east, the lithosphere thickness becomes ~410 km depth again until the easternmost boundary of the annulus. Velocity vectors show a westward direction of the Pacific plate, at the western boundary of the domain, a N-S direction for the East Pacific Rise, where velocity vectors reverse their motion direction in correspondence of the Nazca plate that has an eastward direction of motion. The South American plate has a westward-directed lithospheric motion and its direction inversion occurs below the eastern boundary of the South American coastlines. Thus, lithospheric accumulation in this area can occur in both direction of motion, from E to W and from W-to E. Moreover, velocity vectors show a particularly weak circulation within the upper mantle, whereas an active circulation right above the CMB, in the lower mantle, with a vigorous upwelling of mantle material right below the South American slab can be observed. Temperature of the lithosphere is 0°C at its top and reaches ~1300°C at its bottom. The bottom of the domain has a temperature of about 2330°C as well as almost the totality of the lower mantle. **Pacific (Figure 4.54, lower panel):** looking at this side of the spherical shell the lithosphere is ~410 km thick at the western boundary of the spherical annulus. Under Indonesia a segment of descending lithosphere into the mantle can be seen, reaching a depth of about 1280 km. However, an older and hotter prosecution of it at depth can be seen, being almost mixed with the surrounding mantle, reaching the bottom of the model domain. Eastward, the lithosphere has a thickness of ~410 km, reaching the Japanese area and the Japanese slab. This slab reaches here ~1620 km depth. Right eastward with respect to the slab the lithosphere shows a thickened area that reaches about 670 km depth, after which the lithosphere has a thickness of about 410 km until the end of the spherical annulus. Velocity vectors on the lithosphere surface are eastward-directed for the Indo-Australian plate, whereas they invert their motion direction in correspondence of the Eurasian plate, becoming strictly westward-directed on the Pacific plates surface. This points to a subduction direction that goes from W to E for the Indonesian subduction zone and from E to W for the Japanese subduction zone.

Velocity vectors along the subducting slabs are long and almost comparable with vectors on the surface. Circulation within the upper mantle is weak, except in the area between the two slabs. In fact, the motion of the Japanese slab enhances a vigorous counterflow within its frontal mantle wedge, that influence mantle circulation reaching the Indonesian slab. However, all these vectors flow in the lower mantle, where there is a vigorous circulation down to the CMB. Temperature of the lithosphere is 0°C at its top and reaches ~1300°C at its bottom. The bottom of the domain has a temperature of about 2330°C as well as almost the totality of the lower mantle.

Figures 4.55 and 4.56 show depth and velocity evolution for the South American and Japanese slab, respectively. The depth evolution (Figure 4.55, upper panel) for the South American slab starts at about 50 Myr, at which the lithosphere reaches a depth of ~250 km. Its depth constantly increases up to ~640 km at 10 Myr. This depth is kept also at 0 Myr. Velocity evolution (Figure 4.55, lower panel) starts at 50 Myr, at which the deepest point of the lithosphere assumes a velocity of about 30 mm/yr. This value decreases down to 20 mm/yr at 40 Myr and increases again at 30 Myr, reaching a value of about 40 Myr. This value decreases to 30 (between 20 and 10 Myr) and increases again to 40 mm/yr at 0 Myr. Depth evolution for the Japanese lithosphere (Figure 4.56, upper panel) starts at the beginning of the model run, i.e. 140 Myr, at a depth of ~175 km. The lithospheric depth increases up to ~1310 km (90 Myr), being constant then for 10 Myr between 90 and 80 Myr. Then it starts to deepen again, more rapidly, reaching 2900 km depth (i.e., the CMB bottom of the numerical domain) at 40-30 Myr. Then the deepest point of the Japanese lithosphere becomes shallower, reaching ~1540 km depth between 20 and 10 Myr, reaching about 1620 km depth at the last stage, i.e. 0 Myr. Velocity evolution (Figure 4.56, lower panel) of the deepest lithospheric point of the Japanese area starts at 140 Myr and at a velocity of about 100 mm/yr. This velocity decreases down to 40 mm/yr between 130 and 110 Myr.

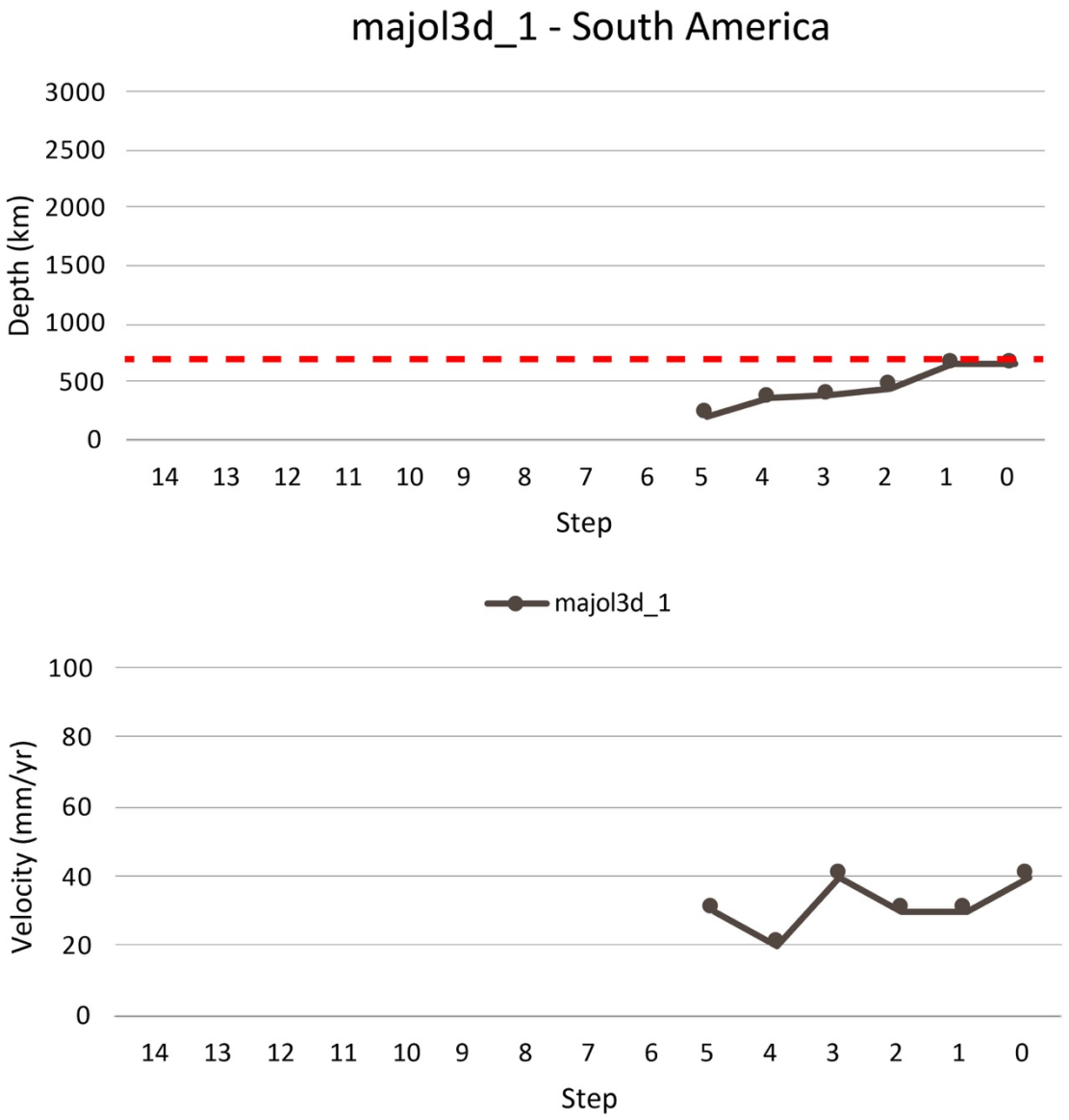

Figure 4.55 – Depth (upper panel) and velocity (lower panel) data for the South American lithosphere of model *majol3d_1*. The South American (upper panel) slab depth evolution starts at about 50 Myr, at which the lithosphere reaches a depth of ~250 km. Its depth constantly increases up to ~640 km at 10 Myr. This depth is kept also at 0 Myr. Velocity evolution (lower panel) starts at 50 Myr, at which the deepest point of the lithosphere assumes the maximum velocity of about 40 Myr at 30 and 0 Myr, whereas its minimum peak is 20 mm/yr at 40 Myr.

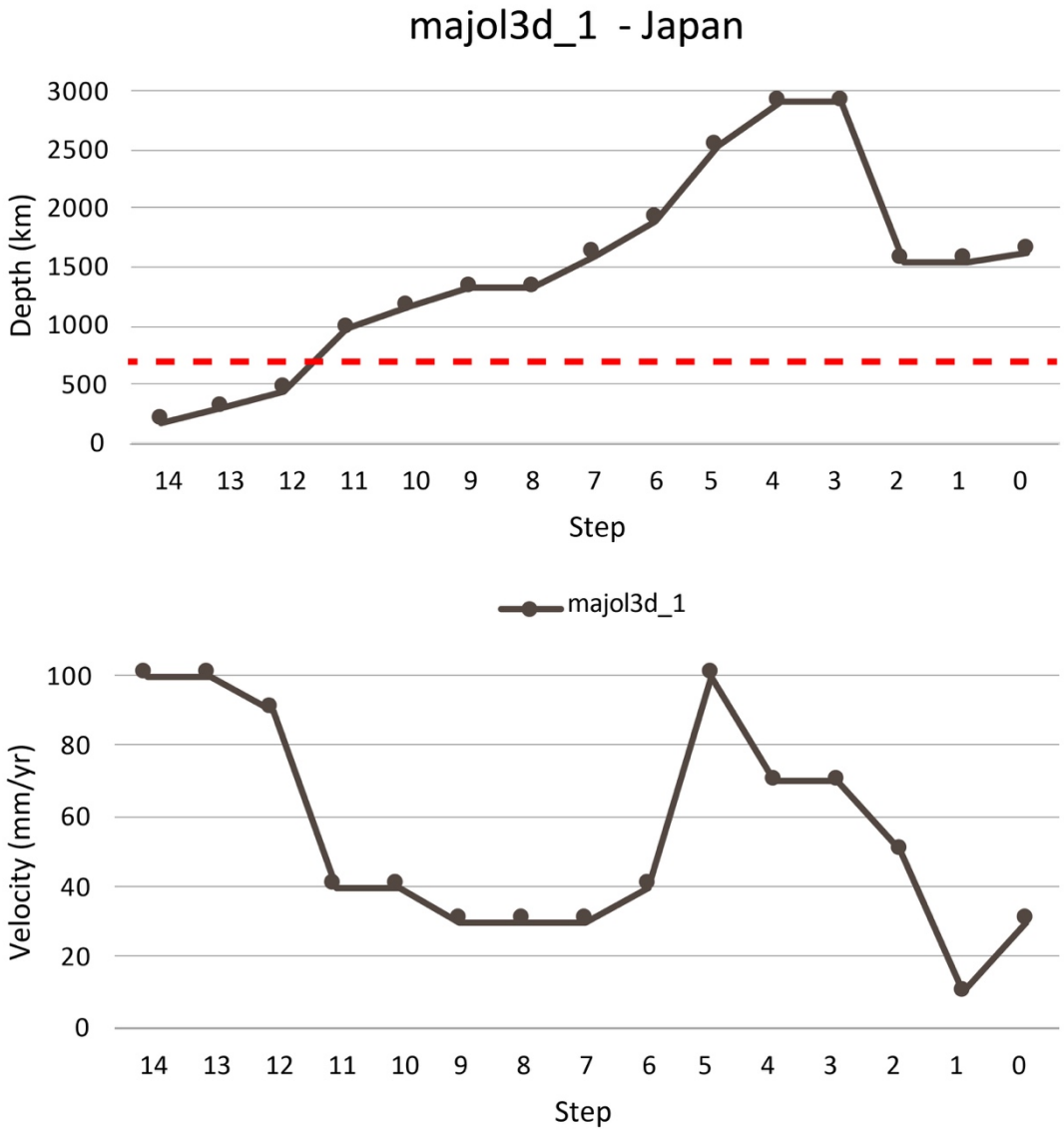

Figure 4.56 – Depth (upper panel) and velocity (lower panel) data for the Japanese lithosphere of model *majol3d_1*. Depth evolution for the Japanese lithosphere (upper panel) starts at the beginning of the model run, i.e. 140 Myr, at a depth of ~175 km. The lithospheric depth increases up to ~1310 km (90 Myr), being constant then for 10 Myr between 90 and 80 Myr. Then it starts to deepen again, more rapidly, reaching 2900 km depth (i.e., the CMB bottom of the numerical domain) at 40-30 Myr. Then the deepest point of the Japanese lithosphere becomes shallower, reaching ~1540 km depth between 20 and 10 Myr, reaching about 1620 km depth at the last stage, i.e. 0 Myr. Velocity evolution (lower panel) shows maximum peaks at 100 mm/yr at 140-130 and 50 Myr, whereas the minimum peak is at 10 Myr, reaching 10 mm/yr

Starting from 100 Myr its value decreases again reaching 30 mm/yr, constant between 90-70 Myr. It increases abruptly up to 100 mm/yr at 50 Myr. Between 50 and 10 Myr the velocity decreases, reaching at 10 Myr 10 mm/yr. At 0 Myr, it increases at 30 mm/yr.

4.7.2 Model *majol3d_2*

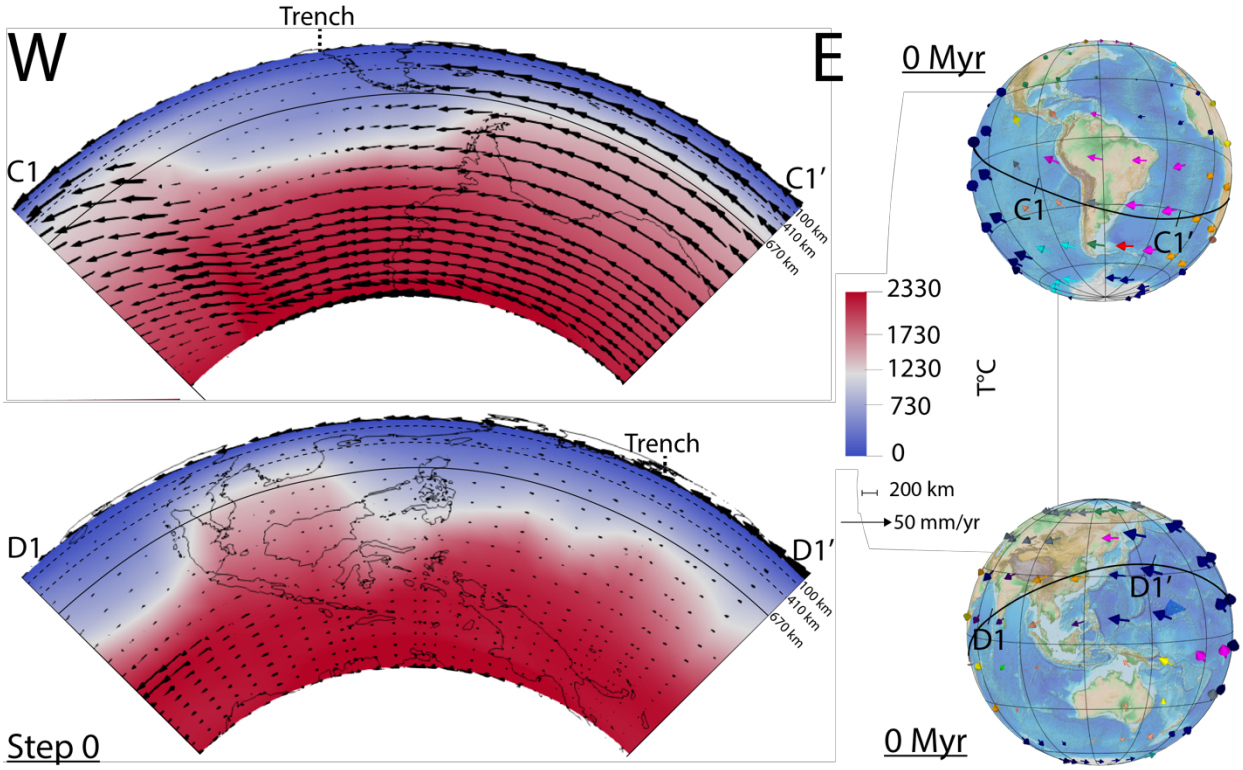

Figure 4.57 - Step 0 relative to model *majol3d_2.* In the upper panel, the South American lithosphere at the western boundary of the numerical domain is about 500 km thick. Westward with respect to the South American coastlines a wide thickened lithospheric area can be observed, with a maximum depth of about 1250 km. It extends from below the plate boundary between Pacific and Nazca plates to the easternmost boundary of the South American coastlines. Going towards the east, the lithosphere thickness becomes ~670 km depth until the easternmost boundary of the domain. Velocity vectors show a westward direction of motion for the tectonic plates, being the Pacific and the South American (at the boundaries) faster with respect to the central slower Nazca plate. Looking at the Pacific side (lower panel) the lithosphere is ~1310 km thick at the western boundary of the spherical annulus, between India and Indonesia. Under the western Eurasian plate the lithosphere is about 600 km depth. In correspondence of eastern Eurasia and Pacific plates an almost homogeneous lithosphere is ~1330 km depth until the end of the quarter annulus. Velocity vectors on the lithosphere surface are westward-directed and their velocity is slower towards the western side of the domain, in correspondence of the Indo-Australian plates, increasing slightly towards the eastern Eurasian and Pacific plates. Globes in the right part of this figure show surface plate kinematics in a shallow hotspot reference frame at this stage, with the black line suggesting the position of the tectonic equator, along which the slice within the 3d model is cut. In profiles C1-C1' and D1-D1' lateral extension and geographical position of the correspondent quarter annulus are shown. The dashed vertical Trench line points to where the subduction trench should be.

Figure 4.57 shows step 0 of the model *majol3d_2*. In this model the evolution of plate motion velocity (from 140 to 0 Myr) in a shallow hotspot reference frame (Table 4.1) is applied as boundary conditions, for a total runtime of 140 Myr corresponding to 14 Steps of 10 Myr each, arbitrarily defined. **South America (Figure 4.57, upper panel):** in model *majol3d_2* the lithosphere at the western boundary of the numerical domain is about 500 km thick. Westward with respect to the South American coastlines a wide thickened lithospheric area can be observed, with a maximum depth of about 1250 km. It extends from below the plate boundary between Pacific and Nazca plates to the easternmost boundary of the South American coastlines. Going towards the east the lithosphere thickness becomes ~670 km depth until the easternmost boundary of the domain. Velocity vectors show a westward direction of motion of the tectonic plates, being the Pacific and the South American

faster with respect to the central slower Nazca plate, pointing to an E to W direction of the lithospheric accumulation. The velocity vectors show a homogeneous circulation within both the upper and the lower mantle except for the western part of the lithospheric thickening. Velocity vectors slightly shortens towards the CMB. Temperature of the lithosphere is 0°C at its top and reaches ~1300°C at its bottom. The bottom of the domain has a temperature of about 2330°C as well as almost the totality of the lower mantle. **Pacific (Figure 4.57, lower panel):** looking of this side of the spherical shell, the lithosphere is ~1310 km thick at the westward boundary of the spherical annulus, between India and Indonesia. Under the western Eurasian plate the lithosphere is about 600 km depth. In correspondence of eastern Eurasia and Pacific plates an almost homogeneous lithosphere is ~1330 km depth until the end of the quarter annulus. Velocity vectors on the lithosphere surface are westward-directed and their velocity is slower towards the western side of the domain in correspondence of the Indo-Australian plates, increasing slightly towards the eastern Eurasia and Pacific plates. Circulation within the entire mantle is weak. Temperature of the lithosphere is 0°C at its top and reaches ~1300°C at its bottom. The bottom of the domain has a temperature of about 2330°C as well as almost the totality of the lower mantle.

Figures 58 and 59 show depth and velocity evolution for the South American and Japanese slab in Figure 57. The depth evolution (Figure 4.58, upper panel) for the South American slab starts at 140 Myr, at a depth of about 175 km. Its depth increases up to ~1450 km, at 100 Myr. This value is constant until 70 Myr. The lithosphere depth then decreases to ~1160 km at 60 Myr, slightly increasing up to about 1250 km until 0 Myr. Velocity evolution (Figure 4.58, lower panel) for this slab starts at the beginning of the model run, i.e., 140 Myr, with a velocity of 110 mm/yr. At 130 Myr the slab tip is faster, reaching 200 mm/yr, whereas it decreases abruptly down to 0 mm/yr at 110 Myr. Then it starts to increase again, reaching 25 mm/yr between 100 and 90 Myr, 50 mm/yr between 80 and 70 Myr and 75 mm/yr at 60 Myr. Velocity value decreases down to 25 mm/yr between 50 and 40 Myr, whereas it assumes a value of 85 mm/yr at 30 Myr, to decrease afterwards down to 0 mm/yr, at 10 Myr and 50 mm/yr at 0 Myr, the end of the model run.

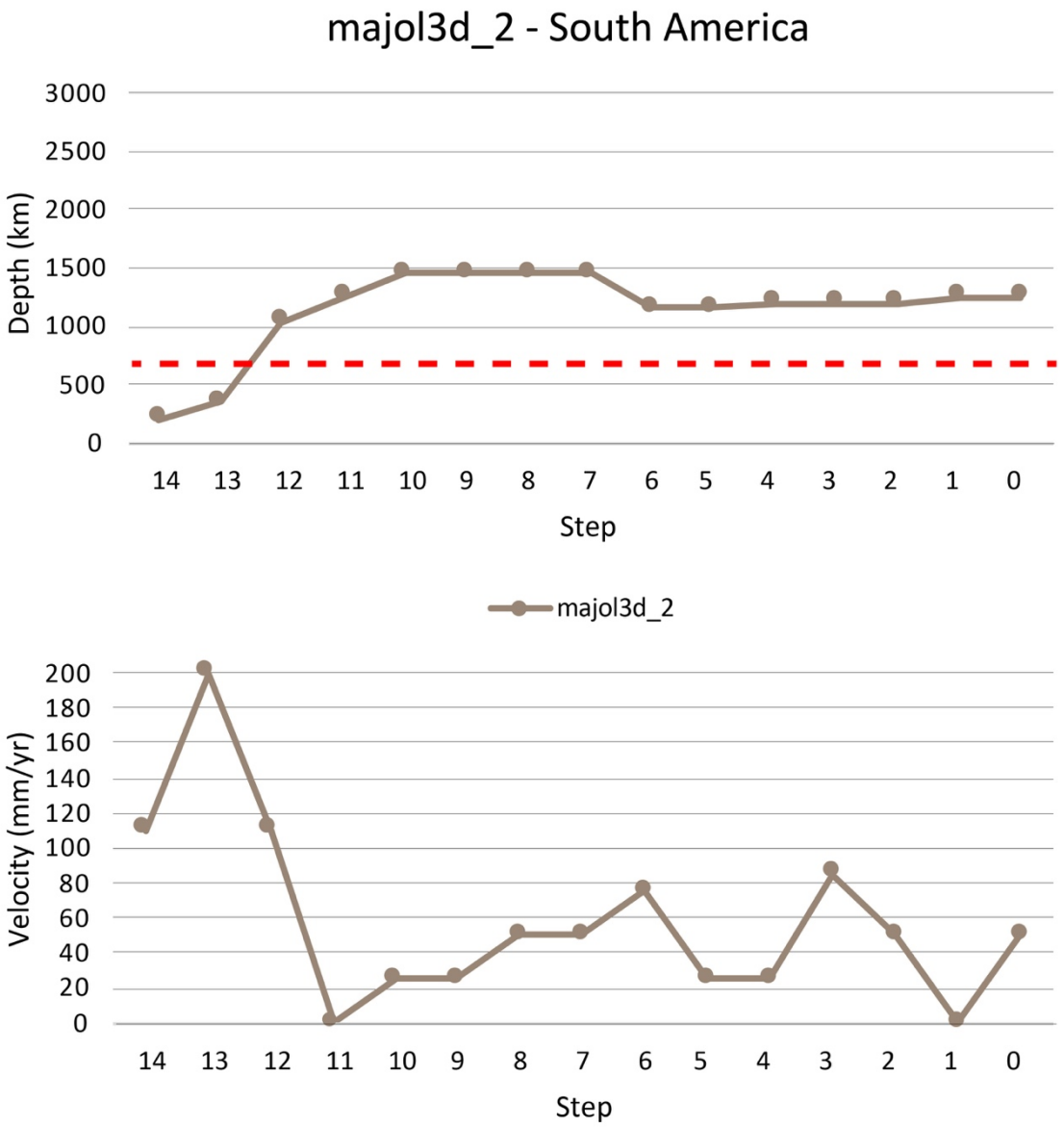

Figure 4.58 – Depth (upper panel) and velocity (lower panel) data for the South American lithosphere of model *majol3d_2*. The South American (upper panel) slab depth evolution starts at 140 Myr, at a depth of about 175 km. Its depth increases up to ~1450 km, at 100 Myr. This value is constant until 70 Myr. The lithosphere depth then decreases to ~1160 km at 60 Myr, slightly increasing up to about 1250 km until 0 Myr. Velocity evolution (lower panel) starts at 140 Myr. For this evolution the deepest point of the lithosphere assumes a maximum velocity of about 200 mm/yr at 130 Myr, whereas its minimum peak is 0 mm/yr at 110 and 10 Myr.

For the Japanese slab, the depth evolution (Figure 4.59, upper panel) starts at 70 Myr at a depth of ~580 km. Its depth increases slowly up to about 725 km, stagnating at the 670 km discontinuity (red dashed line) between 60 and 40 Myr. Lithosphere depth increases abruptly to about 1220 km at 30 Myr, starting to increase slowly again afterwards reaching ~1330 km depth at 0 Myr.

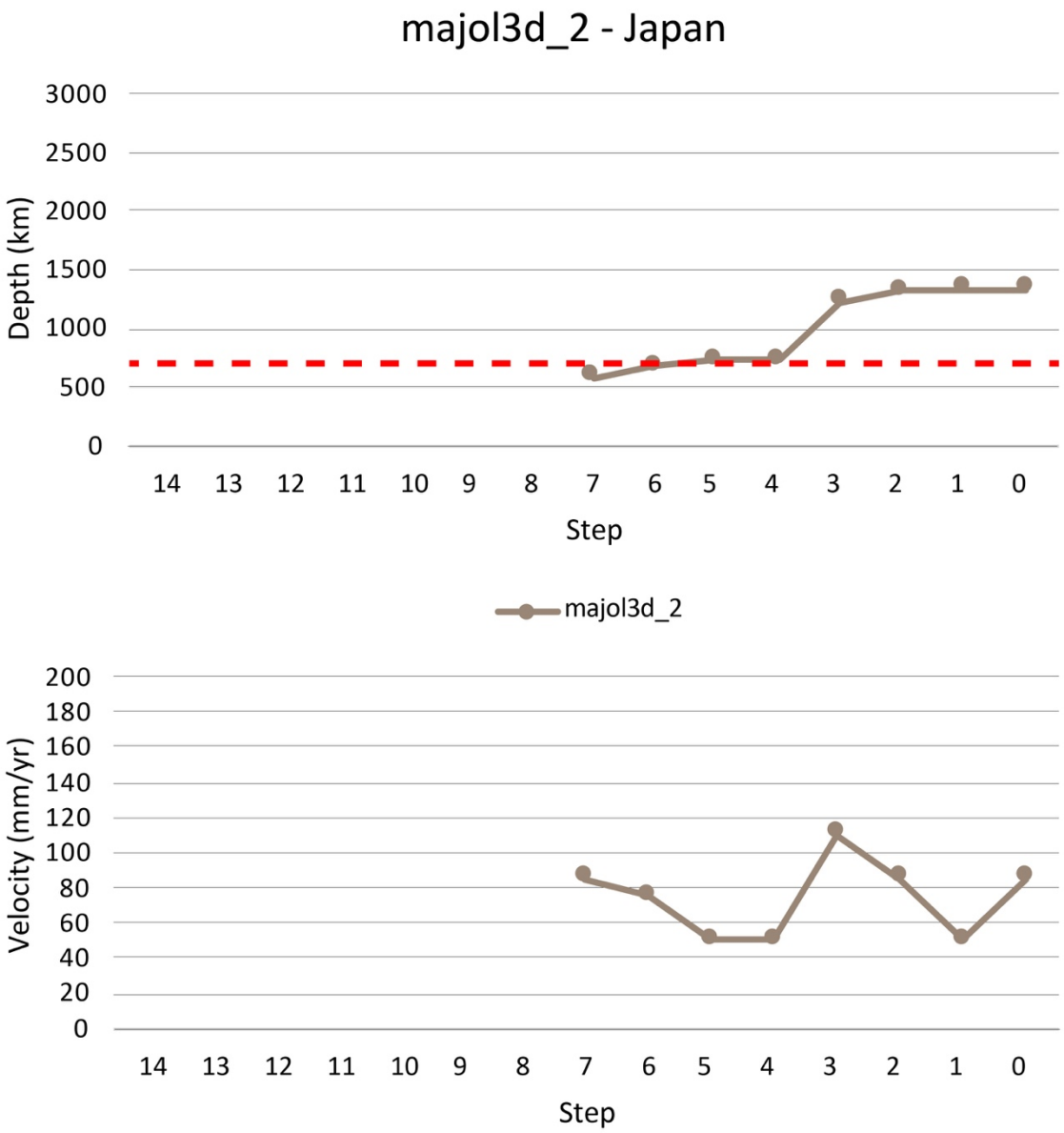

Figure 4.59 – Depth (upper panel) and velocity (lower panel) data for the Japanese lithosphere of model *majol3d_2*. Depth evolution for the Japanese lithosphere (upper panel) starts at 70 Myr, at a depth of ~580 km. Its depth increases slowly up to about 725 km, stagnating at the 670 km discontinuity between 60 and 40 Myr. Lithosphere depth increases abruptly at about 1220 km at 30 Myr, starting to increase slowly again afterwards reaching ~1330 km depth at 0 Myr. Velocity evolution (lower panel) shows its maximum peak at 110 mm/yr at 30 Myr, whereas the minimum peaks are at 50, 40 and 10 Myr, reaching 50 mm/yr

Velocity evolution (Figure 4.59, lower panel) for this slab starts at 70 Myr with a velocity of about 85 mm/yr, that decreases down to 50 mm/yr at 50-40 Myr. The velocity at the slab tip then increases up to 100 mm/yr at 30 Myr, decreases down to 50 mm/yr between 30 and 10 Myr and finally rises again at 0 Myr, reaching 85 mm/yr.

To conclude this results section, recap figures (Figures 4.60-4.63) showing depth (km) vs step and velocity (mm/yr) vs step are shown. First, depth and velocity data relative to models in a deep hotspot reference frame (Figures 4.60-4.61), then data relative to models in a shallow hotspot reference frame will be shown (Figures 4.62-4.63). Data relative to reference frames with respect to fixed South America and Marianas plate are shown together with the deep hotspot reference frame since they have the same velocity order of magnitude.

In Figure 4.60, among seven models in a deep hotspot reference frame (angular vectors provided by Seton et al., 2012) and one in a South America fixed reference frame, in the 37% the lithosphere does not penetrate across the 670 km discontinuity (red dashed line), in 38% of the cases it barely penetrates the 670 km discontinuity and in the remaining 25% the lithosphere exceeds the 670 km discontinuity.

In Figure 4.61, among seven models in a deep hotspot reference frame (rotation data collected by Seton et al., 2012) and one in a Marianas fixed reference frame, in the 12% of the cases the lithosphere does not penetrate across the 670 km discontinuity (red dashed line), in 13% of the cases it barely penetrate the 670 km discontinuity and in the remaining 75% the lithosphere exceeds the 670 km discontinuity.

Velocities are on average higher for the lithosphere on the Pacific side of the spherical shell domain and age of the deepening processes active on the lithosphere seems to be higher for the Pacific side with respect to the South American one.

Of seven models (Figure 4.62) in a shallow hotspot reference frame (Table 4.1), in the 57% of the cases the lithosphere does not penetrate across the 670 km discontinuity (red dashed line), in 43% of the cases the lithosphere exceeds the 670 km discontinuity. In Figure 4.63, among seven models in a shallow hotspot reference frame (Table 4.1), in the 71% of the cases the lithosphere does not penetrate across the 670 km discontinuity (red dashed line), in 15% of the cases it barely penetrates the 670 km discontinuity and in the remaining 14% the lithosphere exceeds the 670 km discontinuity. Velocities are on average higher for the Pacific side whereas the age of deepening processes acting on the lithosphere seems to be higher for the South American side with respect to the Pacific one.

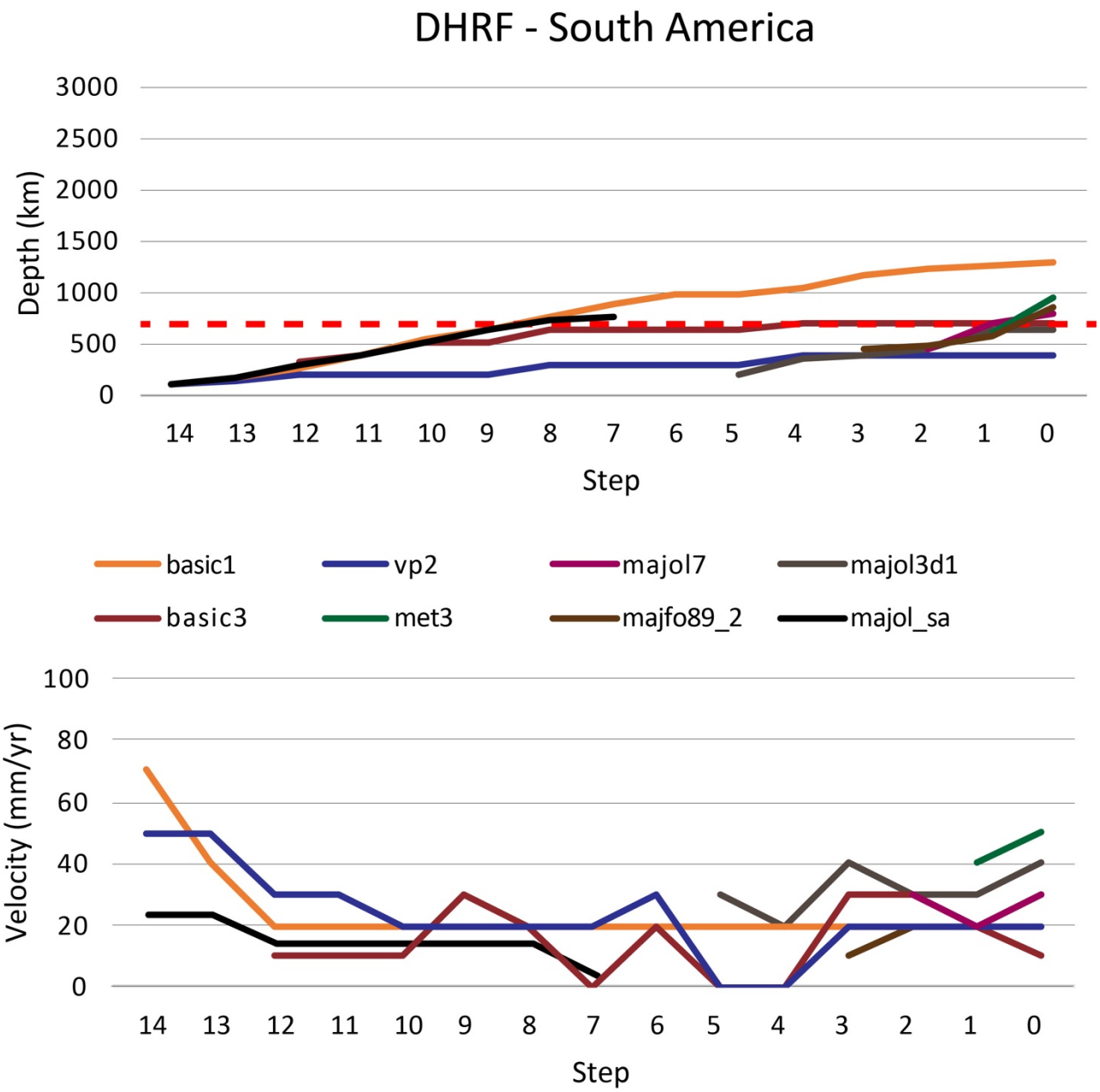

Figure 4.60 – Depth and velocity data relative to deep hotspot reference frame and with respect to South America fixed. Among seven models in a deep hotspot reference frame and one in a South America fixed reference frame, in the 37% the lithosphere does not penetrate across the 670 km discontinuity (red dashed line), in 38% of the cases it barely penetrates the 670 km discontinuity and in the remaining 25% the lithosphere exceeds the 670 km discontinuity.

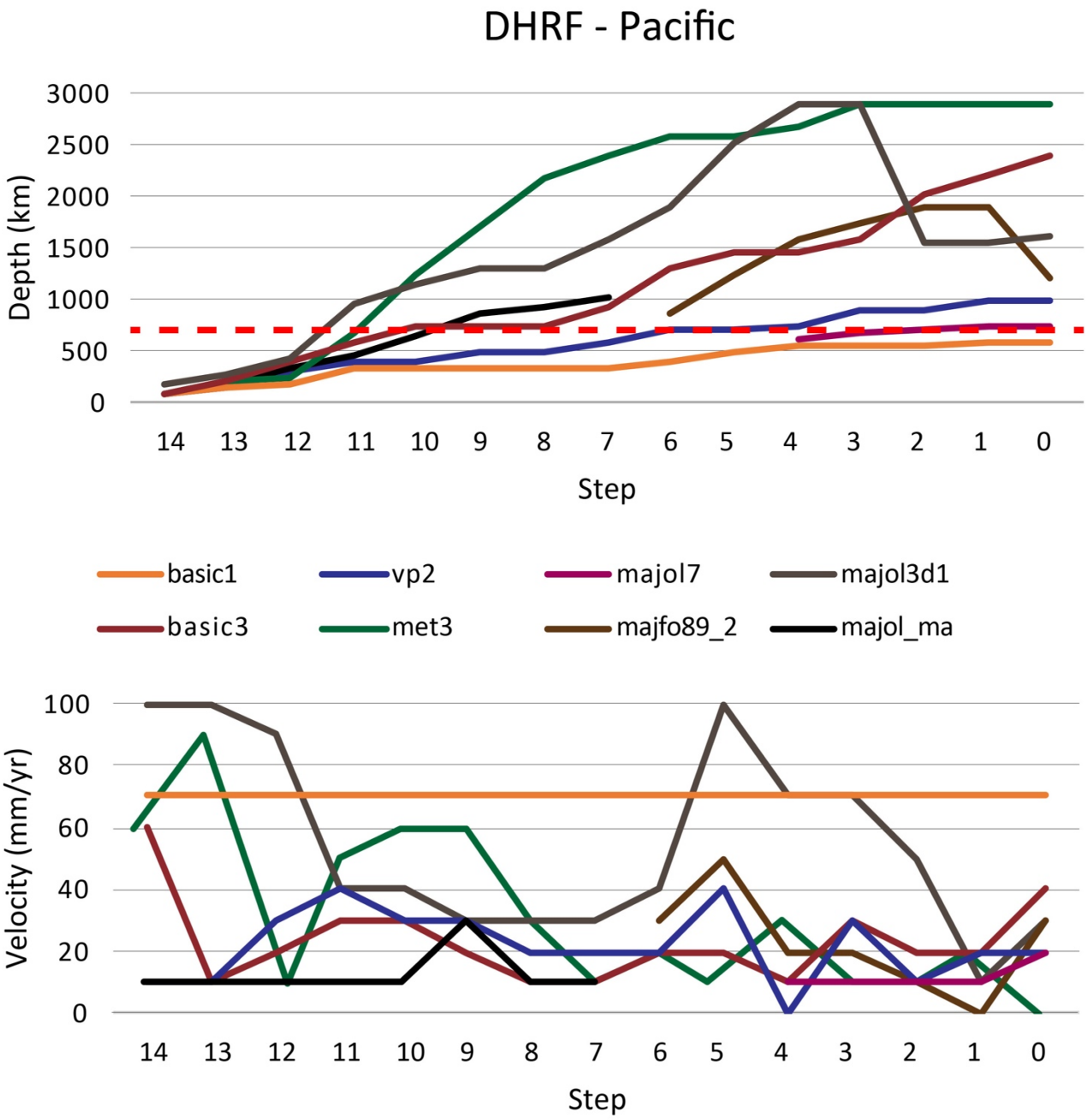

Figure 4.61 – Depth and velocity data relative to deep hotspot reference frame and with respect to Marianas fixed. Among seven models in a deep hotspot reference frame and one in a South America fixed reference frame, in the 37% the lithosphere does not penetrate across the 670 km discontinuity (red dashed line), in 38% of the cases it barely penetrates the 670 km discontinuity and in the remaining 25% the lithosphere exceeds the 670 km discontinuity.

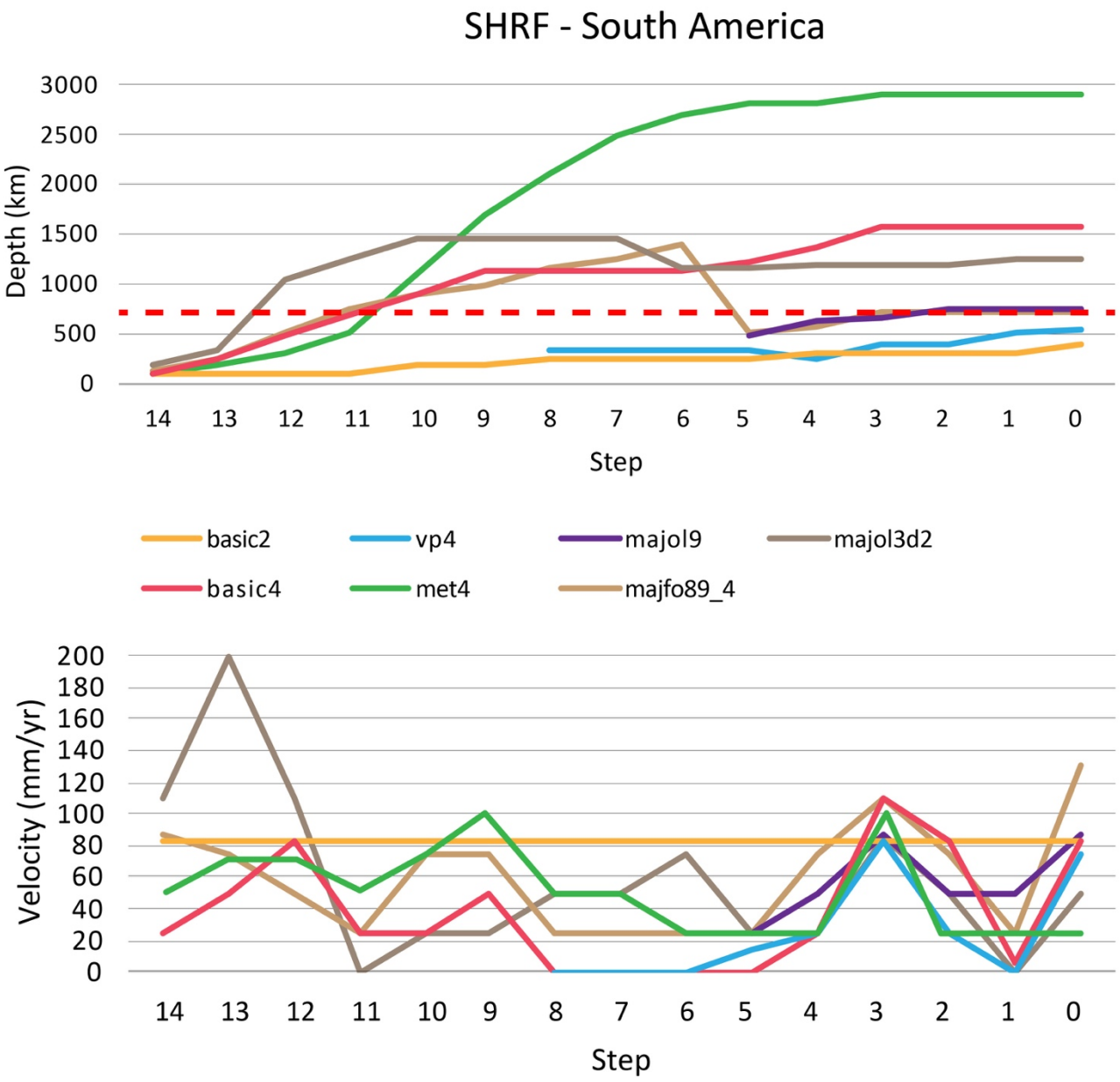

Figure 4.62 – Depth and velocity data relative to shallow hotspot reference frame. Of seven models in a shallow hotspot reference frame, in the 57% of the cases the lithosphere does not penetrate across the 670 km discontinuity (red dashed line), in 43% of the cases the lithosphere exceeds the 670 km discontinuity.

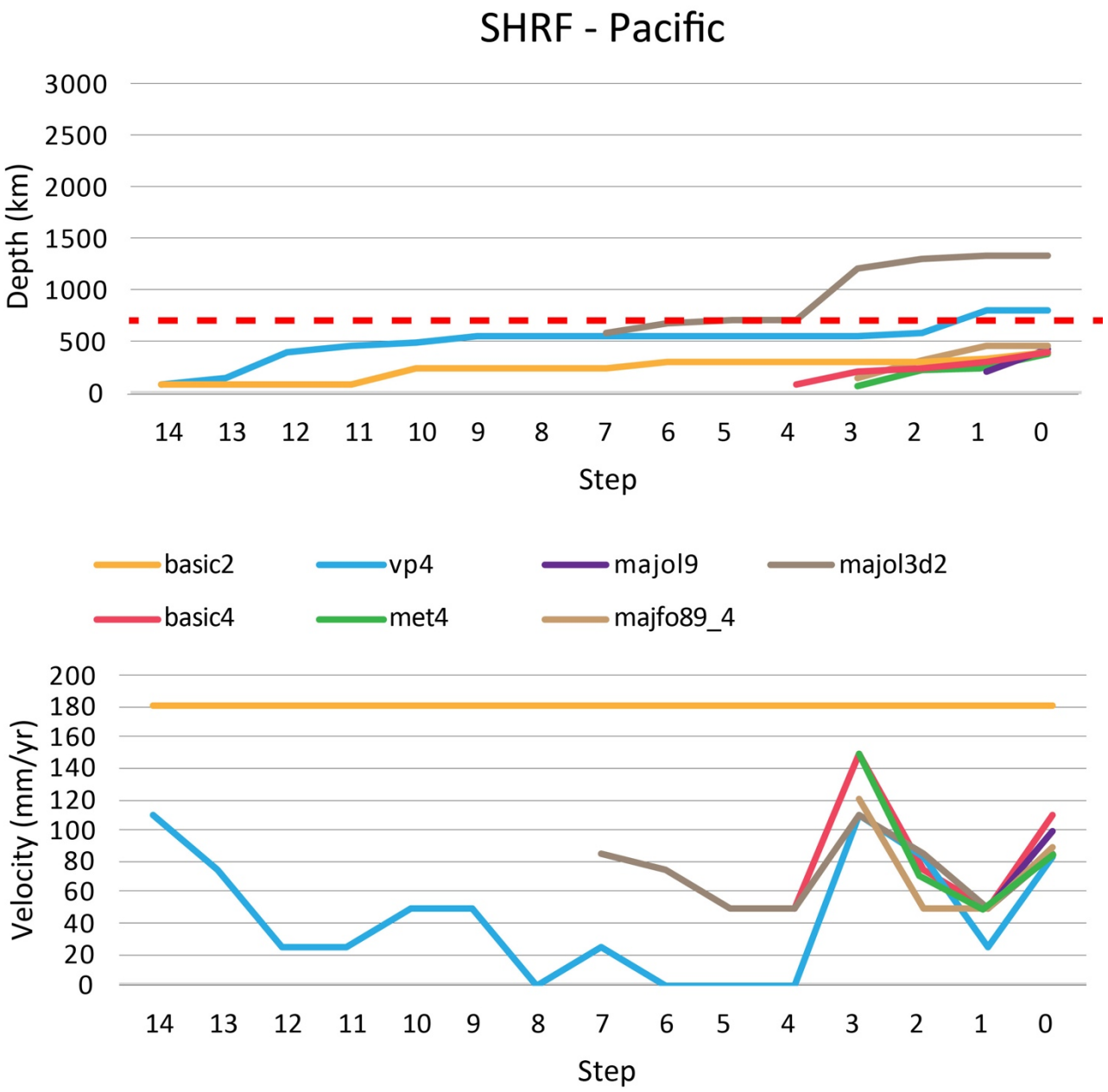

Figure 4.63 – Depth and velocity data relative to shallow hotspot reference frame. Among seven models in a shallow hotspot reference frame, in the 71% of the cases the lithosphere does not penetrate across the 670 km discontinuity (red dashed line), in 15% of the cases it barely penetrates the 670 km discontinuity and in the remaining 14% the lithosphere exceeds the 670 km discontinuity.

4.8 Discussion

Our results show a broad evidence of interactions and interrelations between rheological profiles used for the realization of the numerical models and different surface plate kinematics. For some models, for example, the lithosphere evolution does not show a subducting slab but just a lithospheric thickening and some slabs present opposite subduction direction with respect to what can be observed in nature. This happens more often for models in the shallow hotspot reference frame (Table 4.1) and it is possibly related to the global westward-direction of plate motion and to the higher velocities of plates in this reference frame. The first thing that stands out from this Chapter results is that using the evolution of plate motion in global numerical models simulating interactions between plate tectonics and mantle convection is of first order importance. In fact, as shown from Figures 4.11 and 4.14, the subduction obtained in a spherical shell domain when using a constant velocity for the entire duration of the model run is not comparable with natural observable.

The observable subduction direction for the South American slab is currently towards the east. The deep hotspot reference frame models mostly preserve this observation and, even when there is only just a lithospheric thickening instead of a well-defined subducting slab, the main direction of motion for its lithosphere accumulation is from W to E (e.g., Figures 4.17 and 4.31). The shallow hotspot reference frame models show an opposite direction of motion for the South American lithosphere (e.g., Figures 4.20 and 4.34), which thus accumulates or subducts from E to W. This is probably due to the different surface kinematics in addition to an insufficiently constrained lithosphere. In fact, in this area and with this reference frame both the Nazca and the South American lithospheric plates move towards the west, being the second one faster than the first one. As a result, without any discrimination about the nature of the lithosphere for the upper and lower plates, i.e., continental or oceanic, nor about their thickness, the faster plate is the one that easily subducts, i.e., the upper South American plate. Subduction occurs instead with the correct kinematics in the deep hotspot reference frame because of the faster eastward motion of the Nazca plate that opposes its motion to a slower westward moving South American plate. This allows subduction to occur having the current subduction direction observed in nature even without constraining the lithosphere with its nature or thickness.

Some results show slabs localization problems: subducting slabs, at 0 Myr (i.e., step 0), are not located below their correct current trench position. This likely happens because the surface velocity of the subducting lithosphere is too high with respect to the resistance offered by the lithosphere of the upper plate, thus the trenches move faster than the present ones, especially for Japan where the fast motion of the Pacific plate affects the entire area. This lead to the dislocation of the subducting slab far from

the current subduction zone trenches (e.g., models in Figures 4.20, 4.31 and 4.34, lower panels). Some numerical models, e.g., Figures 4.24 (upper panel) and 4.27 (lower panel), show just a lithospheric thickening in correspondence of one or both the reference subduction zones, i.e., South America and /or Japan. Some models, e.g., Figures 4.41 and 4.48 (both lower panels), show delaminated zones in correspondence of the Pacific area. This is again due to the very fast velocity of the Pacific plate acting on a lithospheric material having the same lateral characteristics along the entire spherical shell domain and thus not opposing any resistance.

The 3d spherical models helped somehow in solving the slabs localization issues in both deep and shallow hotspot reference frame. The use of the 3rd dimension allows to better constrain the surface plate motion and the relative mantle circulation, keeping the subduction area in the right geographical location. The model *majol3d_1* (Figure 4.51) indeed preserves the asymmetric behaviour of the two reference subductions (i.e., shallow South American and deep Japanese subduction zones), whereas wide thickened areas indicate the correct geographical slab locations in model *majol3d_2* (Figure 4.54), although pointing to the already mentioned issues related to the surface kinematic-rheologic profile combination.

Numerical models using relative reference frame, instead, partially solve issues related to the resistance opposed by the upper plate to the subducting one and their results can be overall compared to their respective images in the compilation of slab morphologies at the transition zone (i.e., the 670 km discontinuity) by Goes et al. (2017), even though not reproducing properly their asymmetric behaviour. This further supports problems related to the resistance offered by the upper plate to the lower subducting plate and points to the need to distinguish between upper and lower plate by means of their thickness and/or their continental or oceanic nature in models using absolute reference frames as surface boundary conditions, especially in the faster westward-rotating shallow hotspot reference frame (Table 1).

Viscosities of the lithosphere-mantle system in each numerical model plays an important role on its dynamics and velocity. In fact, for example, in models using the ASPECT's Visco Plastic Material model (Figures 4.24 and 4.27) the viscosity of the mantle is too high whereas the viscosity of the lithosphere is too low leading to a slow or absent circulation within the mantle and to a thick accumulation of the lithosphere below subduction zones. The lithosphere viscosity is of primary importance because of its response to the applied surface velocity boundary conditions. The lower the lithosphere viscosity, the higher is the probability of having a wide area of thickened lithosphere (i.e., blob-like subduction, Crameri et al., 2012) instead of a well-defined subducting lithospheric slab. A second order importance of density has been observed. In each model, in fact, the density of the subducting lithosphere does not seem to play any determinant role in triggering its sinking within

the mantle. The density of the whole system increases at depth, with phase transformation processes, and it seems not to be responsible for the subduction initiation in these models, whereas it rather seems to contribute to the subduction prosecution during the model run. Plate motion with respect to each other and to the mantle seems instead to be a main feature influencing on the dynamics of subduction process.

In these numerical models it is important to notice that the current global tectonic setting of plates, i.e., at step 0, is the final result of a past evolution. This can undoubtedly be related with nature. Plate tectonics and all its features (e.g., subductions, ridges, etc.), as they look now, are just the last steps of a very long-term evolution that brought to several cycles (at least three, Nance & Murphy, 2013 and references therein) of closure and opening of paleo-oceans and supercontinents breakups.

Most of the numerical models resulted from this Chapter analysis show a fast evolution of subduction zones, especially in the Pacific area, which throughout the entire model run form under the Marianas/Japan area and are shifted westward, under Indonesia where the slabs can eventually be swallowed within the mantle (e.g., Figures 4.34, 4.41 and 4.48, lower panels).

Basically, the lithospheric material coming from the east repeatedly starts to subduct and then migrates westward both in the South American (Appendix B, Figures B.1-B.60) and in the Pacific cases (Appendix B, Figures B.1-B.60), albeit with different velocities. If comparing these results with recent tomographic models (Figures 4.64 and 4.65; Moulik & Ekstrom, 2014) across South America and the Pacific area, along the tectonic equator, some common features can be observed. Although a defined slab cannot be identified (Figure 4.64), in the South American area the more rigid material is located eastward with respect to the Nazca plate, below the South American continent and the Atlantic Ocean, the position of the trench is consistent with one of our model (*basic4,* Figure 4.20) taken as reference and plotted in dashed line, even though subduction direction is opposite with respect to the natural observed (Figure 4.64).

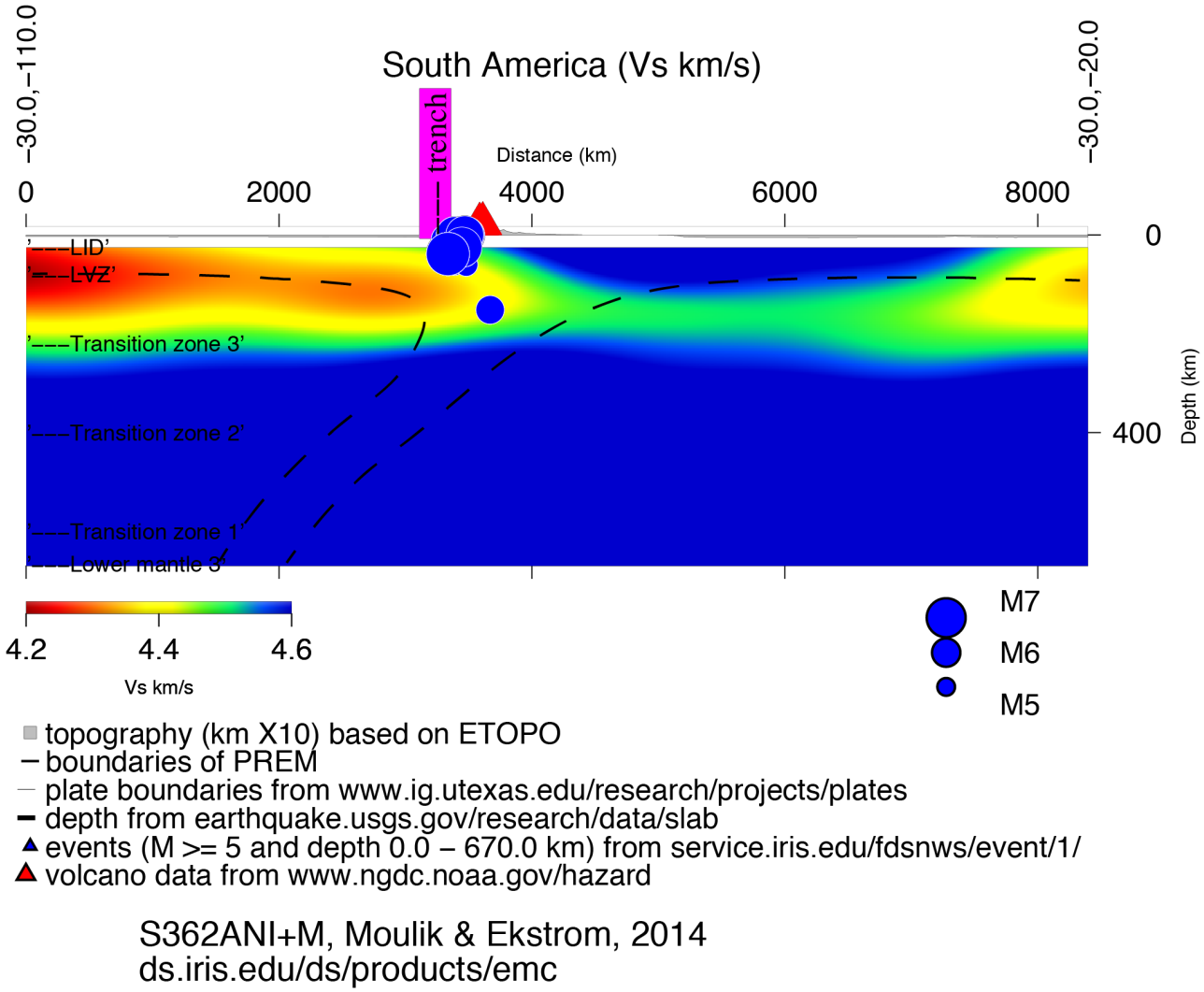

Figure 4.64 – Mantle tomography of the South American area. Here, although a subducting slab cannot be observed, the mantle tomography of the South American area shows that the rigid material is mostly located eastward with respect to the Nazca plate, below the South American plate and the Atlantic Ocean. In dashed line slab of model basic4 (Figure 20, upper panel) is consistently comparable with the position of the rigid material. Vertical exaggeration 4x.

In the Pacific area, the rigid material is mostly located below the Indo-Australian plate (Figure 4.65). This is however consistent with the faster rotation of the lithosphere predicted by the shallow hotspot reference frame (Table 4.1) which leads to the possible accumulation of rigid (lithospheric?) material in those areas (Figures 4.64 and 4.65), as also shown by absolute tomographic models (e.g., Panza et al., 2010).

In models described in this Chapter, mantle circulation is comparable with literature, e.g., Heister et al. (2017), Monnereau and Quéré (2001) and Yoshida (2014), in which there is a top-down motion of mantle material in correspondence of subducting slabs and a rise of it upward, towards spreading ridges. This can be seen quite well in models in a deep hotspot framework, such as model *isehar1* (Figure 4.31), model *majol1* (Figure 4.38), model *majfo89_1* (Figure 4.45), in which a deep circulation involving the shallow parts of the lower mantle moves from the South American slab to

the East Pacific Rise. In models in a shallow hotspot framework, this motion is less evident due to the higher velocities and the opposite direction of the subducting slab with respect to nature (e.g., *isehar2* Figure 4.34. and *majfo89_2* Figure 4.48). Furthermore, it has to be noticed that velocities in our models are referred to the bottom of the spherical domain, i.e., 2900 km, thus surface velocity boundary conditions should be rescaled with respect to the 670 km discontinuity to clearly evaluate any upper mantle circulation.

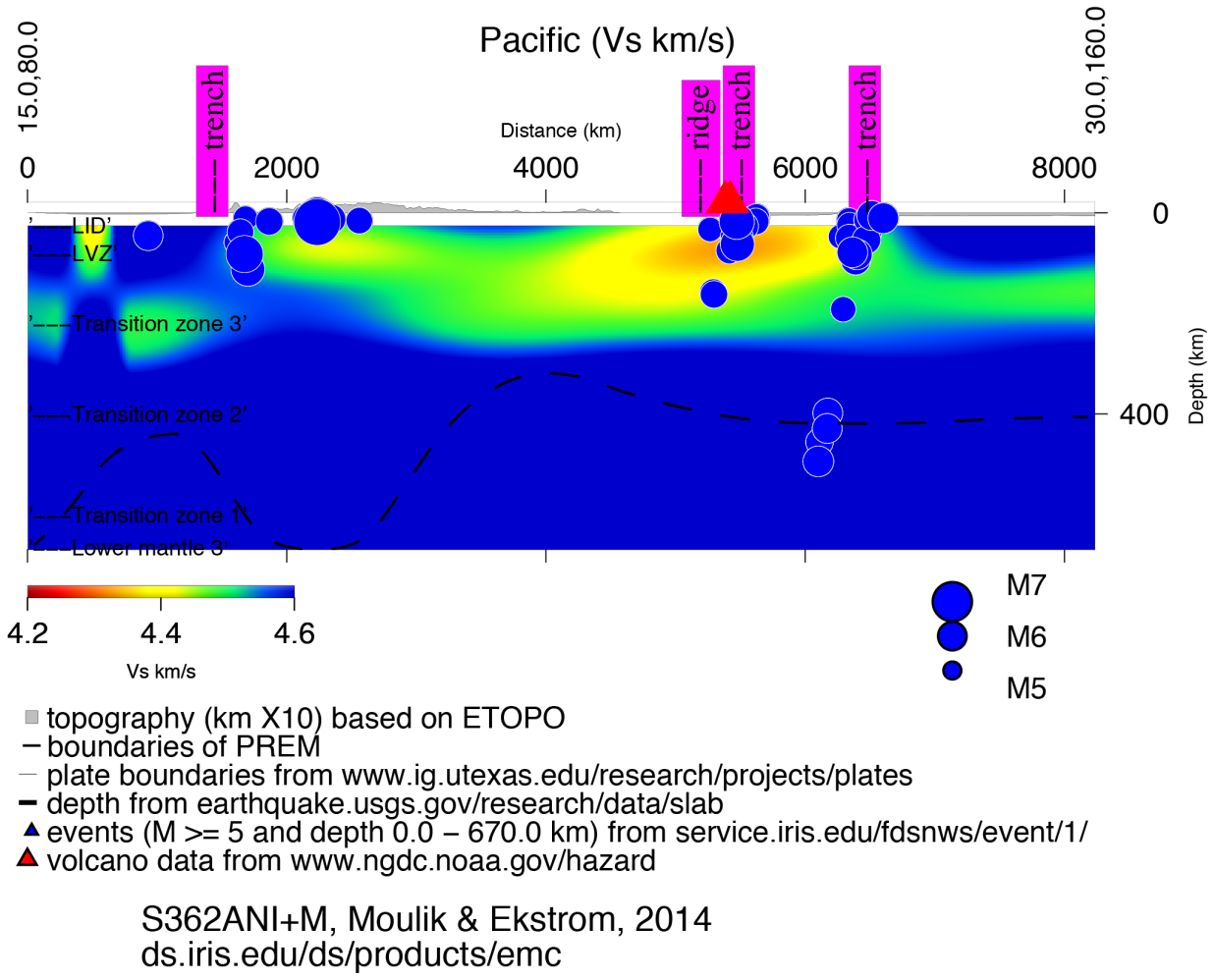

Figure 4.65 – Mantle tomography of the Pacific area. Here, although a subducting slab cannot be observed, the mantle tomography of the Pacific area shows that the rigid material (in blue) is mostly located below the Indo-Australian plates. In dashed line slab of model basic4 (Figure 4.20, lower panel) is comparable with location of the rigid material in this area. Vertical exaggeration 4x.

However, although our numerical models are not sufficiently constrained to analyze subduction zone dynamics and its relation with mantle convection in a shallow hotspot reference frame, i.e., using a global "westward" drift of the lithosphere, they underline the importance of including this feature in numerical models, giving directions for possible successful rheological profiles to use in future experiments. These are: i) the ASPECT's Simple Material model. In fact, model *basic4* (Figure 4.20) presents slab localization issues that could probably be solved including thickness and nature of the

lithosphere. In fact, these two features could change the resistance offered by the upper to the lower plate, together with the density and viscosity contrast between the upper and the lower plate, enhancing or inhibiting subduction of the oceanic plate; ii) the majorite-Fo50 and iii) the majorite-Fo89 rheological profiles. In these latter, the more successful models *majol1* and *majfo89_1*, with their good rheologic approximation and the geographical localization, seem to give advances to solve issues in *majol2* and *majfo89_2* with the introduction of both thickness and nature of the lithosphere. In fact, both models *majol1* and *majfo89_1* show correct subduction direction for the South American slab and well defined lithospheric slab reaching or slightly passing the 670 km discontinuity.

4.9 Final remarks

This Chapter aimed an analysis of the relationship between plate tectonics, i.e., the global westward drift of the lithosphere, and mantle convection using numerical modeling in 2d and 3d spherical geometry. Testing plate motions in different hotspot reference frames contributed to constrain numerical models. In this reference system all plates move towards the west along the tectonic equator although having different velocities. Starting from literature (e.g., Bangerth et al., 2018; Glerum et al., 2018; Heister et al., 2017; Kronbichler et al., 2012), one of the latest and advanced numerical code was used. ASPECT, in fact, is a code built on modern numerical methods, extensible and versatile that can reproduce a wide variety of Earth's processes, from a local to a global scale.
Furthermore, ASPECT allows to test different compositions and rheologies for the Earth's lithosphere and mantle by means of different already provided Material models that can be modified by the user, but the user itself can create its own customized Material models. The main challenge of this study was to find the perfect equilibrium between composition, i.e., viscosity, density, and surface kinematics that could accurately reproduce the dynamics between plate tectonics processes and mantle convection. Starting from simple models using the ASPECT's Simple Material model to the more complicated and customized ASCII Reference Profile Material models, different rheologies were tested. These models were realized using both absolute reference frames, i.e., deep (using rotation data collected by Seton et al., 2012) and shallow (as reported in Table 4.1) hotspots, and relative reference frames, i.e., using fixed South America and Marianas plates, and the 2d slice throughout which the spherical model was cut corresponds to the tectonic equator, i.e., the great circle representing the mainstream of plates towards the W (Doglioni & Panza, 2015, and references therein).
In conclusion, results of these experiments showed a primary importance of the surface kinematics and of the used rheology, together with the strong influence of the lithosphere thickness and nature

(i.e., continental or oceanic) when analyzing subduction zones dynamics using numerical models realized in a spherical shell domain. Models showed here, in fact, present laterally the same rheological and compositional characteristics throughout the entire spherical domain, rather changing at depth. This has a heavy influence on plate tectonics features, i.e., rift and subduction zones, being these first of all a consequence of lateral movements of lithospheric plates. Furthermore, the results obtained in this Chapter helped to select some rheological profiles (Simple Material Model, majorite-Fo50 and majorite-Fo89) that could be considered as a starting point for future research in the field of the interactions between the "westward" drift of the lithosphere and mantle convection.

Conclusions and future directions

The work presented in this dissertation aimed to present numerical models which suggest constraints on subduction zone dynamics. The main starting point for this research was the needs of numerical models which consider i) the horizontal mantle flow which interacts with tectonic plates; ii) the subduction hinge motion, that allows the correct estimation of the effective velocity with which subducting plates enter the mantle; iii) the LVZ decoupling layer between the lithosphere and the mantle, which allows their relative motion; iv) the global "westward" drift of the lithosphere.

To do this, the first step was a 2d numerical analysis using a rectangular box geometry in which the influence of an eastward mantle flow was tested also including a LVZ with a constant viscosity and in the fixed upper plate framework. These models results fit the observable asymmetric behaviour of subducting slabs and their hinge. W-directed slabs are pushed backwards by the eastward mantle flow together with their subduction hinge that moves away from the upper plate. These slabs show steep dip angles, high depths reached and backarc basins opening, i.e., extensional stresses within the upper plate (e.g., subduction zones on the western side of the Pacific Ocean). E-directed slabs, on the contrary, are sustained by the eastward mantle flow and have their hinge moving towards the upper plate. They show low dip angles, shallow depths and strong compressional stresses within the upper plates, which lead to the building of the worldwide highest mountain ranges (e.g., subduction zones on the eastern side of the Pacific Ocean).

This well-constrained scenario opened the possibility for future tests in which this same eastward mantle flow interacts with slabs having opposite geographic polarity attached to lithospheric plates that are laterally free to move. This would allow the observation of the interactions between the slab, the subduction hinge, the subduction trench and the state of stress within the upper plate.

To constrain the volume of lithosphere currently entering within the mantle at subduction zones and, consequently, the amount of mantle material that should be displaced to preserve the mass balancing criterion, the volume of lithosphere currently subducting at subduction zones worldwide has been computed. This computation was made distinguishing subduction zones on the basis of the different kinematics of their subduction hinge with respect to the fixed upper plate (i.e., the hinge H can either move away from the upper plate or towards it). Results highlighted a difference in volumes of subducted lithosphere, i.e., ~190 km^3/yr vs ~91 km^3/yr, and in the subduction rate between the considered end-members subductions, suggesting an asymmetric dynamics at subduction zones. A further 2d numerical modeling analysis in a rectangular box-shaped domain has been made, using the subduction rate in place of the convergence rate as boundary condition. This supported and enforced the obtained asymmetric behaviour. It has also been noted that most of the subduction zones with an

H-divergent behaviour is characterized by a mainly W-directed slab and extensional stresses within the upper plate whereas subduction zones with a H-convergent behaviour are mostly characterized by a mainly E-to-NE-directed slab and strong compressional stresses within the upper plate.

In the last part of this PhD project the passage to 2d numerical experiments using a spherical domain was a further advance. Surface plate kinematics in a shallow hotspot reference frame is the kinematic constraint of the geodynamic model taken as a reference in this dissertation. In this reference frame all the plates follow a "westward" direction along the tectonic equator, albeit having different velocity. This difference in plates velocities is related to difference in the asthenosphere viscosity and, thus, in the degree of coupling between the lithosphere and the asthenospheric mantle. The higher the viscosity of the asthenosphere the lower the velocity of the correspondent plate and vice-versa. This kinematic setting was included in numerical models as surface boundary condition with the attempt of reproducing the asymmetric features of plate tectonics evidenced by geological observations and geophysical signatures. Using the finite elements ASPECT code for mantle convection, we first started testing simple pre-setted rheological profiles, arriving to more complicated and customized rheological profiles at the end of our analysis. This analysis showed the importance of i) the reference frame in which plate motions are computed, ii) the used rheological profile and the introduction of lateral heterogeneities in the models and iii) the lateral variation in thickness and type of lithosphere (i.e., continental or oceanic). Furthermore, iv) a 3d spherical domain helped in solving problems related to localization of subduction zones, whereas v) models with velocities relative to fixed South America and Marianas plates suggested the important role of the upper plate at subduction zones. In fact, the fixed upper plate offered more resistance to the lower subducting plate, allowing a better slab dynamics. The same resistance could be offered by a thicker continental upper plate with respect to a thinner oceanic subducting plate. Thus, it is fundamental to include lateral variation in lithosphere thickness and nature, that represent indeed a consistent starting point for future research work aiming to reproduce interactions between the "westward" drift of the lithosphere and mantle convection.

Appendix A

In this Appendix A data and additional models related to the work presented in Chapter 2 are shown. First will be shown a summary table with main parameters and results of models presented in Chapter 2 (Figure 2.4).

Model	V_a (J/bar)	α (1/K)	Low Velocity Zone	Mantle Flow Direction	Mantle Flow Velocity (cm/yr)	Slab Dip Angle (°)	Back-arc spreading	Oceanic plate age (Myr)
a	1.20	2.00×10^{-5}	Yes	Negative	3.00	74	Yes	20
1	1.40	2.00×10^{-5}	Yes	Negative	3.00	56	Yes	20
2	1.40	3.00×10^{-5}	Yes	Negative	3.00	59	Yes	20
3	1.20	1.00×10^{-5}	Yes	Negative	3.00	63	Yes	20
4	1.40	1.00×10^{-5}	Yes	Negative	3.00	74	Yes	20
6	1.20	3.00×10^{-5}	Yes	Negative	3.00	59	Yes	40
7	1.20	2.00×10^{-5}	Yes	Negative	1.00	45	Yes	40
b	1.20	2.00×10^{-5}	Yes	Positive	3.00	17.5	No	40
8	1.20	3.00×10^{-5}	Yes	Positive	3.00	20.5	No	20
9	0.80	2.00×10^{-5}	Yes	Positive	3.00	30	No	20
10	1.40	2.00×10^{-5}	Yes	Positive	3.00	17.5	No	20
11	1.40	3.00×10^{-5}	Yes	Positive	3.00	17.5	No	20
13	1.20	3.00×10^{-5}	Yes	Positive	3.00	35.5	No	40
14	1.00	3.00×10^{-5}	Yes	Positive	3.00	31	No	40
Ref.1	1.00	3.00×10^{-5}	No	Negative	3.00	78.5	Yes	40
Ref.2	1.20	2.00×10^{-5}	No	Positive	3.00	17.5	No	40
Ref.3	0.80	3.00×10^{-5}	Yes	Null	0.00	67	No	150
Ref.4	0.80	3.00×10^{-5}	No	Null	0.00	52.2	No	150

Table A.1 – Conditions and results of 2D numerical models showed in Chapter 2 and in this Appendix A. Slabs dip in the range of 40°-90° were found for W-directed slabs, while the dip found for E- or SE-directed slabs was within the range of 15°-40°. In bold the reference models commented in Chapter 2.

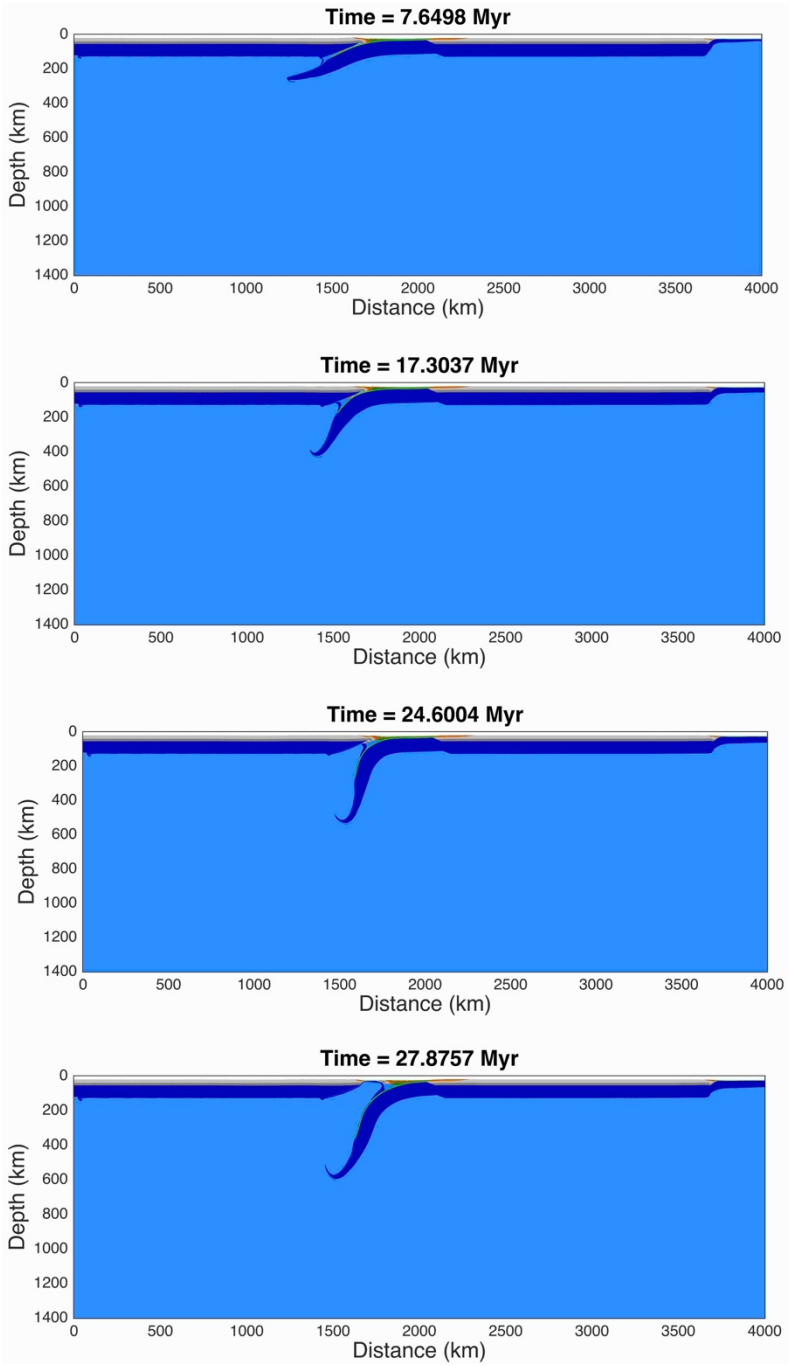

Figure A.1 – Westward-like subduction model with LVZ and horizontal eastward mantle wind. This model has an older age of the oceanic subducting plate and a lower velocity of the mantle wind, with respect to the model in Figure 2.4a in Chapter 2 (Table A.1, model 7 and a, in bold, respectively). In this case the dip angle of the slab is steep (~45°), but not as much as the one of model in Figure 2.4a in Chapter 2, although its older age. This leads to the conclusion that the age of the slab has a minor role in affecting subduction dynamics, with respect to the role of the velocity of the horizontal mantle wind. In fact, model 7 here, has a lower dip angle due to the lower velocity of the mantle flow pushing the slab downward. A backarc basin is opening (as in all westward-like models cases).

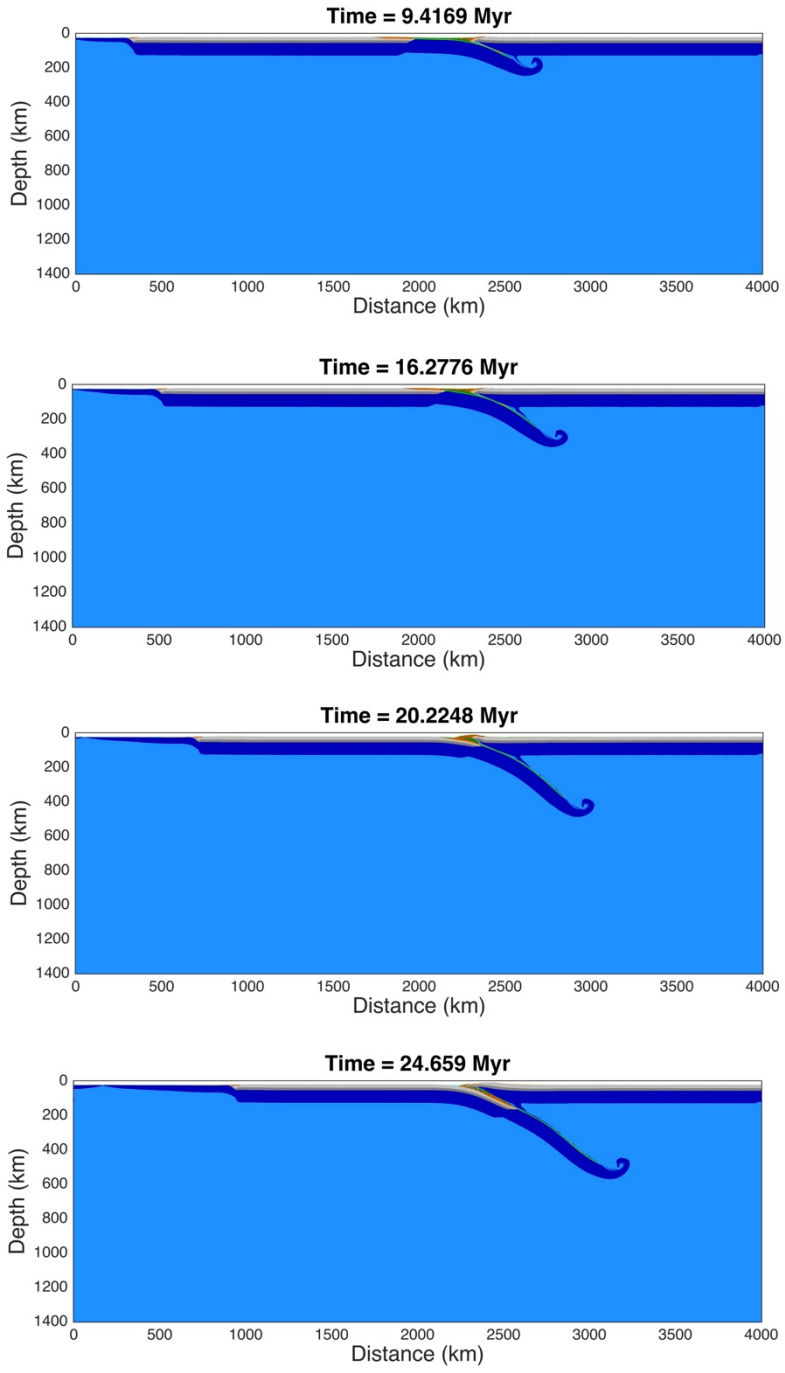

Figure A.2 – Eastward-like subduction model with LVZ and horizontal eastward mantle wind. The slab has a low dip angle (Table A.1, model 13) and at some point (at around 19.5 Myr) collision occurs and, therefore, there is not backarc spreading in the upper plate. In this case, the dip angle is higher than in the "eastward-like" model in Chapter 2 (Table A.1, model b, in bold), probably due to the double effect between a high thermal expansion value and a high activation volume value. Despite this, we have the same sustaining effect of the mantle acting on the subducting slab that model with the eastward-directed subduction shows in Chapter 2 (Figure 2.4b).

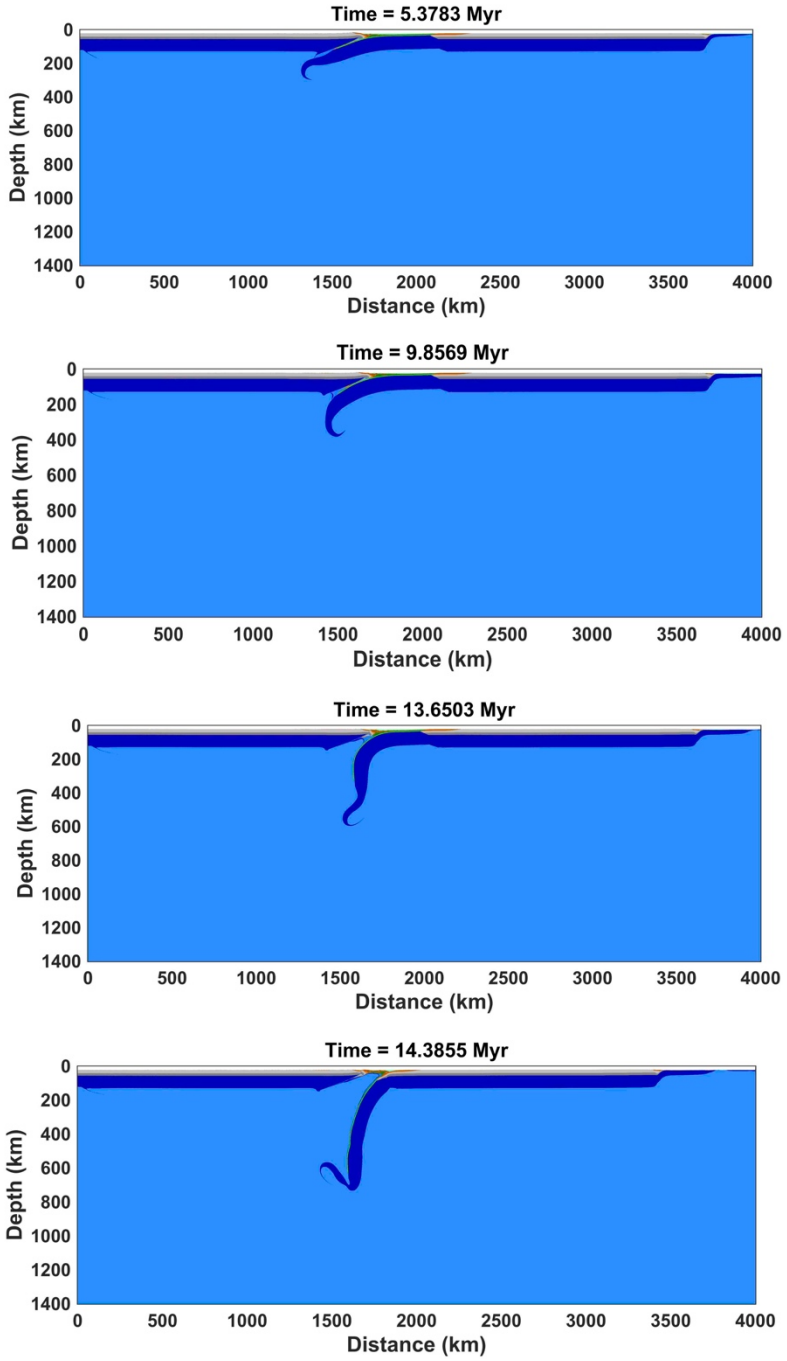

Figure A.3 – Westward-like subduction model without LVZ, with the horizontal eastward mantle flow. Here the mantle flux is considered as negative (i.e., with an opposite direction with respect to the subduction direction): the dip of the slab has a steep angle (Table A.1, model Ref. 1), and there is a backarc opening on the upper plate, like in the other westward-like subduction models (Table A.1). Subduction in this case is very fast.

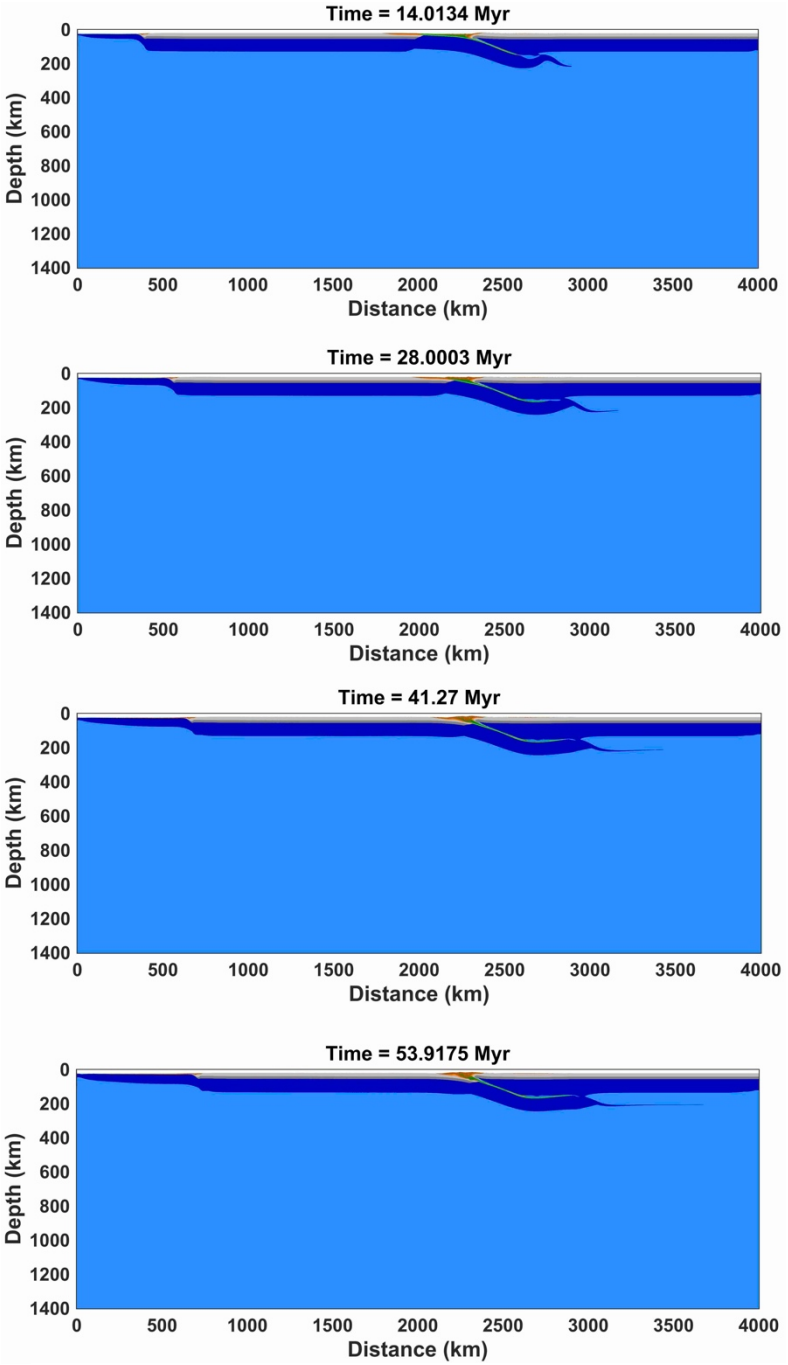

Figure A.4 - Eastward-like subduction model without LVZ, with the horizontal eastward mantle flow. Here (Table A.1, model Ref. 2) mantle flux is considered as positive (i.e., with the same direction of the subducting slab): the oceanic subducting slab is sustained by the mantle flow, but the absence of the decoupling level between the lithosphere and the mantle causes a strong coupling between the upper and the lower plate. In fact, the slab (that has a dip angle of ~17.5°) is right under the upper plate during the whole subduction process.

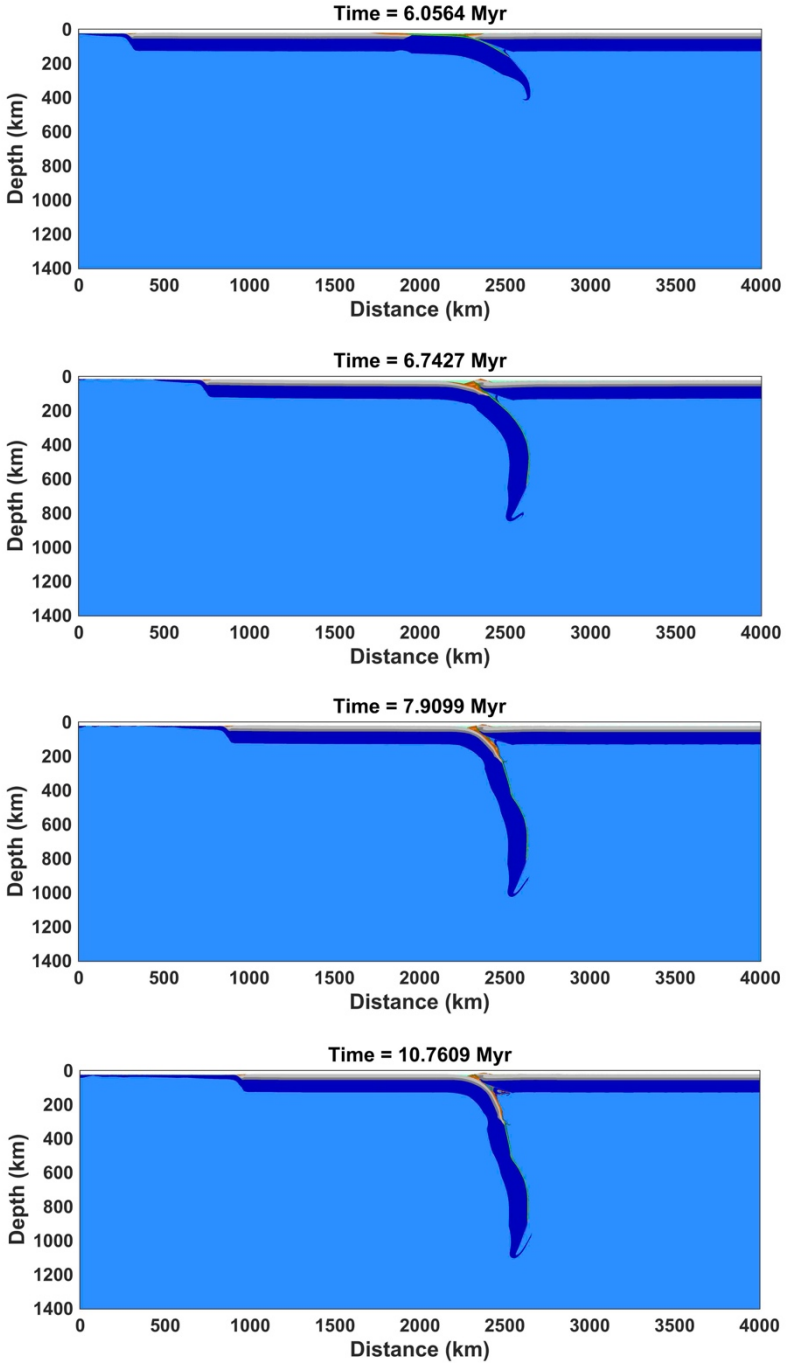

Figure A.5 - Subduction model with LVZ, but without the horizontal eastward mantle flow. For model without mantle wind (Table A.1, model Ref. 3), the age of the subducted lithosphere that facilitate subduction is much more higher (150 Myr) than the one used in models with mantle wind. Substantially, slabs undergo subduction for older age values of the oceanic plate. All the slabs presented in Chapter 2 and Appendix A, instead, could subduct with younger ages (and this is actually what can be observed in nature). For this model the slab dip angle is about 67° (an almost intermediate value).

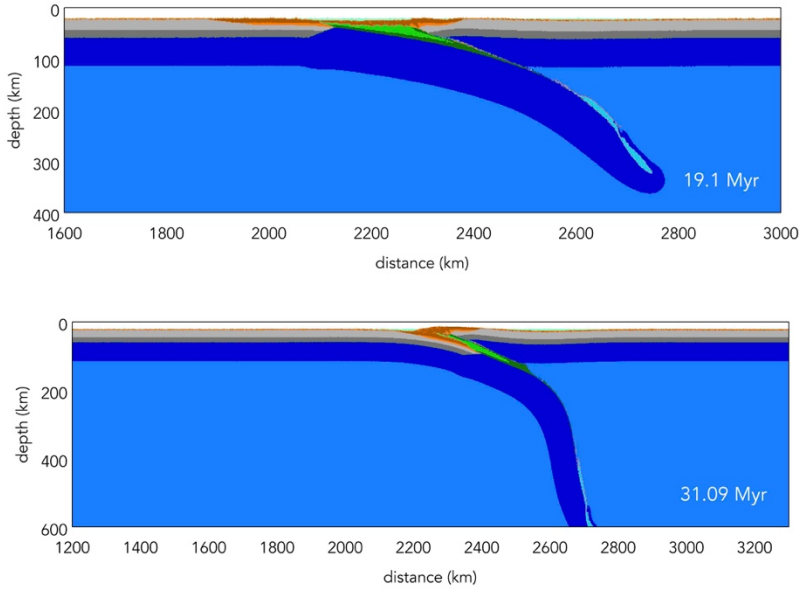

Figure A.6 - Subduction model without LVZ and without the horizontal eastward mantle flow. Also in case of model without mantle flow and without LVZ (Table A.1, model Ref. 4), the age of the subducted lithosphere required for the sinking of the slab is higher (150 Myr) than the one used for the other models (Table A.1). In this reference model the dip angle of the subducting slab has an intermediate value (~52.18°) between the E-directed models and the W-directed ones (Table A.1).

Appendix B

In this Appendix B will be shown velocities and temperature for intermediate steps, i.e., between 140 and 0 Myr, of numerical model results already shown in Chapter 4. Furthermore, models *majfo89_sa* and *ma* will be described. First models in 2d and in absolute reference frames will be shown, then models in 2d and relative reference frames, lastly models in 3d and absolute reference frames.

B.1 2d results in absolute reference frames

B.1.1 basic1 (Simple Material model)

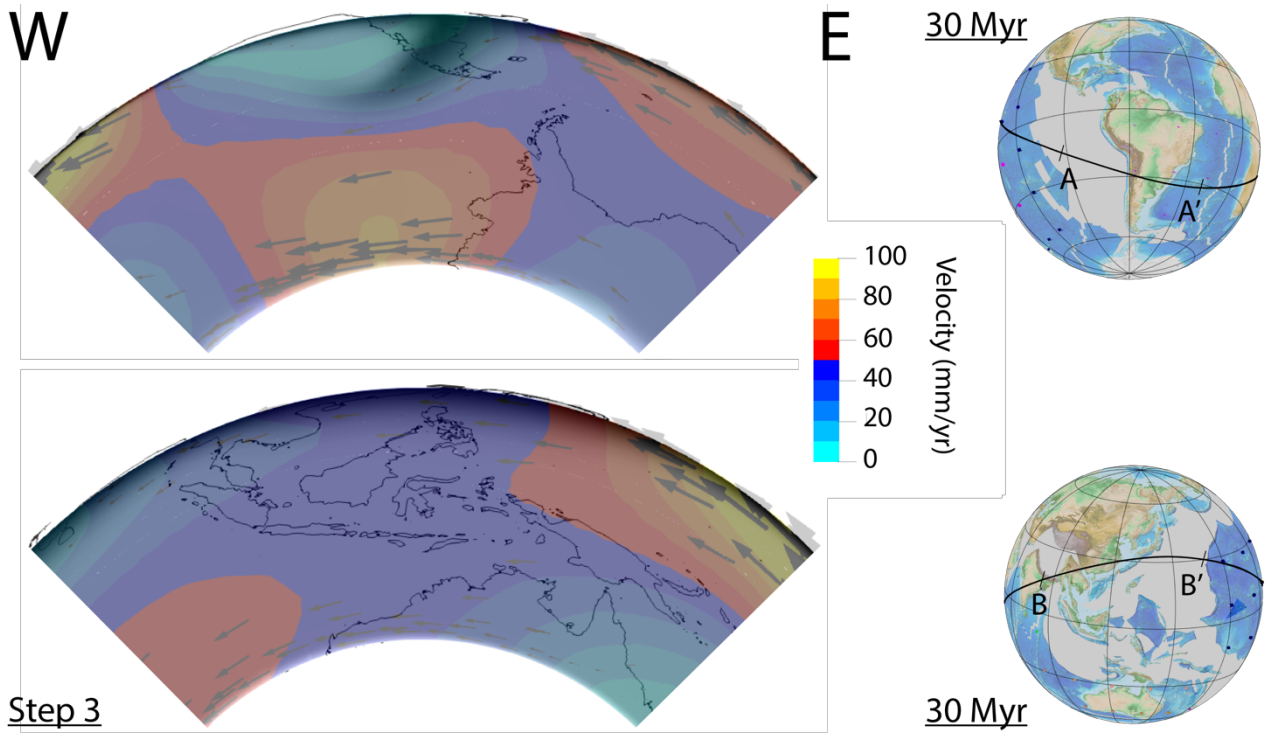

Figure B.1 – Step 3 (i.e., 30 Myr) for South American (upper panel) and Pacific (lower panel) side of model basic1. Temperature (black shadow) and velocity (colored data plus arrows) data are overlapped for step 3 of model basic1. Globes in the right part of the figure shows plate kinematics at 30 Myr in a deep hotspot reference frame. The black line corresponds to the tectonic equator.

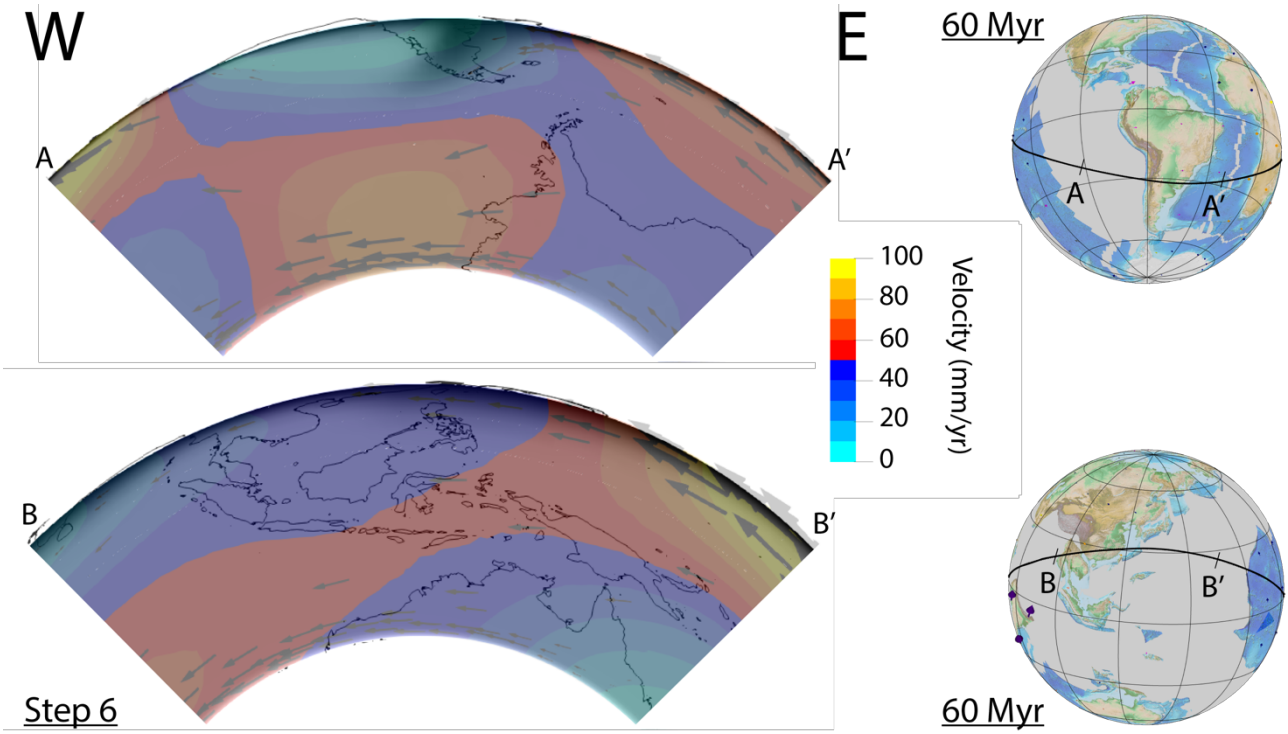

Figure B.2 – Step 6 (i.e., 60 Myr) for South American (upper panel) and Pacific (lower panel) side of model basic1. Temperature (black shadow) and velocity (colored data plus arrows) data are overlapped for step 6 of model basic1. Globes in the right part of the figure show plate kinematics at 60 Myr in a deep hotspot reference frame. The black line corresponds to the tectonic equator.

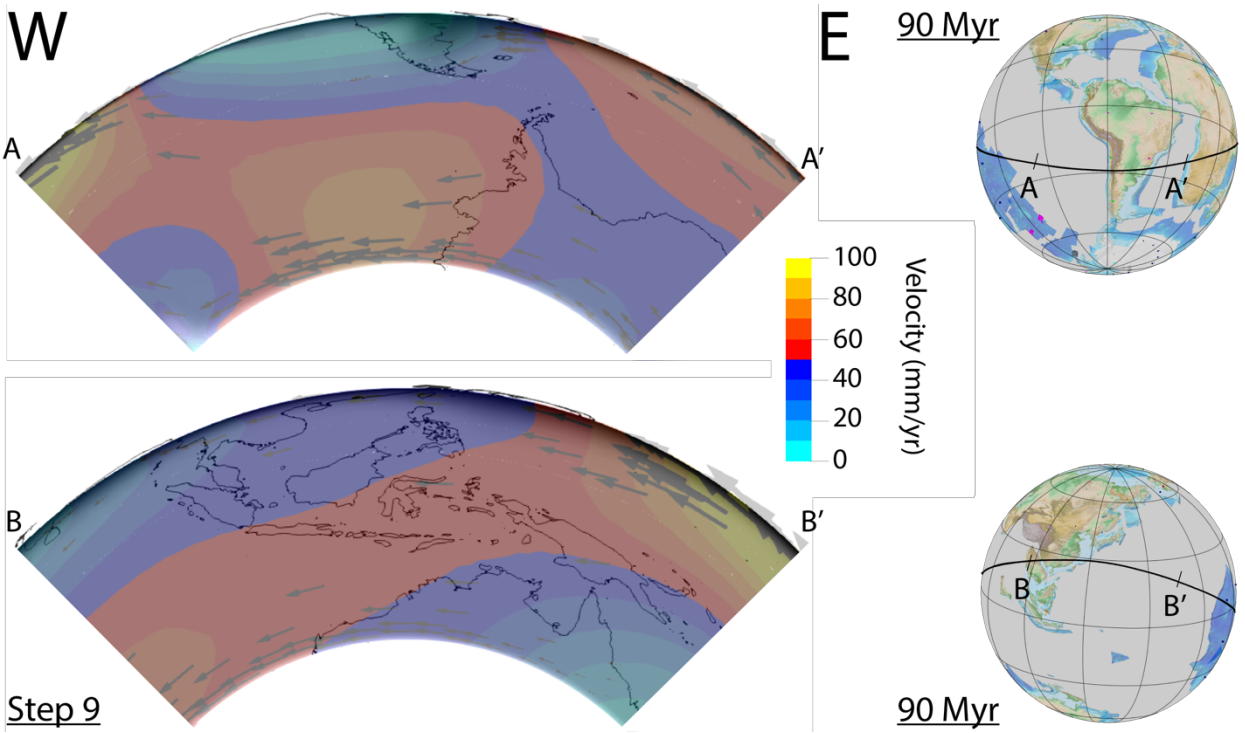

Figure B.3 – Step 9 (i.e., 90 Myr) for South American (upper panel) and Pacific (lower panel) side of model basic1. Temperature (black shadow) and velocity (colored data plus arrows) data are overlapped for step 9 of model basic1. Globes in the right part of the figure shows plate kinematic at 90 Myr in a deep hotspot reference frame. The black line corresponds to the tectonic equator.

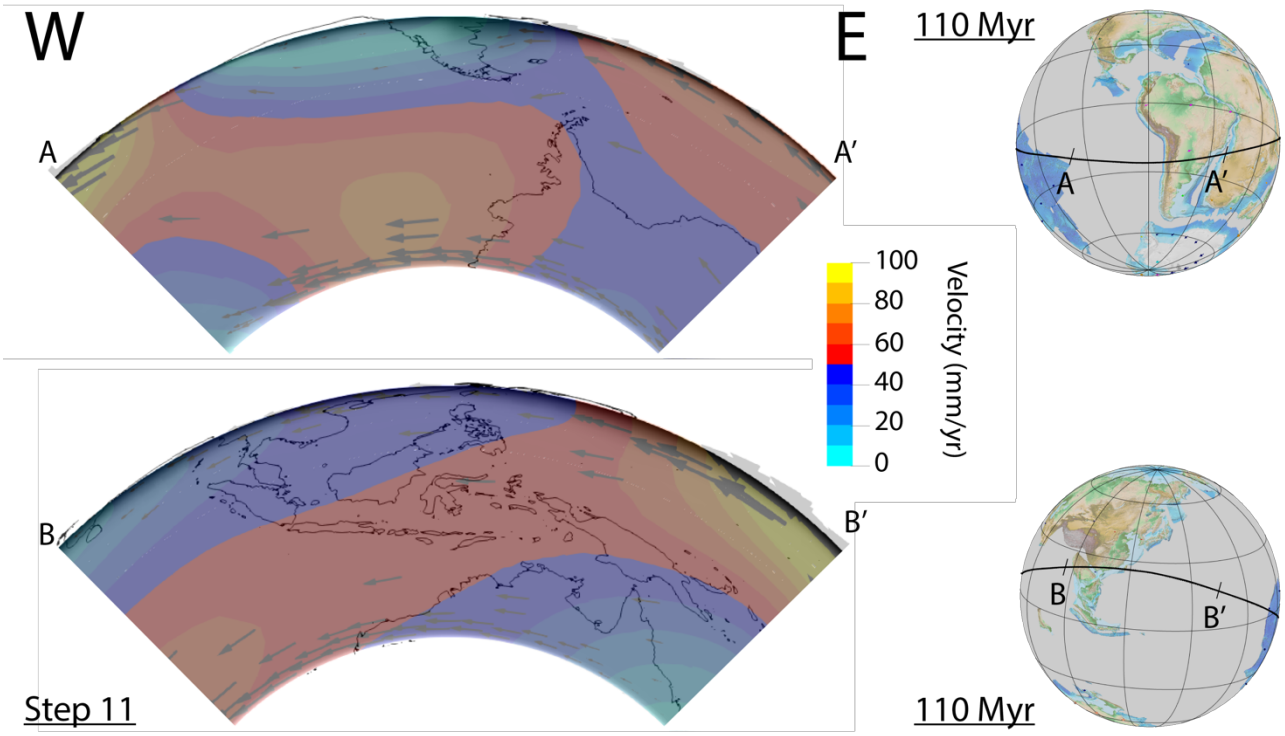

Figure B.4 – Step 11 (i.e., 110 Myr) for South American (upper panel) and Pacific (lower panel) side of model basic1. Temperature (black shadow) and velocity (colored data plus arrows) data are overlapped for step 11 of model basic1. Globes in the right part of the figure shows plate kinematic at 110 Myr in a deep hotspot reference frame. The black line corresponds to the tectonic equator.

B.1.2 basic2 (Simple Material model)

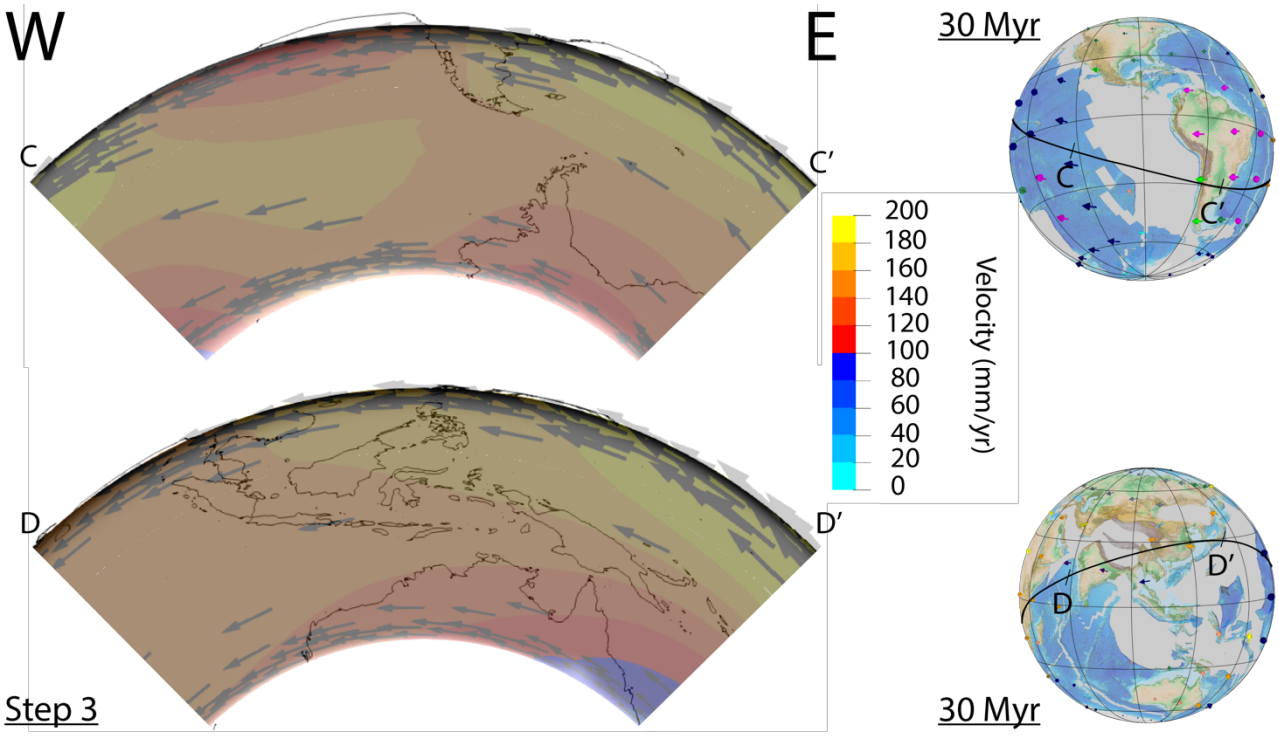

Figure B.5 – Step 3 (i.e., 30 Myr) for South American (upper panel) and Pacific (lower panel) side of model basic2. Temperature (black shadow) and velocity (colored data plus arrows) data are overlapped for step 3 of model basic2. Globes in the right part of the figure shows plate kinematic at 30 Myr in a shallow hotspot reference frame. The black line corresponds to the tectonic equator.

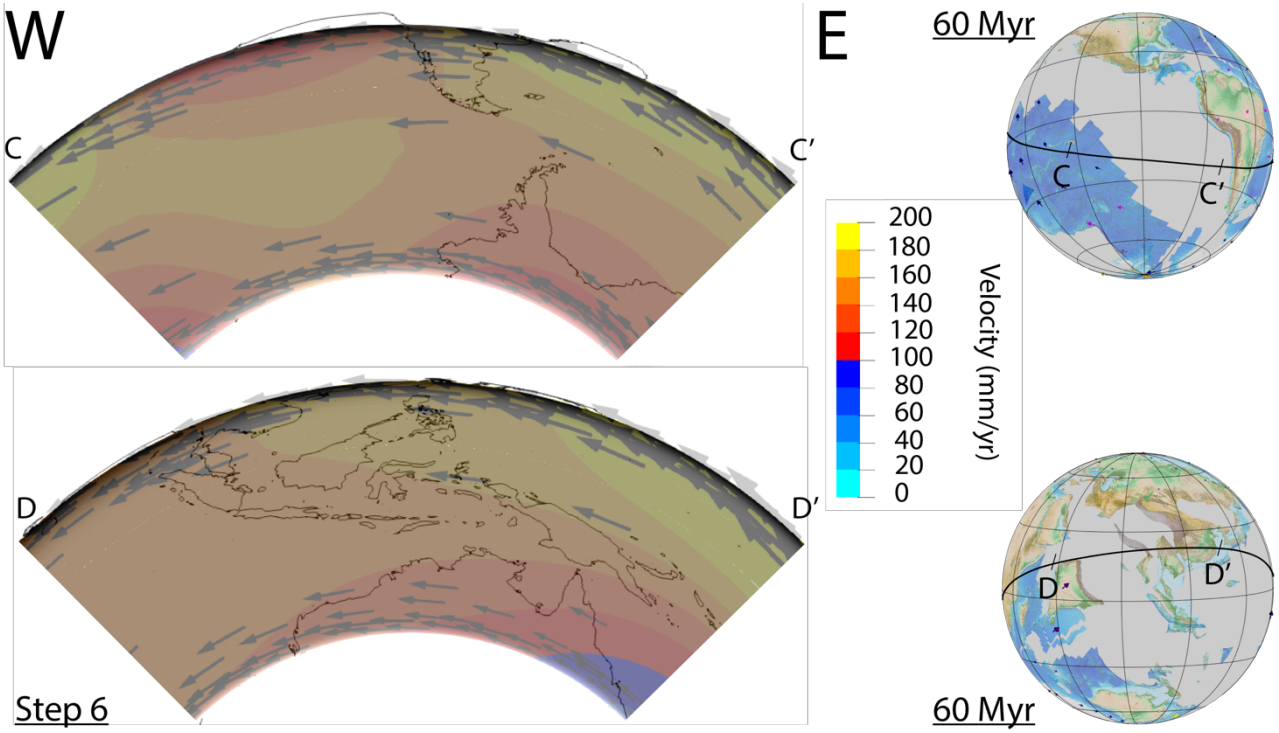

Figure B.6 – Step 6 (i.e., 60 Myr) for South American (upper panel) and Pacific (lower panel) side of model basic2. Temperature (black shadow) and velocity (colored data plus arrows) data are overlapped for step 6 of model basic2. Globes in the right part of the figure shows plate kinematic at 60 Myr in a shallow hotspot reference frame. The black line corresponds to the tectonic equator.

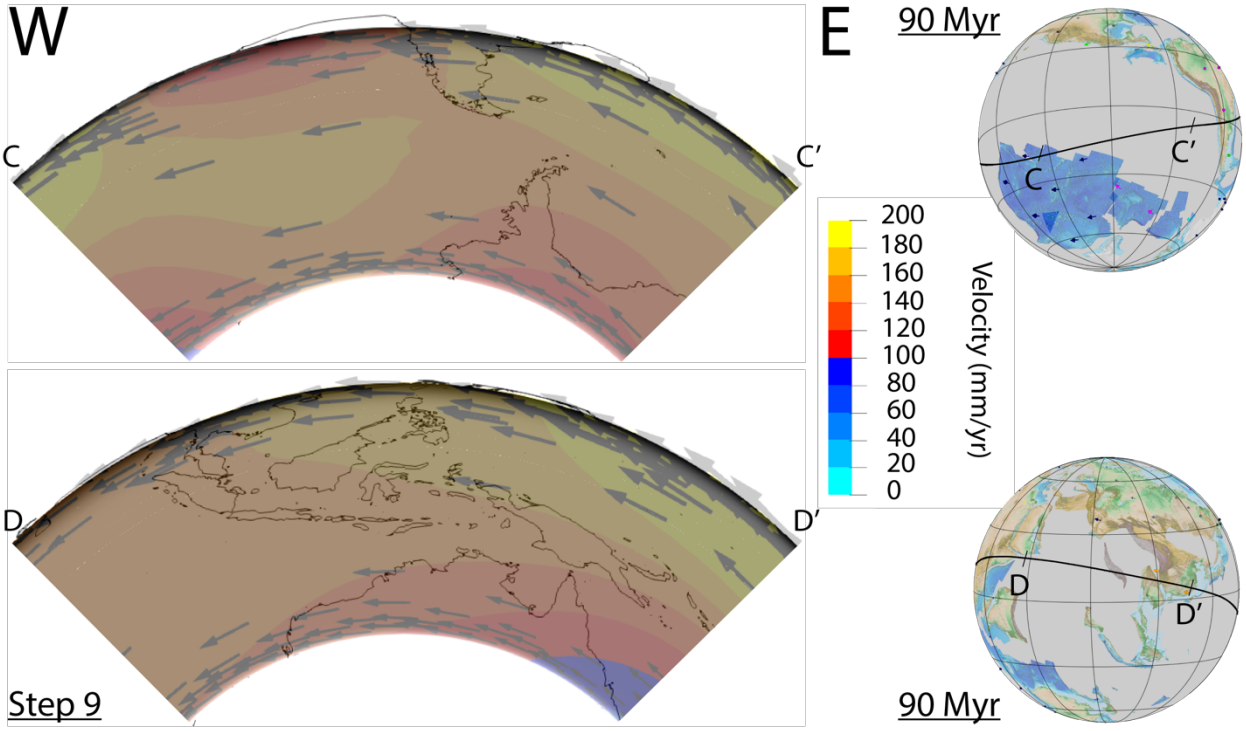

Figure B.7 – Step 9 (i.e., 90 Myr) for South American (upper panel) and Pacific (lower panel) side of model basic2. Temperature (black shadow) and velocity (colored data plus arrows) data are overlapped for step 9 of model basic2. Globes in the right part of the figure shows plate kinematic at 90 Myr in a shallow hotspot reference frame. The black line corresponds to the tectonic equator.

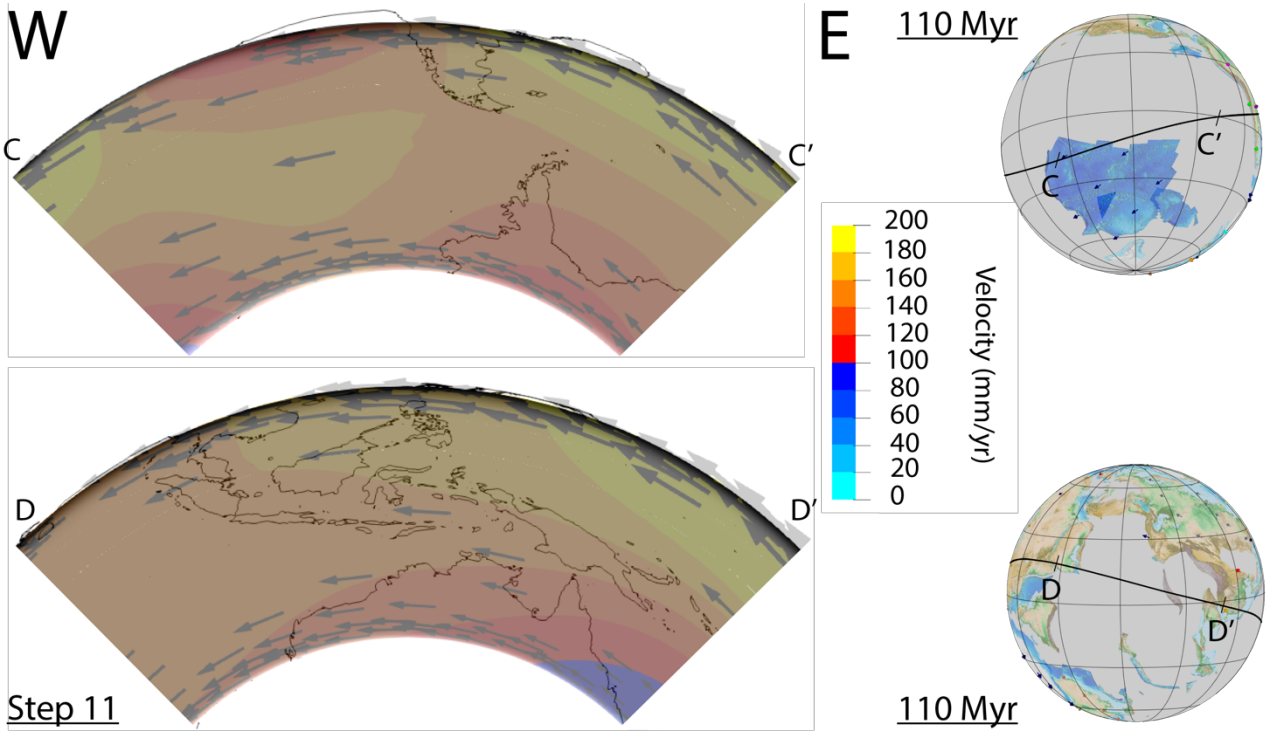

Figure B.8 – Step 11 (i.e., 110 Myr) for South American (upper panel) and Pacific (lower panel) side of model basic2. Temperature (black shadow) and velocity (colored data plus arrows) data are overlapped for step 11 of model basic1. Globes in the right part of the figure shows plate kinematic at 110 Myr in a shallow hotspot reference frame. The black line corresponds to the tectonic equator.

B.1.3 basic3 (Simple Material model)

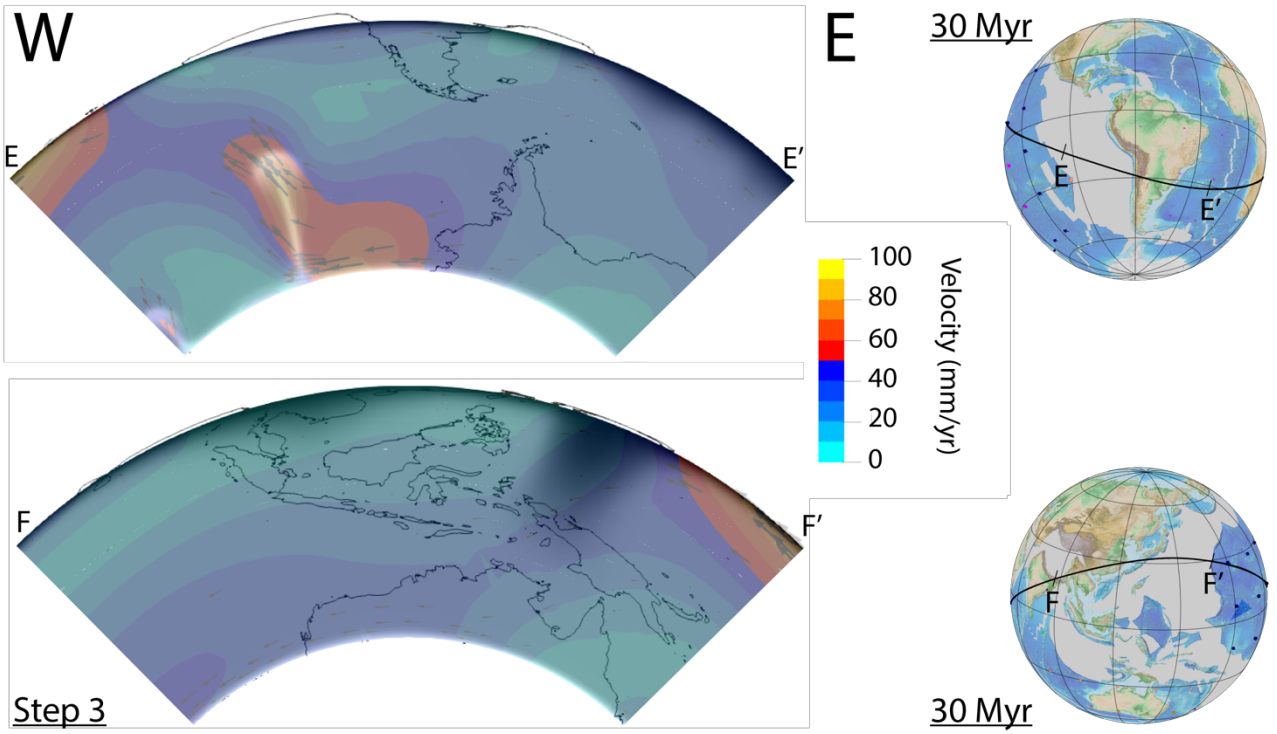

Figure B.9 – Step 3 (i.e., 30 Myr) for South American (upper panel) and Pacific (lower panel) side of model basic3. Temperature (black shadow) and velocity (colored data plus arrows) data are overlapped for step 3 of model basic3. Globes in the right part of the figure shows plate kinematic at 30 Myr in a deep hotspot reference frame. The black line corresponds to the tectonic equator.

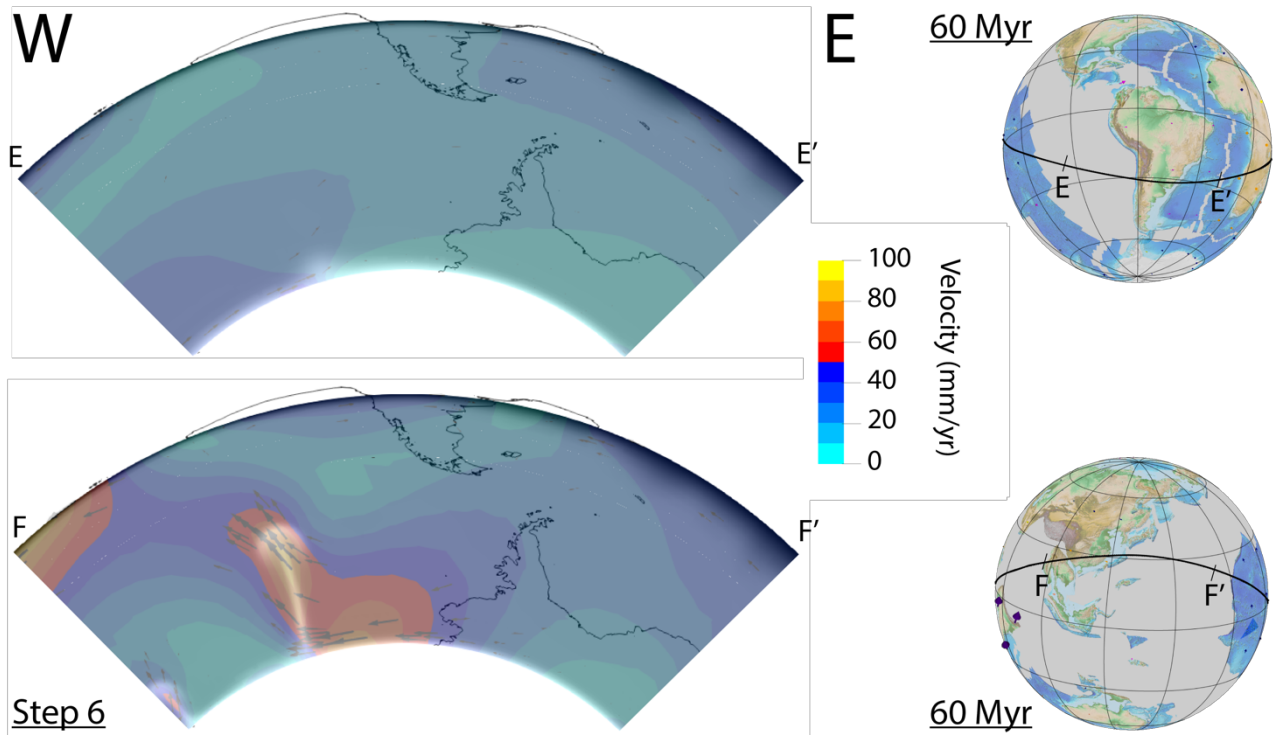

Figure B.10 – Step 6 (i.e., 60 Myr) for South American (upper panel) and Pacific (lower panel) side of model basic3. Temperature (black shadow) and velocity (colored data plus arrows) data are overlapped for step 6 of model basic3. Globes in the right part of the figure shows plate kinematic at 60 Myr in a deep hotspot reference frame. The black line corresponds to the tectonic equator.

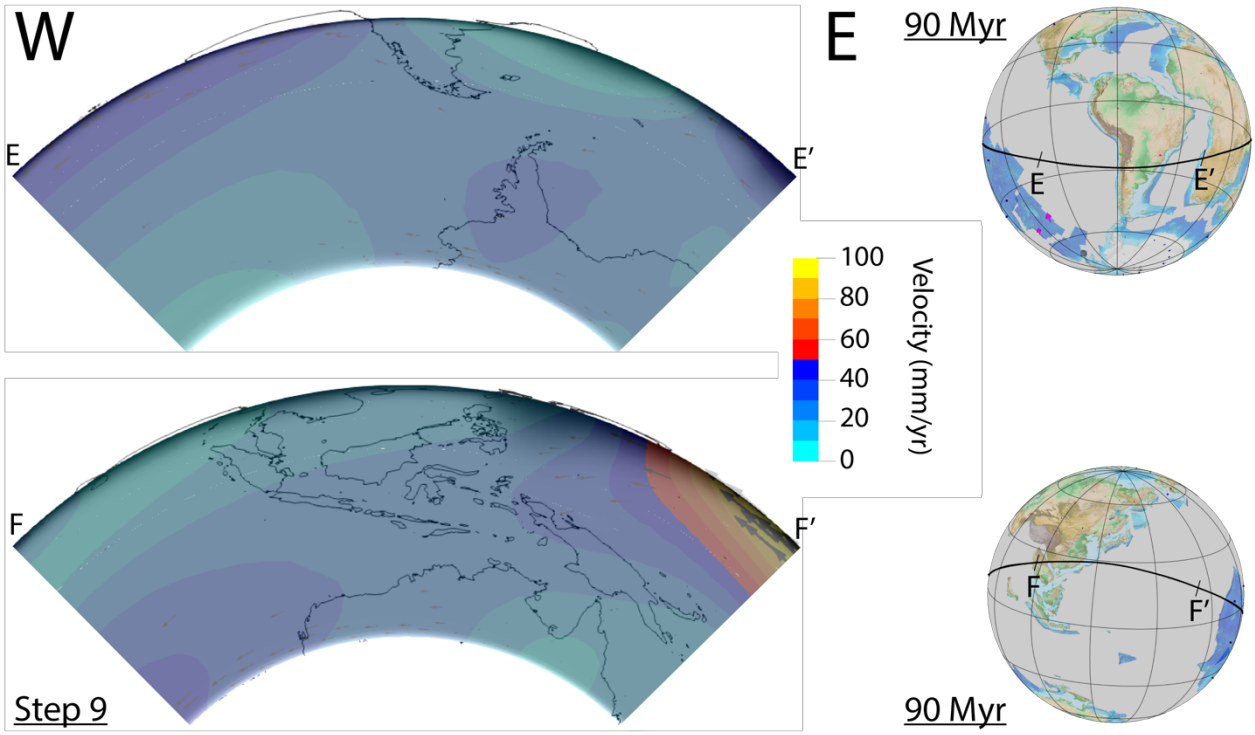

Figure B.11– Step 9 (i.e., 90 Myr) for South American (upper panel) and Pacific (lower panel) side of model basic3. Temperature (black shadow) and velocity (colored data plus arrows) data are overlapped for step 9 of model basic3. Globes in the right part of the figure shows plate kinematic at 90 Myr in a deep hotspot reference frame. The black line corresponds to the tectonic equator.

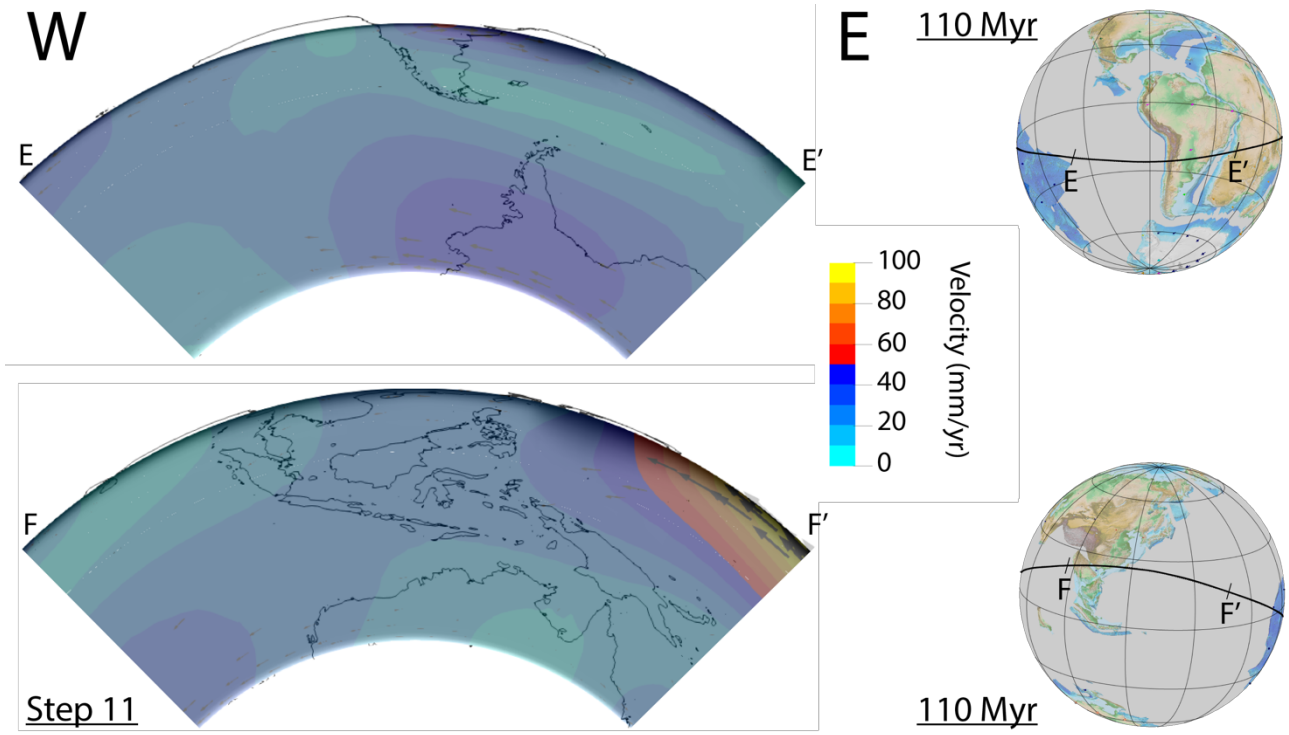

Figure B.12 – Step 11 (i.e., 110 Myr) for South American (upper panel) and Pacific (lower panel) side of model basic3. Temperature (black shadow) and velocity (colored data plus arrows) data are overlapped for step 11 of model basic3. Globes in the right part of the figure shows plate kinematic at 110 Myr in a deep hotspot reference frame. The black line corresponds to the tectonic equator.

B.1.4 basic4 (Simple Material model)

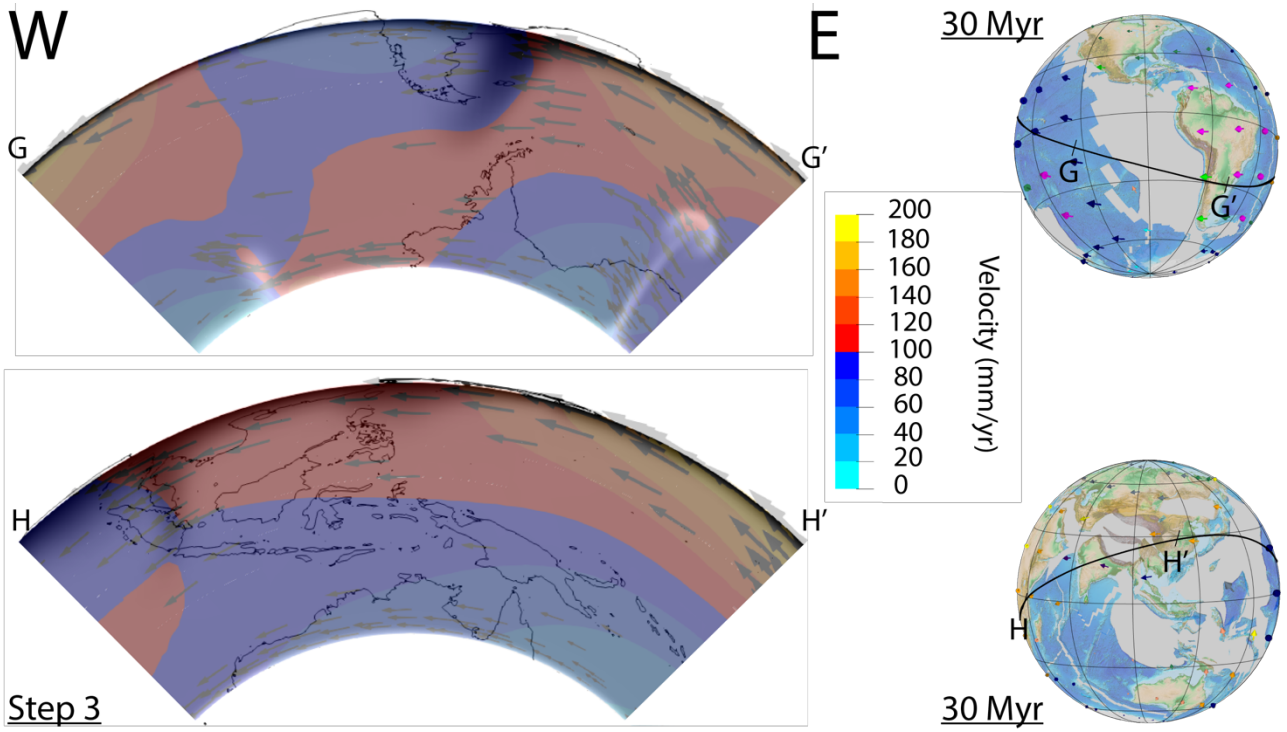

Figure B.13 – Step 3 (i.e., 30 Myr) for South American (upper panel) and Pacific (lower panel) side of model basic4. Temperature (black shadow) and velocity (colored data plus arrows) data are overlapped for step 3 of model basic4. Globes in the right part of the figure shows plate kinematic at 30 Myr in a shallow hotspot reference frame. The black line corresponds to the tectonic equator.

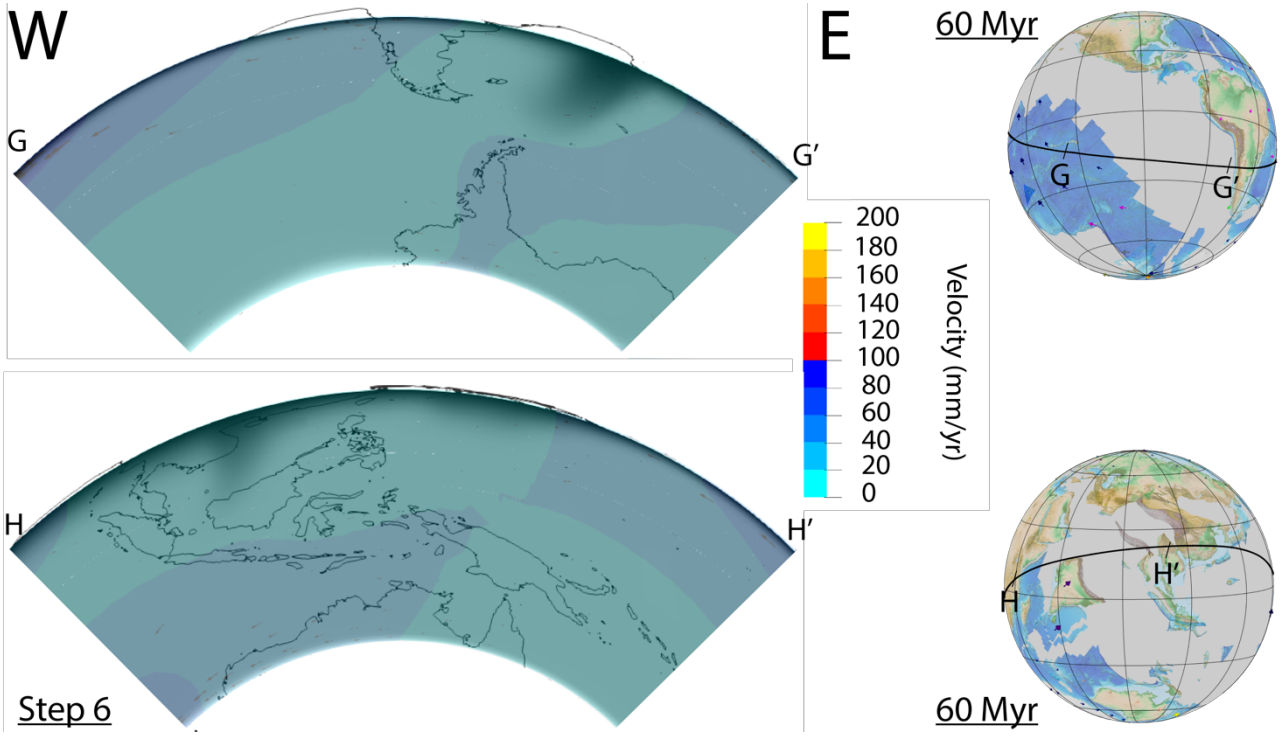

Figure B.14 – Step 6 (i.e., 60 Myr) for South American (upper panel) and Pacific (lower panel) side of model basic4. Temperature (black shadow) and velocity (colored data plus arrows) data are overlapped for step 6 of model basic4. Globes in the right part of the figure shows plate kinematic at 60 Myr in a shallow hotspot reference frame. The black line corresponds to the tectonic equator.

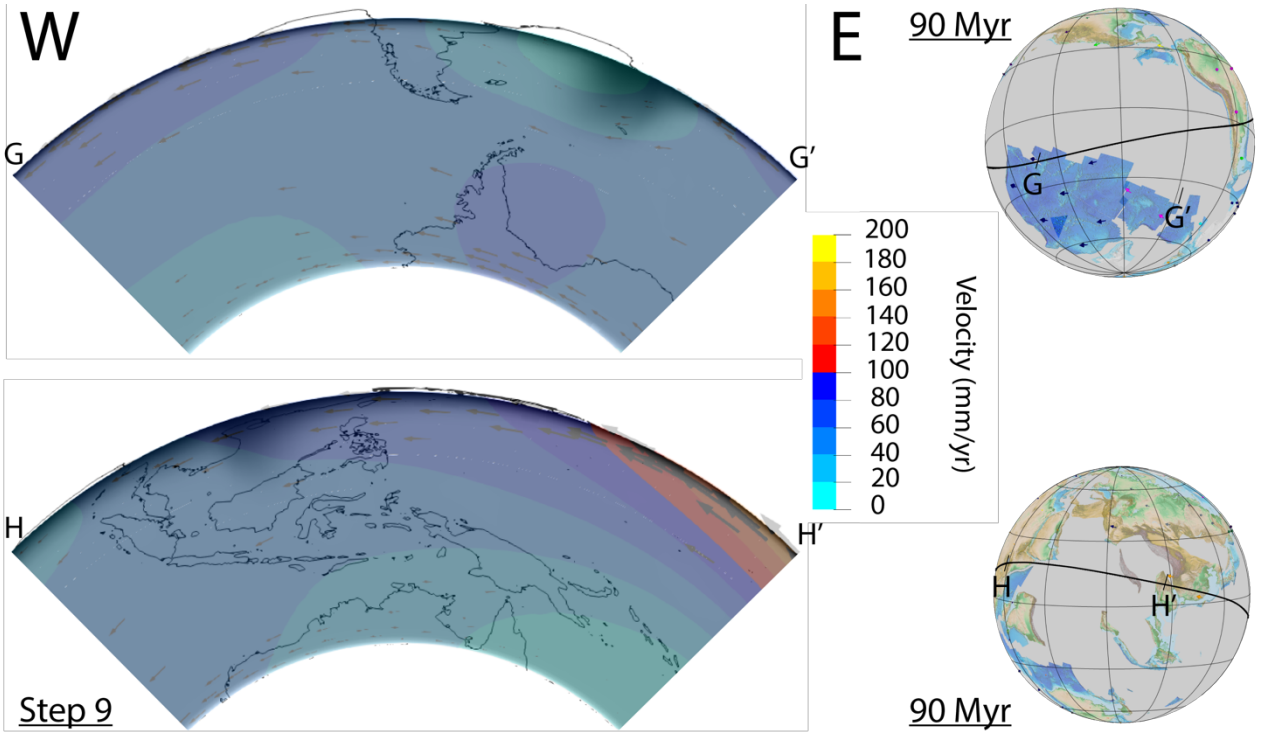

Figure B.15 – Step 9 (i.e., 90 Myr) for South American (upper panel) and Pacific (lower panel) side of model basic4. Temperature (black shadow) and velocity (colored data plus arrows) data are overlapped for step 9 of model basic4. Globes in the right part of the figure shows plate kinematic at 90 Myr in a shallow hotspot reference frame. The black line corresponds to the tectonic equator.

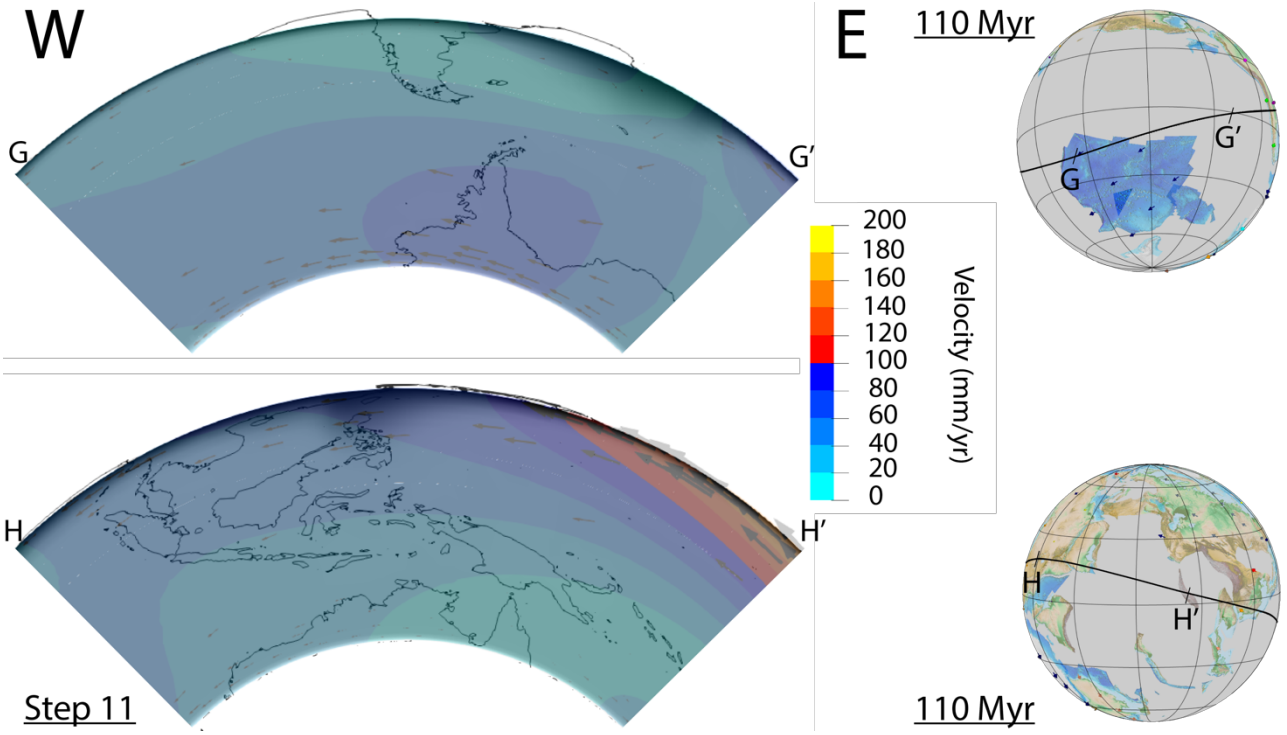

Figure B.16 – Step 11 (i.e., 110 Myr) for South American (upper panel) and Pacific (lower panel) side of model basic4. Temperature (black shadow) and velocity (colored data plus arrows) data are overlapped for step 11 of model basic4. Globes in the right part of the figure shows plate kinematic at 110 Myr in a shallow hotspot reference frame. The black line corresponds to the tectonic equator.

B.1.5 vp1 (Visco plastic Material model)

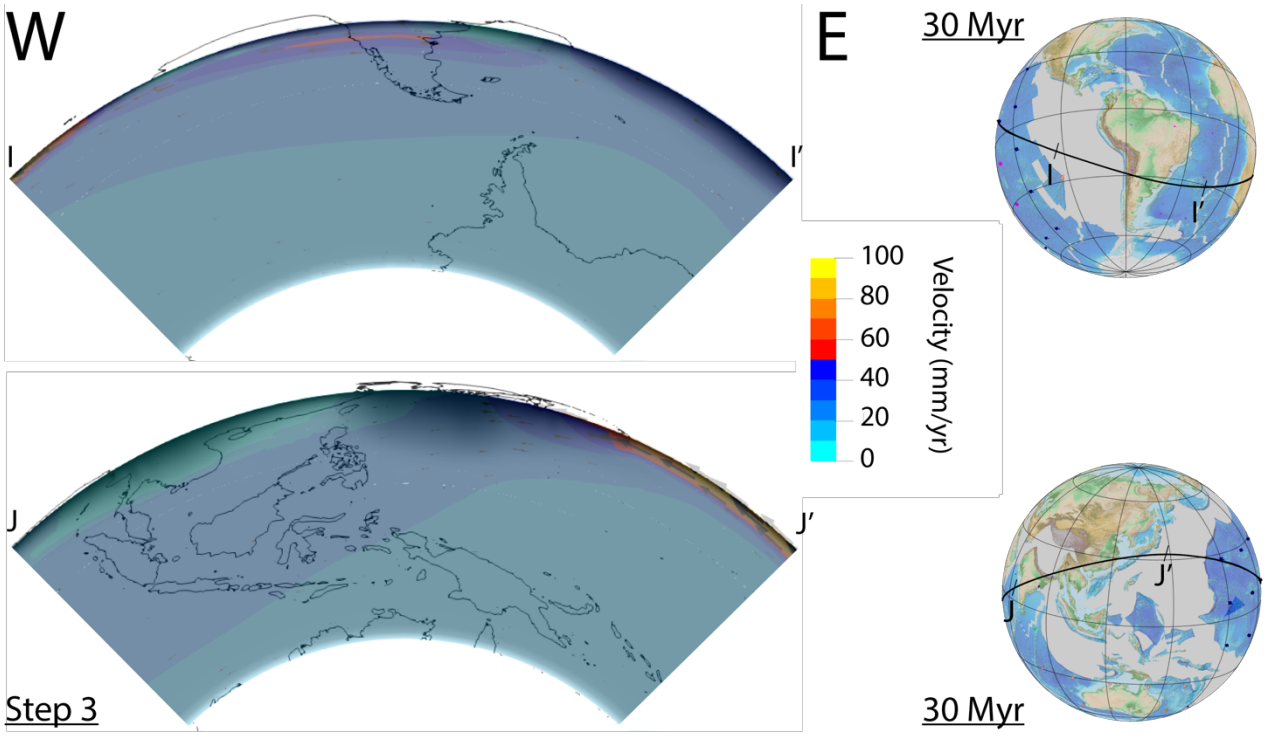

Figure B.17 – Step 3 (i.e., 30 Myr) for South American (upper panel) and Pacific (lower panel) side of model vp1. Temperature (black shadow) and velocity (colored data plus arrows) data are overlapped for step 3 of model vp1. Globes in the right part of the figure shows plate kinematic at 30 Myr in a deep hotspot reference frame. The black line corresponds to the tectonic equator.

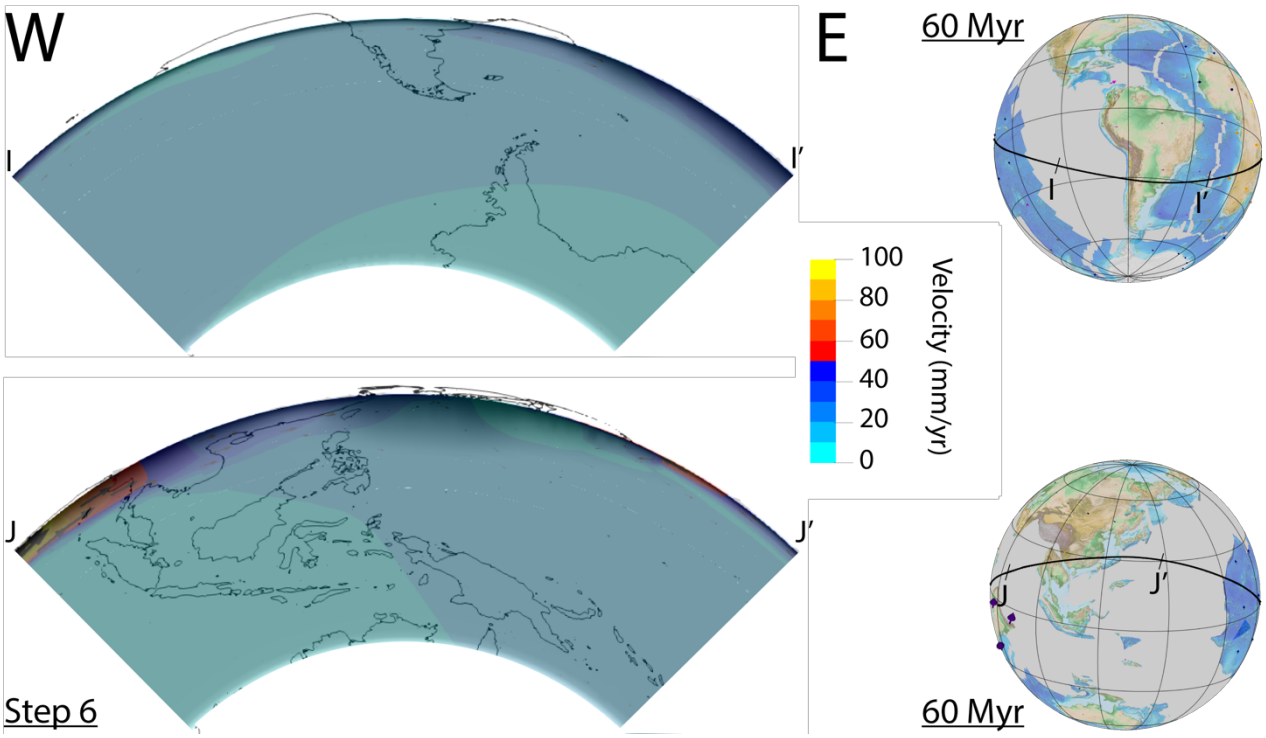

Figure B.18 – Step 6 (i.e., 60 Myr) for South American (upper panel) and Pacific (lower panel) side of model vp1. Temperature (black shadow) and velocity (colored data plus arrows) data are overlapped for step 6 of model vp1. Globes in the right part of the figure shows plate kinematic at 60 Myr in a deep hotspot reference frame. The black line corresponds to the tectonic equator.

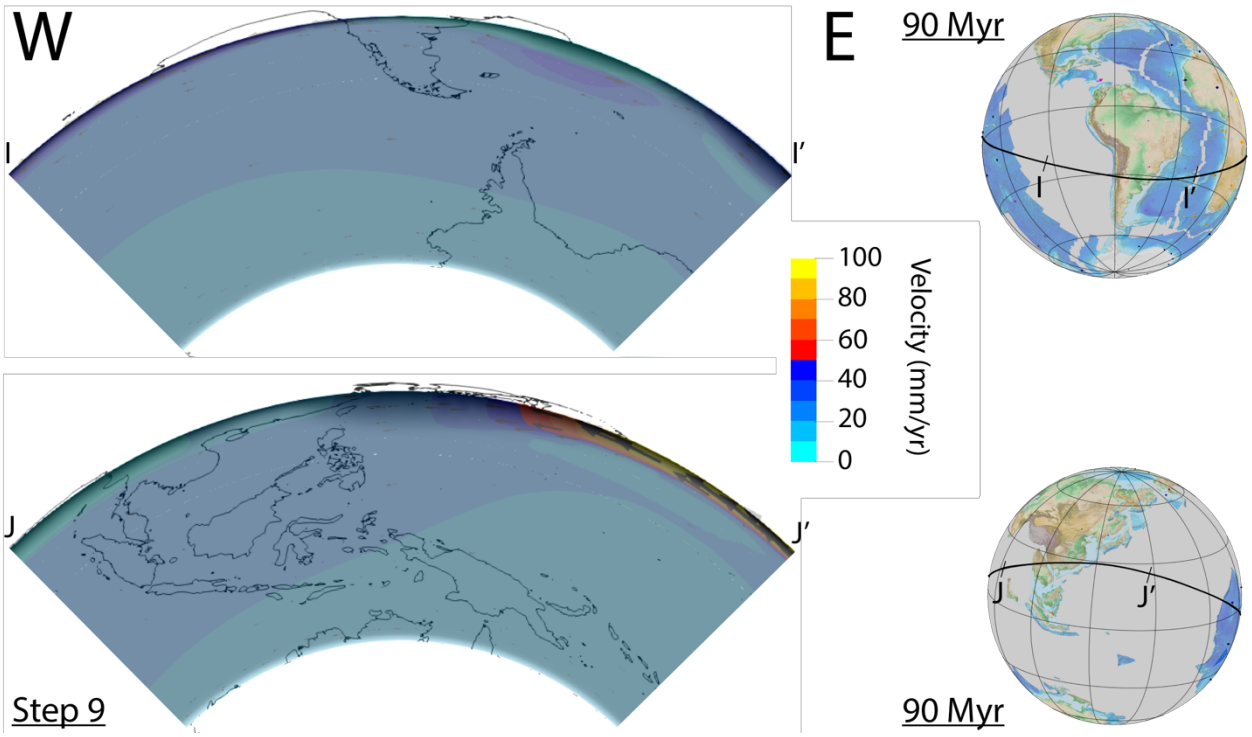

Figure B.19 – Step 9 (i.e., 90 Myr) for South American (upper panel) and Pacific (lower panel) side of model vp1. Temperature (black shadow) and velocity (colored data plus arrows) data are overlapped for step 9 of model vp1. Globes in the right part of the figure shows plate kinematic at 90 Myr in a deep hotspot reference frame. The black line corresponds to the tectonic equator.

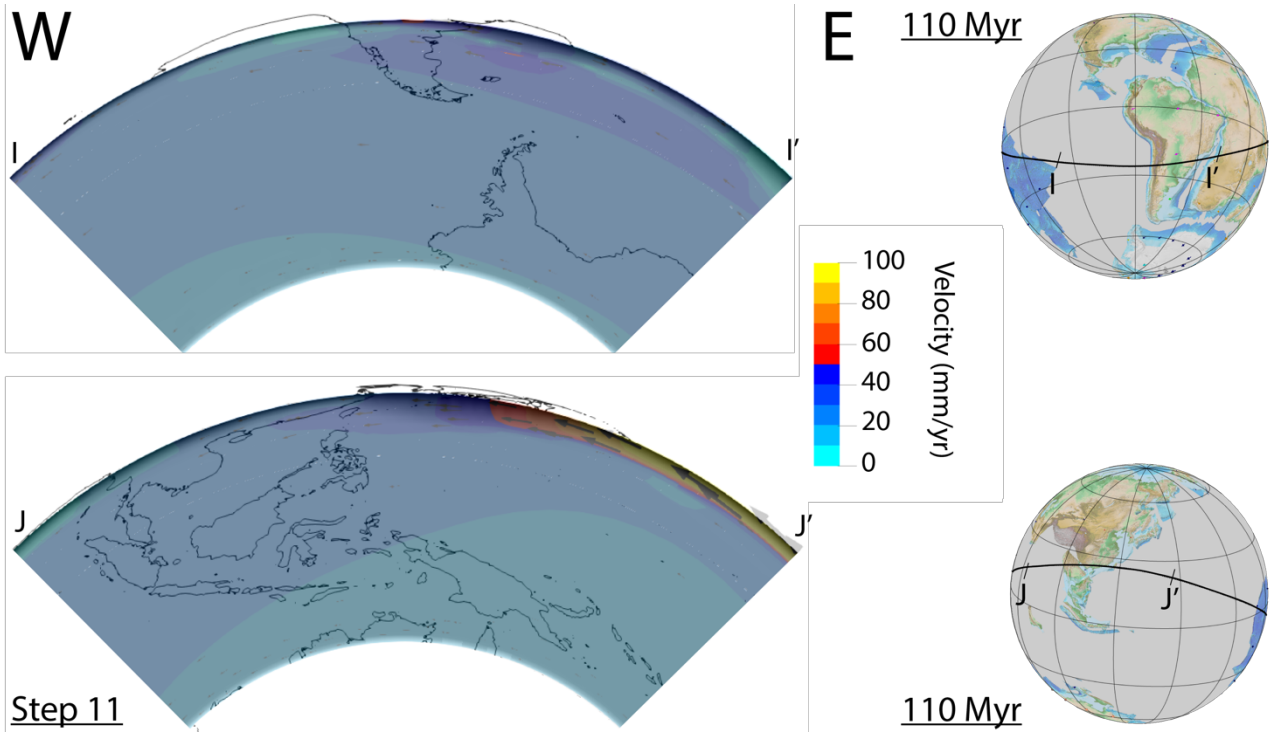

Figure B.20 – Step 11 (i.e., 110 Myr) for South American (upper panel) and Pacific (lower panel) side of model vp1. Temperature (black shadow) and velocity (colored data plus arrows) data are overlapped for step 11 of model vp1. Globes in the right part of the figure shows plate kinematic at 110 Myr in a deep hotspot reference frame. The black line corresponds to the tectonic equator.

B.1.6 vp2 (Visco plastic Material model)

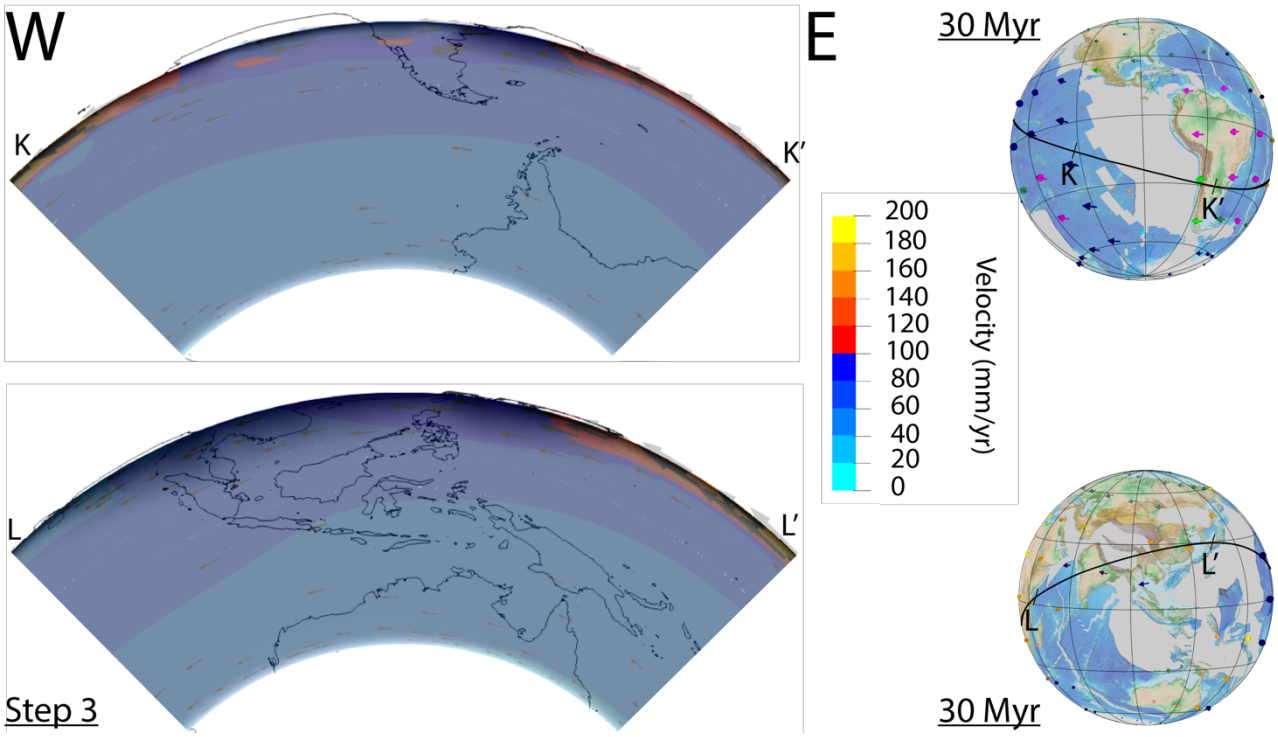

Figure B.21 – Step 3 (i.e., 30 Myr) for South American (upper panel) and Pacific (lower panel) side of model vp2. Temperature (black shadow) and velocity (colored data plus arrows) data are overlapped for step 3 of model vp1. Globes in the right part of the figure shows plate kinematic at 30 Myr in a shallow hotspot reference frame. The black line corresponds to the tectonic equator.

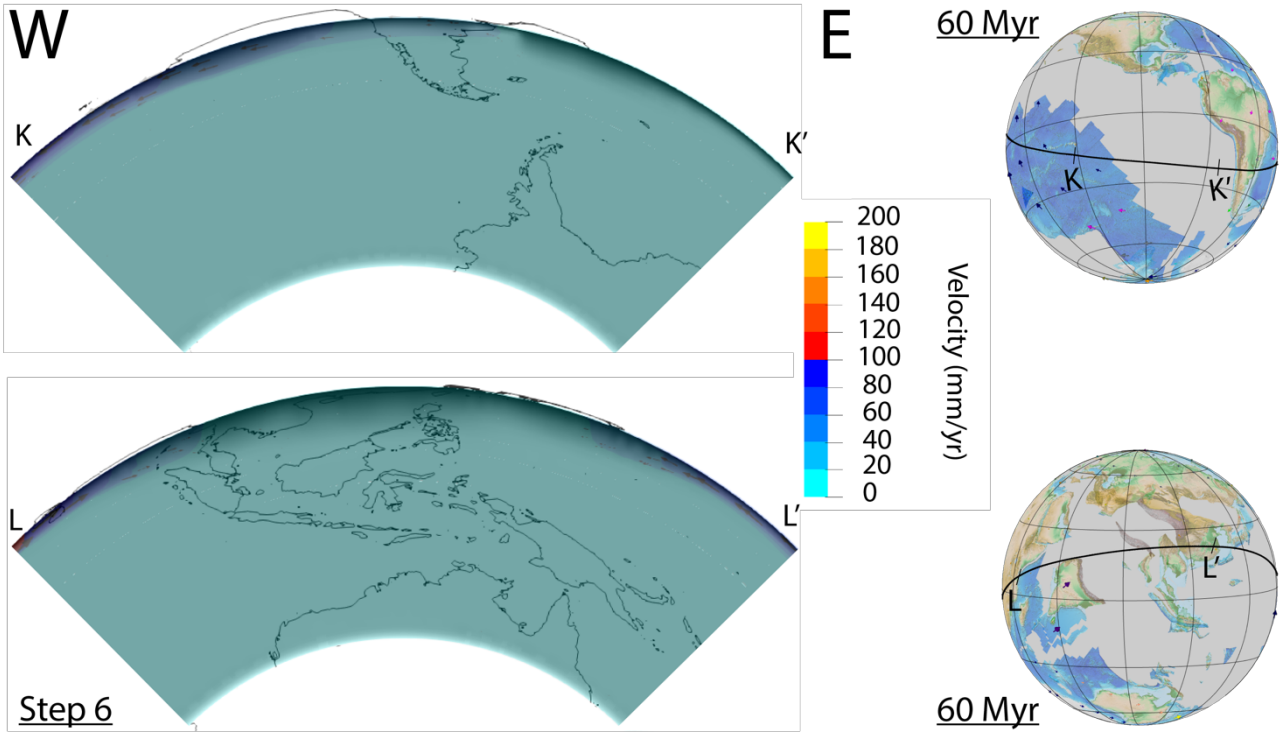

Figure B.22 – Step 6 (i.e., 60 Myr) for South American (upper panel) and Pacific (lower panel) side of model vp2. Temperature (black shadow) and velocity (colored data plus arrows) data are overlapped for step 6 of model vp2. Globes in the right part of the figure shows plate kinematic at 60 Myr in a shallow hotspot reference frame. The black line corresponds to the tectonic equator.

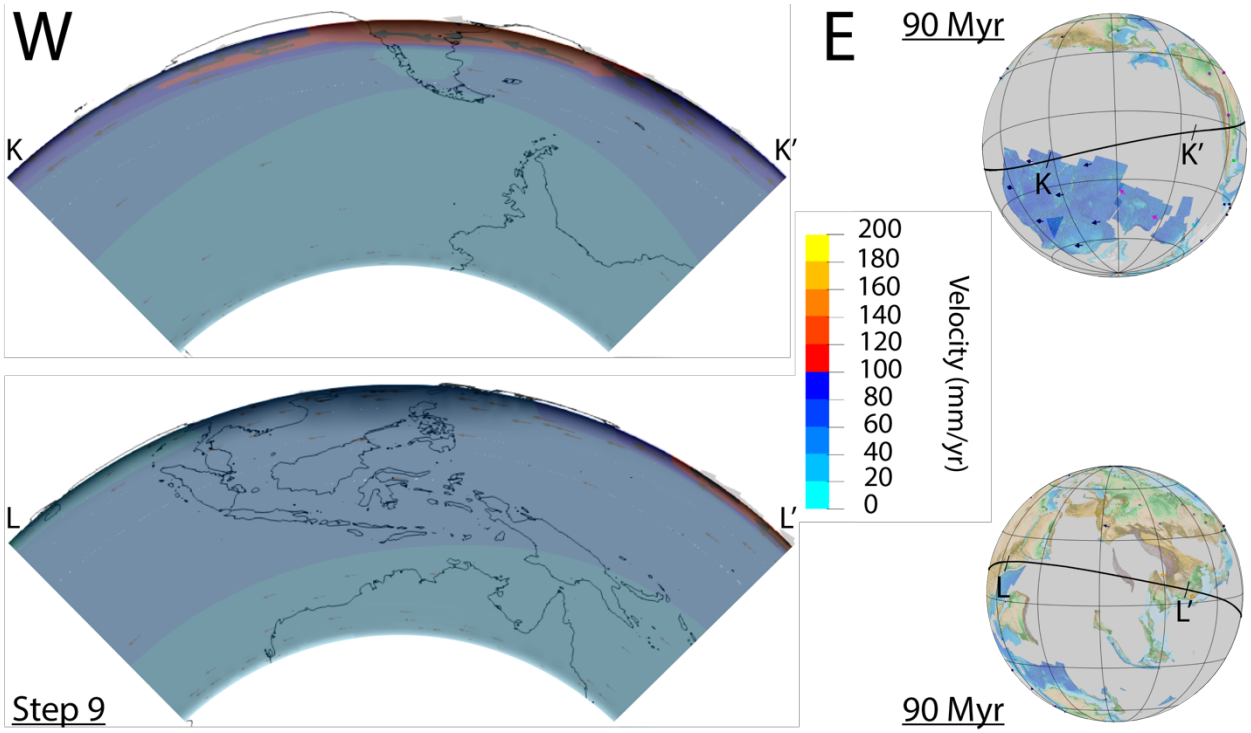

Figure B.23 – Step 9 (i.e., 90 Myr) for South American (upper panel) and Pacific (lower panel) side of model vp2. Temperature (black shadow) and velocity (colored data plus arrows) data are overlapped for step 9 of model vp2. Globes in the right part of the figure shows plate kinematic at 90 Myr in a shallow hotspot reference frame. The black line corresponds to the tectonic equator.

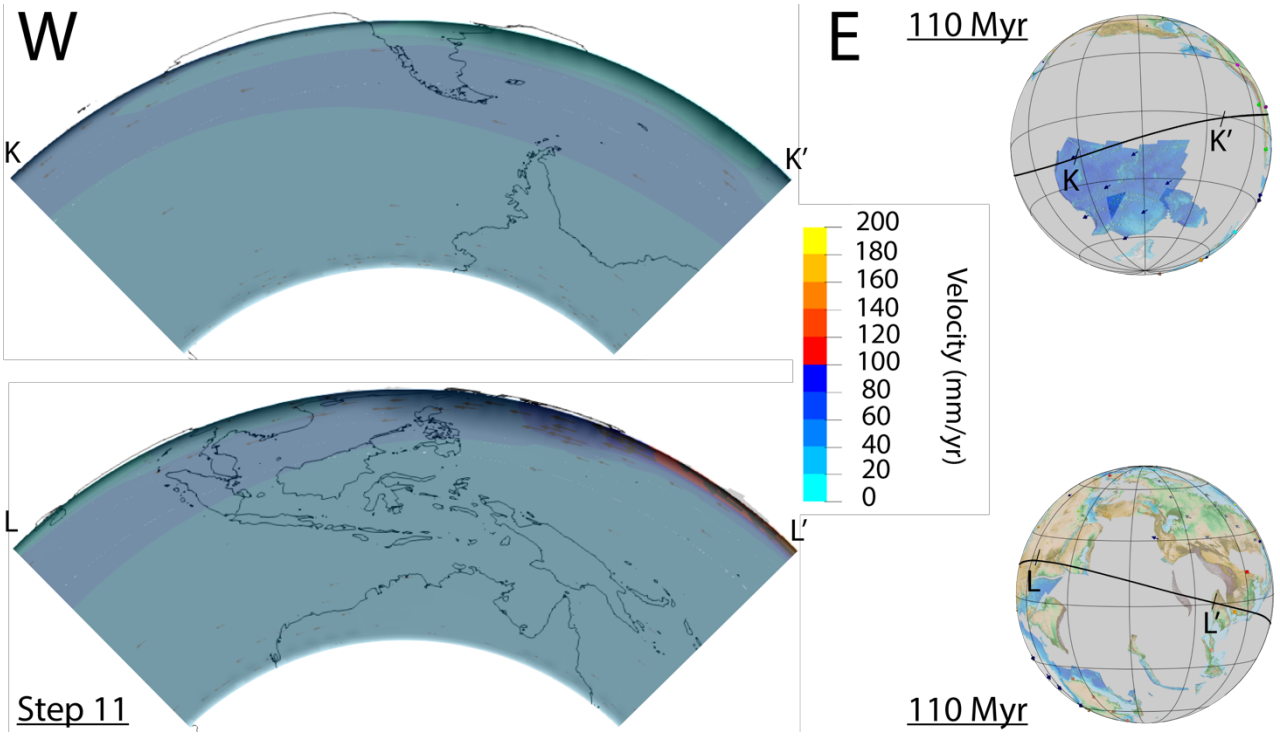

Figure B.24 – Step 11 (i.e., 110 Myr) for South American (upper panel) and Pacific (lower panel) side of model vp2. Temperature (black shadow) and velocity (colored data plus arrows) data are overlapped for step 11 of model vp2. Globes in the right part of the figure shows plate kinematic at 110 Myr in a shallow hotspot reference frame. The black line corresponds to the tectonic equator.

B.1.7 isehar1 (Isentropic Harzburgitic mantle)

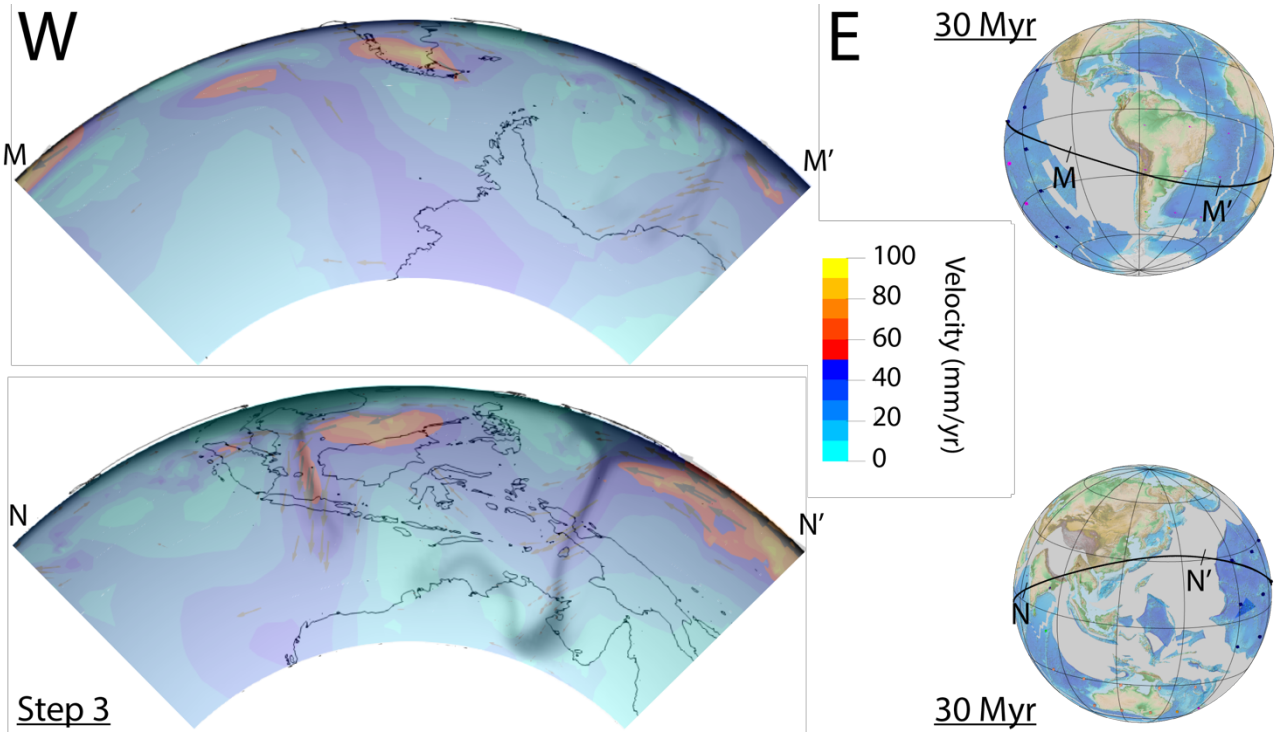

Figure B.25 – Step 3 (i.e., 30 Myr) for South American (upper panel) and Pacific (lower panel) side of model isehar1. Temperature (black shadow) and velocity (colored data plus arrows) data are overlapped for step 3 of model isehar1. Globes in the right part of the figure shows plate kinematic at 30 Myr in a deep hotspot reference frame. The black line corresponds to the tectonic equator.

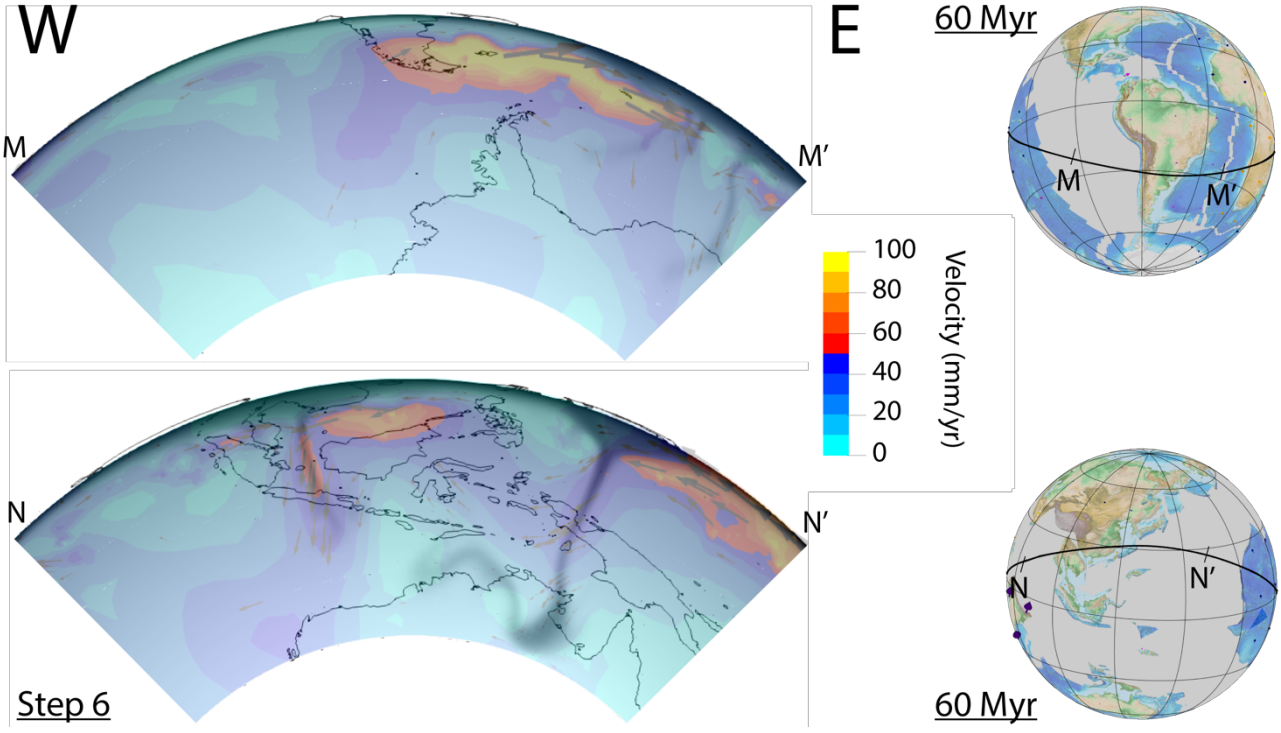

Figure B.26 – Step 6 (i.e., 60 Myr) for South American (upper panel) and Pacific (lower panel) side of model isehar1. Temperature (black shadow) and velocity (colored data plus arrows) data are overlapped for step 6 of model isehar1. Globes in the right part of the figure shows plate kinematic at 60 Myr in a deep hotspot reference frame. The black line corresponds to the tectonic equator.

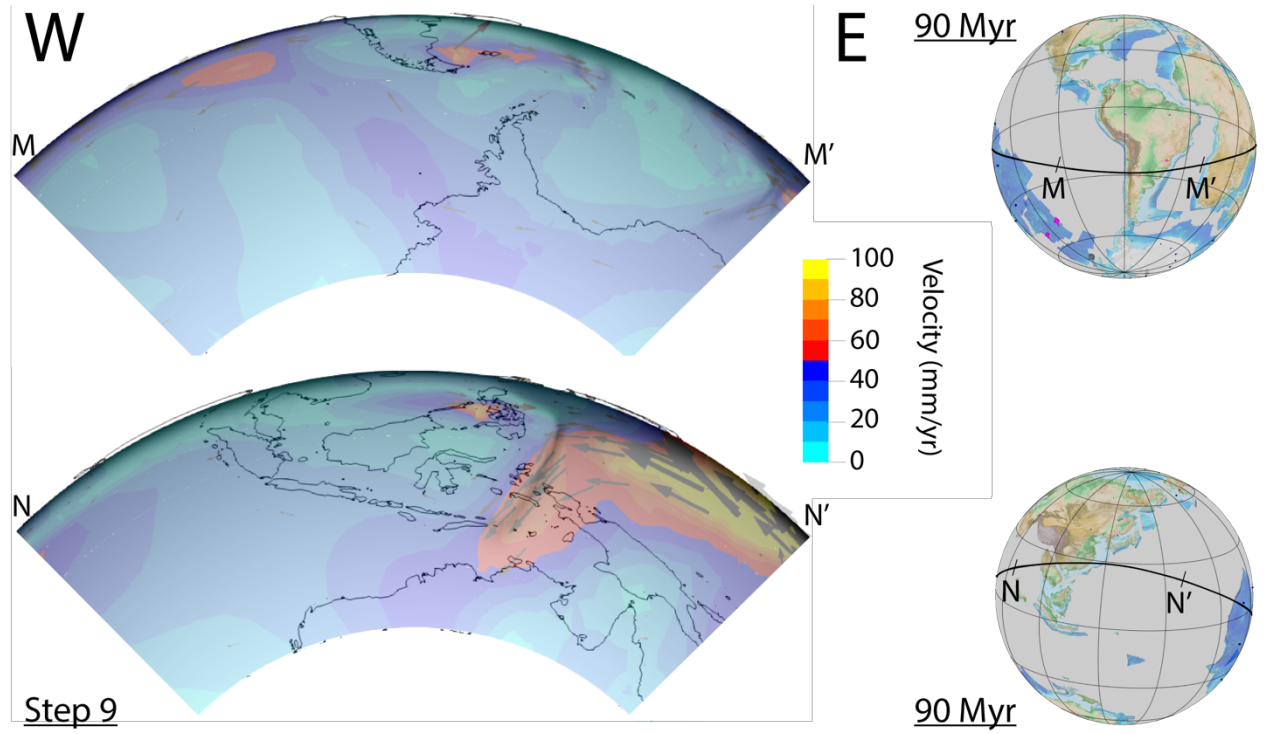

Figure B.27 – Step 9 (i.e., 90 Myr) for South American (upper panel) and Pacific (lower panel) side of model isehar1. Temperature (black shadow) and velocity (colored data plus arrows) data are overlapped for step 9 of model isehar1. Globes in the right part of the figure shows plate kinematic at 90 Myr in a deep hotspot reference frame. The black line corresponds to the tectonic equator.

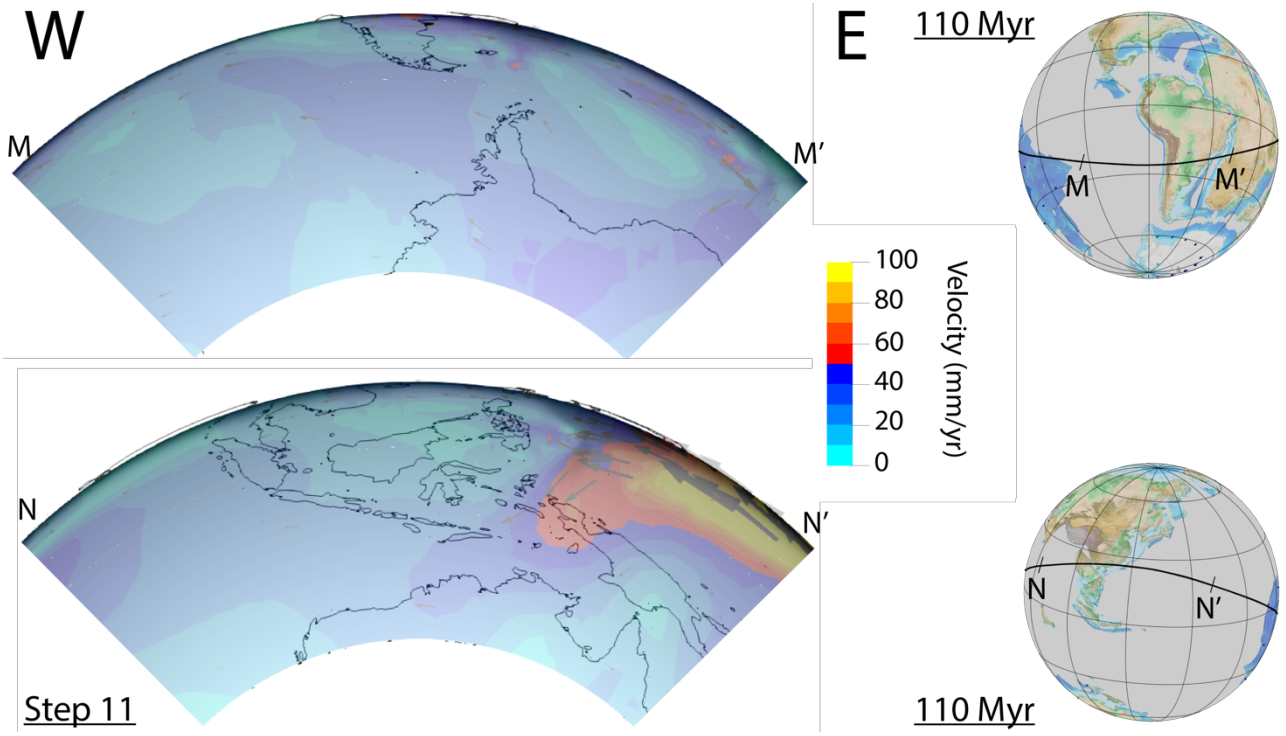

Figure B.28 – Step 11 (i.e., 110 Myr) for South American (upper panel) and Pacific (lower panel) side of model isehar1. Temperature (black shadow) and velocity (colored data plus arrows) data are overlapped for step 11 of model isehar1. Globes in the right part of the figure shows plate kinematic at 110 Myr in a deep hotspot reference frame. The black line corresponds to the tectonic equator.

B.1.8 isehar2 (Isentropic Harzburgitic mantle)

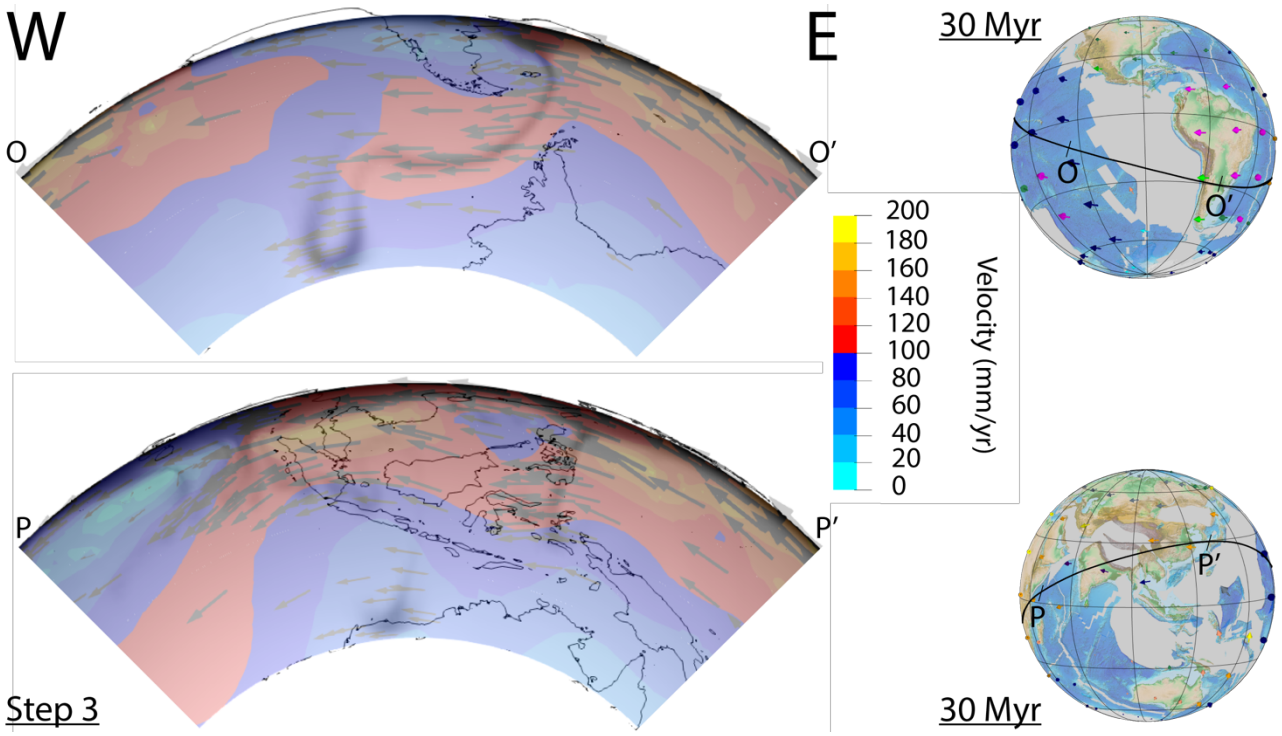

Figure B.29 – Step 3 (i.e., 30 Myr) for South American (upper panel) and Pacific (lower panel) side of model isehar2. Temperature (black shadow) and velocity (colored data plus arrows) data are overlapped for step 3 of model isehar2. Globes in the right part of the figure shows plate kinematic at 30 Myr in a shallow hotspot reference frame. The black line corresponds to the tectonic equator.

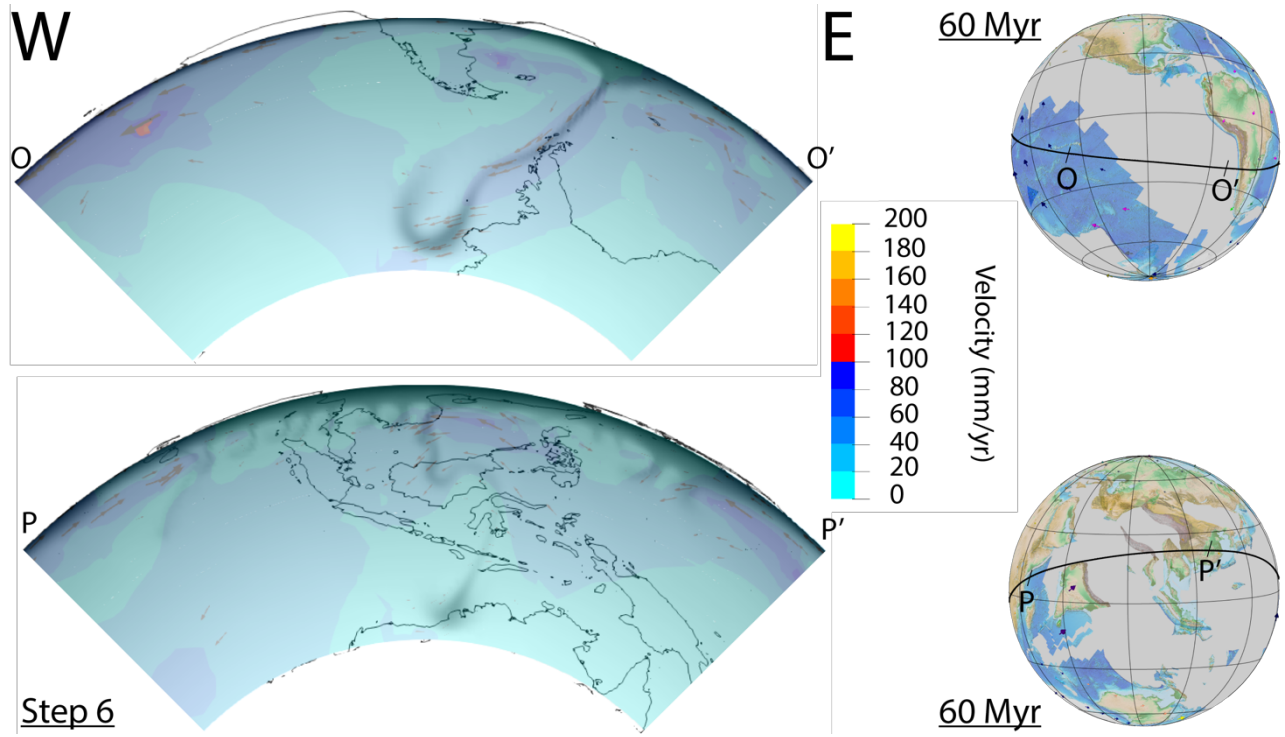

Figure B.30 – Step 6 (i.e., 60 Myr) for South American (upper panel) and Pacific (lower panel) side of model isehar2. Temperature (black shadow) and velocity (colored data plus arrows) data are overlapped for step 6 of model isehar2. Globes in the right part of the figure shows plate kinematic at 60 Myr in a shallow hotspot reference frame. The black line corresponds to the tectonic equator.

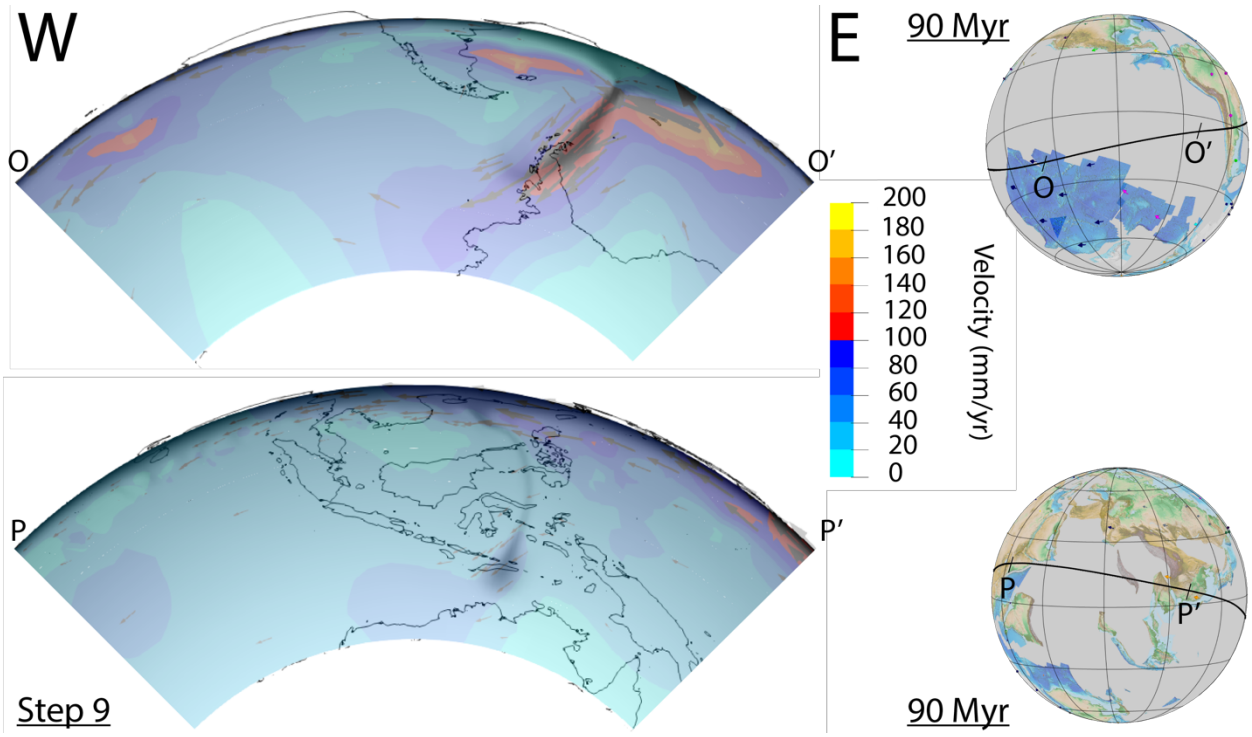

Figure B.31 – Step 9 (i.e., 90 Myr) for South American (upper panel) and Pacific (lower panel) side of model isehar2. Temperature (black shadow) and velocity (colored data plus arrows) data are overlapped for step 9 of model isehar2. Globes in the right part of the figure shows plate kinematics at 90 Myr in a shallow hotspot reference frame. The black line corresponds to the tectonic equator.

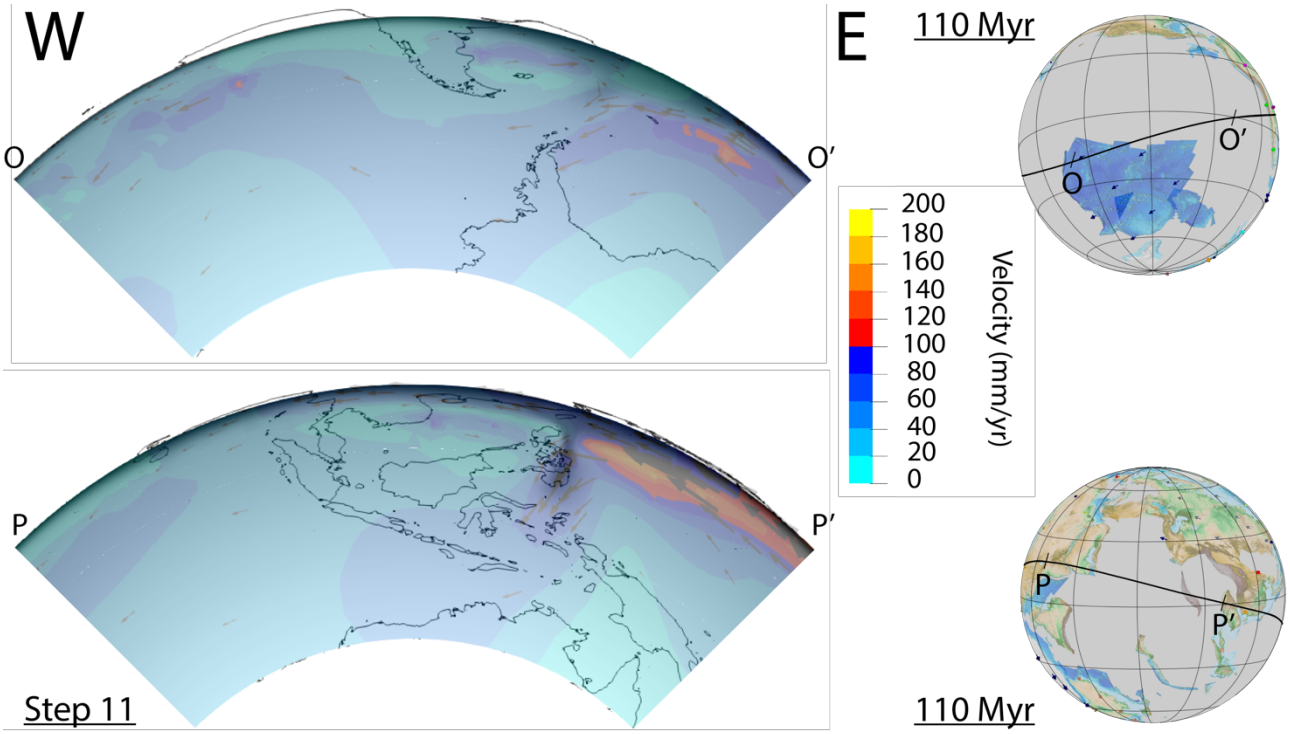

Figure B.32 – Step 11 (i.e., 110 Myr) for South American (upper panel) and Pacific (lower panel) side of model isehar2. Temperature (black shadow) and velocity (colored data plus arrows) data are overlapped for step 11 of model isehar2. Globes in the right part of the figure shows plate kinematics at 110 Myr in a shallow hotspot reference frame. The black line corresponds to the tectonic equator.

B.1.9 majol1 (Majorite-Fo50)

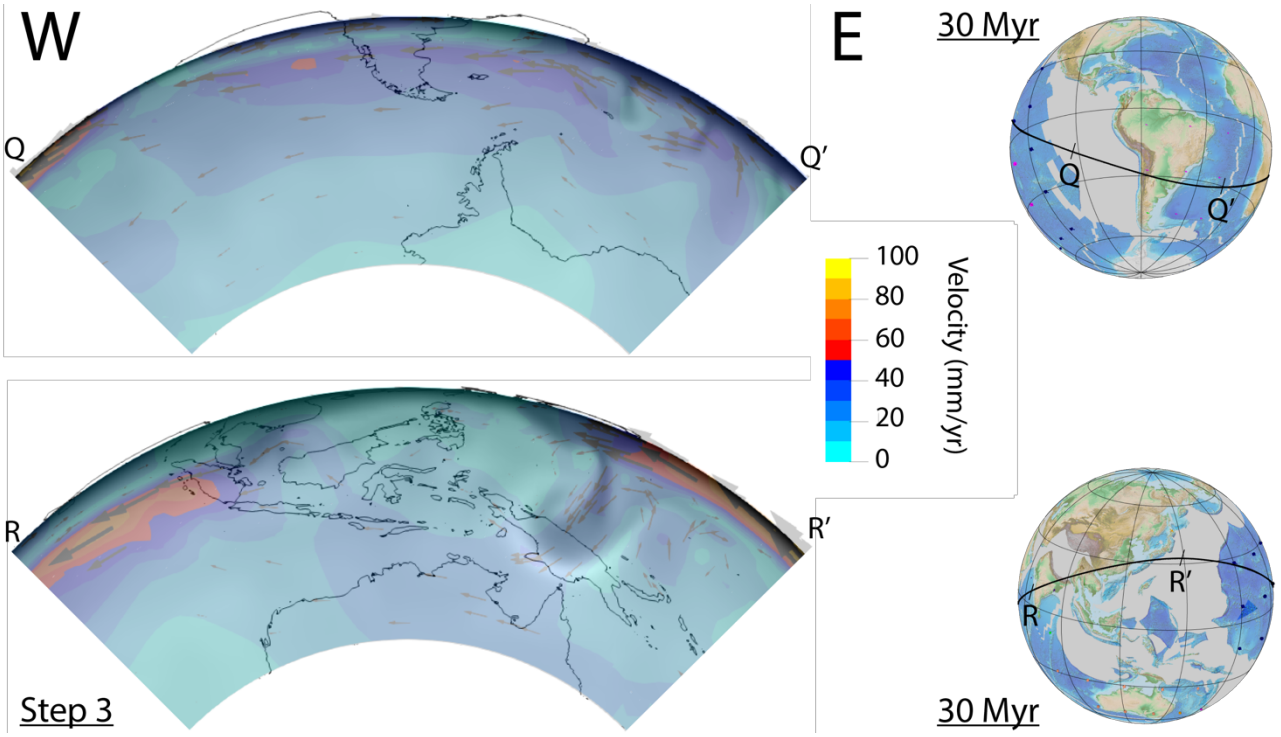

Figure B.33 – Step 3 (i.e., 30 Myr) for South American (upper panel) and Pacific (lower panel) side of model majol1. Temperature (black shadow) and velocity (colored data plus arrows) data are overlapped for step 3 of model majol1. Globes in the right part of the figure shows plate kinematics at 30 Myr in a deep hotspot reference frame. The black line corresponds to the tectonic equator.

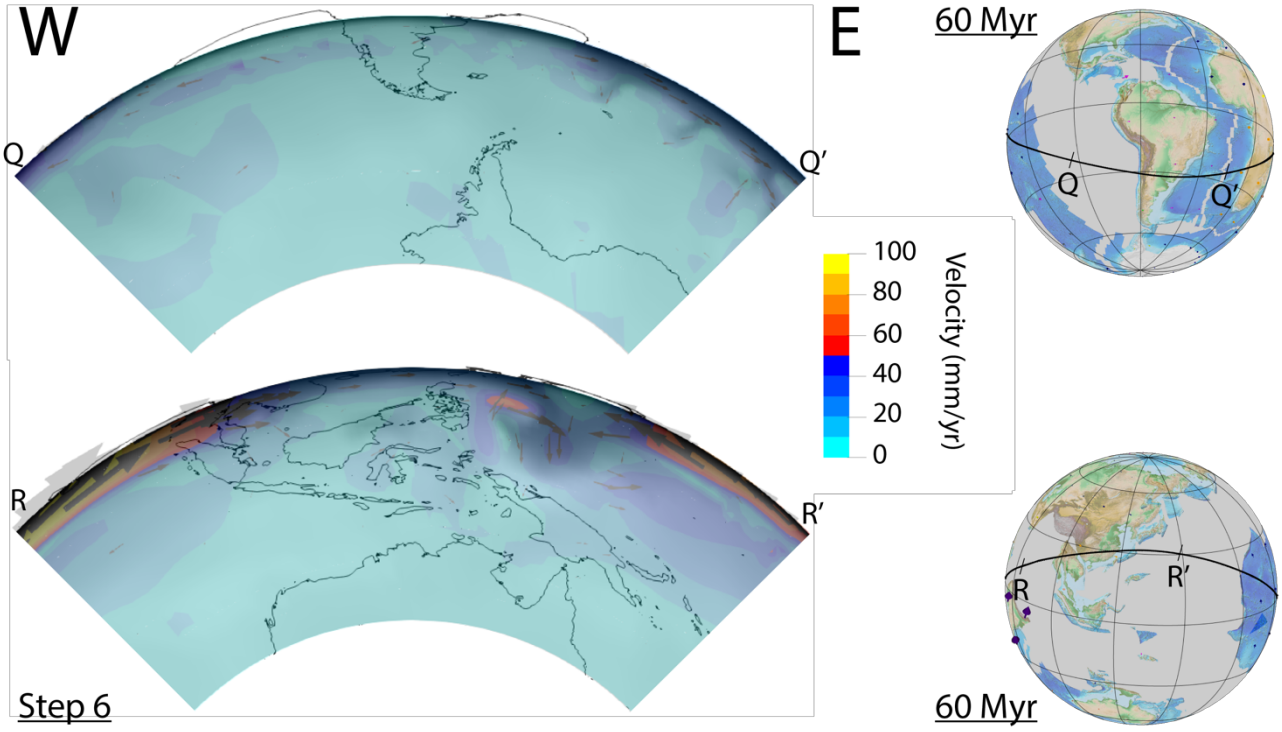

Figure B.34 – Step 6 (i.e., 60 Myr) for South American (upper panel) and Pacific (lower panel) side of model majol1. Temperature (black shadow) and velocity (colored data plus arrows) data are overlapped for step 6 of model majol1. Globes in the right part of the figure shows plate kinematics at 60 Myr in a deep hotspot reference frame. The black line corresponds to the tectonic equator.

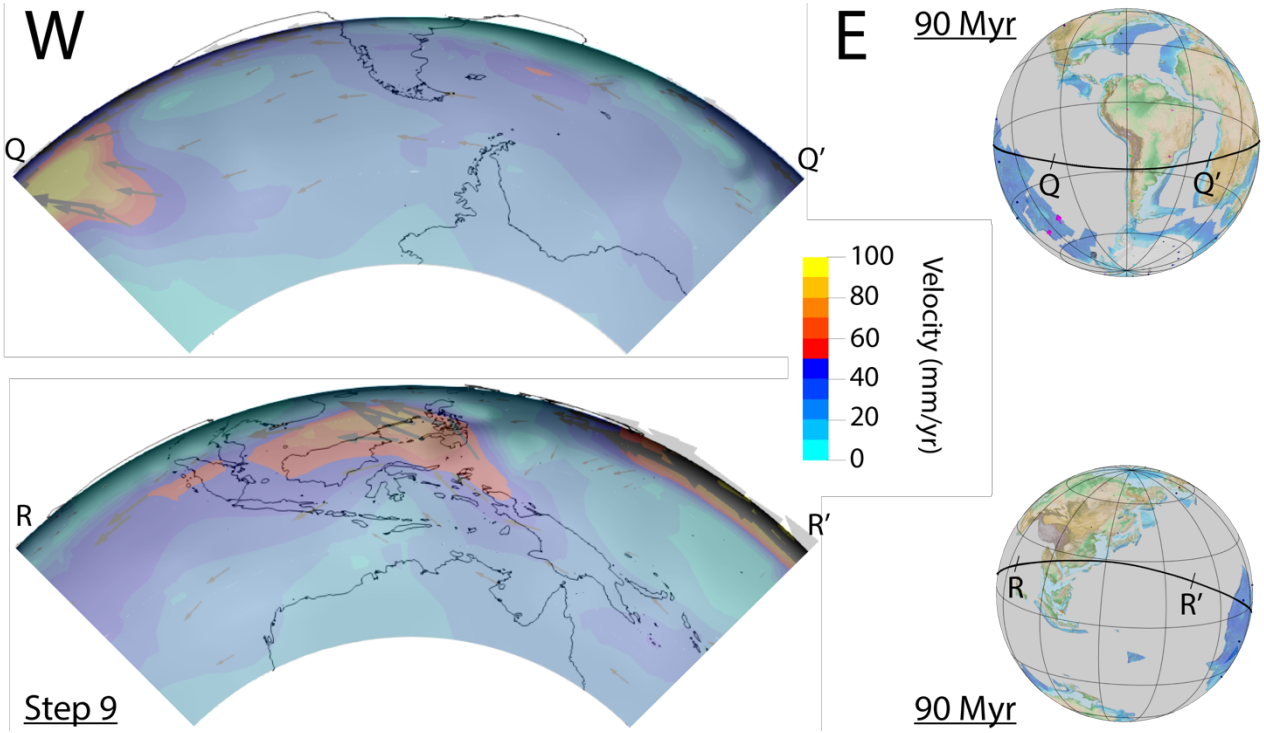

Figure B.35 – Step 9 (i.e., 90 Myr) for South American (upper panel) and Pacific (lower panel) side of model majol1. Temperature (black shadow) and velocity (colored data plus arrows) data are overlapped for step 9 of model majol1. Globes in the right part of the figure shows plate kinematics at 90 Myr in a deep hotspot reference frame. The black line corresponds to the tectonic equator.

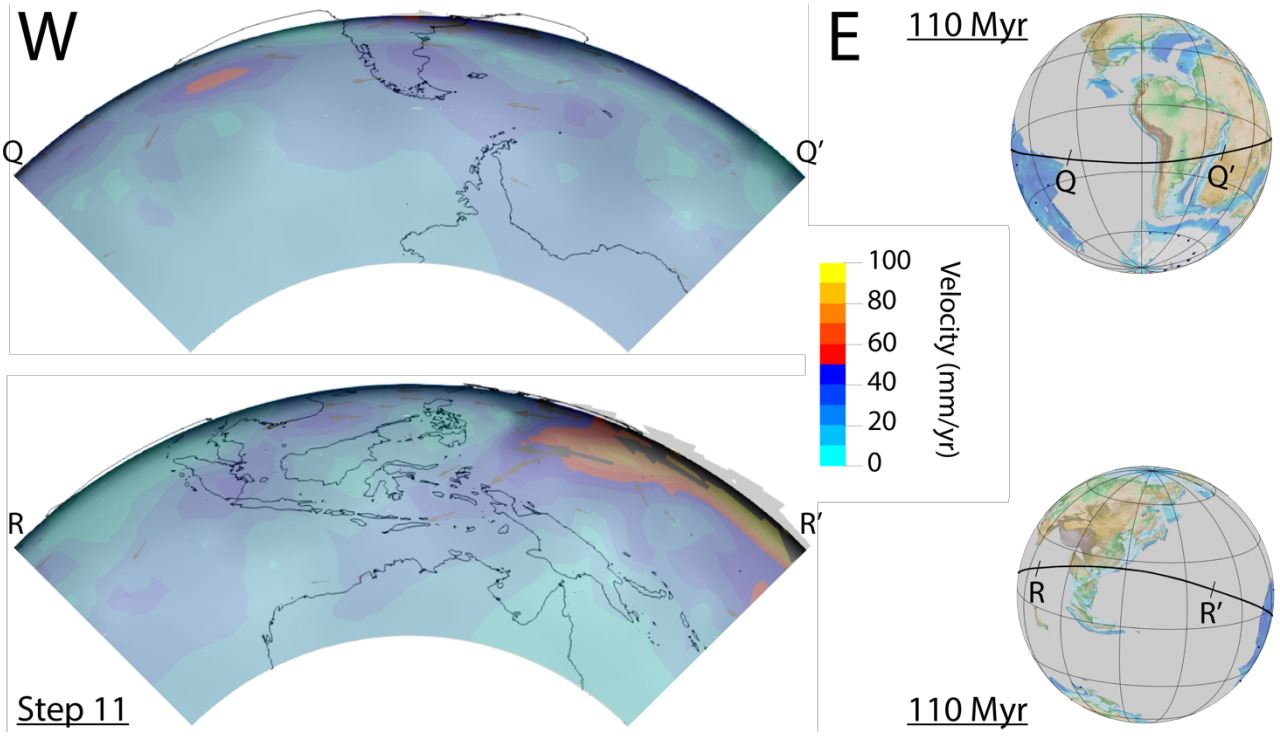

Figure B.36 – Step 11 (i.e., 110 Myr) for South American (upper panel) and Pacific (lower panel) side of model majol1. Temperature (black shadow) and velocity (colored data plus arrows) data are overlapped for step 11 of model majol1. Globes in the right part of the figure shows plate kinematics at 110 Myr in a deep hotspot reference frame. The black line corresponds to the tectonic equator.

B.1.10 majol2 (Majorite-Fo50)

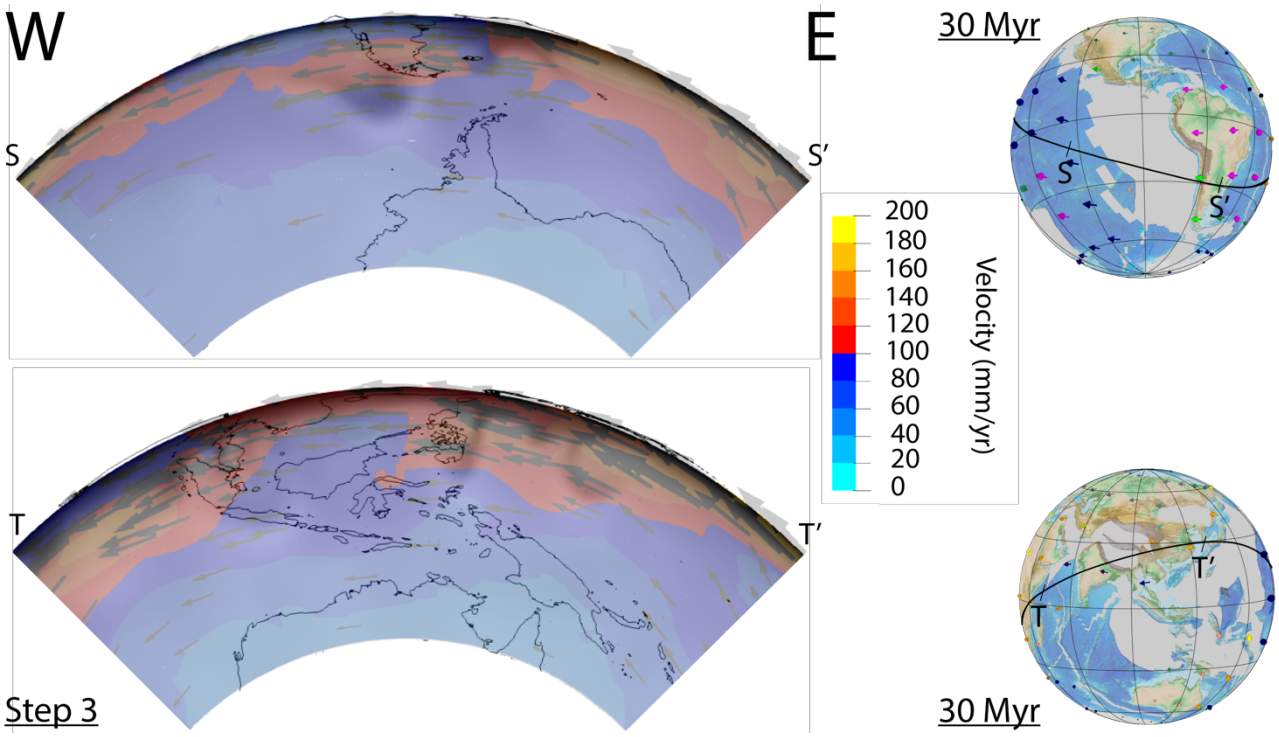

Figure B.37 – Step 3 (i.e., 30 Myr) for South American (upper panel) and Pacific (lower panel) side of model majol2. Temperature (black shadow) and velocity (colored data plus arrows) data are overlapped for step 3 of model majol2. Globes in the right part of the figure shows plate kinematics at 30 Myr in a shallow hotspot reference frame. The black line corresponds to the tectonic equator.

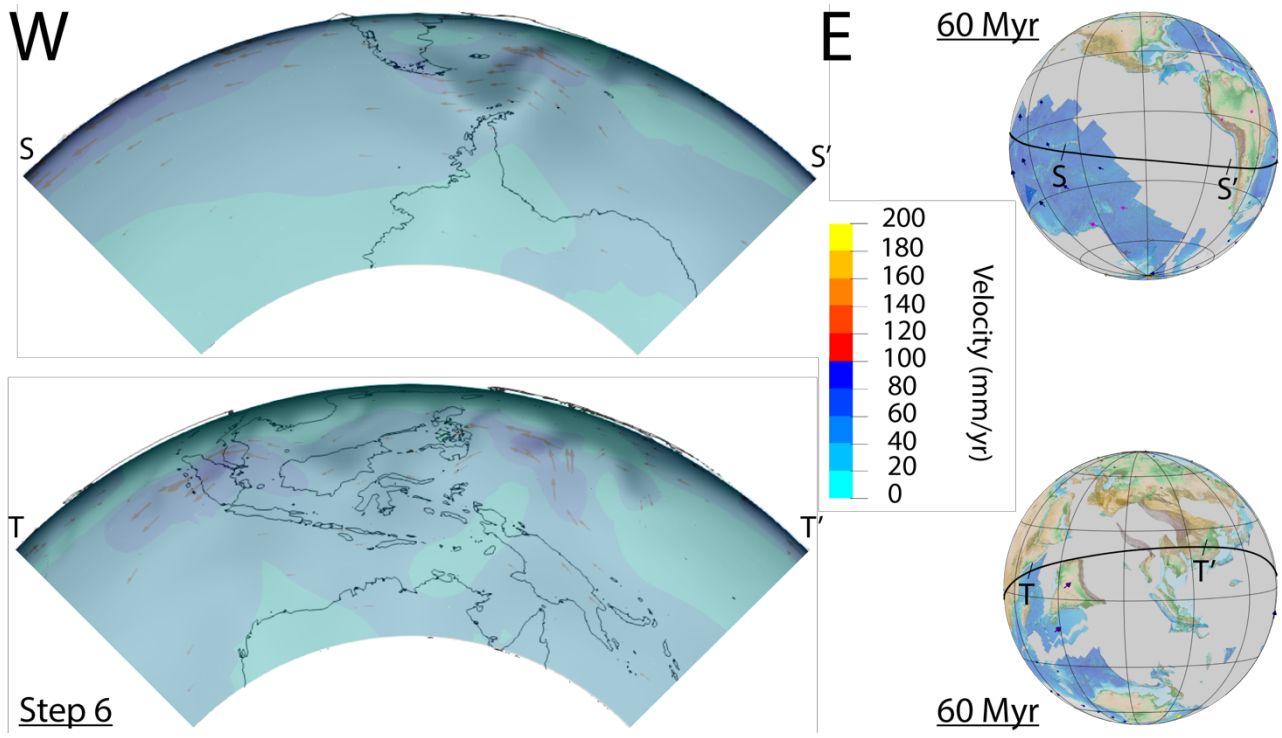

Figure B.38 – Step 6 (i.e., 60 Myr) for South American (upper panel) and Pacific (lower panel) side of model majol2. Temperature (black shadow) and velocity (colored data plus arrows) data are overlapped for step 6 of model majol2. Globes in the right part of the figure shows plate kinematics at 60 Myr in a shallow hotspot reference frame. The black line corresponds to the tectonic equator.

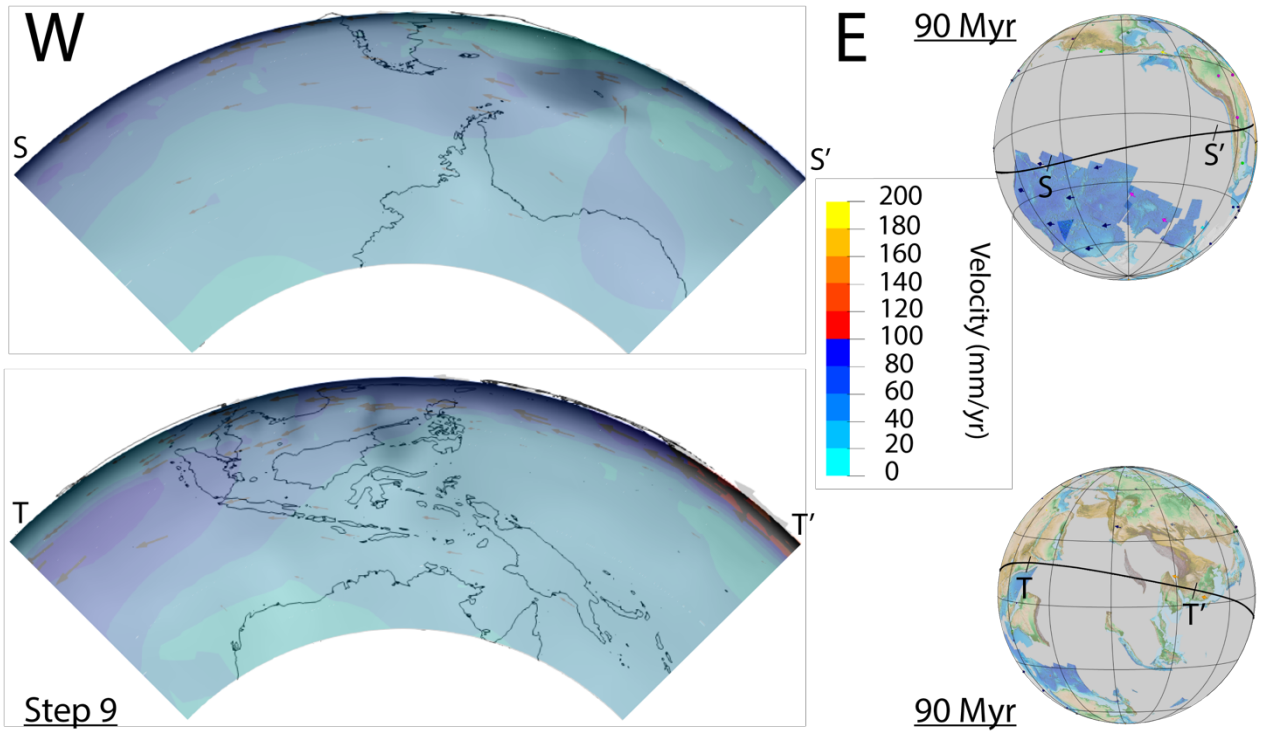

Figure B.39 – Step 9 (i.e., 90 Myr) for South American (upper panel) and Pacific (lower panel) side of model majol2. Temperature (black shadow) and velocity (colored data plus arrows) data are overlapped for step 9 of model majol2. Globes in the right part of the figure shows plate kinematics at 90 Myr in a shallow hotspot reference frame. The black line corresponds to the tectonic equator.

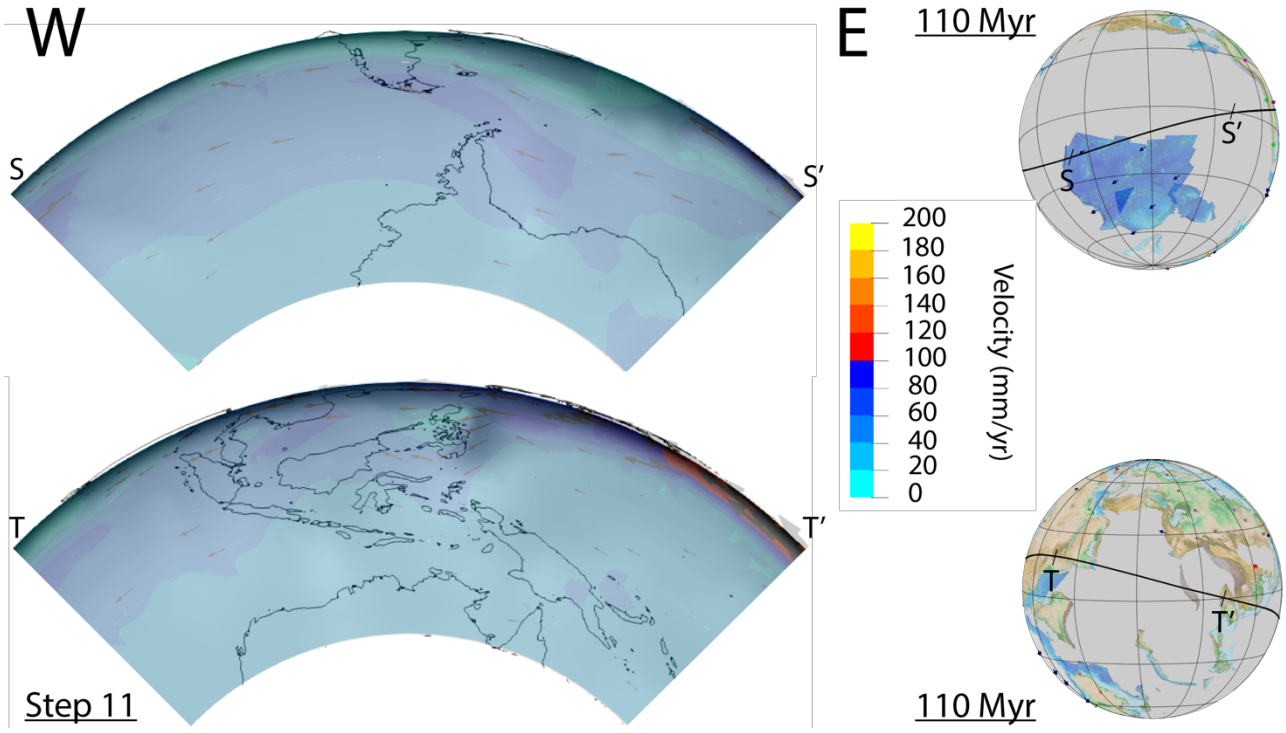

Figure B.40 – Step 9 (i.e., 90 Myr) for South American (upper panel) and Pacific (lower panel) side of model majol2. Temperature (black shadow) and velocity (colored data plus arrows) data are overlapped for step 9of model majol2. Globes in the right part of the figure shows plate kinematics at 90 Myr in a shallow hotspot reference frame. The black line corresponds to the tectonic equator.

B.1.11 majfo89_1 (Majorite-Fo89)

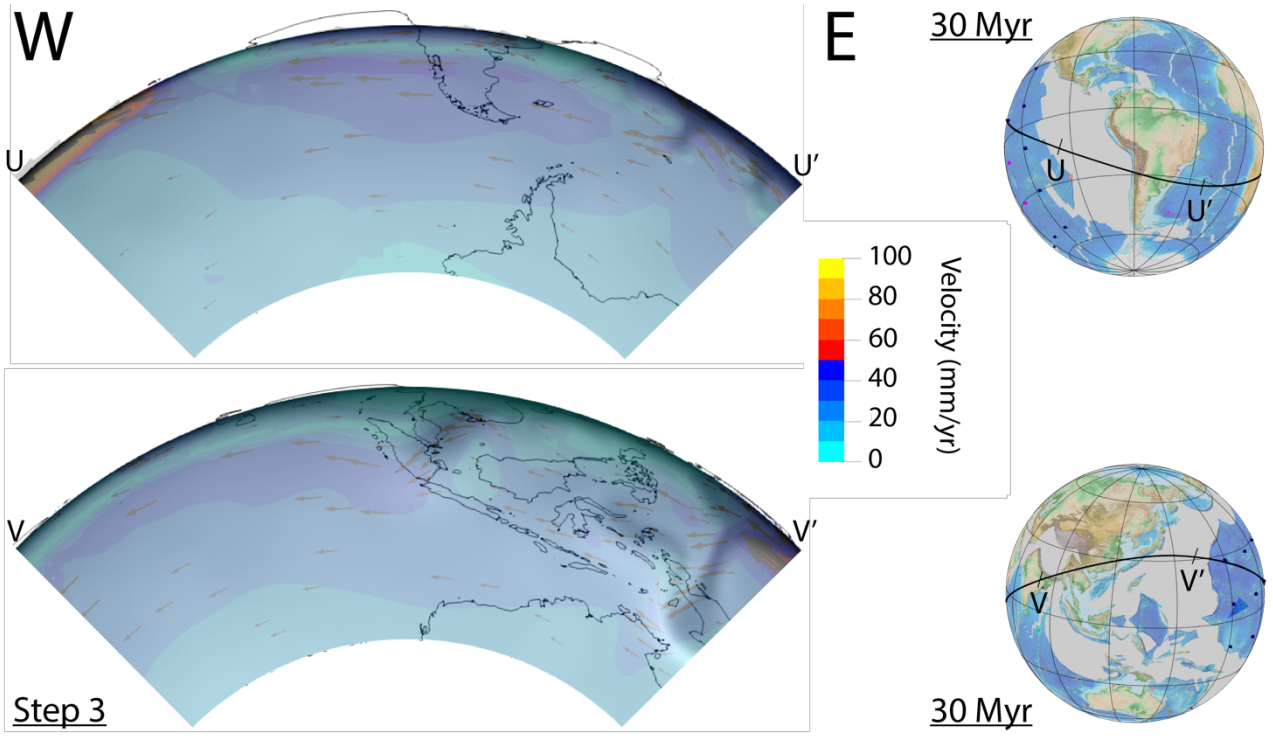

Figure B.41 – Step 3 (i.e., 30 Myr) for South American (upper panel) and Pacific (lower panel) side of model majfo89_1. Temperature (black shadow) and velocity (colored data plus arrows) data are overlapped for step 3 of model majfo89_1. Globes in the right part of the figure shows plate kinematics at 30 Myr in a deep hotspot reference frame. The black line corresponds to the tectonic equator.

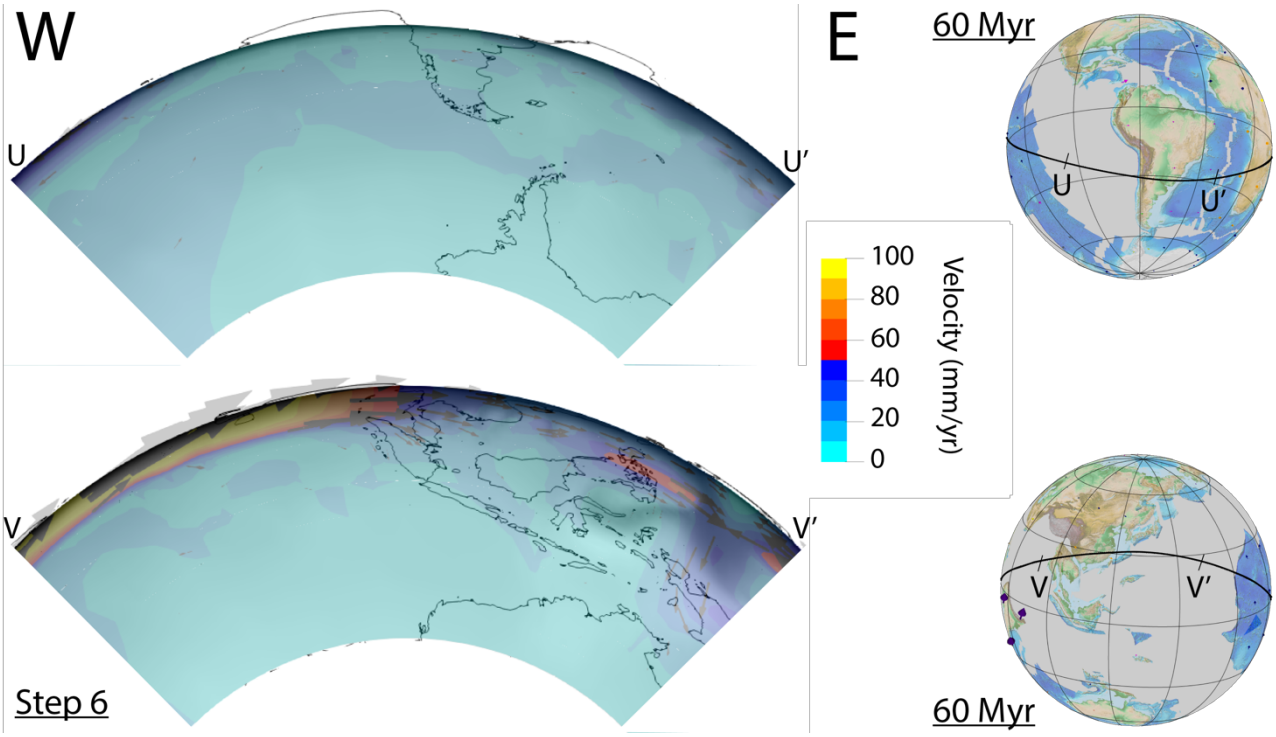

Figure B.42 – Step 6 (i.e., 60 Myr) for South American (upper panel) and Pacific (lower panel) side of model majfo89_1. Temperature (black shadow) and velocity (colored data plus arrows) data are overlapped for step 6 of model majfo89_1. Globes in the right part of the figure shows plate kinematics at 60 Myr in a deep hotspot reference frame. The black line corresponds to the tectonic equator.

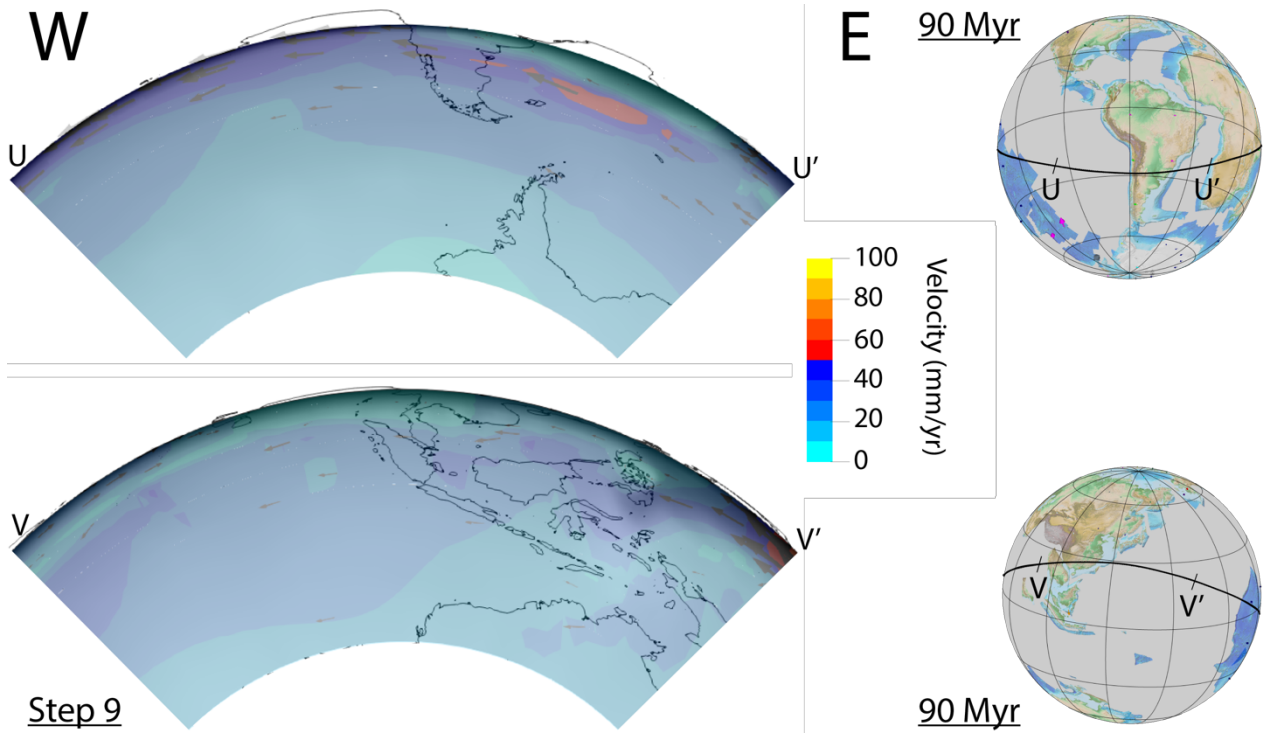

Figure B.43 – Step 9 (i.e., 90 Myr) for South American (upper panel) and Pacific (lower panel) side of model majfo89_1. Temperature (black shadow) and velocity (colored data plus arrows) data are overlapped for step 9 of model majfo89_1. Globes in the right part of the figure shows plate kinematics at 90 Myr in a deep hotspot reference frame. The black line corresponds to the tectonic equator.

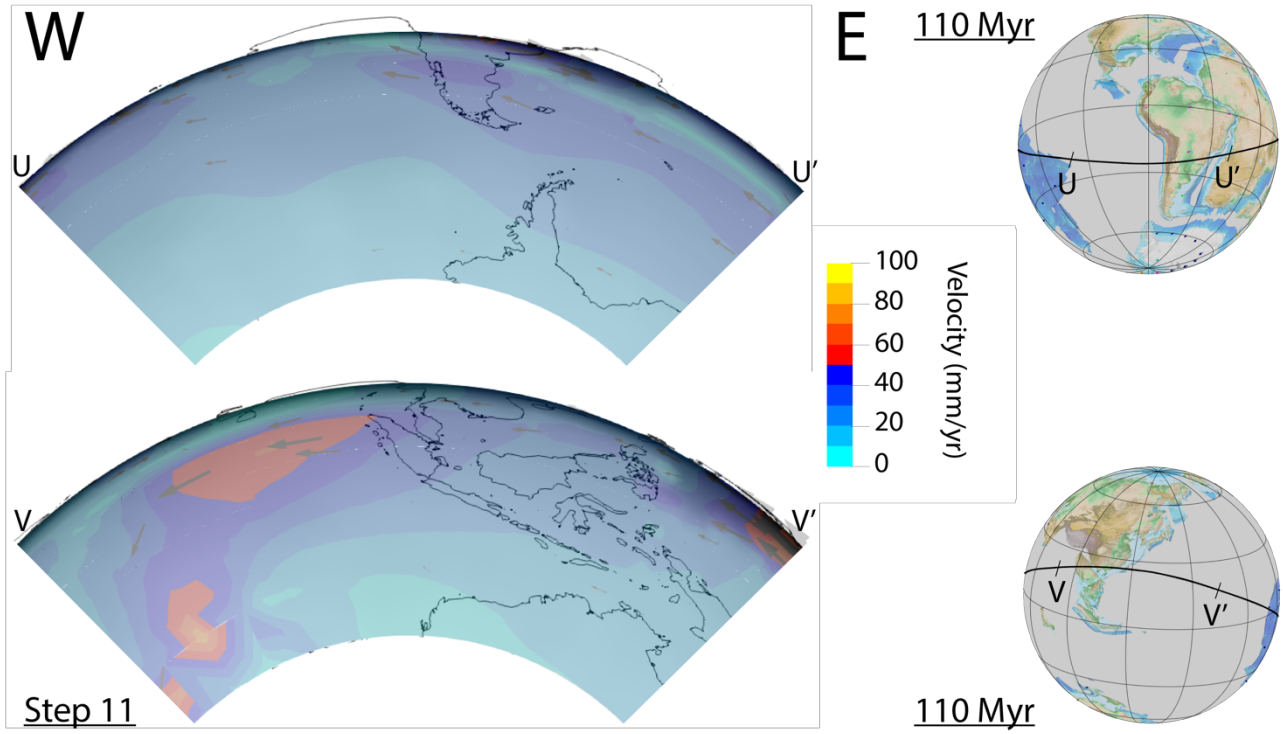

Figure B.44 – Step 11 (i.e., 110 Myr) for South American (upper panel) and Pacific (lower panel) side of model majfo89_1. Temperature (black shadow) and velocity (colored data plus arrows) data are overlapped for step 11 of model majfo89_1. Globes in the right part of the figure shows plate kinematics at 110 Myr in a deep hotspot reference frame. The black line corresponds to the tectonic equator.

B.1.12 majfo89_2 (Majorite-Fo89)

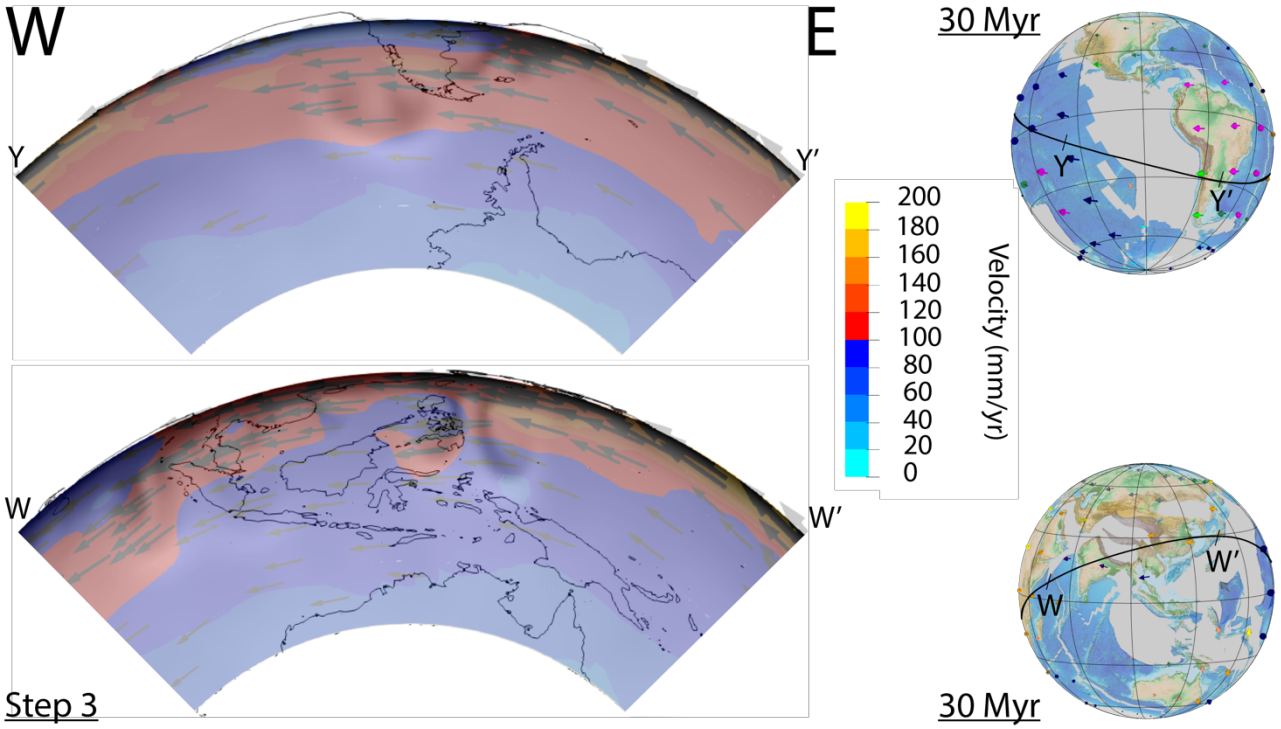

Figure B.45 – Step 3 (i.e., 30 Myr) for South American (upper panel) and Pacific (lower panel) side of model majfo89_2. Temperature (black shadow) and velocity (colored data plus arrows) data are overlapped for step 3 of model majfo89_2. Globes in the right part of the figure shows plate kinematics at 30 Myr in a shallow hotspot reference frame. The black line corresponds to the tectonic equator.

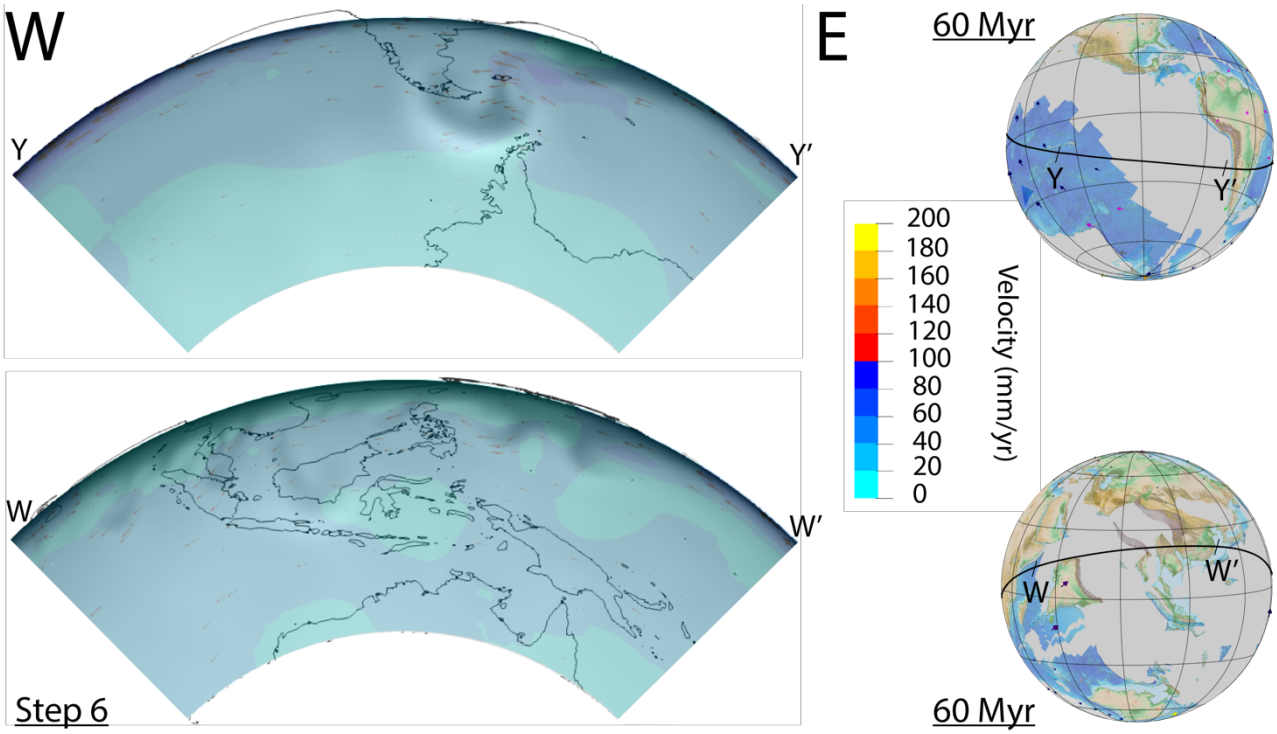

Figure B.46– Step 6 (i.e., 60 Myr) for South American (upper panel) and Pacific (lower panel) side of model majfo89_2. Temperature (black shadow) and velocity (colored data plus arrows) data are overlapped for step 6 of model majfo89_2. Globes in the right part of the figure shows plate kinematics at 60 Myr in a shallow hotspot reference frame. The black line corresponds to the tectonic equator.

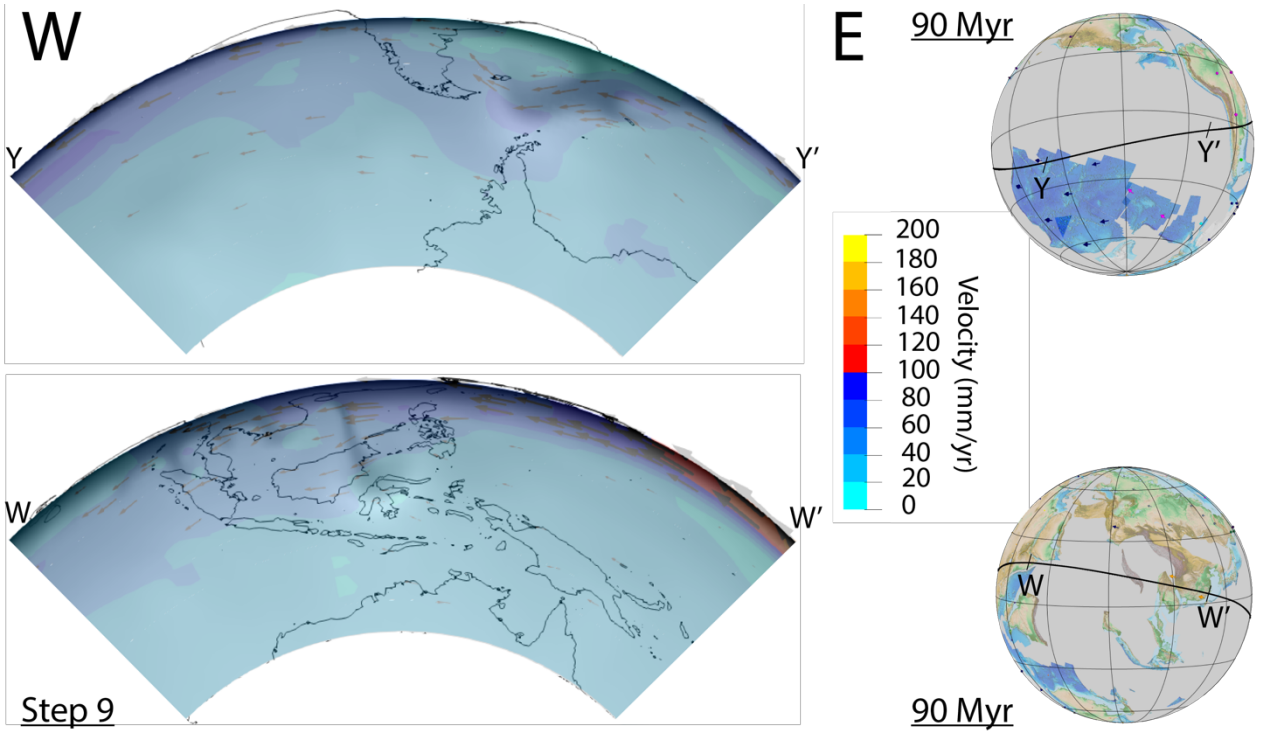

Figure B.47 – Step 9 (i.e., 90 Myr) for South American (upper panel) and Pacific (lower panel) side of model majfo89_2. Temperature (black shadow) and velocity (colored data plus arrows) data are overlapped for step 9 of model majfo89_2. Globes in the right part of the figure shows plate kinematics at 90 Myr in a shallow hotspot reference frame. The black line corresponds to the tectonic equator.

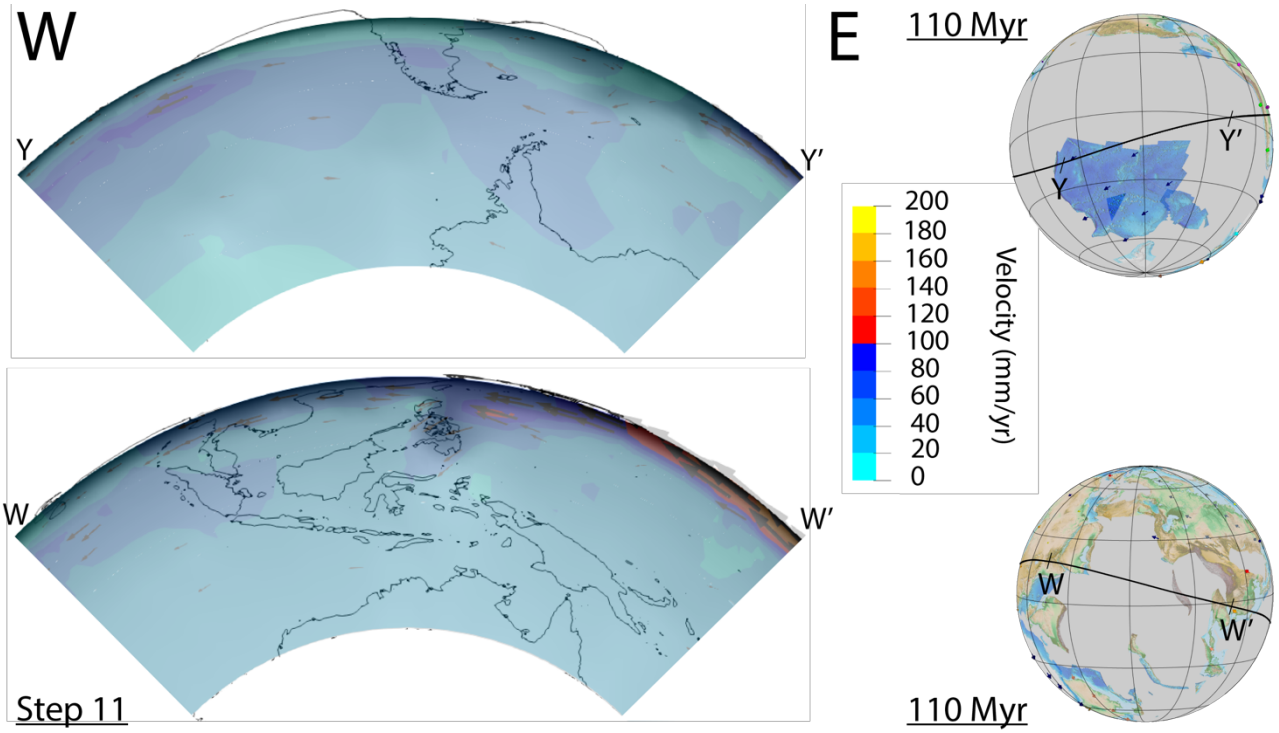

Figure B.48 – Step 11 (i.e., 110 Myr) for South American (upper panel) and Pacific (lower panel) side of model majfo89_2. Temperature (black shadow) and velocity (colored data plus arrows) data are overlapped for step 11 of model majfo89_2. Globes in the right part of the figure shows plate kinematics at 110 Myr in a shallow hotspot reference frame. The black line corresponds to the tectonic equator.

B.2 2d results in relative reference frames

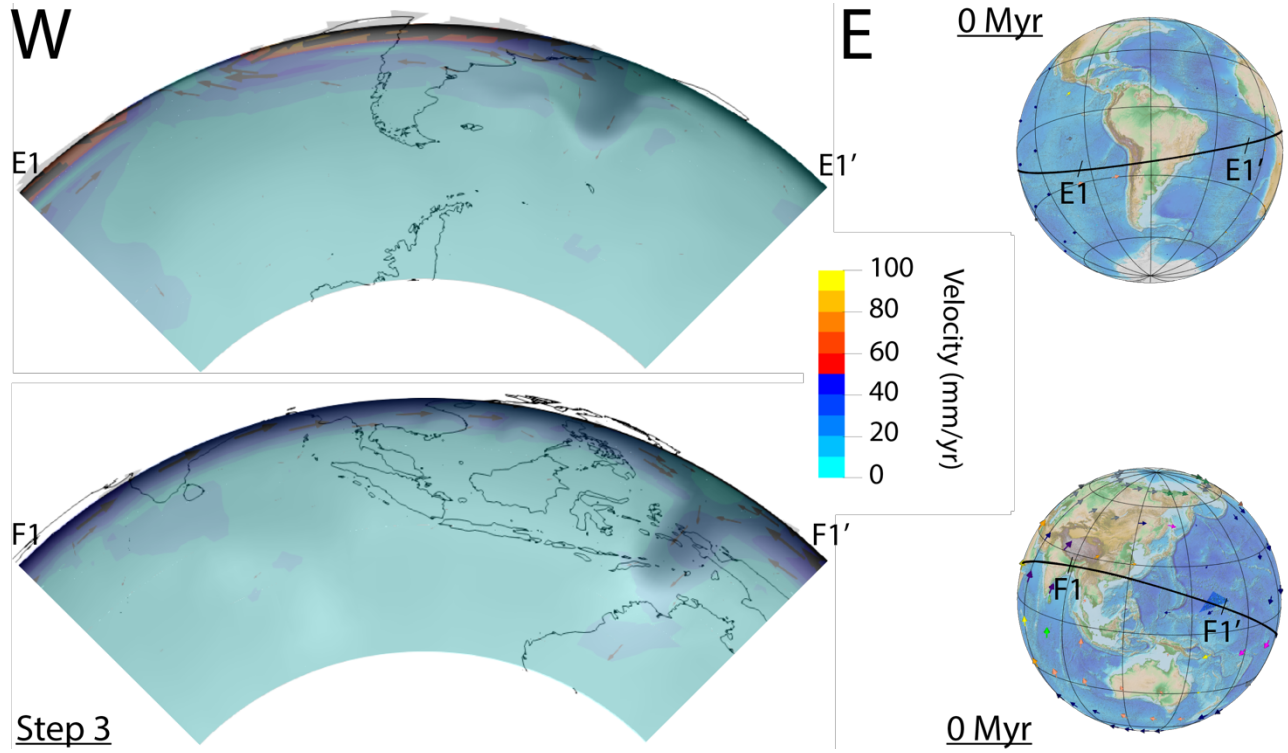

Figure B.49 – Step 3 (i.e., 30 Myr) for South American (upper panel) and Pacific (lower panel) model majol_sa and majol_ma. Temperature (black shadow) and velocity (colored data plus arrows) data are overlapped for step 3 of models majol_sa and majol_ma. Globes in the right part of the figure shows plate kinematics at 30 Myr in reference frames relative to South America (upper panel) and Marianas (lower panel) plates fixed. The black line corresponds to the modified tectonic equator with the rotation pole at longitude 100°E, latitude 65°S.

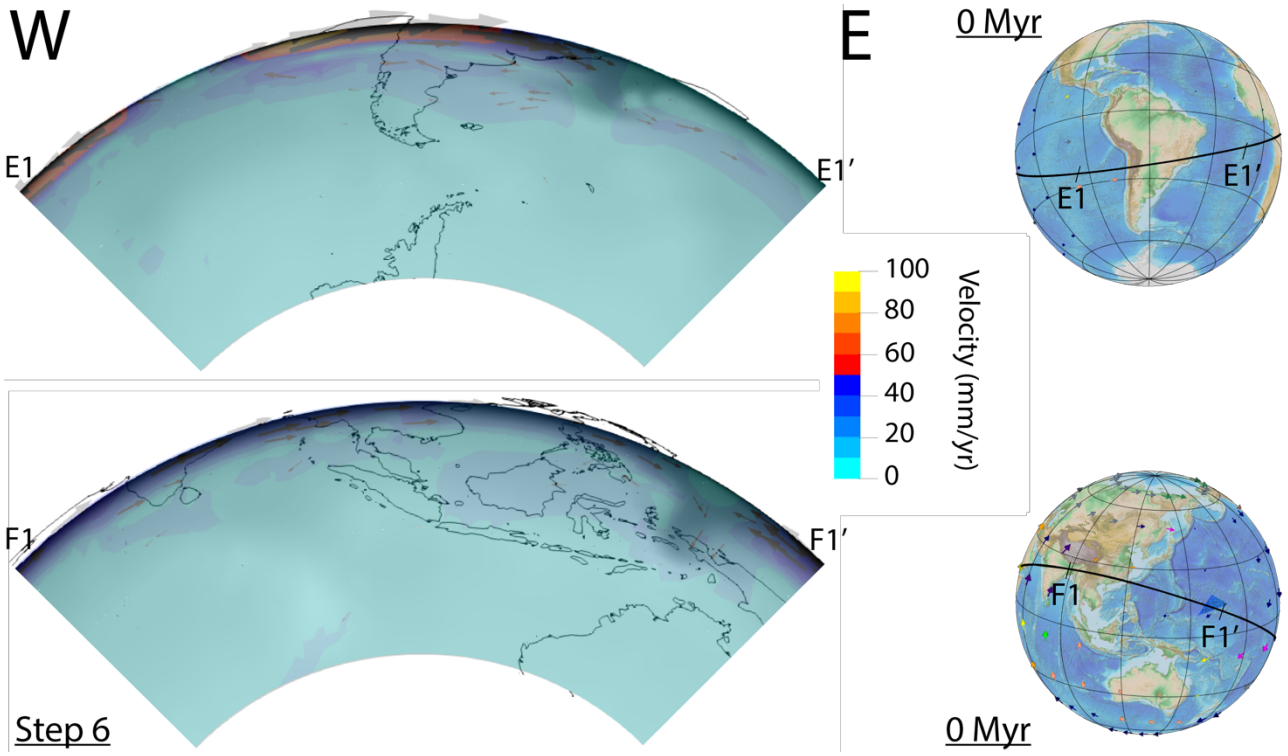

Figure B.50 – Step 6 (i.e., 60 Myr) for South American (upper panel) and Pacific (lower panel) model majol_sa and majol_ma. Temperature (black shadow) and velocity (colored data plus arrows) data are overlapped for step 6 of models majol_sa and majol_ma. Globes in the right part of the figure shows plate kinematics at 60 Myr in reference frames relative to South America (upper panel) and Marianas (lower panel) plates fixed. The black line corresponds to the modified tectonic equator with the rotation pole at longitude 100°E, latitude 65°S.

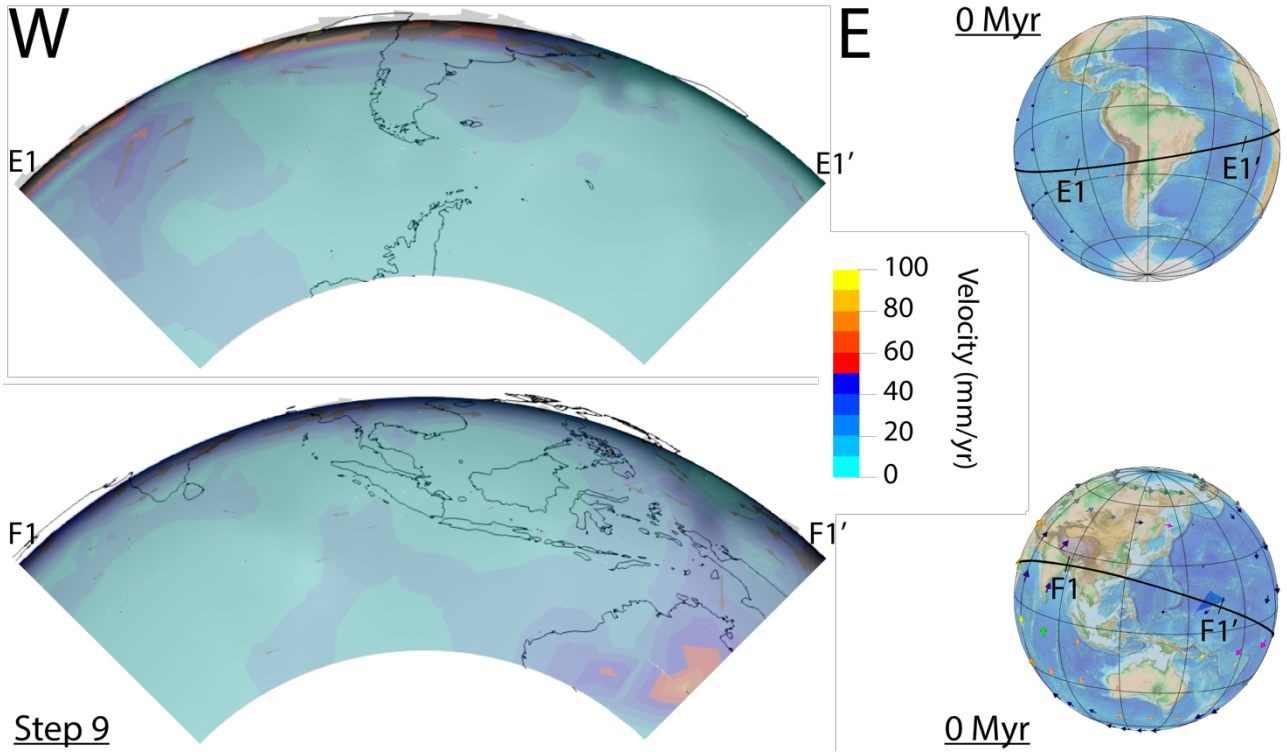

Figure B.51 – Step 9 (i.e., 90 Myr) for South American (upper panel) and Pacific (lower panel) model majol_sa and majol_ma. Temperature (black shadow) and velocity (colored data plus arrows) data are overlapped for step 9 of models majol_sa and majol_ma. Globes in the right part of the figure shows plate kinematics at 90 Myr in reference frames relative to South America (upper panel) and Marianas (lower panel) plates fixed. The black line corresponds to the modified tectonic equator with the rotation pole at longitude 100°E, latitude 65°S.

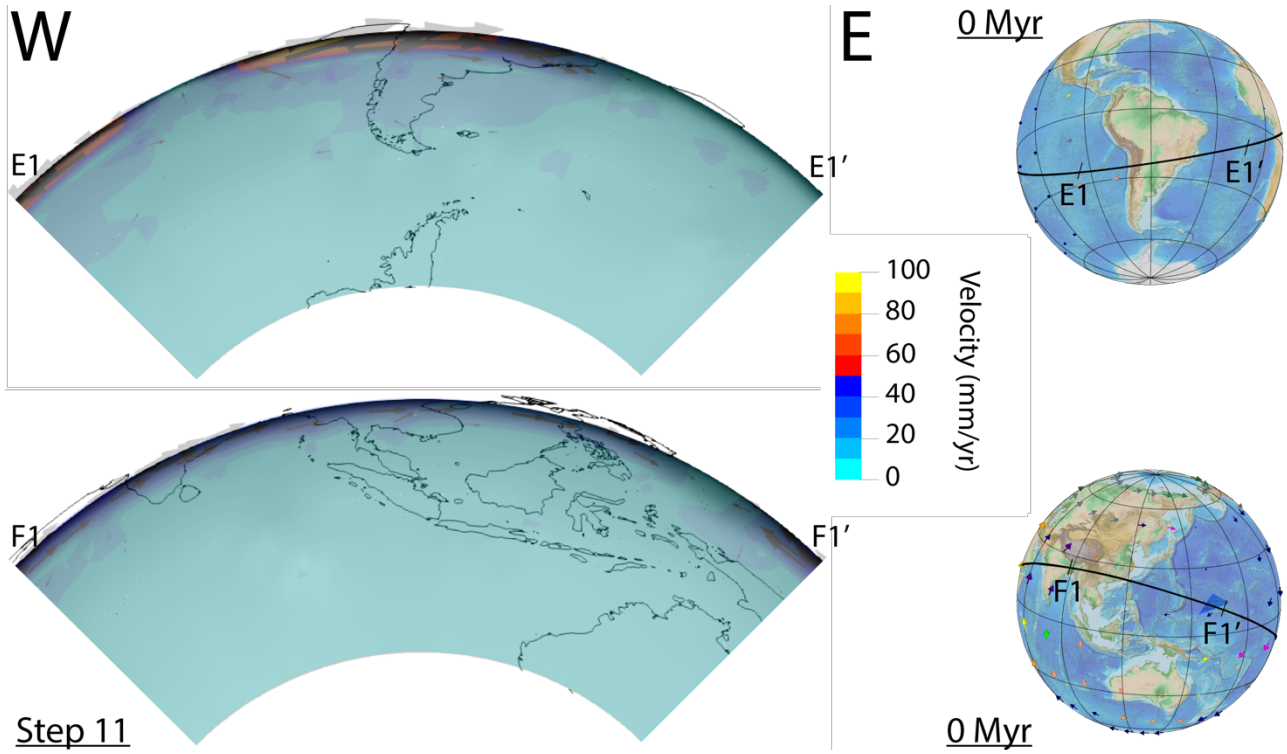

Figure B.52 – Step 11 (i.e., 110 Myr) for South American (upper panel) and Pacific (lower panel) model majol_sa and majol_ma. Temperature (black shadow) and velocity (colored data plus arrows) data are overlapped for step 11 of models majol_sa and majol_ma. Globes in the right part of the figure shows plate kinematics at 110 Myr in reference frames relative to South America (upper panel) and Marianas (lower panel) plates fixed. The black line corresponds to the modified tectonic equator with the rotation pole at longitude 100°E, latitude 65°S.

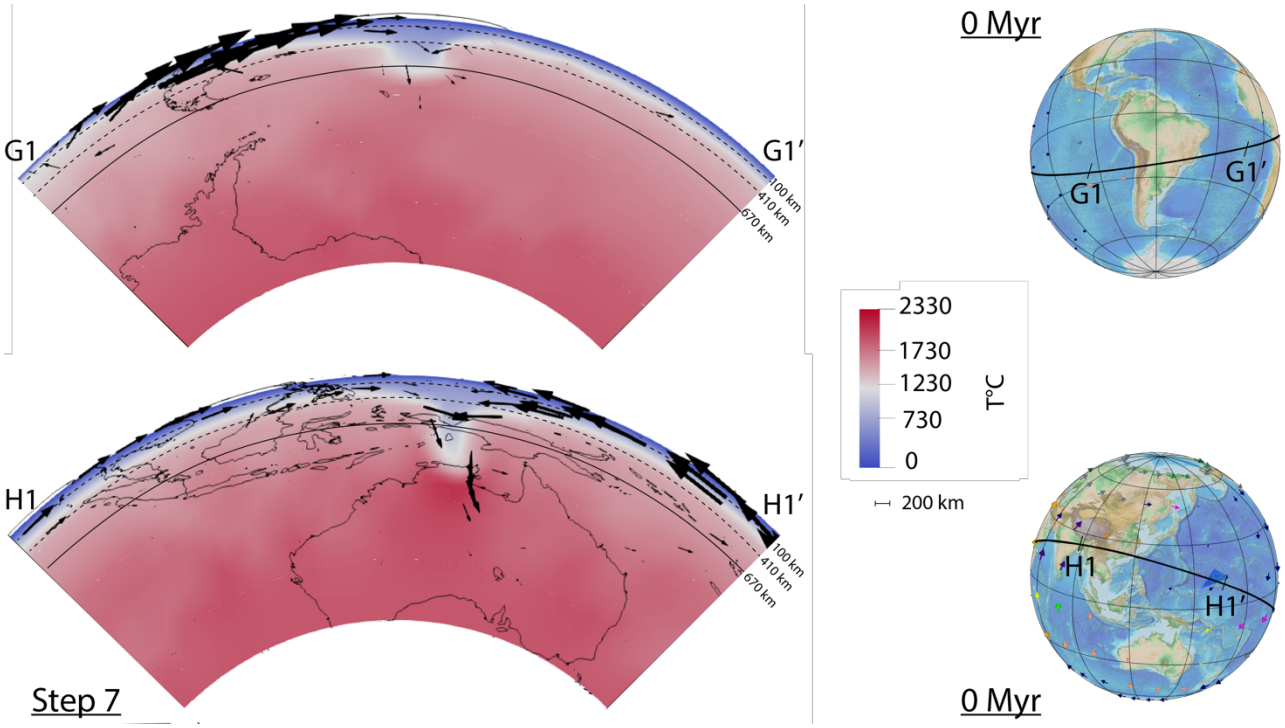

Figure B.53 – Step 7 (i.e., 70 Myr) for South American (upper panel) and Pacific (lower panel) model majfo89_sa and majfo89_ma. Temperature (colored) and velocity (arrows) data are overlapped for step 7 of models majol_sa and majol_ma. Globes in the right part of the figure shows plate kinematics at 70 Myr in reference frames relative to South America (upper panel) and Marianas (lower panel) plates fixed. The black line corresponds to the modified tectonic equator with the rotation pole at longitude 100°E, latitude 65°S.

B.3 3d results in absolute relative frames

B.3.1 majol3d_1 (Majorite-Fo50)

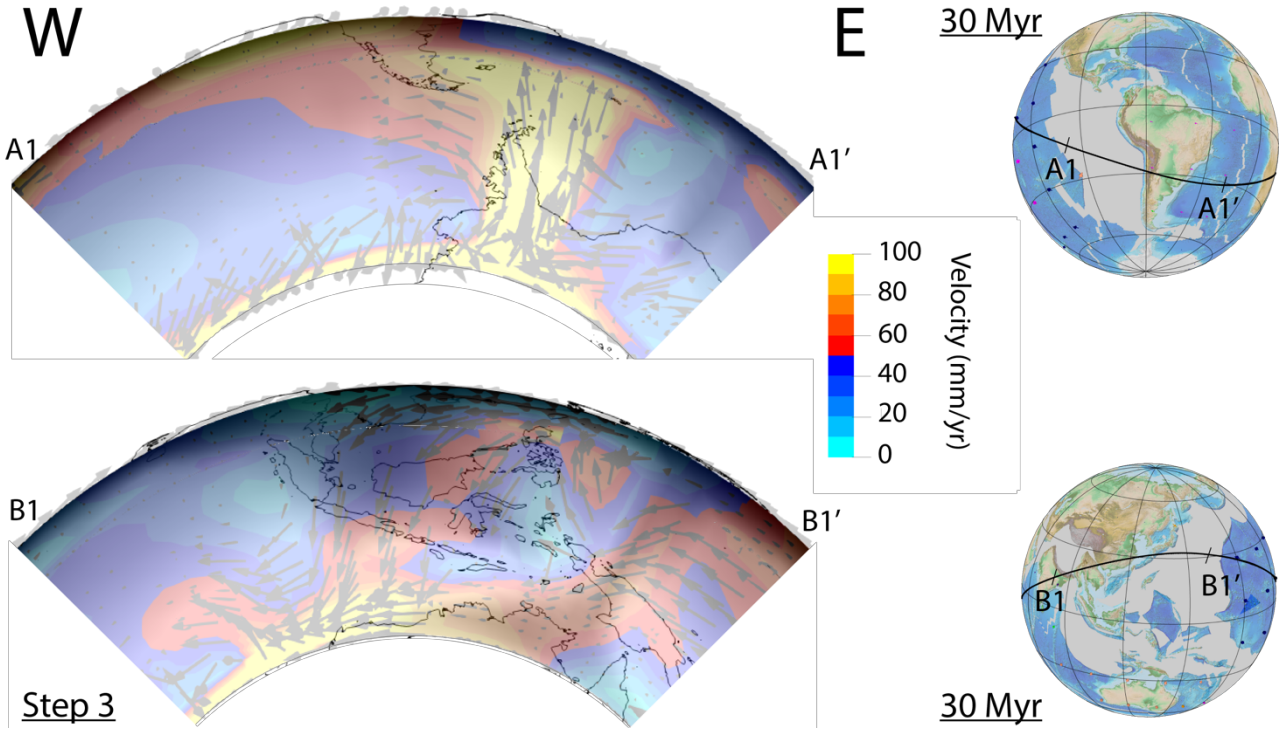

Figure B.54 – Step 3 (i.e., 30 Myr) for South American (upper panel) and Pacific (lower panel) side of model majol3d_1. Temperature (black shadow) and velocity (colored data plus arrows) data are overlapped for step 3 of model majol3d_1. Globes in the right part of the figure shows plate kinematics at 30 Myr in a deep hotspot reference frame. The black line corresponds to the tectonic equator.

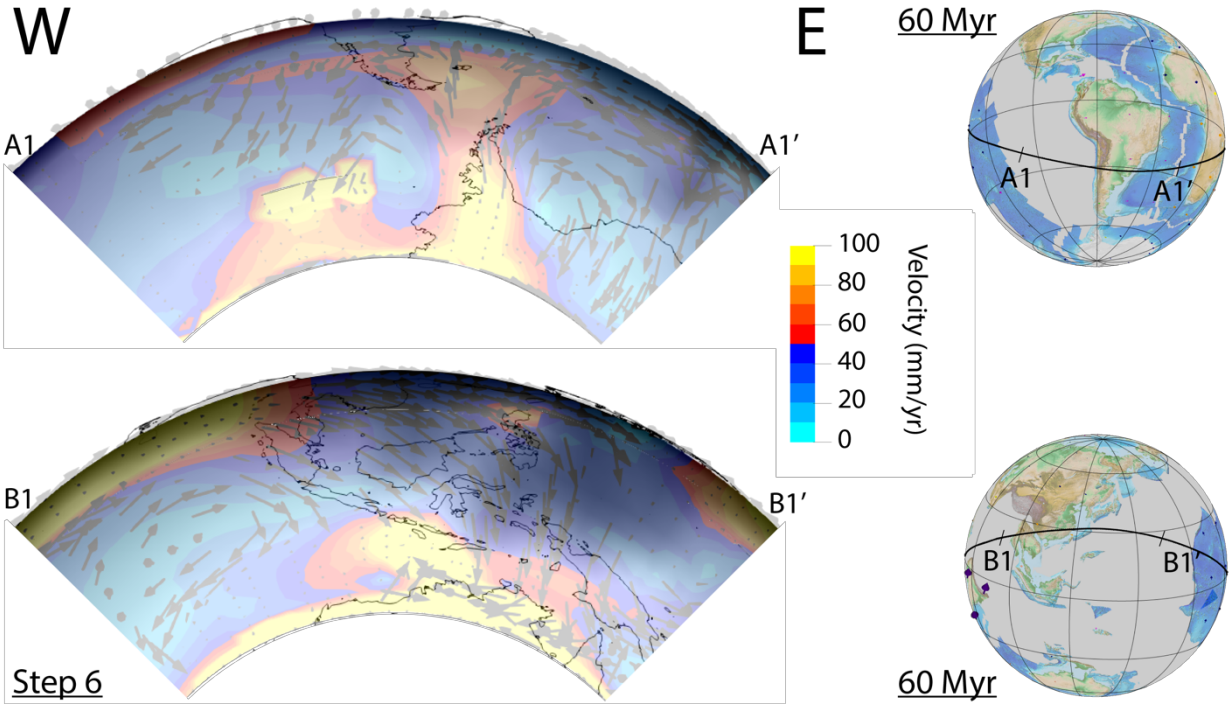

Figure B.55 – Step 6 (i.e., 60 Myr) for South American (upper panel) and Pacific (lower panel) side of model majol3d_1. Temperature (black shadow) and velocity (colored data plus arrows) data are overlapped for step 6 of model majol3d_1. Globes in the right part of the figure shows plate kinematics at 60 Myr in a deep hotspot reference frame. The black line corresponds to the tectonic equator.

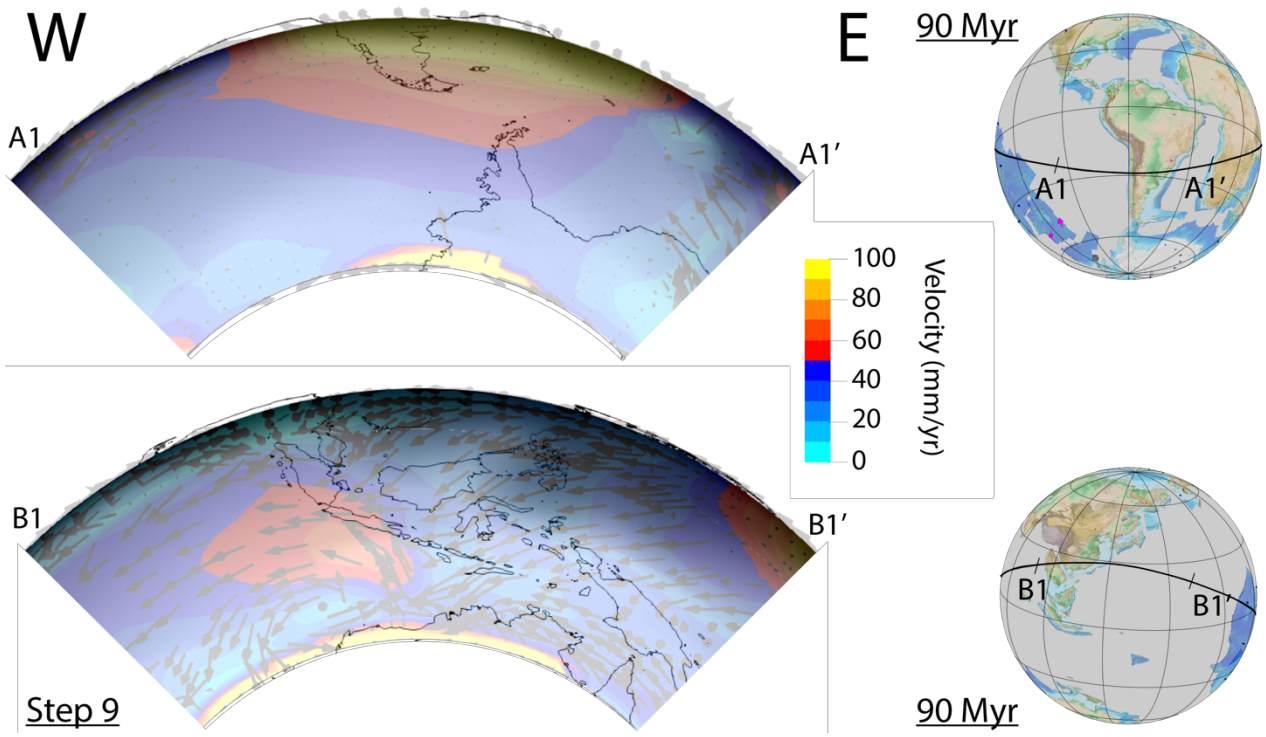

Figure B.56 – Step 3 (i.e., 90 Myr) for South American (upper panel) and Pacific (lower panel) side of model majol3d_1. Temperature (black shadow) and velocity (colored data plus arrows) data are overlapped for step 9 of model majol3d_1. Globes in the right part of the figure shows plate kinematics at 90 Myr in a deep hotspot reference frame. The black line corresponds to the tectonic equator.

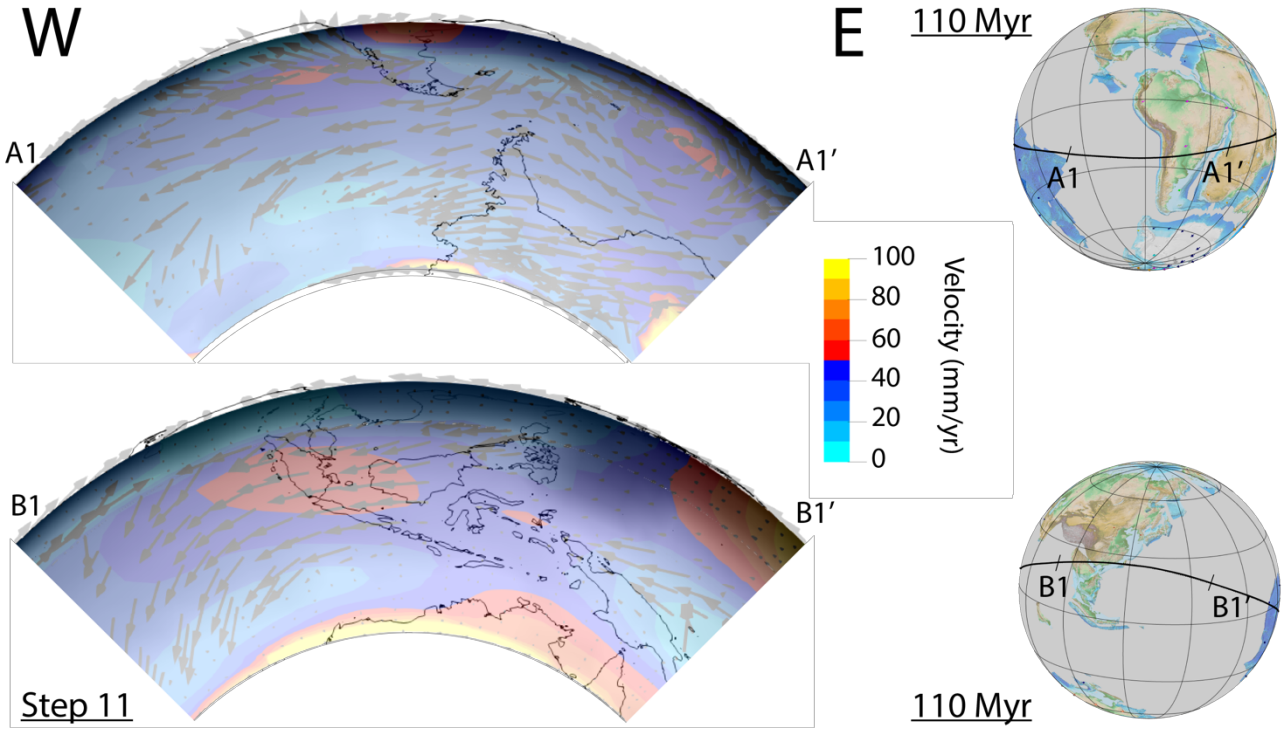

Figure B.57 – Step 11 (i.e., 110 Myr) for South American (upper panel) and Pacific (lower panel) side of model majol3d_1. Temperature (black shadow) and velocity (colored data plus arrows) data are overlapped for step 11 of model majol3d_1. Globes in the right part of the figure shows plate kinematics at 110 Myr in a deep hotspot reference frame. The black line corresponds to the tectonic equator.

B.3.2 majol3d_2 (Majorite-Fo50)

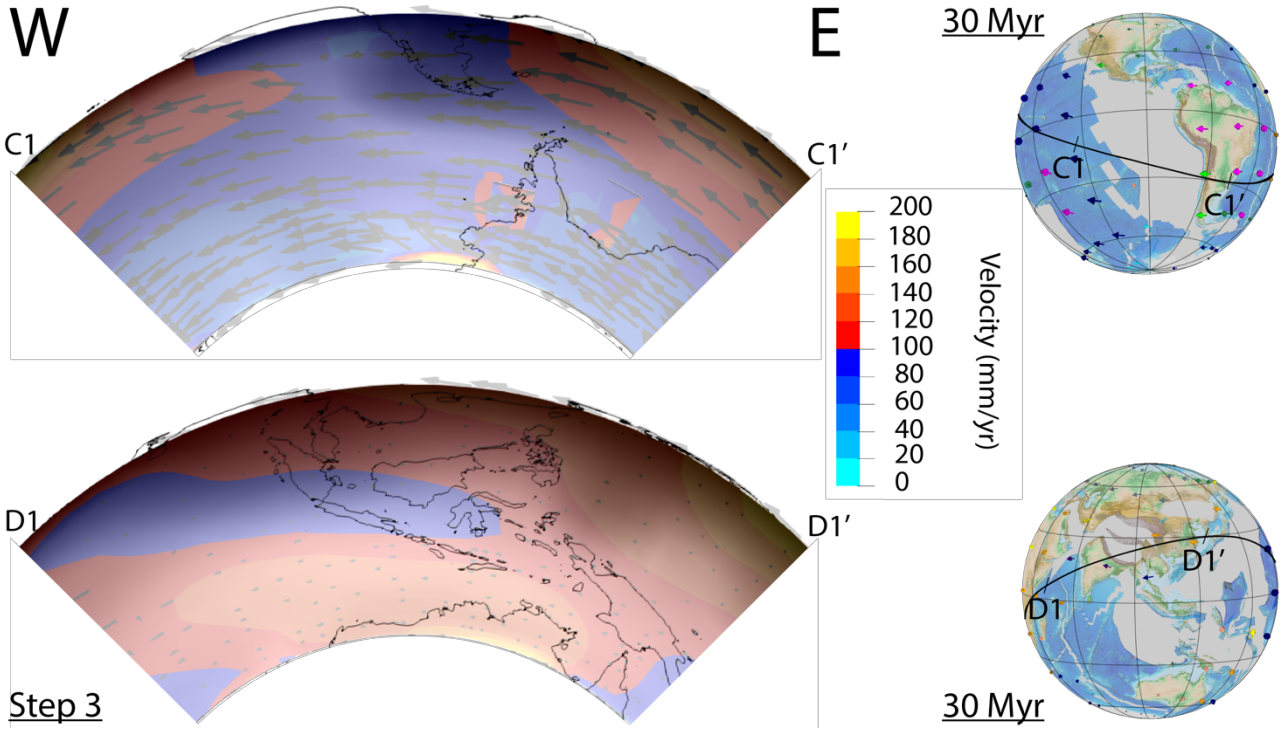

Figure B.58 – Step 3 (i.e., 30 Myr) for South American (upper panel) and Pacific (lower panel) side of model majol3d_2. Temperature (black shadow) and velocity (colored data plus arrows) data are overlapped for step 3 of model majol3d_2. Globes in the right part of the figure shows plate kinematics at 30 Myr in a shallow hotspot reference frame. The black line corresponds to the tectonic equator.

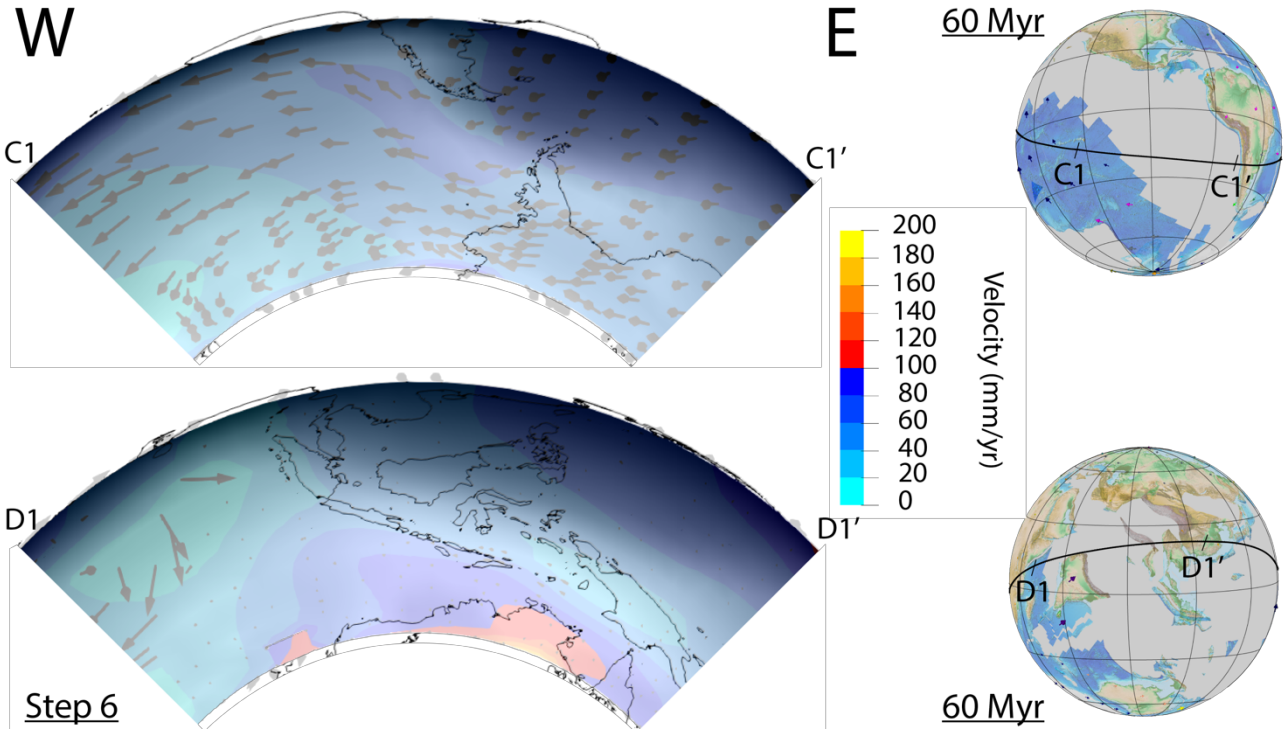

Figure B.59 – Step 6 (i.e., 60 Myr) for South American (upper panel) and Pacific (lower panel) side of model majol3d_2. Temperature (black shadow) and velocity (colored data plus arrows) data are overlapped for step 6 of model majol3d_2. Globes in the right part of the figure shows plate kinematics at 60 Myr in a shallow hotspot reference frame. The black line corresponds to the tectonic equator.

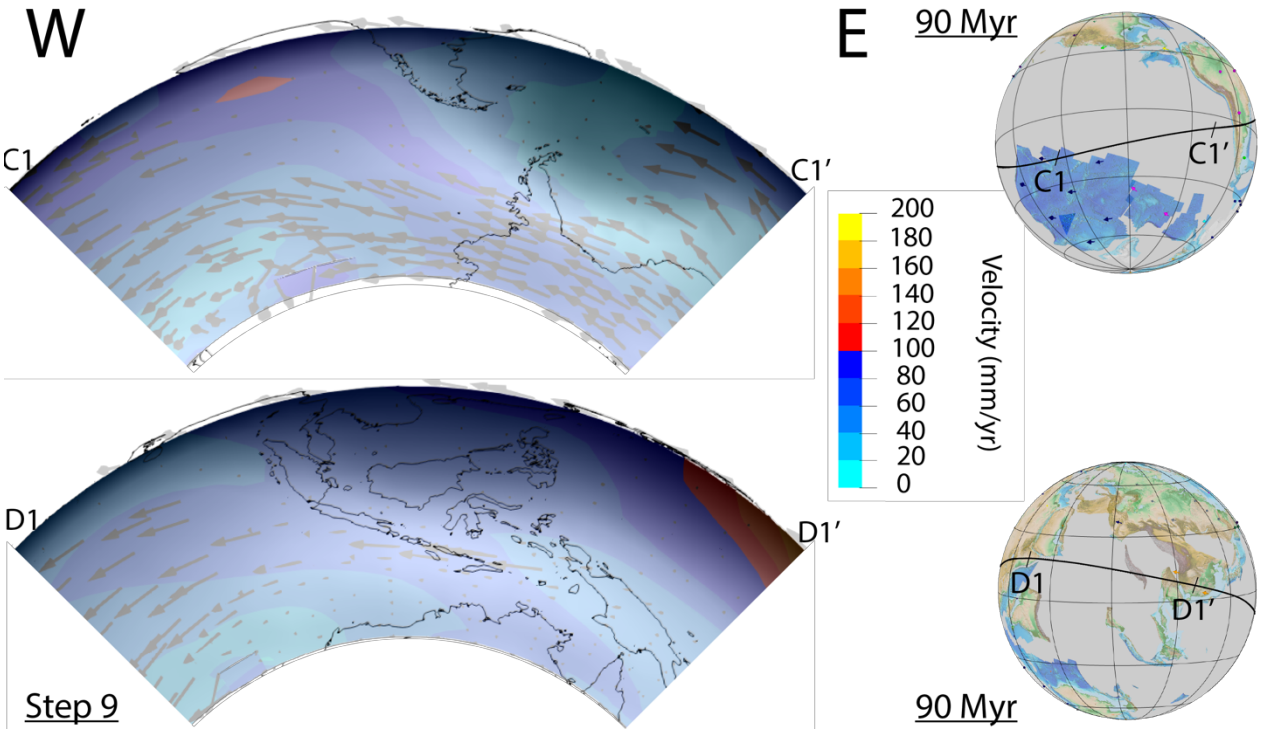

Figure B.60 – Step 9 (i.e., 90 Myr) for South American (upper panel) and Pacific (lower panel) side of model majol3d_2. Temperature (black shadow) and velocity (colored data plus arrows) data are overlapped for step 9 of model majol3d_2. Globes in the right part of the figure shows plate kinematics at 90 Myr in a shallow hotspot reference frame. The black line corresponds to the tectonic equator.

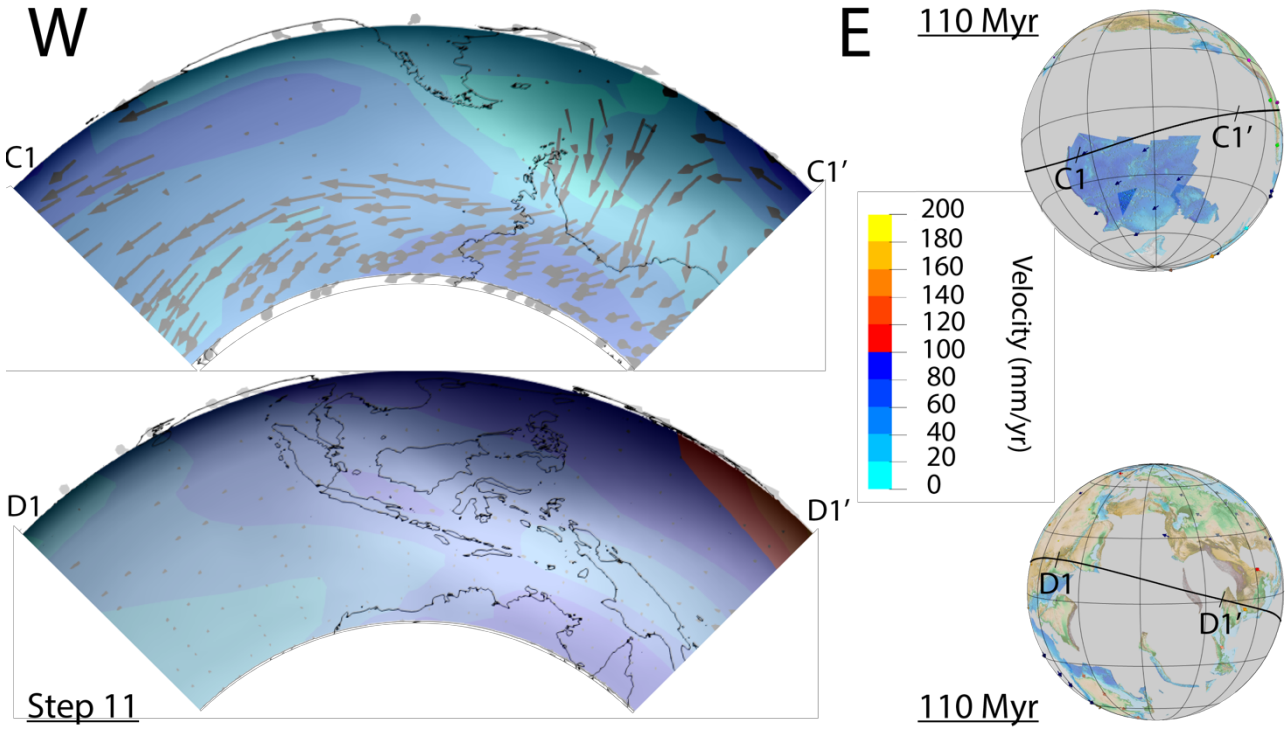

Figure B.61 – Step 11 (i.e., 110 Myr) for South American (upper panel) and Pacific (lower panel) side of model majol3d_2. Temperature (black shadow) and velocity (colored data plus arrows) data are overlapped for step 11 of model majol3d_2. Globes in the right part of the figure shows plate kinematics at 110 Myr in a shallow hotspot reference frame. The black line corresponds to the tectonic equator.

List of Figures

List of Tables

Acknowledgements

I would like to thank *Carlo Doglioni*, who during these three years has always found the time and energy to give me the courage and the passion needed for research, who always believed in me and in my crazy ideas and gave me everything possible to realize them.

One of the biggest thanks (however, nothing will be ever enough to say how much I owe you!) goes to *Marco Cuffaro*: you have always done everything possible to make me survive through all of this, making me stronger and self-conscious. You are one of the best person I have ever met and if I am a better person today it is also because of you.

Thanks to Prof. *Irina Artemieva*, Prof. *Taras Gerya* and Prof. *Alberto Malinverno* whose helpful reviews improved this manuscript.

A big thanks goes to Dr. *Luca Dal Zilio* for the work done together during these three years, Dr. *Vincenzo Stagno* and Prof. *Michele Lustrino* for their advice and help, Prof. *Maurizio Battaglia* for the teaching experience and his trust.

Thanks to everyone at *LaSaGna Lab* (plus affiliated), *Alessia*, *Roberta*, *Giampaolo*, *Lorenzo*, *Luca and Patrizio*: you were the best fellows I could ever ask and every word would be meaningless with respect to what each one of you meant to me.

And endless thanks goes to my parents, *Laura and Giancarlo*: three years ago I promised that the MSc would have been the last time of stress and despair, well…I lied to you! Thank you for all your patience, support and silent resignation, with all my crazy timetables and travels. Once again, I would have never made it without you. I love you to the moon and back!

A big thanks goes to *Daniele* for all his support: no matter what, I will always love you.

Last but not least, I would like to thank all my friends: *Emanuela*, who has always been with me through all of this; *Ylenia and Licia* my long-lived beloved friends; *Giada*, for the evening "relaxing" moments together; *Yelena and Francesco*, for all the time spent together.

References

Ahadov, B. & Jin, S. (2017). Present-day kinematics in the Eastern Mediterranean and Caucasus from dense GPS observations. *Physics of the Earth and Planetary Interiors*, 268, 54-64. http://dx.doi.org/10.1016/j.pepi.2017.05.003

Afonso, J. C., Ranalli, G. & Fernàndez, M. (2007). Density structure and buoyancy of the oceanic lithosphere revisited. *Geophysical Research Letters*, 34, L10302. https://doi.org/10.1029/2007GL029515

Anderson, J. (1995). *Computational Fluid Dynamics*. McGraw-Hill.

Anderson, D.L. (2001). Top-down Tectonics? *Science*, 293, 2016-2018. doi: 10.1126/science.1065448

Anderson, D.L. (2006). Speculation on the nature and cause of mantle heterogeneity. *Tectonophysics*, 416, 7-22. doi:10.1016/j.tecto.2005.07.011

Anderson, D.L. (2011). Hawaii, boundary layers and ambient mantle geophysical constraints. *Journal of Petrology*, 52, 1547–1577. https://doi.org/10.1093/petrology/egq068

Anderson, D.L. (2013). The persistent mantle plume myth. *Australian Journal of Earth Sciences*, 60, 657-673. doi: 10.1080/08120099.2013.835283

Anderson, D.L. & Sammis, C.G. (1970). Partial melting in the upper mantle. *Physics of the Earth and Planetary Interiors*, 3, 41-50. https://doi.org/10.1016/0031-9201(70)90042-7

Apel, E.V., Bürgmann, R., Steblov, G., Vasilenko, N., King, R. & Prytkov, A. (2006). Independent active microplate tectonics of northeast Asia from GPS velocities and block modeling. *Geophysical Research Letters*, 33, L11303. doi:10.1029/2006GL026077

Arisa, D. & Heki, K. (2016). Transient crustal movement in the northern Izu–Bonin arc starting in 2004: A large slow slip event or a slow back-arc rifting event? *Tectonophysics*, 682, 206-213. http://dx.doi.org/10.1016/j.tecto.2016.05.029

Artemieva, I.M. (2011). *The lithosphere: An Interdisciplinary Approach*. Cambridge University Press.

Artemieva, I.M., Thybo, H. & Shulgin, A. (2016). Geophysical constraints on geodynamic processes at convergent margins: A global perspective. *Gondwana Research*, 33, 4-23. https://doi.org/10.1016/j.gr.2015.06.010

Asimow, P.D. & Langmuir, C.H. (2003). The importance of water to oceanic mantle melting regimes. *Nature*, 421, 815-820. doi: 10.1038/nature01429

Bailey, I.W., Alpert, L.A., Becker, T.W. & Miller, M.S. (2012). Co-seismic deformation of deep slabs based on summed CMT data. *Journal of Geophysical Research*, 117, B04404. doi: 10.1029/2011JB008943

Ballmer, M.D., Houser, C., Hernlund, J.W., Wentzcovitch, R.M. & Hirose, K. (2017). Persistence of strong silica-enriched domains in the Earth's lower mantle. *Nature Geoscience*, 10, 236-241. https://doi.org/10.1038/ngeo2898

Bangerth, W., Dannberg, J, Gassmöller, R, Heister, T. et al. (2018). ASPECT: Advanced Solver for Problems in Earth's ConvecTion, User Manual. doi:10.6084/m9.figshare.4865333

Bangerth, W., Hartmann, R. & Kanschat, G. (2007). deal.II — a general-purpose object-oriented finite element library. *ACM Transactions on Mathematical Software*, 33. doi:10.1145/1268776.1268779

Bangerth, W., Heister, T. & Kanschat, G. (2012). deal.II Differential equations analysis library, Tech. rep. http://www.dealii.org/

Barry, T.L., Davies, J.H., Wolstencroft, M., Millar, I.L., Zhao, Z., Jian, P., Safonova, I. & Price, M. (2017). Whole-mantle convection with tectonic plates preserves long-term global patterns of upper mantle geochemistry. *Scientific Reports*, 7, 1870. https://doi.org/10.1038/s41598-017-01816-y

Beavan, J., Wallace, L.M., Palmer, N., Denys, P., Ellis, S., Fournier, N., et al. (2016). New Zealand GPS velocity field: 1995–2013. *New Zealand Journal of Geology and Geophysics*, 59, 5-14. doi: 10.1080/00288306.2015.1112817

Becker, T.W. (2017). Superweak asthenosphere in light of upper mantle seismic anisotropy. *Geochemistry Geophysics Geosystems*, 18. doi:10.1002/2017GC006886.

Bellahsen, N., Faccenna, C. & Funiciello, F. (2005). Dynamics of subduction and plate motion in laboratory experiments: Insights into the "plate tectonics" behavior of the Earth. *Journal of Geophysical Research*, 110, B01401. doi:10.1029/2004JB002999

Bennett, R.A., Hreinsdottir, S., Buble, G., Bašić, T., Bacic, Z., Marjanovic, M., et al. (2008). Eocene to present subduction of southern Adria mantle lithosphere beneath the Dinarides. *Geology*, 36, 3-6. doi:10.1130/G24136A.1

Billen, M.I. & Hirth, G. (2007). Rheologic controls on slab dynamics. *Geochemistry Geophysics Geosystems*, 8, 1525-2027. doi: 10.1029/2007GC001597

Bina, C.R. (1998). Lower mantle mineralogy and the geophysical perspective. In *Ultrahigh-pressure Mineralogy, Physics and Chemistry of the Earth's Deep Interior,* Eds. R Hemley, pp. 205–39. Washington, DC: Mineralogical Society of America.

Birch, F. (1947). Finite Elastic Strain of Cubic Crystals. *Physical Review*, 71, 809–824. doi: 10.1103/PhysRev.71.809

Bokelman, G.H. & Silver, P.G. (2000). Mantle variation within the Canadian Shield: Travel times from the portable broadband Archean-Proterozoic transect 1989. *Journal of Geophysical Research*, 105, 579-605. https://doi.org/10.1029/1999JB900387

Boneh, Y., Wallis, D., Hansen, L.N., Krawczynski, M.J. & Skemer, P. (2017). Oriented grain growth and modification of 'frozen anisotropy' in the lithospheric mantle. *Earth and Planetary Science Letters*, 474, 368-374. http://dx.doi.org/10.1016/j.epsl.2017.06.050

Bonnardot, M.-A., Hassani, R., Tric, E., Ruellan, E. & Régnier, M. (2008). Effect of margin curvature on plate deformation in a 3-D numerical model of subduction zones. *Geophysical Journal International*, 173, 1084-1094. doi: 10.1111/j.1365-246X.2008.03752.x

Bostrom, R. C. (1971). Westward Displacement of the Lithosphere. *Nature*, 234, 536-538. doi: 10.1038/234536a0

Boyden, J.A., Müller, R.D., Gurnis, M., Torsvik, T.H., Clark, J.A., Turner, M., Ivey-Law, H., Watson, R.J., et al. (2011). Next-generation plate-tectonic reconstructions using GPlates. In Eds. G. Keller & C. Baru, *Geoinformatics: Cyberinfrastructure for the Solid Earth Sciences* (pp. 95-114). Cambridge: Cambridge University Press. doi:10.1017/CBO9780511976308.008

Boutelier, D.A. & Cruden, A.R. (2008). Impact of regional mantle flow on subducting plate geometry and interplate stress: insights from physical modelling. *Geophysical Journal International*, 174, 719-732. doi: 10.1111/j.1365-246X.2008.03826.x

Brandmayr, E., Marson, I., Romanelli, F. & Panza, G.F. (2011). Lithosphere density model in Italy: no hint for slab pull. *Terra Nova*, 0, 1-8. doi: 10.1111/j.1365-3121.2011.01012.x

Bunge, H.-P., Ricard, Y. & Matas, J. (2001). Non-adiabaticity in mantle convection. *Geophysical Research Letters*, 28, 879-882. doi:10.1029/2000GL011864

Burstedde, C., Wilcox, L.C. & Ghattas, O. (2011). p4est: Scalable Algorithms for Parallel Adaptive Mesh Refinement on Forests of Octrees. *SIAM Journal on Scientific Computing*, 33, 1103-1133. doi:10.1137/100791634

Cahill, T. & Isacks, B.L. (1992). Seismicity and Shape of the Subducted Nazca Plate. *Journal of Geophysical Research*, 97, 17503-17529. https://doi.org/10.1029/92JB00493

Calmant, S., Pelletier, B., Lebellegard, P., Bevis, M., Taylor, F.W. & Phillips, D.A. (2003). New insights on the tectonics along the New Hebrides subduction zone based on GPS results. *Journal of Geophysical Research*, 108, 2319. doi:10.1029/2001JB000644

Capitanio, F. A., Morra, G. & Goes, S. (2007). Dynamic models of downgoing plate-buoyancy driven subduction: Subduction motions and energy dissipation. *Earth and Planetary Science Letters*, 262, 284-297. doi: 10.1016/j.epsl.2007.07.039

Capitanio, F.A., Stegman, D. R., Moresi, L. N. & Sharples, W. (2010). Upper plate controls on deep subduction, trench migrations and deformations at convergent margins. *Tectonophysics*, 483, 80-92. doi:10.1016/j.tecto.2009.08.020

Carcaterra, A. & Doglioni, C. (2018). The westward drift of the lithosphere: A tidal ratchet? *Geoscience Frontiers*, 9, 403-414. https://doi.org/10.1016/j.gsf.2017.11.009

Carminati, E. & Doglioni, C. (2012). Alps vs Apennines: The paradigm of a tectonically asymmetric Earth. *Earth-Science Reviews*, 112, 67-96. doi: 10.1016/j.earscirev.2012.02.004

Carminati, E. & P. Petricca (2010). State of stress in slabs as a function of large scale plate kinematics. *Geochemistry Geophysics Geosystems*, 11. http://dx.doi.org/10.1029/2009GC003003

Chantel, J., Manthilake, G., Andrault, D., Novella, D., Yu, T. & Wang, Y. (2016). Experimental evidence supports mantle partial melting in the asthenosphere. *Science Advances*, 2, e1600246. doi: 10.1126/sciadv.1600246

Clauser, C. & Huenges, E. (1995). Thermal conductivity of rocks and minerals. In: Ahrens, T.J. (Ed.), *Rock Physics and Phase Relations*. AGU, AGU reference shelf 3, Washington DC, pp. 105–126.

Colli, L., Ghelichkhan, S., Bunge, H.P. & Oeser, J. (2018). Retrodictions of Mid Paleogene mantle flow and dynamic topography in the Atlantic region from compressible high resolution adjoint mantle convection models: Sensitivity to deep mantle viscosity and tomographic input model. *Gondwana Research*, 53, 252-272. https://doi.org/10.1016/j.gr.2017.04.027

Coltice, N., Gérault, M. & Ulvrová., M. (2017). A mantle convection perspective on global tectonics. *Earth-Science Reviews*, 165, 120-150. https://doi.org/10.1016/j.earscirev.2016.11.006

Coltice, N. & Schmalzl, J. (2006). Mixing times in the mantle of the early Earth derived from 2-D and 3-D numerical simulations of convection. *Geophysical Research Letters*, 33, L23304. https://doi.org/10.1029/2006GL027707

Condie, K.C. (2016). *Earth as an evolving planetary system*. Elsevier.

Conrad, C.P. & Behn, M.D. (2010). Constraints on lithosphere net rotation and asthenospheric viscosity from global mantle flow models and seismic anisotropy. *Geochemistry Geophysics Geosystems*, 11, Q05W05, doi: 10.1029/2009GC002970

Conrad, C. P. & Hager, B. H. (1999). Effects of plate bending and faults strength at subduction zones on plate dynamics. *Journal of Geophysical Research*, 104, 551-571. https://doi.org/10.1029/1999JB900149

Conrad, P. C. & Lithgow-Bertelloni, C. (2002). How Mantle Slabs Drive Plate Tectonics. *Science*, 298, 207-209. doi: 10.1126/science.1074161

Cottaar, S., Heister, T., Myhill, R., Rose, I. & Unterborn, C. (2017): BurnMan v0.10.0 [Software]. Computational Infrastructure for Geodynamics. Zenodo.

Cottaar S., Heister, T., Rose, I. & Unterborn, C. (2014). BurnMan: A lower mantle mineral physics toolkit. *Geochemistry Geophysics Geosystems*, 15, 1164-1179. https://doi.org/10.1002/2013GC005122

Crameri, F., Tackley, P., Meilick, I., Gerya, T. & Kaus, B. (2012). A free plate surface and weak oceanic crust produce single-sided subduction on Earth. *Geophysical Research Letters*, 39, L03306. https://doi.org/10.1029/2011GL050046

Crépisson, C., Morard, G., Bureau, H., Prouteau, G., Morizet, Y., Petitgirard, S. & Sanloup, C. Magmas trapped at the continental lithosphere-asthenosphere boundary. *Earth and Planetary Science Letters*, 393, 105-112. https://doi.org/10.1016/j.epsl.2014.02.048

Crespi, M., Cuffaro, M., Doglioni, C., Giannone, F. & Riguzzi, F. (2007). Space geodesy validation of the global lithospheric flow. *Geophysical Journal International*, 168, 491-506. doi: 10.1111/j.1365-246X.2006.03226.x

Cruciani, C., Carminati, E. & Doglioni, C. (2005). Slab dip vs. lithosphere age: No direct function. *Earth and Planetary Science Letters*, 238, 298-310. https://doi.org/10.1016/j.epsl.2005.07.025

Cuffaro, M., Caputo, M. & Doglioni, C. (2008). Plate subrotations. *Tectonics*, 27, TC4007. doi: 10.1029/2007TC002182

Cuffaro, M. & Doglioni, C. Global kinematics in deep versus shallow hotspot reference frames, in Foulger, G.R. and Jurdy, D.M., eds. Plates, plumes, and planetary processes. *Geol. Soc. Spec. Pap.*, **430**, 359-374 (2007).

Cuffaro, M. & Doglioni, C. (2018). On the increasing size of the orogens moving from the Alps to the Himalayas in the frame of the net rotation of the lithosphere. *Gondwana Research*, 62, 2-13. https://doi.org/10.1016/j.gr.2017.09.008

Cuffaro, M. & Jurdy, D.M. (2006). Microplate motions in the hotspot reference frame. *Terra Nova*, 18, 276-281. https://doi.org/10.1111/j.1365-3121.2006.00690.x

Cuffaro, M. & Miglio, E. (2012). Asymmetry of thermal structure at slow-spreading ridges: Geodynamics and numerical modeling. *Computer & Fluids*, 68, 29-37. https://doi.org/10.1016/j.compfluid.2012.07.028

Dahlstrom, C.D.A. (1969). Balanced cross sections. *Canadian Journal of Earth Sciences*, 6, 743-757.

Dahlstrom, C.D.A. (1970). Structural geology in the eastern margin of the Canadian Rocky Mountains. *Bulletin of Canadian Petroleum, Geology*, 18, 332-406.

Dal Zilio, L., Faccenda, M. & Capitanio, F. (2017). The role of deep subduction in supercontinent breakup. *Tectonophysics*. https://doi.org/10.1016/j.tecto.2017.03.006

DeMets, C., Gordon, R.G., Argus, F. & Stein, S. (1990). Current plate motions. *Geophysical Journal International*, 101, 425-478.

DeMets, C., Gordon, R.G., Argus, D.F. & Stein, S. (1994). Effect of recent revisions to the geomagnetic reversal time scale on estimates of current plate motions. *Geophysical Research Letters*, 21, 2121-2194.

DeMets, C., Gordon, R.G., & Argus, D.F. (2010). Geologically current plate motions. *Geophysical Journal International*, 181, 1–80. https://doi.org/10.1111/j.1365-246X.2009.04491.x

Devoti, R., D'Agostino, N., Serpelloni, E., Pietrantonio, G., Riguzzi, F., Avallone, A., et al. (2017). A Combined Velocity Field of the Mediterranean Region. *Annals of Geophysics*, 60, S0215. doi:10.4401/ag-7059

Devoti, R., Riguzzi, F., Cuffaro, M. & Doglioni, C. (2008). New GPS constraints on the kinematics of the Apennines subduction. *Earth and Planetary Science Letters*, 273, 163-174. doi: 10.1016/j.epsl.2008.06.031

Di Bucci, D. & Mazzoli, S. (2002). Active tectonics of the Northern Apennines and Adria geodynamics: new data and a discussion. *Journal of Geodynamics*, 34, 687-707. https://doi.org/10.1016/S0264-3707(02)00107-2

Doglioni, C. (2008). L'interno della Terra. *Treccani Scuola.*

Doglioni, C. (2008). Comment on "The potential influence of subduction zone polarity on overriding plate deformation, trench migration and slab dip angle" by W.P. Schellart. *Tectonophysics*, 463, 208-213. doi: 10.1016/j.tecto.2008.02.012

Doglioni, C. & Anderson, D. L. (2015). Top-driven asymmetric mantle convection. In Foulger, G.R., Lustrino, M., and King, S.D., Eds., The Interdisciplinary Earth: A Volume in Honor of Don L. Anderson: Geological Society of America Special Paper, 514**,** and AGU Special Publication, 71.

Doglioni, C., Carminati, E. & Bonatti, E. (2003). Rift asymmetry and continental uplift. *Tectonics*, 22, 1024. doi:10.1029/2002TC001459

Doglioni, C., Carminati, E., Crespi, M., Cuffaro, M., Penati, M. & Riguzzi, F. (2015). Tectonically asymmetric Earth: From net rotation to polarized westward drift of the lithosphere. *Geoscience Frontiers*, 6, 401-418. https://doi.org/10.1016/j.gsf.2014.02.001

Doglioni, C., Carminati, E. & Cuffaro, M. (2006). Simple Kinematics of Subduction Zones. *International Geology Reviews*, 48, 479-493. doi: 10.1016/j.earscirev.2007.04.001

Doglioni, C., Carminati, E., Cuffaro, M. & Scrocca, D. (2007). Subduction kinematics and dynamic constraints. *Earth-Science Reviews*, 83, 125-175. https://doi.org/10.1016/j.earscirev.2007.04.001

Doglioni, C., Cuffaro, M. & Carminati, E. (2006) What moves slabs? *Bollettino di Geofisica Teorica e Applicata,* 47, 227-247.

Doglioni, C., Green, D.H. & Mongelli, F. (2005). On the shallow origin of hotspots and the westward drift of the lithosphere. In: Foulger, G.R., Natland, J.H., Presnall, D.C., Anderson, D.L. (Eds.), *Plates, Plumes, and Paradigms*. Geological Society of America Special Paper, 388, 735–749. doi: 10.1130/2005.2388(42)

Doglioni, C., Harabaglia, P., Merlini, S., Mongelli, F., Peccerillo, A. & Piromallo, C. (1999). Orogens and slabs vs. their direction of subduction. *Earth-Sciences Reviews*, 45, 167-208. https://doi.org/10.1016/S0012-8252(98)00045-2

Doglioni C., Ismail-Zadeh A., Panza G. & Riguzzi F. (2011). Lithosphere-asthenosphere viscosity contrast and decoupling. *Physics of the Earth and Planetary Interiors*, 189, 1-8. https://doi.org/10.1016/j.pepi.2011.09.006

Doglioni, C. & Panza, G. (2015). Polarized plate tectonics. *Advances in Geophysics*, 56, 1–167. https://doi.org/10.1016/bs.agph.2014.12.001

Doglioni, C., Tonarini, S. & Innocenti, F. (2009). Mantle wedge asymmetries and geochemical signatures along W- and E-NE-directed subduction zones. *Lithos*, 113, 179-189. https://doi.org/10.1016/j.lithos.2009.01.012

Dziewonsky, A.M. & Anderson, D.L. (1981). Preliminary reference Earth model. *Physics of the Earth and Planetary Interiors*, 25, 297-356.

Engdahl, E.R. & Villasenor, A. (2002). Global Seismicity: 1900-1999. In: Lee, H.K., Kanamori, H., Jennings, P.C., et al., Eds., *International Handbook of Earthquake and Engineering Seismology*, Part A, Academic Press, Amsterdam.

England, P., Houseman, G., & Nocquet, J-M. (2016). Constraints from GPS measurements on the dynamics of deformation in Anatolia and the Aegean. *Journal of Geophysical Research Solid Earth*, 121, 8888–8916. doi:10.1002/2016JB013382

Faccenda, M. & Dal Zilio, L. (2017). The role of solid–solid phase transitions in mantle convection, *Lithos*, 268, 198-224. https://doi.org/10.1016/j.lithos.2016.11.007

Faccenda, M., Gerya, T. V. & Burlini, L. (2009). Deep slab hydration induced by bending-related variations in tectonic pressure. *Nature Geosciences*, 2, 790-793. https://doi.org/10.1038/ngeo656

Faccenna, C., Becker, T. W., Lucente, F. P., Jolivet, L. & Rossetti, F. (2001). History of subduction and back-arc extension in the Central Mediterranean. *Geophysical Journal International,* 145, 809-820. https://doi.org/10.1046/j.0956-540x.2001.01435.x

Fan, G., Wallace, C. & Zhao, D. (1998). Tomographic imaging of deep velocity structure beneath the Eastern and Southern Carpathians, Romania: Implications for continental collision. *Journal of Geophysical Research Solid Earth*, 103, 2705-2723. doi: 10.1029/97JB01511

Fischer, K., Creager, K.C. & Jordan, T.H. (1991). Mapping the Tonga Slab. *Journal of Geophysical Research*, 96, 14403-14427. https://doi.org/10.1029/90JB02703

Forsyth, D. & Uyeda, S. (1975). On the Relative Importance of the Driving Forces of Plate Motion. *Geophysical Journal of the Royal Astronomical Society*, 43, 163-200. https://doi.org/10.1111/j.1365-246X.1975.tb00631.x

Foulger, G.R., Panza, G.F., Artemieva, I.M., Bastow, I.D., Cammarano, F., Evans, J.R., Hamilton, W.B., Julian, B.R. (2013). Caveats on tomographic images. *Terra Nova*, 25, 259-281. https://doi.org/10.1111/ter.12041

Frost, D.A., Garnero, E.J. & Rost, S. (2018). Dynamical links between small- and large-scale mantle heterogeneity: Seismological evidence. *Earth and Planetary Science Letters*, 482, 135-146. https://doi.org/10.1016/j.epsl.2017.10.058

Fukao, Y. & Obayashi, M. (2013). Subducted slabs stagnant above, penetrating through, and trapped below the 660 km discontinuity. *Journal of Geophysical Research*, 118, 5920-5938. https://doi.org/10.1002/2013JB010466

Garfunkel, Z., Anderson, C.A. & Schubert, G. (1986). Mantle circulation and the lateral migration of subducted slabs. *Journal of Geophysical Research*, 91, 7205–7223. https://doi.org/10.1029/JB091iB07p07205

Gerya, T.V. (2010). *Introduction to Numerical Geodynamic Modelling*. Cambridge.

Gerya, T.V., Connolly, J.A.D. & Yuen, D.A. (2008). Why is terrestrial subduction one-sided? *Geology*, 36, 43-46. doi: 10.1130/G24060A.1

Gerya, T.V., Stern, R.J., Baes, M., Sobolev, S.V. & Whattam, S.A. (2015). Plate tectonics on the Earth triggered by plume-induced subduction initiation. *Nature*, 527, 221-225. https://doi.org/10.1038/nature15752

Gerya, T. V. & Yuen, D. A. (2003). Characteristic-based marker-in-cell method with conservative finite-differences schemes for modeling geological flows with strongly variable transport properties. *Physics of the Earth and Planetary Interiors*, 140, 293–318. https://doi.org/10.1016/j.pepi.2003.09.006

Gerya, T. V. & Yuen, D.A. (2007). Robust characteristics method for modelling multiphase visco-elasto-plastic thermo-mechanical problems. *Physics of the Earth and Planetary Interiors*, 163, 83-105. doi:10.1016/j.pepi.2007.04.015

Glerum, A., Thieulot, C., Fraters, M., Blom, C. & Spakman, W. (2018). Implementing nonlinear viscoplasticity in ASPECT: benchmarking and applications to 3D subduction modeling. *Solid Earth*, 9, 267-294. https://doi.org/10.5194/se-9-267-2018

Godwin, H., Waszek, L. & Deuss, A. (2018). Measuring the seismic velocity in the top 15 km of the Earth's inner core. *Physics of the Earth and Planetary Interiors*, 274, 158-169. https://doi.org/10.1016/j.pepi.2017.11.010

Goes, S., Agrusta, R., van Hunen, J. & Garel, F. (2017). Subduction-transition zone interaction: A review. *Geosphere*, 13, 3. doi: 10.1130/GES01476.1

Gordon, R. G. (1995). Present plate motions and plate boundaries. In *Global Earth Physics, AGU Ref. Shelf,* 1, edited by T. J. Arhens, 66-87, AGU, Washington, D. C.

Green, D.H. & Falloon, T.J. (1998). Pyrolite: A Ringwood concept and its current expression, in Jackson, I.N.S. (Eds.), *The Earth's mantle: Composition, structure, and evolution*. Cambridge, England, Cambridge University Press, 311–380.

Green, D.H., Hibberson, W.O., Kovacs, I. & Rosenthal, A. Water and its influence on the lithosphere-asthenosphere boundary. *Nature*, 472, 504-504. doi: 10.1038/nature09948

Green, D.H. & Liebermann, R.C. (1976). Phase equilibria and elastic properties of a pyrolite model for the oceanic upper mantle. *Tectonophysics*, 32, 61–92. doi: 10.1016/0040-1951(76)90086-X

Griffin, W.L., O'Reilly, S.Y., Afonso, J.C. & Begg, G.C. (2009). The Composition and Evolution of Lithospheric Mantle: a Re-evaluation and its Tectonic Implications. *Journal of petrology*, 50, 1185-1204. doi: 10.1093/petrology/egn033

Gripp, A. E. & Gordon, R. G. (2002). Young tracks of hot-spots and current plate velocities. *Geophysical Journal International*, 150, 321-361. doi: 10.1046/j.1365-246X.2002.01627.x

Grove, T.L., Chatterjee, N., Parman, S.W. & Médard, E. (2006). The influence of H_2O on mantle wedge melting. *Earth and Planetary Science Letters*, 249, 74-89. https://doi.org/10.1016/j.epsl.2006.06.043

Grüneisen, E. (1912). Theorie des festen Zustandes einatomiger Elemente. *Annalen der Physik*, 344, 257–306. doi: 10.1002/andp.19123441202

Gurnis, M. (1988). Large-scale mantle convection and the aggregation and dispersal of supercontinents. *Nature*, 332, 695-699. https://doi.org/10.1038/332695a0

Gutenberg, B. (1959). The asthenosphere low-velocity layer. *Annals of Geophysics*, 12, 439-460. https://doi.org/10.4401/ag-5730

Hager, B.H. & O'Connell, R.J. (1978). Subduction zone dip angles and flow driven by plate motion. *Tectonophysics*, 50, 111-133. https://doi.org/10.1016/0040-1951(78)90130-0

Hall, C. E., Gurnis, M., Sdrolias, M., Lavier, L.L. & Muller, R.D. (2003). Catastrophic initiation of subduction following forced convergence across fractures zones. *Earth and Planetary Science Letters*, 212, 15-30. https://doi.org/10.1016/S0012-821X(03)00242-5

Harabaglia, P. & Doglioni, C. (1998). Topography and gravity across subduction zones, *Geophysical Research Letters*, 25, 703-706. https://doi.org/10.1029/98GL00137

Hayes, G. P., Wald, D. J. & Johnson, R. L. (2012). Slab 1.0: A three-dimensional model of global subduction zone geometries. *Journal of Geophysical Research*, 117, B01302. doi: 10.1029/2011JB008524

Heister, T., Dannberg, J., Gassmöller, R. & Bangerth, W. (2017). High Accuracy Mantle Convection Simulation through Modern Numerical Methods. II: Realistic Models and Problems. *Geophysical Journal International*, 210, 833-851. https://doi.org/10.1093/gji/ggx195

Heroux, M. A., Bartlett, R. A., Howle, V. E., Hoekstra, R. J., Hu, J. J., Kolda, T. G., Lehoucq, R. B., Long, K. R., et al.(2005). An overview of the Trilinos project. *ACM Transactions on Mathematical Software*, 31, 397-423.

Hess, H. H. (1962). *History of Ocean Basins*. Petrological Studies: Buddington Memorial Volume, New York: Geological Society of America, 609.

Heuret, A. & Lallemand, S. (2005). Plate motions, slab dynamics and back-arc deformation. *Physics of the Earth and Planetary Interiors*, 149, 31-51. doi:10.1016/j.pepi.2004.08.022

Holland, T.J.B. & Powell, R. (2011). An improved and extended internally consistent thermodynamic dataset for phases of petrological interest, involving a new equation of state for solids. *Journal*

of METAMORPHIC GEOLOGY, 29, 333-383. https://doi.org/10.1111/j.1525-1314.2010.00923.x

Honda, S., Yuen, D.A., Balachandar, S. & Reuteler, D. (1993). Three-Dimensional Instabilities of Mantle Convection with Multiple Phase Transitions. *Science*, 259, 1308-1311. doi: 10.1126/science.259.5099.1308

Hsu, Y-J, Yu, S-B, Song, T-R A. & Bacolcol, T. (2012). Plate coupling along the Manila subduction zone between Taiwan and northern Luzon. *Journal of Asian Earth Sciences*, 51, 98-108. doi: 10.1016/j.jseaes.2012.01.005

Hu, Y., Bürgmann, R., Banerjee, P., Feng, L., Hill, E.M., Ito, T., Tabei, T. & Wang, K. (2016). Asthenosphere rheology inferred from observation of the 2012 Indian Ocean earthquake. *Nature*, 538, 368-372. http://dx.doi.org/10.1038/nature19787

Jade, S., Shrungeshwara, T.S., Kumar, K., Choudhury, P., Dumka, R.K. & Bhu, H. (2017). India plate angular velocity and contemporary deformation rates from continuous GPS measurements from 1996 to 2015. *Scientific Reports*, 7, doi:10.1038/s41598-017-11697-w

Jarrard, R. D. (1986). Relations Among Subduction Parameters. *Reviews of Geophysics*, 24, 217-284. https://doi.org/10.1029/RG024i002p00217

Jeffreys, H. (1975). *The Earth*. Cambridge University Press, 1-420.

Jin, Z-M, Green, H.W., & Zhou, Y. (1994). Melt topology in partially molten mantle peridotite during ductile deformation. *Nature*, 372, 164–167. http://dx.doi.org/10.1038/372164a0

Jordan, T. H. (1974). Some comments on tidal drag as a mechanism for driving plate motions. *Journal of Geophysical Research*, 79, 2141-2142. https://doi.org/10.1029/JB079i014p02141

Kárason, H. & van der Hilst, R.D. (2000). Constraints on mantle convection from seismic tomography. *Geophysical Monograph*, 121, 277-288. https://doi.org/10.1029/GM121p0277

Karato, S., Jung, H., Katayama, I. & Skemer, P. (2008). Geodynamics Significance of Seismic Anisotrpy of the Upper Mantle: New Insights from Laboratory Studies. *Annual Review of Earth and Planetary Sciences*, 36, 59-95. doi: 10.1146/annurev.earth.36.031207.124120

Kato, T., Beavan, J., Matsushima, T., Kotake, Y., Camacho, J.T. & Nakao, S. (2003). Geodetic evidence of back-arc spreading in the Mariana Trough. *Geophysical Research Letters*, 30, 1625, doi:10.1029/2002GL016757

Kennedy, L. A., Russell, J. K. & Kopylova, M. G. (2002). Mantle shear zones revisited: The connection between the cratons and mantle dynamics. *Geology*, 30, 419-422. doi: 10.1130/0091-7613(2002)030<0419:MSZRTC>2.0.CO;2

King, S.D., Lee, C., Van Keken, P.E., Leng, W., Zhong, S., Tan, E., Tosi, T. & Kameyama, M.C. (2010). A community benchmark for 2-D Cartesian compressible convection in the Earth's mantle. *Geophysical Journal International*, 180, 73–87. https://doi.org/10.1111/j.1365-246X.2009.04413.x

Knopoff, L. & Leeds, A. R. (1972). Lithospheric momenta and the deceleration of the Earth. *Nature*, 237, 93-95. https://doi.org/10.1038/237093a0

Kogan, M., Frolov, D.I., Vasilenko, N.F., Freymueller, J.T., Steblov, G.M., Ekström, G., et al. (2017). Plate coupling and strain in the far western Aleutian arc modeled from GPS data, *Geophysical Research Letters*, 44, 3176–3183, doi:10.1002/2017GL072735

Korenaga, J. (2008). Urey ratio and the structure and evolution of the Earth's mantle. *Reviews of Geophysics*, 46, RG2007.

Korenaga, J. & Karato, S. (2008). A new analysis of experimental data on olivine rheology. *Journal of Geophysical Research*, 113, B02403. doi: 10.1029/2007JB005100

Koulali, A., McClusky, S., Susilo, S., Leonard, Y., Cummins, P., Tregoning, P., et al. (2017). The kinematics of crustal deformation in Java from GPS observations: Implications for fault slip partitioning. *Earth and Planetary Science Letters*, 458, 69-79. http://dx.doi.org/10.1016/j.epsl.2016.10.039

Koulali, A., Susilo, S., McClusky, S., Meilano, I., Cummins, P., Tregoning, P., et al. (2016). Crustal strain partitioning and the associated earthquake hazard in the eastern Sunda-Banda Arc. *Geophysical Research Letters*, 43, 1943–1949. doi:10.1002/2016GL067941

Koulali, A., Tregoning, P., McClusky, S., Stanaway, R., Wallace, L. & Lister, G. (2015). New Insights into the present-day kinematics of the central and western Papua New Guinea from GPS. *Geophysical Journal International*, 202, 993-1004. doi: 10.1093/gji/ggv200

Kronbichler, M., Heister, T. & Bangerth, W. (2012). High accuracy mantle convection simulation through modern numerical methods. *Geophysical Journal International*, 191, 12-29. doi: 10.1111/j.1365-246X.2012.05609.x

Krogstad, R.D., Schmidt, D.A., Weldon, R.J. & Burgette, R.J. (2016). Constraints on accumulated strain near the ETS zone along Cascadia. *Earth and Planetary Science Letters*, 439, 109-116. http://dx.doi.org/10.1016/j.epsl.2016.01.033

Kuo, Y-T, Ku, C-S, Chen, Y-G, Wang, Y., Lin, Y-N N., Chuang, R.Y., et al. (2016). Characteristics on fault coupling along the Solomon megathrust based on GPS observations from 2011 to 2014. *Geophysical Research Letters*, 43. doi:10.1002/2016GL070188

Lallemand, S. & Funiciello, F. (2009). Subduction Zone Geodynamics. *Subduction Zone Geodynamics*, Eds. Lallemand, S. and Funiciello, F. Berlin: Springer, 2009.

Lallemand, S., Heuret, A. & Boutelier, D. (2005). On the relationships between slab dip, back-arc stress, upper plate absolute motion, and crustal nature in subduction zones. *Geochemistry Geophysics Geosystems*, 6, Q09006. doi:10.1029/2005GC000917

Lambert, I.B. & Wyllie, P.J. (1970). Low-Velocity Zone of the Earth's Mantle: Incipient Melting Caused by Water. *Science*, 169, 764-766. doi: 10.1126/science.169.3947.764

Lebedev, S. & van der Hilst, R.D. (2008). Global upper-mantle tomography with the automated multimode inversion of surface and S-wave forms. *Geophysical Journal International*, 173, 505-518. doi: 10.1111/j.1365-246X.2008.03721.x

Le Pichon, X. (1968). Sea-floor spreading and continental drift. *Journal of Geophysical Research*, 73, 3661-3697.

Li, M. & Zhong, S. (2017). The source location of mantle plumes from 3D spherical models. *Earth and Planetary Science Letters*, 478, 47-57. https://doi.org/10.1016/j.epsl.2017.08.033

Ligi, M., Bonatti, E., Cipriani, A. & Ottolini, L. (2005). Water-rich basalts at mid-ocean-ridge cold spots. *Nature*, 434, 66-69. https://doi.org/10.1038/nature03264

Linzer, H-G. (1996). Kinematics of retreating subduction along the Carpathian arc, Romania. *Geology*, 24, 167-170. https://doi.org/10.1130/00917613(1996)024<0167:KORSAT>2.3.CO;2

Liu, M., Yang, Y., Stein, S., Zhu, Y. & Engeln, J. (2000). Crustal shortening in the Andes: Why do GPS rates differ from geological rates? *Geophysical Research Letters*, 27, 3005-3008. https://doi.org/10.1029/2000GL008532

McCrory, P.A., Blair, J.L., Waldhauser, F. & Oppenheimer, D.H. (2012). Juan de Fuca slab geometry and its relation to Wadati-Benioff zone seismicity. *Journal of Geophysical Research*, 117, B09306. https://doi.org/10.1029/2012JB009407

Malinverno, A. (2012). Evolution of the Tyrrhenian Sea-Calabrian Arc System: The past and the present. *Rendiconti Online della Società Geologica Italiana*, 21, 11-15.

Malinverno, A. & Ryan, W.B.F. (1986). Extension in the Tyrrhenian Sea and Shortening in the Apennines as Results of Arc Migration Driven by Sinking of the Lithosphere. *Tectonics*, 5, 225-245.

Margheriti, L., Nostro, C., Cocco, M. & Amato, A. (1996). Seismic anisotropy beneath the Northern Appennines (Italy) and its tectonic implications. *Geophysical Research Letters*, 23, 2721-2724. doi: 10.1029/96GL02519

Marotta, A. M. & Mongelli, F. (1998). Flexure of subducted slabs. *Geophysical Journal International*, 132, 701-711. https://doi.org/10.1046/j.1365-246X.1998.00489.x

Márquez-Azúa, B. & DeMets, C. (2003). Crustal velocity field of Mexico from continuous GPS measurements, 1993 to June 2001: Implications for the neotectonics of Mexico. *Journal of Geophysical Research*, 108, 2450. doi:10.1029/2002JB002241

Mason, P.R.D., Seghedi, I., Szákacs, A. & Downes, H. (1998). Magmatic constraints on geodynamic models of subduction in the East Carpathians, Romania. *Tectonophysics*, 297, 157-176. https://doi.org/10.1016/S0040-1951(98)00167-X

Mazzotti, S., Henry, P. & Le Pichon, X. (2001). Transient and permanent deformation of central Japan esimated by GPS – 2. Strain partitioning and arc-arc collision. *Earth and Planetary Science Letters*, 184, 455-469. doi:10.1016/S0012-821X(00)00336-8

McKenzie, D. & Parker, R. L. (1967). The North Pacific: An Example of Tectonics on a Sphere. *Nature*, 216, 1276. doi:10.1038/2161276a0

Métois, M., D'Agostino, N., Avallone, A., Chamot-Rooke, N., Rabaute, A., Duni, L., et al. (2015). Insights on continental collisional processes from GPS data: Dynamics of the peri-Adriatic belts. *Journal of Geophysical Research Solid Earth*, 120, 8701–8719. doi:10.1002/2015JB012023

Michel, G.W., Yu, Y.Q., Zhu, S.Y., Reigber, C., Becker, M., Reinhart, E., et al. (2001). Crustal motion and block behaviour in SE-Asia from GPS measurements. *Earth and Planetary Science Letters*, 187, 239-244. https://doi.org/10.1016/S0012-821X(01)00298-9

Mitra, S. (2004). Development in Geochemistry 9. High-Pressure Geochemistry and Mineral Physics – Basics for Planetology and Geo-material Science. *Elsevier*.

Monnereau, M. & Quéré, S. (2001). Spherical shell models of mantle convection with tectonic plates. *Earth and Planetary Science Letters*, 184, 575-587.

Moore, G.W. (1973). Westward Tidal Lag as the Driving Force of Plate Tectonics. *Geology*, 1, 99-100.

Moore, W.B. (2008). Heat transport in a convecting layer heated from within and below. *Journal of Geophysical Research*, 113, B11407. doi:10.1029/2006JB004778.

Mora-Páez, H., Peláez-Gaviria,J-R., Diederix, H., Bohórquez-Orozco, O., Cardona-Piedrahita, L., Corchuelo-Cuervo, Y. et al. (2018). Space Geodesy Infrastructure in Colombia for Geodynamics Research. *Seismological Research Letters*, 89, 446-451. doi: 10.1785/0220170185

Morgan, W. J. (1968). Rises, Trenches, Great Faults, and Crustal Blocks. *Tectonophysics*, 187, 6–22. doi: 10.1016/0040-1951(91)90408-K.

Morgan, W. J. (1971). Convection Plumes in the Lower Mantle. *Nature*, **230**, 42-43.

Moulik, P. & Ekström, G. (2014). Earth's mantle using normal modes, body waves, surface waves and long-period waveform. *Geophysical Journal International*, 199, 1713-1738. https://doi.org/10.1093/gji/ggu356

Murnaghan, F.D. (1944). The Compressibility of Media under Extreme Pressures. *Proceedings of the National Academy of Sciences of the United States of America*, 30, 244–247. doi:10.1073/pnas.30.9.244. JSTOR 87468. PMC 1078704

Naif, S., Key, K., Constable, S. & Evans, R.L. Melt-rich channel observed at the lithosphere-asthenosphere boundary. *Nature*, 495, 356-359. https://doi.org/10.1038/nature11939

Nance, R. D. & Murphy, J.B. (2013). Origins of the supercontinent cycle. *Geoscience Frontier*, 4, 439-448. http://dx.doi.org/10.1016/j.gsf.2012.12.007

Nekvasil, H., Dondolini, A., Horn, J., Filiberto, J., Long, H. & Lindsley, D.H. (2004). The Origin and Evolution of Silica-saturated Alkalic Suites: an Experimental Study. *Journal of petrology*, 45, 693-721. 10.1093/petrology/egg103

Nelson, T.H. & Temple, P.G. (1972). Mainstream Mantle Convection: A Geologic Analysis of Plate Motion. *AAPG Bulletin*, 56, 226-246.

Norton, I. O. (2000). Global hot-spot reference frames and plate motion. In Richards, M.A., R. G. Gordon, and R. D. Van der Hilst, Eds., *The history and dynamics of global plate motions*, American Geophysical Union Geophysical Monograph, 121, 339–357. doi: 10.1029/GM121p0339

Obayashi, M., Fukao, Y. & Yoshimitsu, J. (2017). Unusually deep Bonin eartquake of 30 May 2015: A precursory signal to slab penetration? *Earth and Planetary Science Letters*, 459, 221-226. https://doi.org/10.1016/j.epsl.2016.11.019

O'Connell, R. J., Gable, C.W. & and Hager, B. H. (1991). Toroidal-poloidal partitioning of lithospheric plate motions. In *Glacial Isostasy, Sea Level and Mantle Rheology,* Eds. Sabadini R. and Lambeck, K., 535-551, Kluwer, Amsterdam.

Omori, S., Komabayashi, T. & Maruyama, S. (2004). Dehydration and earthquakes in the subducting slab: empirical link in intermediate and deep seismic zones. *Physics of the Earth and Planetary Interiors*, 146, 297-311. https://doi.org/10.1016/j.pepi.2003.08.014

O'Neill, C., Müller, D. & Steinberger, B. (2005). On the uncertainties in hot spot reconstructions and the significance of moving hot spot reference frames. *Geochemistry, Geophysics, Geosystems*, 6, Q04003. https://doi.org/10.1029/2004GC000784

Outerbridge, K.C., Dixon, T.H., Schwartz, S.Y., Walter, J.I., Protti, M., Gonzalez, V., et al. (2010). A tremor and slip event on the Cocos-Caribbean subduction zone as measured by a global

positioning system (GPS) and seismic network on the Nicoya Peninsula, Costa Rica. *Journal of Geophysical Research*, 115, B10408. doi:10.1029/2009JB006845

Panza, G.F. (1980). Evolution of the Earth's lithosphere. NATO Advanced Study Institute Newcastle, 1979. In: Davies, P.A., Runcorn, S.K., Eds., *Mechanisms of Continental Drift and Plate Tectonics*. Academic Press, pp. 75–87.

Parson, L. & Wright, I.C. (1996). The Lau-Havre-Taupo back-arc basin: A southward-propagating, multi-stage evolution from rifting to spreading. *Tectonophysics*, 263, 1-22. doi: 10.1016/S0040-1951(96)00029-7

Petricca, P. & Carminati, E. (2016). Present-day stress field in subduction zones: Insights from 3D viscoelastic models and data. *Tectonophysics*, **667**, 48-62. http://dx.doi.org/10.1016/j.tecto.2015.11.010

Phillips, B.R. & Bunge, H.-P. (2005). Heterogeneity and time dependence in 3D spherical mantle convection models with continental drift. *Earth and Planetary Science Letters*, 233, 121-135. https://doi.org/10.1016/j.epsl.2005.01.041

Pollitz, F.F., Bürgmann, R. & Romanowicz, B. (1998). Viscosity of oceanic asthenosphere inferred from remote triggering of earthquakes. *Science*, 280, 1245–1249. doi: 10.1126/science.280.5367.1245

Porrit, R.W. & Yoshioka, S. (2016). Slab pileup in the mantle transition zone and the 30 May 2015 Chichi-jima earthquake. *Geophysical Research Letters*, 43, 4905–4912. doi: 10.1002/2016GL068168

Presnall, D.C. & Gudfinnsson, G.H. (2011). Oceanic volcanism from the low-velocity-zone - without Mantle Plumes. *Journal of Petrology*, 52, 1533-1546. https://doi.org/10.1093/petrology/egq093

Raye, U., Anthony, E.Y., Stern, R.J., Kimura, J., Ren, M., Qing, C. & Tani, K. (2011). Composition of the mantle lithosphere beneath south-central Laurentia: Evidence from peridotite xenoliths, Knippa, Texas. *Geosphere*, 7, 710-723. doi: 10.1130/GES00618.1

Ranalli, G. Rheology of the Earth, *2nd ed. Chapman & Hall*, London (1995).

Ranalli, G. (2000). Westward drift of the lithosphere: Not a result of rotational drag. *Geophysical Journal International*, 141, 535-537. doi: 10.1046/j.1365----246x.2000.00091.x

Ribeiro, J.M., Stern, R.J., Martinez, F., Woodhead, J., Chen, M., & Ohara, Y. Asthenospheric outflow from the shrinking Philippine Sea Plate: Evidence from Hf–Nd isotopes of southern Mariana lavas. *Earth and Planetary Science Letters*, 478, 258-271. http://dx.doi.org/10.1016/j.epsl.2017.08.022

Ricard, Y., Doglioni, C. & Sabadini, R. (1991). Differential Rotation Between Lithosphere and Mantle: A Consequence of Lateral Mantle Viscosity Variations. *Journal of Geophysical Research*, 96, 8407-8415. https://doi.org/10.1029/91JB00204

Riguzzi, F., Panza, G., Varga, P. & Doglioni, C. (2010). Can Earth's rotation and tidal despinning drive plate tectonics? *Tectonophysics*, 484, 60-73. https://doi.org/10.1016/j.tecto.2009.06.012

Ritsema, J. (2005). Global seismic structure maps. In Foulger, G.R., Natland, J.H., Presnall, D.C., and Anderson, D.L., Eds., *Plates, plumes, and paradigms*: Geological Society of America Special Paper, 388, 11-18. doi: 10.1130/2005.2388(02)

Rittmann, A. (1942), Zur thermodynamic der orogenese. *Geologiche Rundschau,* 33, 485-498.

Rodríguez-González, J., Negredo, A. N. & Carminati, E. (2014). Slab-mantle flow interaction: influence on subduction dynamics and duration. *Terra Nova*, **26**, 265-272. doi: 10.1111/ter.12095

Rolf, T., Coltice, N. & Tackley, P.J. (2012). Linking continental drift, plate tectonics and the thermal state of the Earth's mantle. *Earth and Planetary Science Letters*, 351-352, 134-146. https://doi.org/10.1016/j.epsl.2012.07.011

Rolf, T., Capitanio, F.A. & Tackley, P.J. (2017). Constraints on mantle viscosity structure from continental drift histories in spherical mantle convection models. *Tectonophysics*, in press. https://doi.org/10.1016/j.tecto.2017.04.031

Royden, L.H. (1993). Evolution of retreating subduction boundaries formed during continental collision. *Tectonics*, 12, 629-638. https://doi.org/10.1029/92TC02641

Russo, R.M. & Silver P.G. (1994). Trench-Parallel Flow Beneath the Nazca Plate from Seismic Anisotropy. *Science*, 263, 1105-1111. doi: 10.1126/science.263.5150.1105

Russo, R.M. & Silver, P.G. (1996). Cordillera formation, mantle dynamics, and the Wilson cycle. *Geology*, 24, 511-514. https://doi.org/10.1130/00917613(1996)024<0511:CFMDAT>2.3.CO;2

Sagiya, T. (2004). A decade of GEONET: 1994–2003 —The continuous GPS observation in Japan and its impact on earthquake studies—. *Earth Planets Space*, 56, 29-41.

Schellart, W.P. (2007). The potential influence of subduction zone polarity on overriding plate deformation, trench migration and slab dip angle. *Tectonophysics*, 445, 363-372. https://doi.org/10.1016/j.tecto.2007.09.009

Schellart, W.P. & Lister, G.S. (2004). Tectonic model for the formation of arc-shaped convergent zones and backarc basins. *Geological Society of America Special Paper*, 383, 237-258.

Schellart, W.P. & Rawlinson, N. (2013). Global correlations between maximum magnitudes of subduction zone interface thrust earthquakes and physical parameters of subduction zones. *Physics of the Earth and Planetary Interiors*, 225, 41-67. https://doi.org/10.1016/j.pepi.2013.10.001

Schellart, W.P., Stegman, D.R., Farrington, R.J. and Moresi, L. (2011). Influence of lateral slab edge distance on plate velocity, trench velocity, and subduction partitioning. *Journal of Geophysical Research*, 116, B10408.

Schubert, G., Turcotte, D.L. & Olson, P. (2001). *Mantle Convection in the Earth and Planets*. Cambridge University Press.

Scoppola, B., Boccaletti, D., Bevis, M., Carminati, E. & Doglioni, C. (2006).The westward drift of the lithosphere: A rotational drag? *GSA Bullettin*, 118, 199-209. doi: 10.1130/B25734.1

Serpelloni, E., Vannucci, G., Anderlini, L. & Bennett, R.A. (2016). Kinematics, seismotectonics and seismic potential of the eastern sector of the European Alps from GPS and seismic deformation data. *Tectonophysics*, 688, 157-181. http://dx.doi.org/10.1016/j.tecto.2016.09.026

Seton, M., Müller, R.D., Zahirovic, S., Gaina, C., Torsvik, T., Shephard, G., Talsma, A., Gurnis, M., et al. (2012). Global continental and ocean basin reconstructions since 200 Ma. *Earth-Science Reviews*, 113, 212-270. doi:10.1016/j.earscirev.2012.03.002

Silver, P. G. & Holt, W. E. (2002). The Mantle Flow Field Beneath Western North America, *Science*, 295, 1054-1057. doi: 10.1126/science.1066878

Smalley Jr., R., Dalziel, W.D., Bevis, M.G., Kendrick, E., Stamps, D.S., King, E.C., et al. (2007). Scotia arc kinematics from GPS geodesy. *Geophysical Research Letters*, 34, L21308. doi:10.1029/2007GL031699

Solomon, S.C. & Sleep, N.H. (1974). Some simple physical models for absolute plate motions. *Journal of Geophysical Research*, 79, 2557-2567. https://doi.org/10.1029/JB079i017p02557

Solomon, S.C., Sleep, N.H. & Richardson, R.M. (1975). On the Forces Driving Plate Tectonics: Inferences from Absolute Plate Velocities and Intraplate Stress. *Geophysical Journal International,* 42, 769-801. https://doi.org/10.1111/j.1365-246X.1975.tb05891.x

Spence, W. (1987). Slab pull and the seismotectonics of subducting lithosphere. *Reviews of Geophysics*, 25, 55-69. https://doi.org/10.1029/RG025i001p00055

Stegman, D.R., Farrington, R., Capitanio, F.A. & Schellart, W.P. (2010). A regime diagram for subduction styles from 3-D numerical models of free subduction. *Tectonophysics*, 483, 29-45. doi:10.1016/j.tecto.2009.08.041

Su, W., Dziewonski, A.M. & Jeanloz, R. (1996). Planet Within a Planet: Rotation of the Inner Core of the Earth. *Science*, 274, 1883-1887. doi: 10.1126/science.274.5294.1883

Sun, W. (1992). Seismic energy distribution in latitude and a possible tidal stress explanation. *Physics of the Earth and Planetary Interiors*, 71, 205-216. https://doi.org/10.1016/0031-9201(92)90077-9

Stegman, D. R., Farrington, R., Capitanio F. A. & Schellart, W. P. (2010). A regime diagram for subduction styles from 3-D numerical models of free subduction. *Tectonophysics*, 483, 29-45. https://doi.org/10.1016/j.tecto.2009.08.041

Steinberger, B. (2000). Plumes in a convecting mantle: Models and observations for individual hotspots. *Journal of Geophysical Research*, 105, 127-152. https://doi.org/10.1029/1999JB900398

Steinberger, B. & Torsvik, T.H. (2008). Absolute plate motions and true polar wander in the absence of hotspot tracks. *Nature*, 452, 620-623. https://doi.org/10.1038/nature06824

Steinberger, B., Torsvik, T.H. & Becker, T.W. (2012). Subduction to the lower mantle – a comparison between geodynamic and tomographic models. *Solid Earth*, 3, 415-432. doi: 10.5194/se-3-415-2012

Stevenson, D. J. (1994). Weakening under stress. *Nature*, 372, 129-130. http://dx.doi.org/10.1038/372129a0

Stevenson, D.J. & Turner, J.S. (1977). Angle of subduction. *Nature*, 270, 334-336. http://dx.doi.org/10.1038/270334a0

Stixrude, L. & Lithgow-Bertelloni, C. (2005).Thermodynamics of mantle minerals–I. Physical properties. Geophys. J. Int., 162(2):610–632, 2005. doi: 10.1111/j.1365-246X.2005.02642.x

Tackley, P.J., Stevenson, D.J., Glatzmaier, G.A. & Schubert, G. (1993). Effects of an endothermic phase transition at 670 km depth in a spherical model of convection in the Earth's mantle. *Nature*, 361, 699-704. https://doi.org/10.1038/361699a0

Tackley, P.J. (2000). Self-consistent generation of tectonic plates in time-dependent, three-dimensional mantle convection simulations. *Geochemistry Geophysics Geosystems*, 1. https://doi.org/10.1029/2000GC000036

Tao, W.C. & O'Connell, R.J. (1992). Ablative Subduction: A Two-Sided Alternative to the Conventional Subduction Model. *Journal of Geophysical Research*, 97, 8877-8904. https://doi.org/10.1029/91JB02422

Thybo, H. (2006). The heterogeneous upper mantle low velocity zone. *Tectonophysics*, 416, 53-79. doi: 10.1016/j.tecto.2005.11.021

Torsvik, T.H., Steinberger, B., Gurnis, M. & Gaina, C. Plate tectonics and net lithosphere rotation over the past 150 My. *Earth and Planetary Science Letters*, 291, 106-112. https://doi.org/10.1016/j.epsl.2009.12.055

Tovish, A., Schubert, G., & Luyendyk, B.P. (1979). Mantle Flow Pressure and the Angle of Subduction: Non-Newtonian Corner Flows. *Journal of Geophysical Research*, 83, 5892-5898. doi: 10.1029/JB083iB12p05892

Trampert, J. Deschamps, F., Resovsky, J. & Yuen, D. (2004). Probabilistic tomography maps chemical heterogeneities throughout the lower mantle. *Science*, 306, 853-856. doi: 10.1126/science.1101996

Turcotte, D.L. & Schubert, J. (1982). *Geodynamics*. John Wiley and Sons, New York.

Turcotte, D. L. & Schubert, G. (2014). Geodynamics. *3rd ed. Cambridge University Press.*

van Keken, P.E., Hacker, B.R., Syracuse, E.M. & Abers, G.A. (2011). Subduction factory: 4. Depth-dependent flux of H_2O from subducting slabs worldwide. *Journal of Geophysical Research*, 116, B01401. https://doi.org/10.1029/2010JB007922

Uyeda, S. (1981), Subduction zones and back-arc basins—a review, *Geologiche Rundschau*, 70, 552–569.

Uyeda, S. & Kanamori, H. (1979). Back-arc opening and the mode of subduction. *Journal of Geophysical Research*, 84, 1049–1061. https://doi.org/10.1029/JB084iB03p01049

van Keken, P. & Zhong, S. (1999). Mixing in a 3D spherical model of present-day mantle convection. *Earth and Planetary Science Letters*, 171, 533-547.

Varga, P., Krumm, F., Riguzzi, F., Doglioni, C., Süle, B., Wang, K. & Panza, G.F. (2012). Global pattern of earthquakes and seismic energy distributions: Insights for the mechanisms of plate tectonics. *Tectonophysics*, 530-531, 80-86. doi:10.1016/j.tecto.2011.10.014

Vine, F.J. & Matthews, D.H. (1963). Magnetic Anomalies Over Oceanic Ridges. *Nature*, 199, 947-949.

Wallace, L.M., Stevens, C., Silver, E., McCaffrey, R., Loratung, W., Hasiata, S., et al. (2004). GPS and seismological constraints on active tectonics and arc-continent collision in Papua New Guinea: Implications for mechanics of microplate rotations in a plate boundary zone. *Journal of Geophysical Research*, 109, B05404. doi:10.1029/2003JB002481

Walters, R.J., England, P.C. & Houseman, G.A. (2017). Constraints from GPS measurements on the dynamics of the zone of convergence between Arabia and Eurasia, *Journal of Geophysical Research Solid Earth*, 122, 1470–1495. doi:10.1002/2016JB013370

Weber, J.C., Dixon, T.H., DeMets, C., Ambeh, W.B., Jansma, P., Mattioli, G., et al. (2001). GPS estimate of relative motion between the Caribbean and South American plates, and geologic implications for Trinidad and Venezuela. *Geology*, 29, 75-78. https://doi.org/10.1130/0091-7613(2001)029<0075:GEORMB>2.0.CO;2

Wegener, A. (1915). Die Entstehung der Kontinente und der Ozeane, 94 pp., Sammlung Vieweg.

Wegener, A. (1924). The origin of continents and oceans, Dutton, New York.

Wessel, P. & Kroenke, L.W. (2008). Pacific absolute plate motion since 145 Ma: an assessment of the fixed hot spot hypothesis. *Journal of Geophysical Research*, 113. https://doi.org/10.1029/2007JB005499

Wessel, P. & Smith, W. H. F. (1998). New, improved version of the Generic Mapping Tools released. *EOS, Transaction American Geophysical Union*, 79, 579. https://doi.org/10.1029/98EO00426

Wilson, J.T. (1963). A possible origin of the Hawaiian Islands. *Canadian Journal of Physics*, 41, 863-870. doi: 10.1139/p63-094

Wilson, J.T. (1965) A New Class of Faults and their Bearing on Continental Drift. *Nature*, 207, 343-347. doi: 10.1038/207343a0

Wilson, J.T. (1973). Mantle plumes and plate motions. *Tectonophysics*, 19, 149-164. https://doi.org/10.1016/0040-1951(73)90037-1

Wolfe, C. J. & Solomon, S. (1998). Shear-wave splitting and implications for mantle flow beneath the MELT region of the East Pacific Rise. *Science*, 280, 1230-1232. doi: 10.1126/science.280.5367.1230

Yong, C.Z., Denys, P.H. & Pearson, C.F. (2017). Present-day kinematics of the Sundaland plate. *Journal of Applied Geodesy*, 11, 169-177. https://doi.org/10.1515/jag-2016-0024

Yoshida, M. (2013). Three-dimensional visualization of numerically simulated, present-day global mantle flow. *Journal of Vision*, 16, 163-171. https://doi.org/10.1007/s12650-013-0160-7

Yoshida, M. (2014). A new conceptual model for whole mantle convection and the origin of hotspot plumes. *Journal of Geodynamics*, 78, 32-41. https://doi.org/10.1016/j.jog.2014.04.004

Yoshida, M. & Santosh, M. (2014). Mantle convection modeling of the supercontinent cycle: Introversion, extroversion, or a combination? *Geoscience Frontiers*, 5, 77-81. https://doi.org/10.1016/j.gsf.2013.06.002

Zhao, D., Fujisawa, M. & Toyokuni, G. Tomography of the subducting Pacific Slab and the 2015 Bonin deepest earthquake (Mw 7.9). *Scientific Reports*, 7, 44487. https://doi.org/10.1038/srep44487